



HAL
open science

Magnetic fabrics and strain associated with thrusting in the Jaca foreland basin, Southern Pyrenees, Spain

Francho Gracia Puzo

► **To cite this version:**

Francho Gracia Puzo. Magnetic fabrics and strain associated with thrusting in the Jaca foreland basin, Southern Pyrenees, Spain. Geophysics [physics.geo-ph]. Université de Pau et des Pays de l'Adour; Universidad de Zaragoza (Espagne), 2024. English. NNT : 2024PAUU3014 . tel-04816341

HAL Id: tel-04816341

<https://theses.hal.science/tel-04816341v1>

Submitted on 3 Dec 2024

HAL is a multi-disciplinary open access archive for the deposit and dissemination of scientific research documents, whether they are published or not. The documents may come from teaching and research institutions in France or abroad, or from public or private research centers.

L'archive ouverte pluridisciplinaire **HAL**, est destinée au dépôt et à la diffusion de documents scientifiques de niveau recherche, publiés ou non, émanant des établissements d'enseignement et de recherche français ou étrangers, des laboratoires publics ou privés.



Universidad
Zaragoza



Tesis Doctoral / Thèse de doctorat

Magnetic fabrics and strain associated with
thrusting in the Jaca foreland basin, Southern
Pyrenees, Spain

*Fabriques magnétiques et déformation associé à la propagation de
failles dans le bassin d'avant-pays de Jaca, Pyrénées méridionales,
Espagne*

*Fábricas magnéticas y deformación asociada a cabalgamientos en la
cuenca de antepaís de Jaca, Pirineos, España.*

Étudiant :

Francho Gracia Puzo

Thèse dirige par :

Charles Aubourg

Antonio Casas Sainz

Président du Jury :

Jean-Paul Callot

ED Sciences Exactes et leurs Applications (ED SEA 211)

2024

TABLE OF CONTENT

ABSTRACT:	7
RÉSUMÉ:	7
RESUMEN:	8
1. INTRODUCTION.....	11
2. SHALE DEFORMATION.....	15
2.1. Shales cleavage	15
2.1.1. Shales	15
2.1.2 Cleavage	16
2.1.3 Temperature domain	20
2.1.4 Regional versus local cleavage.....	20
2.2 Shale fabric	21
2.2.1 Fabric definition	21
2.2.2. Shale fabric techniques.....	25
2.3 Magnetic fabric study	28
2.3.1 Magnetic behaviour of minerals	29
2.3.2 Mineral components of shales and their magnetic behaviour:.....	33
2.3.3 Magnetic minerals in basin evolution	34
2.3.4 The measurement of magnetic anisotropy.	37
2.3.5 Anisotropy of magnetic susceptibility in shales.	38
2.3.6 Magnetic fabric evolution in shaly rocks	44
2.3.7 AMS as a strain gouge, conditions of use.....	48
2.4 The Lehigh Gap, a classical shale-to-slates transition.....	58
2.4.1 Geological setting.....	58
2.4.2 How cleavage is hosted in a shale-to-slate transition?	59
2.4.3 What are the mechanisms responsible for cleavage?.....	68
2.4.4. Comparison with the Sigüés site and concluding remarks con Lehigh Gap.....	70
2.5 The Southern Pyrenees, a natural laboratory of magnetic fabric in shales and slates. ..	71
2.5.1 Foreland basin	71
2.5.2 External Sierras.....	73
2.5.3 Southern Jaca Basin and piggyback basins.....	76
2.5.4. Turbiditic Jaca Basin	82
2.5.5 Internal Sierras.....	86
3. STRUCTURAL STUDY OF THE SIGÜÉS AREA	89
3.1. The Pyrenean Orogen and the Jaca Basin.....	89

3.1.1	General architecture of the Pyrenees.....	89
3.1.2	The Jaca Basin	93
3.1.3.	Geological background in the Sigüés area.....	97
3.2.	Field description of the Jaca Basin sites.	102
3.2.1.	The Sigüés and Leyre Sites.	105
3.3.	Sampling of shales	119
3.3.1	South-western sector: Escó and Llarto cross-section	119
	South central sector: Escalar	122
	South central Sector: San Juan – La Paul.....	124
	Sigüés section.....	126
	Eastern sector: the Orba Range.	128
3.3.2	Preliminary study on secondary thrust zones	130
3.4.	Structural frame and serial Cross -Sections.....	135
3.4.1.	Structural frame and sketch.....	135
3.4.2.	Serial cross-sections	140
3.4.3	Structural synthesis.....	145
3.5.	Conclusions.....	148
4.	SHALE FABRIC	149
4.1	Background	149
4.1.1	Shale mineralogy	149
4.1.2	Shale magnetic fabric.....	151
4.1.3	X Ray Microtomography observations.	153
4.2.	The “sampling by fragments” approach	156
4.2.1	Methodology.....	156
4.2.2.	Rock magnetism	160
4.3.	Sigüés results	162
4.3.1	Sampling.....	162
4.3.2	Results.....	166
4.3.3.	Data treatment and analysis of scalar parameters.....	173
4.3.4	Synthesis of AMS Results near Sigüés footwall.....	178
4.4.	Strain quantification at the Sigüés site	183
4.5	Microtomography results	190
4.5.1	XCT Technique	190
4.5.2	Results.....	192
4.6.	The Jaca thrust	197
4.6.2	Biniés site.....	198

4.6.2 Javierregay Site	204
4.6.3 Jaca-Gas Site	210
4.7 Discussion	211
4.8 Conclusion	214
5. PALEOTHERMOMETRY AND FLUIDS.....	217
5.1 Background	217
5.2 Additional RSCM and Rock-Eval data.	220
5.2.1 Mineralogy	221
5.2.2. RSCM	223
5.3 Calcite-filled faults	225
5.4 Fluid data on calcite faults	233
5.5. Dating calcite faults.	234
5.6 Isotopic data.....	238
5.6.1 Stable isotopes:	238
5.6.2 Chemical mapping:.....	239
5.7 Synthesis.....	241
5.7.1 Burial temperature	241
5.7.2 Isotopes on calcite faults	244
5.8 Conclusions	245
6. DISCUSSION	247
6.1 Introduction	247
6.2 Early deformation	249
6.3 Fault propagation in marls	252
6.4 Characteristics of the calculated deformation.....	254
6.4.1 Extent	254
6.4.2 Fabric development	260
6.5 The origin of deformation: discussion of mechanisms	265
6.6 Folding stage.....	272
6.6.1 Do the conditions under which the strain occurs favour the development of cleavage?.....	277
6.7 General conclusions:.....	279
6.8 General perspectives.....	280
CONCLUSIONES	283
CONCLUSIONS.....	285
7. BIBLIOGRAPHY.....	287

ABSTRACT:

The Leyre thrust is a main structural feature of the Jaca foreland basin incorporated into the system of basement and cover thrust sheets of the Pyrenean orogen. The Leyre thrust presents a local singularity: a thickness of several hundred metres of marls cropping out in its footwall show a cleavage gradient ($>1100\text{m}$ of horizontal distance). Exceptional outcrops allow us to analyse in detail the transition from pencil cleavage to slaty cleavage, over a thickness of several hundred metres. Our analytical approach is based mainly on the magnetic fabric of marls, where we are proposing a statistical study of hundreds of non-oriented fragments weighing just a few grams. Following the sampling and results, secondary faults within this deformation zone are described. We have complemented this approach with a field survey, a mapping study, and by incorporating new analytical data (Raman, microtomography, isotopes, U/Pb dating).

In the Sigüés area, the Eocene marls have undergone advanced diagenesis (burial temperature $\sim 180^\circ\text{C}$), so that magnetic susceptibility is mainly controlled by paramagnetic illite. These illites, which make up a large part of the matrix, were reoriented during the deformation process. The evolution of matrix damage can be plotted using several parameters, including the shape parameter of the magnetic ellipsoid. The development of cleavage at an important angle with bedding enables us to apply a simple model of particle rotation, and calculate a percentage of deformation. We thus obtain a range of deformation from a few percent related to the imprint of layer parallel shortening (LPS), to $\sim 20\%$ in the pencil-type cleavage domain, to almost 80% in the slaty cleavage domain. We thus propose a novel mapping of fault wall in a deformed foreland basin, revealing the existence of unmapped secondary faults. To explain the intense deformation observed in the hanging-wall and footwall of the thrust, we propose a Trishear-type fault propagation model.

In addition, several other sites in the Jaca basin with the same structural configuration are studied in this work: a thrust and its associated deformation in the footwall, provided that marly lithologies crop out. This thesis offers a geometrical and kinematic description of the deformation zones, and warns about the misleading homogeneity of the large marl/shale formations, which can undergo cleavage in large unidentified regions.

RÉSUMÉ:

Le chevauchement de Leyre est un élément structural principal du bassin de l'avant-pays de Jaca, incorporé dans le système de nappes de chevauchement du socle et de la couverture de l'orogène pyrénéen. Le chevauchement de Leyre présente une singularité locale: une épaisseur de plusieurs centaines de mètres de marnes affleurant dans son mur inférieur présente un gradient de clivage ($>1100\text{ m}$ de distance horizontale). Des affleurements exceptionnels permettent d'analyser finement la transition entre la schistosité de type *pencil*, à une schistosité pénétrative de type *slaty*, sur une épaisseur de plusieurs centaines de mètres. Notre approche analytique se base principalement sur la fabrique magnétique des marnes où nous proposons une étude statistique de centaines de fragments non orientés de quelques grammes. Nous avons complété cette approche par une étude de terrain, une étude cartographique, et en incorporant des nouvelles données analytiques (Raman, microtomographie, isotopes, datation U/Pb).

Dans la région de Sigues, les marnes éocènes ont subi une diagénèse avancée (température d'enfouissement $\sim 180^{\circ}\text{C}$) de sorte que la susceptibilité magnétique est principalement contrôlée par l'illite paramagnétique. Ces illites, qui composent une grande partie de la matrice, vont se réorienter sous l'action de la contrainte. On peut tracer ainsi l'évolution de l'endommagement matriciel au moyen de plusieurs paramètres dont le paramètre de forme de la fabrique magnétique. Le développement de la schistosité à un angle important de la stratification permet d'appliquer un modèle simple de rotation des particules, et de calculer un pourcentage de déformation. Nous obtenons ainsi une gamme de déformation de quelques pourcent liée à l'empreinte du raccourcissement horizontale du bassin (LPS), à $\sim 20\%$ dans le domaine de la schistosité de type pencil, à presque 80% dans le domaine slaty. Nous proposons ainsi une cartographie inédite d'un mur de faille dans un bassin d'avant pays déformé, qui révèle l'existence de failles secondaires non cartographiées. Pour expliquer l'intense déformation observée dans le toit et le mur des failles, nous proposons un modèle de propagation de faille de type Trishear.

En outre, trois autres sites du bassin de Jaca présentant la même configuration structurale sont étudiés dans ce travail : un chevauchement et sa déformation associée dans l'éponte inférieure, à condition que des lithologies marneuses apparaissent. Cette thèse propose ainsi une description géométrique et cinématique des zones de déformation, et met en garde contre l'homogénéité trompeuse des grandes formations marneuses, qui peuvent subir de la déformation en grandes sections a priori non identifiées.

RESUMEN:

El cabalgamiento de Leyre es un rasgo estructural principal de la cuenca de antepaís de Jaca, incorporado al sistema de láminas de cabalgamiento de basamento y cobertera del orógeno pirenaico. El cabalgamiento de Leyre presenta una singularidad local: en su zona frontal, un espesor de varios centenares de metros de margas muestra un gradiente de esquistosidad (> 1100 m distancia horizontal). Unos afloramientos excepcionales nos permiten analizar en detalle la transición de la esquistosidad de tipo *pencil* a la esquistosidad penetrativa de tipo *slaty*, en un espesor de varios centenares de metros. Nuestro análisis se basa principalmente en la fábrica magnética de las margas, donde proponemos un estudio estadístico de cientos de fragmentos no orientados de unos pocos gramos. Además, hemos completado este enfoque con un estudio de campo, un estudio cartográfico y la incorporación de nuevos datos analíticos (Raman, microtomografía, isótopos, datación U/Pb).

En la región de Sigüés, las margas del Eoceno han sufrido una diagénesis avanzada (temperatura de enterramiento $\sim 180^{\circ}\text{C}$), de modo que la susceptibilidad magnética está controlada principalmente por la illita paramagnética. Estas illitas, que constituyen una gran parte de la matriz, se reorientaron durante el proceso de deformación. La evolución de la deformación de la matriz puede reconstruirse utilizando varios parámetros, incluido el importante parámetro de forma del elipsoide magnético, que permite aplicar un modelo sencillo de rotación de partículas y calcular un porcentaje de deformación. Obtenemos así un rango de deformación que va desde unos pocos puntos porcentuales ligados a la impronta del acortamiento horizontal (LPS), pasando por $\sim 20\%$ en el dominio de la esquistosidad (clivaje) de fractura, hasta casi 80% en el dominio pizarroso. Proponemos así una cartografía novedosa del bloque inferior del cabalgamiento en una cuenca de antepaís deformada, que

revela la existencia de fallas secundarias no cartografiadas. Para explicar la intensa deformación observada en los bloques superior e inferior de las fallas, proponemos un modelo de modelo de propagación de fallas de tipo Trishear.

Finalmente, en este trabajo se estudian otros emplazamientos de la cuenca de Jaca con la misma configuración estructural: un cabalgamiento y su deformación asociada en el bloque inferior, siempre en afloramientos litologías margosas. Esta tesis ofrece una descripción geométrica y cinemática de las zonas de deformación, y advierte sobre la homogeneidad engañosa de las grandes formaciones de margas/pizarras, que pueden presentar clivaje en amplias regiones no identificada.

1. INTRODUCTION

The geological characterisation of a given rock formation usually involves a more or less developed analysis of the state of deformation of these rocks. This deformation analysis becomes crucial when we are dealing with engineering analysis, or with rocks that are assumed to have certain properties related to their impermeability, homogeneity or stability.

The type of outcrop mostly visited in this thesis consists of grey marls framed within a thick unit sometimes reaching more than 2300 m and often showing deformation features such as cleavage. This type of mudrocks can play a crucial role in many geological settings, and they are very abundant in the sedimentary basins that cover the Earth's crust. Therefore, a superficial look at these rock formations can be misleading, and risks losing important information when looking for geological reservoirs, fluid systems or hydrocarbon studies.

The main issue studied in this work is the strain on the marls of the Jaca Basin, which affects outcrops of several hundred metres of thickness in the study area. The entire study area of this thesis is focused in the Jaca Basin. This is one of the foreland basins of the southern Pyrenees which has undergone an evolution from deep marine, to shallow marine and finally continental deposition. It was then transported within a piggyback structure, in a fold-and-thrust belt in which the thrust sheets have been displaced southwards encompassing the 100 km large basin in thin-skinned thrusts that show a décollement in the Upper Triassic.

These marls of the Jaca Basin correspond to the Larrés Fm and Pamplona Fm, both of Eocene age. They have been considered as monotonous units and have not usually played a leading role in the geological literature of the southern Pyrenees. These formations occupy an intermediate position between the innermost units of the foreland basin (the Hecho Group and the Sierras Interiores both strongly affected by regional cleavage) and the thick series of continental clastic formations (Campodarbe Fm). Articles on structural geology, rock deformation, or tectonic-sedimentation tend to overlook the Eocene marls, with the exception of some of them (see e.g. Pueyo-Anchuela et al., 2011b) that focus on the genesis of the magnetic fabric of these rocks (see Chapter 4.1 Background).

In most part of the Jaca basin the deformation of the Eocene marls is imperceptible and indistinguishable. However, in the footwall of the Leyre thrust and other faults it is very pronounced. The outcrop around the Sigüés site (Aragón) offers excellent conditions for observing a progression from pencil structures, through pencil cleavage, to slaty cleavage over a distance of several hundred metres. It is almost possible to observe this N-S gradient in the same marls bed, since the bedding is subhorizontal. As far as we know, the width of the damaged zone of the fault propagating through clay formations is relatively unprecedented, because the strain halo is usually limited to a few metres in thickness. The strain associated with the movement of these faults contrasts with the absence of strain associated with the minor faults that run parallel to the bedding and have the characteristic of being filled by calcite. Other authors have recognised this cleavage, and have included it within the regional cleavage front characterised for the area immediately towards the hinterland.

CHAPTER 1 - INTRODUCTION

The main hypothesis guiding this work is that the occurrence of this cleavage, with these gradient characteristics, is related to the strain associated with the propagation of the Leyre thrust. For this reason, a multi-proxy study is here developed to characterise this cleavage zone in the footwall of the Leyre thrust and other faults. These are the objectives that have driven the research in this thesis:

- To map the Leyre thrust and surrounding faults.
- To characterise the cleavage zone in the footwall of faults, by visiting outcrops and sampling marls.
- To propose a deformation history associated with the Leyre thrust.
- To compare this geological framework with other similar settings in which thrusts affect marls, and compare the associated deformation zones.

This has led to various means of achieving these objectives, which during the development of the thesis have evolved as the work has progressed.

Firstly, a structural scheme has been drawn up for a site that, despite the quality of its outcrops in the Sigüés Gorge on the river Escá, has not been the subject of numerous articles and studies. We also present the intersection between two structures that have often been taken for the same: the Leyre and Orba sierras with their respective thrusts.

The article by Boiron et al. (2020) contains a starting point for this thesis: the analysis of this cleavage gradient in the same transect. This article presents this outcrop as a natural laboratory to monitor strain intensification within almost literally the same beds. Following the same study, the Anisotropy of Magnetic Susceptibility has been proposed as the key to understanding how Eocene marls host deformation.

In this sense, a sampling method is proposed here to reach numerous sites quickly and easily: the sampling of non-oriented marls fragments (Gracia-Puzo et al., 2021). This has made it possible (i) on the one hand to collect most of the data presented in this thesis, but also (ii) to visit numerous outcrops in the footwall of the Leyre Thrust.

The collection of fragments was completed with a sampling of calcite-filled sub-horizontal faults, present at several points in the studied area. To this aim, it was intended to obtain a new set of fluid, temperature and age data for this deformation zone.

Finally, other areas of the Jaca basin with a similar structure were visited. The Jaca fault crosses the basin with a N100 strike thrusting the Hecho Group onto the same marls. Footwall deformation can be observed in the transects of Biniés, next to the Veral river, and Javierregay, next to the Aragón Subordán river. We also visited a small outcrop next to the Gas River, where the same thrust has the Larrés Fm cut in both walls.

The structure of this thesis is set out in the following chapters:

Chapter 2: Shale deformation, state of the art.

This chapter begins by reviewing the key concepts of this thesis: mudrocks lithology, a history of the shale fabric and cleavage. Following the conceptual introduction, we review studies on magnetic fabrics, especially focusing on the main mineralogy of mudrocks, shales and marls. In a complementary manner, we present a bibliographic compilation of the use of the magnetic fabric as a strain gauge, and the way in which several authors have developed

CHAPTER 1 - INTRODUCTION

methodologies to use AMS to obtain strain quantifications. The chapter concludes with two paradigmatic examples of cleavage gradient studies. One of them is the Lehigh Gap section, which has motivated several studies of cleavage evolution in shales. On the other hand, a summary of the studies of magnetic fabrics carried out on the South Pyrenean zone: from the fabrics of the outer basins to those resulting from orogenic compression in the inner zones of the chain.

Chapter 3: Structural study of the Sigüés area.

This chapter begins with a summary of the background that allows us to have an up-to-date characterisation of the geological framework of our study: the Jaca Basin in the southern Pyrenees. It then presents the outcrops visited during this thesis in the area of the Sigüés gorge and the intersection between the Sierras de Leyre and Orba. The chapter also presents a structural sketch, and the elaboration of parallel cross-sections for this structure.

Chapter 4: Shale fabric:

This chapter is the core of the work in this thesis. It begins with the background of previous studies on the shale fabric in the Sigüés region. We then propose to study the magnetic fabric of more than a thousand marl fragments, mainly located in the footwall of the Leyre thrusts and other faults in Biniés, Javierregay and Jaca-Gas. We propose to quantify the strain in both the footwall and the hanging-wall of the Leyre thrust in several cross-sections, highlighting the role of secondary faults in the footwall.

Chapter 5: Paleothermometry and fluids

The aim of the work summarised in this chapter was to better constrain the Leyre thrust by specifying the burial temperature and fluids, and by dating the system of calcite faults that propagate parallel to the bedding. Although the data is patchy and sometimes unconvincing (the case of Uranium/Lead dating for calcite faults) it has enabled us to better constrain the tectonic agenda of the Sigüés Zone.

Chapter 6: Discussion and conclusion.

The aim of this chapter is to bring together all the data collected (magnetic fabric, characterisation of strain aureoles, structural frame, parallel cross-sections, paleothermometry data, etc...). The discussion starts with a schematic history of fault propagation and associated deformation in the Jaca basin. We make a classification for the three types of studied faults and make a synthesis of the strain calculated in the footwall of the Leyre thrust from the main features previously presented in Chapter 4. Finally, we discuss the hypotheses on the genetics of this deformation zone, and a possible temporal and regional sequence for this Sigüés site. At the end of this chapter we present the general conclusions for this thesis.

This thesis also leaves a number of unknowns open, which for various reasons it has not been possible to study. It must also be acknowledged that some of the sampling has produced insufficient results. However, the hypotheses put forward have been contrasted with the available data, and some future works in relation to the open questions will also be proposed. In any case, **various perspectives** are also raised at the end of the discussion.

CHAPTER 2 - SHALE DEFORMATION

2. SHALE DEFORMATION

2.1. Shales cleavage

2.1.1. Shales

Shales are rocks with a clay matrix that account for 1/3 of all sedimentary basins. The reliefs associated with clay formations are generally depressions (Figure 1a), and outcrops are commonly covered by more recent deposits or vegetation canopies. Furthermore, alteration of these rocks leads to misidentification of bedding surfaces, or structures such as fracturing or cleavage (Figure 1b,c)

Fine-grained sedimentary rocks can be grouped into a large term as “mudrocks”. The prevailing grain size in mudrocks corresponds to silt and clay grain size (<0.063 mm). Within this window, a clay content of >33% is suggested by Potter et al. (2012) for them to be considered as mudstones. Fine grain sizes are a defining characteristic of the shales, with quartzitic, feldspathic or micaceous silt-sized grains accompanying the clays (Figure 1, d.). Organic matter is usually present in shales, and it can give a dark colour to the mudrock beds. Carbonate content may also be present in the fine matrix in the form of micritic mud. Different proportions of quartz grains, iron oxides, or other minerals such as calcite are also frequently present, although the latter are generally not sedimentary grains but rather diagenetic growths.

Mudrocks sediment are deposited in numerous basins around the globe: in lacustrine, deltaic, transitional or marine environments. Shales may occur in intercalation with other coarser detrital deposits, such as sand bars in continental and transitional areas (Figure 1b). Nevertheless they also form large homogeneous bodies with significant thicknesses in mainly marine formations (Figure 1a)

CHAPTER 2 - SHALE DEFORMATION

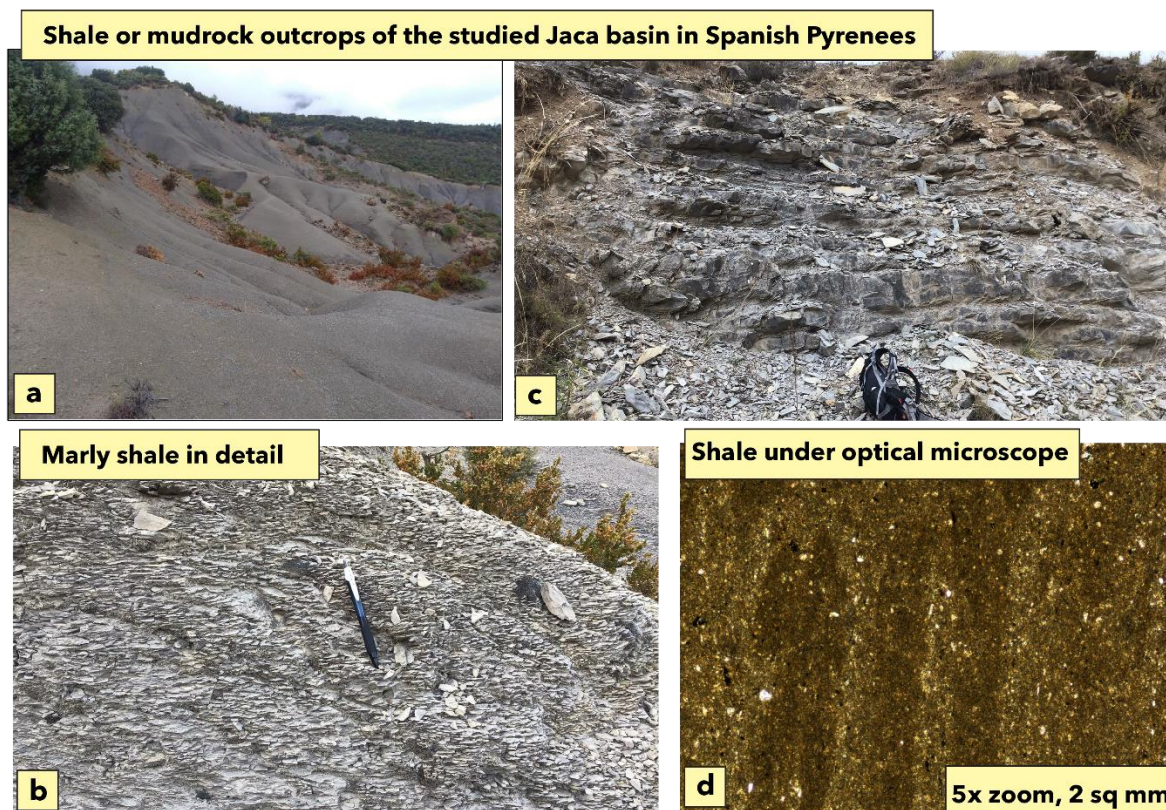


Figure 1: Shale pictures, showing some lithological views. a: Outcrop of homogeneous grey shales. b: Outcrop of carbonated and indurated shales. c: Shale with pencil cleavage. d: Micron scale shales (optical microscope natural light).

There are debates about the boundary between mudrock and shale, and it is generally accepted that although the pressure of the sedimentary column would be the main conditioning factor, there are other environmental factors in the lithification of the formation that affect these deposits from their earlier stages (Aplin and Macquaker, 2011; Flemming, 2000; Moon and Hurst, 1984; Potter et al., 2005, 1980; Weaver, 1989). Main intervening conditions involve the type of clay (since montmorillonite and kaolinite, for example, behave in different ways), and the presence or absence of organic matter. Bioturbation can condition the fissility of the shales. In this sense even laminations of organic matter in the deposit would favour the subsequent splitting of the rock (Spears, 1976).

Moon and Hurst (1984) paper brings together the views of several authors who point to two characteristics such as lamination and fissility as typical for an indurated mudrock to be defined as a shale. The lamination is related to the transformation process of the fabric, generally due to compaction processes, many of them contemporary with the peak burial. This lamination would be between 0.5 and 1 mm thick, but this characterization also accepts the existence of non-fissile shales (Spears, 1980). It is accepted that this fissility is related to the upwelling or extraction of shales, and in buried geological formations it does not manifest itself as an open fracturing.

2.1.2 Cleavage

Tectonic cleavage (S1) is a secondary foliation defined by its superposition on a pre-existing (sedimentary) primary fabric (even if homogeneous), and its recognition is based on repetitive planar and linear structures. This chapter will present a theoretical and

CHAPTER 2 - SHALE DEFORMATION

terminological contextualization, as well as a basic state of the art on the study of shale cleavage.

Cleavage in shales has been particularly studied in the late 20th century. Important elements that provide key steps in the understanding of this deformation can be found in review papers (Gale et al., 2017; Kisch, 1991; Moon and Hurst, 1984; Ougier-Simonin et al., 2016; Wenk et al., 2020, 2010).

Cleavage can be approached from multiple angles, such as temperature and pressure conditions, strain analysis, and the mechanical or chemical aspects of physical transformations. Here, we focus first on the geometry of cleavage in relation to bedding.

2.1.2.1 Angular relationships with bedding

S1 may be parallel, oblique or perpendicular to the bedding (S0). We use examples from the Pyrenean orogen in order to illustrate the various possible configurations.

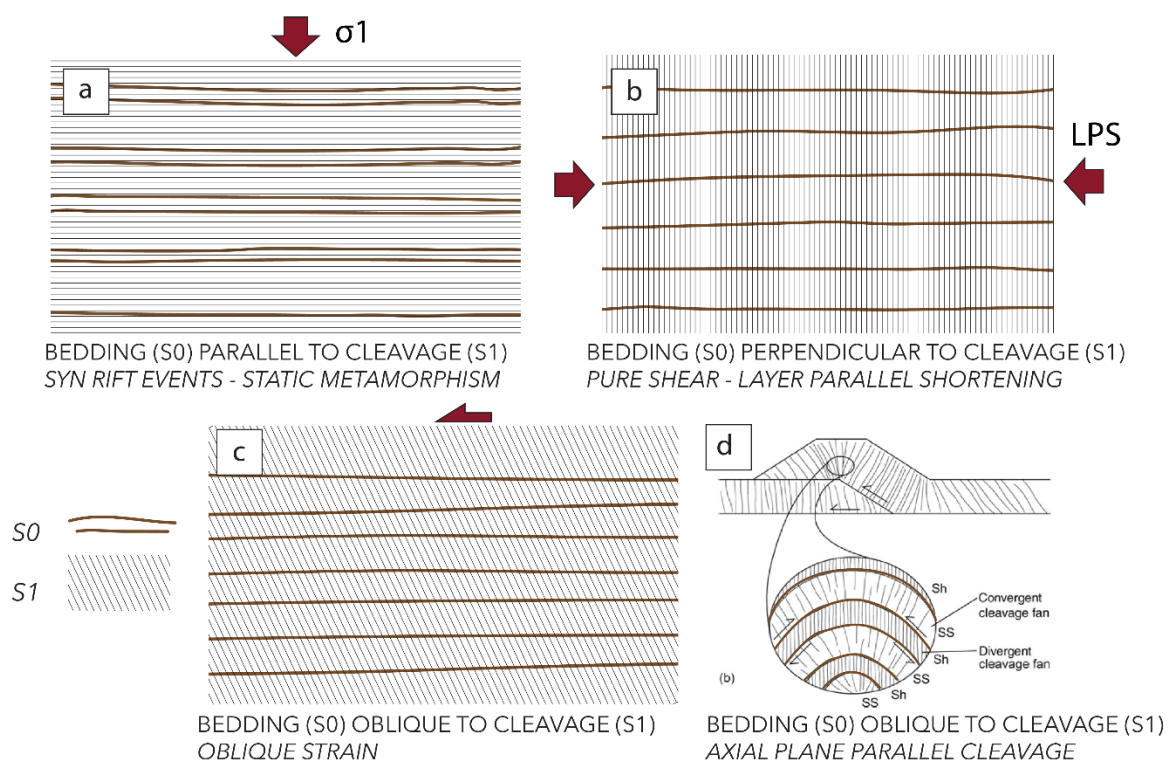


Figure 2: Sketches showing cross-cut relationships between bedding (S0) and cleavage (S1)

- Bedding-parallel cleavage (Figure 2a) In the Pyrenean retrowedge (North Pyrenees), the Mesozoic sediments of the *Chaînons Béarnais*, exhibit frequently S1 parallel to S0 (see Figure 3), particularly in syn-rift Albian shales (Izquierdo-Llavall et al., 2020; Labaume and Teixell, 2020). Interpreted as contemporaneous of the Cretaceous rifting phase by Labaume and Teixell (2020), S1 has been formed in the basin under high temperature (>200°C) (Ducoux et al., 2021) conditions. This can be referred to as a "static metamorphism" a term coined by Beyssac et al. (2007), who documented comparable bedding-parallel S1 in the Taiwan belt. This is a metamorphism imposed by burial condition during basin formation. In the Chaînons Béarnais, a high geothermal flow impacted a 5 km thick sedimentary cover during the rifting stage

CHAPTER 2 - SHALE DEFORMATION

(necking zone), where thermal gradients as high as 80°C/km have been documented (Vacherat et al., 2014). In this type of metamorphism, sedimentary structures can be preserved



Figure 3: Photograph of Albian shales from the Ossau Valley (North on the left). Cleavage is parallel to bedding in these thin shaly layers.

- Oblique-to-bedding cleavage (Figure 2b). In the Pyrenean prowedge, S1 reported in the folded basins is frequently oblique to bedding (Holl and Anastasio, 1995; Parés et al., 1999; Pocoví Juan et al., 2014). In this case, the syn-orogenic sediments have recorded syn-collisional deformation. Therefore, S1 is syn-orogenic. S1 can be perpendicular to the bedding or at an angle $<90^\circ$ to it.
 - A bedding perpendicular to S1 can derive from Layer Parallel Shortening (LPS, Figure 2). One classical example is the LPS-derived cleavage in the Appalachians (see Chapter 2.4 The Lehigh Gap, a classical shale-to-slates transition). This cleavage can be pre-folding (Hirt et al., 2004; Wintsch et al., 1996). In the Burgui Area, North of Sigüés, a bedding-perpendicular S1 cleavage was studied by Saur (2022) (Figure 4). This cleavage develops differently depending on the type of rock, and generally at burial temperatures in excess of 200°C.

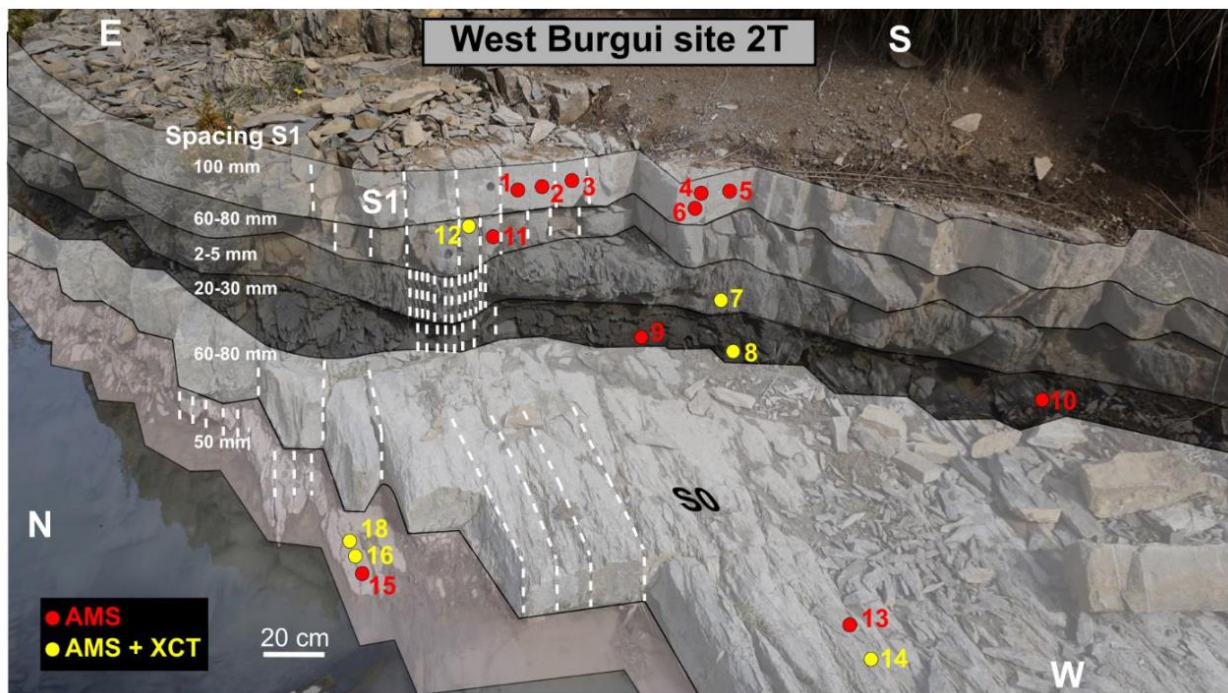


Figure 4: Schema by Saur (2022), Hecho group (Eocene flysch) beds are affected by subvertical LPS-like S1. Note the spacing of S1

- Oblique-to-bedding cleavage (Figure 2c). This cleavage is observed frequently in different tectonic settings including folds (Figure 2d), thrusts, and metamorphism. It relates to simple-shear deformation. This cleavage is widely expressed in the northern part of the Hecho turbiditic basin (Pocoví Juan et al., 2014). This cleavage is also present in the footwall of the Leyre thrust as we will see along this PhD (Boiron et al., 2020; Pueyo-Anchuela et al., 2010).

2.1.2.2 Cleavage spacing and shortening

The spacing between cleavage planes gives an indication of the recorded deformation. However, it should be noted that the same cleavage episode can develop with different spacing in different rock units (Figure 4 and Figure 5 examples). In general, the less competent the rock, the more penetrative the spacing will be. This is why it is important to be careful and precise with the determination of spacing. The shales of the South Pyrenean Basin will be described using the nomenclature proposed by Saur (2022) in fine grained marls. Pencil cleavage refers to spacing from 5 cm to 1 mm; (Figure 5a), and slaty cleavage refers to spacing < 1 mm; (Figure 5b).

It is generally accepted that the rock is hosting cleavage by way of dissolution and neo-growth of grains (Gray, 1997; Mitra et al., 1984; Wenk et al., 2020). In the process that produces soluble ions, these enter the pore system, and they can be carried out of the hosting geological formation through fluid circulation (Gray, 1997; Marshak and Engelder,

CHAPTER 2 - SHALE DEFORMATION

1985; Wood, 1982). Thus, volume losses happens as shown by passive deformation marker studies, as well as other geochemical studies (Gratier, 1983; Gray, 1997). Kisch (1991) proposes a range of shortening for a shaly formation from 10 % (onset of pencil cleavage) to about 75% shortening (slaty cleavage). In the results of this thesis, shortening calculations for our study will be found close to this range of values.

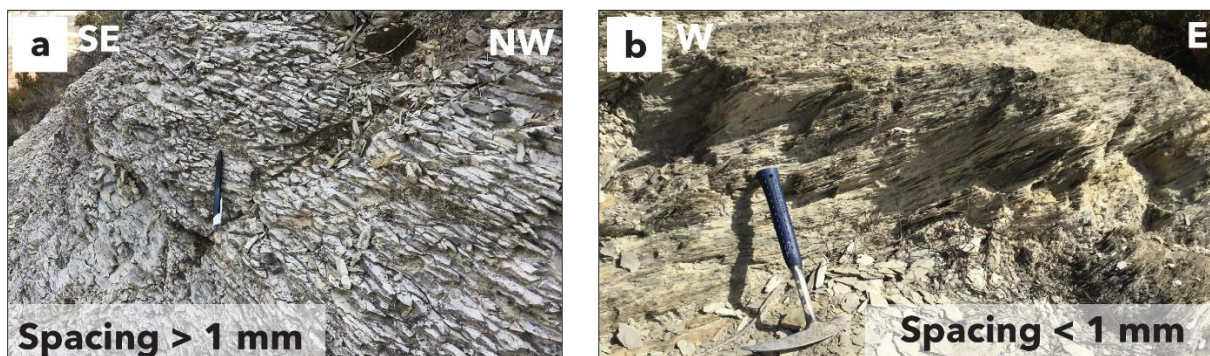


Figure 5: Pencil cleavage (a) vs slaty cleavage (b) and their respective spacing in marls.

2.1.3 Temperature domain

For a detailed description of the analysis of burial temperatures for the Pyrenean case, we recommend reading section 5.1 Background. As a preliminary and taking into account some bibliographical references on this Pyrenean orogen, it is proposed that cleavage marks the upper boundary of diagenesis conditions, for burial temperature near 200°C (Holl and Anastasio, 1995). In the Pyrenees, Izquierdo-Llavall et al. (2013), based on illite thermometry, have correlated a regional cleavage front for burial temperature >230°C in the internal units of the piggyback Jaca Basin. In the Sigüés area, Crognier et al. (2018) proposed that cleavage develops in the range of burial temperature between 150°C to 200°C. It would be then possible that onset of S1 cleavage starts at lower temperatures in this zone of the Jaca basin.

2.1.4 Regional versus local cleavage

Regional cleavage refers to its presence in outcrops larger than tens of kilometre in geological formations. Local cleavage relates to tens of meters extension, usually linked to particular structures.

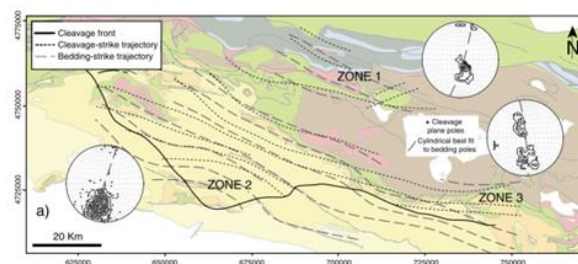
CHAPTER 2 – SHALE DEFORMATION

Fault zones – multiple structures in a few tens of meters of rock thickness



- Monroyo Fault (Vernet et al. 2018), at the picture above 20 m thick
- Daroca Fault (Casas-Sainz et al. 2018) from 0.25 to 40 m thick
- Gavarnie Fault (Marcén et al. 2018) 40 m thick

S1 observed at regional extent.



- Bahamas accretionary prism ($\approx 10\text{km}$) Housen 1997
- Internal Jaca Basin ($>25\text{ km}$) Izquierdo-Llavall et al. 2013
- Northern Apennines ($\approx 50\text{ km}$) Caricchi et al. 2016

Figure 6: Local cleavage vs regional cleavage. Cleavage can vary in width from a few metres to several kilometres.

A typical regional cleavage is observed in the internal part of the South Pyrenean prowedge, where burial temperature is $>200^\circ\text{C}$ (Crognier et al., 2018; Holl and Anastasio, 1995; Izquierdo-Llavall et al., 2013a). The strike of S1 is generally perpendicular to the direction of regional compression (Izquierdo-Llavall et al., 2013) (Figure 6).

In the context of fold-and-thrust belts, cleavage is frequently recognized in fault zones (Figure 6) (Marcén-Albero, 2020; Marcén et al., 2018; Simón et al., 2021). These fault zones can have a remarkable complexity, accumulating multiple markers of deformation. Cleavage is here mainly ruled by mechanical processes (Faulkner et al., 2010; Morley et al., 2017)

2.2 Shale fabric

2.2.1 Fabric definition

The term **fabric** is used to denote the repeating geometric relationship between constituent elements of an object. These constituent parts can be observed at various scales. Generally, in geology we will refer to fabric from the meso (m to mm of observation), to the microscopic ($> \text{mm}$ objects) scales, also defined as microfabric (Fossen, 2010; Van Der Pluijm and Marshak, 2004).

CHAPTER 2 - SHALE DEFORMATION

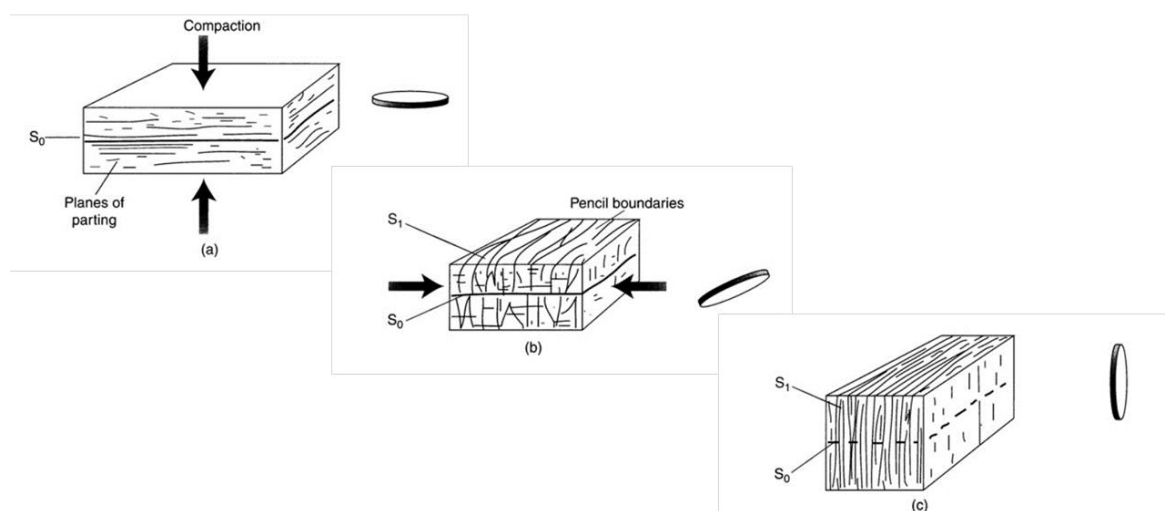


Figure 7: Various shale fabrics as presented by Van Der Pluijm and Marshak (2004). Compactional sedimentary fabric, then, pencil cleavage fabric, and finally, slaty cleavage fabric. A representative strain ellipsoid illustrates its orientation in progressive fabric.

In any sedimentary rock, mineral grains are arranged as a result of sedimentary processes (i.e., energetic environments or calm basins, controlling the deposition of flattened grains, or marked orientation of anisotropic grains) or the deformation that the rock has undergone. Deposition and compaction of the layers in sedimentary history will generate as a rule planar fabric (Figure 7a). These fabrics are usually considered as sedimentary fabrics.

The clay fabric reacts rapidly during compaction. Here, we describe some of the characteristics of this evolution.

Due to their electrochemical architecture, micron-sized clays tend to cluster together forming flakes with irregular shapes, which have been the subject of debate (Bjørlykke, 1998; Meunier, 2005; Weaver, 1989). These flakes are believed to form in aqueous solutions, and the physico-chemical conditions of the water (e.g. whether it is salty or fresh, its pH or Eh) can influence the type of flakes that are formed.

The study of clay particles in sedimentary solutions has also been a challenging issue, but since the 1970s, some experiments such as light-scattering (Schweitzer and Jennings, 1971) have made it possible to observe montmorillonite associations. These observations confirm the model by Van Olphen (1963) who suggested various options for the association of clay lamellae: edge-to-edge (EE), edge-to-face (EF) and face-to-face (FF) associations.

Clays are assumed to form flakes with a "house of cards" shape under general pH and salinity conditions (Figure 8 by Moon and Hurst, 1984), where a cluster of about a dozen clay particles is bonded together in an edge-to-face arrangement. Only at higher pH values, above pH 8 (Flegmann, 1969), are edge-to-edge type flocculants observed.

CHAPTER 2 - SHALE DEFORMATION

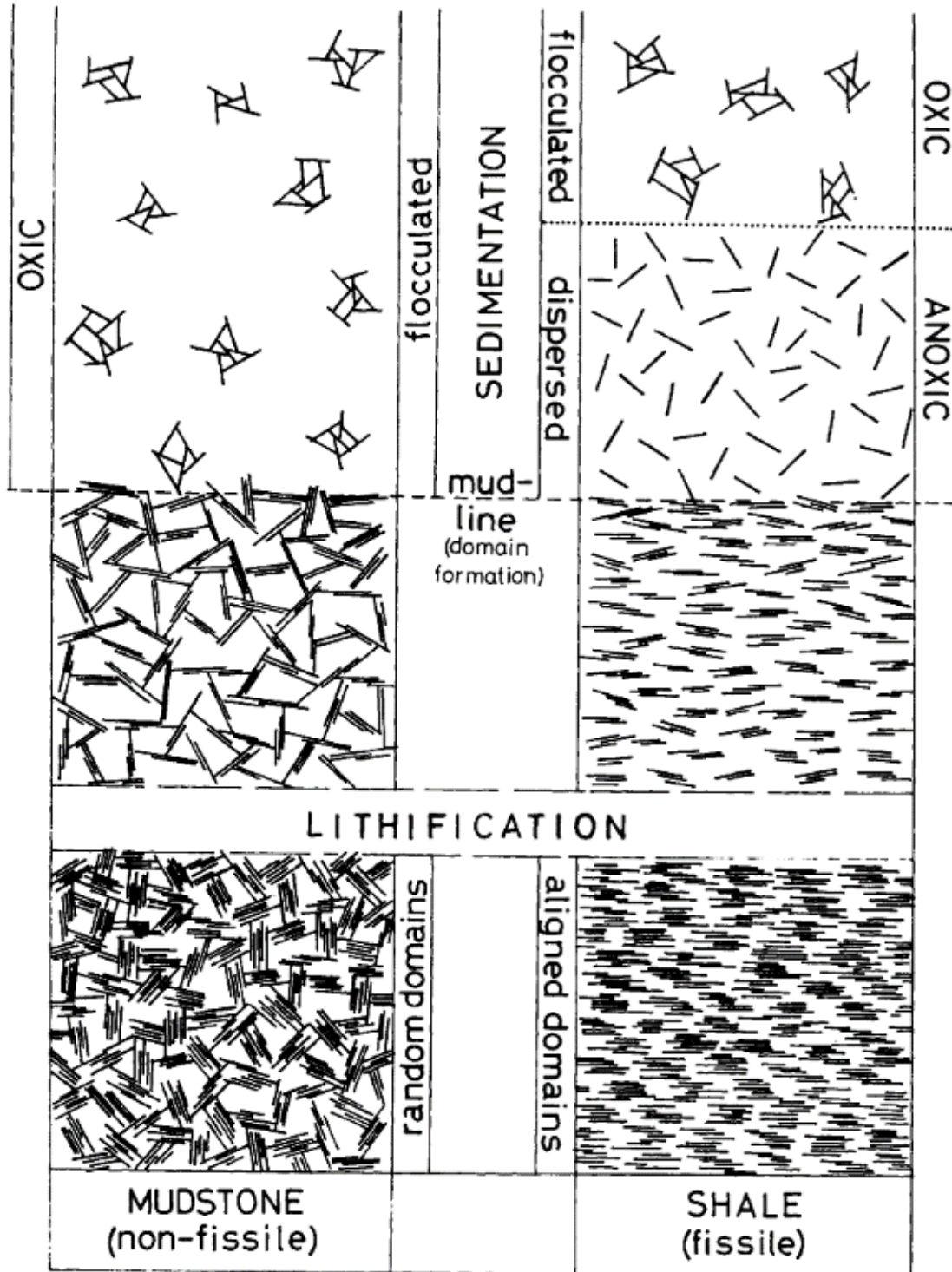


Figure 8: Sketch depicting the major microstructural changes in clay sediments. (Figure from Moon and Hurst, 1984)

The porosity within these flakes is initially 16-20% (Weaver, 1989) but it undergoes rapid changes when these aggregates settle at the depositional interface and their structure begins to transform. The domain structure consists of groups of EF-type aggregates with random orientations, but when they combine at a larger scale, they exhibit a FF structure (Sloane and Kell, 1966; Smalley and Cabrera, 1969). The concept is that even before compaction, this type

CHAPTER 2 - SHALE DEFORMATION

of fabric exists in a new interaction between aggregates, however without notable loss of foliation, and the preservation of the previous electrochemical architecture.

Subsequently, below the depositional surface the gradual burial of the flakes would lead to compaction, resulting in the collapse of EF bonds (see Figure 9). This process leads to a progressive reduction in porosity and volume as the sedimentary column thickness increases. In terms of fabric, this evolution is evident as clay platelets come into contact through FF relationships, consolidating the domains explained earlier into a more uniform planar fabric.

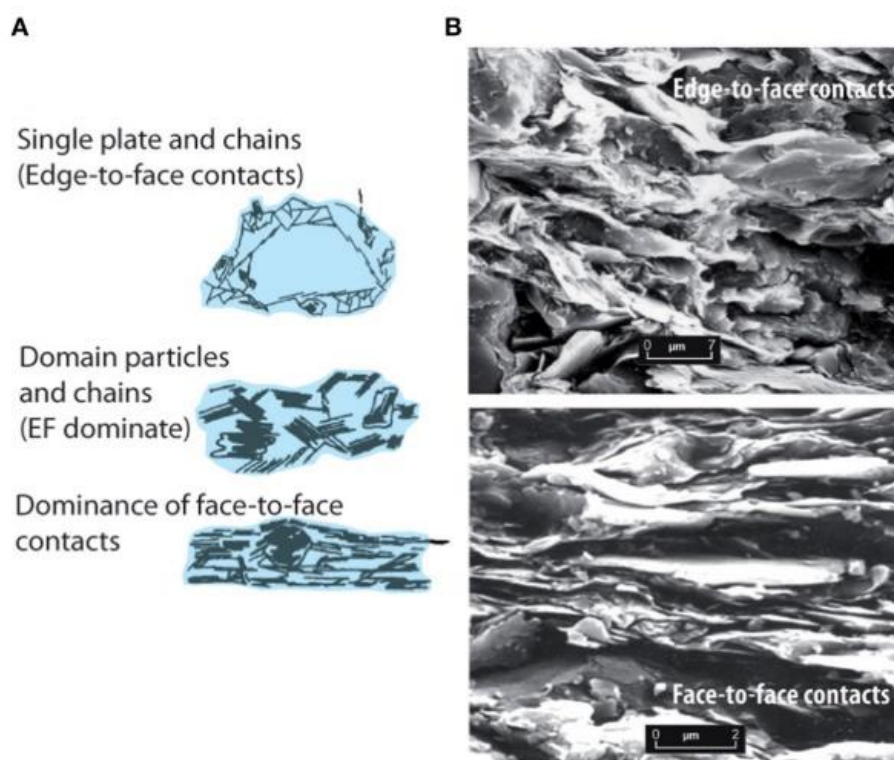


Figure 9: Progressive change of clay microstructure during burial. shortly after deposition A) Vertical evolution of compaction domains B) SEM photos corresponding to the same vertical evolution. Figure from Parés (2015)

In general, shales found in basins with under 100 m burial (Kanamatsu et al., 2012) would undergo these fabric changes. However, exceptions exist, such as over-consolidated sediments, and factors like fluid circulation could influence compaction of the sediments, resulting in relatively isotropic fabrics.

Consequently, studying clay fabrics can lead to more intricate insights into the burial history of a basin. The study of mudrock fabric can therefore prove valuable to geologists from various disciplines, including sedimentologists, geochemists, and structuralists. In this thesis, we aim to delineate this burial and diagenetic history to interpret the fabric accurately and extract the desired information for our structural study.

2.2.2. Shale fabric techniques

Studying shales can be challenging due to the characteristics of the rocks and its fine-grained composition (<0.063 mm). This latter factor makes it difficult to characterize the microarchitecture of shale rocks. The use of electron microscopes since the 1960s has enabled geoscientists to directly observe the nature of clays. Figure 10 summarizes some of the most commonly used techniques in the field of structural geology for studying clay fabric.

A distinction is generally made between the crystal axes preferred orientation (CPO) and the mineral shape preferred orientation (SPO). In the case of certain minerals, such as clays, there is a good correspondence between SPO and CPO (Figure 19). For detrital particles such as quartz, SPO is generally controlled by the rock's diagenesis and deformation history, while CPO is random. Depending on the mineral phase under study, a choice will have to be made between SPO and CPO. Some techniques are dedicated to obtain the bulk fabric of a given sample (mean anisotropic properties), whereas others are dedicated to obtain the grain fabric, i.e. each grain is 3D spatialized. A bulk fabric can also be derived from grain fabric (e.g. Saur et al., 2021).

In shales Saur (2022), has shown that it is possible to extract quartz grain fabric successfully using high-resolution X-ray microtomography (XCT). In this case, the grain fabric is of the SPO type. Extracting SPO from clays with existing techniques seems very complicated. Microtomography, with its micrometre resolution cannot resolve the orientation of a very oblate particle, a few hundred nanometres thick. In theory, the CPO-type structure of clays could be resolved using the EBSD technique (Figure 10), but sample preparation requires a surface finish with a precision of a few tens of micrometres. To our knowledge, no team has yet succeeded in obtaining an SPO fabric of clays using EBSD. That is the reason why we are using bulk techniques to study the fabric of clays.

Restricting this presentation to shales, bulk-type techniques generally make use of the anisotropic properties of certain physical quantities, for example acoustic velocities (Robion et al., 2014), electrical conductivity (Louis et al., 2003) or electromagnetic radiation (Sanjuan et al., 2022). Anisotropy can be modelled simply as a rank-2 tensor, i.e. with 3 eigenvalues that bear a relationship to the rock's fabric. Typically, the acoustic velocities $V_1 > V_2 > V_3$ are tightly controlled by the shale fabric (Sanjuan et al., 2022). V_3 is generally perpendicular to bedding.

Of all the physical quantities that exhibit anisotropy responding to a rank-2 tensor, the magnetic signal is undoubtedly one of the most interesting and unquestionably, the most studied since the 1960s. It is the most interesting because it is very easy to use, and the magnetic response of minerals is very well known. Low-field magnetic susceptibility (close to the Earth's magnetic field) is the most widely used signal. But strong-field magnetic susceptibility (Martín-Hernández and Ferré, 2007) is also occasionally used, as is remanence (Aubourg and Robion, 2002). Among remanent magnetizations (which take longer to imprint in rock, and are sometimes difficult to erase), anhysteretic remanent magnetization remains the most widely used. It is beyond the scope of this thesis to provide a complete state-of-the-art review of magnetic techniques, but the reader will find it in works such as

CHAPTER 2 - SHALE DEFORMATION

the book by Hrouda (1987), that provides all the theoretical bases needed to better understand the advantages and disadvantages of these different techniques.

Figure 10 provides a concise description of some of the most important characteristics of these techniques, along with figures that illustrate the type of observation obtained after their application to the rock.

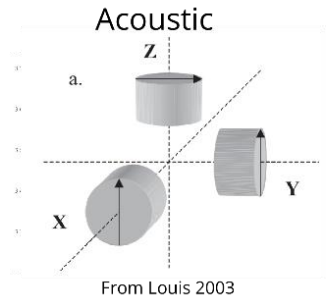
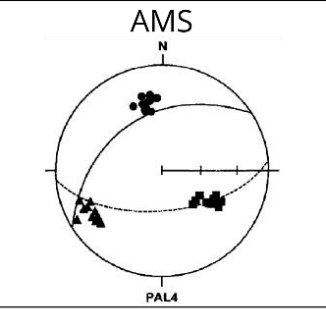
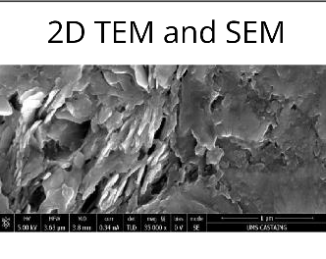
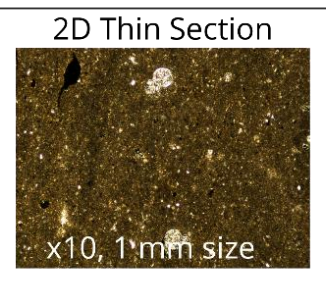
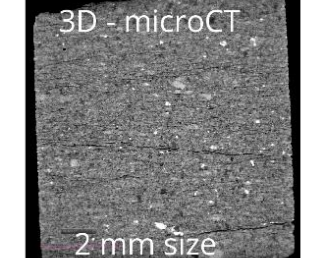
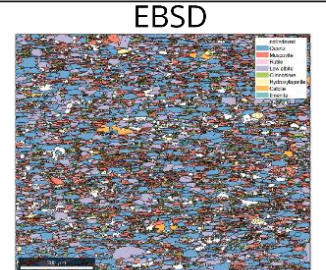
BULK FABRIC	Acoustic	 <p>From Louis 2003</p>	<ul style="list-style-type: none"> - An ultrasonic pulse generator transmits P-waves in rock samples. An oscilloscope sensor obtains the speed. - The samples are rotated in a chosen angle obtaining the velocity anisotropy at various regular positions. - This cycle is repeated in three orthogonal directions, X, Y, Z. Thus, it is possible to project the axes of an ellipsoid that projects the velocity variations in the geometry of the rock.
	AMS	 <p>PAL4</p>	<p>Anisotropy of magnetic susceptibility</p> <ul style="list-style-type: none"> - Measure of bulk magnetic fabric of sampled and oriented cores. - Eigenvalues of magnetic ellipsoid, (k1, k2 and k3) - Magnetic mineralogy (ferromagnetic + paramagnetic + diamagnetic) controls anisotropy. Rock magnetism is crucial to understand preferred orientation of magnetic fabric. - Quick (1 min/measure) and non destructive technique.
SHALE FABRIC	2D TEM and SEM		<ul style="list-style-type: none"> - Various techniques of electronic microscopy: Backscattering, scanning (SEM), transmission (TEM),... - Two-dimensional grayscale images, very high resolution. Up to nm for a pixel. - Backscattering allows to reflect compositional differences. - Or SEM in rough surfaces, reflecting relief and shapes, as clay platelets.
	2D Thin Section	 <p>x10, 1mm size</p>	<ul style="list-style-type: none"> - 2 mm of thin section are shown on the picture (5x) and up to 50x zoom. - Sight of main mineralogical components: - Calcite and quartz could be differentiated (white bright spots). - Clay and micritic matrix is difficult to analyze. Sometimes S1 or S0 is viewed if its present on sampled thin section..
	3D - microCT	 <p>2 mm size</p>	<ul style="list-style-type: none"> - 2 mm of drilled core are shown on the picture. Voxels up to 1.5 μm. - Differences in X-ray attenuation allow to segment mineral phases in a 3D tomography. Quartz, calcite, pores, and pyrite could be separated from matrix attenuation. - 2nd order tensor to orientation of each individual grain segmented is obtained. - For clays and micrite there is qualitative observations on the fabric, but not quantitative.
	EBSD		<ul style="list-style-type: none"> - It combines SEM and EDS (energy dispersive x-ray spectroscopy). It is analysed on surfaces (2d). It can work on phyllosilicates. - It obtains a map of the grains of the section, while it is also possible to obtain compositional and microstructural data. - Mineral phases can be segregated and stereoplot figures can be constructed for the segregated diffraction planes of these phases (Wenk et al., 2020 and references therein).
GRAIN FABRIC			

Figure 10: Table of various shale fabric analysis techniques.

CHAPTER 2 - SHALE DEFORMATION

In general, these techniques complement each other both in the type of results obtained and in their analytical complexities. For this reason, in this PhD three out of five techniques will be presented as part of the methodology: AMS, 2D thin section and 3D XCT. Additionally, there are previous SEM pictures and EBSD data available from other works (Boiron et al., 2020; Saur, 2022) performed in the same study area with the same lithologies.

To clarify, one technique -the analysis of magnetic fabrics in shales using AMS- has received more time and attention and forms a significant part of the results presented here. This choice is attributed to its ease of use, the precision of the data, the speed at which results are obtained, and the new sampling variant that will be introduced later (which is also faster than other methodologies). AMS has become a standardized tool in numerous deformation studies, employed by various research groups in the field of structural geology. The fact that the two universities participating in this international PhD program, situated in close proximity to each other, possess well-equipped magnetic fabric laboratories and have a substantial body of work in this area prior to this thesis, is not coincidental.

2.3 Magnetic fabric study

The use of magnetic fabrics in this PhD research will bring forth both technical and methodological contributions. The novel sampling technique, as previously proposed in Gracia-Puzo et al. (2021) is inscribed within the field of magnetic fabrics studies, specifically, within the field of Anisotropy of Magnetic Susceptibility, the evolution of which will be summarized in the next section.

The study of the magnetic properties of rocks goes back to the beginning of the 20th century, when the correlation between these magnetic properties and the crystalline structures of rocks was already pointed out (Voigt and Kinoshita, 1907). The term magnetic properties includes various parameters: magnetic moment, magnetization or magnetic susceptibility. The conceptual framework for the study of these magnetic properties was in origin especially related to palaeomagnetism s.s., where the analysis of these properties relates to magnetic remanence and allows to obtain data in relation to the terrestrial magnetic field of the past. This has been the basis for the determination of the Apparent Polar Wander Paths of continents and in last instance for the kinematics of plate tectonics. This PhD focuses on a particular aspect of rock magnetism, namely the Anisotropy of Magnetic Susceptibility, while setting aside questions related to magnetic remanence, which are specifically associated with paleomagnetism (although this property has also been used for determining anisotropic properties related to ferromagnetic s.l. minerals).

This work primarily focuses on shales, and as a result, most of the subsequent discussions pertain to this lithological type and its primary constituents: clay minerals (smectite, illite, chlorite), quartz, and carbonates. As accessory phases, there are pyrite (at approximately 0.1%), magnetite, and pyrrhotite (at the order of ppm), which have minimal influence on the bulk magnetic properties of the samples (Aubourg et al., 2019; Boiron et al., 2020; Pueyo-Anchuela et al., 2011a). Minor inherited minerals such as plagioclase, feldspar, etc. will not be considered hereafter.

2.3.1 Magnetic behaviour of minerals

Magnetic susceptibility is related to the application of a magnetic field to substances, which accordingly to their subatomic nature (electron spins) will react in different ways.

The strength of the induced magnetisation (M) in a body can be directly related to the strength of the applied field (H), the proportionality constant is the magnetic susceptibility (K), and the following formula is constructed.

$$\vec{M} = K\vec{H} = K \frac{B}{\mu_0}$$

Equation 1

Where M is the magnetic dipole moment per unit volume (in A/m), H is the magnetic field strength (A/m), B is the magnetic field measured in Tesla and μ_0 is the magnetic permeability of free space (4×10^{-7} Henry/m).

Numerous studies since the 1960s (Fuller, 1963; Hrouda and Tarling, 1993; Stacey, 1960) have shown that K can be satisfactorily represented by a symmetrical second-order tensor. It should be remembered, however, that this is only an approximation, and that the anisotropy may be more complex than an ellipsoid.

$$\begin{pmatrix} M_1 \\ M_2 \\ M_3 \end{pmatrix} = \begin{pmatrix} k_{11} & k_{12} & k_{13} \\ k_{21} & k_{22} & k_{23} \\ k_{31} & k_{32} & k_{33} \end{pmatrix} \begin{pmatrix} H_1 \\ H_2 \\ H_3 \end{pmatrix}$$

Equation 2

Where the first matrix is vector of magnetization (M), the central matrix corresponds to susceptibility tensor (k), and the last matrix (H) is related to field intensity.

Magnetic susceptibility can be measured at different magnetic field magnitudes. Typically, commercially available devices (Saphire, Bartington, Agico... etc.) use a low field value, of an order of magnitude close to the Earth's magnetic field ($\sim 50 \mu\text{T}$). Since induced magnetization is low at these field strengths, the magnetic field is applied in alternating mode (AF), enabling it to be effectively averaged.

The low field magnetic susceptibility K_{lf} can be expressed as the sum of the different contributions:

$$K_{lf} = K_{dia} + K_{para} + K_{ferro}$$

Equation 3

High-field magnetic susceptibility is sometimes used (Ferré et al., 2016), as it allows the contribution of K_{ferro} to be removed, since by definition, the induced magnetization carried by a ferromagnetic phase saturates at high field, and therefore $K_{ferro}=0$.

$$K_{hf} = K_{dia} + K_{para}$$

Equation 4

Diamagnetism

Diamagnetism (K_{dia}) is a universal phenomenon. The mineral responds with an induced magnetization in a direction opposite to that of the applied field. However, this induced magnetization only lasts until the magnetizing field is removed. The diamagnetic susceptibility is negative, on the order of $-10 \mu\text{SI}$ (Figure 11). In shales, diamagnetic susceptibility is generally negligible, although the matrix may contain a majority of only

diamagnetic grains such as calcite or quartz. Therefore, equation 1 can be substituted for the approximation:

$$K_{lf} \sim K_{para} + K_{ferro}$$

Equation 5

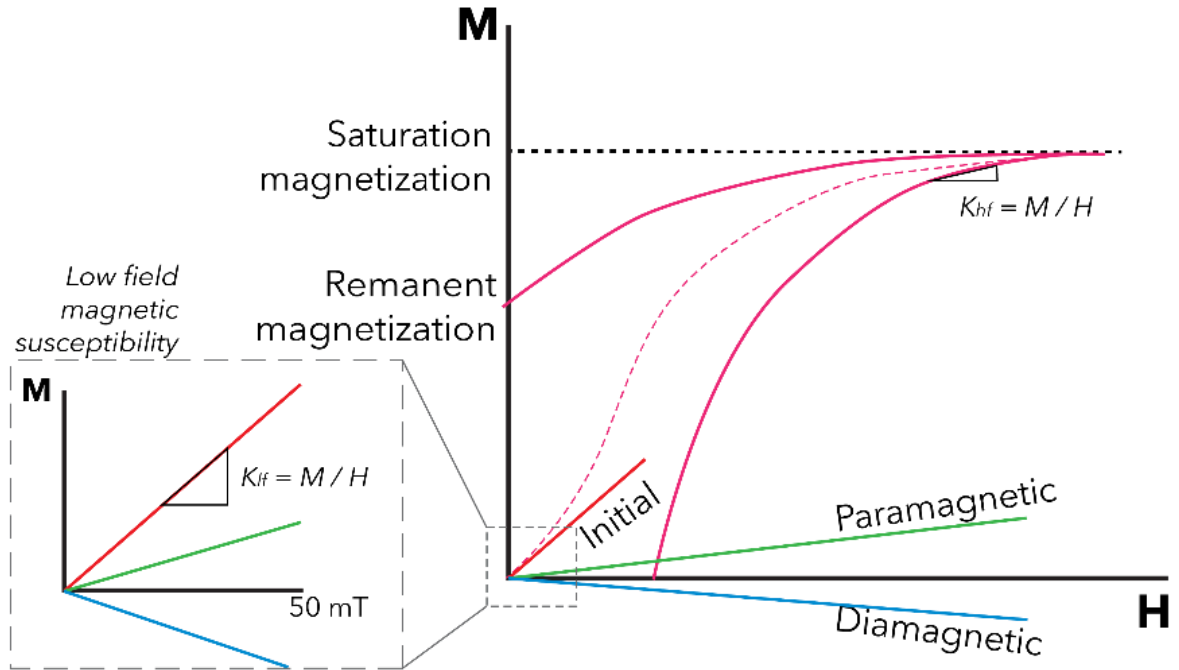


Figure 11: The three main types of magnetic behaviour of a material according to the response to the acquired magnetisation (M) vs. magnetic field (H)

Paramagnetism

Some iron-bearing minerals, under an applied magnetic field, give an induced magnetic moment which has the same direction as the applied field. This is what is called paramagnetic behaviour (K_{para}), conditioned by the incompleteness of subatomic particles. Like diamagnetisms, the induced magnetization disappears together when the applied field is removed. Paramagnetic susceptibility of minerals is 10 to 100 times more important than diamagnetism (Figure 11).

The paramagnetic susceptibility K_{para} is temperature dependant:

$$K_{para} = \frac{C}{T}$$

Equation 6

Where C is the Curie constant and T is the temperature. When T is decreasing, the paramagnetic susceptibility contribution increases. This characteristic is exploited in low-temperature anisotropy measurements (typically obtained with liquid nitrogen -196°C) to enhance the paramagnetic component (Oliva-Urcia et al., 2009; Soto et al., 2007, among many others).

Paramagnetic minerals have positive susceptibilities ranging from 10^{-3} to 10^{-4} SI (0.5 to 5 μ SI after Rochette et al., 1992) for minerals such as pyroxenes, amphiboles and many phyllosilicates, here including clay minerals (Figure 12).

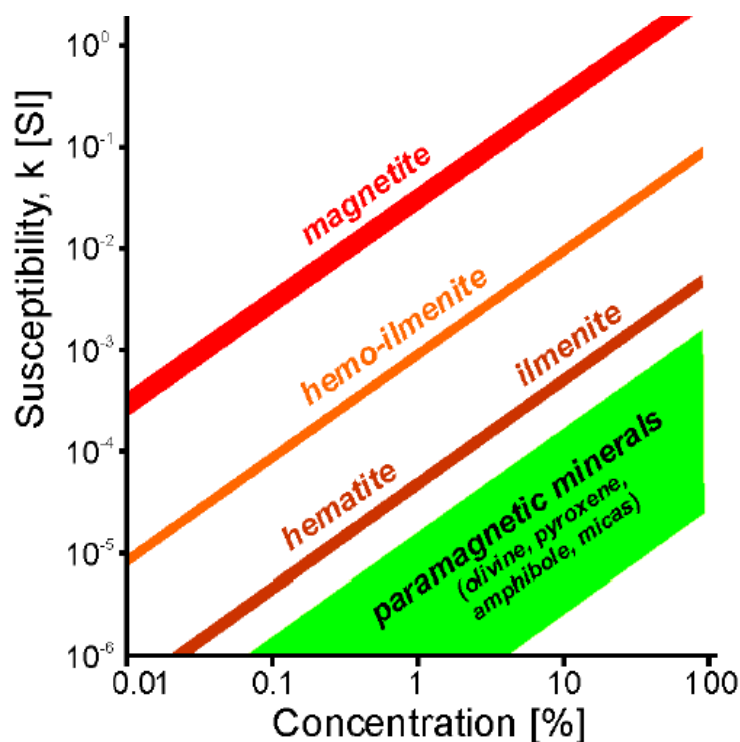


Figure 12: Magnetic susceptibility of various paramagnetic and ferromagnetic minerals, related to their concentration in a sample Taken from AGICO (2019).

Finally, a small number of minerals (iron-titanium oxides and iron sulfides) have a stronger and positive susceptibility, in the order of 10^{-1} and 10^{-3} SI, showing ferromagnetic (s.l.) behaviour:

Ferromagnetism (sensu lato).

By ferromagnetism (s.l.), we mean magnetic minerals capable of retaining a remanent magnetization in zero field conditions. It covers three distinct groups of behaviour: ferromagnetism (*sensu stricto*), antiferromagnetism and ferrimagnetism (Figure 13).

The ferromagnetic *s.s.* behaviour is related with the parallel orientation of the spins of electrons, acquiring and retaining a very strong remanent magnetization (Figure 13a). In practice, ferromagnetic behaviour is not found in shales, as it is observed for iron, cobalt and nickel.

If the magnetic moments are anti-parallel, then antiferromagnetic behaviour is observed (Figure 13b). Misalignments in the antiparallelism lead to remanent magnetization in zero field. Hematite and goethite are antiferromagnetic.

If the antiparallel alignment of the spins is unbalanced (Figure 13c), with different intensities in the two components, ferrimagnetism occurs. In shales, the classic ferrimagnetic minerals are magnetite, greigite and pyrrhotite. It should be noted that pyrite, although very rich in iron, only exhibits low-intensity paramagnetism (10^{-6} to 10^{-5} SI).

Ferromagnetic susceptibility is more complex than diamagnetic and paramagnetic susceptibility, as it exhibits hysteresis and non-linear curves under varying magnetic fields (Figure 9). To avoid the possible contribution of M_r , the remanent magnetization at null field, magnetic anisotropy measurements are made in alternating field (AF). As

CHAPTER 2 - SHALE DEFORMATION

ferromagnetic susceptibility varies according to the applied field (Figure 11), the choice of a weak magnetic field makes it possible to exploit the relatively linear part of the induced magnetization curve.

Ferromagnetic susceptibility depends closely on the nature of the mineral, but also on its size. This is particularly true for magnetite, whose anisotropy is controlled by the shape of the mineral. From the smallest to the largest minerals, a distinction is made between superparamagnetics (SP < 20 nm), monodomains (MD 20-40 nm) and polydomains (PD > 40 nm). While the intensity of magnetic susceptibility does not change much with grain size, anisotropy does. In particular, SDs exhibit a minimum K_3 parallel to the mineral's elongation axis. This is known as axis inversion and has led to numerous publications (Rochette et al., 1992).

Ferromagnetic susceptibility is therefore the potential sum of several ferrimagnetic (magnetite, pyrrhotite) and antiferromagnetic (hematite) phases with very contrasting properties, plus possible complications with grain size. The remanence anisotropy, usually modelled by a rank-2 tensor (but not necessarily verified in practice), allows only the ferromagnetic contribution to be measured. Studies carried out with remanence anisotropy generally give results fairly close to AMS, and in shales, we will see in the Lehigh Gap example, that the latter can make an original contribution.

Ferromagnetic s.l. minerals can strongly influence the magnetic susceptibility of a rock, consequently affecting further analytical interpretations. In shales, clay minerals constitute a significant proportion in terms of weight and volume. Nevertheless, even a small number of ferromagnetic grains can contribute significantly to the overall magnetic susceptibility of the rock. There are numerous examples in the literature where magnetite plays a pivotal role in the studied fabrics (Aubourg et al., 1995; Borradaile and Tarling, 1981; Bruijn et al., 2013; Housen et al., 1993; Lamarche and Rochette, 1987; Moreno et al., 2018; Oliva-Urcia et al., 2011).

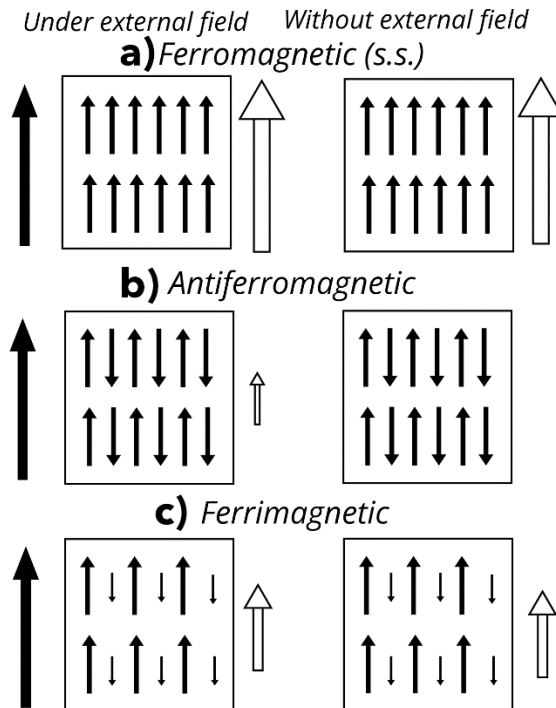


Figure 13: The detailed ferromagnetic (s.l.) behaviours include ferromagnetic (s.s.), antiferromagnetic, and ferrimagnetic. The black arrow represents the applied external field, and the white arrow represents the measured sample magnetization.

2.3.2 Mineral components of shales and their magnetic behaviour:

Diamagnetic minerals:

In shales, all minerals including quartz and calcite, have a diamagnetic component which is a universal phenomenon in matter. However, it should be noted that carbonates containing iron, such as siderite FeCO_3 or ankerite $\text{Ca}(\text{Fe, Mg})(\text{CO}_3)_2$, have paramagnetic susceptibilities.

Quartz	K (μSI) = -0.013 to 0.014	P = 1.01	T = 1	(Hrouda, 1987)
Calcite	K (μSI) = -0.013	P = 1.11	T = 1	(Rochette et al., 1992)

Table 1

These two minerals constitute a fundamental part of shales and can account for more than half the sample's weight, depending on the sedimentary conditions of the deposit. In the Sigüés area, it has been determined that these rocks contain between 60 to 87% of quartz and calcite (Boiron et al., 2020).

Paramagnetic minerals

Smectite / Illite	K (μSI) = 390	P = 1.2 to 1.6	T = 1	(Potter et al., 2004)
Chlorite	K (μSI) = 390-552	P = 1.2 - 1.7	T = 0.25-1	(Martín-Hernández and Hirt, 2003)
Pyrite	K (μSI) = 52	P = x	T = x	(Potter et al., 2004)
Siderite	K (μSI) = 3980	P = 1.56	T = -0.9	(Hrouda and Tarling., 1993)

Table 2

In a marine sedimentary basin, a context similar to that in which shales are deposited, the vast majority of minerals with paramagnetic behaviour corresponds to phyllosilicates. In a less abundant but frequent form, pyrite also appears.

Boiron et al., (2020) estimate that between 15 and 33% of the Sigüés shale is composed of phyllosilicates. According to Saur (2022), pyrite does not exceed 0.5% of the rock volume, and it does not contribute significantly to the magnetic susceptibility in shales.

Ferromagnetic minerals

In shales, ferromagnetic minerals are generally iron sulfides (greigite, pyrrhotite) and iron oxides (magnetite, hematite, and goethite). As we shall see later, for shales that have undergone advanced diagenesis, up to the beginning of the metamorphic domain, the dominant ferromagnetic mineral is magnetite. By comparison, we give hematite, magnetite and pyrrhotite to account for differences in magnetic susceptibility and anisotropy.

CHAPTER 2 - SHALE DEFORMATION

Hematite	K (μ SI) = 1300-7000	P > 100	T = ?	(Hrouda and Tarling, 1993)
Magnetite	K (SI) = 1-3	P = 1.1 - 3	T variable	(Rochette et al., 1992)
Pyrrhotite	K (SI) = 3.2	P > 1000	T variable	(Rochette et al., 1992)

Table 3

The magnetic minerals exhibit susceptibility ranges that are two or three orders of magnitude higher than those of the previous categories. When magnetic susceptibility typically exceeds 1000 μ SI, this indicates the large contribution of ferromagnetic minerals even when they are present in low proportion (often < 0.1%). In the following sections, some studies related to magnetic remanence anisotropy will be discussed.

2.3.3 Magnetic minerals in basin evolution

From the perspective of basin analysis, paramagnetic and ferromagnetic minerals undergo numerous mineralogical transformation (See review by Roberts, 2015 and references therein). Diagenetic processes drive the magnetic fraction of the shale. Some minerals in shales have revealed as reliable paleothermometric indicators (Freed, 1989; Hoffman and Hower, 1979; Kars et al., 2015; Nieto et al., 1996; Velde and Vasseur, 1992)

The process in which the magnetic evolution studied will be framed is as follows:

- Shales are deposited on the sea slope, in a deep (tens to hundreds meters below sea level (after Payros et al., 2006) and anoxic to euxinic environments.
- In the first meters of burial, there is an alteration of iron oxides (Roberts, 2015), principally driven by bacterial activity. Detrital ferromagnetic minerals such as magnetite, hematite, etc.. are mainly destroyed. The proportion of detrital magnetic minerals would be very low, tens of ppmv (parts per million volume). This story is no longer applicable when calcite content is > 50% (Aubourg et al., 2019) .
- Iron sulphides such as greigite or pyrrhotite are the product of early diagenesis, from the first few meters to one or two kilometres. Kars et al. (2015) also point out nanocrystalline goethite. These ferromagnetic phases could contribute to the measured susceptibility K.
- For burial temperatures between $\sim 60^{\circ}\text{C}$ and $\sim 100^{\circ}\text{C}$, i.e. at a depths higher than those where greigite and pyrrhotite are formed, magnetites in the superparamagnetic state (SP, <20 nm) form continuously. The formation of nano-magnetite corresponds to the start of illitization. In this range of burial temperature (the oil window state of maturity), the ferromagnetic contribution can be of importance in shales. Nano-magnetite formation has been identified in a very large number of basins at the same level of maturity, underlining the ubiquitous nature of this process in shales. This led Aubourg et al. (2012) to propose a geothermometer based on the appearance of these

CHAPTER 2 - SHALE DEFORMATION

nano grains, which they named MagEval in reference to the RockEval geothermometer.

- Between $\sim 100^{\circ}\text{C}$ and $\sim 300^{\circ}\text{C}$, the ferromagnetic fraction becomes very low, as shown by Aubourg et al. (2019) on the basis of shale studies. For rocks having a magnetic susceptibility on the order of $100 \mu\text{SI}$, this gives a magnetite contribution of $1\text{--}10 \mu\text{SI}$ (provided that magnetic susceptibility of magnetite is $\approx 1 \text{ SI}$) i.e. less than 10% of the magnetic susceptibility signal and the susceptibility ends up being mainly paramagnetic ($>90\%$). This very low magnetic fraction makes shales, in this temperature range, the rocks containing the fewest ferromagnetic minerals. Isothermal remanent magnetization (IRM) is very easy to obtain in the laboratory. When this IRM in shales is of the order of 10^{-6} to $10^{-5} \text{ Am}^2/\text{kg}$, we can give a burial temperature range of 200°C to 300°C .
- Between 300°C and 350°C , Aubourg et al. (2019) show an increase in the ferromagnetic contribution, with the coexistence of magnetite and monoclinic pyrrhotite. This temperature range is given by Raman spectroscopy (RSCM technique).
- Above 350°C , magnetite is no longer identified in shales, and pyrrhotite becomes the only ferrimagnetic mineral. Pyrrhotite can reach concentrations of the order of few percent, and it is therefore able to dominate magnetic susceptibility.

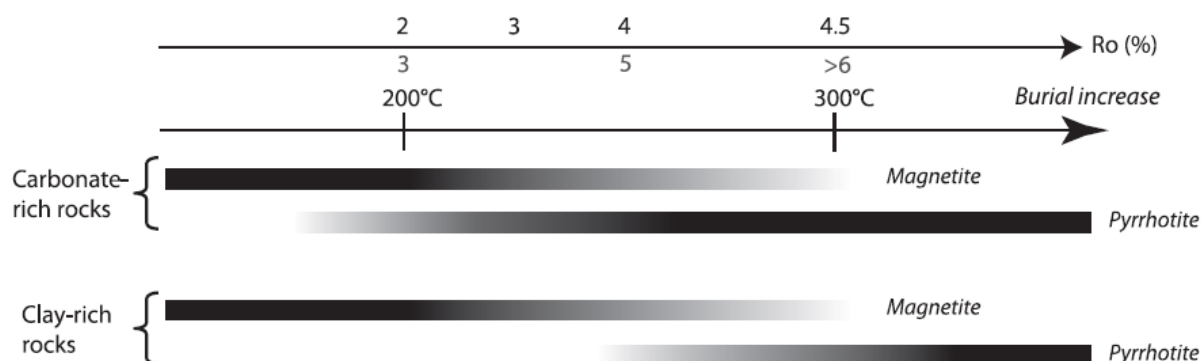


Figure 14. A simplified diagram illustrates the presence of ferromagnetic minerals such as magnetite and pyrrhotite in clay-rich rocks within a burial range of $200\text{--}300^{\circ}\text{C}$. It also includes data on vitrinite reflectance (R0). The calibrations used in this diagram are based on the work of Sweeney and Burnham (1990) and Vassoyevitch (1970). From Aubourg et al. (2019).

- Simultaneously, the diagenetic evolution of phyllosilicates should be described. The most well-documented transformation is illitization, which involves the conversion of smectite into illite. Illitization has been widely used as an indicator of diagenetic processes (Hoffman and Hower, 1979; Hower et al., 1976; Moore and Reynolds, 1997; Reynolds and Hower, 1970; Weaver, 1989). This transformation typically initiates around 60°C , with complete illitization often occurring at approximately 150°C (Hower et al., 1976). However, some geothermometry models, such as those proposed by Horffman and Hower (1979), suggest a broader temperature range, of 50°C to

CHAPTER 2 - SHALE DEFORMATION

180°C. It is important to note that various geochemical and diagenetic factors can influence this evolution

- At higher temperatures (above 210-230°C), approaching the metamorphic domain, chlorite appears and grows at the expense of illite (Hirt et al., 2004). It would be expected that the dominant clay contribution in a shale in the gas window (120-220°C) would be illite (Figure 15).

This theoretical process accounts for the mineralogy observed in sedimentary basins of the type studied in this thesis. The magnetic composition and behaviour align with findings from rock magnetic analyses conducted on the same shale unit (Larrés and Pamplona Fm) of the Jaca Basin (Boiron et al., 2020; Pueyo-Anchuela et al., 2013b), which will be presented in detail in section 4.1.1 Shale mineralogy.

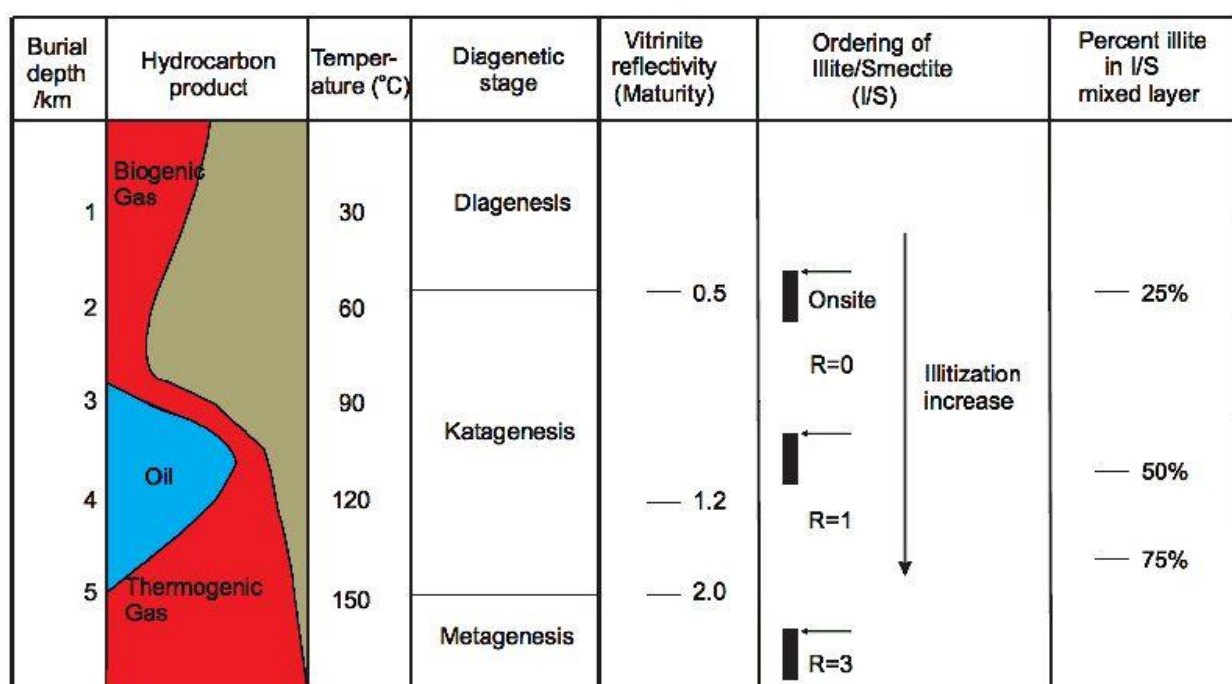


Figure 15: Depth model detailing vitrinite maturity evolutions, illitization stages and I/S percentages; compared to burial temperature, diagenetic stages and expected hydrocarbon product. Taken from Jiang (2012) and references therein.

Despite the complex kinetics involved in the formation and disappearance of these authigenic minerals, observations in the Jaca basin studied in this thesis reveal that the paramagnetic signal accounts frequently for more than 90% of the total (Boiron et al., 2020; Pueyo-Anchuela et al., 2011b). This implies that for shales with magnetic susceptibility ranging from 100 to 300 μSI , the contribution of ferromagnetic minerals is minimal. This mineral assemblage, in conjunction with the specific burial conditions and the measured susceptibilities within this range, can be referred to as the 'illite window'.

Therefore, understanding the genesis of these minerals and how the obtained magnetic signal reflects the geological history of the diagenetic environment, becomes crucial.

CHAPTER 2 - SHALE DEFORMATION

To summarize the above observations, for shales buried between 150°C and 250°C, it is possible to be predictive about magnetic properties, as we will see later in this thesis. These are:

- A ferrimagnetic fraction carried by authigenic magnetite essentially in the superparamagnetic state, with very low concentrations, between 10 and 100 ppmv.
- A clay fraction is largely dominated by illite and, to a much lesser extent, chlorite.
- The magnetic susceptibility is largely dominated by the paramagnetic fraction of authigenic and detrital clays.
- This assemblage has been verified in numerous basins, but the calcite content in the rock seems to be a disruptive element. Magnetite in this case seems to be better preserved.

2.3.4 The measurement of magnetic anisotropy.

This thesis relies on room temperature measurements (abbreviated as RT) of low-field magnetic susceptibility to analyse the samples. Another type of magnetic anisotropy is remanence anisotropy, which is associated with ferromagnetic particles, their internal arrangement, and particle size. Two classical types of remanence are used: the Anhyseretic Remanent Magnetisation (ARM) and the Anisotropy of Isothermal Remanent Magnetisation (AIRM).

In both techniques, a magnetic field is applied to a sample at various orientations. This applied field induces magnetization in the particles within a specific range of coercivities. Typically, it is the ferromagnetic fraction of the magnetic particles that responds to this range, resulting in a spatial analysis of this sub-fabric.

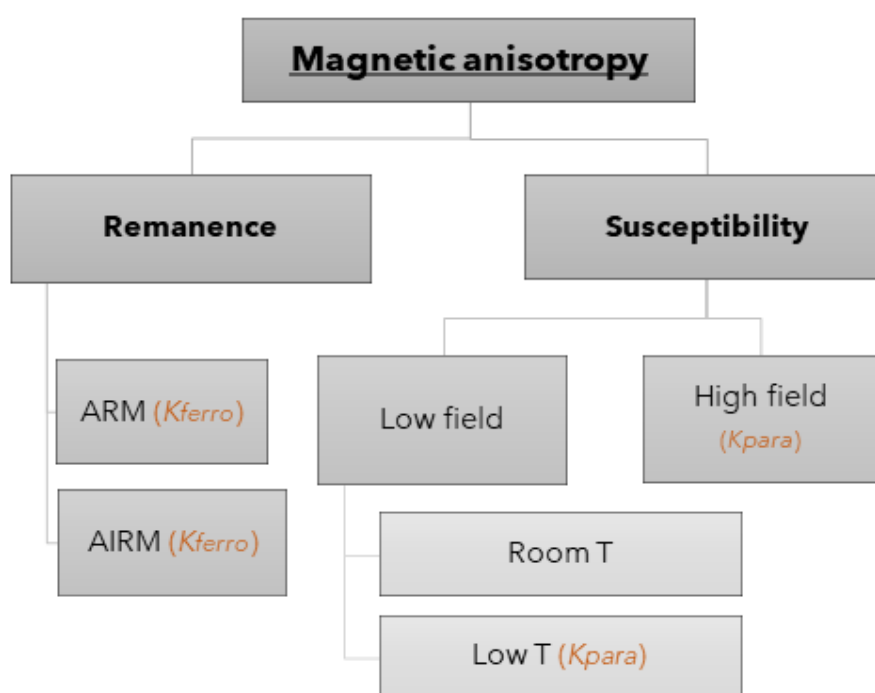


Table 4: Various type of magnetic properties measurements, focusing on anisotropy.

2.3.5 Anisotropy of magnetic susceptibility in shales.

The anisotropy of low-field magnetic susceptibility (AMS) is approached mathematically by a symmetrical second order tensor K_{ij} (Nye, 1957). From the matrix, the three diagonal values K_i are extracted, corresponding to the maximum, intermediate and minimum principal susceptibilities, $K_1 \geq K_2 \geq K_3$. This tensor is represented by an ellipsoid that in its turn is a 3D view of the bulk fabric. The bulk fabric averages the total magnetic contribution of billions of magnetic grains (Figure 16).

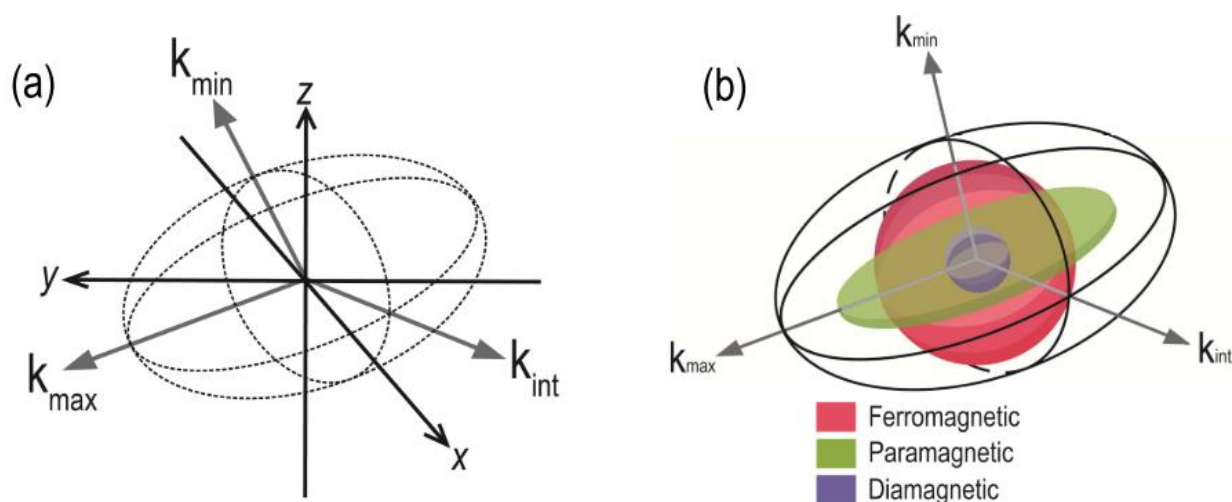


Figure 16: Magnetic ellipsoid, and its three main axes. K_{max} equals to K_1 , $K_{int} = K_2$ and $k_{min} = K_3$ respectively. From García-Lasanta (2016)

Magnetic susceptibility is controlled by the mineral composition of the sample. Each contributing mineral has its own intrinsic properties and preferred orientation. For example, if magnetite dominates the magnetic susceptibility, the maximum theoretical anisotropy will not exceed 40%. Conversely, if pyrrhotite dominates the signal, the theoretical maximum anisotropy will be 2 to 3 orders of magnitude higher. It is therefore not easy to interpret the AMS without precise knowledge of the magnetic carriers.

The magnetic carriers exhibit specific spatial distributions (SPO, CPO), which can range from planar and stretched to isotropic and tilted. Consequently, AMS offers an averaging of the petrofabric orientation, even when it is faintly detectable, complementing kinematic and structural indicators that may not always be easily observable or measurable directly in the outcrop (Oliva-Urcia et al., 2012; Pueyo Anchueta et al., 2010b).

Early studies confirmed that induced magnetization was easier in some significant directions, parallel to bedding or the tectonic foliation (Graham, 1954; Ising, 1942). Interesting examples are shown by Fuller (1963) who exposed commentaries on the relationship between the AMS and the frequency distribution of minerals and Jelínek and Kropáček (1978) whose fundamental contribution on the correct statistical characterization of the obtained tensors is a milestone in this issue. Their parameters for the description of

CHAPTER 2 - SHALE DEFORMATION

magnetic anisotropy are very detailed from the geometrical point of view. Subsequently, numerous studies have developed a working methodology that defines the AMS as a method for determining petrofabrics (Hrouda, 1987; Tarling and Hrouda, 1997). At the same time, numerous papers considered in detail the contribution of diamagnetic, and to a larger extent, paramagnetic mineral phases (Borradaile, 1988; Daly, 1967; Henry and Daly, 1983; Lamarche and Rochette, 1987)

The orientation of K_i axes of AMS tensor (represented generally using a stereoplot), are statistically constrained by errors at 95% confidence (Jelínek and Kropáček, 1978) . The use of an ellipsoid to characterize magnetic fabrics is analogous to the concept of a deformation ellipsoid used in structural geology. However, it is important to note that these two ellipsoids are not inherently equivalent (Borradaile and Jackson, 2010; Lüneburg et al., 1999; Parés and van der Pluijm, 2004a). Most AMS studies applied to rock deformation use terms such as "foliation" or "lineation" with the adjective "magnetic" to geometrically describe the principal planes and axes of the magnetic ellipsoid and their orientations, as well.

To represent and compare the anisotropy of the second rank tensors of magnetic susceptibility, several parameters have been defined. In this thesis, as in a large majority of works, the following parameters are used:

The mean magnetic susceptibility (K_m):

$$K_m = \frac{(K_1 + K_2 + K_3)}{3}$$

Equation 7

K_m is a proxy for magnetic mineral content.

The degree of anisotropy parameter (P):

$$P = \frac{K_1}{K_3}$$

Equation 8

It is common to find in scientific papers the corrected degree anisotropy parameter P_j (or P'), defined as:

$$P_j = \exp^2 \sqrt{2[(n_1 - \eta)^2 + (n_2 - \eta)^2 + (n_3 - \eta)^2]}$$

Equation 9

Where n_x represent $\ln(k_x)$ for each axis and η is the arithmetic mean between those n_x

The magnetic lineation (L):

$$L = \frac{K_{max}}{K_{int}}$$

Equation 10

CHAPTER 2 - SHALE DEFORMATION

The magnetic foliation (F) :

$$F = \frac{K_{int}}{K_{min}}$$

Equation 11

The parameters L and F are generally used in a Flinn diagram, to give an analogy with the shape of the deformation tensor $\mathbf{\epsilon}$ (ϵ_1/ϵ_2 vs. ϵ_2/ϵ_3).

The shape parameter (T):

$$T = \frac{\ln F - \ln L}{\ln F + \ln L}$$

Equation 12

T varies from -1 (prolate, cigar-shape) to +1 (oblate, disc shape).

It is common practice in the literature to associate P (or Pj) and T in a diagram known as the Jelinek diagram (Figure 17). This representation allows us to see both the degree of anisotropy and the shape of the ellipsoid. We will use this representation to illustrate the evolution of a fabric in deformed shales.

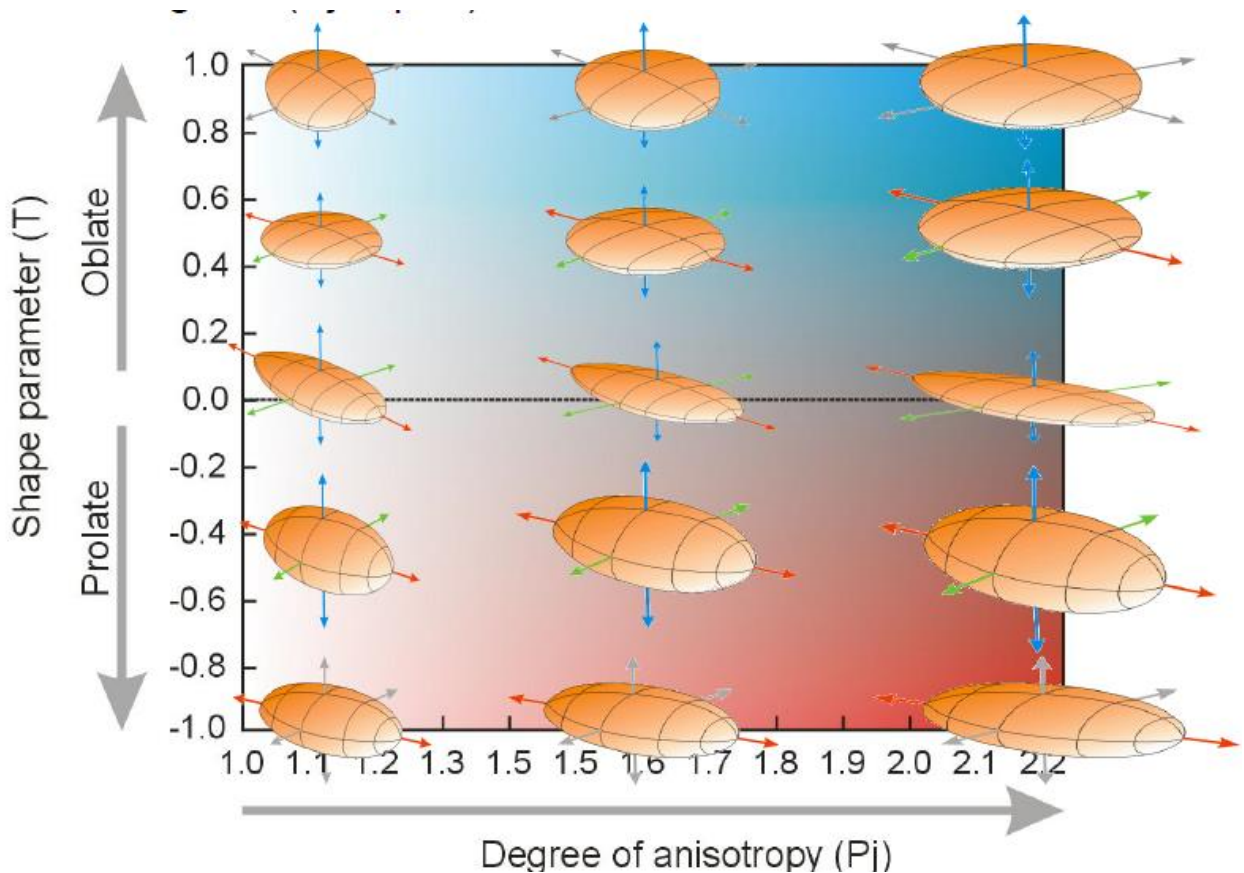


Figure 17: Jelinek's table for scalar parameters. The geometry of ellipsoids is drawn at different positions of the table. Figure from AGICO (2019)

CHAPTER 2 - SHALE DEFORMATION

These scalar parameters provide valuable information. The degree of anisotropy P (or P_j) serves as a proxy for fabric organization. It became evident that this parameter is strongly influenced by the magnetic mineralogy and can be affected by various sources of magnetic minerals with differing properties (Rochette et al., 1992). The intrinsic degree of anisotropy, denoted as P_i , for certain magnetic minerals has a restricted range.

For instance, illite typically has an intrinsic degree of anisotropy, P_i in the range 1.3-1.7 (Tarling and Hrouda, 1997; Debacker et al., 2004). Therefore, the degree of anisotropy in rocks with a high clay fraction is inherently limited by this intrinsic value, up to ~ 1.7 . Magnetite, whose anisotropy is governed by the shape of the mineral, has an intrinsic anisotropy of the order of $P \sim 1.3$, making it comparable to illite and chlorite. This contrasts with the intrinsic value of hematite and pyrrhotite, which can exceed the value of 100. Figure 18 shows the theoretical degree of anisotropy according to the preferential anisotropy degree of classic magnetic minerals. For clay minerals such as chlorite or illite (structurally close to muscovite), it can be seen that, for example, 50% of the minerals aligned according to bedding will have a resulting degree of anisotropy is of the order of 1.05 to 1.08. These values are classically observed in shales.

Another significant scalar parameter is the shape parameter T , which proves particularly useful in the context of shales (Parés, 2015; Parés et al., 1999). Whereas the parameter P is a convolution of the intrinsic properties of minerals and their preferential orientation, the shape parameter T better reflects the preferential organization of minerals. We will see from examples taken from the literature and from our results that T is very sensitive to the loss of preferential orientation when moving from a vertical compaction regime (diagenesis) to lateral compaction (Layer Parallel Shortening, LPS).

In general, phyllosilicates, which constitute one of the primary mineral components in shales (as indicated, with their magnetic properties, in Table 2), tend to exhibit highly oblate shapes in their magnetic anisotropy ellipsoids, often exceeding 0.9. However, it is important to consider that these magnetic parameters can be changed when a significant ferromagnetic contribution is present. Martín-Hernández and Hirt (2003) noted that the degree of anisotropy is governed by the iron and manganese cations within the crystals, with the P_j parameter increasing as the material displays a stronger ferrimagnetic behaviour.

CHAPTER 2 - SHALE DEFORMATION

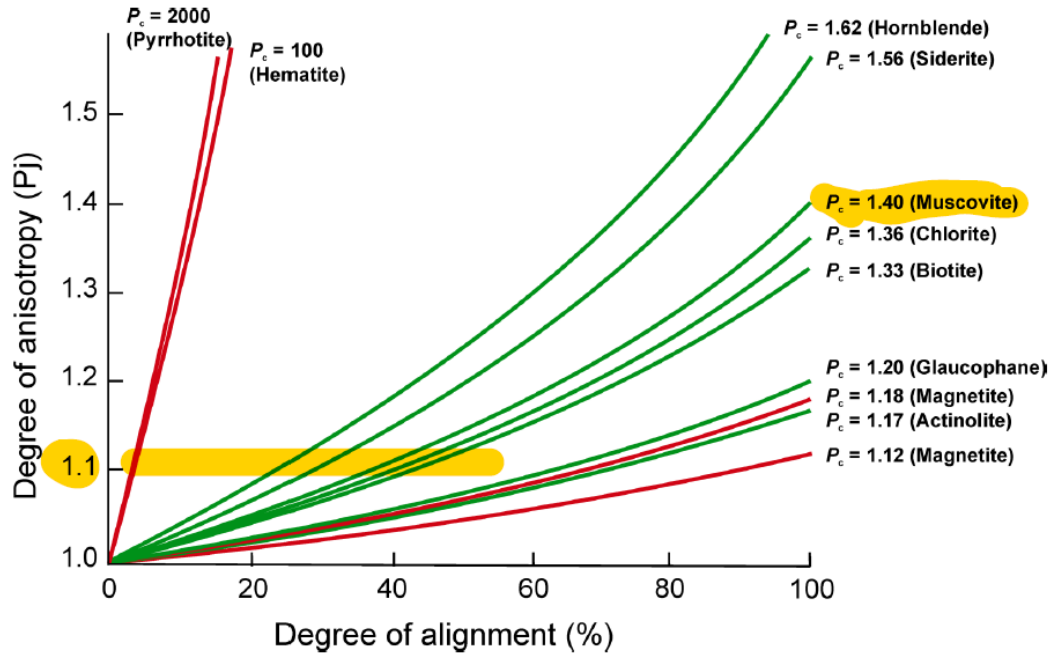


Figure 18: Degree of rock magnetic anisotropy as a function of preferred orientation of its minerals. Muscovite (Illite) is highlighted. From AGICO (2019)

The intrinsic properties of minerals can be dictated by the shape of the mineral (SPO), as in the case of magnetite, or by the crystal lattice (CPO), as in the case of phyllosilicates (Figure 19). In the latter case, the anisotropy of shape and crystal lattice coincide.

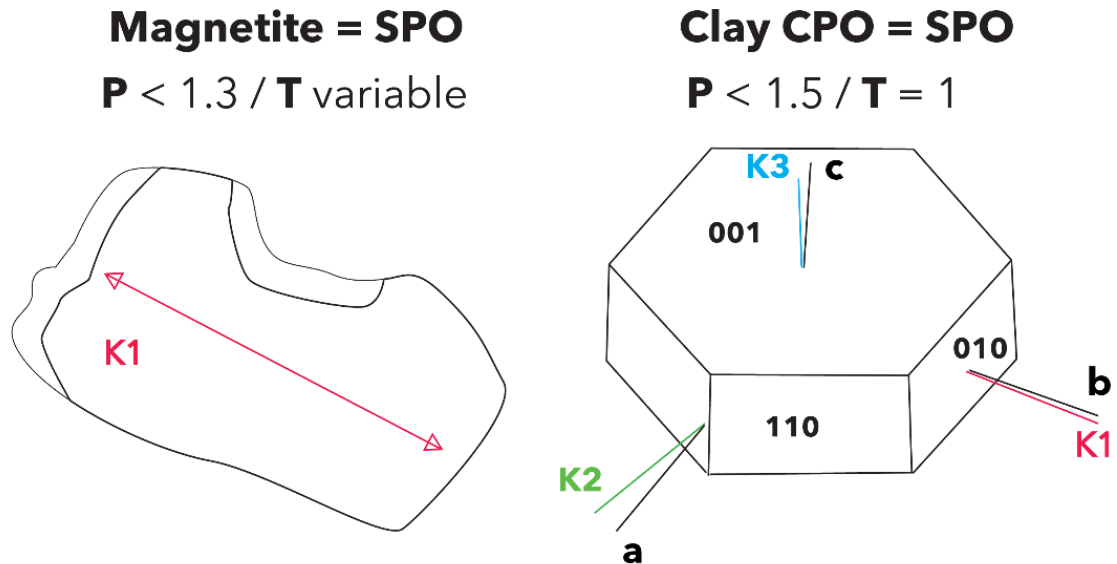


Figure 19: Magnetite can condition the SPO of a sample in AMS, measurements, regardless of its CPO. Meanwhile, in a hypothetical sample governed by clays, it is interpreted that the CPO of the clay is also detectable in the measurement of the magnetic fabric, and the AMS could be punctually equated to the CPO as well.

The measurement of AMS can be applied to the context of this PhD study, particularly to predict planar fabrics like bedding and cleavage (as demonstrated in the influence of cleavage on shale fabric). Scalar parameters within a primarily paramagnetic fabric

CHAPTER 2 - SHALE DEFORMATION

containing minerals such as muscovite can provide insights into the degree of alignment (as depicted in Figure 18). This alignment can be related to how petrofacies are influenced by the disposition of particles during deposition.

Furthermore, some authors define the fabric as a detailed analysis of rock structure that considers crystallographic orientation (Goguel, 1965). The increasing use of this term in the literature is closely linked to advancements in measurement techniques for fabric analysis and their automation. In recent years, techniques such as X-ray goniometry, Electron Backscatter Diffraction (EBSD), and microtomography, which assess the preferred crystallographic orientation of groups of grains, have become more accessible and widely used.

The developments in the techniques and devices for the measurement and analysis of magnetic fabrics (Jelinek, 1977) preceded the widespread use of this technique in different tectonic contexts. Susceptibility bridges, the laboratory tool used to obtain magnetic fabrics, have evolved since the 1960s (see the AC susceptibility bridge by Girdler, 1961) until today (see KLY-5 Kappabridge by AGICO) facilitating the measurement of thousands of samples in a rapid manner

Different measurements strategies have been adopted over time to measure AMS.

1) To optimise the measurement, rapid rotation (of the order of 10 Hz) of a 10 cm³ cylindrical sample was chosen. During rotation, the theoretical signal is that of a sine in 2θ , which makes it possible to obtain maximum (M_{\max}) and minimum (M_{\min}) induced magnetisation in the plane parallel to the axis of rotation. To solve the tensor, 6 values are required, so a minimum of three perpendicular planes are used. Although very popular, this technique has shown limitations linked to the shape of the sample. To simplify, the maximum susceptibility is deviated towards the long axis of the core when the sample is weakly anisotropic.

2) Rather than rotating the sample, Agico proposed an impedance bridge that enabled magnetic susceptibility to be measured very sensitively (10^{-8} SI). To solve the tensor, Agico proposed a redundancy of measurements (15 measurements) which made it possible to obtain the tensor with a reliable statistical description (Jelínek and Kropáček, 1978). This step enabled a threshold to be crossed in the detection of fabrics with very little anisotropy. For example, it was possible to detect a magnetic lineation even though the anisotropy in the magnetic foliation plane was low ($L < 1.05$). The advantage of the impedance bridge is that the magnetic field inside is very uniform. This means that every part of the sample, whatever its position, is subject to the same field. The shape of the sample does not therefore control the axes of magnetic susceptibility, as the spinner did. AMS users are generally unfamiliar with this point, as the shape of the sample must be perfectly cylindrical to optimise the measurement. We will see that the highly variable shape of the shale fragments we are going to study does not change the value of scalar data such as P and T, to name but two parameters.

3) In the 2010s, Agico proposed a hybrid version of the measurement, combining the famous impedance bridge and slow sample rotation (1 Hz). This approach has made it possible to increase sensitivity since, in the rotation plane, the maximum and minimum susceptibility can be determined by inverting the 2θ signal. Today, this approach, coupled with an

automatic sample holder, enables the tensor of a sample weighing just a few grams to be measured in a few minutes, as we shall see in the course of this thesis.

2.3.6 Magnetic fabric evolution in shaly rocks

A common feature in most of these studies is the recognition that AMS can capture the preferred grain orientation in sedimentary rocks, even in the absence of macroscopic strain indicators, and even before embryonic cleavage becomes apparent. Overall, the study of AMS has made substantial contributions to our understanding of deformational processes in mudstones, as it is summarized in the following paragraphs. The Figure 20 summarizes different scenarios as found in the literature (Borradaile and Henry, 1997; Borradaile and Jackson, 2010; Parés, 2015; Pueyo-Anchuela, 2012a; Soto et al., 2022). In this scheme, we specify whether the shales are syn-rift or pre-syn-tectonic.

Syn-rift shales can undergo both extensive and compressive deformation, whereas pre- and syn-orogenic shales will generally only undergo compressive tectonics.

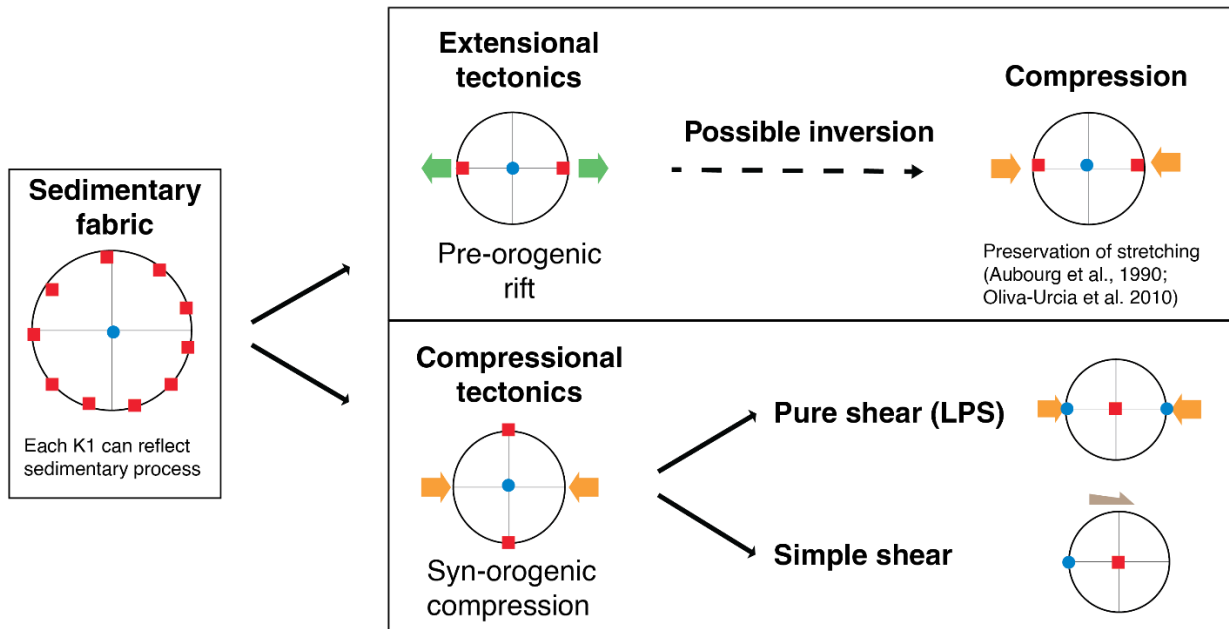


Figure 20: Magnetic fabric cases for various tectonic evolutions.

- **Sedimentary fabric** (Figure 20): The sedimentary fabric results from the combined action of sedimentary processes during deposition (See section 2.2 Shale fabric) and vertical compaction during diagenesis. In this process, magnetic foliation is controlled by bedding (K3 perpendicular to bedding). Magnetic lineation can be very poorly constrained, and if several sedimentary beds are sampled, the K1s may be distributed almost randomly within the plane of magnetic foliation. It is possible, as an exception, that the K1 measurements show some sedimentary lineation parallel to structures such as scour marks or flutes, revealing traction processes, where the grains would indicate paleocurrents (Parés and Van Der Pluijm, 2002; Soto et al., 2009). This type of fabric, that can be found in sandy and silty deposits associated

CHAPTER 2 - SHALE DEFORMATION

with alluvial fans or fluvial activity is quite rare in shales, which are very sensitive to deformation.

- **First tectonic imprint conditioned by extensional tectonics:** The extensional period is favourable to the formation of basins that will undergo extensive processes. Other tectonic contexts can also favour this extensive environment, such as the back-arc basins of subduction zones. Here, we consider the case of shale deposition in this type of environment, i.e. as soon as they are deposited, these sediments will be subject to extension. In these basins, the initial imprint on the magnetic fabric has been detected, with K1 being parallel to the direction of regional stretching (Caricchi et al., 2016; Cifelli et al., 2004; Faccenna et al., 2002; Mattei et al., 1999). The magnetic lineation appears in apparently undeformed (at the macroscopic scale) clayey sediments. In these studies, it is demonstrated that the magnetic lineation reflects the extensional process, starting from an initially oblate sedimentary fabric and progressively evolving into a triaxial-to-prolate ellipsoid as a consequence of stretching. The progressive loss of magnetic foliation, which is reflected by the change in the T parameter from oblate to prolate, can be visualised as follows. If we take a sheet and pull on each side, we will see undulations parallel to $\delta 3$, the minimum stress. Magnetic foliation tends to monitor this pattern.
- **Preservation of stretching lineation on compressional tectonics:** (for a synthesis see García-Lasanta, 2016). A basin can change from an extensive regime to a compressive regime, particularly in the context of an orogen. In the Pyrenees, many Upper Cretaceous basins have been inverted in this way. The initial extension is visible both macroscopically (boudinage) and microscopically (N-S stretching lineation). This extension took place during a high temperature phase, which led to very intense syn-rift metamorphic conditions. Compression is manifested by thrusts, folds and sometimes a second cleavage. In these basins, like the Mauléon Basin, Oliva-Urcia et al. (2010) demonstrated that some extensional fabrics are preserved in Albian shales. A similar example illustrating this transition, with better preservation of extensional fabrics (attributed to the limited development of cleavage) is presented by Oliva-Urcia et al. (2013) in the inverted basin form (Basque-Cantabrian basin, Western Pyrenees), see Figure 21.

CHAPTER 2 - SHALE DEFORMATION

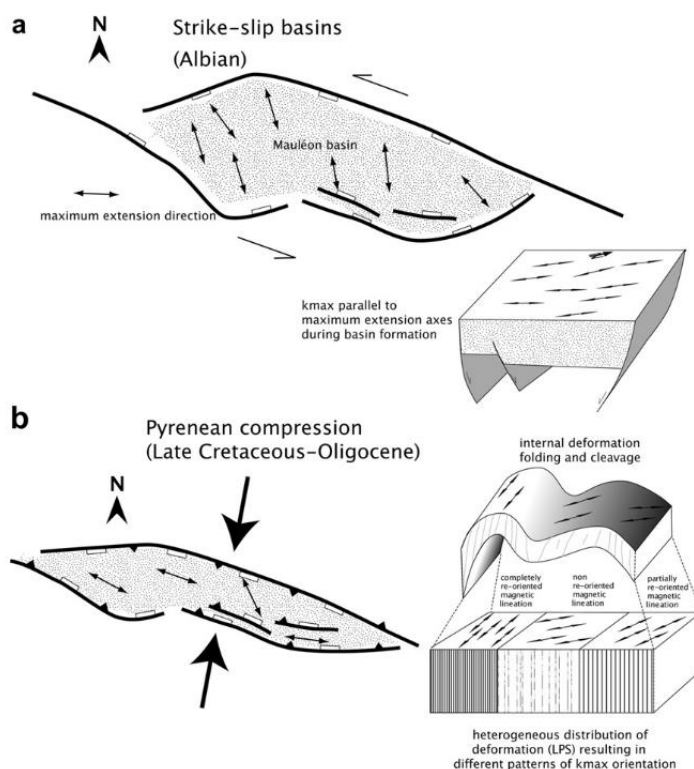


Figure 21: From Oliva-Urcia et al. (2013). Inversion of basin and evolution of magnetic lineations.

- **First tectonic imprint on compressional tectonics:** During an orogenic phase, a foreland basin generally develops and gradually deforms. In this type of basin, the sediments resulting from erosion are syn-orogenic, and will be impacted by compressive deformation. The term "weakly deformed shales" is related to the **first tectonic imprint** of a sedimentary sequence under compression. It was introduced in articles by Borradaile and Tarling (1981) or Kissel et al. (1986). Kissel et al. (1986) conducted an AMS study on shales from non-metamorphosed marine sequences in Greece and Taiwan. Borradaile and Tarling (1981) studied Devonian slates from Germany that had experienced deformation and underwent low-grade metamorphism during the Variscan orogeny. These slates show a fine, penetrative cleavage. Specifically, the authors highlight the existence of sites where a magnetic lineation is oriented perpendicular to the principal compressional stress axis, σ_1 , while the K3 axis is perpendicular to bedding. Kissel et al. (1986) is considered as the first study of the alignment of the K1 axis during the early stages of compressive deformation, even when such alignment cannot be discerned through macroscopic observations of the rock. Since then, numerous studies have confirmed the extraordinary ability of AMS to capture these early orogenic events in shales (Branellec et al., 2015; Oliva-Urcia et al., 2009; Soto et al., 2016; Weil and Yonkee, 2012)
- **Gradients of pure shear, LPS:** While the early appearance of tectonically induced magnetic lineation has been identified in both extensional and compressional basins, magnetic foliation will also change. Under compression, Averbuch et al. (1992) are, to our knowledge, the first to have established four major changes during lateral compaction, named also Layer Parallel Shortening (LPS). From a sedimentary fabric (Type 1), they document an intermediate fabric with the K1 axis perpendicular to

CHAPTER 2 - SHALE DEFORMATION

compression (Type 2). They then define a so-called tectonic fabric, with progressive loss of the magnetic foliation initially parallel to stratification (Type 3). This fabric may evolve into a completely cleavage-controlled fabric (Type 4). This type of evolution has been widely observed in clastic-type sediments such as the Vitrolian facies in the Eastern Pyrenees (Frizon de Lamotte et al., 2002; Robion et al., 2007; Souque et al., 2002) or the Agha Jhari fluvial facies in Iran (Aubourg et al., 2004; Bakhtari et al., 1998).

Parés et al. (1999) and Parés (2015) documented a similar evolution in shales from the Southern Pyrenean Foreland, further East. A complete cross-section was presented illustrating the magnetic fabric evolution for non-metamorphosed mudrocks subjected to Layer Parallel Shortening (Figure 22). Sampling of geological units with outcrops extending over several kilometres allowed the identification of deformation gradients, which were subsequently confirmed by magnetic fabric analysis. This model encompasses three types of magnetic fabrics that develop in weakly deformed mudrocks undergoing progressive deformation: cleavage free, pencil cleavage and “cleavage” *s.s.* This evolution has served as a starting point for other authors in recent years (Aubourg et al., 2004; Oliva-Urcia et al., 2009; Pueyo Anchueta et al., 2010b; Robion et al., 2007; Weil and Yonkee, 2012).

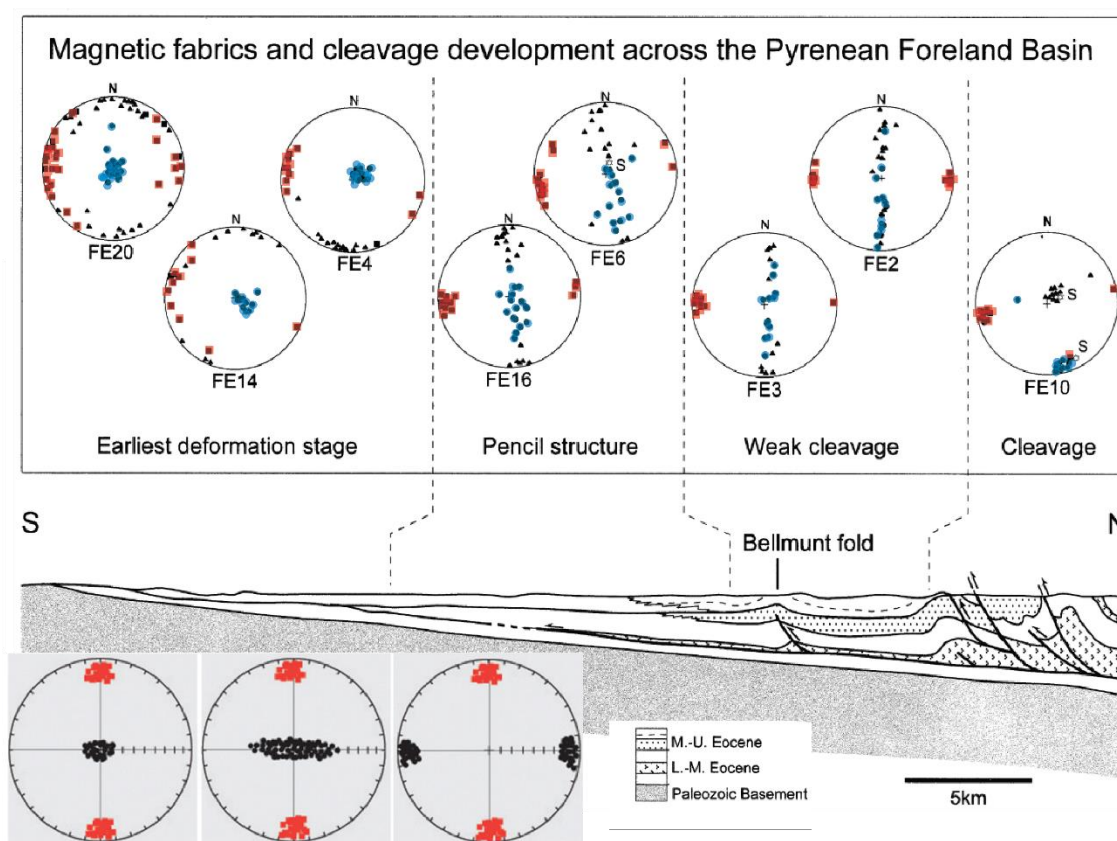


Figure 22: Model for evolution of LPS magnetic fabrics by Parés et al. (1999). Bottom left, there are modelized stereoplots by Parés (2015) for early compression fabrics. Top plots are from Eastern Pyrenees measurements: K1 are in red, while K3 are highlighted in blue.

The phases of this evolution are as follows (Figure 22). The K1 axis in the initial stage does not show a preferred direction, but it lies rather randomly in the bedding plane, and therefore distributed within a girdle. The K3 axes, meanwhile, are well clustered

CHAPTER 2 - SHALE DEFORMATION

for the set of samples, and corresponds to the pole of the bedding in the initial stage, arranged in a vertical position by the compaction of the sampled rocks. This matches with sedimentary fabric (Figure 20) and type 1 of Averbuch et al. (1992). It should be noted in passing that site FE4 already shows an E-W magnetic lineation linked to Pyrenean compression. If we were to combine the 3 sites, the mean lineation would also be E-W, and would therefore reveal the early stages of Pyrenean compression. We are therefore on the borderline between a purely sedimentary fabric and an LPS-type fabric. In the classification of Averbuch et al. (1992), these three sites would correspond to a stage 1-2.

During this early stage of deformation, the K1 axes define a magnetic lineation that is sometimes not detectable at the macro- or mesoscopic (or even the microscopic) scale in the rocks but is well reflected in the magnetic fabric. As the shortening progresses, the K1 remains perpendicular to the shortening direction. This would correspond to the intersection lineation at the mesoscale, when it is expressed. It is from an intermediate degree of shortening, corresponding to pencil cleavage, that a girdle can be detected in the distribution of the population of the K3 axes. It is at this stage that the magnetic fabric can be considered to be imprinted by tectonics (fabric of type 3 of Averbuch et al., 1992).

This girdle increases in size as the deformation increases, until in samples where the cleavage is penetrating, as in the case of slaty cleavage, it is possible to detect the K3 axes completely controlled by the cleavage and clustered around its pole (fabric of type 4 from Averbuch et al., 1992).

- **Simple shear on compressional tectonics:** Examples of shearing can be found in the limbs of folds or associated with faults. Such fabric types have been interpreted on the Chelungpu fault (Chou et al., 2020) where the magnetic foliation is oblique to the gouge plane. In a different way, but also related to fault shear, Marcén et al. (2018) find that in S-C shear structures the magnetic lineation coincides with the intersection of these planes, in the Gavarnie fault zone in the Axial zone of the Pyrenees.

This non-exhaustive overview of magnetic fabric in shales shows that they are very sensitive to deformation. This has led Aubourg et al (1991), for example, to speak of 'cryptic' fabrics, since no counterpart is visible on a macroscopic scale. All these geometries (Types 1 to 4) have been observed by numerous teams, and it is therefore possible to predict the evolution of these fabrics. In a deformed foreland domain, shales will respond very quickly to the development of the LPS. We will see from examples in the Pyrenees that the LPS can be detected up to several tens of km from the last emerging thrust. However, although the direction of the LPS has been extensively studied by various teams (Anastasio et al., 2016; Humbert et al., 2014; Pocoví Juan et al., 2014; Pueyo Anchuela et al., 2010a; Weil and Yonkee, 2012), it provides little information for the structural geologist, as this direction is found in other markers (fold axes, fracturing, stylolites, to name but a few). Scalar information, on the other hand, has received little attention. This is the subject of the next section. It would indeed be possible to calculate a deformation rate, which is much more difficult to obtain. Are we talking about a few percent of LPS, 10% or more?

2.3.7 AMS as a strain gouge, conditions of use.

CHAPTER 2 - SHALE DEFORMATION

Shales are of significant scientific and economic interest due to their commonly ductile behaviour, making them able to preserve the effect of weak stresses or weak deformational features. The primary manifestations of matrix damage are fissility, pencil structures and cleavage. Cleavage was extensively studied between the 1970s and the 1990s, and its interest is demonstrated by the huge number of works analysing this issue (Alvarez et al., 1978; Elliott, 1976; Holl and Anastasio, 1995; Marshak and Engelder, 1985; Mitra, 1987; Powell, 1979; Rutter, 1983; Tullis, 1976... among many others).

So, what is the contribution of AMS to the study of petrofabric in shales? Classical structural strain analysis involves examining indicators in field exposures, polished samples or thin sections. As mentioned earlier, the relationship between AMS axis and structural orientations has been proposed since the mid 20th century (Balsley and Buddington, 1960; Ising, 1942). Many of the classical methods for determining the deformation or general rock fabric require the presence of pre-tectonic markers at the microscopic or mesoscopic scale and a sufficient number of samples for adequate representativeness and 3D reconstruction of the deformation ellipsoid. In contrast, magnetic fabrics offer the advantage of analyzing a large number of sites and samples, thereby providing a higher level of representativeness for the distribution of deformation along and across sedimentary basins. Comparison between the magnetic and visual methods has been a good way of obtaining additional information about the origin of fabrics. For instance, Borradaile and Tarling (1981) used worm tubes as strain markers in addition to AMS (Figure 23).

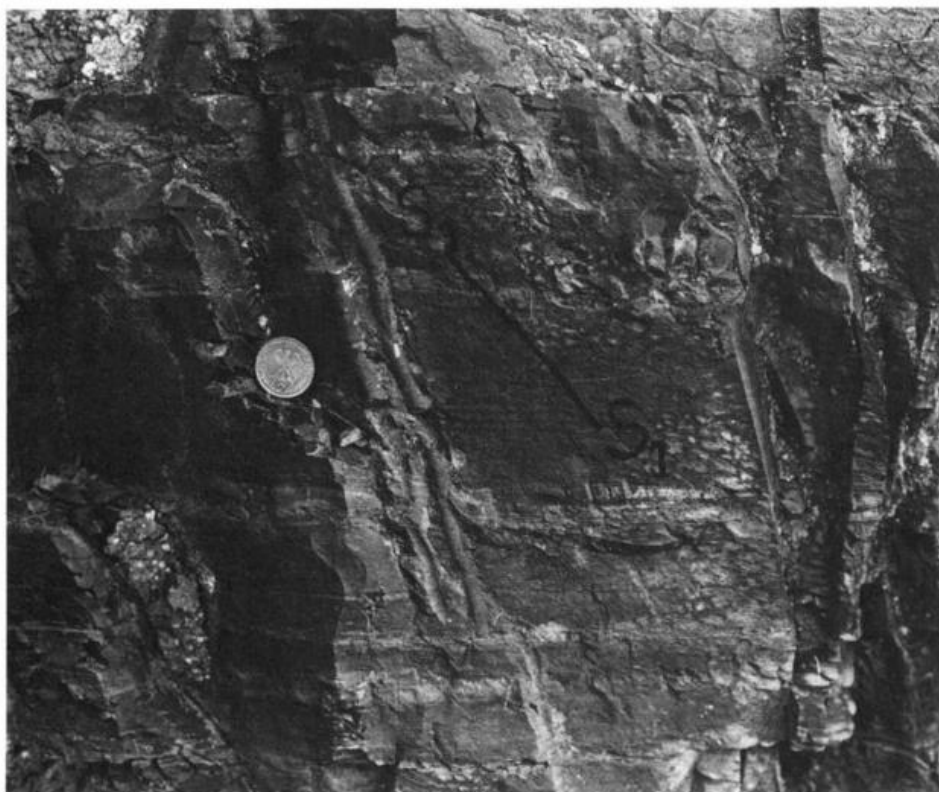


Figure 23: Worm tubes are used as a strain marker in Borradaile and Tarling (1981)

Nevertheless, converting AMS data into a quantitative estimate of strain or a measurable deformation parameter has been a subject of debate in the study of magnetic fabrics.

CHAPTER 2 - SHALE DEFORMATION

Understanding the internal deformation mechanisms of shales is a prerequisite for establishing a model to explain the measured magnetic fabrics and their translation into strain quantification. In this respect, there is a significant difference between rocks in which the metamorphic grade allows for the growth of mineral grains (para-, ferro- or diamagnetic) and rocks in which the magnetic (and tectonic) fabric results either from the re-orientation of components within the rock or from the concentration of specific ferro- or para-magnetic minerals within the preferred anisotropy surfaces. In this PhD the evolution of shales in diagenetic conditions is the chosen environment, and therefore only the re-orientation mechanisms are discussed.

Some bibliographical references that have dealt with this problem will be presented in the next paragraphs. Beforehand, Hrouda (1993) listed several theoretical models:

- The **passive model**, assumes that there is no viscosity contrast between the magnetic particles and the matrix, so the magnetic grains deform in the same way as the matrix. This model is a magnetic equivalent of the Ramsay strain model.
- The **ductile model**, assumes that the magnetic particles and the matrix have different viscosities, with the difference that the deformation of each part depends on the viscosity contrast between them. The ductile model was developed only for strain conditions that give rise to rotational ellipsoids.
- The **“flat-line” model** assumes that magnetic particles behave as lines or planes in a homogeneously deformed material. During deformation, the particles do not change their shape, only their orientation, and this change of orientation is independent of the shape of the particle. A graphic representation of this model can be seen in the Figure 24 taken from Borradaile (1988). This is known as the March model, from March (1932). For mathematical reasons, the grains are simplified to spheroidal particles.
- Finally, **the viscous model** assumes that during rock deformation, the magnetic grains behave as isolated rigid particles embedded in a slowly flowing viscous liquid. The particles do not change their shapes, but they do change their orientations, depending on the shape of the particle. Spheroidal shapes for the particles are also assumed.

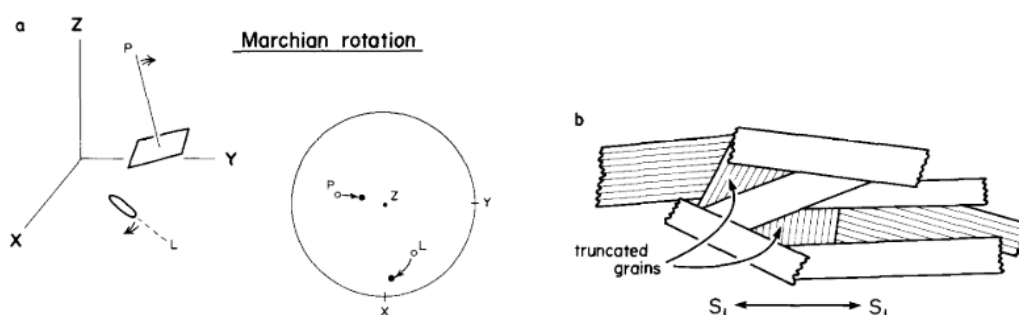


Figure 24: Geometry of March model and rigid rotation of bodies. From Borradaile (1988). X-Y-Z are the axis of strain.

Hrouda (1993) explained how the mathematics of these models can generate anisotropies similar to those observed in nature. However, there is no direct evidence confirming that these three models accurately represent natural processes.

CHAPTER 2 - SHALE DEFORMATION

Kneen (1976) and Wood et al. (1976) conducted sampling on North Wales slates (United Kingdom), in order to establish a correlation between slaty cleavage strain and three methods of fabric analysis: degree of preferred orientation (X-Ray goniometry), AMS, and seismic anisotropy. These studies established a mathematical correlation with muscovites measured by X-ray goniometry. Strain can be inferred using:

$$e = p_i^{-\frac{1}{3}} - 1$$

Equation 13

where e_i is the strain for an i -axis of the previously measured deformation ellipsoid, while p_i are the intensities of the measured goniometry X-ray axes. Kneen (1976) worked on the same lithology, establishing a graph using logarithmic ratios (shown in Figure 25). However, the obtained magnetic anisotropy is lower than the calculated strain. A correlation of $r=0.053$ is found, which the author assumed "is only valid for this rock formation and cannot be extrapolated to other lithologies."

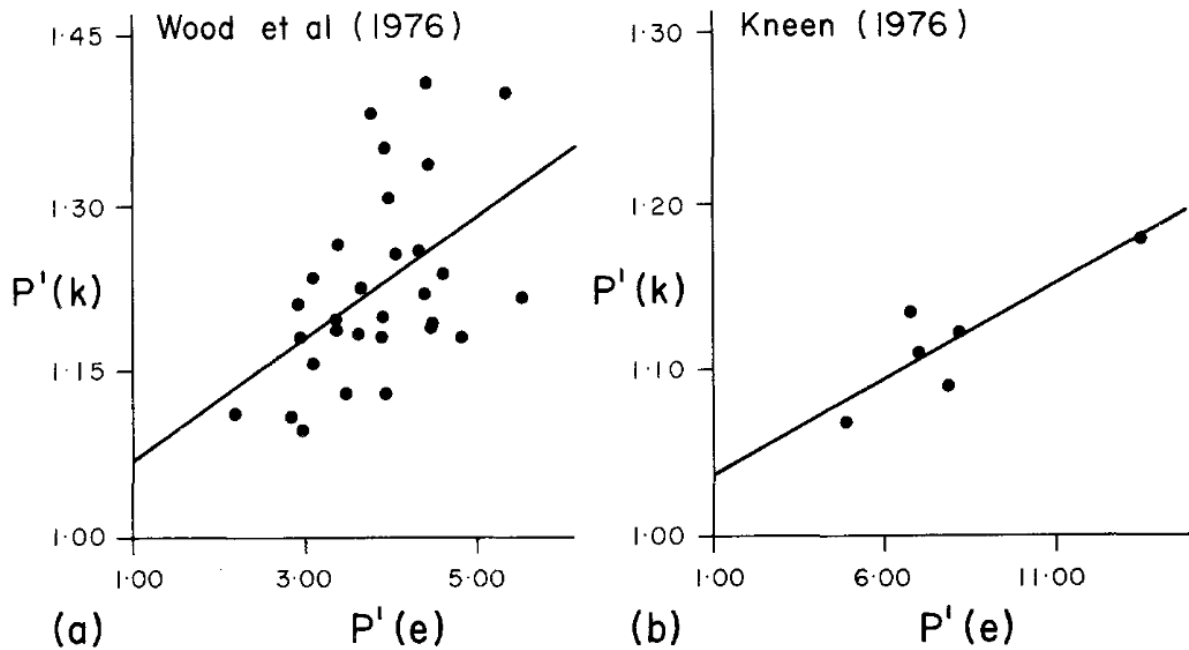


Figure 25: Wood et al. (1976) and Kneen (1976) correlations after Borradaile (1991) using P' parameter (corrected degree of anisotropy) to compare strain and magnetic fabrics.

Rathore (1979) drew upon the mathematics of March (1932) rigid rotation model, including a comparison of the measured strain axes with the axes of the magnetic anisotropy ellipsoid. The author therefore proposes the following formula

$$\left(\frac{X_{fi}}{X_0}\right) = \left(\frac{l_{fi}}{l_0}\right)^a$$

Equation 14

Being X_{fi} final susceptibility along axis i ; l_{fi} = final and l_0 initial axial dimensions in the same direction of a principal strain axis, $X_0 = \sqrt[3]{X_{max} X_{int} X_{min}}$; [9] and a is a parameter for slates, different proposed for each geological site (0.145 for North Wales slates).

CHAPTER 2 - SHALE DEFORMATION

Kligfield et al. (1981) proposed a comparison of finite strain calculated from reduction points, and magnetic susceptibility values, for Permian shales and slates in SE France. As they sampled along a deformation gradient, they established two linear relations for two different sites, with varying degrees of deformation. Thus, the equation remains:

$$\epsilon_i = 20.6 \Delta K_i$$

$$\epsilon_i = 43.0 \Delta K_i$$

Equation 15

Being ϵ_i natural strain, and $\Delta K_i = (K_i - K_{mean}) / (K_{mean})$

Equation 16

Hrouda (1987) established a mathematical model to establish a relation between paramagnetic anisotropy and strain in slates. The paper presented a relationship corresponding to bulk anisotropy in weakly magnetic slates, considering the nature of the rocks. To achieve this, the author derived and simplified the formulas of Rathore (1979), resulting in:

$$(k_{\max} / k_{\text{int}}) = (X/Y)^a \text{ solve for } X / Y: (X/Y) = (k_{\max}/k_{\text{int}})^{1/a}$$

$$(k_{\text{int}} / k_{\min}) = (Y/Z)^a \text{ solve for } Y / Z: (Y/Z) = (k_{\text{int}}/k_{\min})^{1/a}$$

$$(k_{\max} / k_{\min}) = (X/Z)^a \text{ solve for } X / Z: (X/Z) = (k_{\max}/k_{\min})^{1/a}$$

Equation 17

Where "a" is a constant related to the sampled rock unit.

The relationship between paramagnetic anisotropy and strain is depicted by curved lines on the graph shown in Figure 26. The calculated degree of anisotropy values align with those measured in natural slates.

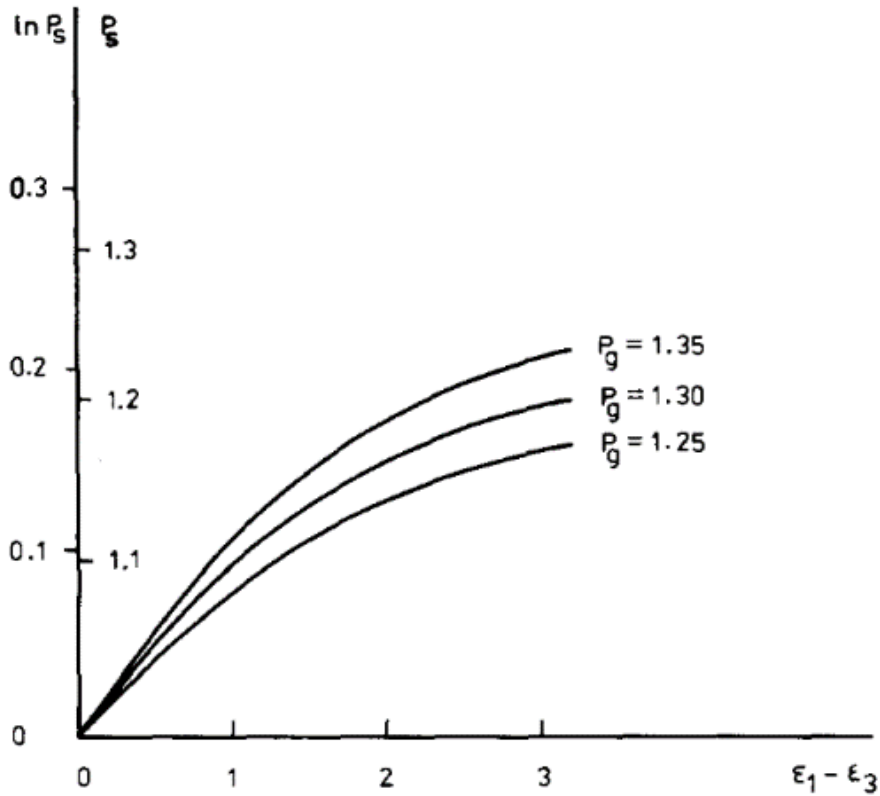


Figure 26: The relationship between the degree of paramagnetic anisotropy in slates (P_s) and strain ($\epsilon_1 - \epsilon_3$) for variable grain anisotropy of a paramagnetic mineral. From Hrouda (1987)

The author acknowledges that this model has limitations, such as the case of a ferromagnetic susceptibility, which could result in a different type of correlation, possibly more linear, rather than the curved shapes shown in Figure 26.

Housen and van der Pluijm (1990) proposed the use of equations by Hrouda (1987) and Rathore (1979). As previously presented, research on the Martinsburg Formation (Ordovician) at Lehigh Gap (USA) has demonstrated the sensitivity of clays to increasing deformation (Hirt et al., 2004; Housen and van der Pluijm, 1990; 1991). However, in this case, the metamorphic conditions led to complex phenomena of clay recrystallization. The paramagnetic mineral responsible for AMS, chlorites, underwent recrystallization. As a result, the fabric does not conform to previous assumptions, which are somewhat based on the March-strain model of rigid rotation.

Subsequently, Borradaile (1991) reviewed these and other articles, comparing the accuracy of these correlations. The paper proposes another fabric parameter to compare AMS and strain ellipsoids. In this case, the parameter P' (corrected degree of anisotropy) is favoured:

$$P' = \exp \sqrt{\{2(a_1^2 + a_2^2 + a_3^2)\}}$$

Equation 18

Where $a_i = \ln(k_i/kb)$ for $i = 1$ to 3 and $kb = (k_1 k_2 k_3)^{1/3}$ or $kb = (k_1 + k_2 + k_3)/3$ (for the usual range of K , the different definitions of kb make little differences) and $a = X/Y$, $b = Y/Z$ for strain and $L = k_1/k_2$, $F = k_2/k_3$ for AMS.

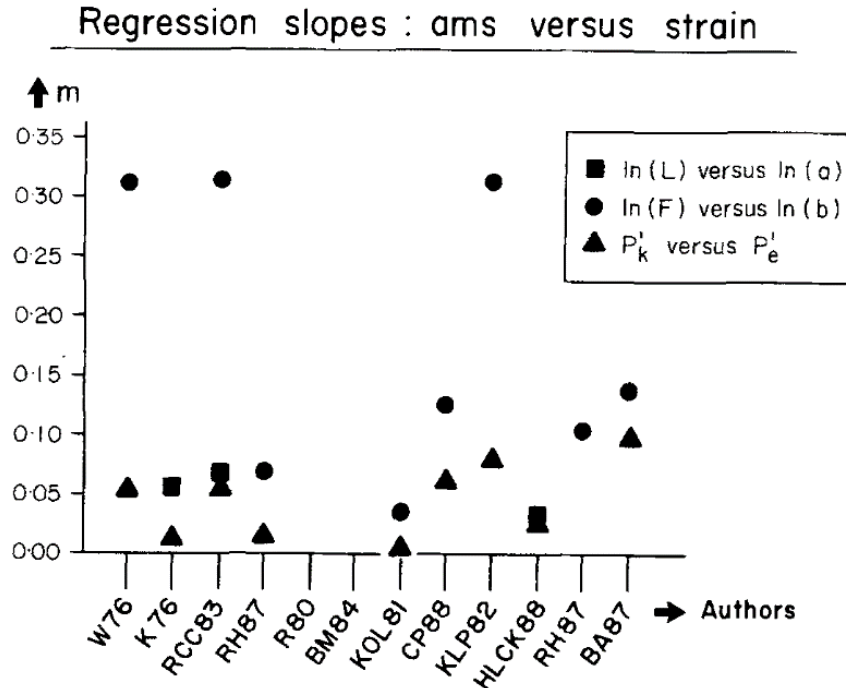


Figure 27: Borradaile's (1991) review of regression slopes (m) from previous literature. See Figure 23 for example of regression slopes. W76 = Wood et al. (1976); K76 = Kneen (1976); RCC83= Rathore et al. (1983); RH87 = Rathore & Hughon (1987) ; KOL81 = Kligfield et al. (1981) ; CP88 = Cogné & Perroud (1988); KLP82 = Kligfield et al. (1982) , HCL88 = Hirt et al. (1988) ; RH87 = Rathore & Hugon (1987) ; BA87 = Borradaile & Alford (1987).

However, Borradaile (1991) emphasized the precautions required when utilizing AMS as a strain quantifier. This involves (i) avoiding metamorphosed areas where crystal growth overlays the signal resulting from grain rotation and (ii) possessing a thorough understanding of the minerals responsible for the magnetic signal. Some subsequent references also explore the correlation between AMS and strain (Aranguren et al., 1996; Hirt et al., 1993; Lüneburg et al., 1999). New relationships between the orientations and magnitudes of AMS and the principal axes of finite strain are established, with normalized magnitudes of the finite strain axes being presented (Lüneburg et al., 1999). However, limitations emerge in relation to the fabric's nature or the minerals involved (such as hematite, magnetite, etc.) that are responsible for these effects.

Parés and van der Pluijm (2002, 2004b) highlight the challenges in quantifying strain, including uncertainties in establishing accurate relationships between the AMS ellipsoid and the sources of magnetic susceptibility, along with potential recrystallizations and growth of these key minerals. In their work, these authors propose correlating magnetic fabrics obtained from AMS analysis with the study of pencil structures exhibiting known finite strain. They use histograms of eigenvalues to compare magnetic ellipsoids, suggesting the potential to associate strain with the susceptibility tensor of the analysed rocks. In this case, the comparison is based on the symmetry of the shape parameter T (as defined by Jelinek, 1981) with shortening, in contrast to the parameter P defined by Borradaile (1991). Thus, they obtain a curve (Figure 28) with

$$\text{Shortening (\%)} = 17 \times \exp(T)$$

Equation 19

CHAPTER 2 - SHALE DEFORMATION

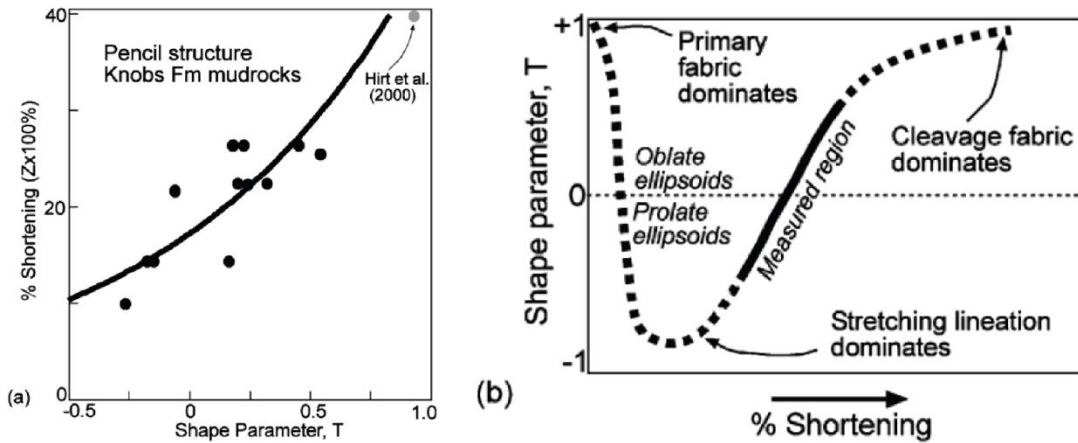


Figure 28: a) Correlation between longitudinal shortening in percentage vs T parameter. B) Note the path in the Jelinek diagram. Both figures from (Parés and van der Pluijm, 2003).

These data correspond to a sequence of Appalachian shales. A quantitative relationship was determined in a shortening window between 10% and 25%. Again, the authors do not recommend extrapolating this correlation to other rocks, but do suggest using this parameter as a proxy for shortening at low-strain sites. This is the first quantitative correlation in shales, by comparing the shape parameter T and strain, measured from pencil structures. The length/width ratio of pencil structures turns out to be a measure of strain, with:

$$Y/Z = 0.913 \times 0.019 (1/w)$$

Equation 20 from Reks and Gray (1982).

We note that the prolate domain in the shales corresponds to a percentage of deformation in the order of 10% to 20%. We will see that we obtain similar values with a different approach based on the rigid rotation of the clay particles.

Humbert et al. (2014) investigated the mathematics derived from March's model. In this paper the rigid rotation model is the initial model, but instead of a uniaxial compression applied on a "flat line vector", a "geometric collapse" is presented, where only the starting and end points of the flat line vector are fixed (Figure 29).

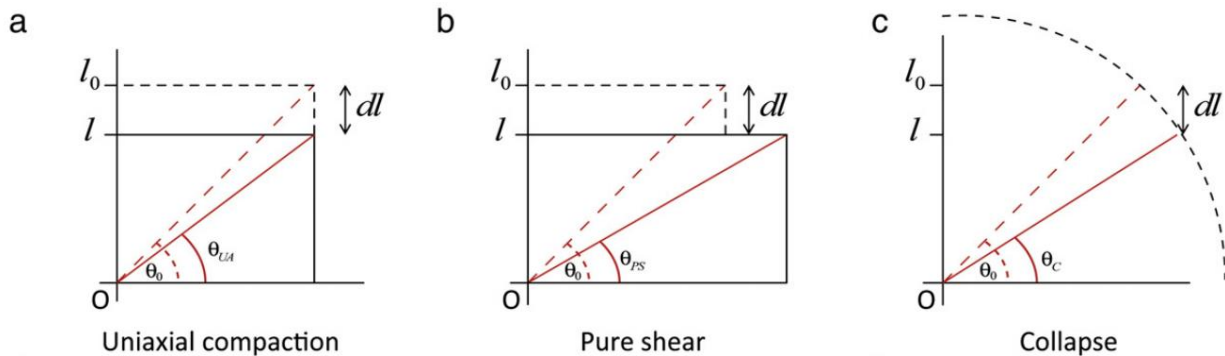


Figure 29: March model, in which the reference vector displacement is following the collapse model, differentiated from uniaxial or pure shear compressions. From Humbert et al. (2014).

CHAPTER 2 - SHALE DEFORMATION

The authors establish the three conditions necessary to apply this method: (1) the main carrier of the magnetic signal should be platy; generally it corresponds to paramagnetic phyllosilicates particles, but some ferromagnetic grains (such as hematite) can also meet this condition; (2) the platelets must rigidly respond to horizontal strain with no bending, no twinning or intragrain fracturing; and (3) there has been neither recrystallization nor formation of new magnetic minerals disturbing the initial signal, being this rotation comparable to an undeformed fabric. So, as Figure 29 shows,

$$\varepsilon = \frac{dl}{l} = \frac{l - l \cos \alpha}{l} = 1 - \cos \alpha$$

Equation 21

Thus, using this idea, they apply the derivative to the axes of the magnetic ellipsoid to obtain an estimate of the incremental horizontal strain defined by:

$$\varepsilon \left(\frac{dl}{l} \right) = 1 - \sqrt{\frac{K_1 - K_3}{3(K_1 - 1)}}$$

Equation 22

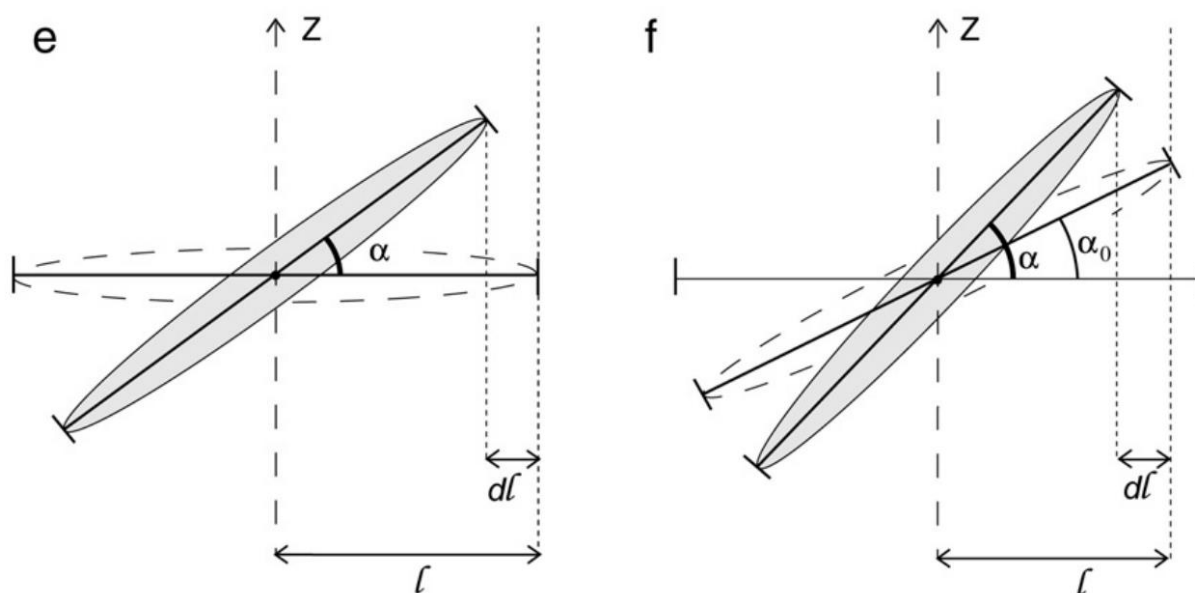


Figure 30: Geometric characteristics of shortening calculations by Humbert et al (2014). It requires platy particles, generally corresponding to paramagnetic shales, which undergo rigid rotation, accordingly to March's approach.

These mathematics are revisited by Boiron et al. (2020) who studied shales in the Larrés formation (at Sigüés, in the same site as this PhD). This paper investigates the burial conditions of shales, and demonstrates the absence of recrystallisation of paramagnetic clays.

Given the existence of the deformation gradient described in this thesis, Boiron et al. (2020) propose to adapt the shortening calculation formula of (Humbert et al., 2014) according to the layout of the internal fabric and its conditioning on the magnetic fabric measurements.

CHAPTER 2 - SHALE DEFORMATION

In other words, in outcrops where bedding appears to be the dominant fabric, the K_3 axes can still serve as a reference for rigid rotation. However, in outcrops where a distinct cleavage (either pencil or slaty) is prominently visible, the reference for rigid rotation shifts to the K_2 which corresponds to the vertical axis of the AMS measurements taken, according to the orientation of the clay particles (Figure 31)

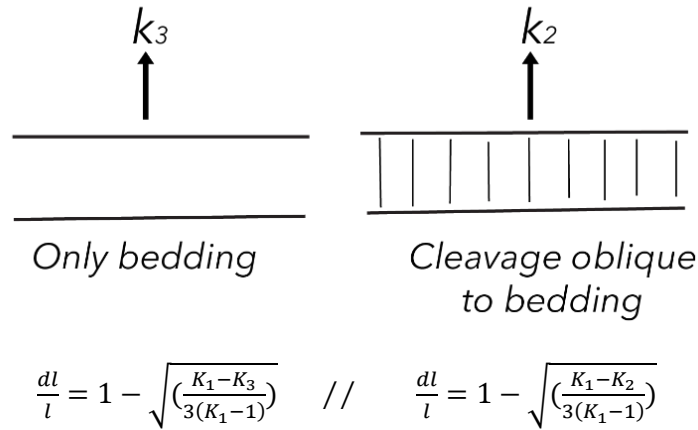


Figure 31: The formula proposed by Humbert et al. (2014) is divided into two end-members by Boiron et al. (2020) in which the K_3 axes are vertical or the k_2 axes of the measured fabric is vertical.

Shales are, therefore, excellent candidates for strain vs. magnetic fabric studies because their magnetic mineralogy is generally dominated by paramagnetic clays. Clay particles of detrital origin, or formed early during diagenesis, can rotate rigidly during deformation. Magnetic susceptibility in clays can thus be used as a significant strain marker (Boiron et al., 2020; Parés, 2015; Wenk et al., 2020).

The South-Pyrenean shales were chosen for the new approach proposed in this PhD, involving the study of non-oriented fragments and the application of AMS parameters to understand deformational processes. In this PhD, a novel methodology will be applied to investigate the deformation associated to the footwall of the Leyre thrust (Southern Pyrenees), building the new findings upon the previous research by Boiron et al. (2020).

2.4 The Lehigh Gap, a classical shale-to-slates transition

2.4.1 Geological setting.

This thesis focuses on deformation gradients within shales. One of the most notable example is undoubtedly the Lehigh Gap outcrop, which was extensively studied from the 1950s to the early 2000s.

It is important to delve into the literature concerning this site, as various techniques have been employed to understand the formation of cleavage in shale-to-slate transition. Therefore, the available data and interpretations will be reviewed to address a geological problem similar to the one posed in this PhD: a shale gradient that aims to elucidate the rocks' deformation history

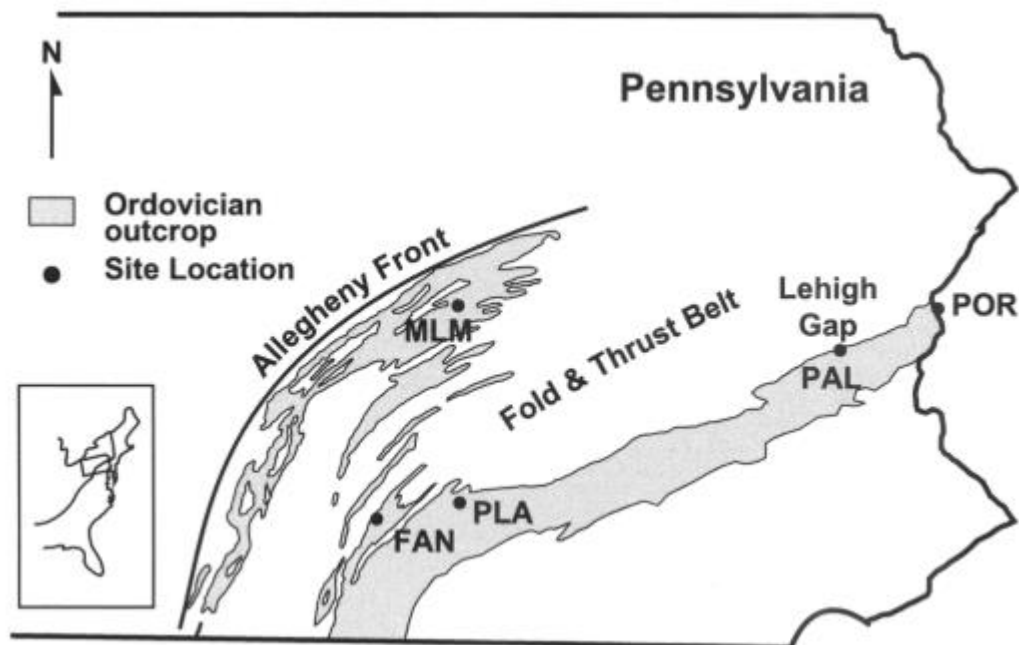


Figure 32: Regional Map of the Pennsylvania state (USA) Lehigh Gap is named PAL point. From Hirt et al (2004)

The Lehigh Gap outcrop is located at Pennsylvania, USA; in the central sector of the Appalachian fold-and-thrust belt- a mountain range predominantly consisting of Paleozoic rocks that underwent folding during the Alleghanian orogeny (see Figure 32). This outcrop encompasses two distinct geological formations. The Martinsburg Formation comprises a series of thin greywackes and primarily mudstones, characteristic of marine slope deposits. Specifically, the upper part of this formation, known as the PenArgyl Member, is exposed at Lehigh Gap. Directly overlying this member, in a conformable manner, is the Shawangunk Formation—a quartz-rich sandstone composed of coarser-grained, clastic deposits (Hirt et al., 2004). Between these two units, there is a centimetre-thick gouge, indicative of thrusting that took place at this location.

CHAPTER 2 - SHALE DEFORMATION

In structural terms, the region features a significant regional thrust cutting across the Martinsburg Formation, which has undergone a regionally detectable Layer Parallel Shortening (LPS), marked by the development of cleavage perpendicular to bedding and parallel to the regional folds. Generally, the area has experienced the Alleghenian orogeny, and several authors (Epstein and Epstein, 1967; Lash, 1978; Maxwell, 1962; Mitra, 1987; Wintsch, 1978) have attempted to describe the compressional sequences responsible for the Appalachian architecture. The Lehigh Gap holds particular interest due to the presence of a cleavage gradient, spanning over 200 m within the Martinsburg Formation series (refer to Figure 33). In this outcrop in the northern section, adjacent to the Shawangunk Formation sandstones, no macroscopically detectable foliation is present in the rocks. Around the 60-meter mark, S1 planes, perpendicular to S0, begin to emerge, forming a subtly pervasive pencil cleavage. Beyond 100 meters, a pervasive slaty cleavage appears, affecting the entire formation, including certain outcropping turbiditic beds.

It is accepted that the quartzitic lithology of the Shawangunk Formation serves as a barrier to the development of cleavage in the shales of the underlying Martinsburg Formation, which is generally less affected by the LPS within these initial meters. However, as presented throughout this chapter, most of the attention in the literature has been directed toward the mineral mechanisms responsible for cleavage formation. The reorientation of the mineral components within the shales giving rise to gradient fabrics, and whether these correspond to the observations made at the mesoscale, have been the central focus of the previous research.

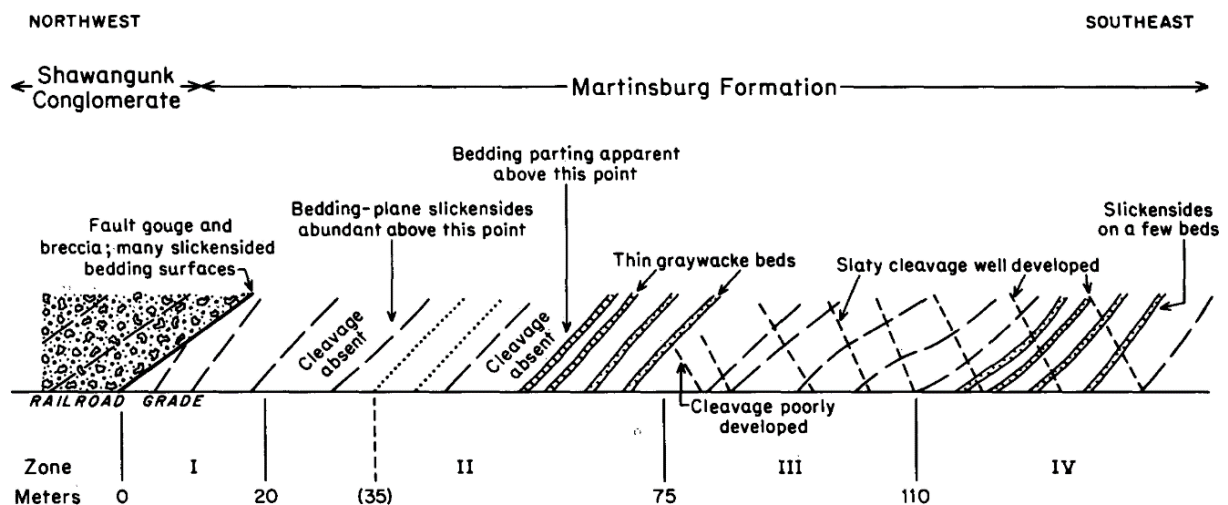


Figure 33: Lithological sketch of the complete Lehigh Gap outcrop, taken from Wintsch et al. (1991)

2.4.2 How cleavage is hosted in a shale-to-slate transition?

As shown in the sketch in Figure 33, the lithology in the Martinsburg Fm is slightly changing: centimetric layers of sandstones appear corresponding to turbidity currents that were deposited on the marine slope. The Martinsburg formation is composed of quartz, clay minerals and feldspar according to observations from Lee et al. (1986) in proportions that are constant over the transect. The clay mineralogical assemblage consists of very elongated detrital chlorites, authigenic chlorites, and authigenic illites that progressively change to muscovites in the most deformed part of Lehigh Gap (Ho et al., 1995; Lee et al., 1986).

CHAPTER 2 - SHALE DEFORMATION

Various techniques are used to describe these components: optical microscopy, for the largest grains; electron microscopy; X-ray fluorescence (Lee et al. 1986) which allows to quantify in weight percent some chemical components; X-ray diffraction (Lee et al. 1986) which differentiates and makes a semi-quantitative estimation of the different types of clays present in the sampled shale. Finally, X-ray microtomography has also allowed the addition of observations, both on the image itself and the quantification of the fabric (Saur, 2022).

In general, various techniques are available to determine how the fabric is controlled by the cleavage or remains as the primary fabric of the shales. Since the first paper by Holeywell and Tullis (1975) several works have used X-ray textural goniometry techniques presented in pole figures (Beutner, 1978; Ho et al., 1995, 1996; Housen and van der Pluijm, 1990; Lee et al., 1985; Van Der Pluijm et al., 1998; Wintsch, 1978; Woodland, 1982). This technique has seen advancements, and methodological corrections have been proposed (van der Pluijm et al., 1994). Additionally, a complementary approach using synchrotron X-ray diffraction, as used by Wenk et al. (2007) provides more precision and intensity in the measurement of materials that are weakly detected in standard goniometry, offering quantitative insights as well.

All of these techniques share the ability to study the mineral fabric of shales, particularly by examining the basal planes of the clay minerals and their spatial orientation. Hand samples are prepared, solidified with epoxy resin and vinyl, then polished and cut. A polished section of the samples is then exposed to the X-Ray beams, and by rotating the sample in the goniometers, differentiated diffractions for spatial analysis are obtained. Thanks to these diffractions, and the ability to program the machine for specific basal plane separations (each clay mineral is organised at a nanometric separation), distinct orientations have been identified, especially for chlorites, and muscovites, in their 001 or 002 planes. It is possible to determine fabric ellipsoids, along with their shape factors and principal axial orientations (t_1 , t_2 and t_3) by obtaining eigenvalues and eigenvectors of the intensity distributions. These values are comparable with those of the magnetic fabric ellipsoid, being represented in the lower hemisphere (Hirt et al., 2004).

Goniometry results, together with TEM and SEM electron microscopy observations (Hirt et al., 2004; Ho et al., 1995; Holeywell and Tullis, 1975; Lee et al., 1986) indicate that:

- In the first tens of metres, the chlorite grains are identified as being at an angle of $\sim 30^\circ$ to the bedding (Hirt et al., 2004; Ho et al., 1995; Holeywell and Tullis, 1975, see Figure 34). The t_1 of both phyllosilicates is sub-parallel to the lineation of the pencil structure, which appears here as an open separation of fractures (Hirt et al., 2004). It is also noted the t_3 of the mica (mostly represented by illite) is parallel to the pole of the S_0 (Hirt et al., 2004). This would be in agreement with microscopic observations of TEM and SEM.
- In zone 2, the phyllosilicates lie on the S_0 or some kinks are visible, with a mineral fabric similar to the main zone. Although in this case, the t_3 of the chlorite is closer to the S_0 pole than in zone 0. The t_3 of the phyllosilicates are well clustered around the S_0 pole, and the t_1 are aligned with the intersection lineation.
- Further ahead, at 90 m, slaty cleavage and lineation are visible. The phyllosilicate kinking is behind the girdles exhibited intersecting by the mica plotted distribution. The chlorite fabric is very weak and may be controlled by a few large crystals, in any

CHAPTER 2 - SHALE DEFORMATION

case, with a t_3 that is subparallel to the S_0 pole. In contrast, the t_3 of mica is intermediate between S_0 and S_1 .

- At a fourth point, with slaty cleavage, signals such as kinking, grains, and rotation in the cleavage plane are found. In general, the mineral fabrics are aligned with the cleavage, although the intersection lineation is visible.

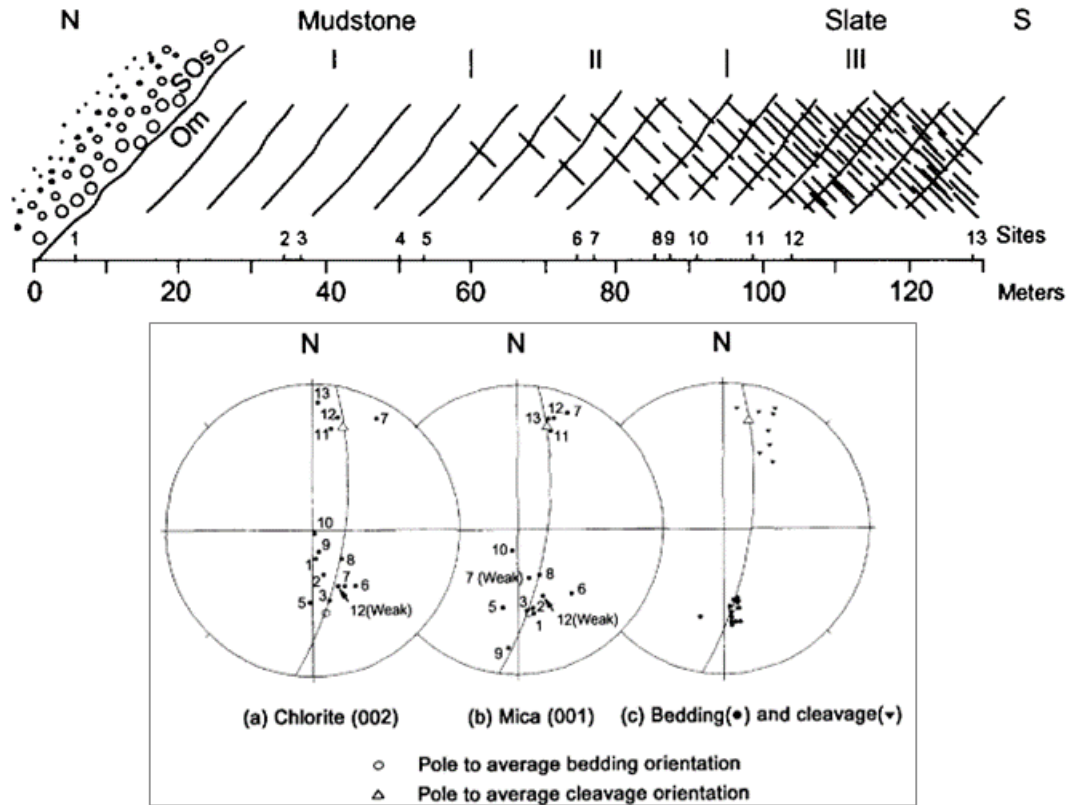


Figure 34: a) preferred orientation of chlorite (002) b) preferred orientation of mica (001); and c) bedding and cleavage orientations. From Ho et al. (1995).

The evolution of X-ray fabric data can be observed in Figure 34 (Ho et al., 1995). These authors attempted to quantify this migration by applying the rigid rotation March model to clay particles. When the shortening calculations obtained from this model are projected, a progression of V-shaped shortening of the sampled rocks becomes apparent (Figure 35), although it may be obscured by recrystallization phenomena. This represents one of the earliest attempts to quantify shortening in a deformation gradient zone where both rigid rotation of grains and dynamic recrystallization phenomena associated with deformation coexist.

CHAPTER 2 - SHALE DEFORMATION

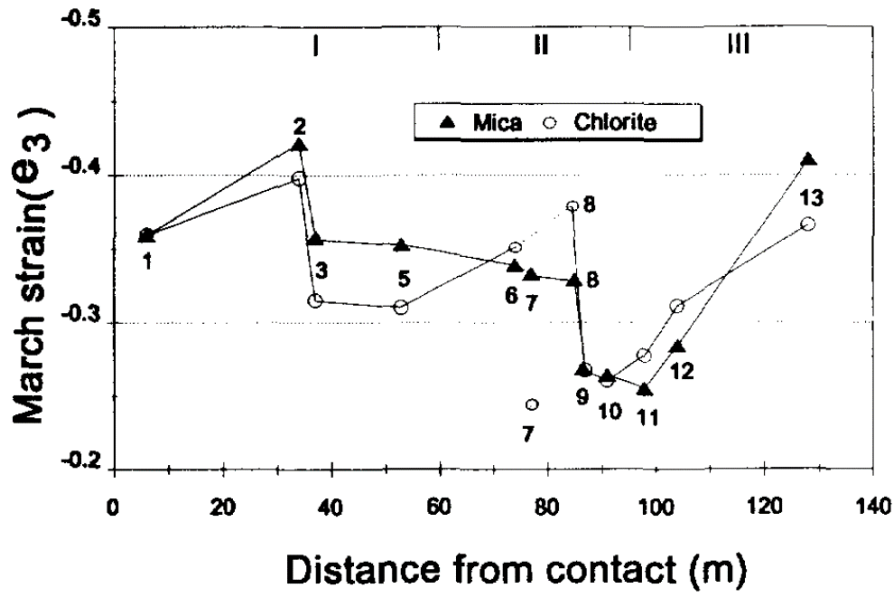


Figure 35: March strains along the Lehigh Gap transitions, same sample sites numbers as Figure 33. From Ho et al. (1995).

The study of magnetic fabric (Hirt et al., 2004; Housen and van der Pluijm, 1990; Housen and Van Der Pluijm, 1991) provide additional information. AMS and AARM (Anisotropy of Anhysteretic Remanent Magnetization) were carried out to discriminate the ferromagnetic fabric and the bulk fabric (Housen and Van Der Pluijm, 1991). The data can be summarised in the following sequence of AMS:

- An initial fabric next to the lithological contact is measured, in which the minimum axis (K_3) is $\sim 20^\circ$ more inclined than the pole of the S_0 , indicating rotation.
- Then, a second fabric is detected. K_3 axis remains intermediate between the S_0 and S_1 poles, with the magnetic lineation also appearing parallel to the lineation intersection of the pencil cleavage. This change is detected abruptly at 75 m from the contact, in contrast to what is detected with goniometry (Housen and van der Pluijm, 1990).
- Finally, this fabric is accentuated towards more distant positions, finding a more anisotropic and oblate fabric controlled by the cleavage.
- Housen and Van Der Pluijm (1991) plot AARM and AMS data (Figure 36). The ferromagnetic fabric is controlled by bedding for distance < 60 m. Then, there is a quite regular change from bedding-parallel to cleavage-parallel (at distance > 90 m). This magnetite evolution contrasts with AMS pattern, governed by clays. The gradient is more similar to that of goniometry as it contains "intermediate" steps in the pencil cleavage zone (74-94 m) (Housen and Van Der Pluijm, 1991).

CHAPTER 2 - SHALE DEFORMATION

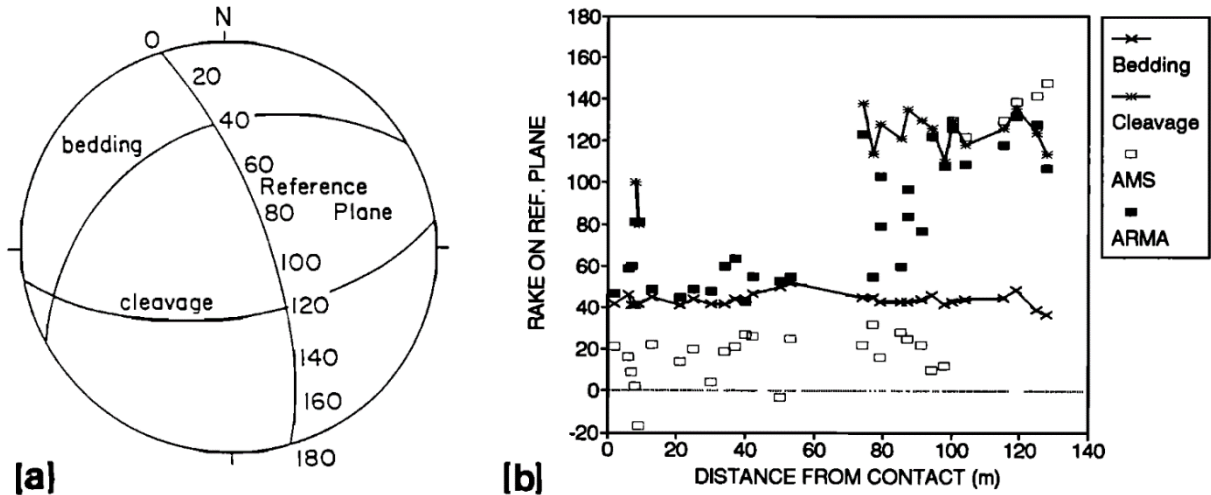


Figure 36: a) Stereoplot including orientation of bedding, cleavage and reference plane for orientations plotted on the table to the right. b) plot of bedding, cleavage, AMS, and AARM orientations. AMS and AARM orientations are contained in the "magnetic foliation" plane. From Housen and van der Pluijm (1991).

In any case, Housen and Van der Pluijm (1991) conclude that the bulk magnetic fabric coincides with the orientation of the chlorite planes measured in goniometry (Holeywell and Tullis, 1975). It is the chlorite signal that dominates the paramagnetic behaviour measured in the rocks.

These data were subsequently supplemented by Hirt et al. (2004), who, with a larger number of samples per site, provided new data. Consequently, the transition towards the magnetic fabric being completely controlled by the cleavage was not as pronounced as observed previously. Instead, a slower K_3 rotation was observed.

The contribution of these two fabrics is combined in the bulk AMS, highlighting one of the challenges of using the bulk fabric approach for AMS. When examining the data presented by Hirt et al. (2004), it becomes evident that the AMS is primarily influenced by chlorite, resulting in a foliation orientation that is notably oblique to the bedding. Nonetheless, the AMS effectively characterizes the transformation of the clay fabric during cleavage development, revealing a distinctive arrangement of K_3 poles in a girdle-like pattern within the intermediate zone (two central plots in Figure 37).

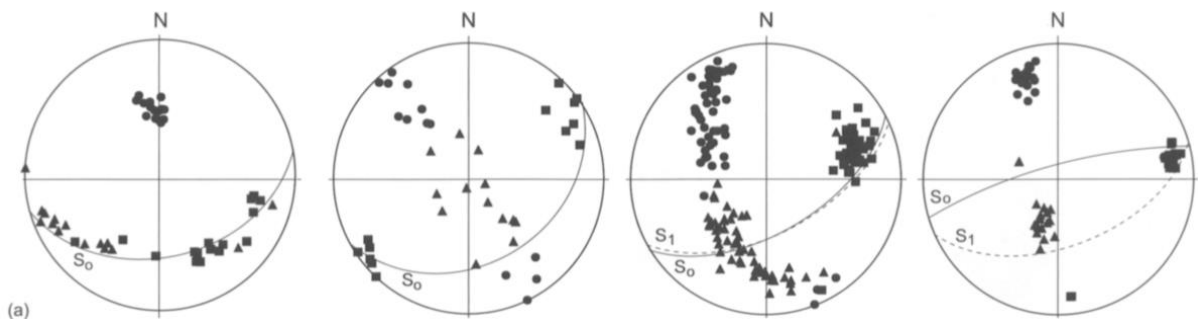


Figure 37: AMS data from Hirt et al. (2004). K_1 axes are shown by squares, K_2 axes by triangles, and K_3 axes by circles. Bedding plane is shown with a solid line, cleavage plane with a dotted line, and pencil lineation with a white diamond. From left to right, the data correspond from least to most deformed sampling sites.

In the slaty cleavage zone (zone 3), the AMS is completely governed by cleavage. The AMS parameters including the degree of anisotropy (P) and shape parameter (T) have been

CHAPTER 2 - SHALE DEFORMATION

recalculated from the data of Housen and van der Pluijm (1990) and presented on Figure 38. Both parameters exhibit a decreasing trend from the onset of zone 1 to the slaty cleavage (zone 3). This might initially seem paradoxical, as the lowest the degree of anisotropy is observed in the most deformed zone of Lehigh Gap. It is also notable that the most prolate shape is found in the most deformed area.

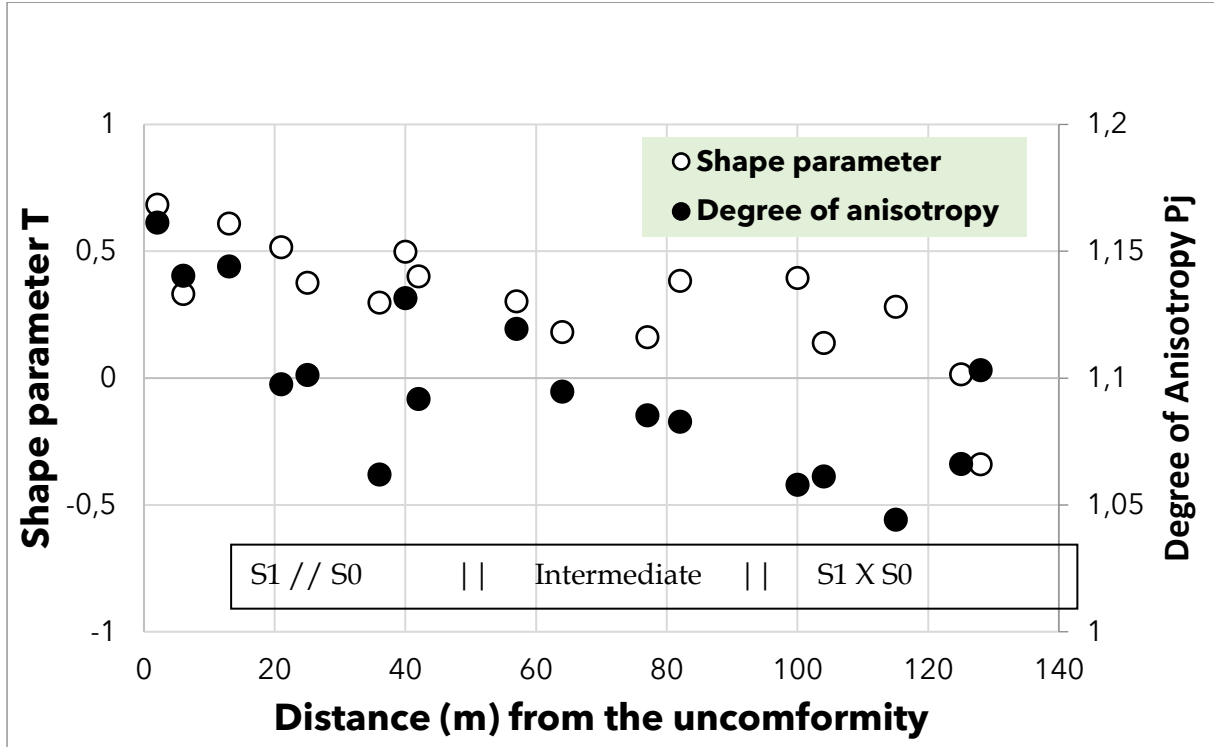


Figure 38: Data from Lehigh Gap. Computed from AMS Data by Housen and van der Pluijm (1990).

CHAPTER 2 - SHALE DEFORMATION

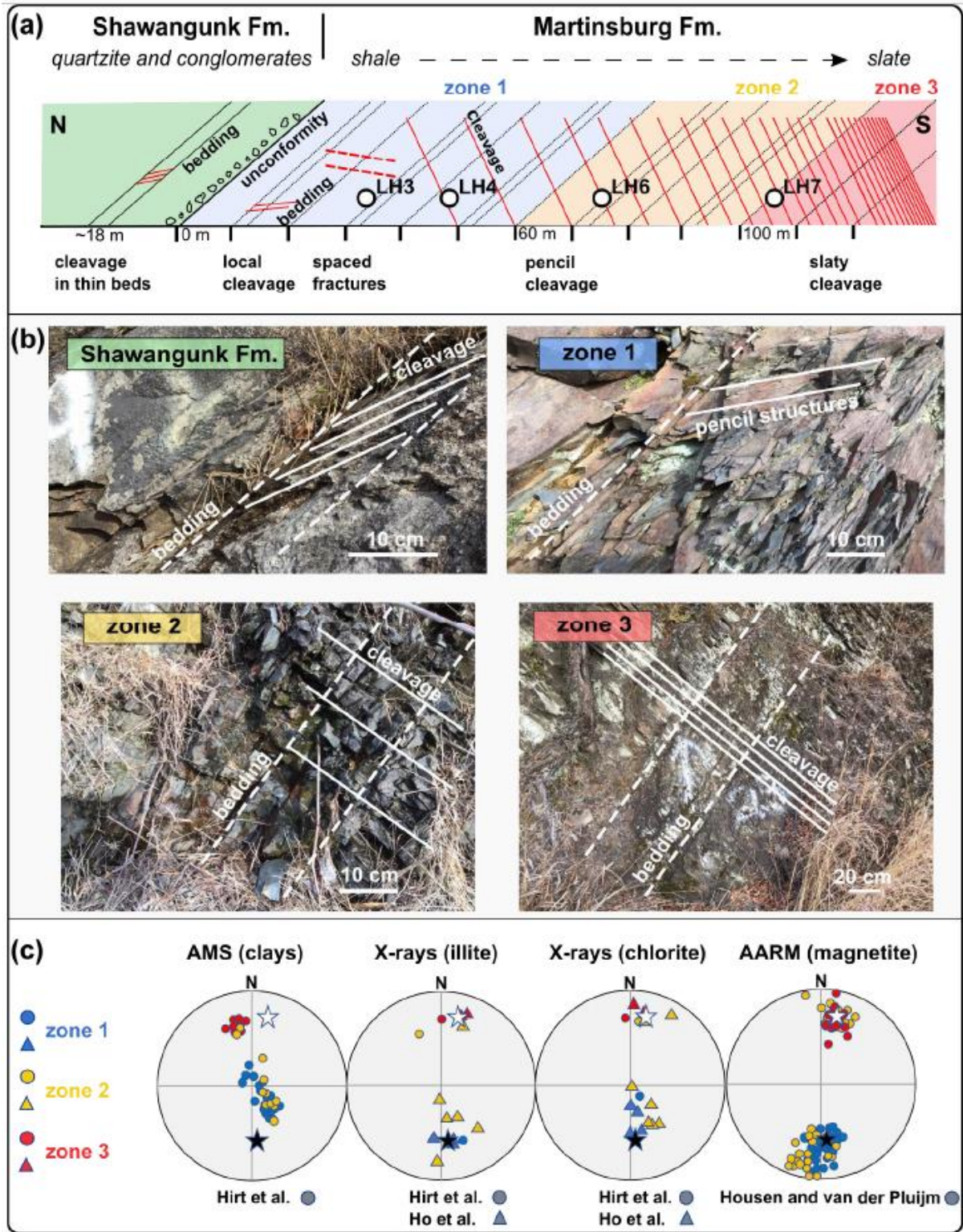


Figure 39: Summary of data from various fabrics measured in the bibliography; with outcrop pictures and new sampling. From Saur (2022).

All these techniques performed on the Lehigh Gap transect and the data obtained on these sub-fabrics are compiled in Saur (2022) PhD (Figure 39). X-ray microtomography of four samples have been studied (Saur et al., 2021). SPO fabrics of quartz, pyrite and shale pores have also been analysed.

CHAPTER 2 - SHALE DEFORMATION

One of the most interesting results is that quartz exhibits an oblique orientation to bedding in Zone 1, aligning with chlorites (Figure 39 and Figure 40). This contrasts with the fabric of pyrites, which is controlled by stratification in Zone 1. The microtomography data therefore confirm the AMS and X-ray diffraction data, i.e. that in Zone 1 two fabric coexist, one controlled by the stratification (illite, pyrite), the other oblique at around 20-30° to the stratification (detrital elongated chlorite, quartz).

CHAPTER 2 - SHALE DEFORMATION

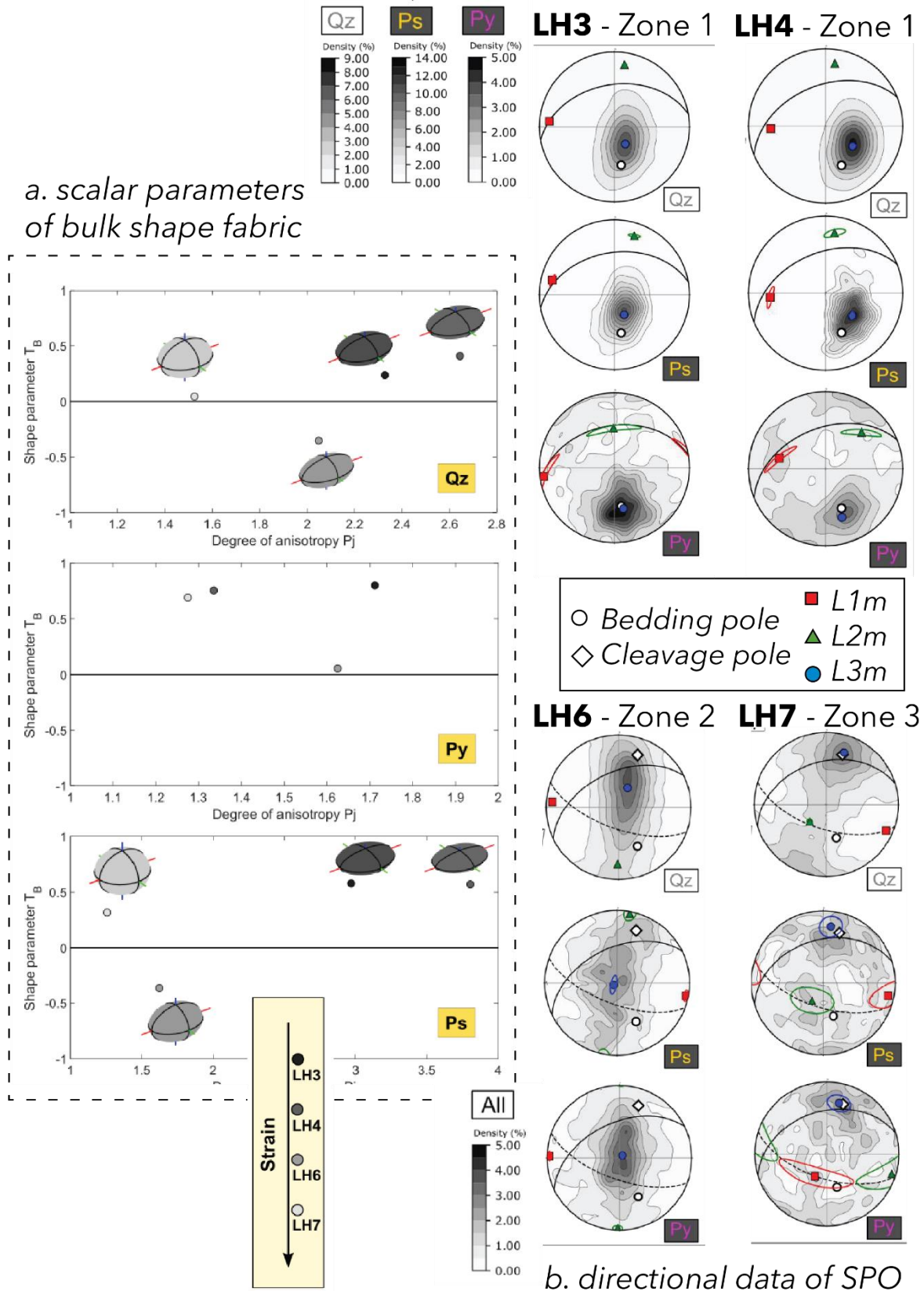


Figure 40: Scalar parameters for Quartz, Pyrite and pores, from Saur (2022). Besides, SPO data for the same shale components are shown.

CHAPTER 2 - SHALE DEFORMATION

2.4.3 What are the mechanisms responsible for cleavage?

The examination of shale components across the Lehigh Gap transect has revealed various mineral and fabric evolutions. Consequently, the mechanisms attributed to them will be presented, also explaining how the Martinsburg Formation hosts cleavage.

Clay minerals	Chlorite	Chlorite is extensively dissolved and recrystallised back into the S1 fabric (Holeywell and Tullis, 1975; Housen and Van der Pluijm, 1991) . However, some passive rotation of detrital chlorite grains can also be observed (Ho et al. 1995; Hirt et al. 2004)
	Muscovite/Illite	Grain kinking and passive rotation of large detrital phyllosilicates grains (Hirt et al. 2004).
Ferromagnetic mineral	Magnetite (Housen and Van der Pluijm 1991)	The passive rotation of magnetite, transitioning from a position parallel to S0 to aligning alongside S1, mirrors the gradual increase in penetrative nature of the slaty cleavage.
Diamagnetic mineral	Quartz	Dissolution-precipitation creep mechanism is suggested along the Lehigh Gap transect (Saur, 2022)
Paramagnetic mineral	Pyrite	Rigid rotation is suggested. (Saur, 2022)

Table 5: Mineral components of shale and their deformation mechanisms

The array of mechanisms present in the Lehigh Gap poses an unresolved challenge, as different interpreted mechanisms could potentially coexist without a clear sequence. Ho et al. (1996) and Van Der Pluijm et al. (1998) proposed that chemical processes, such as dissolution-crystallization, could become active in energetically intense environments. Conversely, when thermal energy and strain decrease, mechanical processes like rigid rotation would become dominant.

The classical interpretation of the gradient exposed at Lehigh Gap remains somehow unclear. The starting point is that the Shawangunk Formation might create a strain shadow effect on the underlying shales. Interestingly, the authors don't place their emphasis on detailing the cleavage present in the thin layers of the Shawangunk Formation (Figure 39 by Saur, 2022). The angular relationship with the bedding bears resemblance to that of a reverse stratigraphic sequence. This specific relationship, commonly observed in reverse-flanking folds, appears illogical at Lehigh Gap due to the chronological sequence—Shawangunk Formation being younger than the Martinsburg Formation.

Chemical conditions: In their study, Wintsch et al. (1991) report no significant volume changes within the Lehigh Gap transect. They compute a mass balance that indicates a low differential mobility for aluminum, iron, magnesium, and other metal oxides. While there are observable transfers of silica between distinct lithologies, including mudrocks and greywackes, these transfers have limited influence, largely due to the slow and gradual P-T and permeability conditions considered in the study.

Burial conditions (Epstein et al., 1977; Kars et al., 2015; Stamatakos et al., 1996; Wintsch et al., 1996): The mineralogical assemblage aligns with expectations for conditions along the border of the greenschist metamorphic domain, where illitization initiates around 60°C, and chloritization becomes significant at temperatures exceeding 200°C. This cleavage is linked

CHAPTER 2 - SHALE DEFORMATION

to pre-folding Layer Parallel Shortening (LPS), see Hirt et al. (2004). Lee et al. (1986) proposed a peak burial temperature ranging from 230 to 300°C. In collaboration with R. Stockes, Saur (2022) determined Raman Spectroscopy (RSMC) temperatures of approximately 280°C, which corresponds to the higher range of published temperature.

There is no real discussion about the temporal relationship between clay formation and deformation. The LPS episode at the origin of the cleavage postdates the illitization and is probably contemporary with the chloritization. It is therefore reasonable to assume that illite acted as a passive marker during deformation, and that authigenic chlorite recrystallized during deformation. Van Der Pluijm et al. (1998) suggest that recrystallization phenomena are activated in the most deformed part of Lehigh Gap.

Considering that clays are generally aligned with the cleavage, two hypotheses have been formulated for cleavage formation: either through the rigid reorientation of grains or via pressure-solution mechanisms. The hypothesis put forth by Van Der Pluijm et al. (1998) suggests that clays underwent recrystallization under stress, supported by favourable burial conditions. Similarly, in Saur's thesis (2022), 3D microtomography studies reveal how other fabric components, such as quartz and pyrite, also experience reorientation within strongly deformed zones of the transect. This implies flexural slip and flexural flow mechanisms contributing to the development of cleavage.

2.4.4. Comparison with the Sigüés site and concluding remarks con Lehigh Gap

We compare the two sites after learning about the in-depth study of the Lehigh Gap site in the Appalachians, with the idea of also highlighting the site where this thesis has been developed: the Sigüés transect. Consequently, some differentiations that may be of interest and reveal new ideas for the study of strain in shales are the following:

- ✓ In the case of Sigüés, the gradient is related to the main thrust of the Leyre system, although the exact conditions of strain remain controversial.
- ✓ The length along with the gradient detected on Lehigh Gap is ~100 m, whereas it is on the order of several hundreds of meters for Sigüés (pencil cleavage is observed at more than 1000 m from the fault contact);
- ✓ the gradient is observed in the same stratigraphic unit for Sigüés (continued lateral observation of a few decametre thick beds), whereas for Lehigh Gap, it develops over a stratigraphic thickness on the order of 200 m
- ✓ the facies are silty for Lehigh Gap (dominance of quartz and phyllosilicates in composition after Lee et al, 1986) and marly for Sigüés (30-50% calcite, 30-35% quartz and 15-33% phyllosilicates).
- ✓ the burial temperature is higher for the Lehigh Gap (~280°C) than for the Sigüés sites (~180°C).

At a time when a strong community of structural geologists was interested in the development of cleavage in shales, Lehigh Gap appeared as a typical example of a zone with a fairly clear gradient, showing over 100 m an evolution of cleavage. A wide range of techniques were used to better understand the processes at work in the development of cleavage. These approaches have proved fruitful, but attempts to quantify deformation have come up against complex recrystallization processes. For example, the evolution of the degree of anisotropy P of the ASM shows a decrease where the geologist sees an intensification of deformation. Recent microtomography has given us a new perspective on this zone, and it is likely that Zone 1, described as lacking cleavage, is in fact home to a more subtle cleavage, slightly oblique to the stratification.

2.5 The Southern Pyrenees, a natural laboratory of magnetic fabric in shales and slates.

The Southern Pyrenean region has been the subject of numerous magnetic fabrics studies. In this chapter, a primarily focus will be put on the central sector of the chain, encompassing the Jaca-Pamplona basin, the Aínsa basin, as well as other sites of interest.

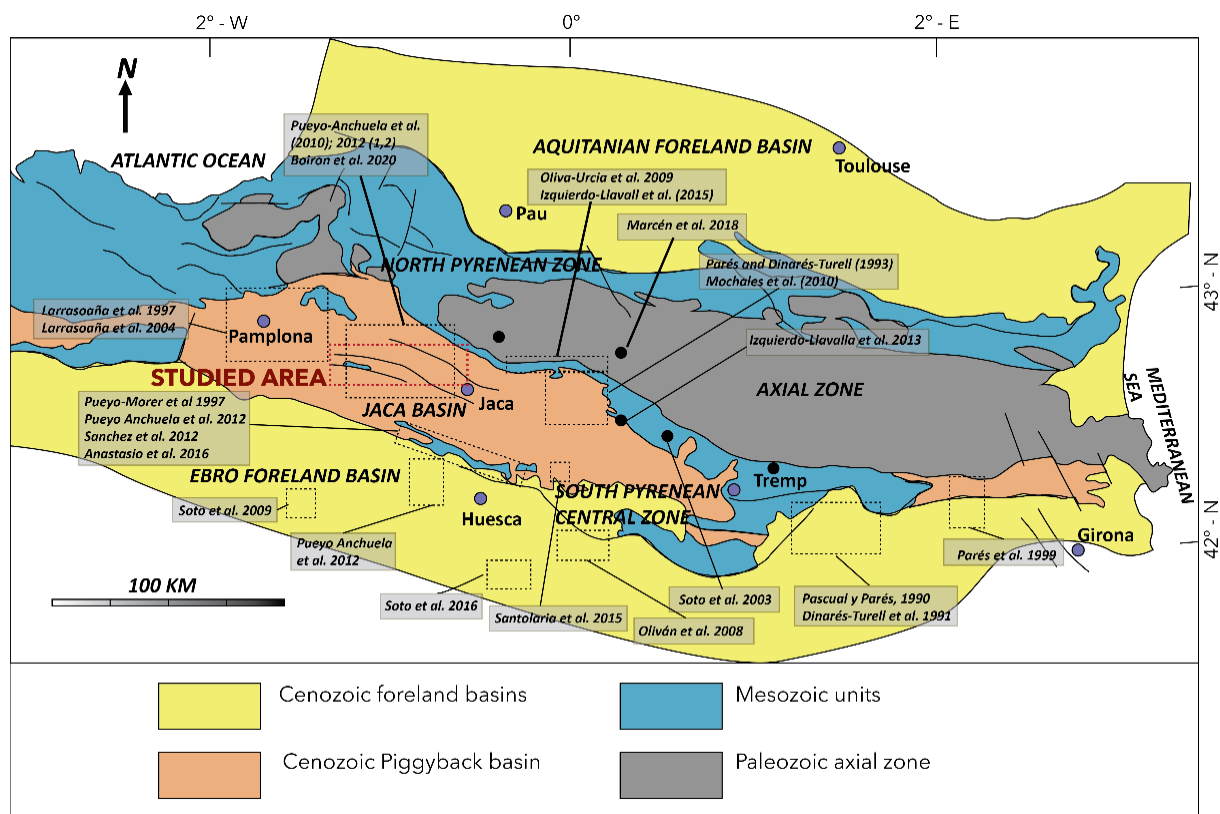


Figure 41: Pyrenean orogen map, modified from Teixell (1996). Research papers described in this chapter are localized.

2.5.1 Foreland basin

This “natural laboratory” starts from the “undeformed” areas, in the foreland basin south of the orogenic wedge: the Ebro foreland basin (See Figure 41). The Ebro basin is a morphological depression of more than 500 km between its upstream and downstream margins (considering the Ebro river), and more than 200 km in its transverse profile, NE-SW. Practically all the sediments studied in the Central Ebro Basin correspond to the Miocene, and only occasionally near the margin of the South Pyrenean frontal thrust are Oligocene sediments found. Eocene and Oligocene materials dominate, conversely, towards its eastern margin. Since its active margins were its northern, southern and eastern boundaries, it is therefore to be expected that in its central sector there is a stable tectonic content and fabrics would be governed by the sedimentary configuration. In the following paragraphs we summarise the main studies carried out from the point of view of AMS in this area.

Pascual and Parés (1990) present a preliminary work carried out on the SE edge of the Ebro Basin. The data are not available today, but it sets a precedent in the study of magnetic properties in the centre of the Ebro Basin, which the authors interpret as reflecting a sedimentary fabric, as well as paleocurrent-controlled magnetic lineations.

CHAPTER 2 - SHALE DEFORMATION

This situation is confirmed by Soto et al. (2009) and Pueyo Anchuela et al. (2010b). These authors reported stratification-controlled AMS pole, and randomly oriented K1 axes. However, both studies point out some localities in the Ebro basin where the K1 does appear to be oriented subperpendicular to the shortening direction of the South Pyrenean frontal thrust. Soto et al. (2009) report some sites in the Bardenas area (45 km south from the frontal thrust) with this “orientated” lineation (Figure 42). Lower and Middle Miocene lacustrine mudrocks were sampled, flat-lying beds chosen for their “sensitivity” to LPS as it was demonstrated.

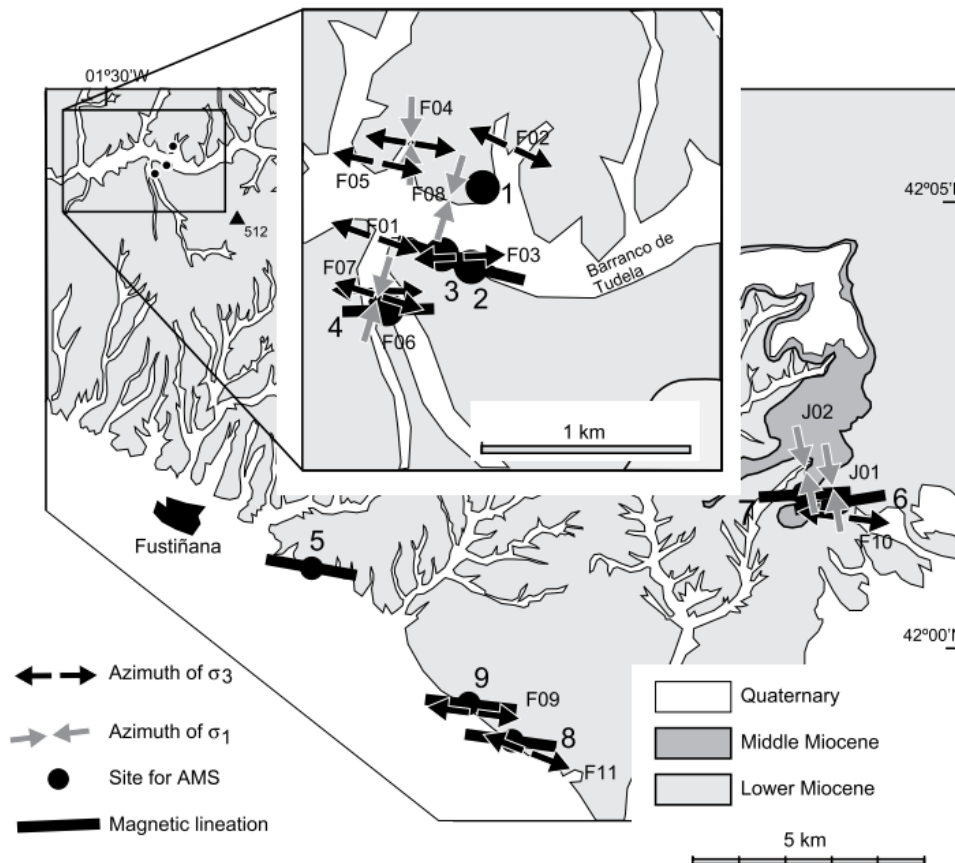


Figure 42: Sampling sites on Bardenas Reales (central Ebro Basin). The authors show the orientation of the deduced σ_1 , determined from structural observations of joints and strike-slip faults, with the K1 axes being exactly perpendicular. The magnetic lineation is also marked by the thick black lines. From Soto et al.(2009).

Pueyo Anchuela et al. (2010b) provided two sampling sections south of the South Pyrenean frontal thrust in the range 0 to 80 km south of the frontal thrust. Oligocene to Middle Miocene sandstones, mudstones and carbonate rocks were sampled. They reported an E-W magnetic lineation compatible with an LPS record as far as ~30 km from the thrust (Figure 43). The authors also point to a dispersion of the fabric linked to younger materials, where deformation is not so well expressed.

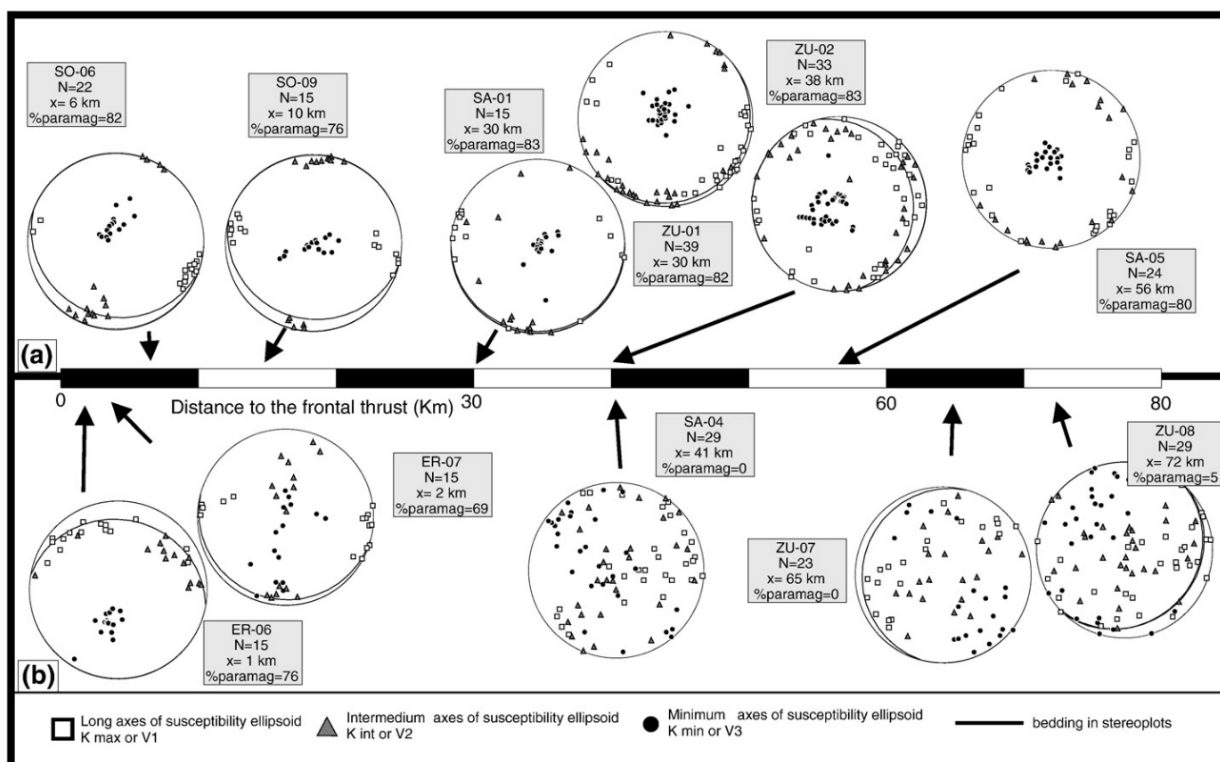


Figure 43: Magnetic fabrics of sampling sites in the two sections (a) corresponds to Ayerbe sections (b) corresponding to Ebro section. In both cases, the southern, and therefore the most central positions of the Ebro foreland basin are located to the right. We observe how the stereoplots of these positions show scattered K1 without magnetic lineation. Meanwhile, K3 is generally subvertical. From Pueyo-Anchuela et al. (2010)

Soto et al. (2016); sampled various sites in the central Ebro basin. Lower to Middle Miocene mudstones were targeted, tens of kilometres south the South Pyrenean frontal thrust at the Monegros region. LPS-like magnetic lineation is observed at 47% sites studied. The authors suggest that these lineations are related to Miocene deformation regime related to convergence between Europe or Africa.

All these studies show that horizontal shortening (LPS) very rapidly imparts deformation to the rather clastic facies of the Ebro Basin. A distance of around 30 km from the position of the outermost overrides visible on the ground can be invoked.

2.5.2 External Sierras.

The External Sierras (Sierras Exteriores) constitute the hanging-wall of the South-Pyrenean frontal thrust (Gurga thrust), comprising Mesozoic and Cenozoic carbonate and clastic rocks. This unit maintains continuity to the north with the broader Pyrenean piggyback, and is distinguished structurally by the presence of numerous north-south oriented folds. This phenomenon has captured the attention of structural geologists due to its noteworthy characteristics.

Pueyo-Morer et al. (1997) conducted an AMS study on the Pico del Águila Anticline to understand folding mechanisms. The Eocene syntectonic marls were sampled to explore these mechanisms. In doing so, they linked the fabric to flexural flow processes resulting from the fold's geometry, identifying mechanical distinctions based on lithology. Additionally, they established correlations between the scalar fabric parameters and the

CHAPTER 2 - SHALE DEFORMATION

overall shortening that the formations have experienced (Figure 44). Note the wide dispersion of the P and T data for a maximum calculated strain of ~15%. It should also be noted that T is triaxial to prolate, which is probably an underestimate of the deformation if we refer to the results of Parés and van der Pluijm (2003).

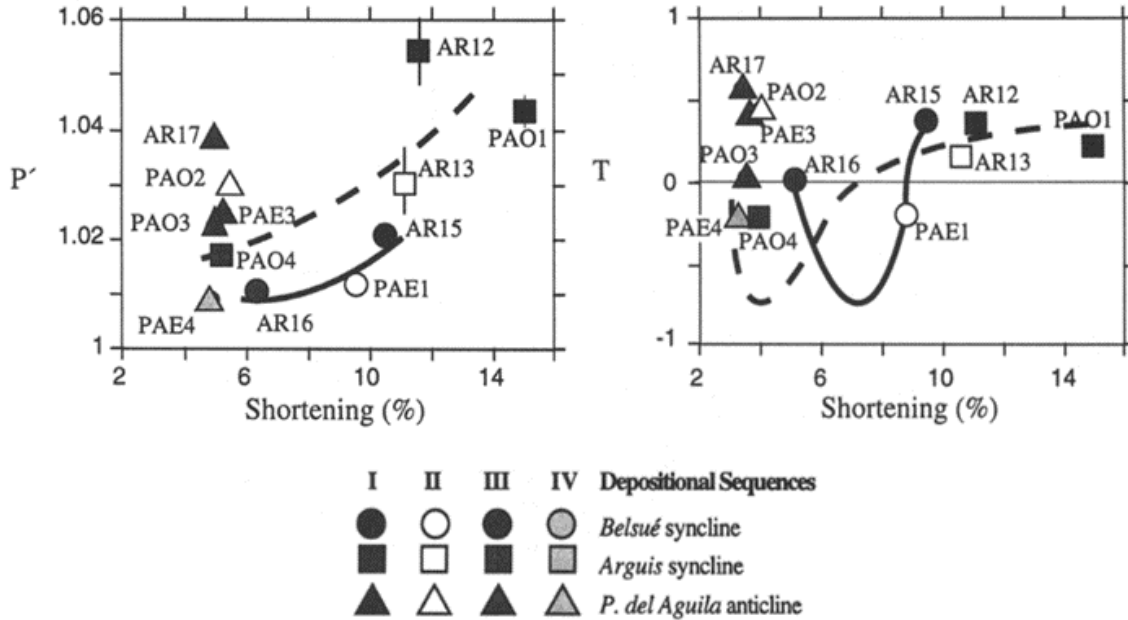


Figure 44: Scalar parameter (P' and T) are plotted against shortening calculated in fold geometry. An interpreted path of deformation is drawn. From Pueyo-Morer et al. (1997).

Anastasio et al. (2016) further investigated the deformation of the Arguis marl formation around the Pico del Águila fold. Their objective was to understand whether the deformation resulted from the N-S fold or the South Pyrenean frontal thrust, the predominant fault structure in the region.

Sampling within the same Eocene Arguis Marls formation adjacent to the fold revealed that the orientation of K1s is parallel to the axial plane of the anticline. However, in locations distant from the limbs, the K1s orientation is oblique to that of the fold, yet aligned with the overall strike of the External Sierras (see Figure 45). This implies that K1 is perpendicular to the shortening direction of the South Pyrenean frontal thrust.

CHAPTER 2 - SHALE DEFORMATION

AMS Fabric History	AMS Orientation (bedding corrected)	AMS Ellipticity (Jelinek Plot)	Deformation Regime
Compaction and Layer-Parallel Shortening			
Folding			
Thrusting	<div style="display: flex; flex-direction: column; align-items: center;"> <div style="margin-bottom: 5px;">limbs</div> <div style="margin-bottom: 5px;">hinge</div> </div>		

Figure 45: The study by Anastasio et al. (2016) shows how the magnetic fabric and the positions of the magnetic axes corresponding to the different phases of compression could be disentangled: LPS, folding or thrusting

Mochales et al. (2010) conducted a study on the N-S trending Boltaña Anticline, situated along the eastern margin of the Jaca basin. They sampled Bartonian turbidites from the western limb of the fold. The magnetic lineations exhibit trend variability and are attributed to various deformation events (stages a, b and c in Figure 46) associated with compression resulting from significant internal structures such as the thrust units of the Axial Zone or the Cotiella sheet, which lies northwards. The sampled turbidite beds do not display cleavage, and overall, the fabric retains sedimentary characteristics.

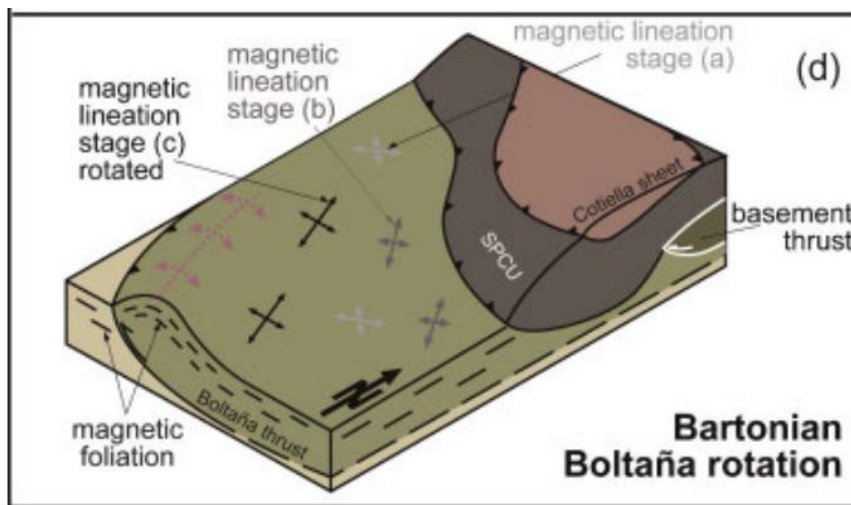


Figure 46: The Boltaña anticline with multi-directional magnetic lineation drawn on the Eocene units. From Mochales et al. (2010).

CHAPTER 2 - SHALE DEFORMATION

Sánchez et al. (2012) investigated the Santo Domingo anticline in the External Sierras (same units as the ones appearing in the Pico del Águila anticline), revealing a multimodal magnetic lineation orientation pattern that depends on the dipping axis within the periclinal closure of this structure. Consequently, the magnetic lineation displays variations, transitioning from subhorizontal orientation on the vertical flanks to a pronounced dip at the western termination of the fold.

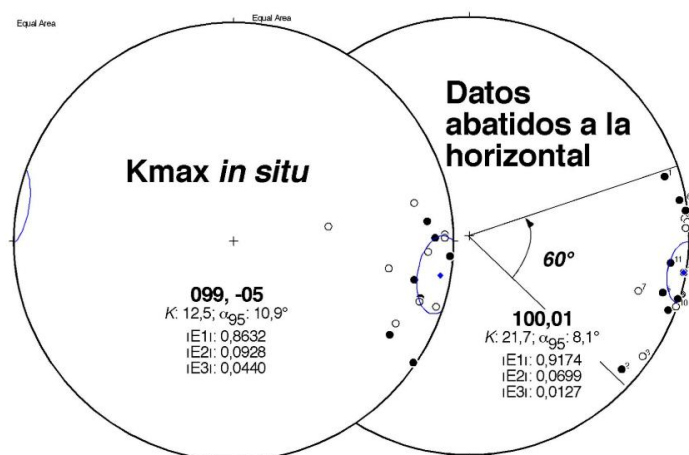


Figure 47: Magnetic lineation (described as *Kmax*) data in the Barbastro Anticline. From Oliván et al. (2008).

Oliván et al. (2008) discovered that the magnetic lineation orientation within the Barbastro anticline (southernmost structure of the South Pyrenean Central Unit, westward continuation of the External Sierras) varies when the axes are adjusted to the original horizontal of the folded layers (i.e. bed restoring). Sampling was conducted on the Oligocene-Miocene Peraltilla and Sariñena formation, both comprising alternations of sandstones, limestones and shales. This adjustment reveals a dispersion of up to 60° (Figure 47). Consequently, the study observes that these layers had recorded Layer Parallel Shortening (LPS) before the fold formation, serving as a passive marker of the initial compression.

2.5.3 Southern Jaca Basin and piggyback basins

Within the Pyrenean piggyback basins (such as Jaca-Pamplona, Ainsa, Tremp, and others), the intensity of LPS increases significantly, resulting in a variety of fabric types with more intricate evolutions at both regional and local scales. For this reason, the previously published models of fabric evolution are revisited in this chapter, focusing specifically on the one initially introduced by Parés et al. (1999). This same model has undergone further development and was incorporated into Jelinek's scheme (Parés and van der Pluijm, 2004b). The fabric evolution model, encompassing these five fabric types, is adopted in the paper by Gracia-Puzo et al. (2021) (see section 4.3.3. Data treatment and analysis of scalar parameters). The numbering of fabric types (1 to 5) will be employed for correlation with those described in the existing bibliography.

For additional detail, the sampling conducted by Parés et al. (1999) covered a transect spanning ~25 kilometres along the Ter River in the Eastern Pyrenees (~230 km east of Jaca).

CHAPTER 2 - SHALE DEFORMATION

The sampled units primarily consisted of mudstones from the Middle and Upper Eocene. From numerous sampling sites along this transect, a model was developed, categorizing fabrics into five distinct types that illustrate the transition from sedimentary fabric to cleavage fabric (Figure 48).

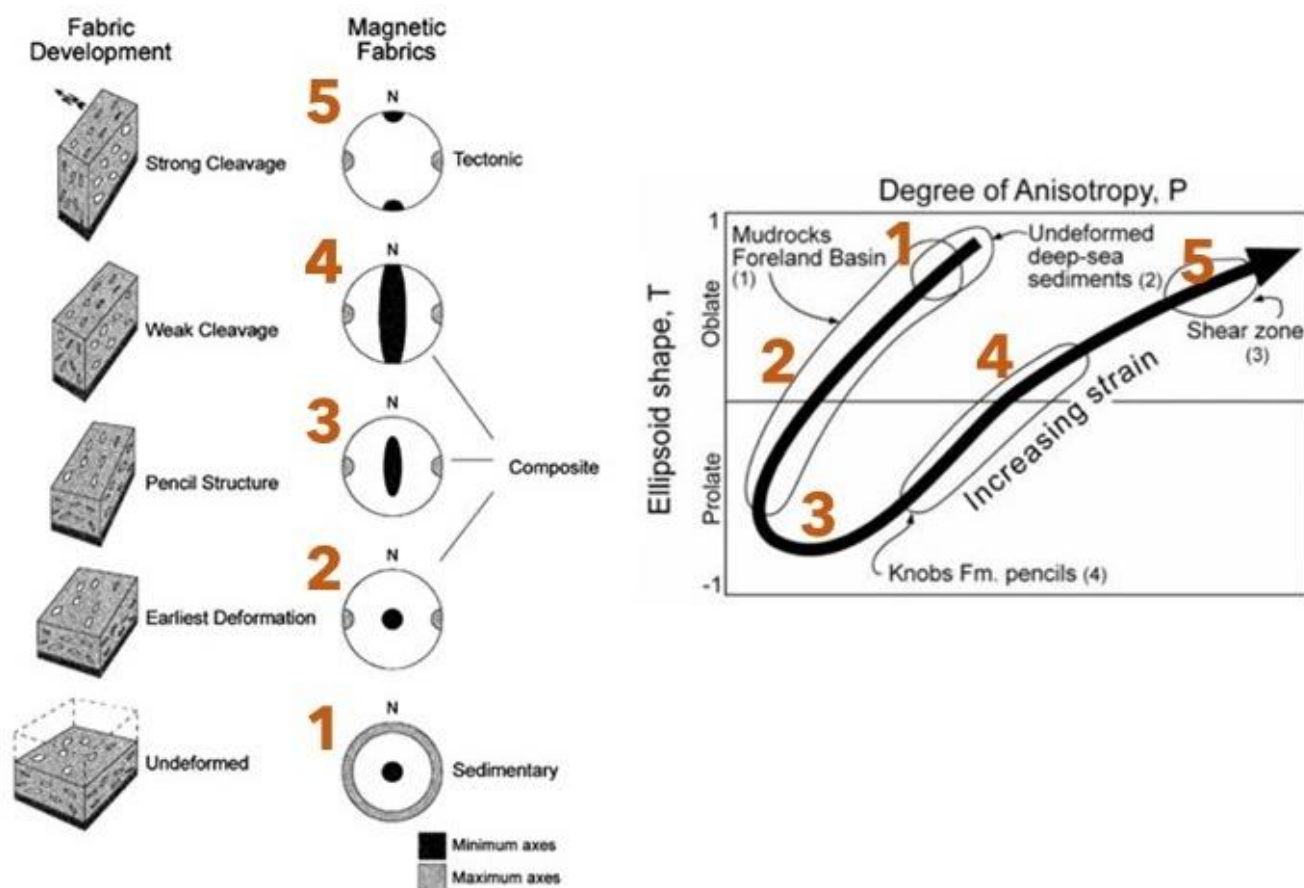


Figure 48: On the left we show the fabric evolution model presented by Parés et al. (1999), while on the right there is a comparable Jelinek diagram illustrating the increase in deformation expressed through the parameters P and T, as introduced by Parés et al. (2004). The orange numbers serve as correlating references between the two models.

An essential bibliographical reference for comprehending the evolution of fabrics in this region of the chain, encompassing the Jaca basin and extending transversally from the Ebro basin to the Sierras Interiores, is Pocoví Juan et al. (2014). This article compiles various samplings conducted within the Jaca Basin, offering a geographically comprehensive and expanded overview of magnetic fabric studies on the southern slope of the Pyrenees. Thus, Pocoví-Juan et al. (2014) not only provide insights into the condition of fabrics formation within the Jaca basin but also contextualize the broader framework presented in this chapter (Figure 49). It demonstrates that while fabrics may be influenced by local heterogeneities and orogenic evolution, they are generally governed by bedding unless cleavage predominates (making them a reliable strain indicator). Their results are comparable with the complete fabric evolution model (1 to 5 fabric types) proposed by Parés et al. (1999).

CHAPTER 2 - SHALE DEFORMATION

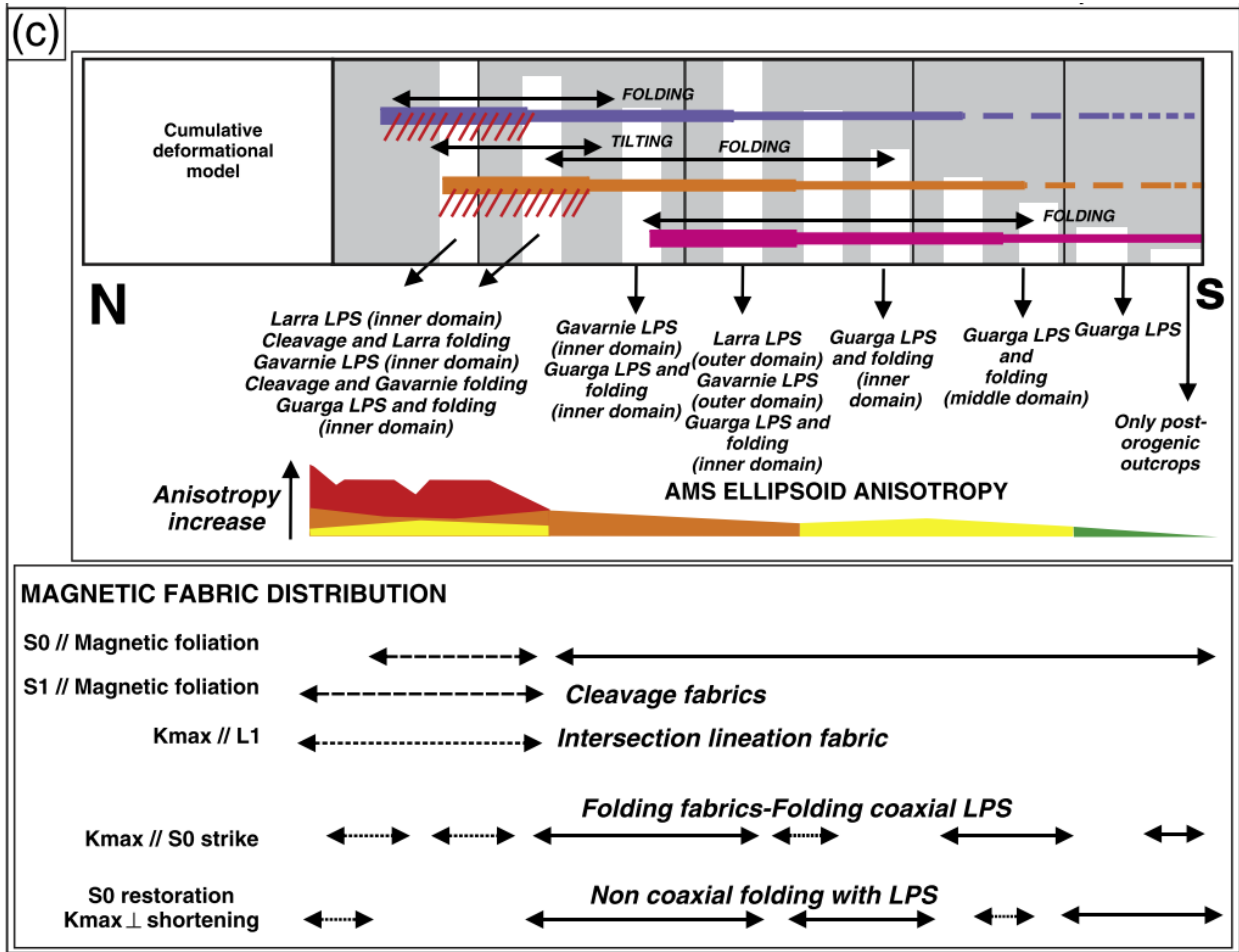


Figure 49: The article by Pocoví-Juan et al. (2014) provides an overview of the deformation characteristics within the Jaca Basin. This figure serves as a summary of the mechanisms and LPS episodes associated with orogen emplacement, correlated with AMS results, and detailing the magnetic fabric characteristics.

Several studies examining magnetic fabrics associated with folding processes have been presented, primarily focusing on the External Sierras. However, the study by Larrasoña et al. (1997) specifically concentrates on the Jaca Basin, situated between the molasse and turbiditic subbasins. In this area, multiple marine Eocene units were sampled, including the marls of the Pamplona Formation and the Hecho Group, both affected by folding.

The article highlights that the magnetic fabric complexity can vary based on folding mechanisms and the position within the fold: longitudinal strain in the hinge, flexural slip, and simple shear on the flanks. In general, pure shear results in a fabric normal to the axial surface, with K1 aligning parallel to the strike of this surface. In Figure 50 (top left), the authors use Jelinek's diagram to categorize various fabric types corresponding to the deformation mechanism associated with the fold and LPS shortening. The fabrics presented in the model are not organized by intensity, but it is possible to correlate some of these 'mechanism' of fabrics with a various types of the model proposed by Parés et al. (1999).

CHAPTER 2 - SHALE DEFORMATION

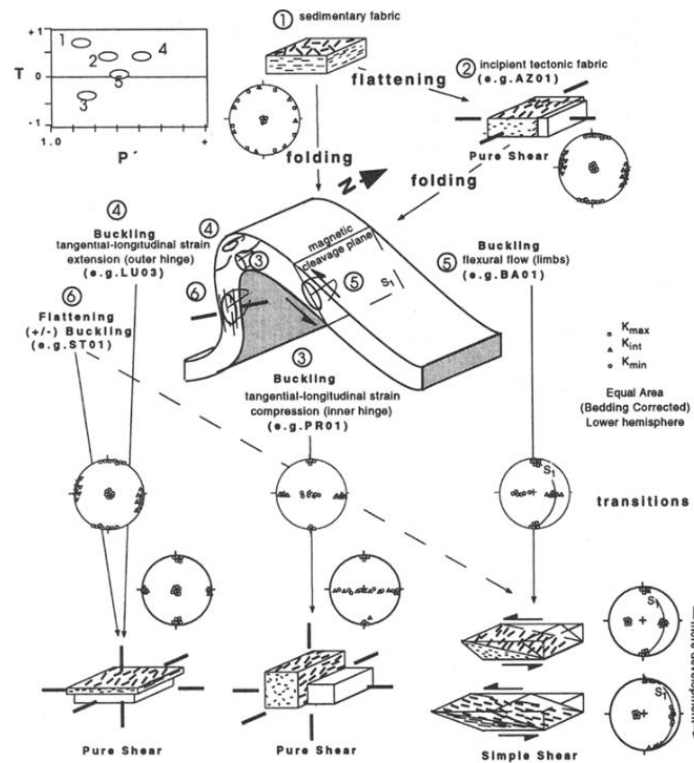


Figure 50: A fold is hosting various strain mechanisms; consequently it could be detected and described with magnetic fabric analysis. From Larrasoana et al. (1997).

Parés and Dinarés-Turell (1993) sampled the Eocene marls of the Aínsa basin, which is located to the east of the Jaca Basin. Although the structural architecture differs between the two areas, the sampling was undertaken to examine whether the marls closer to the internal thrusts of the orogen (north of the basin) displayed any changes in their fabric.

Some distant sites exhibit an oblate sedimentary fabric (represented by square symbols in Figure 51), characterized by compaction, with K_3 aligned parallel to the bedding pole. This fabric gradually rotates to oblique positions, with K_1 aligning with the intersection lineation, marking the beginning of a subtle pencil cleavage and an oblate fabric (indicated by triangular symbols). Finally, in the innermost part of the basin (at site J35), where cleavage is present, an oblate fabric is observed, interpreted as controlled by LPS cleavage, as evidenced by K_3 aligning with the pole of the shale cleavage. The fabrics described in the article exhibit characteristics that coincides with fabric evolution types 1 to 5, as later described by Parés et al. (1999).

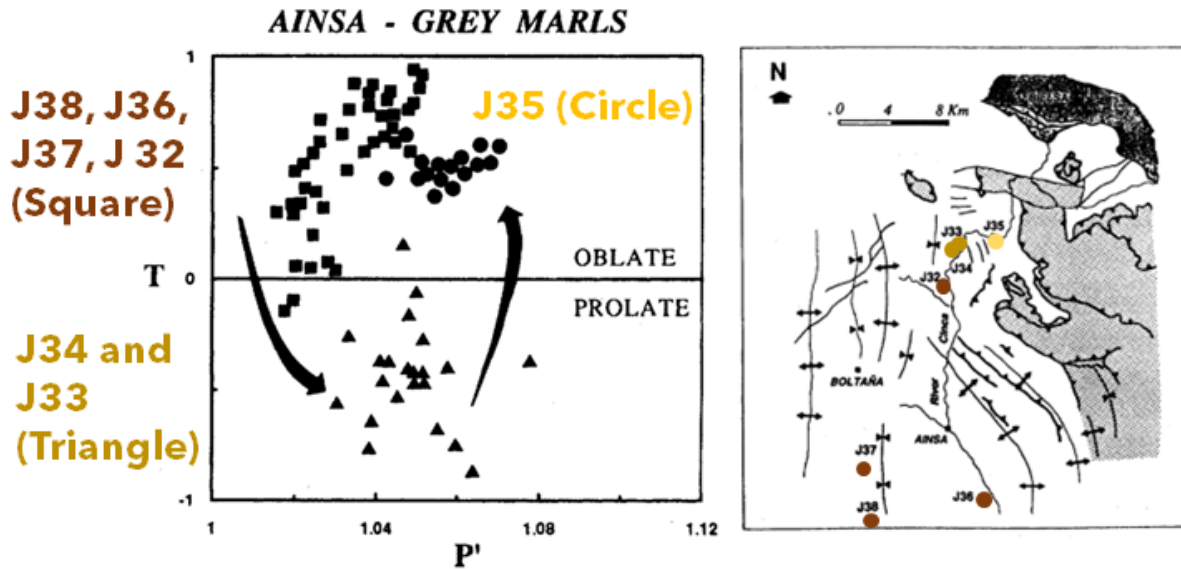


Figure 51: Sampling on the Ainsa Basin has led to a path of deformation marked by arrows in Jelinek's diagram (left). Magnetic fabrics are affected in proximity to internal nappes of South Pyrenean prowdedge (north of right map). From Dinarés Turell and Parés (1993).

Larrasoña et al. (2004) conducted sampling in the Eocene Pamplona Formation shales within the Pamplona Basin, which represents the western continuation of the Jaca Basin. Their study encompassed a comprehensive AMS analysis. Their findings indicate that the signal is predominantly controlled by paramagnetic minerals such as chlorite and illite-muscovite.

They proposed a classification of four fabric types, reflecting a progressive increase in deformation (refer to Figure 52). However, it is important to note that this model of fabric evolution is based on the Woodcock diagram, not Jelinek's diagram, resulting in a different arrangement of fabric elements in the diagram on the right. As such, this model does not align with that presented by Parés et al. (1999).

Furthermore, Larrasoña et al. (2004) argue that magnetic fabric elements were developed and locked during the early stages of strain, specifically in the Middle-Late Eocene compression period. They contend that subsequent cleavage would undergo passive rotation, supporting the use of fabric measurements as a proxy for strain.

CHAPTER 2 - SHALE DEFORMATION

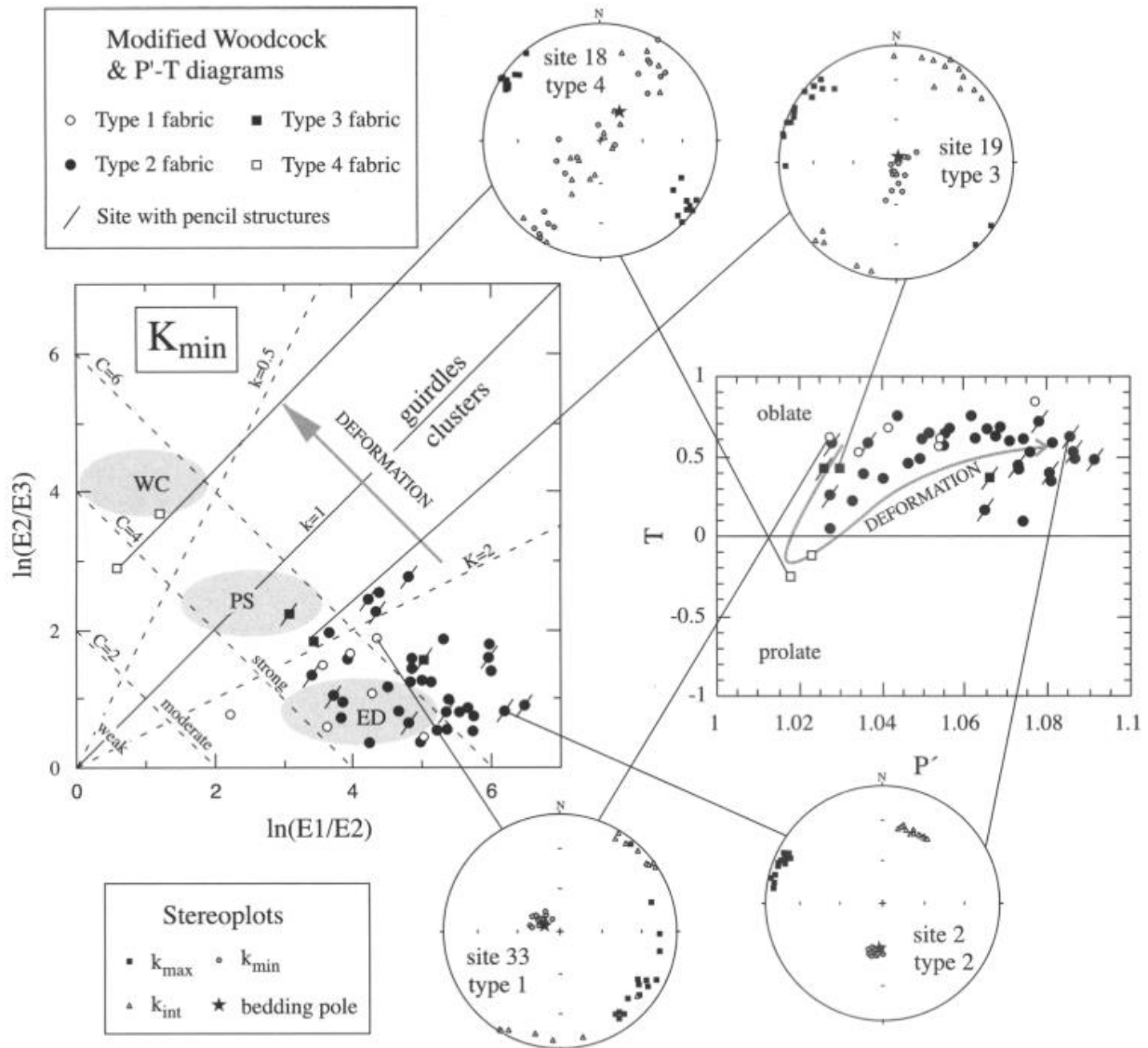


Figure 52: Types of magnetic fabric in the Jaca Basin. ED: earliest deformation; PS: pencil structure and WC: weak cleavage. From Larrasoña et al. (2004).

Pueyo-Anchuela et al. (2011b) conducted sampling in the Eocene Larrés Formation within the Canal de Berdún, which is located near the sampling sites of this PhD study. This paper investigates how the magnetic fabric preserved the evolutionary history of this syntectonic basin. These authors specifically analysed the paramagnetic contribution, which they attributed to be responsible for 80 to 98% of the magnetic fabric signal.

Results suggest that the magnetic fabric is influenced by slumps and other intra-sedimentary phenomena on the marine slope. This observation implies that the locking of the fabric occurred shortly after sedimentation and before the widespread folding and tilting of the orogenic basin. In general, the identified fabrics in their study correspond to Parés et al. (1999) Type 1 (“Sedimentary” in Figure 53), Type 2 (comprising “Type 1A and 1B”), and Type 3 (related to “gravitational structures or Type 2” by Pueyo-Anchuela et al., 2011)

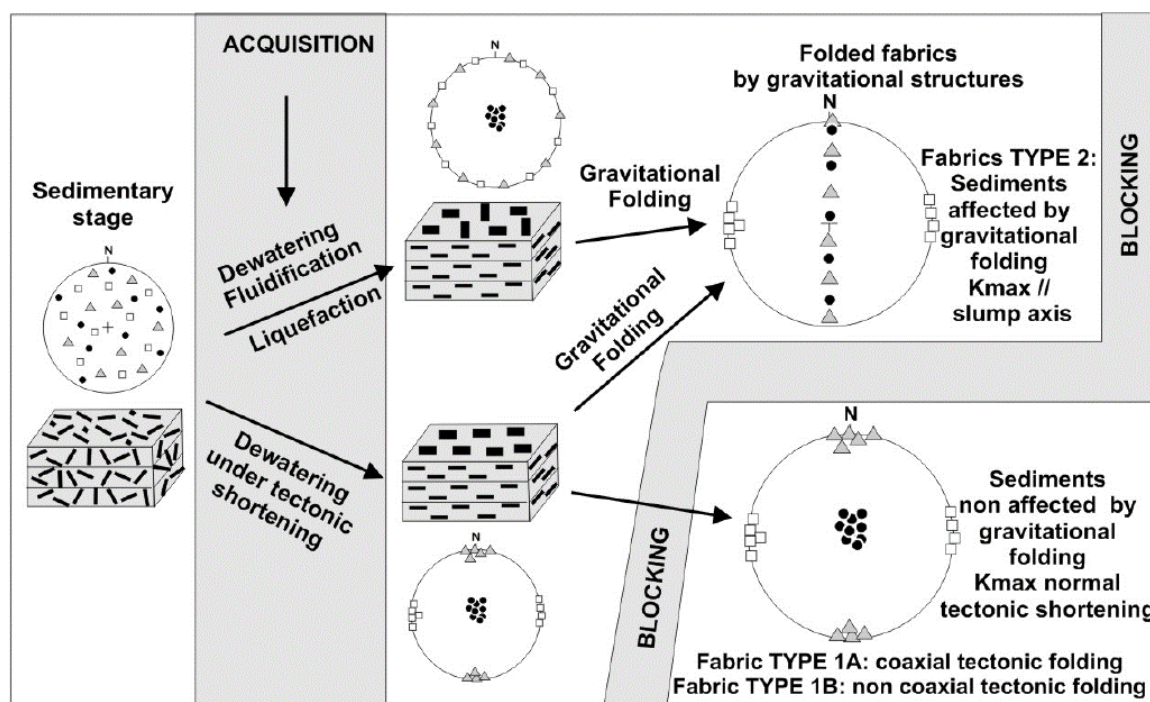


Figure 53: A model for evolution of magnetic fabrics measured on Eocene marls. Sedimentary processes such as dewatering, fluidifications and folding (slumps) create a fabric of type 2. Fabric of Type 1 is interpreted related to first LPS. From Pueyo-Anchuela et al. (2011b).

Recently, in the Molasse-Turbiditic interface of the Jaca Basin, Boiron et al. (2020) analyzed the footwall of the Leyre thrust, where the marls of the Jaca molasse basin underwent intense deformation. This work served as the precursor to this thesis and its results show a deformation gradient within these Eocene Larrés Fm shales. It was observed that the shales exhibited a more penetrative cleavage in the vicinity of the Leyre thrust.

2.5.4. Turbiditic Jaca Basin

Some of the articles mentioned earlier involve sampling conducted within the Hecho Group and other molasse formations. Drawing from the conclusions of Pueyo-Anchuela (2012b), Izquierdo-Llavall et al. (2013), and the comprehensive review by Pocoví Juan et al. (2014), it is broadly asserted that the cleavage front aligns, or slightly deviates to the north, to the boundary between the Jaca molassic basin and the thick turbidites of the Hecho Group. These turbidites thrust southward over the molasse deposits. It is worth noting that the presence of 'local irregularities,' as described by Pueyo (2012), may lead to deformed fabrics south of this boundary. Nevertheless, within this turbiditic zone, numerous studies have been conducted to establish regional cleavage patterns and understand deformation mechanisms, with a methodological focus primarily on magnetic fabrics and rock magnetism.

The paper by Pueyo-Anchuela et al. (2011a) indicates that Bouma sequence levels exhibit similar behaviour in terms of orientation and AMS scalar parameters. The paramagnetic contribution to susceptibility demonstrates consistent values and does not display differential patterns between lithologies. These paramagnetic grains (various phyllosilicates) are likely sedimentary and detrital rather than autigenic. In general, paramagnetic

CHAPTER 2 - SHALE DEFORMATION

phyllosilicates and fine-grained magnetites are susceptible to cleavage development. It's possible that certain beds of the turbidites are influenced by ferromagnetic behaviour, but mainly the sandstones show a high paramagnetic contribution (resulting from clay minerals content) that are highly sensitive to cleavage development within the turbidites. As a result, the development of cleavage in outcrops may not directly correlate with the definition of the magnetic fabric (Pueyo-Anchuela et al., 2011a).

Two more papers by the same author (Pueyo-Anchuela et al., 2013b, 2013a) describe in detail the magnetic behaviour of the measured fabrics across the entire South Pyrenean transversal. Notably, these papers delve into the segregation of paramagnetic and ferromagnetic contributions to fabric measurements. It becomes apparent that the ferromagnetic contribution tends to be more prominent in the inner zones of the turbidite basin (Figure 54), a phenomenon linked to variations in P-T conditions (Pueyo-Anchuela et al., 2013b).

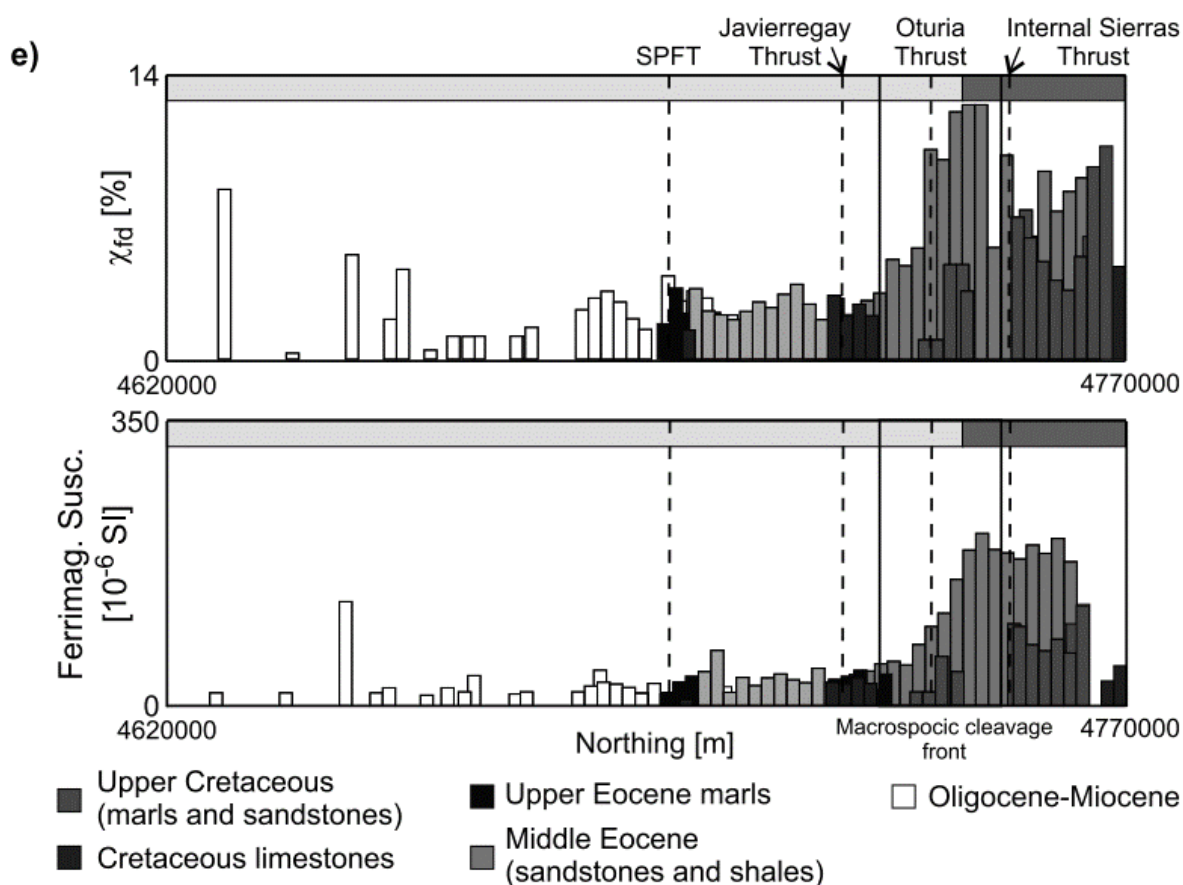


Figure 54: The Javierregay thrust could occupy a structural position similar to that studied in this PhD. Upper Eocene Marls are the shale formations object of study. From Pueyo-Anchuela et al. (2013b).

Overall, Pueyo-Anchuela et al. (2013a) generally attribute the majority of the signal to paramagnetism in most samples, with this dominance being particularly pronounced in samples from the Larrés Formation, the upper Eocene marls highlighted in black in Figure 55. In these shale samples, the paramagnetic signal can account for up to 99% of the bulk susceptibility, as revealed through High vs. Low field susceptibility measurements (HF vs. LF) conducted on the rock samples from the Jaca Basin.

CHAPTER 2 - SHALE DEFORMATION

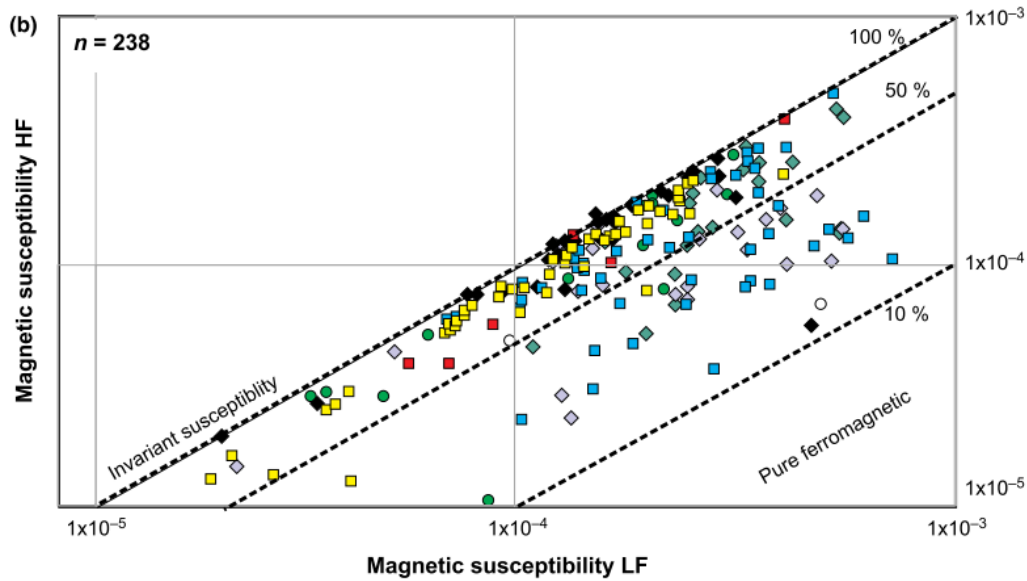


Figure 55: Black diamonds correspond to Eocene Marls, such as Arro-Fiscal Fm in Jaca Basin. From Pueyo-Anchuela et al. (2013a).

In relation to the syntectonic shortening within the Eocene Hecho Group, Pueyo Anchuela et al. (2010a) conducted sampling solely within the turbidites, encompassing both sandstone and mudstone lithologies. The primary aim of this study was to discern the LPS events that have affected the Hecho Group, which present cleavage in their outcrops. As a result, the author identified four distinct fabric types that serve to highlight 'the inhomogeneity of the strain progression.' This heterogeneity in fabric types is attributed to localized phenomena such as faults, folds, and variations in the signal, primarily driven by paramagnetic minerals (phyllosilicates). However, there were occasional occurrences of ferromagnetic signals, which contribute to the observed differences in what would theoretically constitute a deformation gradient within the inner zones of the turbiditic basin.

Comparing Pueyo Anchuela et al. (2010a) AMS groups with the evolutionary model proposed by Parés et al. (1999): Group 1 and Group 2 are consistent with type 2 (Figure 56), although it is important to note that the orientation of the magnetic lineation (K1) varies in relation to the emerging cleavage observed in Group 2. Group 3 aligns with either type 4 or type 5 within Parés's model.

CHAPTER 2 - SHALE DEFORMATION

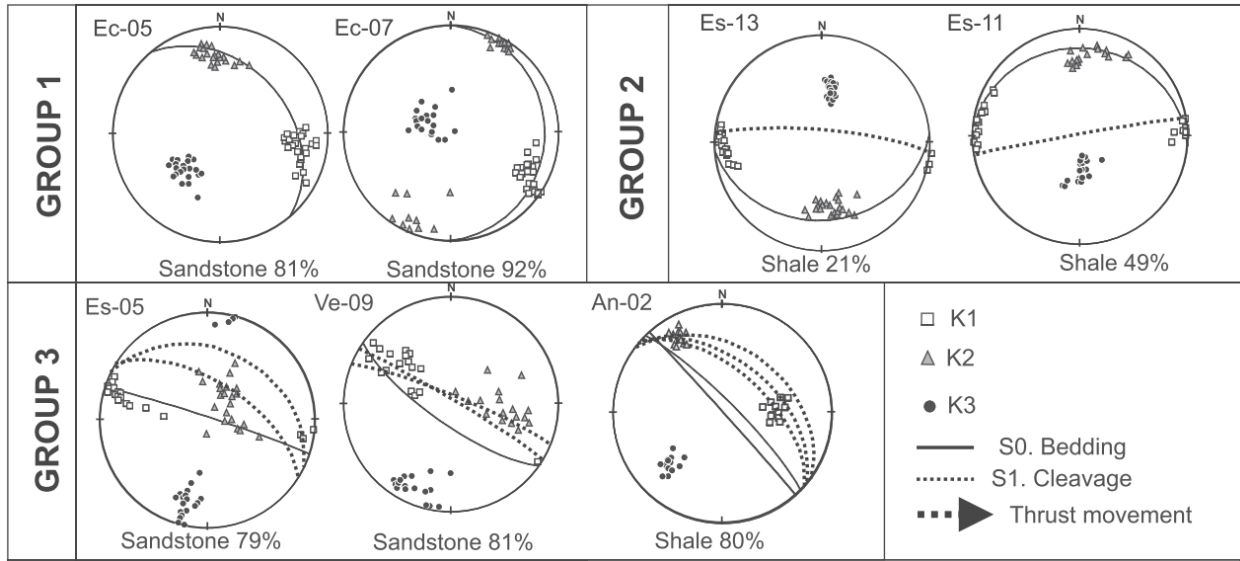


Figure 56: 3 of the groups of magnetic fabrics presented in the paper by Pueyo Anchuela et al. (2010a). Comparing with the model of Parés et al. (1999): Group 1 and group 2 would correspond to type 2, although the orientation of the magnetic lineation (k1) varies with respect to the incipient cleavage of group 2. Group 3 corresponds to type 4 or 5.

Pueyo Anchuela et al. (2012) delve into the domain of cleavage and examine how magnetic fabrics record these phenomena. They sampled similar sites in the Eocene Hecho Group as in the previously presented paper, also including a few sites in Upper Cretaceous and Palaeozoic rocks. Their investigation revealed variability in the magnetic signal, detecting both ferromagnetic and paramagnetic behaviour coexisting and calculating their respective contributions. Consequently, they identified several deviations from the expected results, such as magnetic lineations not always coinciding with the intersection lineation. They attributed these deviations to factors such as the ferrimagnetic contribution to susceptibility in carbonate-dominated shales, leading to the presence of competing 'sub-fabrics' or 'inhomogeneous' deformation caused by local structures. The authors differentiated between various strain processes, including LPS, penetrative cleavage, and shear fabrics. As a result, they proposed a model (Figure 57) that corresponds to types 2, 3, 4, and 5 of the Parés et al. (1999) model.

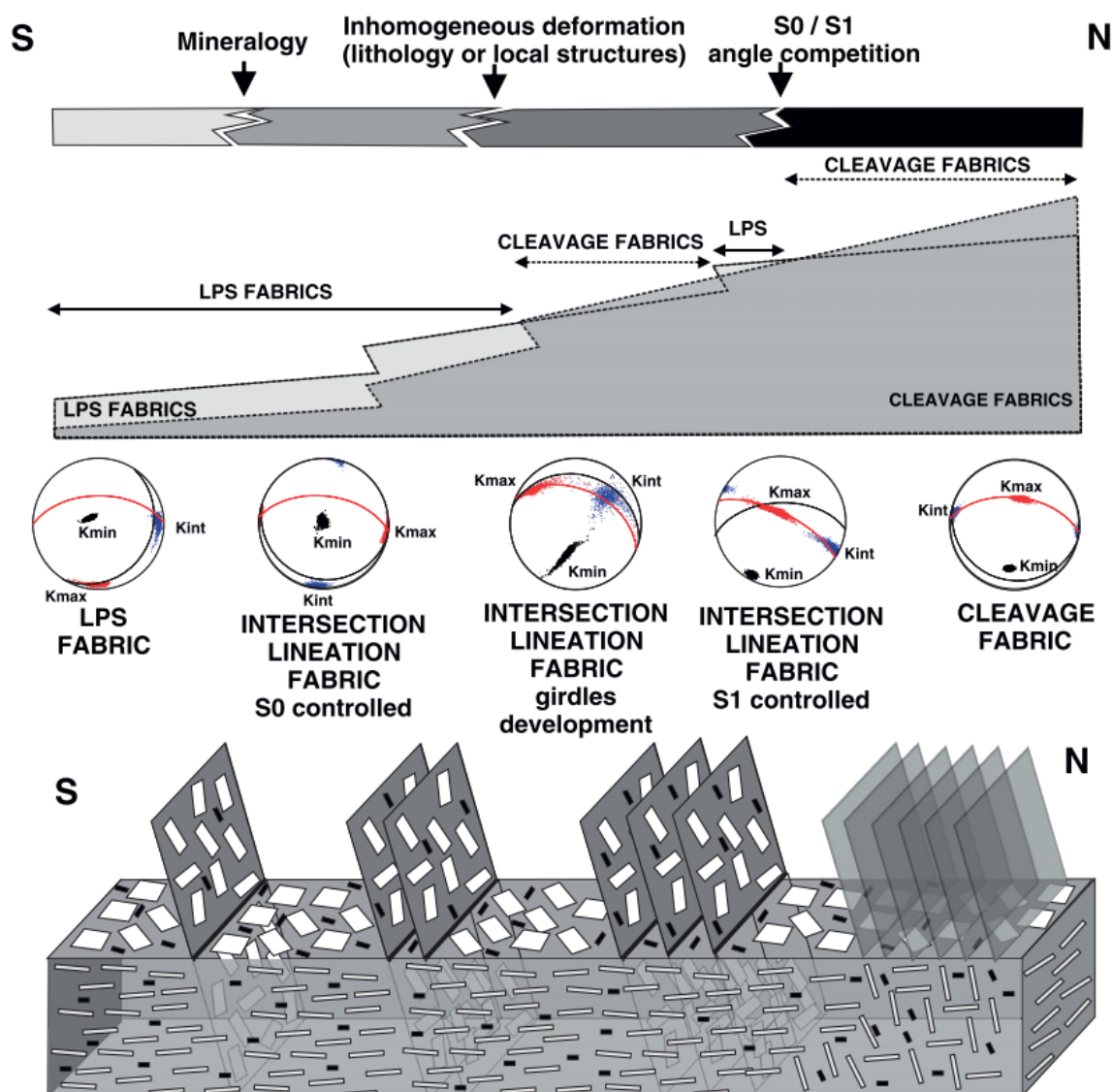


Figure 57: Model of fabric evolution of cleavage domain of South Pyrenean domain. A distinction is made between LPS fabrics and 'cleavage fabrics.' LPS fabrics exhibit magnetic lineations that correspond to the intersection lineation, whereas cleavage fabric K3 aligns with the pole of the outcropping cleavage. From Pueyo-Anchuela et al. (2012).

2.5.5 Internal Sierras

The Internal Sierras and the Axial Zone can be included in the context of the 'evolution of the southern slopes of the Pyrenees. However, due to the age of the deposits (Paleogene, Mesozoic and Paleozoic) and the complexity of the deformation mechanisms that they have undergone (Variscan orogeny in the Axial Zone, extensional basins during the Cretaceous), the existing literature focuses on issues somewhat different to the deformation gradient described in this work.

For instance, studies have examined the expression of the K1 magnetic lineation in relation to the emplacement of the Cotiella-Bòixols thrusts. Soto (2003) investigated Upper Cretaceous limestones in the central sector of the South-Pyrenean zone. Oliva-Urcia et al. (2009) distinguished between paramagnetic sub-fabrics (using LT-AMS) and ferromagnetic sub-fabrics (using AARM) to describe the complex composite fabric observed in the Zuriza

CHAPTER 2 - SHALE DEFORMATION

Shales, which exhibit cleavage (Figure 58). Similarly, Marcén et al. (2018) focused on the Gavarnie fault, which outcrops in the Axial Zone, primarily affecting Paleozoic rocks (Silurian and Devonian phyllites). A complex fabric comprising phyllosilicate (paramagnetic) and ferromagnetic elements is analysed using AMS, LT-AMS, and AIRM. In a shear zone up to 80 m thick, a strain gradient was detected with more significant deformation toward the thrust plane. Scalar parameters (P_j and T) data is also examined, noting that these parameters exhibited higher values in areas with increasing strain, while K_1 of the magnetic fabrics is aligned parallel to the transport direction.

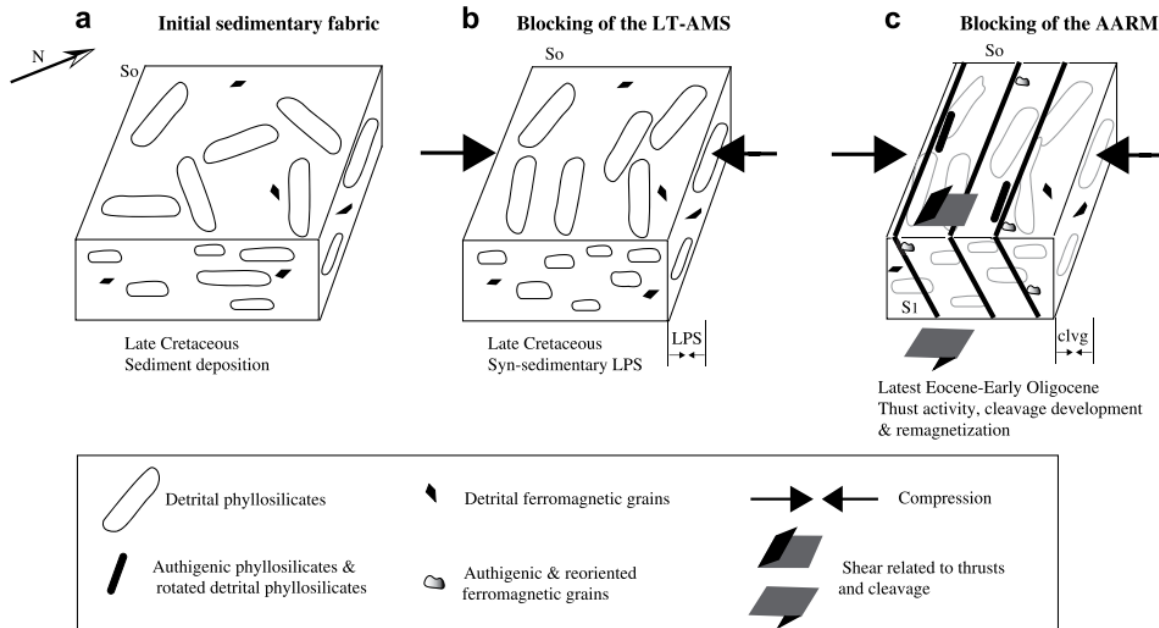


Figure 58: Zuriza Shales exhibit a coexistence of various subfabrics. AMS comprises a bulk of various grain components, including paramagnetic detrital phyllosilicates, detrital ferromagnetic grains, authigenic phyllosilicates, and authigenic ferromagnetic grains. In the paper, both LT-AMS and AARM techniques are employed to separate ferromagnetic and paramagnetic behaviours. Consequently, the authors present a fabric evolution model. From Oliva - Urcia et al. (2009).

3. STRUCTURAL STUDY OF THE SIGÜÉS AREA

3.1. The Pyrenean Orogen and the Jaca Basin

3.1.1 General architecture of the Pyrenees

The continental Pyrenees (Muñoz et al., 2002) constitute a mountain range that separates the Iberian Peninsula from the European continent, marking the geographical border between the south of France and the north-east of Spain. Nevertheless, the geological impact of the Pyrenean orogeny is broader and extends farther than the isthmus. The effects of the Pyrenean orogeny are interpreted and detected from the Cantabrian mountain range hundreds of kilometres west of the isthmus (Alonso et al., 1996; Pulgar et al., 1999; Quintana et al., 2015; Séranne et al., 1995; Teixell et al., 2018), to the Provençal chains in south-eastern France, with many mountainous reliefs associated to this geological event.

The global configuration of the Pyrenean chain has traditionally been interpreted as the result of the continental collision between the Iberian plate and the Eurasian plate, now welded together (Choukroune, 1992, 1989; Choukroune et al., 1990; Choukroune and Séguret, 1973; Muñoz, 1992). This orogen is framed (i) as the western continuation of the massive Alpine orogen, together with (ii) other SW European and North African structures such as the Iberian and Betic systems in the Iberian Peninsula; all of them are included in the continental-scale collision frame between the African plate and the Eurasian plate (Casas Sainz and Faccenna, 2001; Macchiavelli et al., 2017; Roure et al., 1989; Teixell et al., 2018).

Precisely, at the isthmus Pyrenees (as shown in Figure 59) the structure of the chain exhibits a highly variable orogenic structure, both longitudinally and across-strike. The three major along-strike units are (i) the Axial Zone, which comprises Paleozoic rocks in the central axis of the chain. On each flank of the chain there is (ii) the retrowedge (North Pyrenean Zone) mainly consisting of Mesozoic units, often detached over the basement by means of the Upper Triassic detachment, and (iii) the prowedge (South Pyrenean Zone), which also consists of Mesozoic units, and a significant thickness of Cenozoic syntectonic rocks to the south. On the northern and southern margins of the Pyrenees lie the Cenozoic foreland Aquitaine and Ebro basins, respectively.

CHAPTER 3 - STRUCTURAL STUDY OF SIGÜÉS AREA

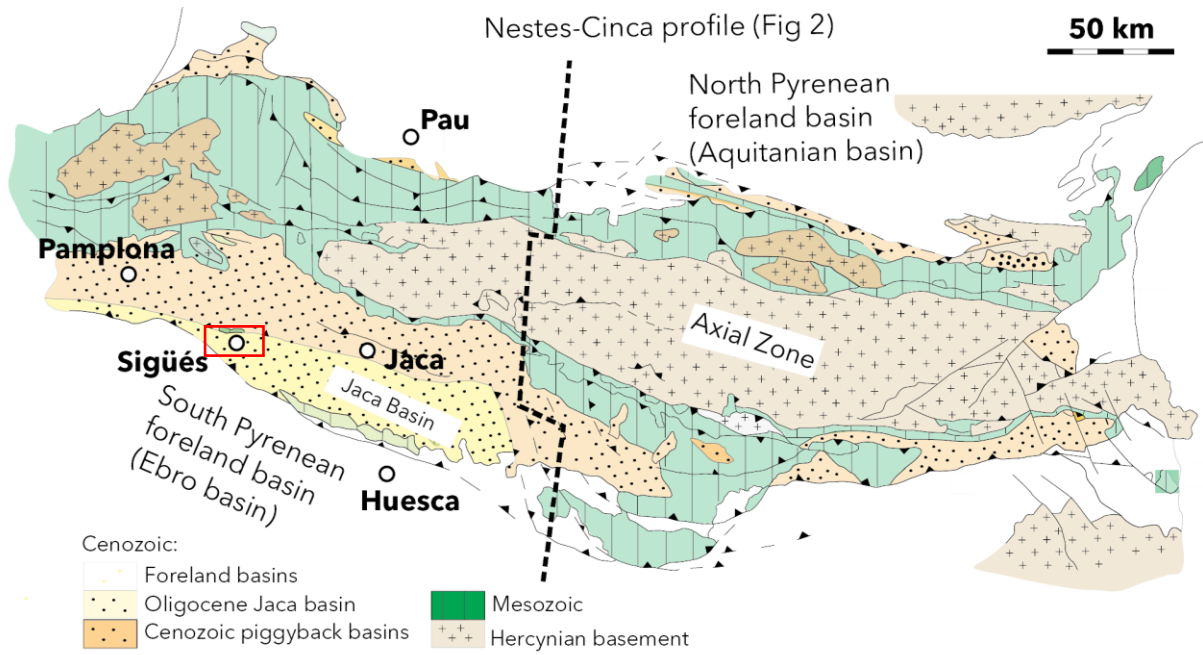


Figure 59: Map of Pyrenees. Redrawn from Pocoví-Juan et al. (2014). Studied area is in square. Note the location of this study area at the boundary between the turbidite basins in piggyback, and the molassic basins to the south. Cross-section of Figure 2 is the N-S black line.

The important seismic campaigns in the 1980-90s allowed to understand the crustal architecture of the Pyrenees (Choukroune, 1989; Daignières et al., 1994 respectively ECORS, 1989, ECORS Anso-Arzacq, 1989). There are also dozens of regional seismic lines, usually promoted by hydrocarbon companies, but the three main ones used on academic domain are as follows. There is the ECORS-Pyrenees, which crosses the entire mountain range from N to S in its central sector, from Lleida to Toulouse approximately. Further to the west, another section complements this one, the ECORS-Arzacq, which covers the western North Pyrenees region, in the Béarn-Navarre Provinces. A third section called ECORS - Bay of Biscay, runs parallel to a few kilometres of the Basque-French coast. The three lines have served as the starting point for the major crustal cross-sections of the orogen (Daignières et al., 1994; Muñoz, 1992; Roure et al., 1989; Teixell, 1998, 1996, among others).

CHAPTER 3 - STRUCTURAL STUDY OF SIGÜÉS AREA

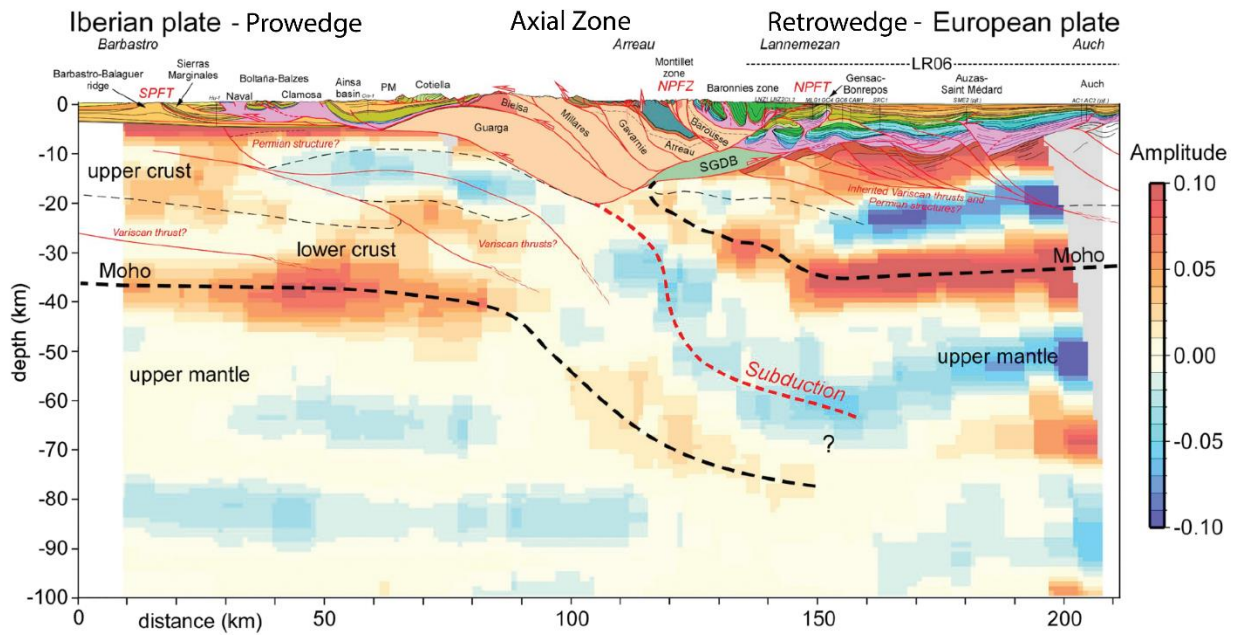


Figure 60: Stack crustal profile of OROGEN west profile by Espurt et al., 2019, done in central Pyrenees (see trace Nestes-Cinca in Figure 59). Data acquisition by Chevrot et al., 2018 includes PYROPE project, who plots amplitude of P-to-S waves conversion phases. Also, seismic reflection, tomographic studies, exploration wells, shallow profiles and surface geology.

In the last decade, new tomography, reflection seismic and geophysical campaigns by means of different techniques (Calvín et al., 2018; Campanyà et al., 2012, 2011; Chevrot et al., 2018, 2014; Clariana et al., 2022; Diaz et al., 2016; Muñoz et al., 2013; Piña-Varas et al., n.d.; Wang et al., 2016) campaigns have expanded and refined the available information. In Figure 60, a cross-section by Espurt et al. (2019) is shown, integrating geophysical data such as deep seismic reflection profiles, tomographic studies, exploration wells, shallow profiles and surface geology. All this have led to the interpretation that the Pyrenees are formed by a double bivergent tectonic wedge, where the Iberian crust subducts about 55-60 km (Chevrot et al., 2018, 2015) below the European crust. This determines the configuration of the basement thrust sheets, that are disposed in fan-shape, and crustal thickening is observed in the central sector of the orogen, the Axial zone (Figure 60), as recognized in the classical works of the past century (Choukroune, 1992; Mattauer, 1990, 1985; Séguret and Daignieres, 1986). The orogen has a visible asymmetry in the sections: to the N, the retrowedge it extends less (30 km) than to the S, where the prowedge thrust sheets incorporate piggyback basins advancing into the foreland (60 km). The Axial Zone is composed of the Hercynian basement, mainly Paleozoic rocks that underwent the Variscan orogeny (Ábalos et al., 2002; Carreras and Capella, 1994; Matte, 2002), as well as plutonic units emplaced during the Carboniferous and the Permian (Denèle et al., 2014, 2012; Gil-Imaz et al., 2012; Gleizes et al., 1998, 1997; Pereira et al., 2014) and their volcanic counterparts (Bixel and Lucas, 1983; Lago et al., 2005, 2004).

The shortening associated with the orogenic stage is not laterally uniform, being smaller in the eastern section (100 km; Roure et al., 1989), than in the central section, where it reaches more than 165 km (Beaumont et al., 2000), diminishing again towards the west, although some other factors such as the thickness of the continental crust involved in deformation have also been invoked as responsible for along-strike changes in the Pyrenean structure (Soto et al., 2006). In simple terms, the Axial Zone is larger in the central-eastern part of the

CHAPTER 3 - STRUCTURAL STUDY OF SIGÜÉS AREA

chain and the thrust sheets propagate tens of kilometres to the south in the South Pyrenean Central unit (SPCU). In the western part of the chain, outcrops of Mesozoic and Cenozoic units, corresponding to basin inversions, dominate (Daignières et al., 1994; DeFelipe et al., 2018; Gómez-Romeu et al., 2019; Jammes et al., 2009). In some cases thrust sheets involve the Paleozoic materials of the Axial Zone (Oliva-Urcia et al., 2010; Saspiturry et al., 2022). The difference in shortening is explained by the collisional history responsible for the orogen. The most widely accepted version is that the Iberian plate rotated counterclockwise in its collision with the Eurasian plate (Mouthereau et al., 2014; Rosenbaum et al., 2002; Roure et al., 1989). The construction of the chain through the collision of plates starts in the East and progressively advances towards the West, in a period that spans from the Cretaceous to the Miocene (Bosch et al., 2016; Oliva-Urcia et al., 2019; Roure et al., 1989; Vergés et al., 1995).

Comparing the retrowedge and prowedge of the Axial zone incorporated into the orogen, they show an asymmetrical growth towards the north and south and their geometries are also different (Figure 60) (Grool et al., 2018; Hoth et al., 2008; Saspiturry et al., 2020; Sinclair et al., 2005). The difference in structural style between the northern and southern Pyrenees is conditioned by its previous history and Mesozoic palaeogeography (Canérot et al., 2004; Lescoutre and Manatschal, 2020): It is generally accepted that the northern Pyrenees were subjected to pre-alpine, Mesozoic rifting, especially during the Cretaceous, characterized by hyperextension processes (Canérot, 1991; Jolivet et al., 2007; Labaume and Teixell, 2020; Lagabrielle et al., 2010; Teixell et al., 2016). Rifting also involved other sectors of the European plate (i.e. Parentis basin, Basque-Cantabrian Basin; Ábalos, 2016; Almar et al., 2008; Ducoux et al., 2019; Ferrer et al., 2012; Gómez et al., 2002; Jammes et al., 2010; Masini et al., 2014; Tavani and Muñoz, 2012). In general, to the north, the Northern Pyrenean basin includes pre-rift and syn-rift units, from Triassic to Cretaceous, and it does extend an average of 30 km northward (Biteau et al., 2006; Bosch et al., 2016; Saspiturry et al., 2019).

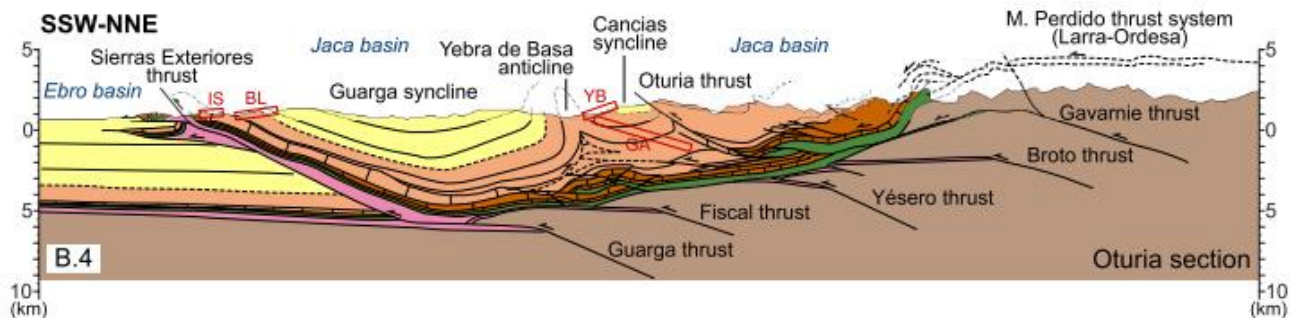


Figure 61: Oturia cross-section from Vinyoles et al. (2021) Structure of the Pyrenees at the central zone, ~80 km east of the studied zone. Section corresponds to line B on Figure 59.

In the prowedge domain (Figure 61) the thrusts show mainly S vergence, except for a few points where the Mesozoic cover is in contact with the basement units and the southwards movement of the basement induced a relative northwards displacement of the cover favoured by the Upper Triassic detachment (“*têtes plongeantes*” area, Muñoz, 1992; Séguret, 1972). The foreland basins, the progressive piggybacks, and the tectosedimentary evidence are progressively younger from the east towards the west (Barnolas and Gil-Peña, 2001; Montes, 2002; Vinyoles et al., 2020). The South Pyrenean zone coincides mainly with the foreland basin that opened up contemporarily with the stacking of the large thrust units in

CHAPTER 3 - STRUCTURAL STUDY OF SIGÜÉS AREA

the Axial Zone (Larra-Ordesa, Gavarnie, Broto, Guarga...). The cumulated thickness of syn-compressional deposits can exceed ~10 km (Barnolas and Gil-Peña, 2001; Montes, 2002; Muñoz, 2019; Puigdefábregas, 1975), that in some areas (South Pyrenean Central Unit) were added to the ~5 km thick Mesozoic syn-rift units. A sequence of piggyback thrusts that advanced towards the south mobilized all these units, incorporating them into the orogen thanks to an efficient detachment level in the Middle-Upper Triassic (Labaume et al., 1985a; Muñoz, 1992; Teixell, 1996).

3.1.2 The Jaca Basin

The Jaca Basin is a region of the South Pyrenean foreland, located in the central-western part of the orogen. Some of the towns located in this basin are, from E to W, Fiscal, Sabiñánigo, Jaca, Berdún or Sangüesa and it spans ~125 km along its E-W length and ~50 km in its N-S traverse. Several rivers cut across the structure in a N-S directions, thus revealing its geological features at surface. In Figure 62, its central-eastern part is shown, from the Ara to the Salazar river. The Jaca Basin is bounded to the north by the Internal Sierras, built up by Cretaceous-Palaeocene-lowermost Eocene units in contact (by means of an unconformity of Cretaceous units either lying onto the pre-Variscan units or onto the Permo-Triassic red beds) with the Axial Zone (Oliva Urcia and Pueyo Morer, 2007 and references therein). These mountain ranges form an alignment with a Pyrenean, N110 orientation (locally changing to E-W, Izquierdo-Llavall et al., 2013b; Oliva Urcia and Pueyo Morer, 2007; Teixell and Garcia-Sansegundo, 1995; Ten Haaf et al., 1971; Van der Voo, 1966), that corresponds to the pink-green band on Figure 62.

To the south, the Jaca basin is bounded by the Sierras Exteriores, a strip of Triassic to Eocene units (mainly limestones) that crop out in the hanging-wall of the Frontal South Pyrenean Thrust. This structure bounds the Mesozoic-Paleogene series in the hanging-wall with the Cenozoic deposits of the Ebro basin in the footwall (Garcés et al., 2020; Millán-Garrido et al., 2000; Oliva-Urcia et al., 2019). In between, the Jaca Basin can be divided into two large units. The lower one (located in its northern half) is the turbiditic piggy back basin, mainly composed of the Hecho Group. This includes more than ~5 km of flysch sediments with numerous folds, cleavage, and some carbonate megabeds detached from the platforms surrounding the Eocene syntectonic trough (Barnolas and Gil-Peña, 2001; Labaume et al., 1985b; Payros et al., 1999). To the south, there appears the second unit, the molasse basin, which contains the deposits (marine at the beginning and progressively continental) of the progressive shallowing and continentalization of the Pyrenean foreland (Costa et al., 2010; Montes, 2002; Puigdefábregas, 1975; Roigé et al., 2017).

The boundary between the molasse Guarga sector and the turbiditic piggy-back Hecho sector is marked by a fairly segmented fault. To the east is the Oturia fault. This fault, which marks a displacement of ~5 km (Labaume et al., 2016), is connected to the Gavarnie crustal fault. It operated during the Rupelian Priabonian (~34-28 Ma). To the west, in the main study area of this thesis, the faults affecting the Sierra de Leyre mark this boundary between the two basins. This thrust will be the focus of this thesis study.

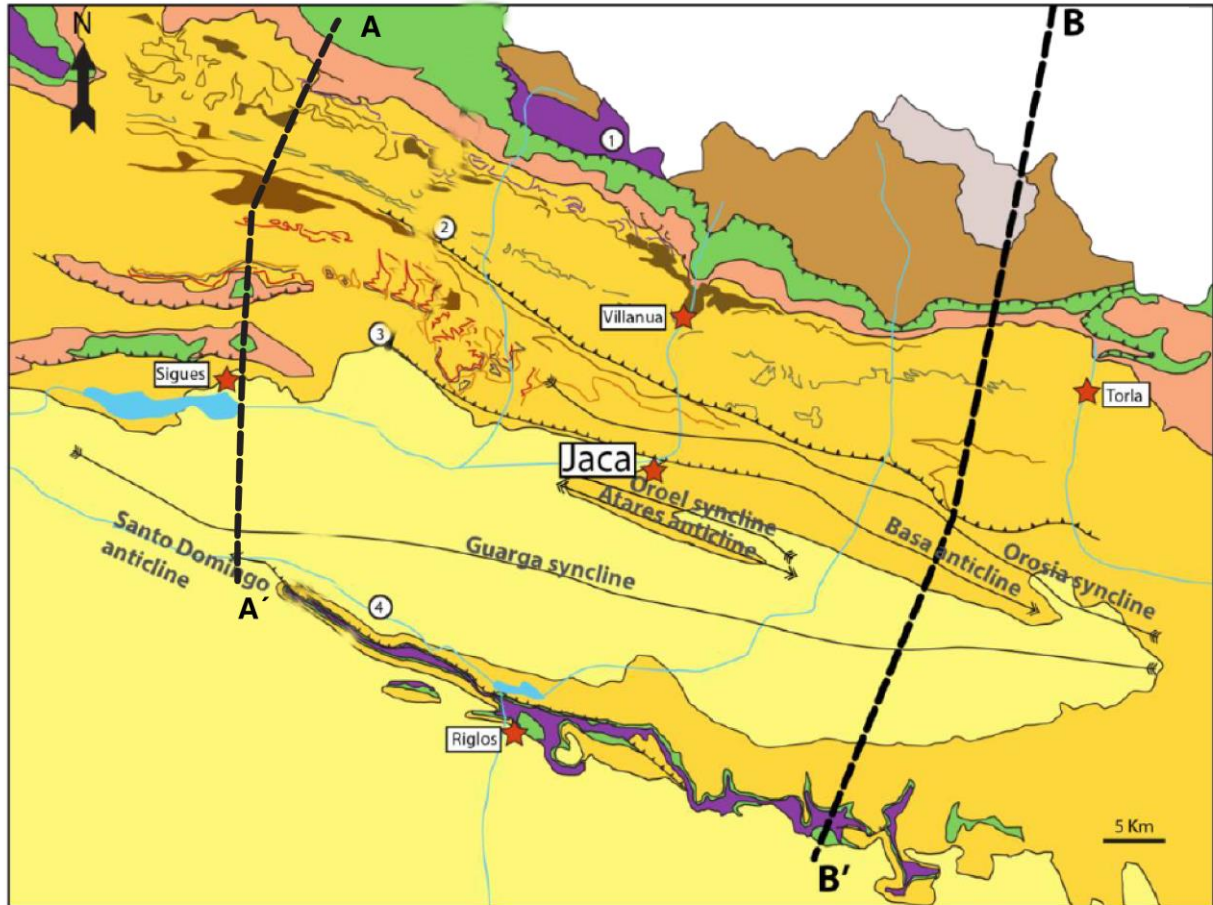


Figure 62: Geological map of the central-eastern part of the Jaca Basin, from Crognier (2018). Roncal-Escá sections (Fig 7 and 9) are along the trace A-A', and the Oturia cross-section from Fig 3 is along the B-B' transect.

To describe the geological units of the Jaca basin in its entirety, the chronostratigraphic frame proposed by Labaume and Teixell (2018) will be used. These authors revisited chronostratigraphic data from other previous references (Figure 63). This frame also includes pre-Eocene units, which underlie the thick syn-tectonic units, and which correspond to the Cretaceous and Palaeocene pre-compressional sequences. We also use the Roncal borehole (Lanaja, 1987) to give realistic formation thicknesses in our study area.

The Paleozoic basement and the Permo-Triassic tegument (related to the post-Variscan transtensional or extensional evolution, Lago et al., 2004; López-Gómez et al., 2019) do not crop out in the Jaca Basin, but are visible in the Axial Zone, north of the Sierras Interiores (Cantarelli et al., 2013; Gisbert Aguilar, 1983; Valero-Garcés and Gisbert Aguilar, 2004). Nevertheless, they have been found in exploration wells (e.g. Roncal, Broto, Serrablo or San Vicente Wells), underneath the Mesozoic series (Lanaja, 1987).

The Middle-Upper Triassic is the regional detachment level, consisting of shales and evaporites of the Muschelkalk and Keuper facies (Cámara and Flinch, 2017). This level also crops out sparsely, and only at the margins of the basin, as in the Sierras Exteriores (Millán, 1996). As said before, it worked as a detachment level for the main thrusts in the South Pyrenean foreland, and its thickness strongly changes from a few meters to hundreds of meters (Calvín et al., 2018; Labaume and Séguret, 1985; Teixell, 1996... among others)

CHAPTER 3 - STRUCTURAL STUDY OF SIGÜÉS AREA

The Triassic is overlain by the carbonated formations from the Upper Cretaceous, Cenomanian to Santonian, called the Canyons Limestones (*Calcaires des Cañons* by Souquet, 1967). The sedimentary gap between the Triassic and the Cretaceous is probably the result of a non-sedimentation stage, although some outcrops of marine Jurassic strata in the External Sierras (Barbed et al., 1988; Comas et al., 1988) rather point to an erosional stage. In the Santo Domingo anticline, which marks the southern limit of the Jaca Basin, outcrops of Lower Jurassic (Lias) indicate a strong energy (the beds are unstructured). It is probable that the Lias was deposited in a normal fault system, which later served to activate a diapiric system (Aubourg, pers. comm. 2023). The Upper Cretaceous limestones crop out also in the northern edge of the Jaca basin (Internal Sierras), between the turbiditic basin and the Axial Zone, as a result of the uplift of the latter. In the Roncal well (Lanaja, 1987) the measured thickness of this unit is ~70 m.

A relevant unit that appears in the NW of the Jaca basin is the Zuriza marls, a Campanian unit that played a significant role in the mechanical stratigraphy of the series. They are considered to be the detachment level of some of the Sierras Interiores thrusts (Izquierdo-Llavall et al., 2015; Rodríguez Méndez, 2011; Teixell, 1992). It is also considered as the lateral equivalent to the Marboré Sandstones, the oldest formation among those that crop out in the study area. The latter is composed mostly of quartzitic sands reaching a thickness of ~300 m (Roncal well, Lanaja, 1987). In other areas of the basin its thickness changes, since in the Campanian-Maastrichtian the first signs of compressional tectonic activity in the Pyrenean domain are detected in this unit (Puigdefàbregas and Souquet, 1986; Souquet, 1967; Teixell, 1992), e.g. it is 120 m thick in the northern part of the Ansó Valley (de Rojas and Latorre, 1972).

The K-Pg transition is pinpointed in the southern margin of the Jaca basin by the Garumnian facies corresponding to the Tremp Fm, which in the northern half of the basin are usually thinner, less than 10 m thick. It shows reddish colours and includes continental and transitional facies (Puigdefàbregas and Souquet, 1986).

Overlying this Mesozoic units, there appear the widespread Palaeocene-Ilerdian limestones, consisting of platform limestones with numerous bioclasts and alveolines. This unit is divided into different lithostratigraphic units, depending on its position in the southern Pyrenean basin. In the studied area they are included within the Ager Fm. (Garcés et al., 2020; Pujalte et al., 2014 and references therein).

The evolution of the sedimentary sequence towards the Eocene is strongly conditioned by the geometry of the basin. An underfilled stage of the basin begins (Aguirre et al., 2019; Coll et al., 2020; Vergés et al., 2002) where the opening of a deep trough generated a turbiditic slope composed by up to ~ 5 km of sediments of the Hecho group flysch (Payros et al., 2009; Remacha and Fernández, 2003). At the palaeogeographic margins there were carbonate platforms of Eocene age, which cannot be seen in the center of the basin, but crop out extensively in the Sierras Exteriores (Montes, 2002; Silva-Casal et al., 2021, 2019).

CHAPTER 3 - STRUCTURAL STUDY OF SIGÜÉS AREA

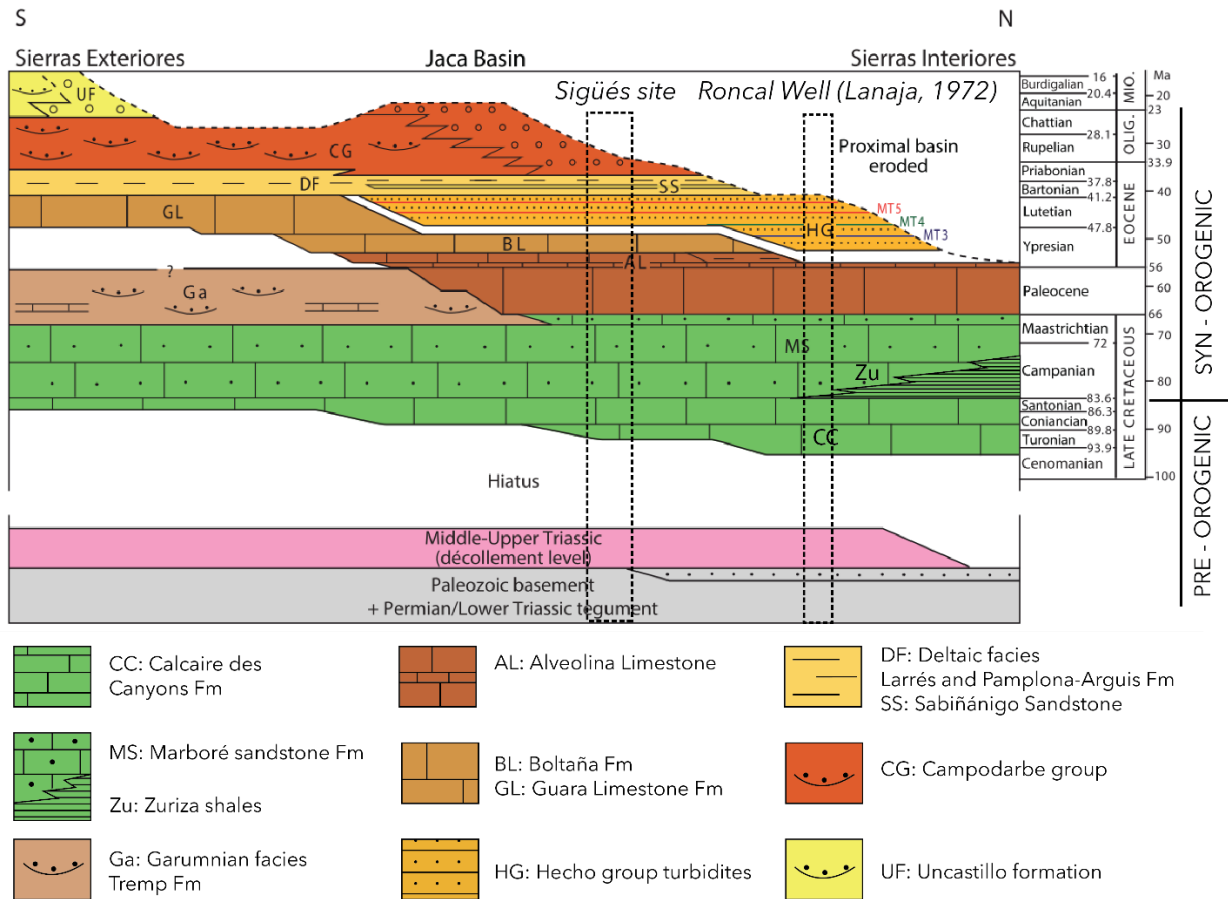


Figure 63: Chronostratigraphic sketch for the Jaca Basin, and its evolution from N to S, from Labaume et al. (2018) . The geographical extent of this units corresponds mainly to the Map on Figure 62.

The progressive filling of the basin towards the Bartonian-Priabonian favored the progradation of marine facies and we find the shales of the Larrés and Pamplona-Arguis Formations (Barnolas and Gil-Peña, 2001; Puigdefábregas, 1975). These shales can be more than ~1 km thick in the Canal de Berdún/Aragón valley area. Above these marine formations lies the Belsué-Atarés Formation, consisting of sandstones deposited in a delta environment that represent the transition from a marine to a continental basin (Puigdefábregas, 1975). This final progradation is responsible for the sedimentological environment that dominated the rest of the sedimentary fill of the Jaca Basin (Casas-Sainz and Pardo, 2004).

Subsequently, during the Oligocene a significant thickness of syntectonic fluvial and alluvial sediments was deposited (related to an underfilled stage of the basin). This sedimentation occurred contemporarily with the emplacement of new thrust sheets that incorporate the previous units into the chain and the uplift of the Axial Zone (Teixell, 1998). These sediments are integrated within the Campodarbe Group, and the overlying Uncastillo and Bernués formations, which can exceed ~ 4km in thickness in the depocentre of the basin (Montes, 2002).

The tectonic evolution of the Jaca basin is closely linked to its filling history at the foreland basin of the Pyrenean chain (Deramond et al., 1993). A general sequence of basement thrusting and crustal flexure has been proposed (Espurt et al., 2019; Labaume and Teixell, 2018; Teixell, 1996) in relation to the different stages of basin evolution in the Jaca basin

CHAPTER 3 - STRUCTURAL STUDY OF SIGÜÉS AREA

transect (see below): the Lakora-Eaux Chaudes thrust system would be related to the deposition of the turbiditic sedimentary basin, the Gavarnie thrust would be responsible for the deposition of the molasse basin and finally the Guarga thrust generated the final uplift of the chain (Millán-Garrido et al., 2006; Teixell, 1992). A particular feature is the propagation of the deformation associated with the Guarga thrust, favored by the existence of the Upper Triassic detachment. The surface expression of this final shortening is therefore the South Pyrenean Frontal thrust in the Sierras Exteriores area. The Lakora-Eaux-Chaudes thrust system also propagates through the Upper Cretaceous low-strength levels (Rodríguez Méndez, 2011), whereas the Gavarnie thrust only shows shorter splays within the turbiditic basin (Teixell, 1998, 1996).

3.1.3. Geological background in the Sigüés area

The geological maps (2nd Magna Series by de Rojas and Latorre, 1972) published by the IGME (Instituto Geológico y Minero de España, Spanish Geological Survey) can be used for a first approach to the geological background of the area. Furthermore, the key work by Puigdefàbregas (1975) in the Jaca Basin is focused in the molasse units described in this area. The map presented by Puigdefàbregas (1975) goes beyond the mapping of the molasse units and constituted a milestone in the knowledge of the geology of the Jaca basin. His cartography is here used (and complemented) and the stratigraphic units defined therein, as the geological reference.

In terms of structural geology, the first interpretations of the structure of the study area were presented in the Roncal cross-section by Labaume et al. (1985) (section 1 on Figure 64).

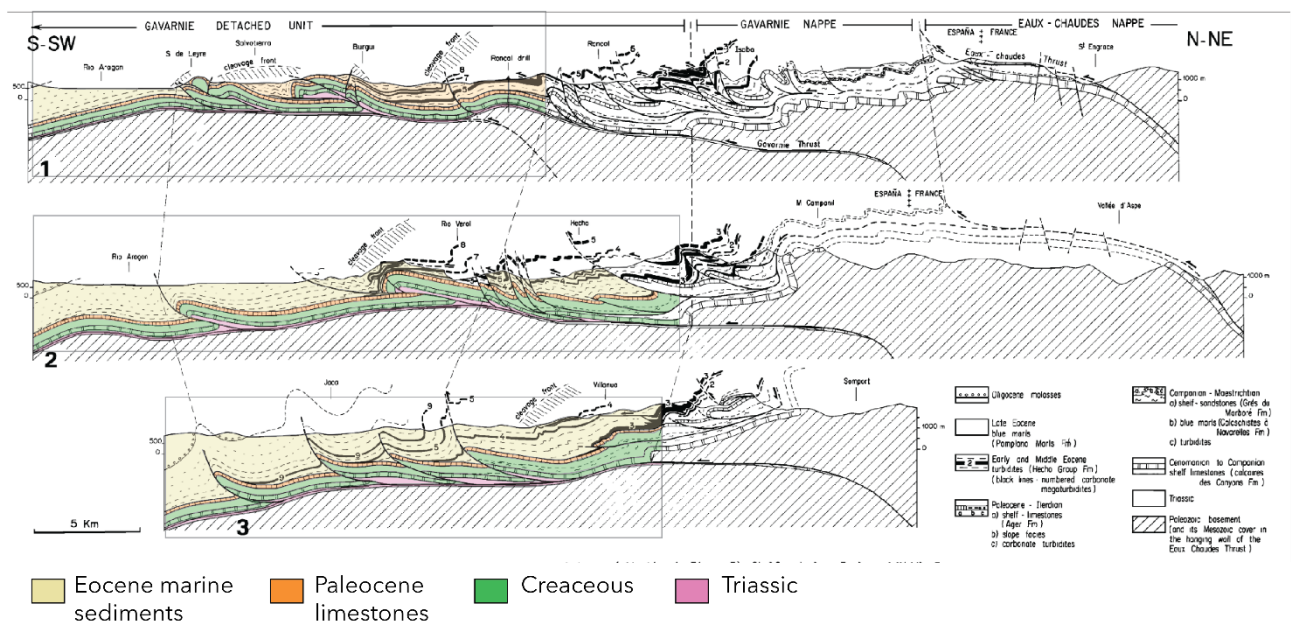


Figure 64. Modified (coloured) Labaume et al. (1985) cross-sections, in the southern slope of the Pyrenees. N°1 corresponds to the Roncal (Escá river) cross-section. N°2 to the Hecho (Aragón Subordan river) cross-section. N°3 to the Aragón river cross-section.

In these cross-sections, the Middle-Upper Triassic and intra-Cretaceous units are considered the main detachment levels for the Leyre and Illón (Burgui) structures. However, further

CHAPTER 3 - STRUCTURAL STUDY OF SIGÜÉS AREA

north, basement-involved thrusts such as the Eaux Chaudes or the Gavarnie thrusts can be seen. The thrust surfaces are subhorizontal and increase their dip in the northern sector of the cross-sections. This is in agreement with the in-vogue paradigm at the moment, when a ductile-deformation thick-skinned tectonics was considered for the Axial Zone of the orogen, originally accompanied by gravity sliding of the cover favoured by the Middle-Upper Triassic detachment level (Séguret, 1972). The structure of the Axial zone and other zones of the Pyrenees changed subsequently to a model of “thin-skinned” (in a broad sense, considering that thrust sheets show thickness of several kilometres) structure of basement thrust sheets that prevailed during the subsequent decades (Graham et al., 1987; Labaume and Teixell, 2018; Muñoz, 1992). Labaume et al. (1985) cross-section shares both interpretations, implicitly considering the compressional deformation of the Mesozoic-Cenozoic cover by means of a fold-and-thrust system that propagates from the basement thrust sheets and the ductile deformation of the basement, associated with high-angle faults. In this model, long-wavelength undulations of the basement can be also considered as the result of ductile deformations.

The fold geometry in the southern part of the sections, and in particular in the Leyre and Illón sierras, reflects a succession of flats and ramps, with a main level of detachment in the Triassic (Labauume et al., 1985). The general geometry suggests a fault-bent-fold, which appears multiphase. In the thesis, we will take up these geometries in greater detail to propose alternative geometries.

The Paleozoic basement would be relatively shallow (<1 km) in the southern sector of the turbiditic basin, as indicated by the Roncal well (Lanaja, 1987). The turbidites also show superficial thrusts that are not detached in the Triassic, using local detachment levels. From cross-section 1 to cross-section 3 of Figure 64 it is shown how the structure evolves along strike, since in the Roncal section the Marboré Fm (Upper Cretaceous) is exhumed, and the basement is less than 1 km deep from the surface. However, to the east in the Jaca Basin, the Marboré Fm does not crop out, and the top of the basement also deepens to >2500 m from the surface.

In addition, Labaume et al. (1985) also depict several areas with well-developed cleavage, thus improving the milestone in the geological structure by Choukroune and Séguret (1973). In the westernmost sections presented by Labaume et al. (1985) the cleavage front is more advanced to the south, whereas to the east the cleavage front remains in a more northward position, close to the Axial Zone although always within the turbiditic basin. In the southern section of Roncal, Labaume et al. (1985) identified several cleavage zones that do not appear to be continuous to first order.

The structural geology in this area has included the more detailed description of the cleavage front by Izquierdo-Llavall et al. (2013a), re-interpreting Labaume et al. (1985) cross-section (Figure 65). Also, with the aim of obtaining paleo-temperatures to add more information on the conditions of cleavage development, both the turbidites of the Hecho group and the Eocene shales cropping out to the south of the Leyre range thrust were sampled.

CHAPTER 3 - STRUCTURAL STUDY OF SIGÜÉS AREA

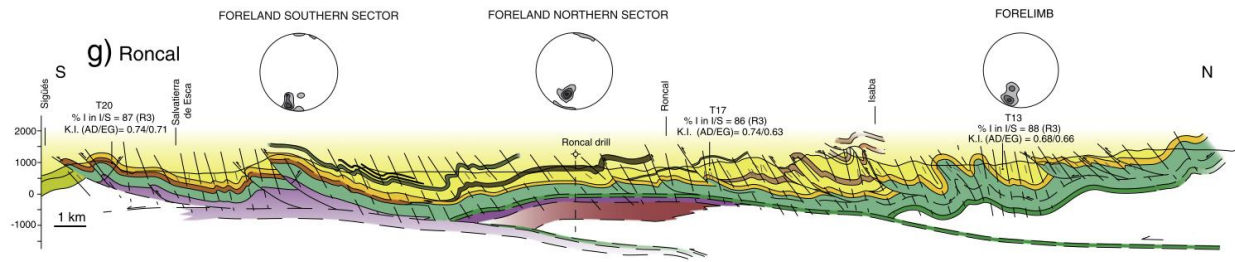


Figure 65: Roncal cross-section from Izquierdo-Llavall et al. (2013). Cleavage measurements are plotted. The basement thrusts are drawn, such as the one underlying the Roncal Well where the basement (painted in red) overthrusts the Trias (purple).

Izquierdo-Llavall et al. (2013) propose thermicity data (X-ray diffraction, vitrinite, fluid inclusions) in the Jaca basin to constrain the conditions under which the cleavage front will develop, particularly at Sigüés. They establish two types of cleavage: one related to the axial plane of the fold, and the other of the LPS type (i.e. perpendicular to bedding). The mechanisms involved in the formation of this cleavage are pressure-solution and rigid particle rotation. Based on thermicity data, they propose a temperature between 140-160°C near the cleavage front in the Sigüés area (Figure 66). The fluid inclusion data were challenged by Crognier et al. (2018), who found higher temperatures. As we shall see in this thesis, new Raman data support the idea that the cleavage front is closer to a temperature of 180-200°C than 140-160°C.

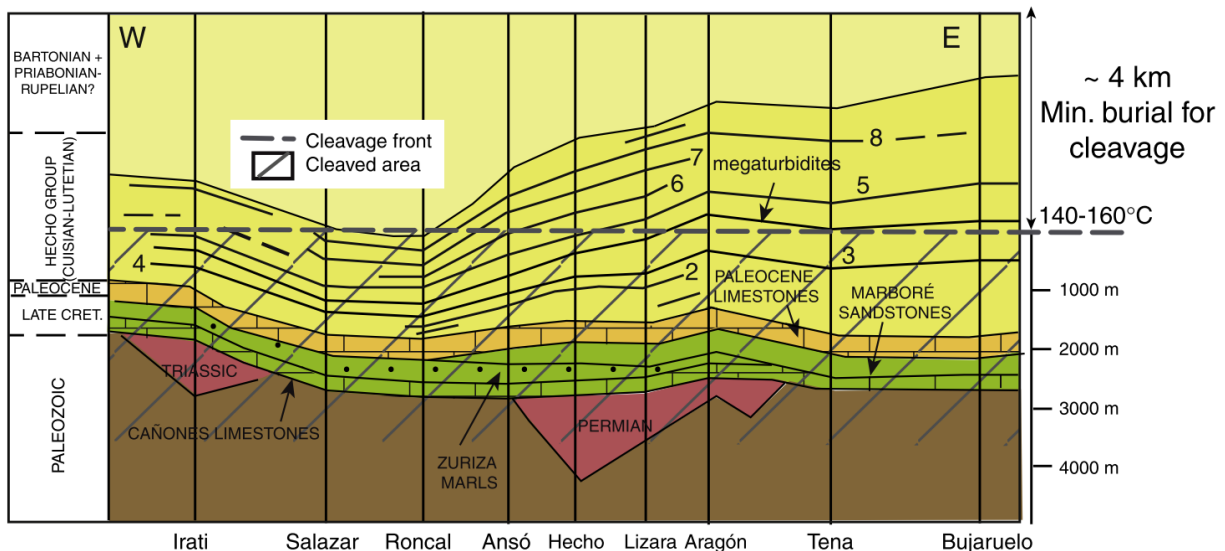


Figure 66: Burial sketch for the Axial Zone, Internal Sierras, turbiditic basin, in the southern slope of the Pyrenees. From Izquierdo-Llavall et al. (2013).

Three more cross-sections use the Roncal-Escá transect in order to interpret the structure of this part of the Pyrenees, as shown in Figure 67.

The first one, chronologically, corresponds to the sections presented together with the 1:50.000 MAGNA Map (n° 175) published by the IGME. In this case the authors (de Rojas and Latorre, 1972) show a N-S cross-section, and propose a detailed interpretation of the Leyre structure (Figure 67a). However, this cross-section does not take into account the evolution at depth of the structures, neither does it take into account the geometrical constraints that thrust structures must honor (Boyer and Elliott, 1982; Butler, 1987; Cooper

CHAPTER 3 - STRUCTURAL STUDY OF SIGÜÉS AREA

and Trayner, 1986). And in a rudimentary way, this cross-section interprets differently the relationships between the involved units, especially between the Cretaceous (painted in dotted white) with the overlying Cenozoic units. In this case, they seem to be discordant, while in the rest of the cross-sections, the rest of the units remain in geometric concordance.

Oliva-Urcia et al. (2012) aimed to study the structure and kinematics of the South Pyrenean frontal thrust, for which they presented three cross-sections with calculated shortenings combining basement and cover thrusts (Figure 67b). The Leyre structure is drawn imaging a single structure with the Paleozoic basement close to the eroded surface but not involved in deep thrust sheets. Similarly, to Izquierdo-Llavall et al. (2013) the Leyre and Illón structures are detached in a thick Triassic unit, and rooted in and a single thrust sheet, that branches next to the surface.

Finally, there is the local section by Boiron et al. (2020) which only analyses the Leyre structure (Figure 67c). The authors based their analysis on the geometry proposed by (Labaume et al., 1985), which involves a detachment level in the Triassic and a double system of thrust sheets. In this cross-section, the authors use the Trishear concept (Hardy and Allmendinger, 2011), which provides a theoretical framework to explain deformation in the footwall of the Leyre fault. This structure will be discussed at greater length in this thesis, but it should be noted that in this description, the Leyre fault is blind. The surface fault, which is quite steep, corresponds in this model to the upper part of the triangular zone, i.e. the zone where shear is concentrated. More details on the footwall of this structure are explained in the following pages.

CHAPTER 3 - STRUCTURAL STUDY OF SIGÜÉS AREA

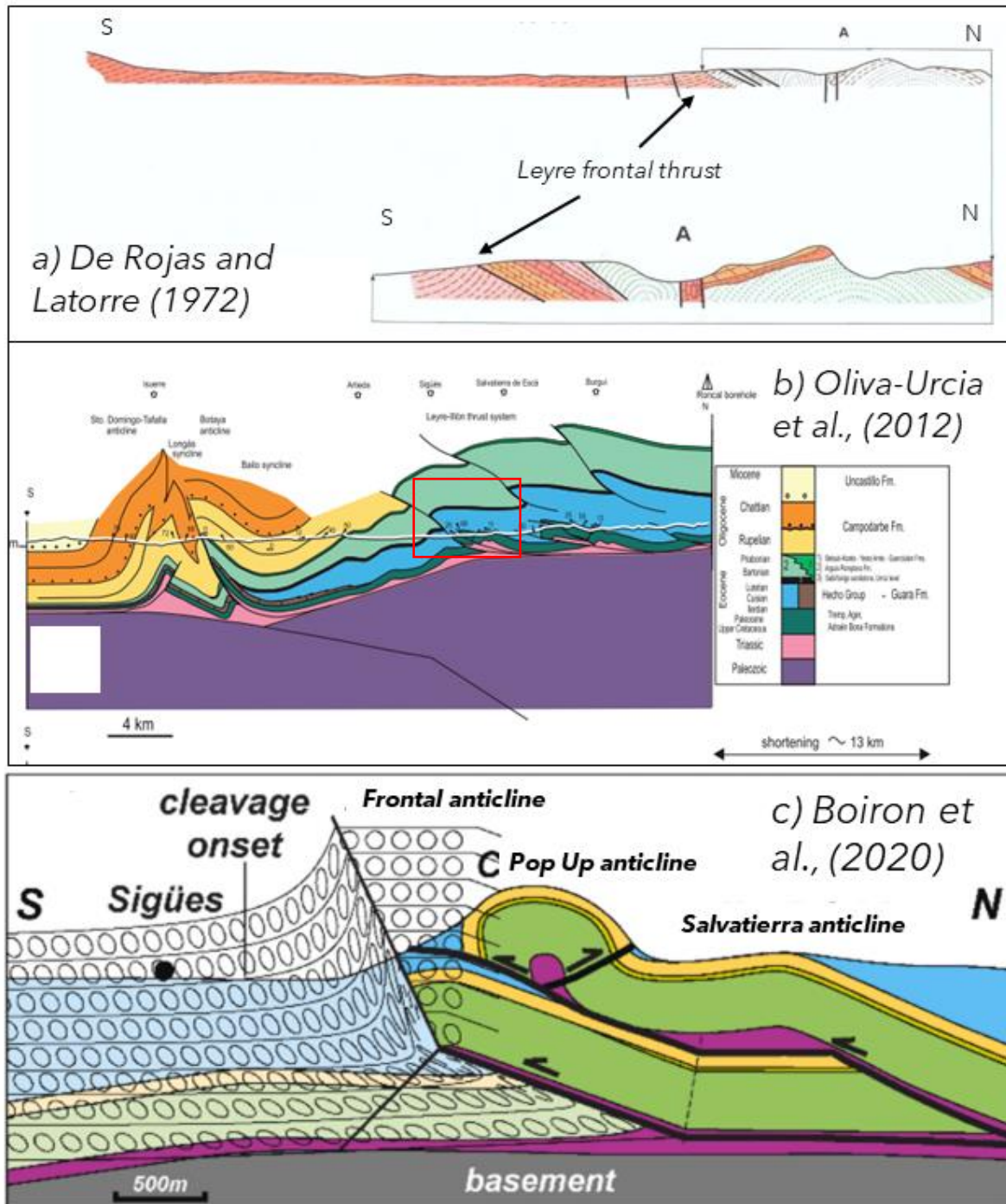


Figure 67: Three cross-sections of the Roncal-Escá transect (Fig 3). a) Cross-section from the published geological map, Magna cartography by the IGME (de Rojas and Latorre, 1972) b) Regional Cross-section from Oliva-Urcia et al. (2012); the Sigüés section presented at a and c is framed in a red square; and c) Local cross-section for the Leyre Unit from Boiron et al. (2020).

3.2. Field description of the Jaca Basin sites.

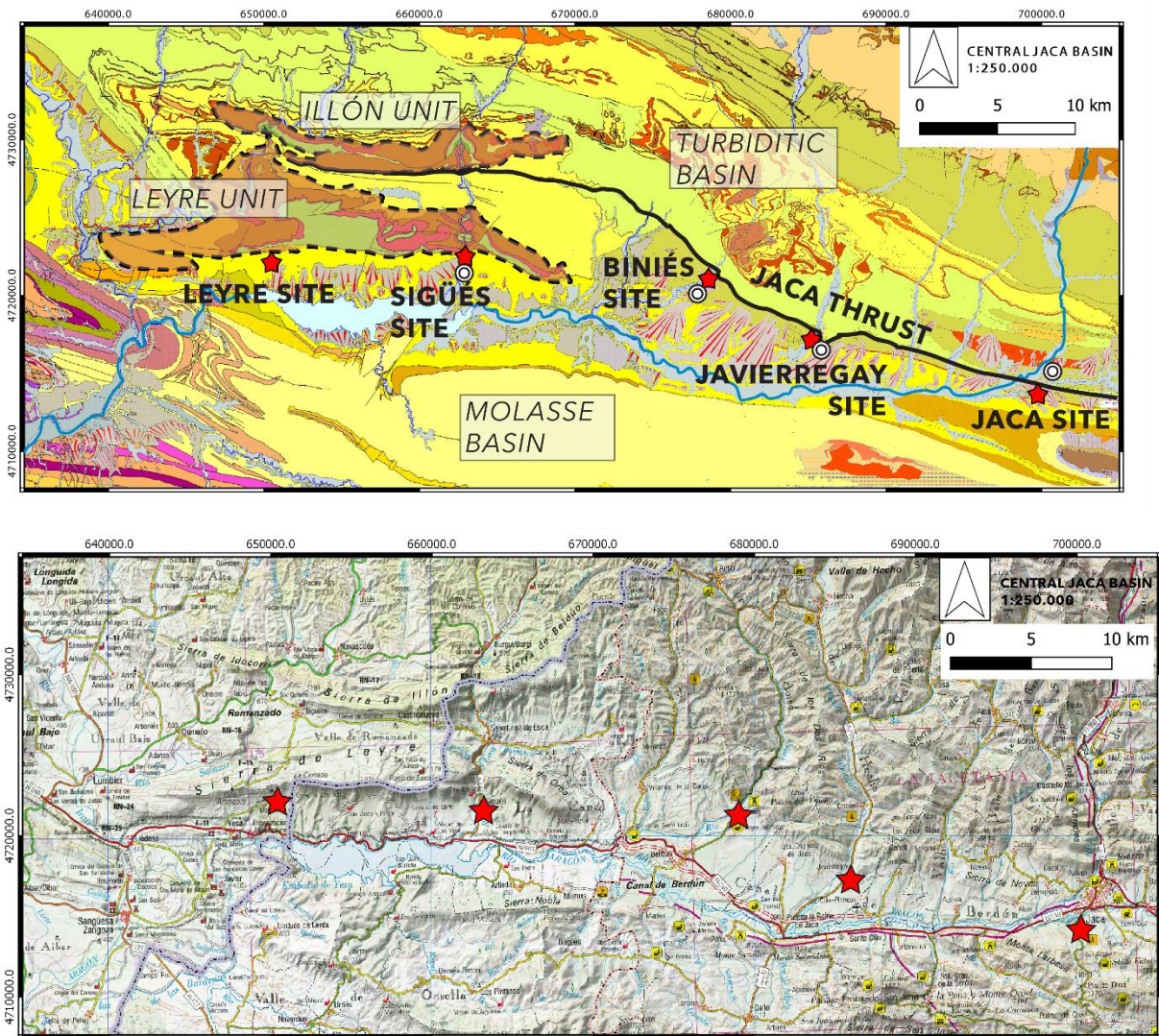


Figure 68: Geological map showing the location of the studied sites in the Jaca Basin. Geological map from GEODE continuous cartography (IGME).

The Illón and Leyre units, each associated with an outcropping thrust, are the main structures in the studied area (Figure 68). These units correspond to the structural transition between the Jaca Turbidite Basin and the Jaca Molasse Basin (Labaume et al., 1985; Puigdefábregas, 1975). The Jaca thrust marks this contact between the two subbasins to the east, whereas to the west this thrust is located within the turbiditic basin. On the other hand, there is also an East-West transition because the Pamplona Basin (to the west of the studied area) contains deposits that reflect a different palaeogeographic stage of the syntectonic Pyrenean foreland, containing in general deeper facies (Payros et al., 1999). However, in this work we will not deal with this western basin evolution.

The site studied thoroughly in this work is located around the village of Sigüés and the gorge of the Escá river where it passes through the Leyre unit. In addition to this site, the

CHAPTER 3 - STRUCTURAL STUDY OF SIGÜÉS AREA

outcrops at the footwall of the Leyre frontal thrust, next to the abbey of the same name, have been visited. Other studied sites are located in the footwall of the Jaca thrust, farther east, near the villages of Biniés, Javierregay and Jaca (Figure 68). In general, the stratigraphic units in the study area are similar to those shown in the chronostratigraphic sketch in Figure 63 of this chapter, along with the descriptions provided there. However, the thicknesses observed in the work area are also indicated in the next paragraph.

The description corresponds to the regional synthetic log shown in Figure 69. The Triassic evaporites and the Cretaceous *Calcaire des Canyons* Fm do not crop out in the study area, and their thicknesses (~30 m and ~70 m respectively) are inferred from the log of the Roncal well (Lanaja, 1987). The thickness of the Marboré Fm. is ~340 m in the Leyre unit (325 m in the Roncal well). Also in the Leyre unit there is an interval of the Tremp Fm (Garumnian facies) ~10 m thick. It is overlain by the ~80 m sequence of Paleocene-Ilerdian Ager Fm limestones.

CHAPTER 3 - STRUCTURAL STUDY OF SIGÜÉS AREA

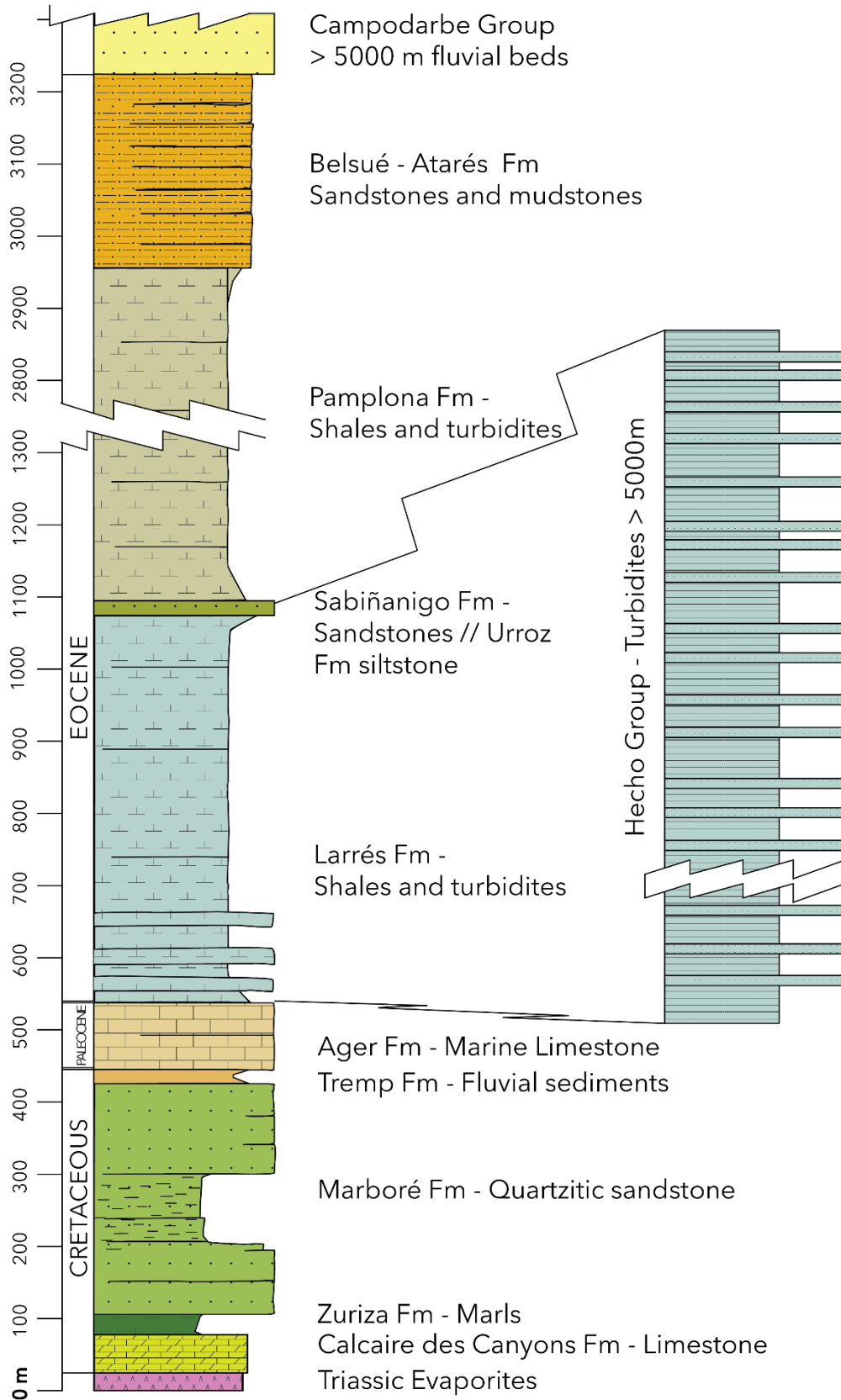


Figure 69: Schematic sedimentary log for this region of Jaca Basin. Same colours as Puigdefàbregas, 1975, and map on Figure 70.

The thicknesses of the marls and shales of the Larrés and Pamplona Fms. (Puigdefàbregas, 1975) is difficult to evaluate.

CHAPTER 3 - STRUCTURAL STUDY OF SIGÜÉS AREA

Oliva-Urcia et al. (2012) estimate a thickness of ~4 km for the Eocene marly formations on their restored geological section (Figure 67b). This agrees with thermal data obtained in the Sigüés region and modeled in 1D by Crognier (2016). The report of Magna Map n°175 (2nd Magna Series, by Rojas-Tapia and Martínez-Díaz, 1973) suggests a total thickness of ~1 km for all the Eocene shales (Larrés and Pamplona Fms.), including the Sabiñánigo Sandstone intercalation. In fact, the Sabiñánigo Sandstone changes in this area of the Canal de Berdún to a lateral equivalent called the Urroz Siltstone (Gabaldón et al., 1985). We will use this term because there is no sandstone layer in this area. More recent detailed studies such as the paleomagnetic sampling for these formations by Sierra-Campos (personal communication) suggest more than 2.3 km of total thickness for the whole of the shale units. In their preliminary stratigraphic logs carried out in the Berdún area (10 km to the east of the Sigüés transect) they calculate ~400 m for the Larrés Fm, ~100 m for the Urroz siltstone and ~1800 m for the Pamplona Fm. The Larrés Fm would be the lateral equivalent to the deeper, turbiditic sediment of the Hecho Group, which can reach thicknesses up to 5 km in the subbasin located immediately to the N. Finally, the local series can be completed with the deltaic deposits of the Belsué-Atarés Fm (~230 m), and the fluvial facies of the Campodarbe Group (≥ 4 km), which crop out to the S of the Canal de Berdún (Aragon river). These thicknesses are used in the cross-sections presented in section 3.4. Structural frame and serial Cross -Sections.

3.2.1. The Sigüés and Leyre Sites.

The main geographical and geological feature in the study area is the Leyre Unit (Figure 68), a minor mountain range with an E-W direction, which to the west of the Esca river is called Leyre Range (Sierra de Leyre), and to the east Orba Range (Sierra de Orba). More specifically, the Orba range has an ENE-WSW direction, slightly oblique to the Leyre alignment. Both ranges are separated by the gorge of the river Escá, that excavated a canyon almost 500 m deep, in which the geological structure that composes both ranges is spectacularly exposed in a natural cross-section. Some of the highest points of the Leyre range reach 1300 m at the western end of the map, and 1220 m at the eastern end of the map in the Orba range. In the following subsections, some of the outcrops of this study area will be presented.

CHAPTER 3 - STRUCTURAL STUDY OF SIGÜÉS AREA

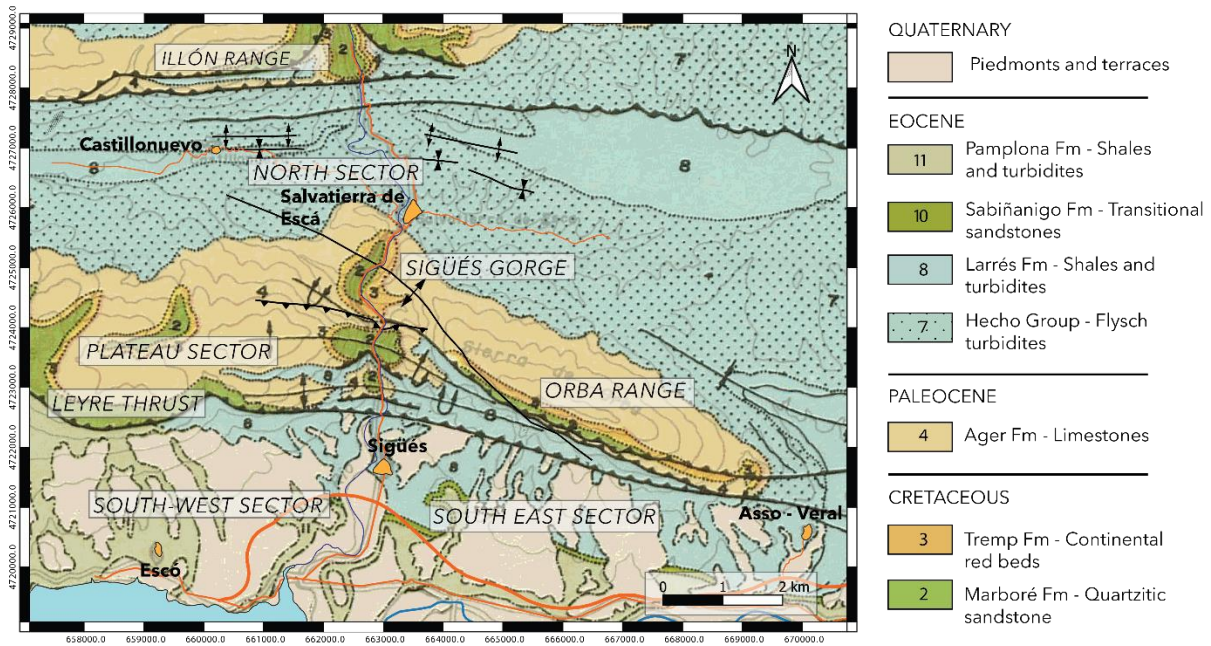


Figure 70. Geological map (from Puigdefàbregas, 1975) of the main Sigüés site. Leyre Abbey site and other Jaca fault sites are excluded, see context in Figure 68.

3.2.1.1 North sector – Salvatierra de Escá Valley

Several sites have been visited on the northern side of the Leyre unit. From the ridge of the Leyre range, the topography descends to Salvatierra de Escá, which stands at an elevation of 580 m and marks the confluence of two minor streams that flow in an east-west direction, and the Escá river that flows in a north-south direction. This area is called the Salvatierra valley in this work (Figure 71), an E-W valley with badlands excavated on shaly ground, flanked to the south by the Leyre and Orba ranges (see Northern sector in Figure 70). The outcrops in this area correspond to the turbidites of the Hecho Group, which consist of sandy and shaly strata with changing thickness.

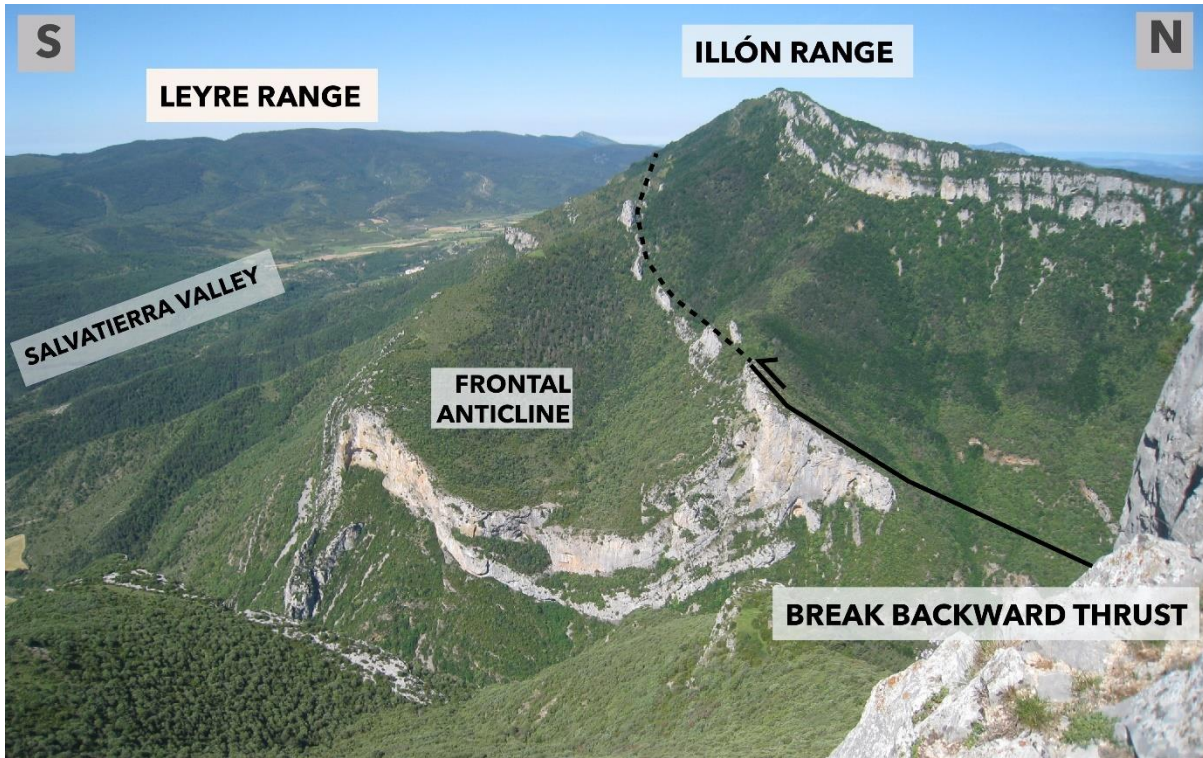


Figure 71: Southern front of Illón range. Paleocene units show hanging-wall anticline in two ramps.

To the north is the Illón mountain range, which is structurally similar to the Leyre mountain range, and is made up of the same geological units, with a parallel E-W strike, also cut by the River Escá in a N-S direction. The Illón Range is slightly higher (1420 m), and in parallel, the compressive structures (thrusts and associated hanging-wall anticlines) that build up the structure crop out in the Salvatierra-Burgui gorge (Figure 71). Different cross-sections (Figure 65 and Figure 67) interpret the double-stack thrust system that builds up this mountain range. The cross-section of the Sierra de Illón can be left to at first order “fault-bend-fold” with a lower level (the main Triassic detachment), a $\sim 30^\circ$ ramp and an upper level that does not emerge at the surface. This structure is complicated by the break in the ramp (break backward thrust), which allows the series to be redoubled. This structure therefore has a geometry of flats and ramps, complicated by what may appear to be a late out-of-sequence overlap.

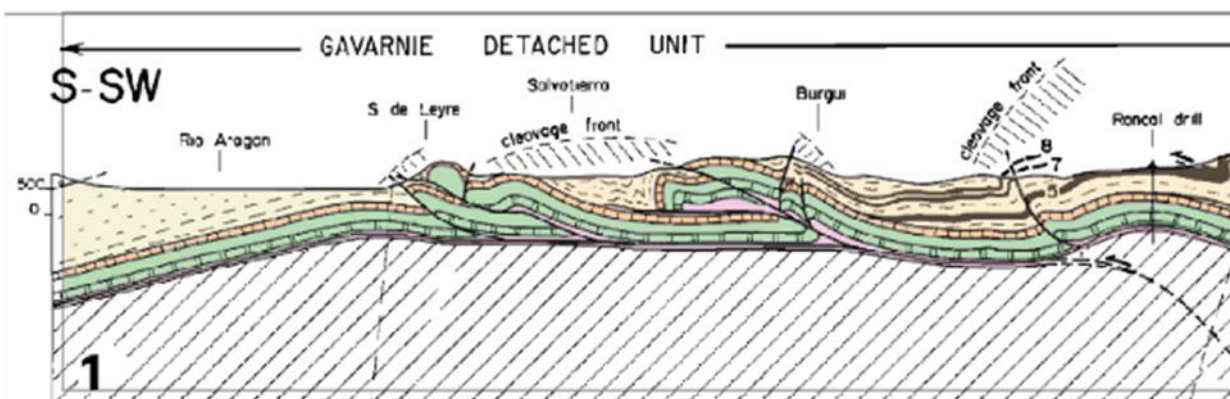


Figure 72: Zoom on the Roncal Section of the Figure 64. Same colour legend applies.

CHAPTER 3 - STRUCTURAL STUDY OF SIGÜÉS AREA

The Labaume et al. (1985) cross-section (Figure 72) shows two cleavage zones: between the Sierra de Leyre and Sierra de Illón and on the back limb in the Burgui region. Our field observations confirm the presence of this LPS-like cleavage.

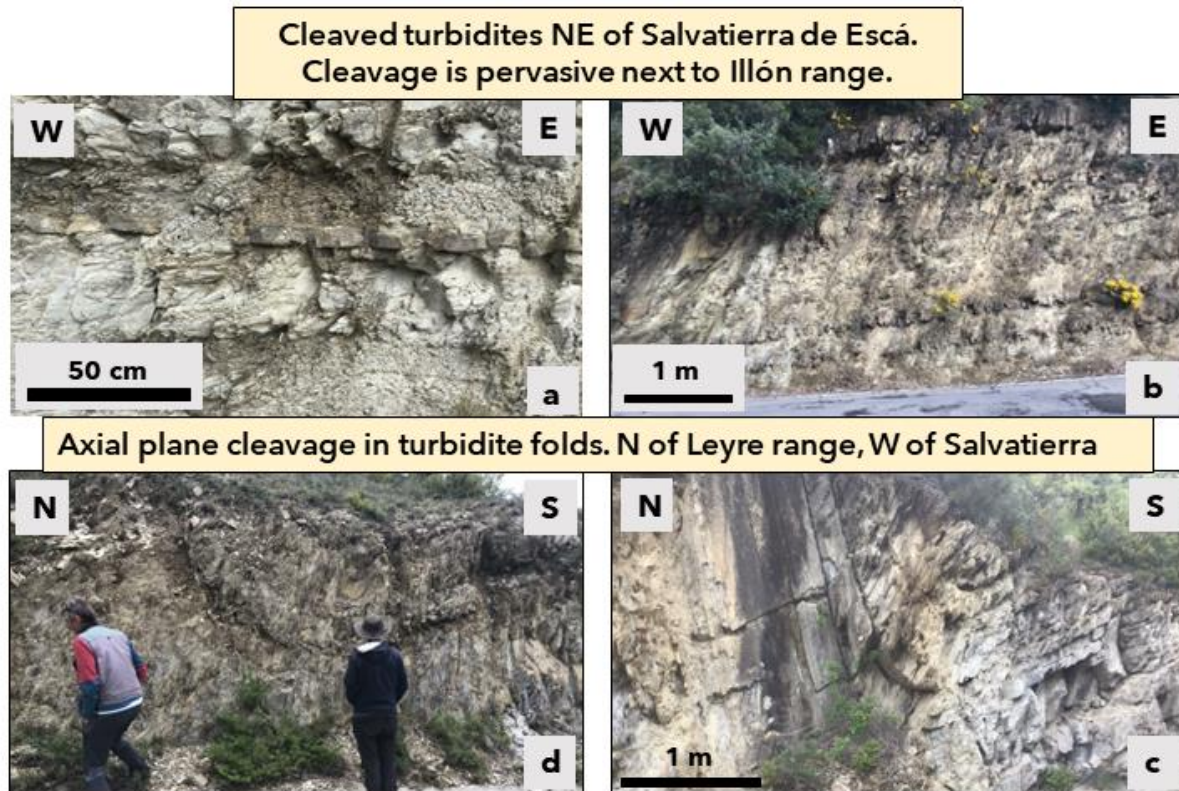


Figure 73: Outcrops of shales and turbidites of the Hecho Group in the Salvatierra area.

The flysch outcrops in the Salvatierra valley form a south-verging syncline whose northern limb shows an average dip of 25° and whose southern limb shows an average dip of 10° (Figure 93). Roughly, the turbidite sedimentary sequence involved in the core of the fold shows a preserved thickness of 200 m. Most of the series here corresponds to the turbidites of the Hecho Group arranged in typical Bouma sequences (Figure 73). This unit shows a pervasive cleavage, that maintains the main regional orientation N100-N110 (see stereoplot in Figure 93). In Figure 73 (photos c and d) the axial planes of folds, a few meters in wavelength, coincide with the planes of cleavage. It is also observed how the cleavage shows different geometry in shales (more penetrative) and in sandstones (more spaced planes), occasionally manifesting refraction -i.e. changes of the S1 dip. Finally, in outcrops close to the Illón range, near the thrust that bounds the structure to the south, it is observed how the cleavage is more penetrative in shales (slaty cleavage) and also affects the sandstones (Figure 73b).

In the Burgui zone, the cleavage is pencil-shaped and perpendicular to bedding (Figure 74). This geometry, which we were able to verify by walking up a canyon for several kilometers, is of the LPS type (S1 perpendicular to S0). Quartz and clay fabric have been studied by Saur, (2022). He shows that, depending on the facies, quartz orientation can be controlled by cleavage or bedding. In contrast, clays, measured by AMS, are on average controlled by

CHAPTER 3 - STRUCTURAL STUDY OF SIGÜÉS AREA

bedding. The fabric is triaxial and corresponds to stage 2 to 3, which we will define in our study. Since the cleavage is perpendicular to the bedding, we can calculate a strain (See section 4.4. Strain quantification at the Sigüés site). This gives a shortening range of the order of 20 to 30%, which corresponds to LPS values documented in the Appalachians (e.g. Hirt et al., 1993).

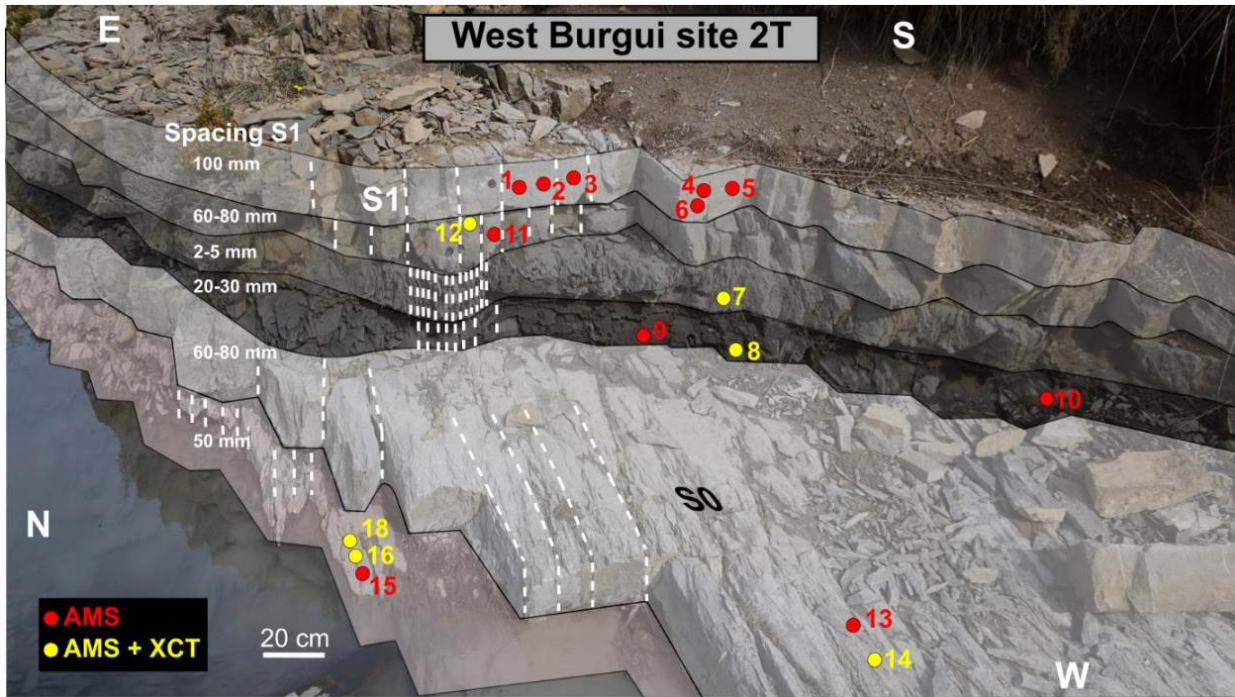


Figure 74: Photograph of the sampling area in the West Burgui site. Multiple lithologies of carbonate turbidites with similar bed thickness but various cleavage intensities at the bed scale (Saur, Phd, 2022).

3.2.1.2 Leyre Range - Plateau Sector

The Leyre range, as seen from the south, is characterized by cliffs where the harder, most erosion-resistant units crop out. At the top of the range the yellowish quartzitic sandstones of the Marboré Fm and the grey limestones of the Ager Fm (Figure 75, top picture), which form a cliff above the shaly units of the footwall of the Leyre thrust can be seen. The Leyre thrust trace is recognizable in almost any view from the Canal de Berdún, just below the rock cliff.

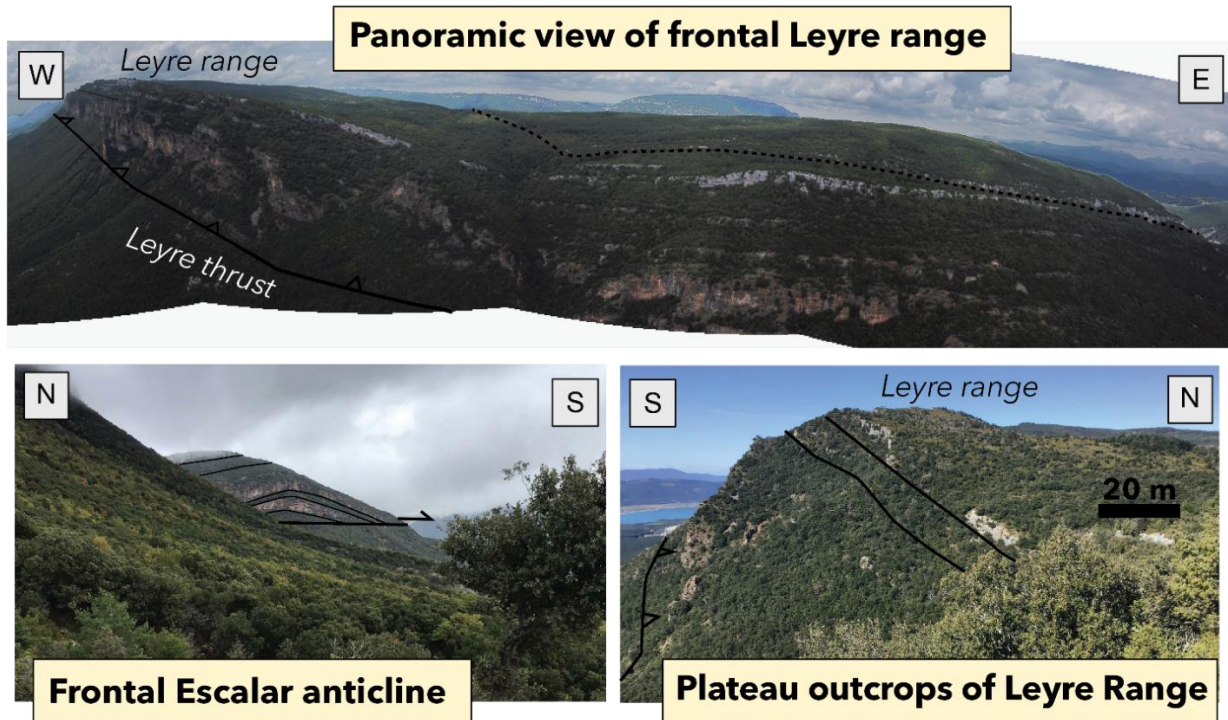


Figure 75: View of the plateau sector of the Leyre Range. Photo on top is a panoramic view of the rock walls that appear to the S of the mountain range. Lower left photo is the frontal Escalar anticline where the Cretaceous sandstone layers of the Marbore Fm. are in the hanging-wall, of the sub-horizontal surface of the Leyre frontal thrust. The forelimb is eroded towards the observer, to the W, as can be seen, in the lower right photo, at the backlimb.

The hanging-wall anticline of the Leyre thrust is particularly pronounced in the areas near the Sigüés gorge (Figure 77). In the Escalar area, it is possible to see the fold with an open geometry, thrusting over, by means of a subhorizontal thrust, the shales in the footwall (Figure 75, bottom left picture). To the W, the axial trace of the anticline is eroded and only backlimb is present.

In the higher areas of the range, the landscape is characterized by a "plateau" limited by these rock cliffs. In them, grey limestones generally crop out. It is possible to recognize the gentle folding of the layers that top it, which are generally responsible for the changes in the landscape features (Figure 75, bottom right picture). This is what is called a "conformable relief", also detected in the hillsides towards the N. This relief is also recognized towards the E, in the areas near the gorge excavated by the Esca river.

In this gorge, two anticlines (described in detail further on) can be seen (Figure 76). The main anticline is the pop-up anticline showing a box-fold geometry, with the horizontal layers of its hinge zone coinciding with the plateau on top, and vertical layers limiting on both sides this area.

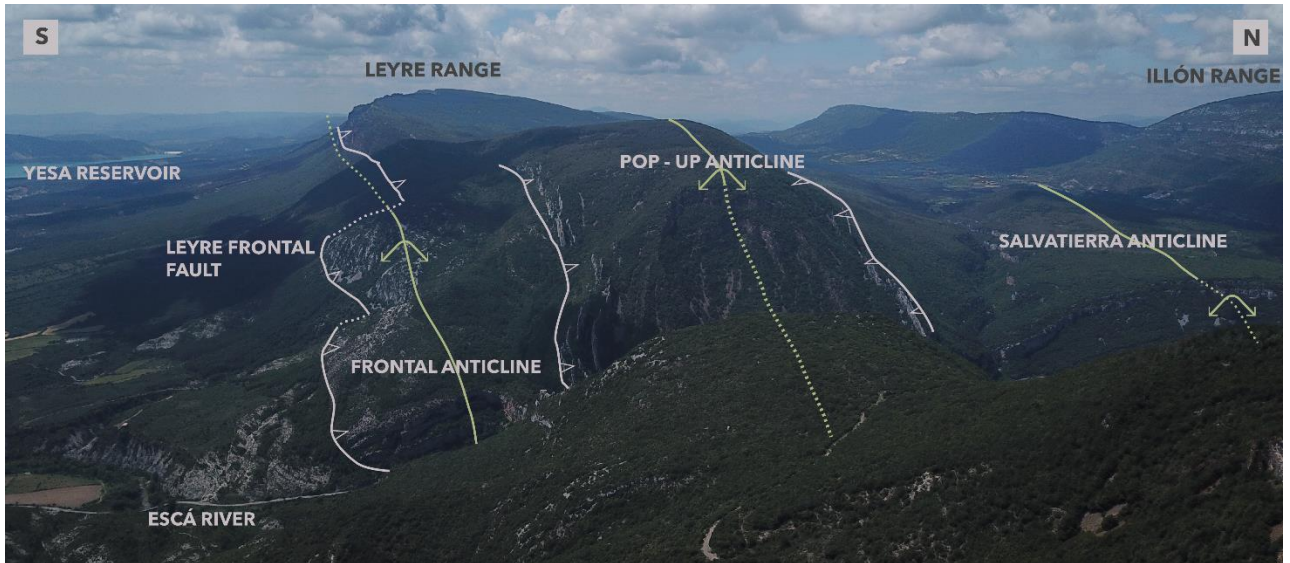


Figure 76: General aerial oblique photograph of the Leyre range, viewed towards the West. The plateau remains in the background, showing subhorizontal beds and dipping 20° to the N in the northern edge of the plateau. In the central part of the photograph the cluse generated by the river Esca is observed, and it shows what the interior structure of the mountain range looks like, expressed by the three folds described in the text. The frontal fold is eroded towards the W, while the other two dissolves into the landscape of the range and its N slope.

3.2.1.3 Sigüés Gorge

Visiting the Sigüés gorge provides magnificent information on the internal architecture of the Leyre range (i.e. the hanging-wall of the Leyre thrust), and its relationship with the footwall of the Leyre frontal thrust. It is possible to cross the structure along the road parallel to the Escá river, finding outcrops of different stratigraphic units. However, there is also a path on the left bank of the Escá river, which runs along the gorge at a higher altitude, providing better views of the structures, as well as key outcrops for understanding them. As previously mentioned, three successive anticlines can be found along the gorge, two of which can be followed longitudinally along the Leyre mountain range, and the third one, located to the north, with a slightly oblique direction (see map in Figure 70). The rocks observed inside the gorge correspond to the Marboré Fm and the Ager Fm, although reddish layers of the Tremp Fm are found in some areas. It is also possible to see the first meters of the turbiditic Hecho Group, which lie on top of the Ager Fm, at the frontal fold (Figure 77) and the Salvatierra anticline.

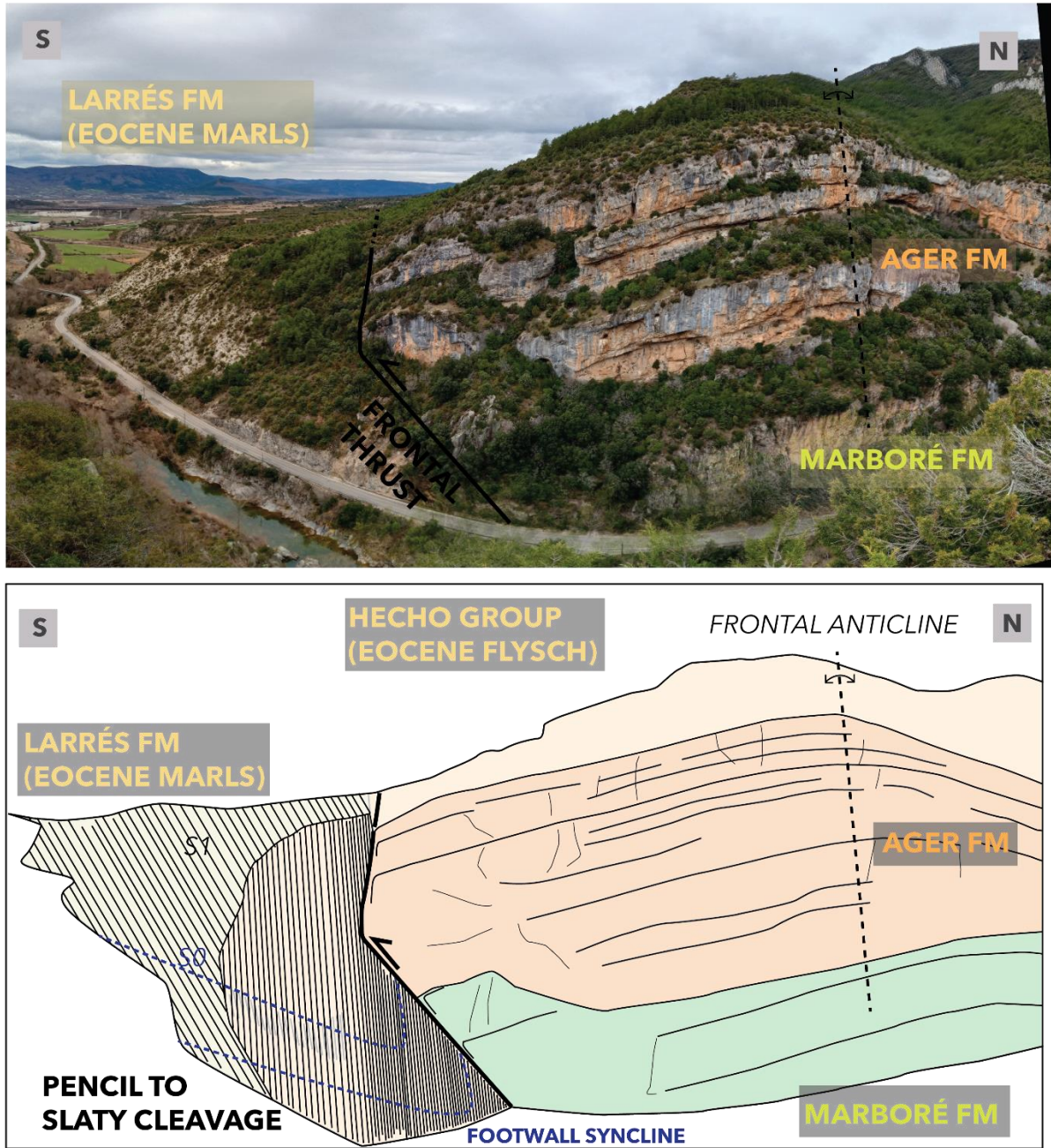


Figure 77: Frontal anticline and Leyre frontal thrust, thrusting over the Larrés Fm shales.

At the southernmost end of the transect, the Leyre frontal anticline (Figure 77) appears as a gentle fold with a southern limb dipping 20-30° S and being cut by the south-verging Leyre frontal thrust. Secondary shear structures appear on the last few meters of this forelimb. This end of the forelimb has a significant shear zone, with a drag fold over several metres (S0 drawn as blue line in Figure 77). This limb thrusts over the Eocene shales, which crop out showing a highly penetrative cleavage (that can be considered as a fault gouge where the bedding cannot be recognized).

From the road or path on the left bank of the Esca River, it is possible to see the faulted contact between the carbonate formations and the Larrés formation, in the footwall of the fault. Along the road, the syncline footwall at the fault contact is marked by the presence of

a spring to the north. In the southern part of the structure the carbonates are bent (not visible in the photo) over a few meters, with the formation becoming vertical. This geometry is illustrated in Figure 76. These two geometries (footwall syncline in the footwall and steep drag fold in the hanging-wall) led Boiron et al. (2020) to identify a structure compatible with the trishear model (Figure 67c). In this way, the emerging fault would be the top part of the triangular zone; the Leyre fault being in this model, at depth, and therefore blind.

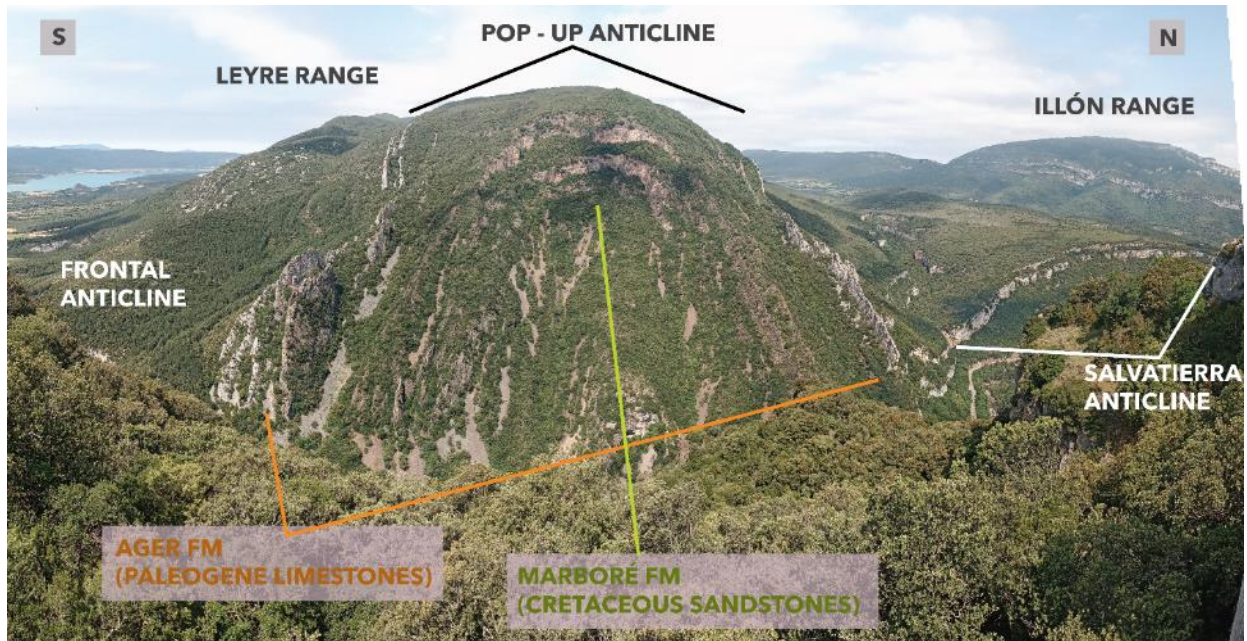


Figure 78: View of the gorge of the river Escá, photograph towards the W. This is a local zoom of Figure 76, with a view of the internal structures of the Leyre range. Figure 77 view is under "Fontal Anticline" label, not visible.

The second and central fold, with an amplitude of ~500 m (see Figure 78) displays subvertical limbs. The structure is bounded by a forethrust to the South and a backthrust to the North. This structure, with its vertical faulted flanks, thus presents a pop-up geometry, that will be modelled with two versions of cross-sections (see section 3.4. Structural frame and serial Cross -Sections.). This pop-up fold brings to the surface the entire Marboré Fm. The Triassic or Zuriza Fm are not visible in the heart of this fold, which suggests that the detachment takes place between the Marboré and Zuriza formations.

Finally, the third and northernmost fold, the Salvatierra anticline, is a gentle fold with a wide hinge zone, except for areas next to the pop-up, where Paleocene beds are verticalized (Figure 79). The backlimb of this fold faces the village of Salvatierra, and in general, it constitutes the entire northern slope of the Leyre and Orba mountain ranges.

3.2.1.4 Orba Range

This mountain, located in the vicinity of the Leyre Range, exhibits a similar relationship between structure and topography. From the village of Sigüés, it is striking to see the continuity between the Sierra de Leyre, which overrides the Larrés marls, and the Sierra de Orba, armed by the same Marboré and Ager carbonate formations, and also overriding the

CHAPTER 3 - STRUCTURAL STUDY OF SIGÜÉS AREA

Larrés marls. This continuity nevertheless represents two folds, the frontal Anticline to the west and the Salvatierra fold to the east. The hinge is visible in both cases, towards the Esca Gorge, and has since been eroded. Essentially, therefore, only the backlimbs of the two folds are visible.

The strike of the Orba range is oblique by about 20° clockwise with respect to the Leyre range (see map in Figure 70). Moreover, its internal structure is not entirely visible in the Esca river gorge. On the southern slopes, there are extensive Quaternary pediments and outcrops of Eocene shales. Cartographically, the Sierra de Orba was mapped differently between Puigdefábregas' early work (Puigdefábregas, 1975) and the latest version of the geological map (GEODE from IGME, see Figure 92: Comparison of three previous maps covering the newly mapped study area presented in Figure 70. The Geode mapping was published in 2008. The Magna cartography is presented by de Rojas and Latorre (1972). The Puigdefábregas cartography dates from 1975.).

Figure 79 shows how the Ager and Marboré Fm on the summit of the range are thrusting over the folds of the Leyre range, whose axes exhibit a downward plunge towards the East. The entire northern slope of the range is dipping 20°N, which coincides with the northern limb of the Salvatierra anticline. In general, the strike of the Salvatierra anticline is aligned with the trend of the Orba range, suggesting that the forelimb of the Salvatierra anticline is eroded, and this N structural ramp coincides with the backlimb. Some outcrops of the Marboré sandstones on the eastern limit of the range correspond to vertical layers which would form part of this forelimb, which is almost completely eroded.

The second picture in Figure 79 presents the view from the Escá gorge towards the boundary between the forelimb of the Salvatierra fold, and the backlimb of the Pop-Up anticline. Although the forelimb is cut by the backthrust of the pop-up (and overlain by its hanging-wall), at some point, a bulge in the limb (probably caused by the incipient Orba thrust) leads to the overlap of the Ager Fm over the backthrust. Unfortunately, this location is not identifiable due to dense forest coverage.

Figure 79 also highlights the cleavage in the shaly layers at the base of the footwall of the backthrust, where S1 is observed to dip towards the south (the only place in this area where a southward cleavage is observed), parallel to the pop-up fault, and likely generated by the backthrust.

CHAPTER 3 - STRUCTURAL STUDY OF SIGÜÉS AREA

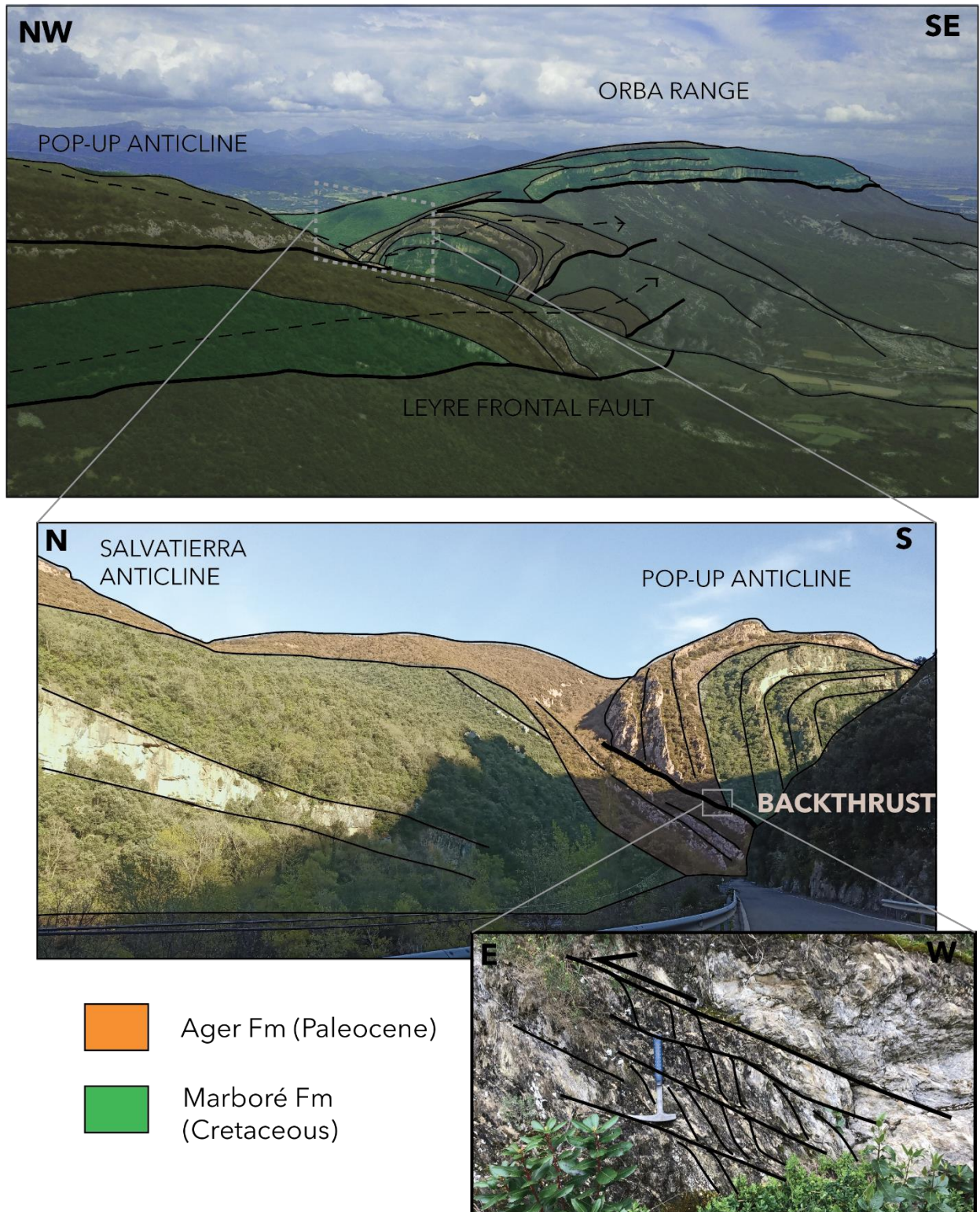


Figure 79: 1) View of the Orba range to the E, in a oblique aerial photograph. 2) View highlighted in the grey square, from inside the Escá gorge, towards the backlimb of the Pop-Up anticline. 3) Detailed picture of the outcrop of the backthrust in the Larrés formation, with cleavage dipping to the South. This is the only place in the Sierra de Leyre or Illón where we have documented cleavage dipping to the south. This demonstrates that at least part of the cleavage is controlled by fault propagation.

3.2.1.5 Southern zone of the Leyre thrust

To the south of the Leyre-Orba system, the foothills of the mountain range show gentle slopes towards the Canal de Berdún where the Aragón river flows from E to W. The E-W Canal de Berdún depression (sometimes also called *Depresión Intermedia* in the geographical literature) is a wide valley (~6-7 km in the Sigüés area), where shale outcrops of Larrés, Urroz/Sabiñánigo and Pamplona Fms can be found. On its right bank, the Escá river, is a N-S tributary of the Aragón river, that displays an alluvial plain and several stepped fluvial terraces.

From the mapped trace of the Leyre thrust (N of Sigüés) to the S, cleavage is present in the Eocene shales. There is slaty cleavage which persists for several tens of meters from the Leyre thrust to the south. Moving away from the thrust, cleavage is progressively less penetrative, and at about 200 m from the thrust, pencil cleavage is found. Finally, this cleavage is missing in the shale outcrops at about 600 m from the fault, next to the village of Sigüés. This gradient of cleavage can be clearly observed along the A-136 road, and is the subject of the study by Boiron et al. (2020). This gradient zone has also been studied by Saur et al. (2021). Cleavage spacings can be found in these publications. Since this gradient is one of the targets of this PhD, in the present work, we visit several other outcrops, at the footwall of this fault to the E and W of the Esca river transect.

On this southern side of the Leyre range, shale outcrops are found in badlands and gullies that cut through the Quaternary pediments, and allowing the exposure of the underlying substrate. This is where most of the sampling for the dataset in this PhD was carried out (see 4.3. Sigüés results), including the AMS analysis of shale fragments and the calcite veins embedded in the Larrés and Pamplona formations. The gullies running perpendicular to the strike of the Leyre range influenced the sampling campaign, and as a result, field work was carried out along transects perpendicular to the Leyre range. This allowed us to see how the outcrops evolve in the vicinity of the main fault along strike, in a direction perpendicular to the road section studied by Boiron et al. (2020). An extra sector will be described, which corresponds to outcrops on the western margin of the range near the Leyre Abbey, 13 km west of the town of Sigüés and the Escá river transect.

Generally, the strata of the Larrés and Pamplona formations dip at an angle of 10-20° to the south. However, there may be variations in the dip of the S0, and it can be challenging to detect it in the thick homogeneous banks of the shales. Outcrops have been observed in this southern part of the Leyre range in which there are very gentle folds, having locally a monocline shape as shown in Figure 80.



Figure 80: Dipping limb of a monocline fold on Larrés Fm shales, at the Escó section, south of Leyre thrust.

3.2.1.6 Leyre Abbey Sector

At this westernmost sector, only one sampling transect was carried out perpendicular to the strike of the Leyre frontal fault. Shale outcrops appear with facies that range between finely stratified and completely homogeneous, in addition to some beds having more carbonate content and a bluish colour (Figure 81a). In general, the shales appear without detectable cleavage, although with a fracturing that could be confused with pencil cleavage. Only in areas close to the fault, in the upper part of the transect, a more conspicuous cleavage is observed (Figure 81b), which becomes much stronger and penetrative in the final tens of meters before reaching the mapped thrust trace.

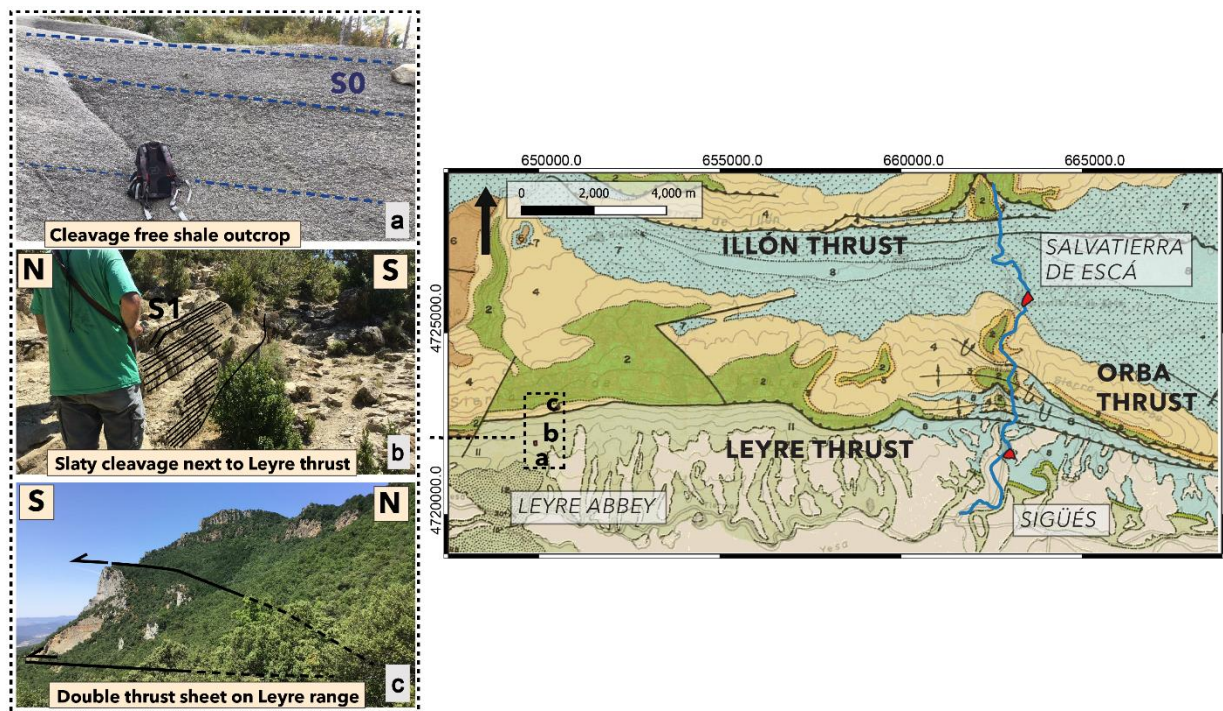


Figure 81: Leyre Abbey sector located at western termination of the Leyre Thrust. Pictures of shale outcrops show cleavage associated to the Leyre thrust footwall. Also, the hanging-wall anticline of the Leyre thrust is depicted.

CHAPTER 3 - STRUCTURAL STUDY OF SIGÜÉS AREA

In a quarry near the fault contact and the first outcrops of the Paleocene Ager Fm., what appears to be a hanging-wall anticline is observed (Figure 81c). There are not outcrops that allow to define the geometry of the fault, as the contacts are covered by debris. On the other hand, the geometry of the hanging-wall is more complex than that observed in the Sigüés sector. The Ager Fm appears duplicated in the cliff, suggesting a possible duplex structure. However, the intermediate thrust sheet disappears towards the E, where the Cretaceous-Paleocene series is only visible in the hanging-wall of the Leyre thrust.

3.3. Sampling of shales

In what follows, the different sections of the sampling campaigns performed on Sigüés will be presented. More than 1400 non-oriented fragments were collected and measured. Generally speaking, it is very difficult to detect the appearance of pencil cleavage on these facies. Indeed, the alteration of these marls makes it difficult to interpret the cleavage planes. It was only in the slaty cleavage phase that there was no ambiguity, as the rock is more resistant to erosion. Bedding can be identified morphologically, but in the most deformed zones, only cleavage is observed. In the footwall of Leyre thrust, numerous horizontal faults with N-S striations were identified, and sometimes with several kinematics. The most striking feature of the sections studied, especially the Esca section, is the appearance of slaty cleavage framed by pencil cleavage. This conformation has been interpreted as the presence of a blind fault. However, some secondary faults are clearly emergent. It therefore appears that the footwall of the Leyre fault, then the Orba fault, is affected by secondary faults, some emerging, others blind, and finally by horizontal faults that are a few mm thick.

3.3.1 South-western sector: Escó and Llarto cross-section

These two transects begin similarly, with shale outcrops in gullies, where the bedding can be identified (Figure 82 a and b). However, it is often challenging to check the strike of bedding in the shale beds, which are metric in thickness and very homogeneous. In this area of the range, no lithological differences have been detected along the section. A characteristic feature of these sections is the abrupt changes in deformation of the outcrops. In the Escó section, shale beds hosting pencil cleavage are observed at about 200 m of vertical distance from the thrust. In some adjacent outcrops, a deformation zone approximately 10 m thick appears in the shales. The cleavage is highly penetrative and undergoes changes in orientation and dip. Several folded and sheared calcite veins are also present (Figure 82c). Nevertheless, the deformation seems to be restricted to this zone, and in upper outcrops, the marls exhibit their sedimentary aspect, hardly distinguishable from a spaced pencil cleavage (Figure 83a).

The Llarto cross-section has a greater number of outcrops, allowing the emergence of secondary faults to be detected at ~100 m of vertical distance from the fault. Again, signs of intense shearing are detected within a few meters (Figure 83c). Finally, in the upper outcrops of the Llarto section, the pencil cleavage is more penetrative, and the shale beds are progressively more foliated (Figure 83d), reaching a slaty cleavage area in the last tens of meters before reaching the Leyre frontal thrust. In both sections, the cleavage dip varies between subvertical and 20°. This variability is attributed to facies changes (cleavage refraction). In some cases, we detected the presence of two cleavages in the clay matrix.

CENTRAL ZONE: ESCÓ SECTION

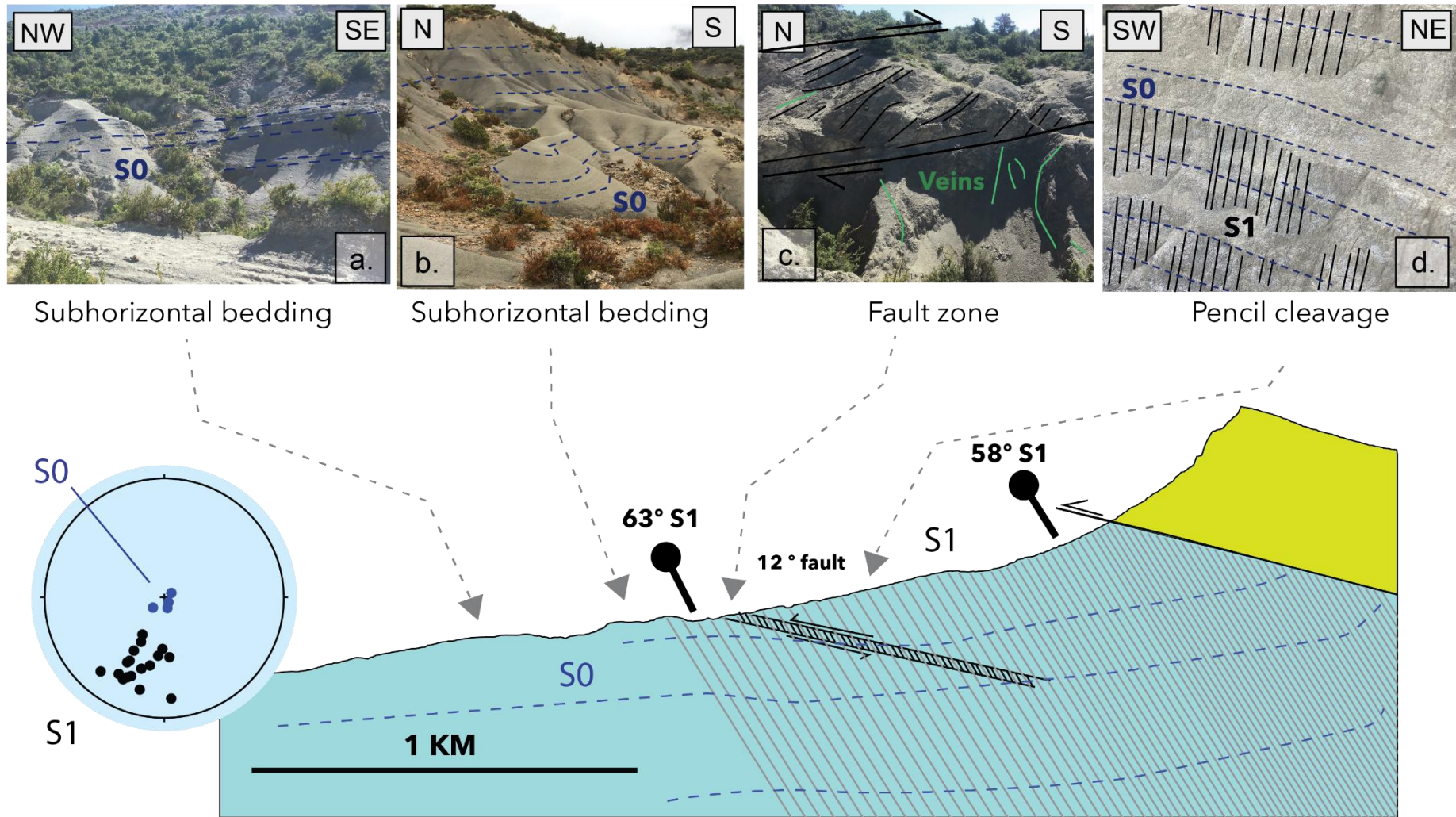


Figure 82: Scaled sketch of the Escó section, with field photographs and shale cleavage drawn. The stereonet shows various bedding (S0) and cleavage (S1) orientations.

CENTRAL ZONE: LLARTO SECTION

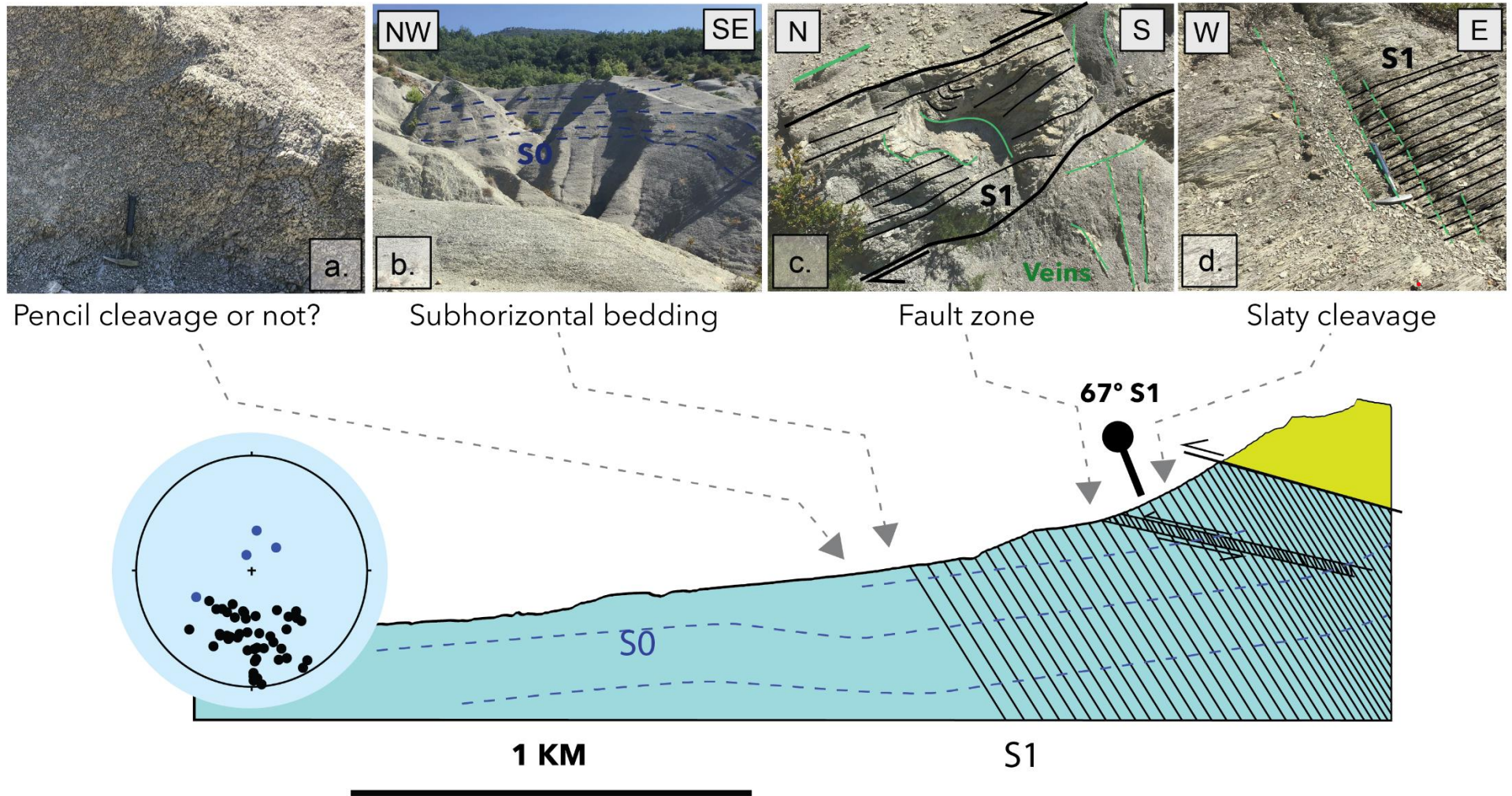


Figure 83: Sketch of the Llarto section. The stereonet shows various bedding (S0) and cleavage (S1) orientations with same colours as in Figure 82.

South central sector: Escalar

The Escalar transect has been the most intensively sampled of all those described. Throughout the outcrops visited, the cleavage gradients described in the footwall of the Leyre frontal thrust can be found with an acceptable continuity. For this reason, this transect has been re-sampled on two occasions to obtain a denser grid. In lower areas (to the south), outcrops without deformation can be found. At a distance of 300 m (vertically) from the Leyre thrust, pencil cleavage can be distinguished, what leads to a certain hardening of the shales, which are more competent than in other areas (Figure 84b).

At about 230 m of vertical distance from the thrust, the cleavage becomes very penetrative, with millimetre spacings giving the shale outcrops a slaty appearance. At higher positions, this penetrativity is reduced, although the planar slaty cleavage is maintained up the last few meters before the thrust (Figure 84c and d)

CENTRAL ZONE: ESCALAR SECTION

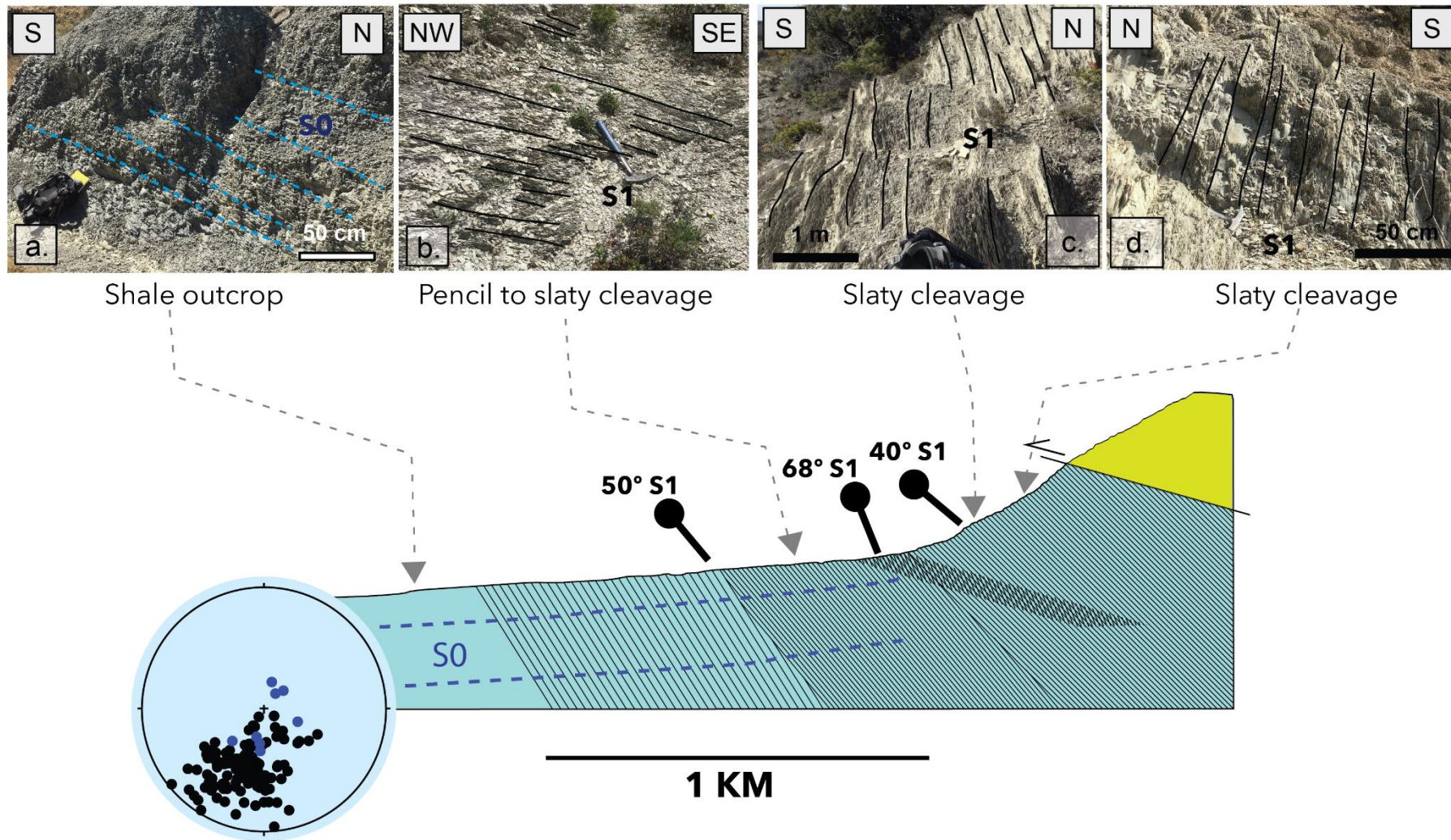


Figure 84: Sketch of Escalar Section. Cleavage is observed almost at all outcrops.

South central Sector: San Juan - La Paul

The La Paul site is located one kilometre east of these outcrops, where pencil cleavage is more penetrative, in transition to a slaty cleavage (Figure 85c)

Overall, in both the upper parts of the La Paul and Escalar profiles, attempts were done to find an exposure of the Leyre thrust surface. However, due to the outcrop conditions of the shales, and areas where the geological structure is covered by either the vegetation canopy or slope deposits, basic structural features of the Leyre frontal thrust, such as the fault plane, cannot be observed. In this place, shales display slaty cleavage underlying the first observed outcrop of the Marboré sandstones in the Escalar section (or the Ager limestones in La Paul, since they are in contact with the forelimb of the frontal fold).

The San Juan sampling section cuts across shale outcrops to the N of Sigüés, on the right bank of the Escá river (Figure 85b). The river's erosion allows to observe a vertical wall of shales, where the bedding is dipping to the south while the cleavage is subvertical. However, many of the sampling points were actually placed in the hanging-wall, on carbonated shales that crop out overlying the Ager Fm, which at that point appear in the frontal anticline. Only three sampling sites were taken in the footwall of the Leyre frontal thrust. Slaty cleavage is observed, which becomes more pronounced when approaching the thrust (Figure 85a and c). The Leyre frontal thrust is only distinguishable by features such as intense shear and deformation accumulated in a few meters of thickness. However, there are no discrete fault planes or other structural or kinematic markers apart from cleavage planes.

CENTRAL ZONE: SAN JUAN AND LAPAUL SECTION

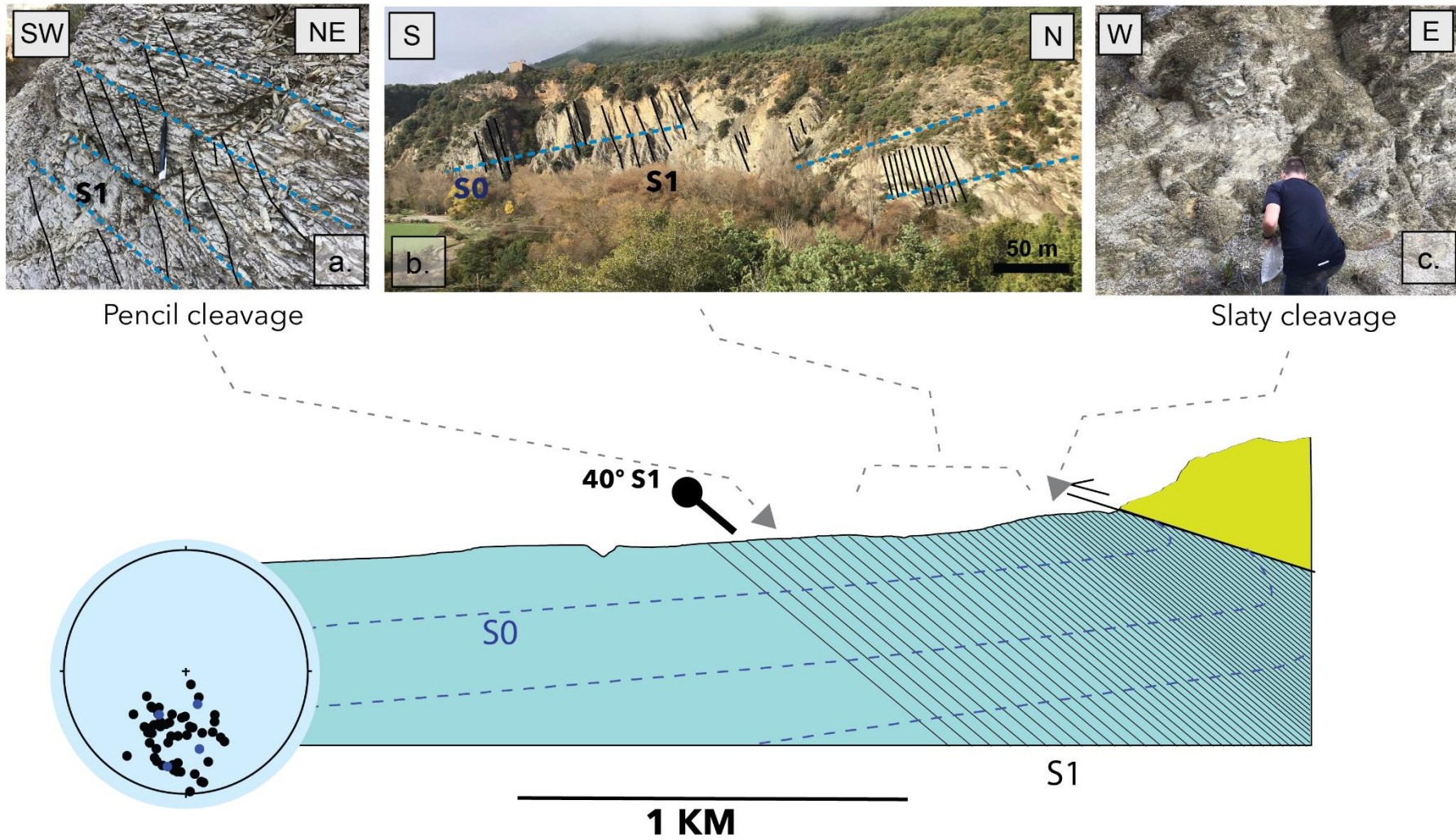


Figure 85: San Juan and LaPaul sketched section. A panoramic photograph is displayed showing the outcrops next to Escá River. Same legend as in Figure 82

Sigüés section.

In the area of Sigüés, other outcrops different from the ones next to the road (already sampled by Pueyo-Anchuela (2012) or Boiron et al., (2020) were visited. All of them are located a few hundred meters east of the road where the Larrés Fm crops out. Here, a gradient of cleavage is observed, which is expressed in the form of pencil cleavage next to the Sigüés village (Figure 86a and b), although it progressively diminishes in spacing when approaching the Leyre thrust. In the last tens of meters of shale exposure before reaching the fault contact, the overturned beds indicate a footwall syncline with the shales showing slaty cleavage (Figure 86c). Once again, it is difficult to appreciate the fault plane, because shales crop out both in the hanging-wall and the footwall, and no discontinuities or measurable planes can be seen. There is only one site; an outcrop next to the gorge (Figure 94), where the hanging-wall of the forelimb anticline is in contact with the footwall shales, a clean fault plane separating them. These data are presented later on in section 3.4. Structural frame and serial Cross -Sections.

Sigüés Section

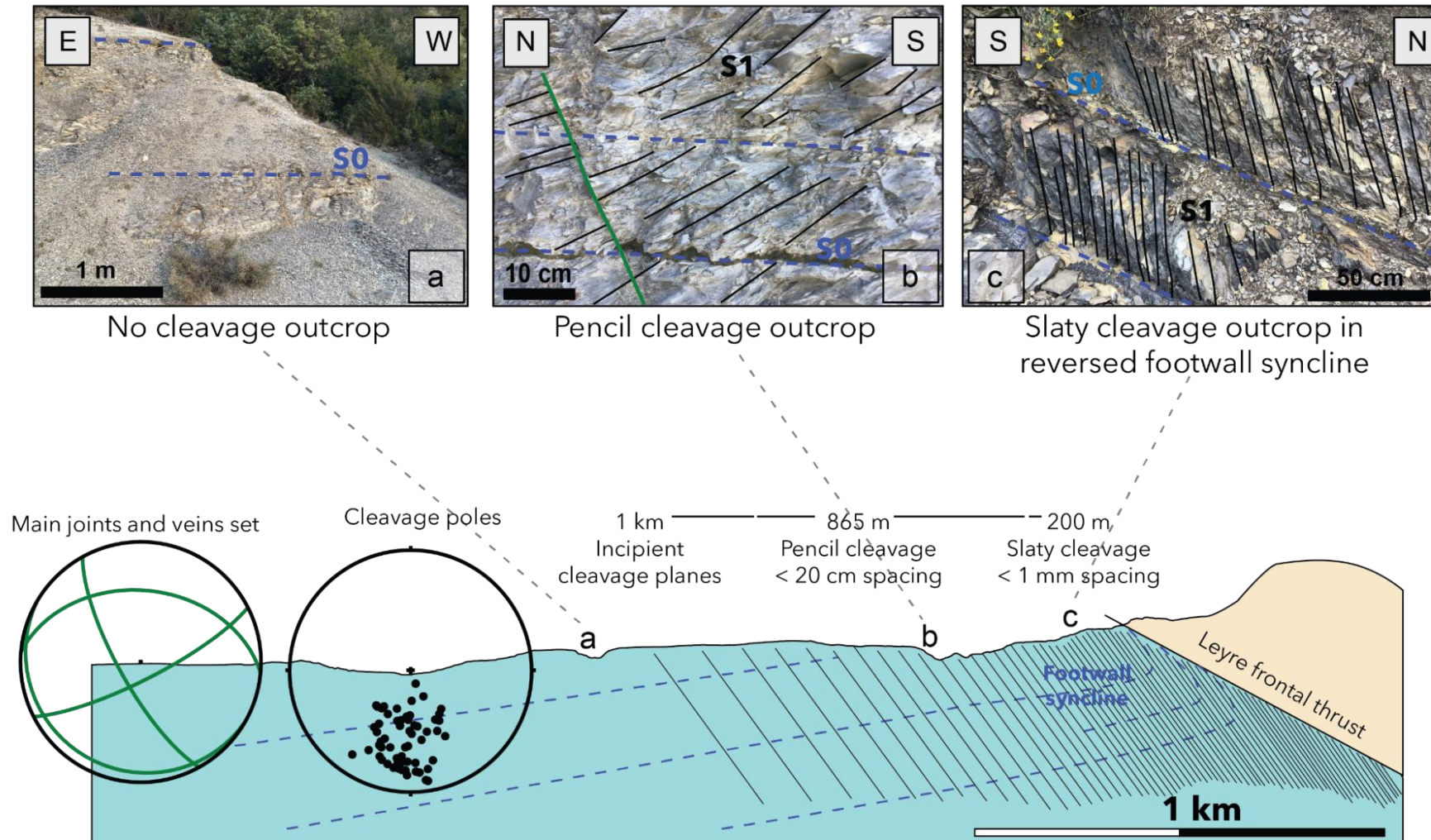


Figure 86: Sketch of Sigüés section, same outcrops as Boiron et al. (2020).

Eastern sector: the Orba Range.

As seen in Figure 79, at the left bank of the river Escá the landscape begins to increase in altitude in the area near the Pop-up anticline, indicating that the main thrust that builds it up is between them and is thrusting over the structures of the Leyre range. Therefore, it is considered that there is a transition in the area where the pop-up still crops out, but then it is thrust over in the footwall of the Orba Range.

In areas at ~2.5 km from the Orba frontal thrust, it is difficult to recognize the deformation associated with cleavage. Bluish shale outcrops, with fracturing sub-perpendicular to bedding that can be confused with pencil cleavage (Figure 87a and b) dominate. Pencil cleavage is clearly distinguishable to the eye at ~900 m from the Orba frontal thrust trace. This cleavage again becomes more penetrative closer to the fault (Figure 87c and d). Once again, partly because of the outcrop conditions no outcrops of the thrust are found, preventing the detailed characterization of the main Orba thrust.

In the transition zone between the Leyre and Orba structures, signs of what could be a hanging-wall anticline, are observed and expressed as verticalization of beds of the Marboré Fm right above the fault trace. As mentioned before, the Orba frontal thrust corresponds to the continuation of the Salvatierra anticline, and although the forelimb would be completely eroded, there is little evidence of it.

EAST ZONE: ORBA SECTION

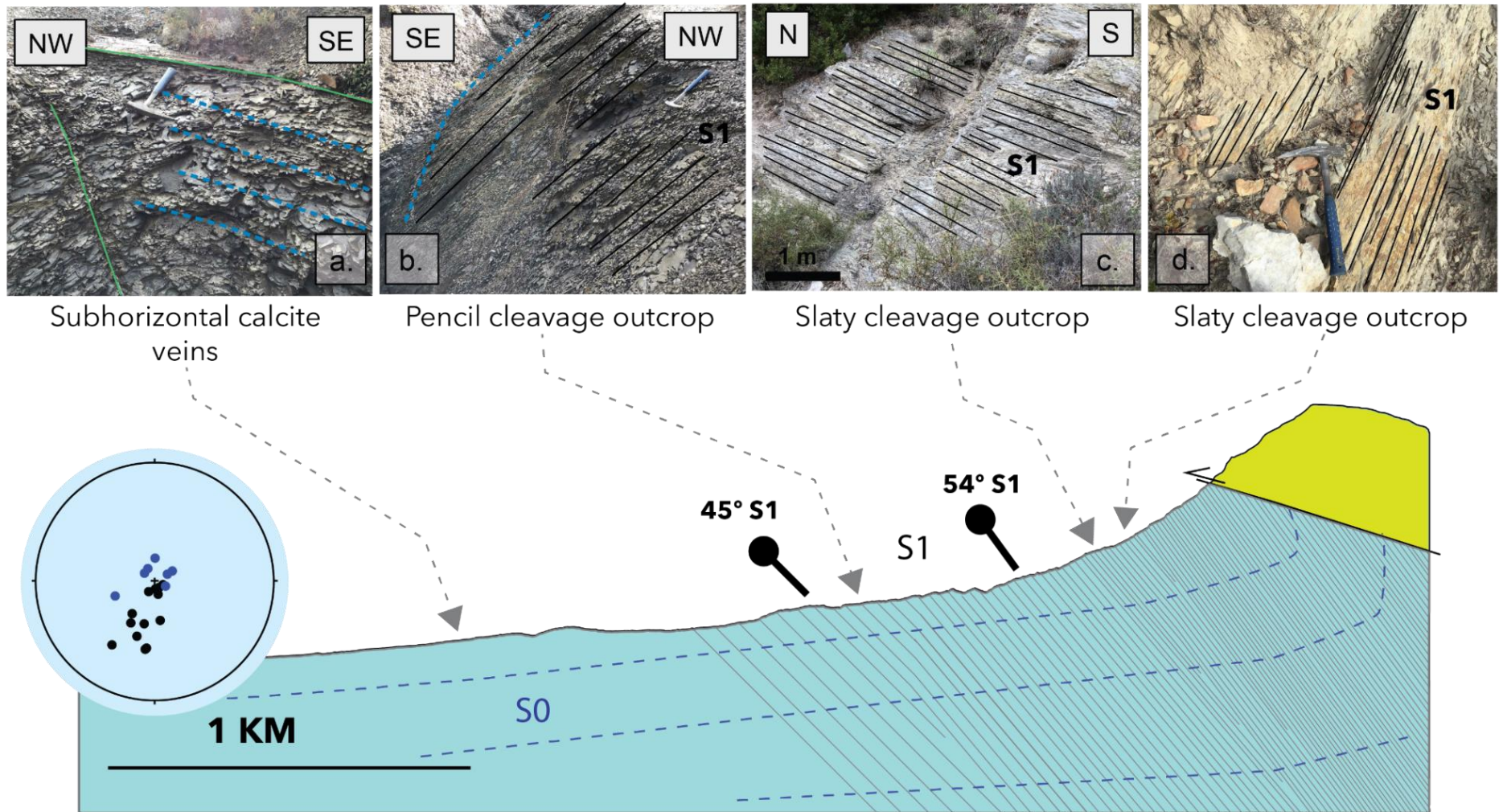


Figure 87: Sketch of Orba section with field photographs and structural data. Same legend as previous sketches.

3.3.2 Preliminary study on secondary thrust zones

A secondary target of this PhD is to explore other similar fault zones, i.e. where the Eocene shales are close to a thrust and consequently could host the deformation associated to it. Besides, we have aimed to compare the effects of the deformation that the marls or shales have probably underwent. Therefore, in the same orogenic context and in the same basin, other outcrops are proposed to be studied. The application of AMS analysis is presented in the next chapter (4. SHALE FABRIC).

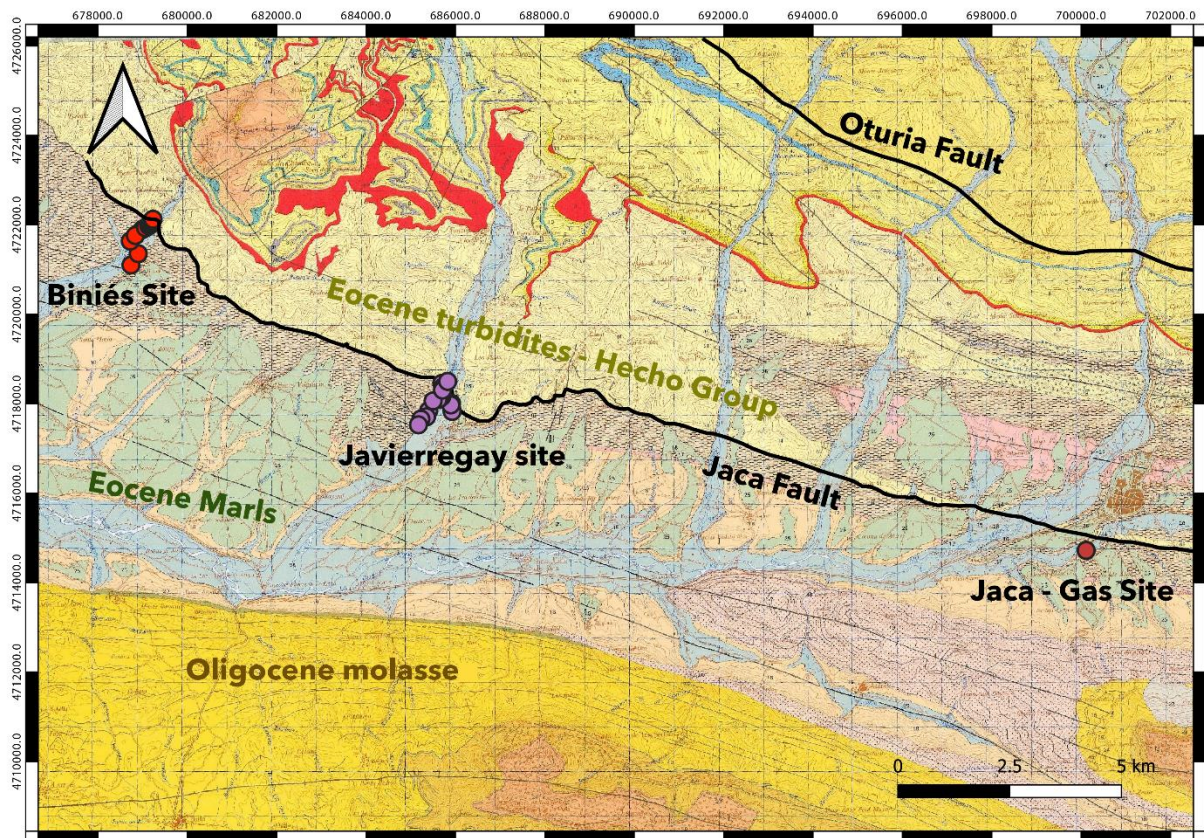


Figure 88: Jaca Basin geological map from: MAGNA 1:50.000 (Jaca, nº 176), eastwards of Leyre unit. The Jaca fault separates thrusting turbiditic basin over Eocene shales. Three sites in the footwall of this thrust were visited.

Both the Leyre thrust and the Orba thrust map trace disappear to the east, due to the plunge of the structure. Thus, no new outcrops seem to be found nor show evidence of these contacts between the Cretaceous and Eocene units. However, following the basin eastwards a new fault trace is detected. A thrust that brings the turbiditic basin (Hecho Group) in the hanging-wall in contact over the shale formations (either the Larrés or Pamplona Shales) to the south. This thrust has different names in the literature (Javierregay thrust, Pueyo-Anchuela 2012; Jaca thrust), but it is clearly recognizable in the cartography. In this PhD it will be referred to as Jaca thrust.

The strike of the Jaca thrust is Pyrenean, N100, and in the same way that the Orba thrust, its trace disappears within the Eocene shales at Jaca (Aragón river transect). Meanwhile a new fault further north, the Oturia thrust (see Casas-Sainz and Pardo, 2004), shows a relay geometry with the Jaca thrust, by continuing the contact between the two Jaca sub-basins: turbiditic and molasse.

CHAPTER 3 - STRUCTURAL STUDY OF SIGÜÉS AREA

Along the trace of the Jaca thrust three observation points will be presented: (i) the Biniés section, along the A-1602 road; (ii) the Javierregay section, exactly the same layout but this time next to the A-176 road in the valley of the Aragón Subordán river, and finally, (iii) to the south of the town of Jaca close to the Gas River, where the thrust brings shales into contact both in the hanging-wall and the footwall. Sampling points are plotted on Figure 88.

The Biniés transect includes 1.5 km of sampling sites southward from the fault outcrop; from the turbidites on the hanging-wall (which show cleavage in their shaly members), to the shales of the Larrés Fm in the footwall, close to the Biniés village (Figure 89b). These shales appear to be intensely deformed in the area immediately adjacent to the fault, but further south, it is difficult to characterize the deformation, because some syn-sedimentary structures such as slumps, make it difficult to interpret the fracturing of the shale. The contact between the turbiditic and molasse units appears to be an intensely sheared zone, where more penetrative cleavage and a fault gouge are found (Figure 89a). Pebbles and blocks from the hanging-wall are also incorporated into the fault zone. This structure dips about 40° towards the North, but no other structural markers are distinguished.

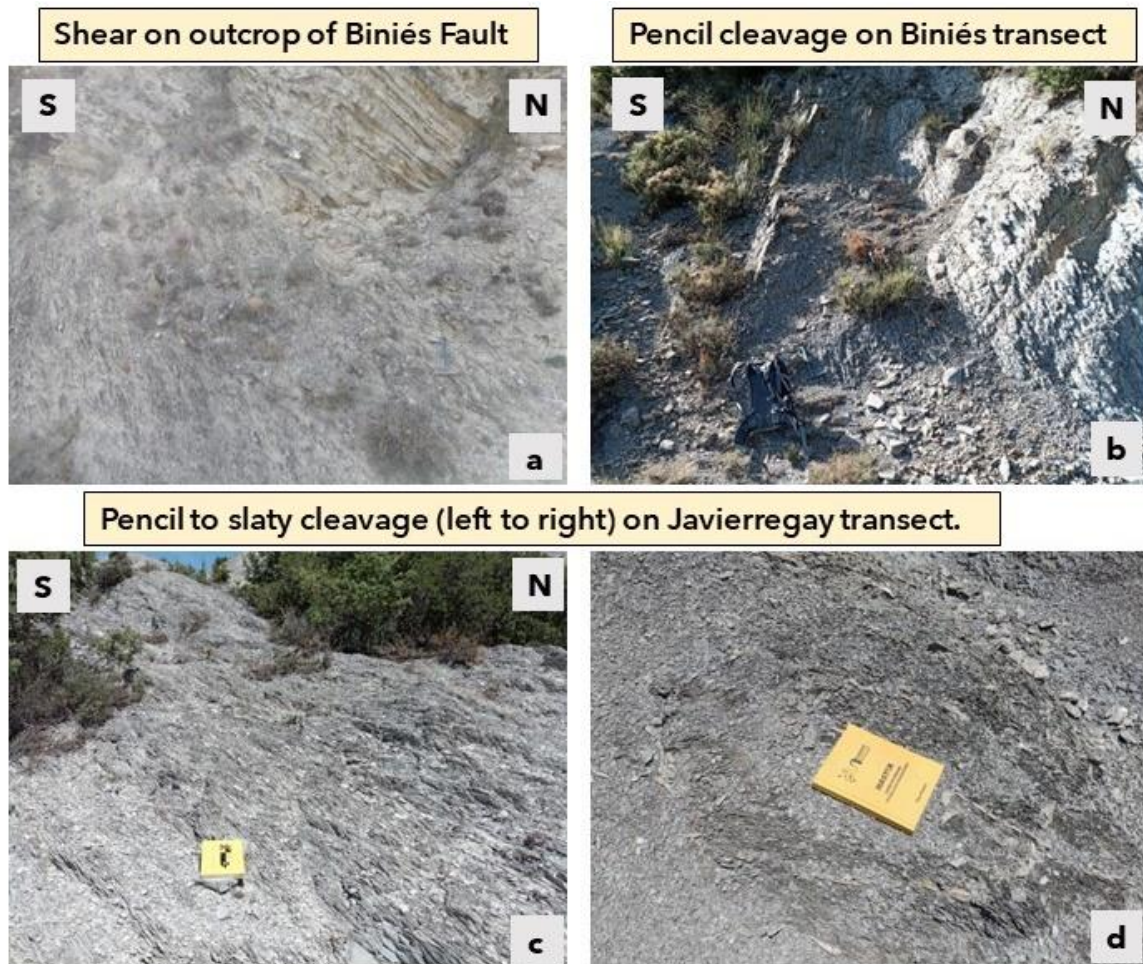


Figure 89: Outcrops on Biniés and Javierregay sites.

CHAPTER 3 - STRUCTURAL STUDY OF SIGÜÉS AREA

Similarly, other sampling sites distributed along a few hundred meters were sampled south of the Jaca thrust between the Hecho Group and the Eocene shales near the village of Javierregay, on the right bank of the Aragón Subordán river.

Here, hundreds of metres of shale outcrops appear to have “weathering” fracturing (it is doubtful to distinguish purely lithological fracturing, related or not to de-compression, from some tectonic phenomenon) and calcite veins. About 800 m from the contact, there are clear S1 planes forming pencil cleavage in the shale units. This cleavage becomes more penetrative in the vicinity of the thrust, especially in several clayey layers (Figure 89d) where spacing decreases.

On the left bank of the Aragón Subordán river and next to the road, the Jaca thrust (which on the right bank is hardly recognizable because of the homogeneous lithology) is clearly observed. In this outcrop, a shear zone dipping 25°N, and 1 m thick (similar in size to the Biniés section) is found. In the footwall Eocene shales are cleaved and sheared in several blocks. A few meters to the south, the outcrop of the thrust trace is lost. In general, folds are observed in the Eocene shales, something which is common in the Canal de Berdun, where the Larrés Fm. exhibits gentle Pyrenean-trending folds with a wavelength of about 50-100 m. Usually, given the homogeneity of the shale rock formations, and the scarcity of good exposures these folds are not easy to define and could blur the interpretation of the deformation data in the Arro-Fiscal Fm.

A third site, in along-strike continuation of the Jaca thrust, was explored to the south of the city of Jaca. Driving along the A-1205 road, one kilometer south of Jaca, a fault that emerges within the Eocene shales is found. In this outcrop, unlike what happens north of Jaca, the thrust does not bring the shales into contact with the turbidites of the Hecho Group, which lie to the north of the city. A 1 m-thick fault zone with intense shearing and cleavage is observed. The cleavage, in less penetrative form, is also detected in a 2 m thick damage zone in both fault walls, making total of 5 m of deformation zone (Figure 90). In other nearby outcrops, no local cleavage or shear structures are found, suggesting that deformation is restricted to the zone closest to the thrust. In this case, it was decided to implement a different sampling approach. Instead of doing a kilometer-long transect, eight sampling points were obtained in the fault zone, and 2 samples at a distance of 5 and 10 m in the footwall (Figure 90).

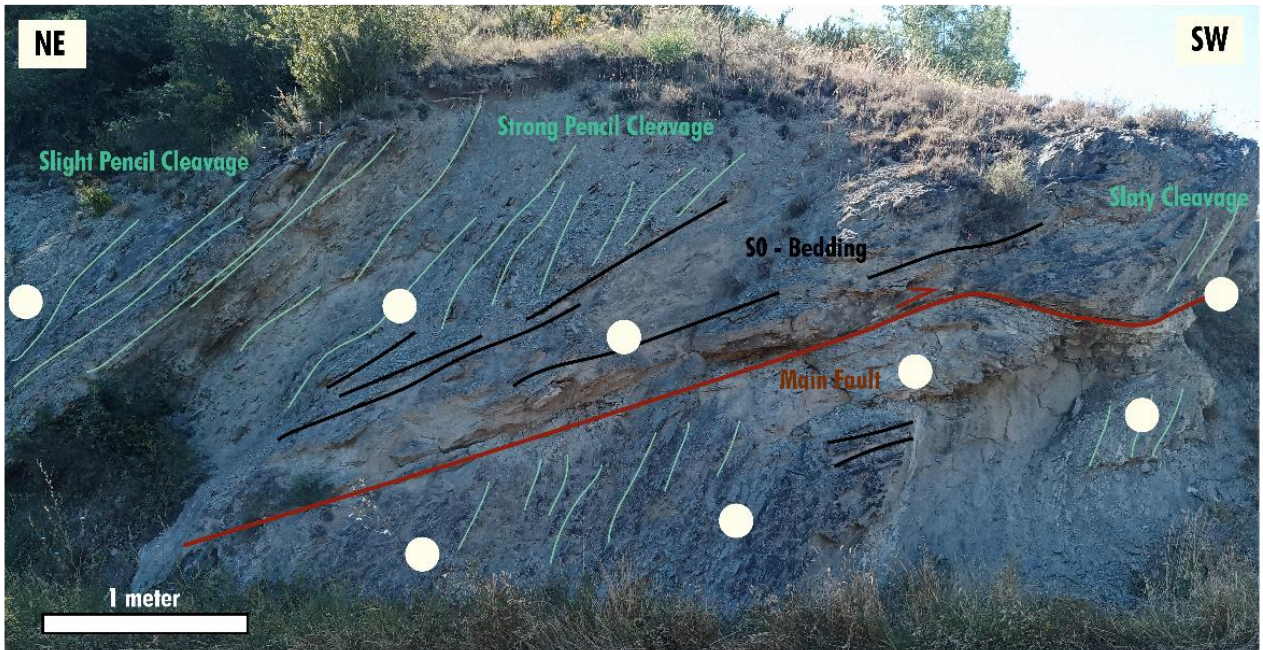


Figure 90: Jaca Gas fault. An outcrop with 20 m of shales with a thrust (red line). Ten sites were sampled on shales. Two of them are 5 and 10 meters right of pictured outcrop.

In short, a number of similar geological contexts were visited: a thrust superimposing sedimentary geological units, and in the footwall a large group of shale sites hosting the deformation associated with compression and shear.

In these cases, the hanging-wall varies in geometry and facies: the units in the Leyre - Orba system are sandstones and limestones, very competent. Subsequently, in the next fault; the Biniés-Javierregay thrust, the hanging-wall is composed by the turbidites of the Hecho Group, generally folded and cleaved. Finally, in the Jaca thrust, the hanging-wall is also composed of the Eocene marls of the Arro Fiscal formation, and no cleavage is observed.

In the case of the footwall, there are fewer differences. In all cases the Eocene shale formations are found: Arro-Fiscal or Pamplona. However, the geometry and local lithological changes are an important factor in controlling the development of cleavage and deformation, and therefore, facilitating its study.

Figure 91 shows a sketch that simplifies some of these geometrical elements: the dip of the main thrust, the occurrence of cleavage in the shaly footwall, and the geometrical relationship with the bedding (painted in green).

The cross-cut relationships between S0 and S1 are variable, but remain interpretable in the Escalar or Sigüés sections. There is a parallelism, or slight obliquity between bedding and cleavage in the areas where there is a footwall syncline. In more distant areas, the S1 and S0 are sub-perpendicular, where the more widely spaced pencil cleavage also appears.

These cleavage relationships are not so well perceived where the bedding is not clearly expressed (in the Biniés section, where there are slump structures within the series) or where the bedding is folded (in the Javierregay section). Although a deformation gradient is observed by comparing the penetrativity of cleavage in the outcrops of a section, it can be confusing in order to have accurate information on shortening.

CHAPTER 3 - STRUCTURAL STUDY OF SIGÜÉS AREA

For all these reasons, the area of Sigüés is the most favourable place to study the gradual evolution of the deformation of the shales, where the state of deformation of the rocks can be observed in a transparent and almost continuous way.

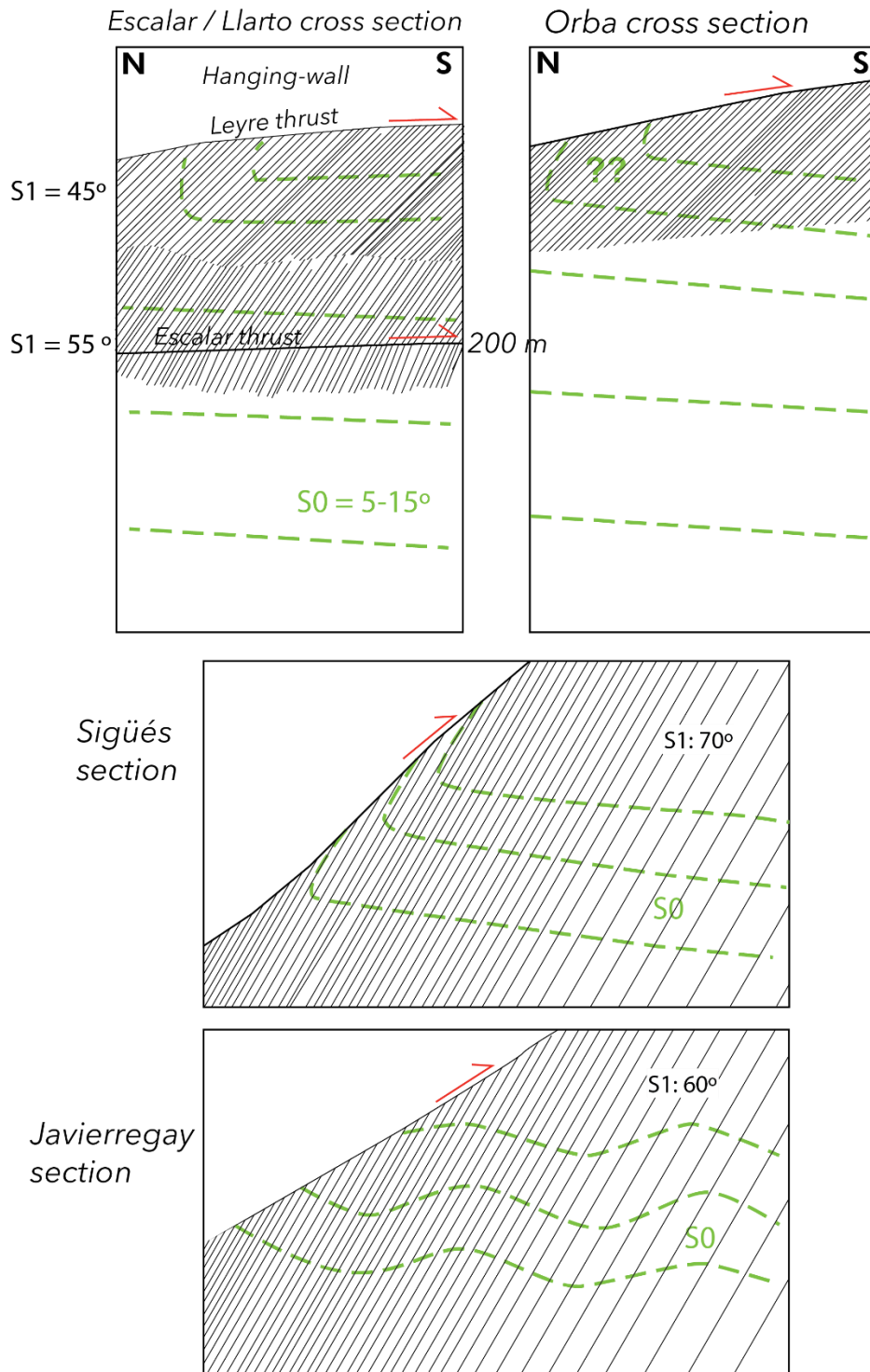


Figure 91: Simplified sketches of the various thrust footwall cleavage/bedding relationships in the transects studied during the PhD field work along the Jaca Basin.

3.4. Structural frame and serial Cross -Sections.

3.4.1. Structural frame and sketch

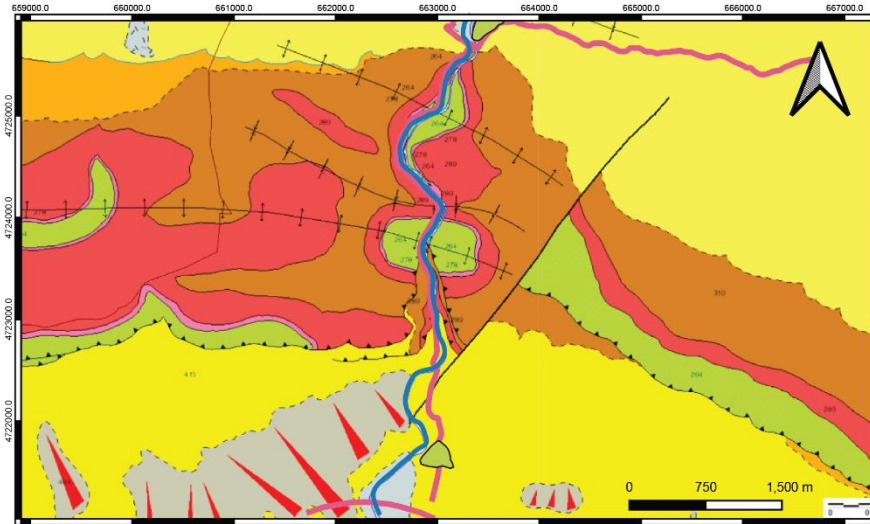
The observations presented throughout this Chapter 3 are summarized in a structural map. The map has at its centre the gorge of the Escá river, which marks the intersection between the Leyre and the Orba ranges. Other sites outside this intersection and presented in the previous section (Leyre, Binies, Javierregay, Jaca) are not represented on this map. More than 90% of the shale sampling for AMS (presented in section 4.3. Sigüés results) and the calcite vein sampling has been carried out in this mapped area. This structural map has been constructed taking into account the three previous maps existing in the area: Magna – Sheet number 175 (de Rojas and Latorre, 1972, IGME), Geode (IGME, 2008) and Puigdefàbregas (1975). These three maps are shown in Figure 92. Following the field work carried out in this thesis, which has included more than 30 working field days, and numerous observations throughout the area framed by the maps, this PhD is proposing some modifications and corrections to the cartographies, as shown in Figure 92.

These are some of the key indications for the interpretation of the structures depicted in Figure 92:

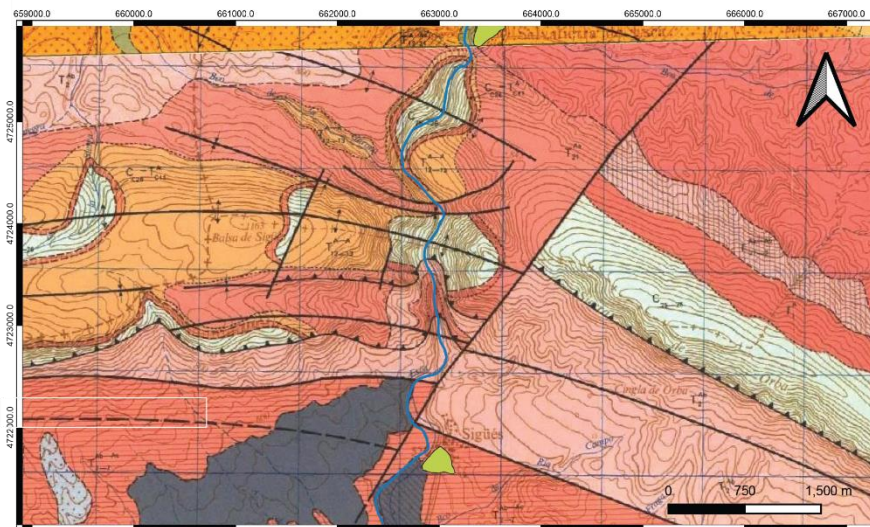
- The Leyre structure and the Orba structure are two independent thrust-fold systems with a different trend, and with no apparent lateral continuity between them. The hanging-wall anticlines of both thrusts have their forelimbs generally eroded as seen on Figure 79. The Leyre hanging-wall anticline can be seen in areas to the W of the Escá river as seen on Figure 76.
- As described before on section 3.2.1. The Sigüés and Leyre Sites., the Leyre thrust sheet evolves from West to East from a relatively simple geometry reflected by the K-Pg units (Marboré Fm, Tremp Fm and Ager Fm) at the W boundary of the area, towards a more complex pattern, with an anticline fold succession in the centre of the map, next to the Escá river gorge.
- The Orba structure is in concordance (and continuity) with the Salvatierra anticline. This fold crops out completely next to the Escá river. East of it, a thrust cuts it (Figure 79) and leaves its southern forelimb eroded, with its northern backlimb outcropping in most of the Orba mountain range.
- Although it has not been sampled, to the N of the Leyre-Illón structure, there appears the lateral transition from marls of the Larrés formation (Puigdefàbregas, 1975) to the turbidites of the Hecho Group (described on section 3.2.1). This area shows decameter-wavelength folds and axial plane cleavage, which is more developed in the vicinity of the Illón range. The penetrativity of the pencil cleavage observed to the N of Salvatierra de Escá increases, evolving towards slaty cleavage near the Illón Thrust.

CHAPTER 3 - STRUCTURAL STUDY OF SIGÜÉS AREA

**GEODE CONTINUOUS
CARTOGRAPHY (IGME)
1:50.000**



**MAGNA CARTOGRAPHY
(IGME)
1:50.000**



**Puigdefábrigas (1975) - JACA
BASIN CARTOGRAPHY
1:50.000**

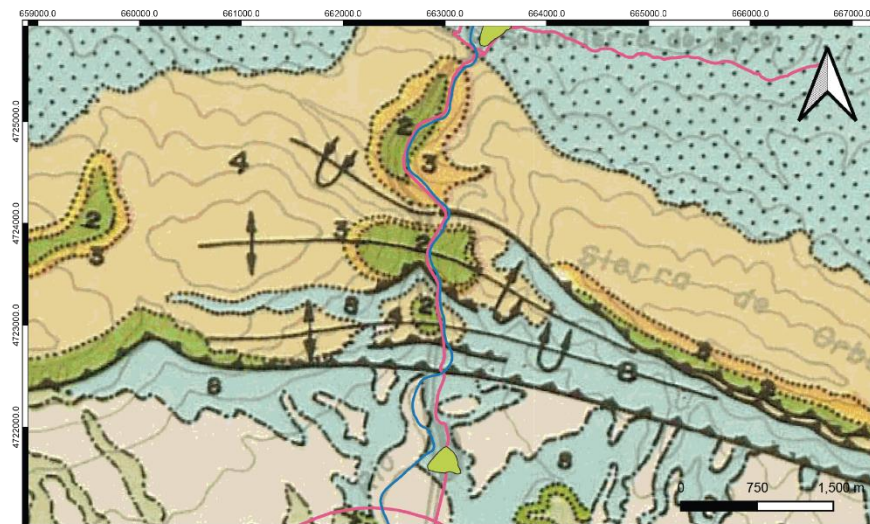


Figure 92: Comparison of three previous maps covering the newly mapped study area presented in Figure 70. The Geode mapping was published in 2008. The Magna cartography is presented by de Rojas and Latorre (1972). The Puigdefábrigas cartography dates from 1975.

CHAPTER 3 - STRUCTURAL STUDY OF SIGÜÉS AREA

Some differences with respect to the maps shown in Figure 92, however, are worth highlighting

- The trace of the frontal Leyre thrust drawn by Puigdefábregas (1975) should be adjusted in the areas near the Sigüés gorge. This trace is difficult to track given the shaly nature of outcrops, as described on 3.2. Also, the “Geode” map (IGME) confuses the Leyre frontal thrust with the one corresponding to the forelimb of the Pop-up anticline (the second structure found in the south-north profile). The frontal and pop-up forethrust are well mapped in Magna by de Rojas and Latorre (1972).
- In the same way, none of the previous cartographies establishes a continuous relationship between the Salvatierra anticline and the Orba range. This Salvatierra anticline is not depicted in Puigdefábregas (1975) cartography.
- On the other hand, the Geode and MAGNA maps shows a long subvertical fault, striking N030, which crosses the study area, in continuity with the Ruesta fault, which crops out to the south of the Aragón River in the Canal de Berdún area (Turner, 1990). According to this mapping, this fault would abruptly separate the Orba from the Leyre structure.

In the map in Figure 93 this Ruesta fault is included, since it is observed in the Quaternary fluvial terraces corresponding to the Escá river and the Aragón river in the southern sector. The fault trace is rectilinear, and is probably related to a deformational episode much younger than the rest of the Leyre unit, which is the focus of our study. According to our interpretation (in agreement with Carbonel et al., 2019) the Ruesta fault does not affect the hanging-wall of the Leyre-Orba thrusts, and therefore it cannot be drawn in the Orba mountain range, maintaining our interpretation of the W sector of the Orba structure.

Figure 93 includes several stereoplots that show the compilation of field-measured orientations for S0 and S1 in the Eocene units. On the northern margin, measurements correspond to the Hecho Group outcrops (Figure 73 and stereoplots on S1 on Figure 93). The average for all measurements in this sector indicates an overall dip of about 20° to the N, and a fold with an approximate N100 axis. The S1 generally dips more than 50°, and is sub-parallel to the axial planes of the folds in the turbidites.

In the southern part, in the Eocene shales (Pamplona and Larrés Fm.) there is a general shallow of the bedding dips to the S (between 5 and 15°) although locally there may be sub-horizontal or shallow northward dips. This also indicates very gentle folds with strike N100 as seen in Figure 80 in section 3.3.1 South-western sector: Escó and Llarto

The plots of S1 are divided into three sectors on the southern footwall, as there are numerous measurements with a certain variability. In general, the strike of S1 can vary but on average it is sub-parallel to the fold axes, and to the prevailing structural direction in each sector. This is especially evident in the footwall of the Orba range where the Pyrenean N110 direction is better defined, whereas in the central area, in Sigüés, the average strike of foliation planes is subparallel to the trend of the Leyre Range (N090).

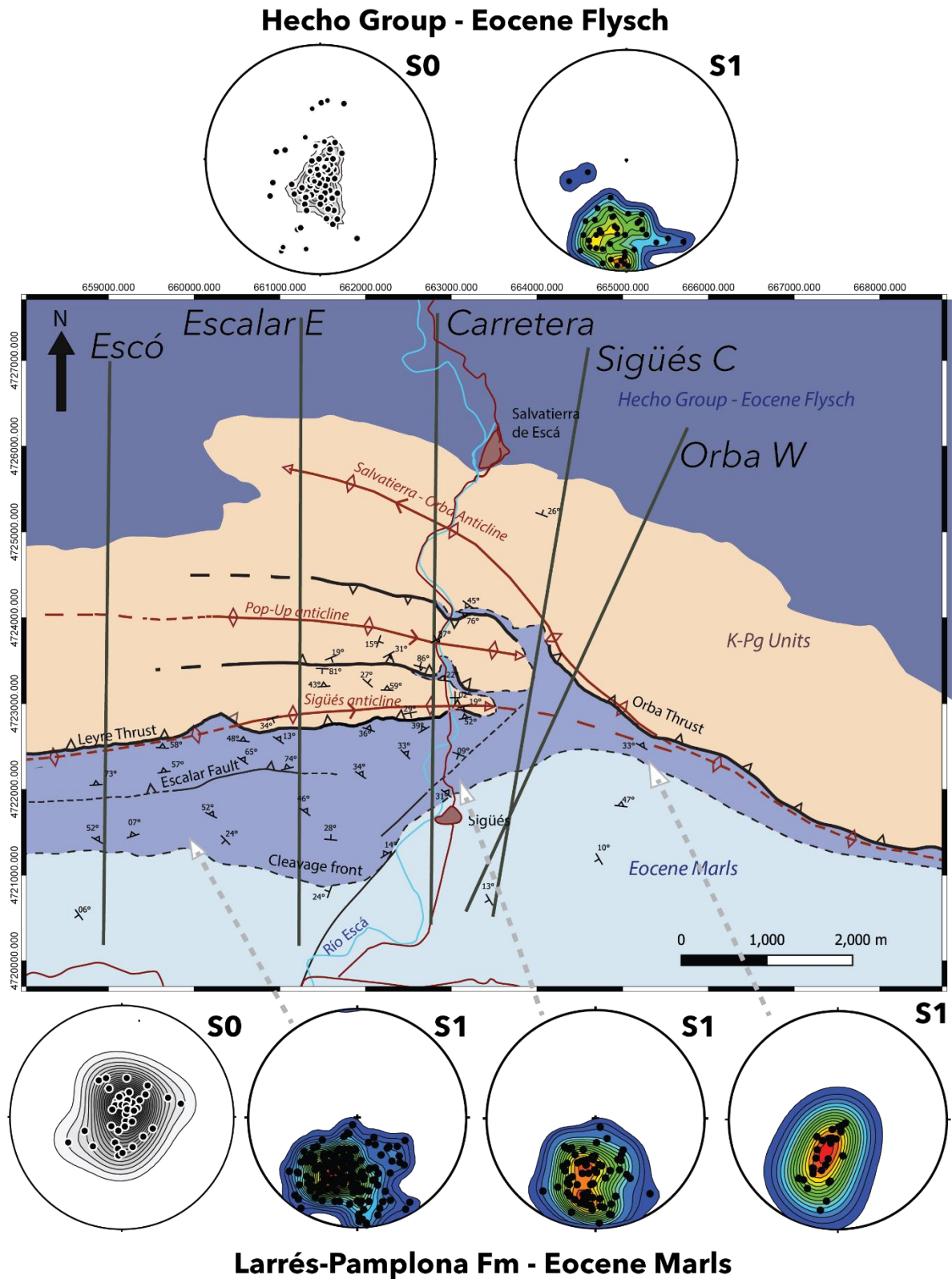


Figure 93: Structural sketch for the Sigüés Area. Stereoplots are shown for the Hecho group, on the N margin of the Leyre range, and for the Eocene marls (Larrés and Pamplona Fm) on the southern footwall. Attached to the Leyre and Orba thrusts, the area where clear pencil cleavage has been observed in the shale outcrops, is painted in dark blue and delimited as “cleavage front”.

CHAPTER 3 - STRUCTURAL STUDY OF SIGÜÉS AREA

Macroscopic cleavage is more extensively found in the footwall of the Leyre frontal thrust, up to more than 1 km horizontal distance from the fault trace (Figure 93). This zone is narrower in the shale outcrops at the footwall of the Orba thrust. The precise extent of the cleavage front could be disputed as the observation of cleavage in outcrops can be challenging, considering the natural fracturing of the shales and its possible confusion with pencil cleavage.

It is also possible to find cleavage in the shales in the outcrops next to the Pop-up anticline. Some of these outcrops correspond to the shale-rich turbidite levels overlying the Ager Fm, i.e. they would be located in the hanging-wall of the Leyre thrust as seen in Figure 77. The cleavage in this area is parallel to the two thrusts that delimit the Pop-up. In the forethrust, the cleavage dips to the N, but in the backthrust, conversely, the cleavage dips to the S (Figure 79).

In the absence of exposures of the Leyre and Orba frontal thrusts, as described in section 3.2.1. The Sigüés and Leyre Sites., only one key point remains: a fault outcrop next to the Leyre frontal anticline, to the N of the town of Sigüés.

At this site, the forelimb of the frontal anticline of the Leyre unit thrusting over intensely sheared turbidites of the Hecho Group is observed. Geometrically, strata of the Hecho group, which correspond to the hanging-wall, show subvertical bedding in the sheared forelimb, but the propagation of the fault plane towards this forelimb, would cause it to be thrust over as shown in Figure 94. With a thickness between 2 and 3 m, a fault gouge that incorporates blocks of the Ager limestones of the hanging-wall into the intensely foliated turbidites of the foot wall can be distinguished. Two lineations are observed in the fault plane, which would indicate two episodes of movement with an overall top-to-the-south direction.

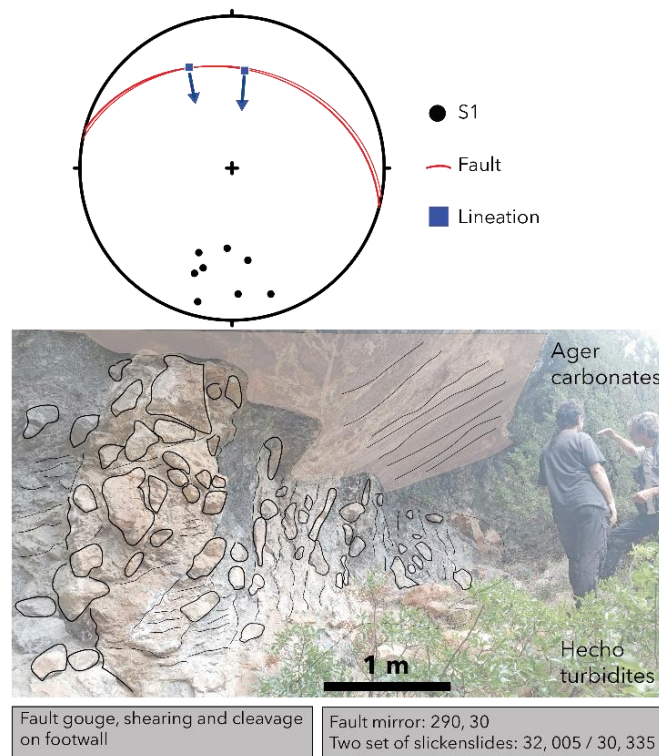


Figure 94: Leyre frontal thrust outcrop on the Sigüés gorge.

3.4.2. Serial cross-sections

Based on the structural data collected in the field, and the geological maps, a number of cross-sections were drawn to define the geometry of the Leyre Unit. The orientation data collected at surface, along with the field photographs, panoramic views, and drone pictures enable us to propose these cross-sections. Furthermore, the differential erosion of the Ager and Marboré formations (which are much more resistant) allows to interpret the conformable landscape in accordance with the structure.

Nevertheless, it must be taken into account that some key locations are covered by a dense vegetation canopy, and that the geology below it is not visible. One crucial point is the western termination of the Orba thrust trace, where the Pop-Up anticline is plunging east at the end of its eastern trace. Additionally, the geometrical evolution of the pop-up to the west, in the hanging-wall of the Leyre thrust, appears to be rapidly changing. Consequently, in the western margin of the map, these folds lose amplitude or die out completely.

The previously existing cross-sections (Figure 67 with Boiron et al., 2020; Izquierdo-Llavall et al., 2013a; Labaume et al., 1985a) run along the gorge of the river Escá. In this work the geometrical analysis of the structure has been extended towards the East and West of that cross-sections. Consequently, four parallel cross-sections are here presented, called, from West to East, Escó Escalar E, Carretera (whose trace coincides with cross-sections of the above-mentioned previous studies), and Orba. The first three cross-sections cut across the Leyre structure and the fourth one traverses the Sierra de Orba thrust.

To interpret at depth the Leyre structure we have kept the two possible end-member interpretations, that can be summarized as follows:

- The single sheet geometry, in which there is an only major thrust and footwall ramp and several minor thrusts planes (both forethrusts and backthrust). It probably results from the rupture of the hanging-wall. In this model the uplift of the whole structure is closely related to basement deformation (see also Izquierdo-Llavall et al., 2013a)
- The two-sheet geometry, in which two superimposed thrust sheets, according to a thin-skin model, are responsible for the uplift of the whole structure, although some contribution from basement deformation must also exist (see Boiron et al., 2020; Labaume et al., 1985)

The cross-sections, whichever the chosen model, have to fulfil a series of conditions, some of them common to consistently balanced cross-section (see e.g., Dahlstrom, 1969; Judge and Allmendinger, 2011; Lopez-Mir, 2019; Woodward et al., 1989):

- the location of structures and the dips measured in the field (either as individual dips or as envelopes in the case of short-wavelength folding) must correspond with those in the cross-sections. The calculation of the envelope for a series of folds can also have a dose of interpretation, but it is extremely important in order to locate the hinge zone and axial surfaces of long-wavelength folds.
- a consistency must exist both in terms of geometry and shortening, of the different along-strike geometrical reconstructions. In spite of not presenting a thorough 3D reconstruction, provisional 3D models were done in this work to check this consistency (see, e.g. Egan et al., 1997).

CHAPTER 3 - STRUCTURAL STUDY OF SIGÜÉS AREA

- In each cross-section, shortening and line-length must be consistent. This is critical when considering thrust systems where there are different *décollements*. The line-length balancing must be as “natural” as possible to avoid ad-hoc solutions. Area compensation for detachment levels is not so critical because lateral migration along structures is also probably to occur in this area.
- Internal deformation (analysed in different chapters of this work) must be consistent with the assumed transport directions and the particular structures at each point.
- The different cross-sections must be kinematically feasible, also taking into account the regional deformation frame.

The field data collected in this PhD allow the reconstruction of structural cross-sections, in which surface data fit the two end-members. Particularly, the observation of the structure in the Escá river gorge does not compromise either of the two models, since the imbrication between the thrusts would be a few hundred metres below the present topography.

Cross-sections have been constructed according to the two geometries, with the same surface data, except for the unknown inclination of the frontal thrust and the pop-up forethrust. Precisely, it is difficult to provide reliable data for these key structures, since for both structures, only one outcrop has been visited where to directly measure their attitude.

All data on bedding and cleavage orientations measured during the fieldwork of this PhD are provided in annexed documents.¹

¹ Supplementary Material

One-flat geometry

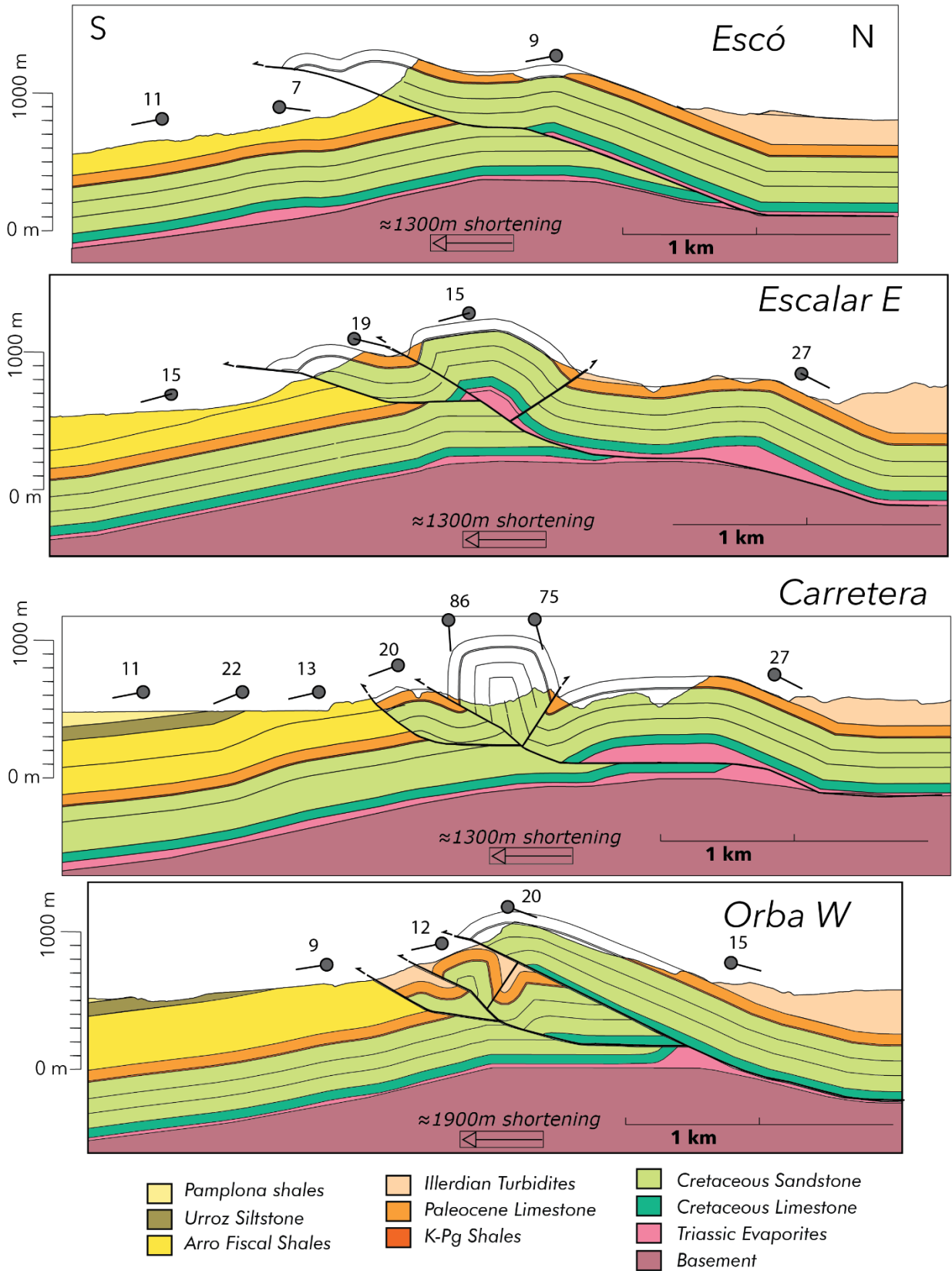


Figure 95: Single sheet geometry cross-sections. Traces on map of Figure 93.

Two-flat geometry

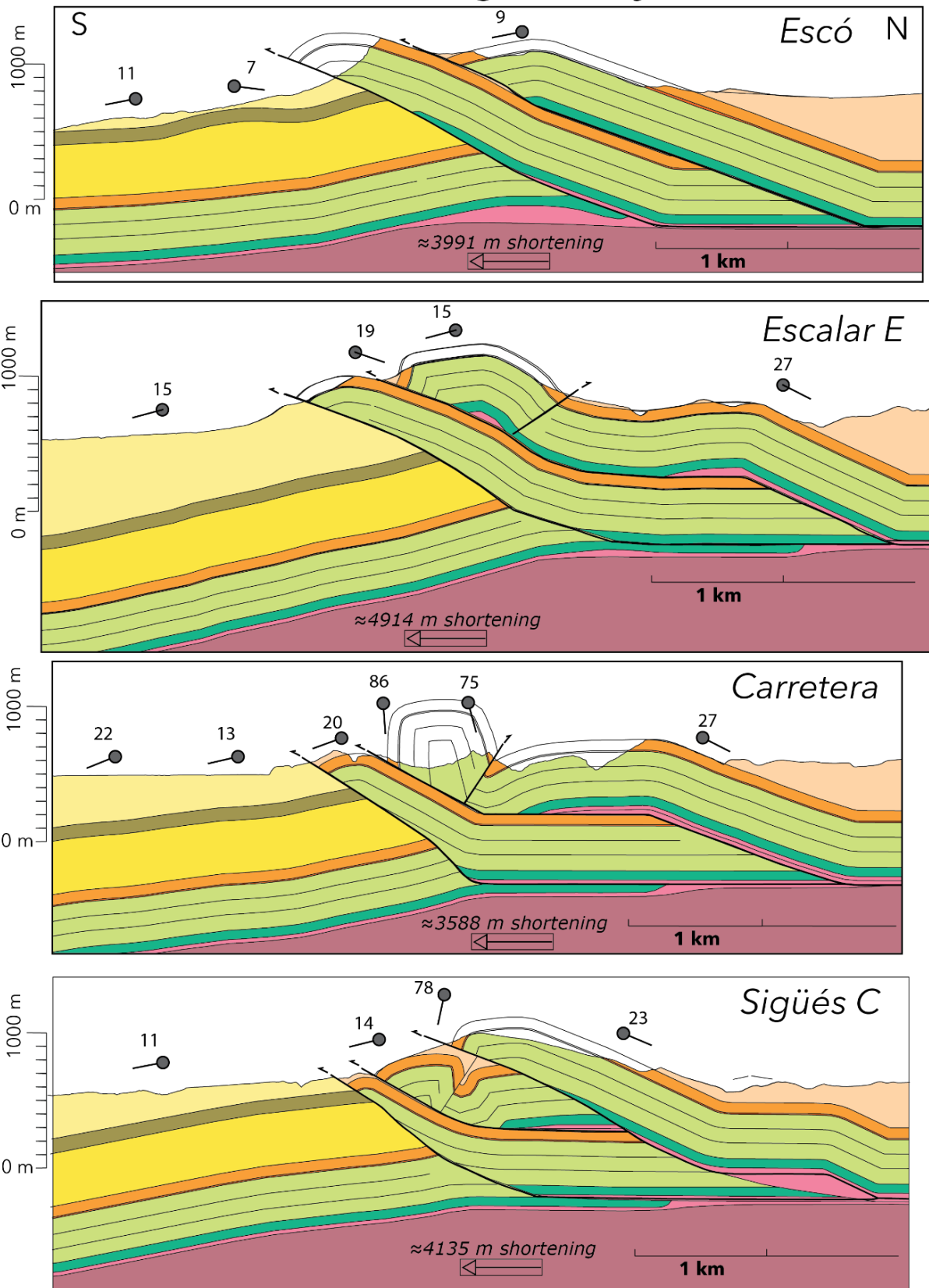


Figure 96: Double sheet geometry cross-sections. Traces on map of Figure 93.

CHAPTER 3 - STRUCTURAL STUDY OF SIGÜÉS AREA

Here some key structures and the implications that they have it has on their geometry changes along-strike, as well as their interpretation according to the two proposed models are described:

- The Leyre frontal thrust shows a shallow dip in the observed exposures (Escalar anticline in Figure 75). Besides, this is generally interpreted according to the attitude of bedding of the units in its hanging-wall, which varies from 10 to 20° N (Plateau section in Figure 75, Escalar hanging-wall data). It appears that this thrust involves the Ager Fm and part of the Marboré Fm in its hanging-wall anticline. A shaly layer within the Marboré sandstones or just the bedding planes could act as a local detachment, as observed for example, in outcrops along the Aragon river. Farther N, as it gains depth, this thrust would also involve the whole Cretaceous series, finally rooting in the Triassic (as drawn in all cross-sections of Figure 95 and Figure 96). According to the single sheet model, the Leyre frontal thrust would have a hanging-wall flat geometry in the Calcaire des Canyons Fm that changes to a ramp and a very low-angle ramp in the Marboré Sandstone, and a similar pattern can be interpreted in the double-sheet model, although in this case the low-angle ramp also involves the Canyon Limestones. The main difference between the two models in the case of the Leyre thrust is that in the single sheet model there are two horizontal segments linked by the 30°N panel whereas in the two-sheet model the frontal ramp shows a rather homogeneous dip.
- To the east, the hanging-wall of the Leyre thrust plunges to the east, and descends progressively dying out in the Larrés shales north of Sigüés. Therefore, the Leyre frontal thrust geometry is more difficult to define east of the Escá river.
- The spectacular pop-up cut by the Escá river shows varying geometries along strike:
 - In general, from west to east, the hanging-wall of the Leyre thrust is progressively retreating towards the north. In the Escó and Escalar sections, the anticline is gentle and its backthrust has very little displacement. Consequently, the Calcaire des Canyons are interpreted to be within the core of the anticline. Conversely, in the Escá river gorge, the anticline is almost 600 m in amplitude, and its two limbs are thrusting up the rest of the Leyre hanging-wall unit.
 - In these sections, the core of the Pop-up must be the Marboré sandstone, since there is no room for the Calcaire des Canyons. If the double thrust-sheet model is considered, the forethrust of the Pop-up would correspond to the upper thrust of the double sheet system. The backthrust and the subvertical limbs of the fold would grow progressively and are tightened to the E as in the other situation.
 - The main difference between the two possible structural geometries is to consider this Pop-up anticline as belonging to a thrust sheet different from the frontal thrust sheet (in the double-sheet model), or as forming part of the same sheet, as occurring in the simple sheet model. This has implications for the deep geometry and for the displacement of the second thrust of the system. Disgracefully, field data do not allow to distinguish between a slightly thrust syncline (Escarlar cross-section, simple sheet geometry) and a thrust with kilometer-scale displacement because the same unit is found in

CHAPTER 3 - STRUCTURAL STUDY OF SIGÜÉS AREA

the hangingwall and the footwall (Escalar cross-section, double sheet geometry).

- The Salvatierra anticline appears in the northern half of the map and in the cross-sections (Escalar E, Carretera). The Escó cross-section does not include it, since its periclinal termination would occur to the W of this section trace. The Escalar E cross-section finds a frontal anticline with a very open geometry. The trend of the Salvatierra anticline is N110 and shows gentle dips at its limbs, except at the contact with the backthrust limiting to the south the Pop-up. In the Carretera cross-section, limbs with a dip $>25^\circ$ are interpreted. Finally, at some point between the Escá river and the Sigüés C cross-section, the anticline is faulted at its hinge, showing in fact two hinges. The backlimb (northern limb of the anticline) is interpreted to coincide with the footwall ramp of the second thrust in the case of the double-thrust model (that would show a similar dip according to the template constraint), and can be related with a décollement from the basement in the case of the single-sheet model. However, in the Carretera cross-section a certain backlimb-ramp association can also be considered because an extra length of the Canyons Limestones is necessary at the core of the anticline for length balancing the cross-section.
- In the Orba range cross-section (Orba W or Sigues C) the backlimb of the Salvatierra anticline corresponds to the main body of the range, with a partially eroded forelimb in its hanging-wall anticline. To the E, this thrust progressively advances over the rest of the structures of the Leyre range, which are thrust over (and probably tightened) by this thrust sheet, and the shaly outcrops of the footwall as described before.

The geometry is quite simple in its hanging-wall: a single thrust sheet in which the Orba thrust would dip $5-10^\circ$ more at surface, including all the Paleocene-Cretaceous formations involved in the Salvatierra anticline. A hanging-wall anticline is also formed, with punctual outcrops of its forelimb appearing very occasionally next to the Eastern termination of the Orba thrust trace. In order to make room for the Paleocene-Cretaceous units, up to the Triassic in the two-sheet geometry, the Orba forethrust or pop-up forethrust would have to dip $>30^\circ$

Note that in the two models the general structure of the Leyre unit, which includes the frontal anticline of Leyre and the Pop-up anticline, plunges to the E and is over-thrust by the Orba unit (Figure 95 and Figure 96). The Calcaires des Canyons Fm does not crop out neither in the Orba nor in the Leyre frontal thrust, and the same happens in the case of the Triassic. While drawing the thrust traces, the Triassic evaporites is in both models the main detachment, showing lateral thickness changes. On the other hand, the Calcaires des Canyons Fm. needs to be compensated in cross-sections shortenings. It is not involved in the shallowest part the frontal thrusts, as can be assessed from surface data. As a result, the Cretaceous Limestone is assumed to be “captured” beneath the faults and overlying folds in the footwall unit as seen in most of the cross-sections.

3.4.3 Structural synthesis

The general structural characteristics for the Leyre mountain range have been presented along with the local cross-sections of Figure 95 and Figure 96. As has been said, the most

CHAPTER 3 - STRUCTURAL STUDY OF SIGÜÉS AREA

direct surface observations cannot be used to promote exclusively one of the two geometrical models. In fact, most of the structural features of this area are taken into account in both models. For example, the along-strike changes, the formation of the pop-up backthrust, or the out-of-sequence overthrusting of the Orba range fit in both models.

In this chapter, however, one of the two geometries will be prioritised so that it can be used in the rest of the thesis, to integrate other results and for the general discussion.

In first instance, the overall accumulated shortening is summed up for the set of structures in the presented cross-sections. For the one-flat thrust model, shortenings obtained range between 1300 m (for the Carretera section) and 1900 m (for the Orba W section). While for the two-flat model, shortenings range between ~3.5 km (for the Escó section) and ~5.0 km (for the Sigüés C section).

The proximity of the Illón structure (as we have seen in Figure 71), which has a two-flat geometry architecture (cross-section from Labaume and Séguret, 1985), suggests that the Leyre unit could have been built in a similar way. The way in which the Pop-up structure thrusts over the frontal anticline in the Escá gorge may suggest that double-sheet model can be applied to this unit as well.

Nevertheless, the lateral evolution of the Pop-up to the west, where the two limbs are reduced and arranged sub-horizontally, suggests that this structure is not completely allochthonous in relation to the frontal anticline. In fact, the western end of the map in Figure 93, corresponds to the plateau sector (Figure 75), and suggests that the backlimb of the Leyre frontal anticline is only a homogeneously-dipping limestone panel, without detecting significant tectonic discontinuities.

In addition, the geometry with two flats (double thrust sheet) requires a large slip on the front fault to ensure the restitution of the cross-sections. This means that the Urroz Siltstone located below the Pamplona shales, should always be at the surface. Although it is not included in the structural sketch, this observation does not agree with Puigdefábregas (1975) mapping and field observations at the foot of the Orba range, where the Larrés Marls (lateral equivalent to the Arro-Fiscal Fm) are actually found at surface.

Furthermore, the geometry of the Leyre frontal thrust in the Escó and Escalar E cross-sections corresponds to the subhorizontal dip that has been observed in the southern cliffs of the Leyre mountain range (Figure 75). Here, the units of the hanging-wall define a hanging-wall anticline thrusting over the Eocene shales.

Regarding the feasible kinematics, as it has been previously stated there is not a strong difference between the two models, and the late, out-of-sequence emplacement of the Orba range must be considered in both cases. In the case of the single-sheet model, deformation of the hanging-wall in break-back sequence seems more feasible and would explain the tightening of some structures as for example the Pop-up or the frontal limb of the Salvatierra anticline. In this model this also fits well with the detachment of the Mesozoic-Cenozoic cover in the northernmost sector of the structure. However, a normal piggyback sequence is not incompatible with the development of the structure according to this model. In this case, tightening of structures could be related to changes in inclination of the footwall ramp during the advance of the single thrust sheet.

CHAPTER 3 - STRUCTURAL STUDY OF SIGÜÉS AREA

In the case of the two-sheet model, a piggyback sequence for the two thrusts defining the Leyre structure seems easier to adapt to the geometrical features in the two westernmost cross-sections. However, the Carretera cross-section is more compatible with a break-back sequence, with the Pop-up structure developing on top of the underlying thrust sheet, after the blocking of the movement on this one. This favours the break-back interpretation for the whole of the Leyre structure also for this model.

In summary, these observations have led us to decide in favour of the one-thrust geometrical option, which is the one that will be presented in the subsequent structural representations for the study area. Besides, after the incorporation of data on the analysis of the footwall shale fabrics (section 4.3. Sigüés results), or on the calcite veins (section 5.3 Calcite-filled faults), they will allow us to refine in detail the structural history of the Leyre frontal fault.

To conclude, and to inscribe the local cross-sections into its regional frame, a general cross-section is presented in Figure 97. Its trace extends beyond the main study area. It begins to the N of the Illón Range and it includes, to the south, the norther margin of the Guarga synclinorium (molasse basin), with the Bagüés Syncline (Figure 97) . The aim of this cross-section is to contextualize the local cross-sections on Figure 95 and Figure 96. For this reason, data from other maps and field information made by colleagues at the University of Pau and the University of Zaragoza (Aubourg, pers. comm.; Sierra-Campos, pers. comm) are incorporated in this cross-section.

The Illón unit, the twin structure north of the Leyre Unit, has been observed at surface (Figure 71) and together with the IGME map (143 Magna 2nd series sheet by de Rojas and Latorre, 1972), and adapting the cross-section that appears in Labaume et al. (1985), this structure has been drawn. It is also composed of a series of thrusts and folds involving the same units as the Leyre Unit (Paleocene to Cretaceous Fms, with local Cretaceous detachment, and an interpreted main Triassic detachment for the whole structure. A slightly different geometry with two thrust sheets outcropping on the forelimb can be interpreted in this case, as well as higher shortening associated with thrusts than in the case of the Leyre thrusts.

In the Aragón Valley, to the S of the study area, bedding measurements (Pablo Sierra and Juan Cruz Larrasoña, pers. comm.) indicate that despite the apparent monotonous homogeneity of the Larrés marls, deca- to hectometer scale folds may appear, and in general the dip of the S0 increases towards the S, from 10° in the central Aragón Valley to 45° next to the contact with the overlying (mostly continental) Upper Eocene-Oligocene units.

Finally, regarding the Bagüés syncline, we have defined it from only cartographic and aerial photo observations, which have allowed us to interpret its overall geometry towards its hinge, where this cross-section approximately ends.

From the presented cross-section (Figure 97) a strong difference in the level of the basement (at least 2.5 km) is inferred. This strong structural difference must be related to a south-verging basement thrust that can be related to the Guarga thrust defined farther east (Teixell, 1998). This thrust is in last instance the responsible for the configuration of the whole structure and the final emplacement and uplift of the Leyre and Illón systems.

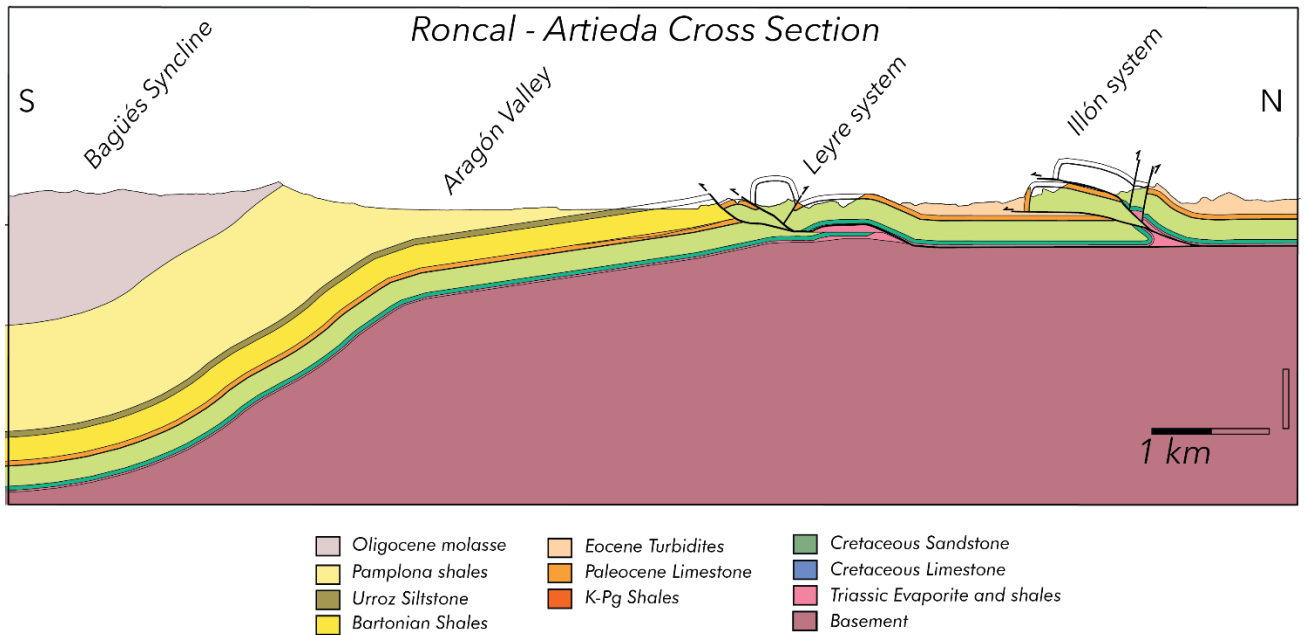


Figure 97: Regional cross-section, from Roncal Valley (Escá River) to Guarga sinclorium, at the Bagüés Anticline. See trace in the map (with Geological cartography from GEODE-IGME), which is parallel to the Carretera cross-section.

3.5. Conclusions

The river Escá is the geographical intersection between two structures of regional importance: the Leyre thrust and the Orba thrust (each with their respective mountainous reliefs). The previous mapping shows the difference in strike, but in this chapter we have emphasised the complexity of this link between two thrusts that have a different position in the sequence of thrusts in the Jaca basin.

Similarly, the appearance of the pop-up fold in the hanging-wall of the Leyre thrust is noteworthy. A fold that a few kilometres to the east disappears into the hanging-wall ramp. The along-strike changes in this structure are profound, and can be interpreted as heterogeneous kinematics for the same thrust ramp.

The characterization of the deformation in the Larrés Fm and Pamplona Fm has allowed us to visit numerous outcrops and to describe shale-on-shale faults and gradients. The visit to these sites reveals features not revealed by previous mapping. These will also be described in detail and from the sampling data in Chapters 4 and 5.

4. SHALE FABRIC

4.1 Background

In this chapter we will mainly refer to the study of samples from the Larrés Formation, Eocene marls/shales, marine fraction of the molassic Jaca Basin. As described in previous chapters, the Larrés Formation is given other names in the literature (Arro-Fiscal Formation) or can be confused in the field with the overlying marly Pamplona Formation. For this reason, the term Eocene Marls/Shales will also be used, as adopted by some other authors (Pueyo-Anchuela, 2012b).

Bibliographical references related to this issue have been previously described in chapter 2.5 The Southern Pyrenees, a natural laboratory of magnetic fabric in shales and slates. In this chapter of results of this thesis, we will start by re-presenting briefly these published data, to which we will also add those obtained after the new samplings presented in this work.

4.1.1 Shale mineralogy

Several observations on the lithology of the Eocene Marls can be found in the literature:

Pueyo-Anchuela et al. (2011) described the "homogeneous outcrops" sampled at Berdún, Biniés and Javierregay, with parallel laminations that the authors attribute to sedimentary processes. "Processes of activity during sedimentation detected by changes in thickness, onlap geometries, or folds with high ductility" are described within the Eocene marls.

Boiron et al. (2020) estimate that clays vary between 15-33% of the mineral content, quartz between 29-37% and calcite between 30-50%.

Bauluz et al. (2008) carried out several microscopic studies (SEM, XRD optical microscopy) and found lithological composition for the Hecho Group: 40-60% calcite, 15-40% quartz, 10-40% phyllosilicates and <5% for albite and dolomite (to the N of the study area). It is also noted that the phyllosilicates are $\approx 70\%$ illite and $\approx 30\%$ chlorite, with no differences between sandstones and marls in the Flysch.

Izquierdo-Llavall et al. (2013) sampled in the Sigüés area and reported an illite/smectite ratio of $\sim 90\%$ after XRD data in I-S mixed layers.

In some of these papers, by studying the susceptibility signal or magnetic remanence of these rocks, analyses on rock magnetism and magnetic mineralogy were done. The authors assume the very dominant paramagnetic behaviour of the signal measured in the Eocene marls.

Bulk susceptibility values range from 100 to 200 μSI according to Pueyo-Anchuela et al. (2011). There is no correlation of susceptibility and anisotropy values (Figure 98b). Susceptibility measurements in LF and HF alternating fields show values consistent with a high paramagnetic component, between 80 and 98% (Figure 98a).

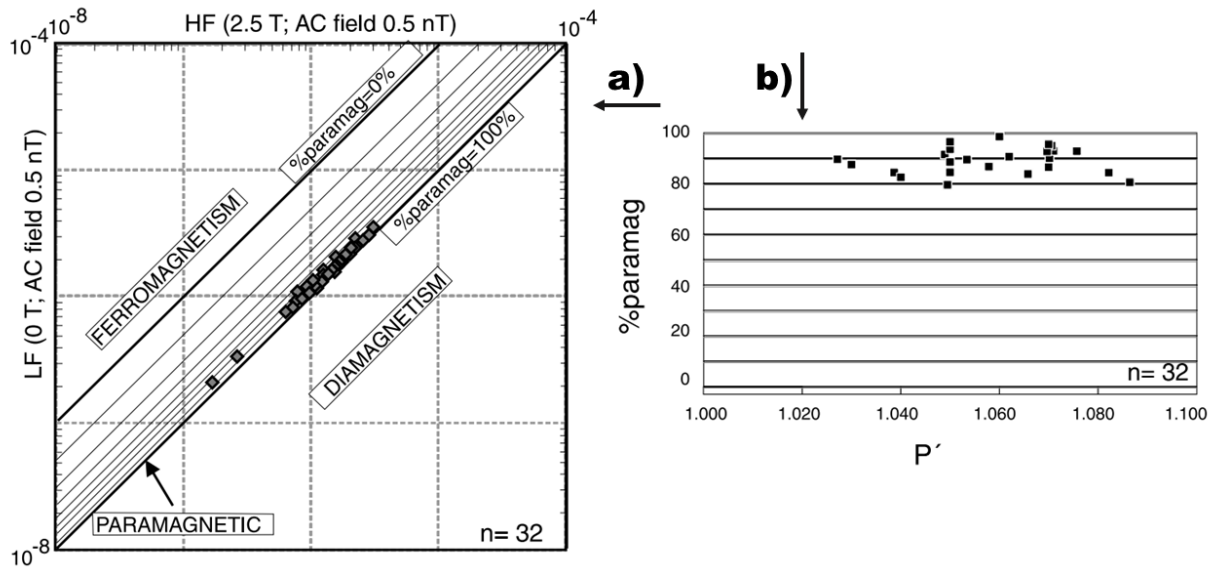


Figure 98: Rock magnetism measurements on Eocene Marls (Larrés Fm) that allow to check the strongly paramagnetic behavior that dominates this unit. On the left, a) is the projection of the measured HF-LF samples. On the right, b), there is no correlation between the magnetic behaviour and the corrected anisotropy P' . From Pueyo-Anchuela et al. (2011)

Hysteresis cycle analyses presented by Boiron et al. (2020) also indicate a dominant paramagnetic signal (Figure 99), which together with X-ray diffraction results indicate a dominance of illite, over a very secondary content of biotites and chlorites. This result coincides with the previously mentioned works.

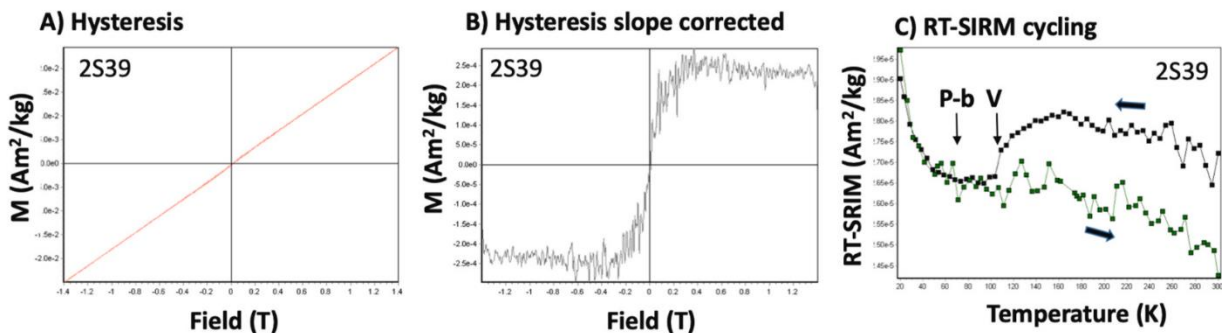


Figure 99: Hysteresis cycles and RT-SIRM cycling from Boiron et al., (2020).

Several authors (Boiron et al., 2020; Pueyo-Anchuela et al., 2013b, 2011b) also discuss the presence of a ferromagnetic s.l. phase detected by its remanence. Boiron et al. (2020) observed a Verwey transition at 120K thanks to RT-SIRM cycling curve (Figure 99C) corresponding to stoichiometric magnetite, although its contribution to the bulk fabric is not substantial. Pueyo-Anchuela et al. (2011b) by using IRM found a ferromagnetic phase related to MD magnetite and iron sulphides, but which does not control the AMS. In fact, they found that this signal does not control the directional patterns of the bulk RT-AMS magnetic fabric, and they finally used the remanence anisotropy (AARM) to highlight this ferromagnetic sub-fabric.

All these rock magnetism results, which can be summarized by a very low ferromagnetic contribution and the presence of stoichiometric magnetite, are consistent with the magnetic diagenesis model proposed by Aubourg et al. (2019).

4.1.2 Shale magnetic fabric.

Various authors (Boiron et al., 2020; Pueyo-Anchuela, 2012a; Saur et al., 2021) have targeted the 2 km segment immediately South of the Leyre thrust, in its outcrop at Sigüés. Boiron et al. (2020) obtained up to 281 samples from 37 sites, with the following results.

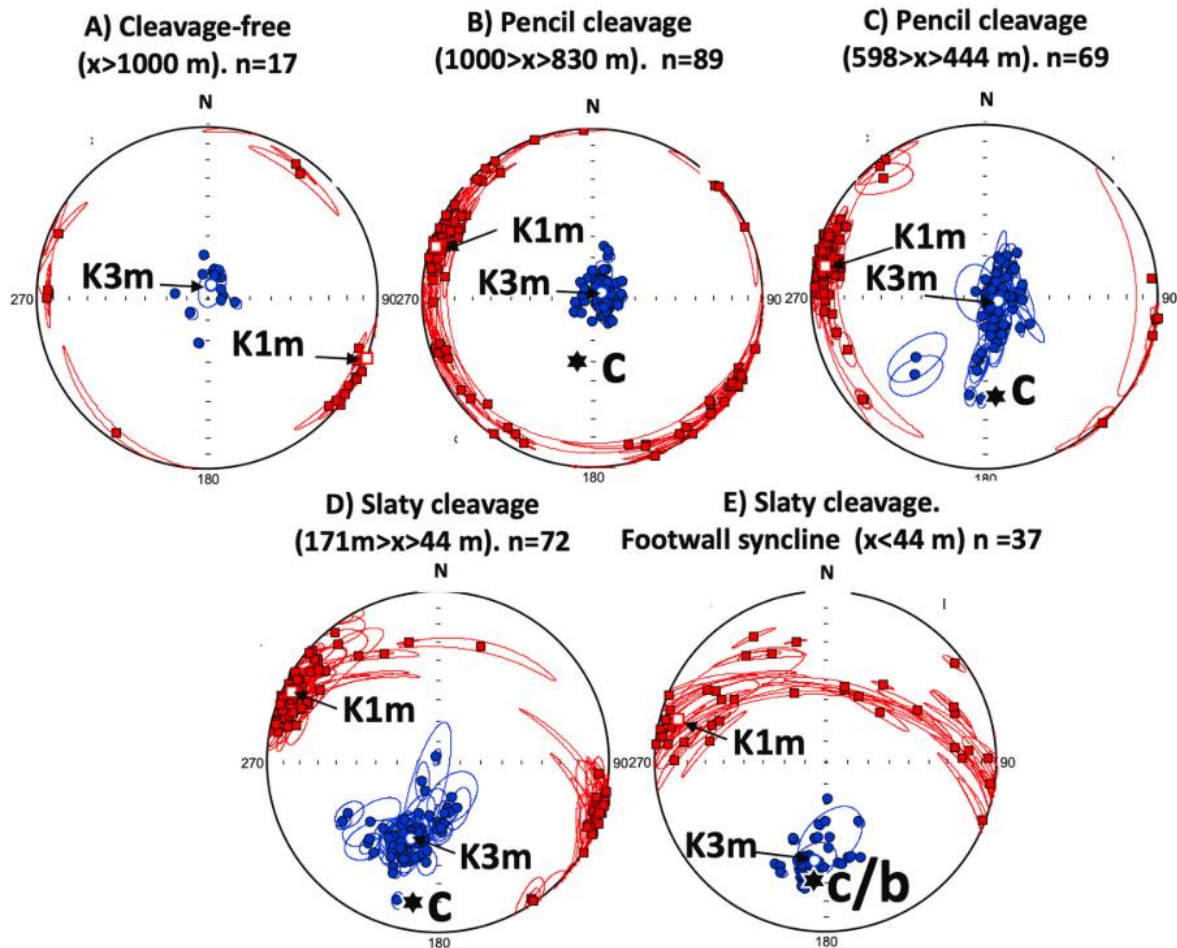


Figure 100: AMS K1 and K3 axes for five stages in the Leyre frontal thrust footwall; from Boiron et al. (2020). X refers to the distance of the emergent Leyre thrust ($x=0$). Note that confidence ellipse at 95% of every samples is represented.

To our knowledge, these authors were the first to draw confidence ellipses for each sample (Figure 100). This information, which was generally provided in the very first versions of the measurement acquisition programme (Agico), could not be visualised in the very latest versions of the Anisoft software. This shows the lack of interest of the community in this scalar quantity. In fact, it is common practice to take a tensor mean and draw the 95% confidence ellipse. However, this results in a loss of information for each sample, information which, as we shall see, is of interest when the fabric is intermediate between stratification and cleavage.

- The AMS show K1 axes with some dispersion, although the average of its axes is aligned with the main structural direction (N110). Meanwhile, K3 is parallel to S0 in the southernmost part of the section. In closer positions it starts to rotate, distributed in a girdle-shaped pattern in intermediate positions between S1 and

CHAPTER 4 - SHALE FABRIC

S₀, and in the final meters (closer to the Leyre thrust) it is parallel to S₁. It is interesting to see the evolution of the confidence ellipse for each sample. Between cases B and C in Figure 100, we can observe a perceptible elongation of the ellipse in the K₂-K₃ plane, or along the dispersion girland of K₃ axes. This means that a single sample can provide this information, provided that its confidence ellipse is taken into account. In the area of slaty cleavage (Figure 100D), the K₃ axes are located on average between the bedding pole and the cleavage pole.

- A graph is also presented in which the P_j (Corrected degree of anisotropy) and T (shape parameter) data are plotted with respect to the distance to main thrust (Figure 101). Finally, given the fabric conditions (paramagnetic particles carrying the signal), a finite strain calculation is proposed from March's rigid rotation model (see 2.3.7 AMS as a strain gauge, conditions of use. of this thesis, Figure 31 from Humbert et al., 2018). Thus, the axes of the magnetic ellipsoid are used to calculate the shortening (also plotted in Figure 101). To our knowledge, this is the first successful attempt to quantify deformation in marls.

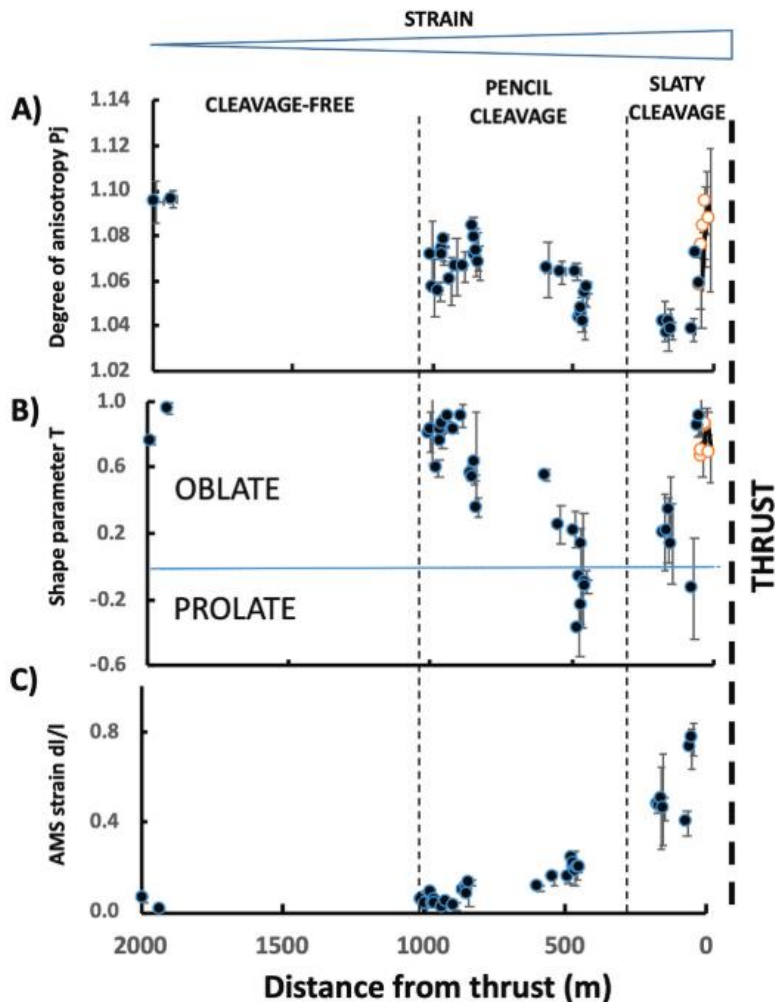


Figure 101: Lateral evolution of scalar parameters (P_j and T) of the magnetic fabric of the Larrés and Pamplona Fm shales. Below, the shortening calculated from the same fabrics (dl/l) is shown. From Boiron et al. (2020). The empty circles correspond to AMS data where S₁ and S₀ are parallel, in the footwall syncline. Note the general decrease in the P parameter up to about a hundred metres from the Leyre Thrust. This development, which contradicts the observation of increasing deformation, is the result of increased competition between two, almost perpendicular, planes: bedding and cleavage.

4.1.3 X Ray Microtomography observations.

Saur's (2022) PhD thesis includes two articles on Sigüés shales (Saur et al., 2021, 2020), and also provides the X-ray microtomography (abbreviated to XCT) dataset following the study of five marls samples taken along the Sigüés section, samples inherited from Boiron et al. (2020). After performing the acquisition of X-ray images, Saur (2022) compiled:

- Individual grain analysis on 5 XCT drill cores images (Saur et al., 2020).
- Individual gran analysis on a second set of 5 XCT drill core images.
- Bulk shape fabric results of the two sets in relation to the bulk magnetic measurements obtained by Boiron et al. (2020).
- Results of the spatial distribution of quartz grains.
- Comparison between the SPO of calcite and quartz and their CPO measured by means of EBSD technique in two samples.

In relation to this thesis, we will highlight some of the most important results, which complement previous studies and will be taken up in the discussion.

Saur (2022) proposes to study the grain fabric of different phases (pores, pyrite, quartz, calcite) with a resolution 1 μm /voxel, and to compare it with the bulk illite fabric. This comparison between different mineral phases is a novelty in the study of shales.

To study scalar parameters in the so called Jelinek diagram (P, T), Saur (2022) calculated the tensor mean of grain fabrics. In this way, the XCT tensor can be directly compared with that obtained by the AMS technique.

For the 5 samples, the illite P parameter varies from ~ 1.04 to ~ 1.09 (See Figure 102). For quartz, P has a higher amplitude of around ~ 1.2 to ~ 1.5 . For pyrite, P varies from 1.4 to 1.9, for calcite from 1.2 to 2.6, and for pores from ~ 2 to 14. This indicates that the anisotropy measured by XCT is greater than that measured by AMS. This is due to a degree of preferential organization of the mineral phases, but also, and above all, to the fact that quartz, pyrite, calcite and pores have aspect ratios that can frequently go beyond 2, whereas in illites, the degree of intrinsic anisotropy is of the order of 1.4.

In samples A1 to A2, all mineral phases have oblate shapes. In sample A3, a generalised evolution towards a triaxial anisotropy ($T \sim 0$), is observed. Generally, the degree of anisotropy remains the same or decreases slightly. In samples A4 and A5, an increase in anisotropy for all phases, but quartz, is also observed. Almost all phases return from a triaxial anisotropy to an oblate anisotropy.

Alternatively, there is the exception of the quartz shape fabric that remains essentially in the oblate domain in the consecutive samples of the transect. However, in the sites with stronger deformation (in other words, the strongest deformation stages, A4 and A5) the shape fabric appears close to the triaxial domain, indicating reorientation to this mineral phase.

CHAPTER 4 - SHALE FABRIC

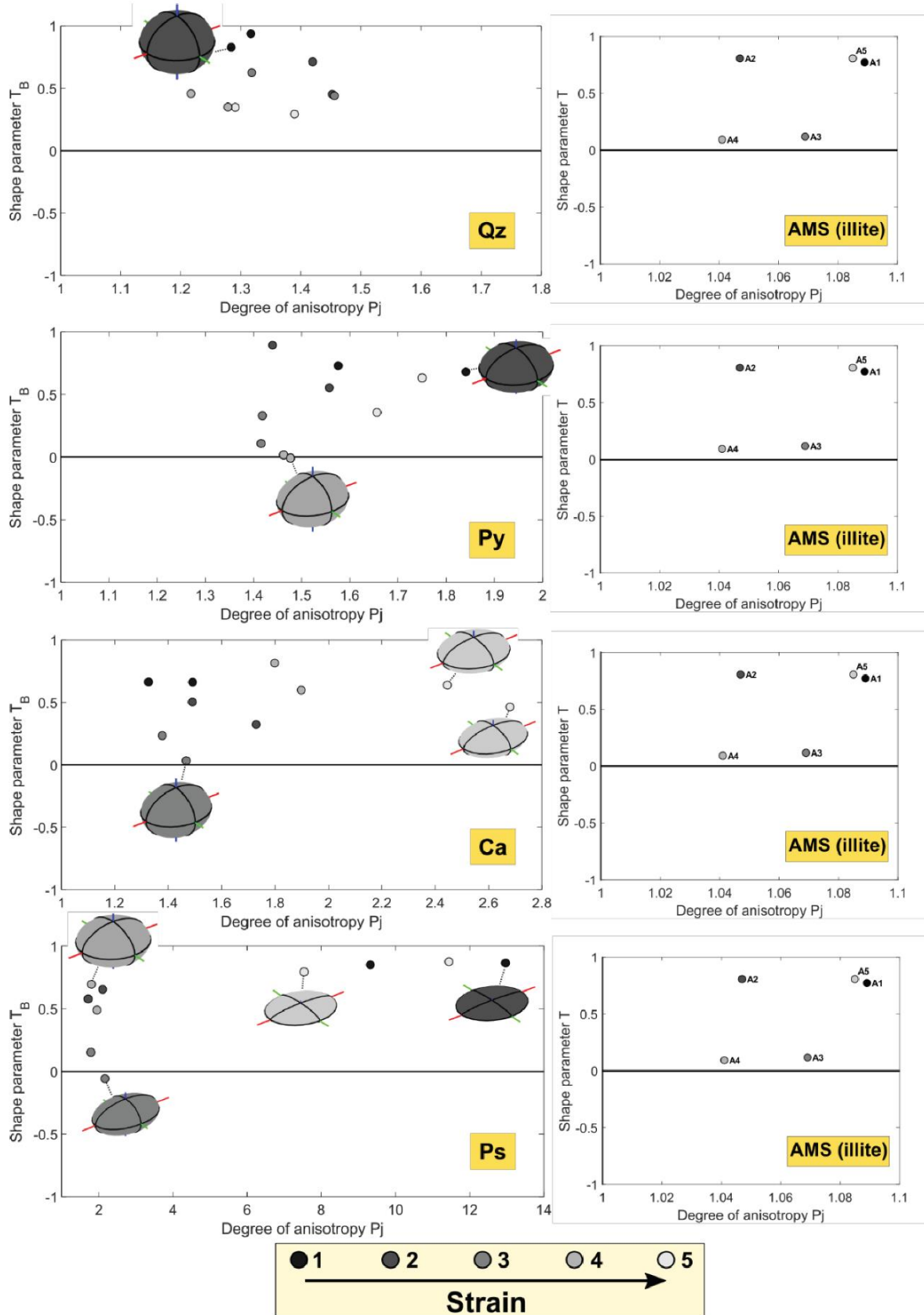


Figure 102: Comparison of various shale phases with the AMS scalar parameters (P_j and T). Qz: Quartz, Py: Pyrite, Ps; pore space, Ca: Calcite. From Saur (2022).

CHAPTER 4 - SHALE FABRIC

The bulk fabric of the matrix components and the bulk magnetic fabric mostly coincides. Considering that AMS is mainly governed by illite, and comparing the various separated phases, Saur (2022) describes the cleavage onset on the 5 sampled sites. In the non-deformed part of the transect, the scalar parameters and orientations of the ellipsoid match.

In the 5 phases studied (calcite, quartz, pyrite, pore, illite), there is a general agreement between quartz and pyrites, which are themselves fairly close to the behaviour of illites. Pores and calcites, on the other hand, seem to react much more quickly to deformation, as early as the pencil cleavage range. In other words, the fabric remains essentially governed by stratification for samples A1 to A3 (Figure 103) for quartz-type behaviour, whereas calcites reorient very rapidly parallel to cleavage, from A3 onwards. Saur et al (2021) have proposed that calcite reacts by solution pressure to deformation, while quartz, like illites and pyrites, much less so. These particles therefore act as rigid markers in the matrix.

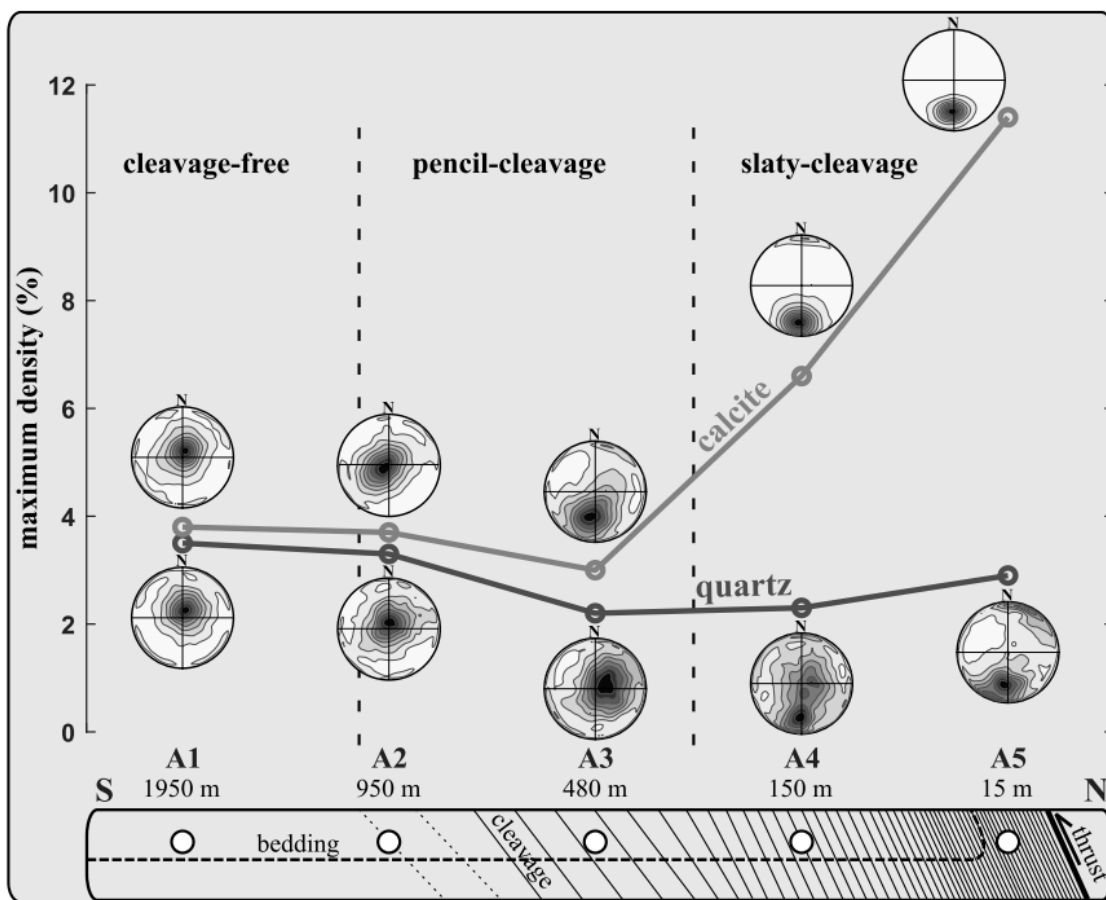


Figure 103: Calcite shows changes on SPO when approaching the main thrust, but quartz remains with the same SPO. Mechanisms of pressure-solution are interpreted on calcite, but not on quartz. From Saur et al. (2021).

4.2. The “sampling by fragments” approach

Since the pioneering studies in the 1950s, authors have been interested in orientated samples, so as to be able to compare directional data with macrostructures such as fold axes, bedding and cleavage to name but a few. In orogenic accretionary prisms, the correspondence of magnetic foliation with bedding, or magnetic lineation with horizontal shortening (LPS) has been widely demonstrated (see section 2.3.7 AMS as a strain gouge, conditions of use.). In more deformed domains, where cleavage occurs, reading the magnetic fabric is more complicated because of competition between bedding and cleavage. However, the lineation remains perpendicular to the direction of the LPS.

In other words, we can say that AMS directional data in a deformed prism (foliation and lineation) are generally predictable. On the other hand, quantitative data derived from scalar data remains under-exploited. This is because the quantitative data results from the organisation of the fabric, but also from the magnetic carrier. Our approach in this thesis is based on the constancy of the paramagnetic component in moderately buried shales. This is a very simple signal, carried by a clay mineral (illite) whose magnetic properties are very stable. So, rather than sampling and orienting the most clayey facies with difficulty, we decided to collect more samples from the most clayey facies, in order to obtain better regional statistics.

4.2.1 Methodology

The sampling scheme of picking fragments is appropriate to cover a larger extent and a more continuous profile from the above-cited works. It results that the magnetic mineralogy is homogeneous and largely dominated by clays in the most clay-rich facies of these marls (Aubourg et al., 2019; Boiron et al., 2020; Pueyo-Anchuela et al., 2011a). Consequently, during sampling, we picked up by eye the most clay-rich fragments and ruled out carbonate-rich fragments.

In each sampling site, about 15–19 non-oriented fragments of shales were taken. Over an area of about 10 m², within a radius of about 2-3 m from a georeferenced point (Figure 104a), we selected fresh cuts of the most clayey facies. Fragments that present oxidized faces were discarded. In areas dominated by slaty cleavage, fragments are smaller, and it was more difficult to distinguish between clay-rich and carbonate-rich fragments. During sampling, the outcrops generally did not offer suitable exposure for standard drilling procedure, a necessary condition to collect oriented cylindrical cores 10 cm³ in volume.

Sampling velocity depends on several factors, such as the separation distance between sampling sites, the spacing between sections if a sampling grid is defined... etc. But in optimal conditions it has been possible to sample up to 20 sampling sites in one day, with the equipment of a hammer, a tablet, and sample bags. Each properly characterised sampling point should take no more than 10 minutes of time.

In the laboratory, these fragments are carved and cut, to a size between 0.5 and 2 cm³ in volume, which corresponds to a mass range from 0.6 to 5.4 g (Figure 104b, Supplementary Material). These fragments of irregular shape are adapted to fit into a 10 cm³ nylon sample holder (Figure 104c) having low diamagnetic susceptibility. Fragments are fixed with cotton inside the capsule to avoid movement and rattling during the measurement.

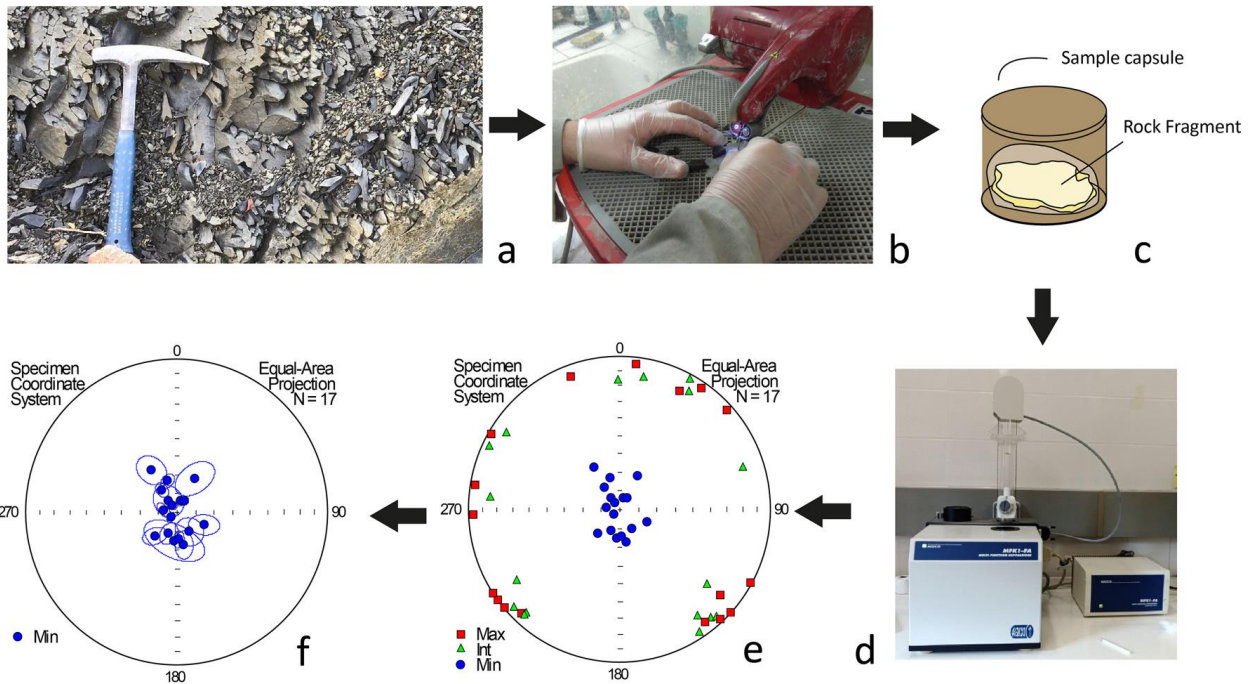


Figure 104: Steps of the sampling and measuring methodology for fragments. a: surface where samples are collected, b: Cutting of samples by means of a trim saw with non-magnetic diamond blade, c: Positioning of sample, d: Magnetic susceptibility measurement on the MFK1-FA (Agico), e and f: AMS data plotted on stereoplots.

The AMS instrument used is the MFK1-FA susceptibility bridge (Agico- Advanced Geoscience Instruments Company, Figure 104d) which is located at the UPPA (University of Pau). For measurement, we used the standard magnetic field strength (200 A/m) and frequency (976 Hz). A 3D rotator arm is available to measure the components of the magnetic susceptibility ellipsoid in less than 2 min. Interestingly, during this procedure, the cylindrical holder is not removed, allowing a better accuracy to calculate the tensor.

In ~45 min, up to 20 fragments can be measured and their tensors fully resolved. AMS data are plotted using Anisoft software (Chadima, 2019) (Figure 104e). The sensitivity of the MFK1-FA bridge is 0.5×10^{-8} SI and its accuracy for resolving anisotropy is less than 0.1%. It is known that this measure is not sensitive to the shape of samples (Tarling and Hrouda, 1997). The reason for that is the sample is submitted to a homogeneous, well-controlled magnetic field in the impedance bridge during the bulk susceptibility measurement. As we shall see, we have experimentally verified this point, which generally raises questions among scientists working on AMS.

The tensor resulting from each fragment is described according to Jelinek (1977) theory. Each K_i axis is calculated with two E_{ij} confidence ellipse axes at the 95% level. In this study, we are only focusing on the K_3 axis, since it evolves between the poles to bedding and cleavage. This mode of dispersion has been well described in the AMS studies (Boiron et al., 2020; Pueyo-Anchuela et al., 2011b). The K_3 axis is specified by an ellipse with two axes, E_{31} in the K_1 - K_3 plane and E_{32} in the K_3 - K_2 plane (Figure 104f). The magnitude of E_{32} and E_{31} does not depend on the coordinate system. The K_3 orientation quality is also defined by F_{23} and F_{31} statistical tests (Jelinek, 1977). A threshold value $F_{test} > 4.6$ is generally required for the reliability of the measurement.

CHAPTER 4 - SHALE FABRIC

The output results provide K1, K2, and K3 with their associated confidence value, dK1, dK2, and dK3 according to Jelinek (1977). Using standard equation for the error propagation, the standard error for the degree of anisotropy P and the shape parameter T are calculated. Error on P, dP, can be calculated from

$$dP = \left(\left(\left| \frac{1}{K_3} \right| * dK_1 \right) + \left(\left| \frac{K_1}{K_3^2} \right| * dK_3 \right) \right)$$

Equation 23

To calculate error on T, the expression on T can be rearranged, as :

$$T = \frac{\ln F - \ln L}{\ln F + \ln L}$$

Equation 24

Where $L=K_1/K_2$ and $F=K_2/K_3$

If we take the error propagation equation of a quotient as for P, and applying it to L (dL) and F (dF), it is possible to find the error propagation equation of T, such that:

$$dT = \left(\left(\left(\frac{\left(\frac{1}{F} \right) * (\ln L + \ln F) - \left(\frac{1}{F} \right) * (\ln F - \ln L)}{(\ln L + \ln F)^2} \right) \right) * dF + \left(\left(\frac{-\left(\frac{1}{L} \right) * (\ln L + \ln F) - \left(\frac{1}{L} \right) * (\ln F - \ln L)}{(\ln L + \ln F)^2} \right) * dL \right) \right)$$

Equation 25

The representativeness and repeatability of the data were checked by carrying out sets of measurements on three fragments (Figure 105). The fragments EL12-15 and EL6-11 have about the same weight (~2 g) but respond differently to the statistical test F23 (Figure 105a, b). Two types of measurement sequence were performed. Firstly, the fragment was measured 10 times in a row with a fixed and immovable position inside the capsule (fixed-position). Secondly, the same fragment was introduced several times into the capsule and measured in 10 different random positions (Figure 105 a-b).

EL12 sample displays a well-defined K3, with the axes of the ellipse of confidence lower than 5° (Figure 105a). The F23 statistical test yields a value of 341. The shape parameter is oblate and the degree of anisotropy is high (P=1.18). When measuring according to the fixed-position protocol, the K3 remains remarkably within the area defined by the ellipse of confidence at 95% level. When the random-position protocol is applied, the ellipse of confidence remains the same. The scalar data P and T remain within the 95% level of uncertainty for both random-position and fixed position. It appears therefore that a fragment of ~2 g with a high F23 statistical test displays the same scalar data whatever its orientation.

Provided that the fragment is irregular in shape, this rules out a possible artifact due to the shape of the sample. EL6-11 sample, measured with the random-position protocol (Figure 105b), displays a poorly defined K3 with the long axis of the confidence ellipse higher than 10°. Accordingly, its shape is prolate and P is close to 1.08. The F23 test is here low (6.6) near the acceptable threshold of 4.6 proposed by Jelinek (1977). The random-position protocol shows that K3 displays comparable elongated shapes of the ellipse of confidence. P and T are also contained within the error bars. When applying the random-position protocol, the

CHAPTER 4 - SHALE FABRIC

size of K3 ellipses and P-T error bars recover similarly, excluding a possible bias due to the shape of the fragment.

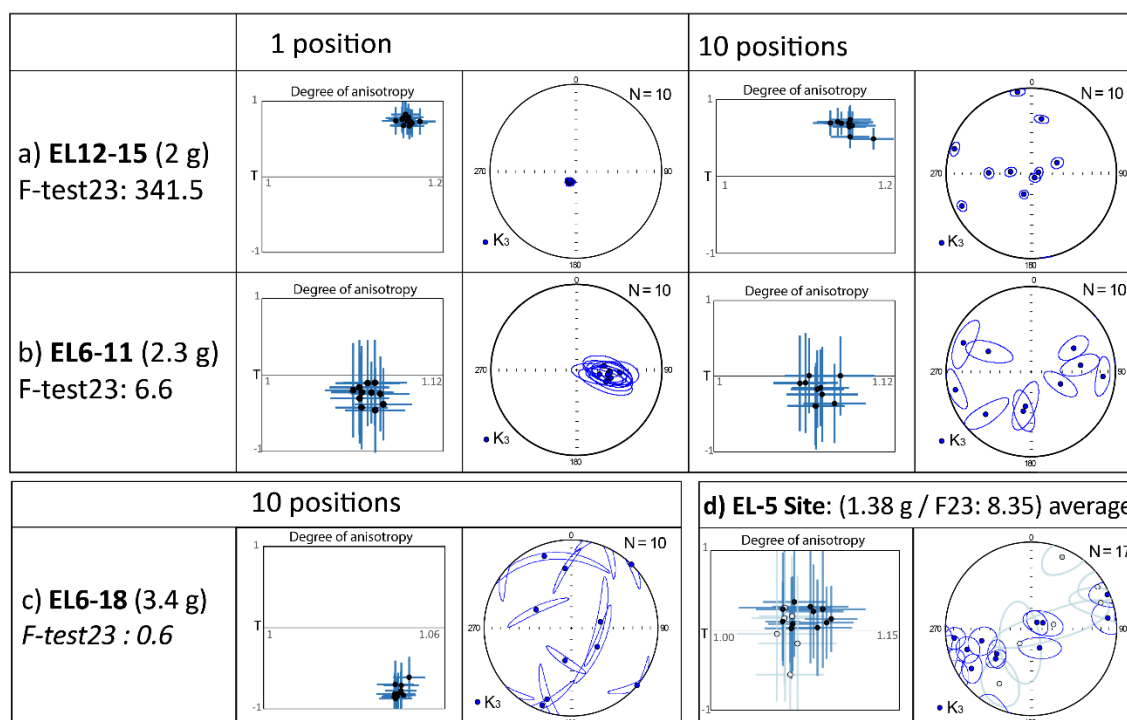


Figure 105: a) Fragment EL12-15 has been collected in an area displaying slaty cleavage. It has been measured 10 times in the same position (fixed-position protocol) and 10 times by changing each position (random-position protocol). Scalar data (degree of anisotropy P and shape parameter T) are plotted with their confidence value calculated from equations (1) and (2). Minimum axis K_3 with its confidence ellipse at 95% level is plotted in equal-area stereonet. The minimum axis K_3 is here well-defined ($F_{23} = 341.5$) and the shape is oblate. One can note that error bars and ellipses display the correct distribution of data in both fixed-position and random-position protocols. B) Fragment EL6-11 has been collected in an area displaying pencil cleavage. This fragment has been measured using both fixed-position and random-position protocols. The competition between bedding and cleavage results in a poor definition of K_3 (large ellipses of confidence), low value of F_{23} ($F_{23} = 6.6$), and prolate shape ($T < 0$). It can be seen that both the error bars and the ellipse of confidence reflect properly the distribution. c) Fragment EL6-18 has been collected in pencil cleavage area. K_3 is poorly defined with a statistical test $F_{23} = 0.6$ below the threshold value of 4.6. Repeated measurements using the random-protocol reveals that the distribution framed by error bars and ellipses remains the same. d) EL5 site corresponds to a pencil cleavage area. This site has been chosen because it has the smallest fragments in average, and a rather poor statistical resolution. Five out of 17 samples have an F_{23} parameter lower than 4.6 (light blue circles in the diagrams).

To go further in the consistency of fragment measurement, we measured repeatedly (random-position protocol) sample EL6-18, characterized by a very low F_{23} test ($F_{23} = 0.6$; Figure 105c). Sample EL6 displays the same scalar values (ellipse size, P , T) within 95% level (Figure 105). This indicates that even samples with low F_{23} statistical test values can be measured with some reliability. In addition, we present a sampling site, EL-5 (17 fragments) characterized by small fragments and poor statistical resolution (five out of 17 samples display $F_{23} < 4.6$) (Figure 105d) This site shows a dispersion similar to the repeated measurement of the EL6-11 fragment (Figure 105b). Samples with an unfavourable F_{23} test have comparable scalar magnitudes except for one fragment with a negative T parameter value. The statistical approach with an average including more than 10 fragments smooths out outlier points. To honour the data set, we have kept all samples, even those with a large deviation from the mean values. The reason for this is that they may represent a deviation from the values for reasons other than mineralogy (and, for the moment, unknown to us).

We do not exclude further research to solve this problem. This test on 3 fragments and one site (17 fragments) allows to conclude that the measurement of a small fragment of irregular shapes does not alter the significance of AMS scalar parameter.

4.2.2. Rock magnetism

Rock magnetism of seven samples from the Larrés Formation marls was performed by C. Aubourg during a stay at the MRI (Minneapolis) in 2016. He performed hysteresis cycles at room temperature, and measurements at low temperature on an MPMS. Thus, magnetic transitions such as Verwey's (120K, magnetite), Besnus' (35 K, pyrrhotite) or Morin's (250K, hematite) were highlighted.

The hysteresis cycles (Figure 106, lower part) show a remarkable linearity with a paramagnetic susceptibility between 60 and 80 micro SI (average= 70.7 ±10.2). The ferromagnetic contribution is very low, less than 5%. The remanent magnetization at saturation acquired at 300K and with the application of a magnetic field of 2.5 Tesla (RT-SIRM) is on average 47±21 μAm²/kg .

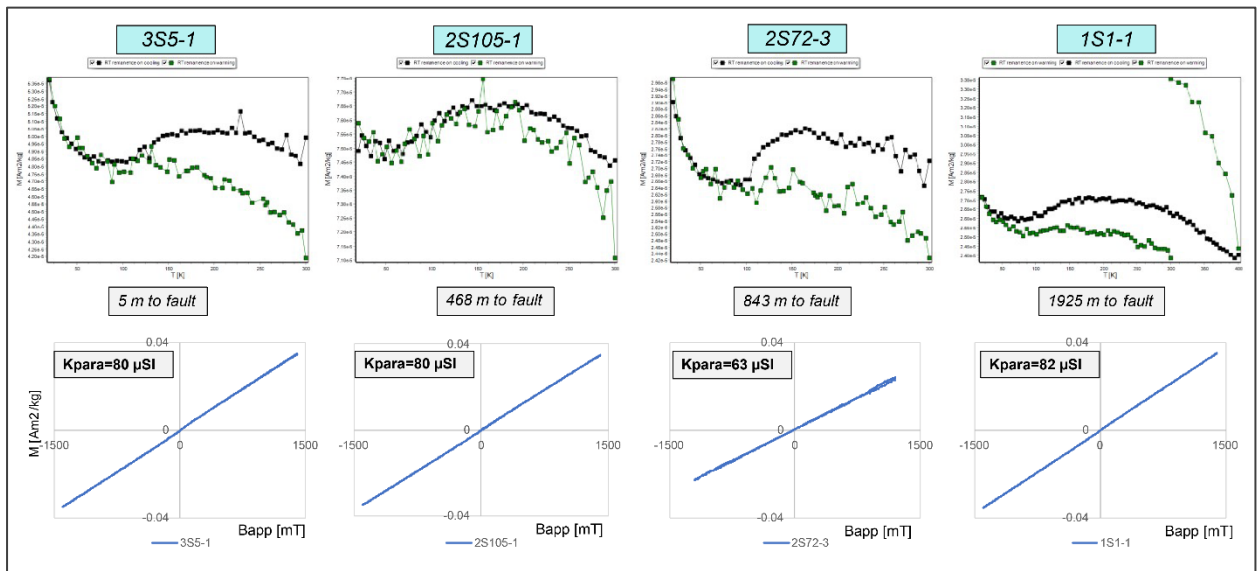


Figure 106: Four representative samples and their magnetic features (IRM in the upper set of diagrams and hysteresis cycles in the lower set) in the shales corresponding to the footwall of the Leyre frontal thrust. The 3S, 2S and 1S samples are at increasing distances from the fault.

When the RT-SIRM is subjected to a cooling and heating cycle, we note the presence of a Verwey transition at 120K (sample 3S5), sometimes poorly constrained (sample 1S1). This indicates the presence of stoichiometric magnetite, possibly altered in some samples. Among the other visible transitions, we note the presence of a P-transition which indicates the presence of a magnetization induced by the residual field in the magnetometer. This P-transition (Kars et al., 2015) has been interpreted as being related to the presence of grains in a superparamagnetic state, which is classically found in shales (Aubourg et al., 2019). We also find a probable signature of goethite (sample 1S1-1). In any case did we find the Morin transition (~250K), which would indicate the presence of hematite.

This magnetic assemblage is consistent with that observed in many shales (Abdelmalak and Polteau, 2020; Kars et al., 2011). The ubiquitous presence of mainly stoichiometric magnetite indicates that we are in the magnetite window that extends from a few tens of degrees to

CHAPTER 4 - SHALE FABRIC

about 300°C burial temperature (Aubourg et al., 2021). Magnetic diagenesis results in progressive dissolution of magnetic iron oxides without the process being fully understood. Aubourg et al. (2021) discuss these transformations. In particular, these authors show that there is a sort of concentration minimum of ferromagnetic minerals around a burial temperature of about 200°C to 300°C (Figure 107). With an RT-SIRM value around 50 $\mu\text{Am}^2/\text{kg}$ we can observe a good agreement between the RSCM temperature ($\sim 200^\circ\text{C}$, see section 5.2 Additional RSCM and Rock-Eval data.) and the low RT-SIRM values (Aubourg et al., 2019).

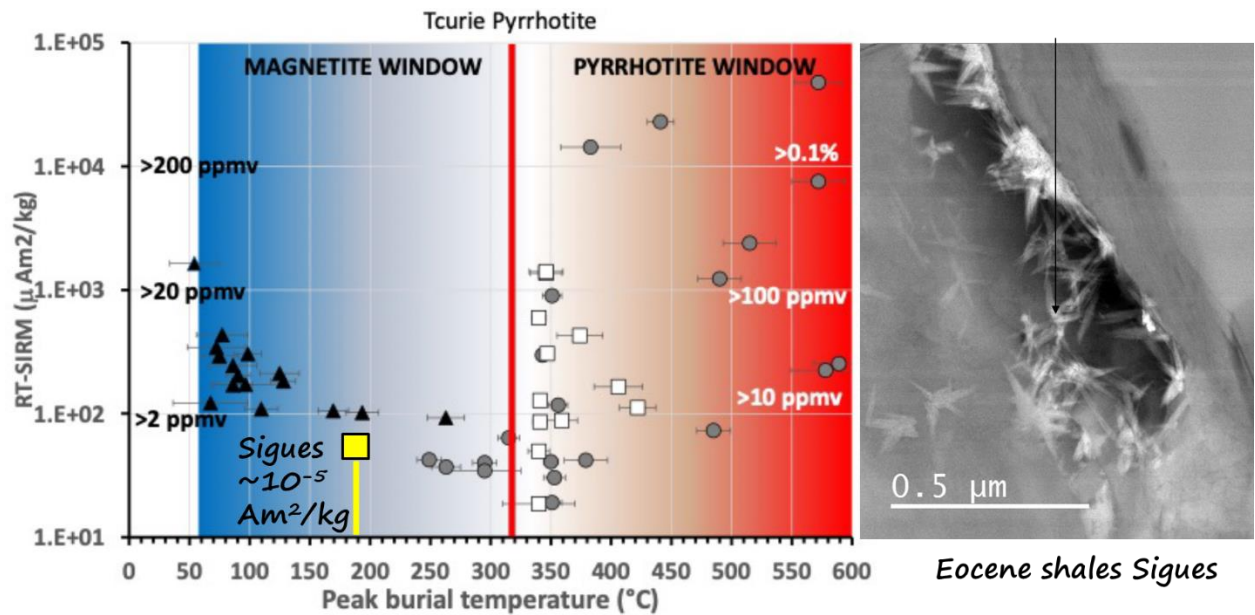


Figure 107: RT-SIRM data VS Peak burial (from vitrinite reflectance and RSCM data) from the Pyrenees and Taiwan samples from Aubourg et al. (2019). Right picture corresponds to SEM observation of Larrés marls. Magnetite crystal are signalled (Aubourg, Pers. Comm.). Aubourg et al. (2021, 2019) have observed that nano-magnetites develop around iron sulphide (pyrite). Here, nano-magnetites are observed growing in micrometric pores.

These results, similar to those of Boiron et al. (2020), support the idea that shales in the temperature window between 200°C and 300°C show a minimum concentration of ferromagnetic minerals and a magnetic susceptibility largely governed by the clayey suite, mainly illites. The properties are very homogeneous, and show no differences between the part without cleavage and the samples near the fault (Figure 106).

Our observations, along with those of Boiron et al. (2020) and Pueyo-Anchuela (2012a) therefore support the idea that Eocene marls have a very largely dominant paramagnetic component, mainly carried by illite.

4.3. Sigüés results

4.3.1 Sampling

More than 1500 fresh shale samples were collected at 99 sampling sites on the footwall of the Leyre thrust. Most of these sampling sites are aligned on transects perpendicular to the fault. These are the Leyre, Escó, Llarto, Escalar, Sigüés B and Orba transects (See location on Figure 108). Some sampling sites are scattered over the map, with no vocation for transect, such as the La Paul area. Also, out of the count there are about thirty sampling sites whose AMS has not been measured. Some belong to the Sigüés area, others to areas close to the Leyre frontal thrust, in shales that are probably incorporated into the hanging-wall.

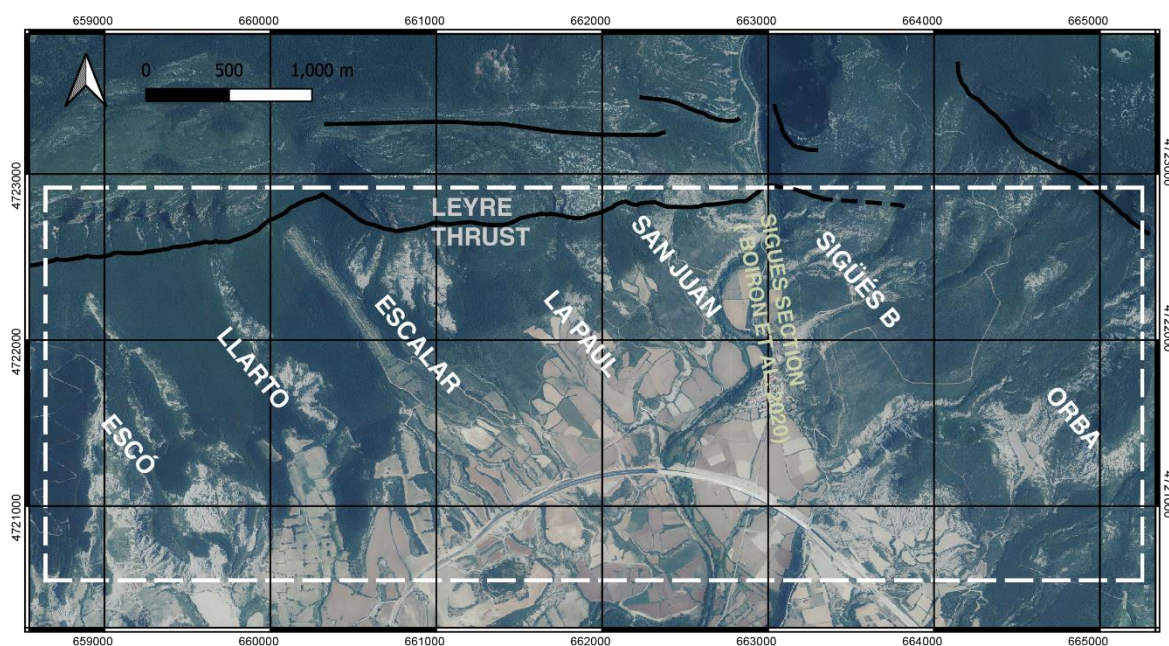


Figure 108: Aerial photo of the Leyre-Orba footwall outcrops. The sampling paths coincide with the layout of the labels on the map. The black traces indicate the main thrusts in the structure.

The lithology is composed exclusively of marls, with rare carbonate-rich centimetre-thick layers. As mentioned in section 3.4.3 Structural synthesis, it is possible that in this area there is a transition between different stratigraphic units according to Puigdefabregas (1975). It would be the top of the Larrés Formation, and the base of the Pamplona Formation, both of which are slope marls of the South Pyrenean Basin. In between, there are transgressive sediments corresponding to the Sabiñánigo Sandstones (Puigdefábregas, 1975), or to the Urroz Siltstone, a lithology more commonly found towards the W of the Jaca Basin. However, in the field it is very difficult to establish the difference between them; the facies do not vary, and the deformation is easily expressed in the soft marly sediments (Figure 109).



Figure 109: A view of the marl outcrops in the Escó section (see map in Figure 108). It is not always easy to distinguish recurrent structures such as bedding or cleavage.

These Eocene grey marls experienced a peak burial temperature near 180°C (see data in 5.1 Background, and also references from Boiron et al., 2020; Crognier et al., 2018; Izquierdo-Llavall et al., 2013b) and hosted fluid circulation events. Shales generally show homogeneous grey facies, and are crossed by calcite veins and fractures with different orientations as described in Chapter 3 and section 5.3 Calcite-filled faults.

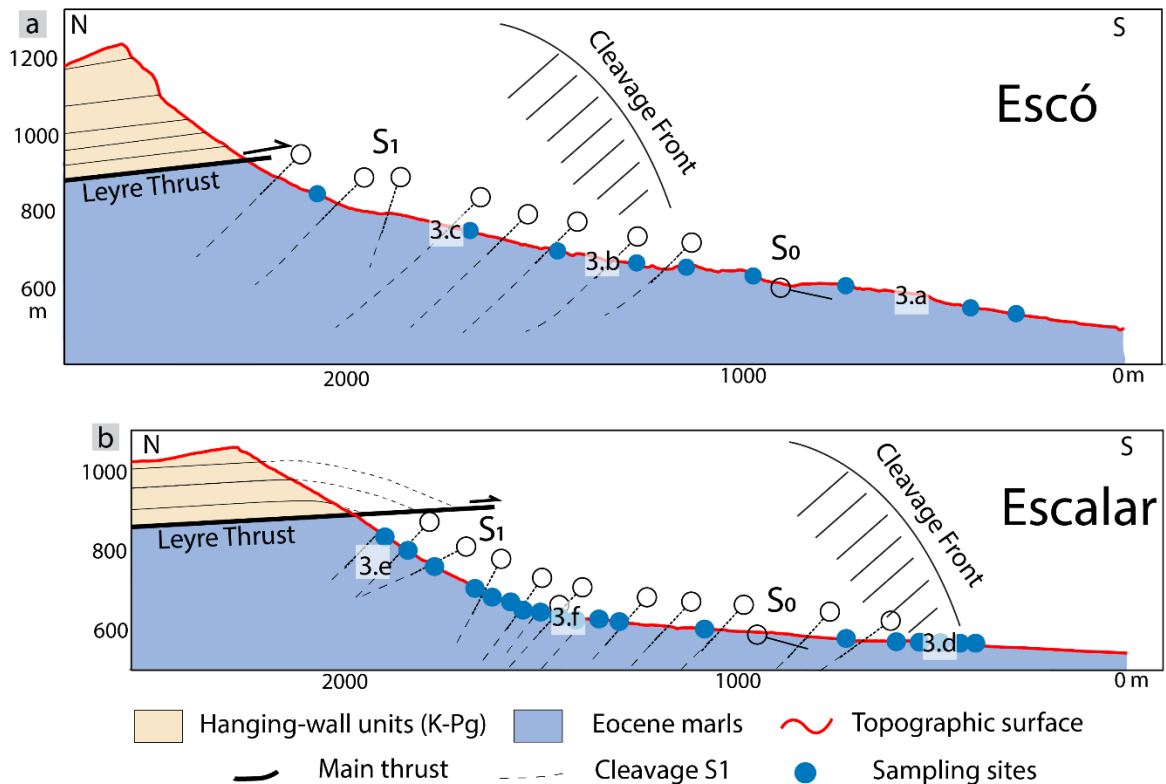


Figure 110: Simplified cross-sections for the sampling on the footwall of the Leyre thrust. Escó and Escalar sections located on Figure 108. The stratification dips gently to the south on the order of 5° to 15° . The general northward dip of the cleavage is marked by dotted lines. The approximate position of the cleavage front is indicated. For the Escó section, this front is located farther north.

In the footwall of the Leyre thrust, bedding shows shallow dips, being horizontal (Figure 111), shallowly dipping to the south ($<15^{\circ}$) or rarely dipping to north, with gentle folds. As cleavage development increases, it is difficult to detect bedding (Figure 111c-e), that is completely overprinted by the slaty cleavage (Figure 111f). However, by observing the general geometry (e.g. Figure 111a) and noting subtle changes in facies, we were able to verify that the general dip of the bedding does not change all along the two sections ($<15^{\circ}$ S). A drag fold has also been detected in the vicinity of the Leyre frontal thrust, resulting in a N-dipping reverse limb (Boiron et al., 2020).

The sampled outcrops have been described in section 3.2. Field description of the Jaca Basin sites., and in the following paragraphs we will describe the features of each profile and the number of sampling sites in each section from W to E.

- The Leyre transect includes nine sampling sites from the main fault to 1.9 km south, close to the Yesa reservoir. It is separated 9 km to the west of the Escó transect. In this section, little deformation was detected in the marls of the footwall, and only slightly more intense deformation close to the main thrust.
- The Escó transect (Figure 111) includes 10 sampling sites over a horizontal distance of 2 km. Some other sites, not presented in Gracia-Puzo et al. (2021) have also been sampled in this work. We found mainly pencil cleavage sites, locally more penetrative.

CHAPTER 4 - SHALE FABRIC

- The Llarto transect is composed of 12 sampling sites, in a line of shale outcrops between Escó and Escalar sections of 1.5 km in length. Here we found the first slaty cleavage sites, and a “damage zone” outcrop.
- The Escalar transect (Figure 111) consists of 20 sampling sites covering ~2 km of horizontal length. There are more sites because the lower part of this section reveals the presence of pencil cleavage (Figure 111), while the lowest part of the Escó section is cleavage free. Our sampling scheme was based on a tighter grid to obtain better resolution of the deformed area. Along the section, slaty cleavage is observed at about 1.5 km from its southern limit (the local cleavage front). According to the results obtained previously, as described in the above-cited article, it was decided to extend the sampling again, up to a metric vertical separation; 16 new sites were added during a field campaign in 2022. These results are shown in this PhD thesis, modifying the figures of Gracia-Puzo et al. (2021).
- La Paul sampling sites, are three sampling sites on shaly outcrops to the E of the Escalar Section, corresponding to its middle part. San Juan sampling sites comprises only three sites between La Paul and Sigüés section. All of them show at least pencil cleavage, and one site is very close to the main thrust trace.
- This PhD section does not include those data published by Boiron et al. (2020) and obtained in the Sigüés section, although they will be included in the further analysis about the strain quantification section.
- Next to the Sigüés section, some 200 m further E is the transect Sigüés B, which adds eight sites, but only four in the footwall.
- Finally, in the footwall of the Sierra de Orba, and perpendicular to it, is the Orba transect with 10 sampling sites distributed along a 2.5 km line.

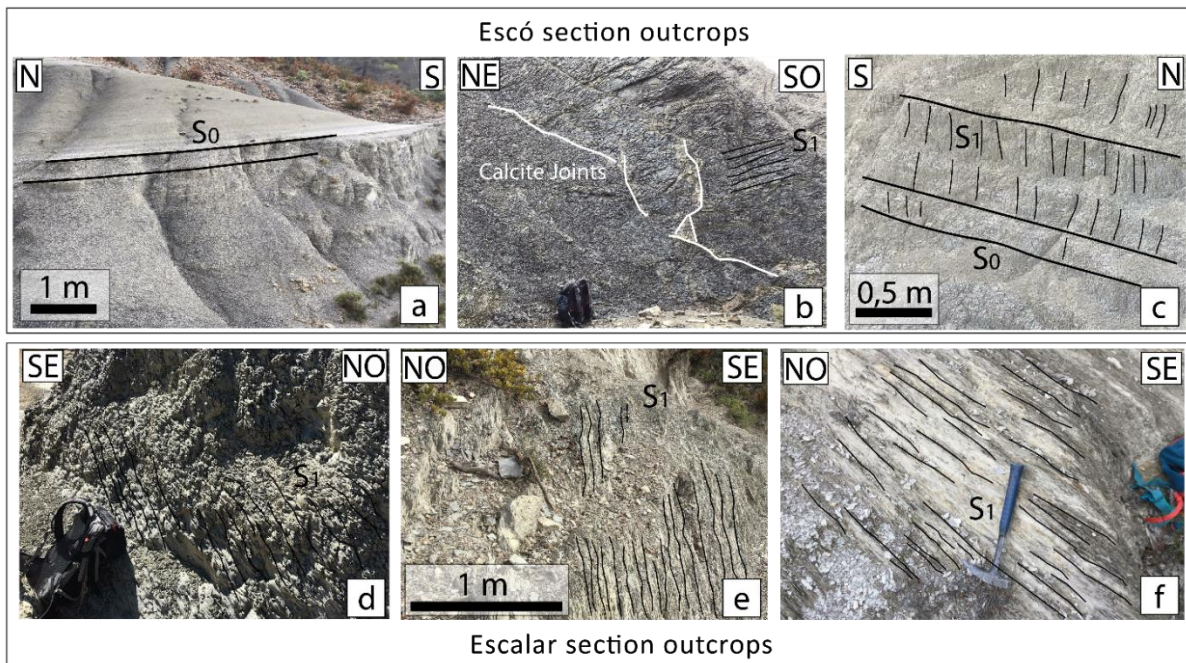


Figure 111: Photographs of outcrops with different degree of deformation. A) Beds of marls in the lower part of the Escó section. B) Middle part of the section, outcrop with fracturing and incipient cleavage C) Penetrative pencil cleavage outcrops D) Marls in the lower part of the Escalar section, bedding and cleavage are not visible, camouflaged by the homogeneity and surface fracturing of the marls. E) Slaty cleavage with centimetric spacing in the middle-bottom of the section. F) Highly penetrative slaty cleavage 220 m from the main thrust

CHAPTER 4 - SHALE FABRIC

The complete list of sampling sites, with the number of measured fragments, geographical coordinates and section will be detailed in the annex.

4.3.2 Results

This section of the thesis presents the data for the above-mentioned sections, summarizing the results of the analysis of a total of 1500 samples.

The following table shows some characteristics of the sampling sections

Table 6: Summary of data for each sampling section

SECTION	Number of sites	Number of fragments	Latitude / Longitude	Altitude of southern site m	K norm μ SI	K average μ SI	Mass of fragments g
Leyre	8	139	42°37'24.36"N 1°10'21.27"W	506	57 - 216	154	0.7 - 6
Escó	9	155	42°37'15.94"N 1° 3'55.89"W	559	119 - 220	133	1.6 - 5.4
Llarto	12	197	42°37'41.94"N 1° 2'33.64"W	506	109 -233	147	0.5 - 3.3
Escalar	34	672	42°37'29.97"N 1° 1'52.11"W	538	37- 180	133	0.9 - 5.4
La Paul	4	51	42°38'8.25"N 1° 1'31.63"W	603	81-120	97	1.7 - 5.8
San Juan	3	54	42°37'57.81"N 1° 0'58.90"W	521	77-201	130	1.1 - 5.1
Sigüés B	8	137	42°37'55.14"N 1° 0'33.61"W	586	-		-
Orba	10	162	42°37'20.54"N 1° 0'10.47"W	545	36-220	142	0.5 - 5.2
TOTAL	88	1513	-	506	3.6-233	134	0.5 - 6

This chapter integrates more data than the article by Gracia-Puzo et al. (2021). Tables with all detailed data of the measured samples will be presented in Annex. Here, in this section, a brief compendium, which contains data related to the mean of measurements of each parameter for a sampling point with its standard deviation, will be presented.

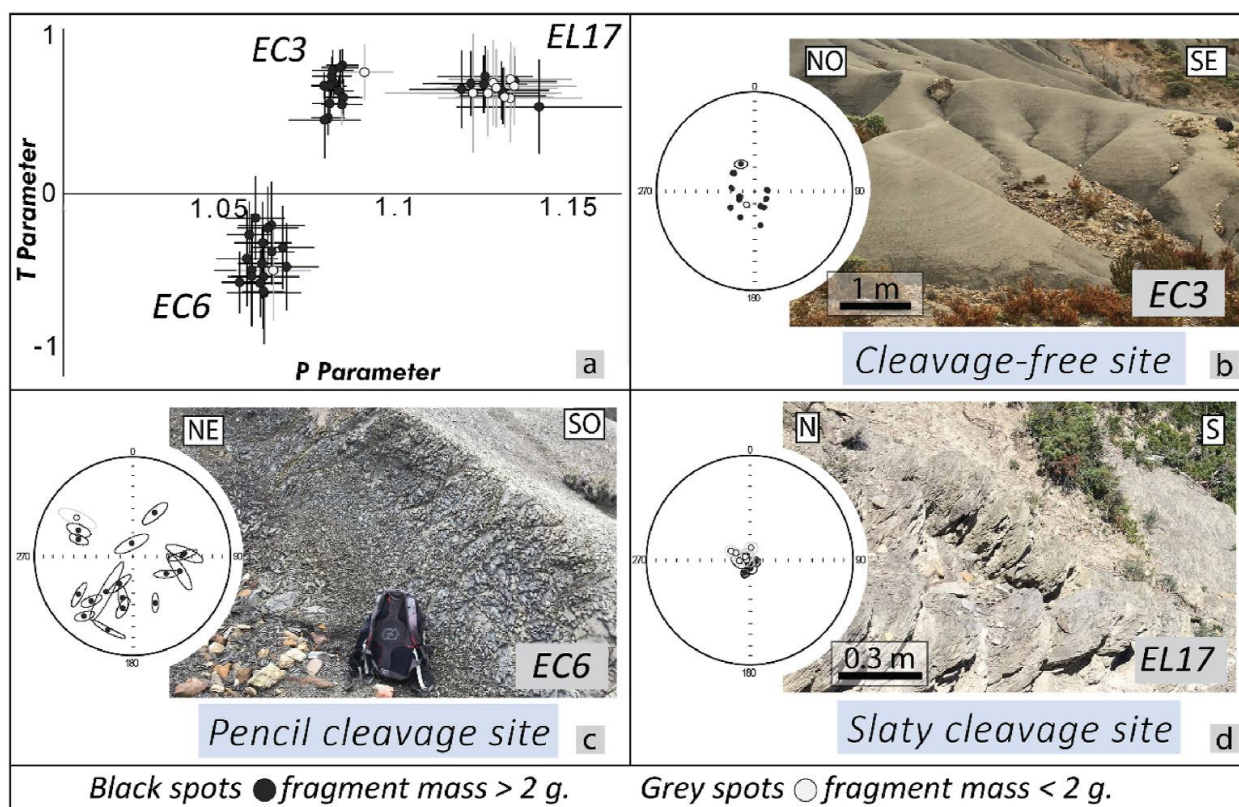


Figure 112: Three representative examples of outcrops with different degrees of cleavage development. a) Jelinek's diagram (P vs T parameters). Errors bars are plotted according to Equation 23 and Equation 25. b-c-d) photographs of each outcrop, the stereonet shows the K3 axes with their confidence ellipses, without spatial reference. White dots indicate fragments < 2 g.

Three main types of representative magnetic fabrics can be distinguished, depending on the state of deformation (Figure 112). In these plots, samples with $F_{23} < 4.6$ and mass < 2 g are marked in light grey colour to assess their reliability. Site EC3 corresponds to an outcrop where cleavage is not observed (Figure 112b), site EC6 is an example of an outcrop with pencil cleavage (Figure 112c), and site EL17 located near the main thrust shows slaty cleavage (Figure 112d). The scalar parameters P and T show little variation (Figure 112a), with a distribution comparable to the repeated measurements (Figure 105). This indicates little variability at the scale of the sampling site. Note that low-weight fragments (< 2 g) display similar results. Cleavage-free and slaty-cleavage sites display oblate fabrics. The degree of anisotropy is higher for slaty-cleavage site EL17. Pencil-cleavage site EC6 has a prolate shape and a rather low anisotropy. The other important scalar data for the description of the deformation state is the parameter E_{23} which marks the elongation of the confidence ellipse in the K2-K3 plane.

We present in the stereoplots (Figure 112) the K3 axis with the confidence ellipse, whose maximum elongation gives an idea of the magnitude of E_{23} . It must be emphasized that the directions obtained for the K3 axis are not useable information because the fragments are not oriented. For the EC3 site (Figure 112b) and for the EL17 site (Figure 112d), ellipses have a very small size (i.e. $< 5^\circ$). However, for the EC6 site (Figure 112c), elongated ellipses of enlarged size are observed, in agreement with the prolate nature of the shape of the AMS ellipsoid. The grouping of K3 along the vertical direction comes from the fact that a visible plane was used on the fragment, and that the sample was placed with this horizontal plane in the sample holder. Cleavage-free site EC3 reveals well-defined K3 axes grouped near the

CHAPTER 4 - SHALE FABRIC

vertical (Figure 112b). Pencil-cleavage site EC6 reveals poorly defined K3 axes (Figure 112c). The K3 are predominantly oblique, and never close to vertical. Slaty-cleavage site, EL17, reveals well-defined K3 axes tightly grouped near the vertical (Figure 112d). For further analysis of the trend of scalar parameters P, T, and E23, we propose to plot these data relative to the main Leyre thrust (see Figure 113 and Figure 114).

Because of the above, the orientations of the axes of the magnetic ellipsoid cannot be directly related to bedding of cleavage; instead, several sketches and occasionally stereoplots will be used to visualise the evolution of the selected scalar parameters. These parameters were described in section 2.3 Magnetic fabric study: P, T, L and the angle of confidence of K3, E23.

Boiron et al. (2020) chose the horizontal distance from the Leyre fault to plot the scalar data because the section is horizontal. Here, we prefer to take the elevation reference in m from the known location of the nearest point of the trace of the Leyre thrust. The reason for this choice lies in the type of projection that is classically used in drilling studies with vertical sections. This projection does not accurately reflect the distribution of the scalar data, but the field data (Figure 113 and Figure 114) show that 1) the Leyre thrust is approximately at the same elevation for both sections, 2) the Leyre thrust is subhorizontal where it emerges, 3) the hanging-wall of the Leyre thrust, eroded at present, beyond the mapped thrust front probably reached the southernmost studied sites. Our projection mode can therefore be likened to a virtual borehole, to illustrate the fact that our approach is quite applicable to the measurement of cuttings in boreholes. A description of these sampled outcrops is given in section 3.2.1.

The **Leyre section** is located at the western end of the Leyre thrust (see location in section 3.2.1. The Sigüés and Leyre Sites., not visible in Figure 108) and the associated folded structure. This section was not extensively studied during the thesis fieldwork. However, we were able to see a slaty-type cleavage close to the fault, comparable to the footwall of the Leyre fault towards Sigüés. This cross-section is therefore indicative, as we have not documented the transition with the Escó cross-section.

Parameter P varies between 1.06-1.08 except for the site sampled next to the fault where it is strongly anisotropic, up to $P=1.11\pm 0.02$. Slaty cleavage is here observed, a feature that can be found within a few tens of metres from the fault trace. Parameter T remains stable between oblate and triaxial (~ 0.6); furthermore, in the last two sampling sites, a rebound from 0.1 to 0.7 is observed, indicating a change of fabric. We also observe homogenous values of the L parameter, between 1.02-1.03 (Figure 114). The E23 parameter is also quite stable and low (≥ 8) compared to that obtained in other sampling sections.

At the **Escó section** (this and the following sections visible on Figure 108), there are some worth noting parameter evolutions. As described above, a fault zone is observed in the intermediate zone at ~ 250 m depth with respect to Leyre thrust (Figure 111b, see also section 3.2.1.5 Southern zone of the Leyre thrust). A transition from marly rocks to pencil cleavage-like outcrops is observed from a vertical distance of 250 m to the frontal thrust mapped trace. Parameter P obtained is $P = 1.07 \pm 0.01$, shows a constant decrease upwards from ~ 1.10 down to ~ 1.06 . Parameter T shows a negative peak value (prolate) at ~ 230 m from the fault, and a similar value ($T=-0.2$) at 90 m, creating a double ramp trend. The same trend is found, but in reverse for the L-value and E23 (Figure 114): a positive peak of these parameters at

CHAPTER 4 - SHALE FABRIC

230 m and a final rebound, with maximum values at the 230 m peak for $L \sim 1.045$ and for $E23 \sim 12 \pm 5^\circ$.

In the **Llarto section**, the P parameter increases increasing gradually, from ~ 1.07 to ~ 1.12 , with an outlier peak at 140 m from the fault ($P \sim 1.13$). This trend is consistent with outcrop observations of progressively more penetrating cleavage from the lower to the upper part of the transect. The shape parameter T remains in the triaxial to oblate domain (from ~ 0.2 at the bottom to ~ 0.6 at the top) with a prolate peak at 260 m from the main fault. This would be in relation to the cleavage front, which has the appearance of a pencil cleavage in the field.

For parameter L, no trend is observed and data are obtained within a range between 1.02 and 1.04, with a peak of 1.05 at 260 m from the fault. Parameter E23 does have a decreasing trend towards the top of the section, from 21 to 8, and a peak also at 260 m.

For the **Escalar section**, the average value of P is on average higher than that observed in the other section ($P = 1.10 \pm 0.03$). P shows a generally increasing trend towards the fault, from ~ 1.05 to ~ 1.15 . However, there are two segments where P values are high: between 230 m and 175 m ($P \sim 1.14$) and in the last two sampling sites, 60 m below the Leyre thrust ($P \sim 1.13$). The evolution of T has a double branch. A peak of prolate values stands out at 334 m from the fault ($T = 0.46 \pm 0.21$), and there are two maxima of positive oblate shapes: at 222 m ($T = 0.79 \pm 0.08$) and at 60 m ($T = 0.5 \pm 0.27$). These maxima coincide with slaty cleavage observations in outcrops. In this profile, the L parameter shows the largest deviations of all samples, with a mean value of 1.05. The same peak (in this case, negative) is observed at 230 m from the main thrust. Parameter E23 also shows large standard deviations ($8 \pm 12^\circ$ at 40 m from the fault) although a maximum is observed at 330 m from the fault. This could coincide with the point where the outcrops show a pencil cleavage. Then, a decreasing tendency is detected in the rest of the transect towards the main frontal thrust.

The **San Juan profile** shows an increasingly penetrative pencil cleavage up to a slaty cleavage zone in the vicinity of the frontal Leyre thrust. The general increase in P (~ 1.06 to ~ 1.10) can be linked to a very deformed general state of the cross-section. The T parameter shows a triaxial fabric (between -0.1 and 0.2) at 180 m from the fault, and above it, we see prolate fabrics with $T > 0.5$. For the L parameter a roughly decreasing trend is observed, from 1.04 to 1.02 when approaching the fault. This slightly decreasing trend is also observed in the values of the E23 angle, which has a relatively low mean with respect to other sections, from 12 ± 6 to 5 ± 3 .

The **Sigüés B section** corresponds to a long horizontal distance (1 km) but little extent on the vertical. So the most relevant is the horizontal distance from the thrust. In general, the rocks sampled show progressively more penetrative pencil cleavage, and finally slaty cleavage close to the fault trace. The P parameter has rapid changes near the fault, from 1.02 to 1.10 in a few metres, as a result of the short stratigraphic distance sampled. The T parameter also undergoes rapid changes, with a large standard deviation. Some points remain in the prolate zone, especially far from the fault (-0.1 to 60 m from the fault), but we observe that above the fault, the slightly oblate domain seems to be dominant (T between 0.3 and 0.5). The parameter L is also different in the distance ($L = 0.4$) and the proximity of the fault (L around 1.02). Finally, parameter E23 starts from a relatively small angle in most of the transect ($E23 = 10^\circ$ at 80 m from the fault) reach high values close to the fault ($50 \pm 40^\circ$).

CHAPTER 4 - SHALE FABRIC

The **Orba section** (Figure 108), crosses the foot of the Orba mountain range, covering a long vertical distance. This time, the vertical distance is associated with the emerging Orba fault, not the Leyre fault (see cross-sections on Figure 95 from section

3.4. Structural frame and serial Cross -Sections.). The P parameter decreases generally from 1.11 to 1.05 towards the main fault. The T parameter is variable, and although it is generally oblate (mean $T \sim 0.7$), it has a triaxial shape, with values of 0.2 at 100 m from the fault. The L parameter is rather constant ($L_{\text{mean}} \sim 1.02$). The E23 parameter has a value of 4° , except at distances of 90 m and 100 m away from the fault, where it shows a jump to $29 \pm 13^\circ$, indicating a wide opening of the E23 angle. This would coincide with slaty cleavage, with signs of shearing at these upper sampling sites.

CHAPTER 4 - SHALE FABRIC

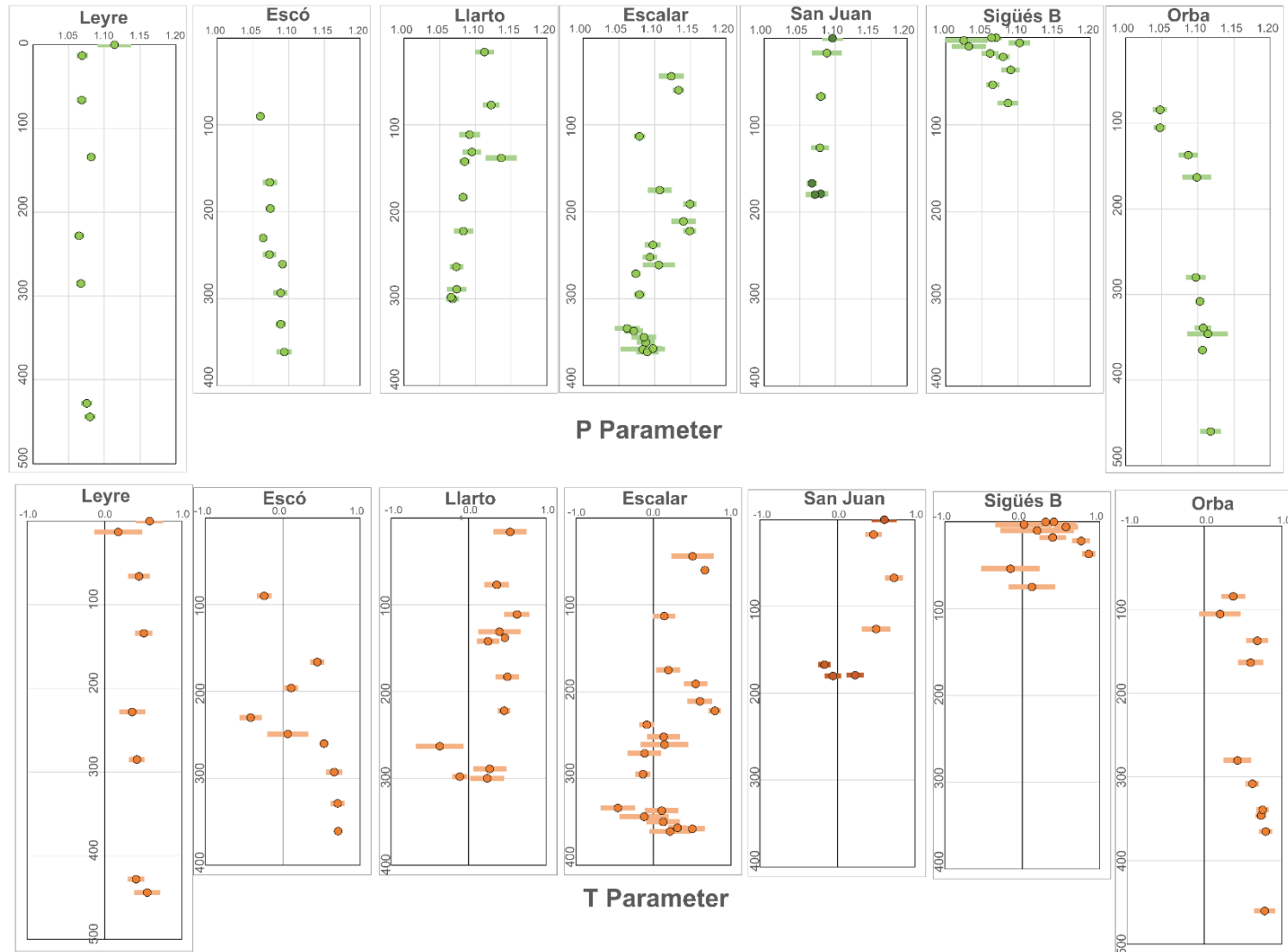


Figure 113: Virtual boreholes: i.e. vertical projection of the results of scalar parameters obtained for the sampling sections. In the ordinates we represent the vertical distance up to the projection of the trace of the Leyre thrust.

CHAPTER 4 - SHALE FABRIC

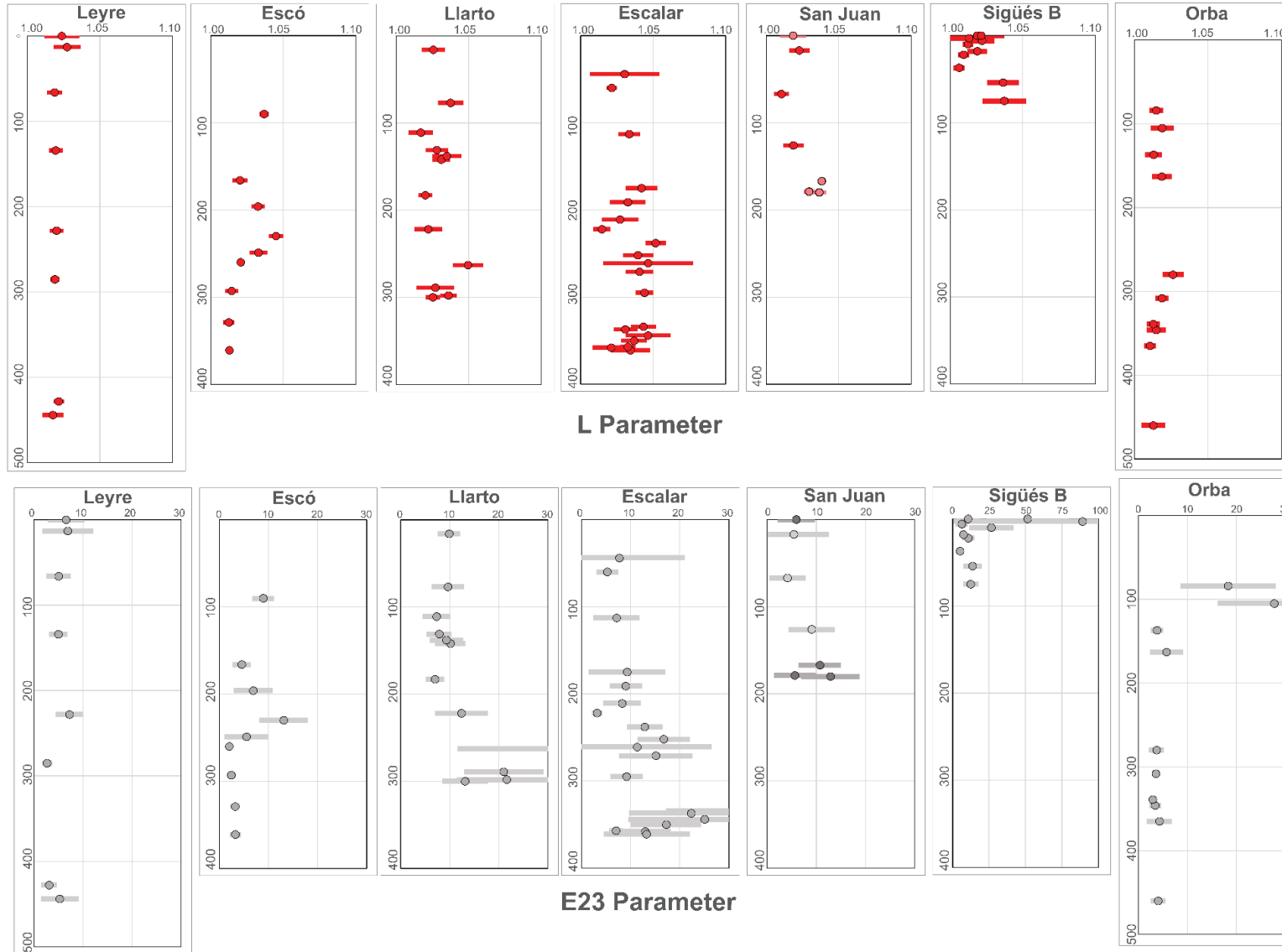


Figure 114: As in Figure 113, a vertical projection of the results of scalar parameters obtained for the sampling sections is shown for these parameters

4.3.3. Data treatment and analysis of scalar parameters

When plotting the degree of anisotropy P as a function of the shape parameter T in Jelinek's diagram, the sampling transects can be analysed to detect differences in the fabrics.

From the results obtained in the two transects presented in the former paper, we proposed a five-step evolution of deformation in the footwall of the Leyre thrust. The deformation evolutionary model is very similar to the one presented in previous bibliographical references (Parés et al., 1999; Parés and van der Pluijm, 2004)

In step 1, there is no cleavage (Figure 115 a). The magnetic fabric of sedimentary origin shows an oblate ellipsoid with a degree of anisotropy close to 1.10. The directions of K_3 are well defined and grouped in the vertical. The main anisotropy of fragments is controlled by the bedding plane (Figure 115a). In step 2, pencil structures are barely detected in field exposures. The degree of anisotropy decreases slightly, but the most remarkable trend is the shift towards a triaxial shape of the susceptibility ellipsoid. The E_{23} angles are mostly $>5^\circ$ indicating a progression towards a conflictive fabric. In step 3, pencil structures are well developed (Figure 115c). The shape parameter evolves to negative values indicating a prolate shape. As a result, the E_{23} angles are larger $> 15^\circ$. Inclination of K_3 is still variable, indicating that the main plane visible on the fragment can be either bedding or cleavage. In step 4, the susceptibility ellipsoid is triaxial, and the degree of anisotropy slightly increases. The main difference with step 2 is that cleavage is well expressed in the outcrops and bedding planes are almost indistinguishable (Figure 115d). We note here a significant reduction in size of the confidence ellipses. The magnetic foliation is primarily, but not totally, controlled by the cleavage planes. In step 5, the slaty cleavage is penetrative. The shape of the ellipsoid is oblate and the degree of anisotropy can reach much higher values than observed in step 1. The K_3 axes show a very important reduction of the E_{23} angle. The evolution of steps 1 to 2 is interesting because the scalar parameters allow to detect a gradual matrix damage that is not evident from field observations. Step 3 shows pencil structures that can still go unnoticed either in the field or in drilling cuts. Steps 4 and 5 can be more easily detected from field observations or by a simple examination of the fragment.

All five of these steps will be referred to as "Fabric stage n°X" in the following sections of this manuscript.

CHAPTER 4 – SHALE FABRIC

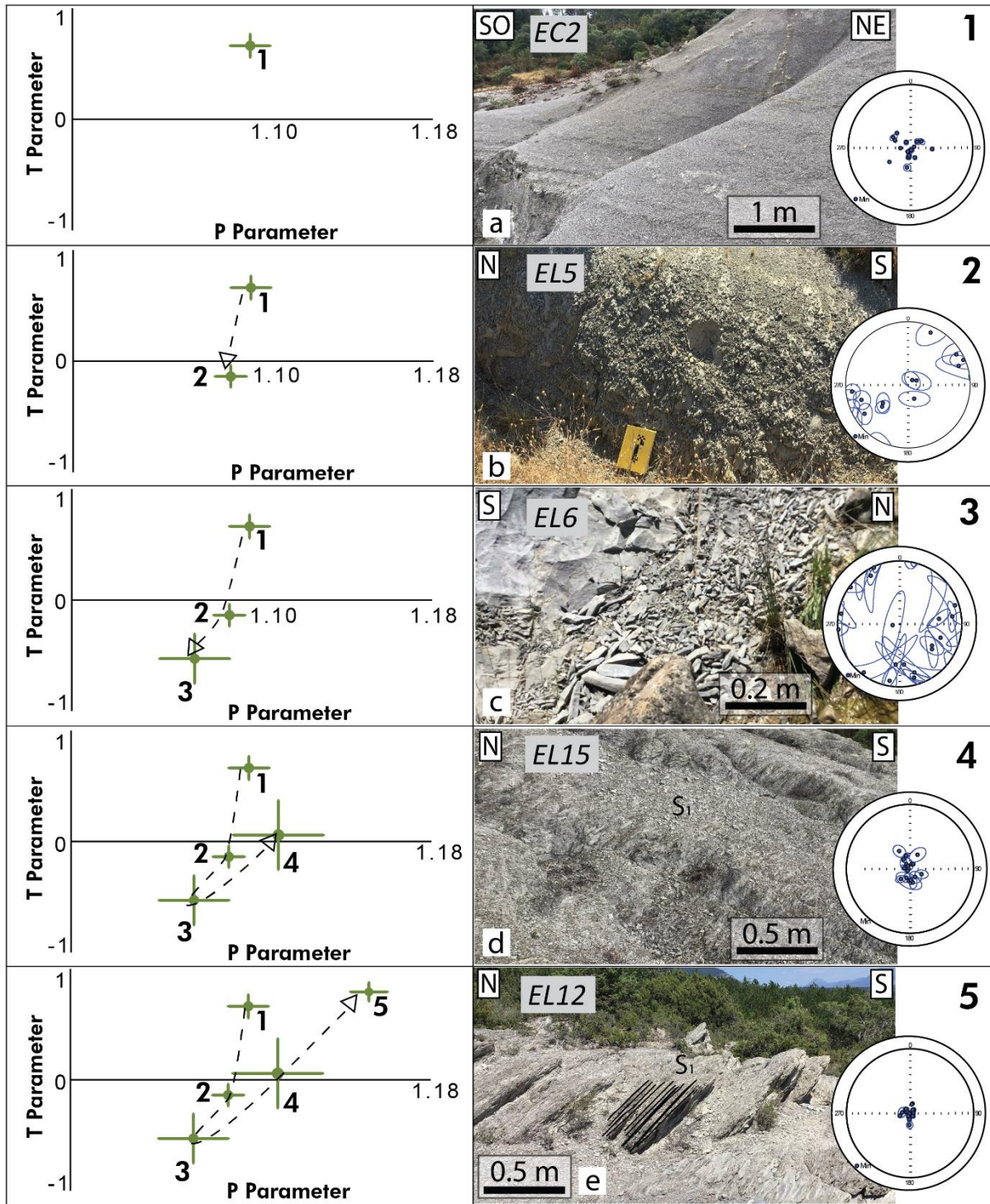


Figure 115: Five-step evolution of the magnetic fabrics in the footwall of the Leyre thrust.

This allows for a new visualisation of the data, beyond the virtual boreholes presented in Figure 113 and Figure 114. For this purpose, we have separated the data into four sectors corresponding to the sampling area in Figure 108.

Firstly, separated by its geographical distance (11 km to the east), we separate the data for Leyre, which can nevertheless be compared with the rest of the figures. The data from each sampling site are plotted in Figure 116.

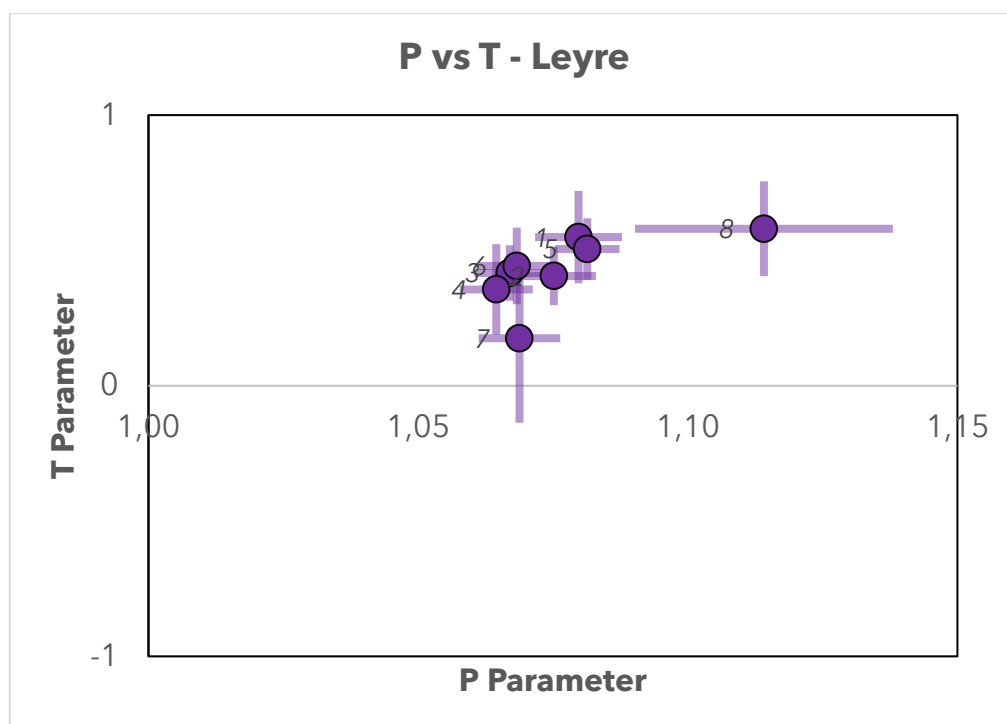


Figure 116: Jelinek diagram (P-parameter vs T-parameter) for the Leyre Section. Sites are numbered from 1 (farthest south) to 8 (close to the footwall) see distances in Figure 113.

Most of the P-T results in agreement with what was observed in the field prove to correspond to stage 1 fabrics (although not as oblate as in the model in Figure 115). However, for site 7 we do have a slightly more oblate value (T 0.2) and for site 8 the anisotropy peak P 1.11 described above, which would make it a stage 4 or 5 fabric.

Secondly, in the western sector there are the Escó and Llarto sections (Figure 117). The most oblate positions coincide with the lower part of the Escó sector, coinciding with areas without cleavage, probably corresponding to the sedimentary fabric of the Eocene shales (sites 1, 2, 3 and 4).

Then, a group of fabrics have slightly lower anisotropy (1.06-1.08) and a shape parameter around triaxial (-0.1 to 0.3). These correspond to the middle zone of the Escó section (sites n° 5, 7) or to the lower part of the Llarto section (sites a, b and c). This can be attributed to a subtle pencil cleavage, sometimes not detected in the outcrop, but corresponding to the stage 2 fabric.

Some sampling sites correspond to clearly prolate fabrics ($T < -0.2$), and coincide with the upper part of the Escó section (sites 6 and 9), and the beginning of macroscopic pencil cleavage in the Llarto section (site d). This would correspond to stage 3.

Finally, from the East to the last sampling site of the Llarto transect, a T parameter between 0.4 and 0.7 is measured with increasing anisotropy (>1.08); it coincides with the middle and upper parts of the Llarto section. The higher anisotropy can be attributed to fault zones (maybe stage 5), but in general it would correspond to the stage 4 fabric.

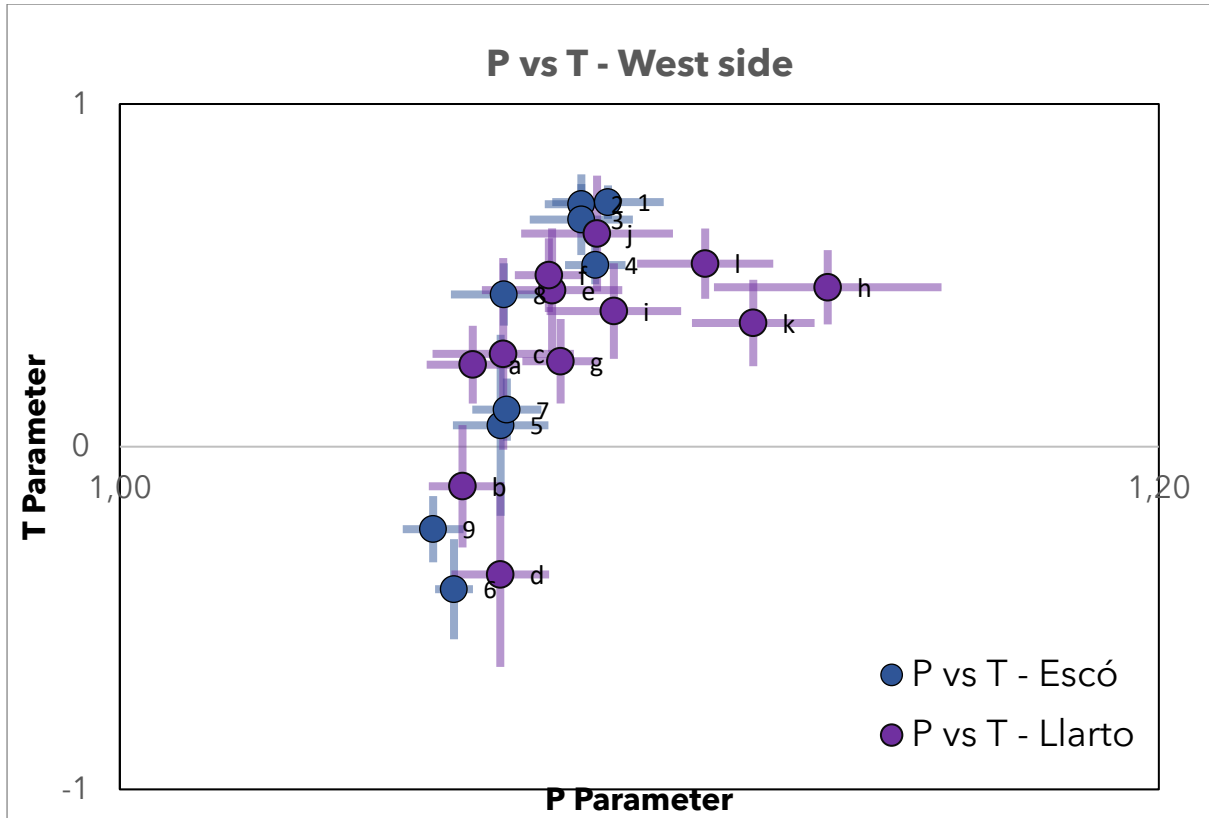


Figure 117: Jelinek diagram for the Escó and Llarto sections. The Escó section is numbered from 1 (farthest) to 9 (closest to the fault). The Llarto section from the letter "a" (farthest) to the letter "l" (closest).

The Escalar transect contains results representing almost all five stages. From EL1 (site farthest from the frontal thrust) which is between stage 1 or stage 2 fabric, to site EL6, which represents a stage 3, to the progressively increasing anisotropy and oblate fabrics of the sites between EL9 and EL18. It is the transect that contains the most sampling points, and the vertical distance between sampling sites does not exceed 20 m, where shales crop out continuously. For this reason, many of the Escalar sites have been used as examples to prepare the model in Figure 115.

The sites sampled in the San Juan transect include samples whose shape factor is in the oblate domain, but less anisotropic than in Escalar section (Figure 118). They should correspond to stage 1, in spite of having been collected in outcrops of shales with slaty cleavage. Fabric shows an oblate shape ($T > 0.5$) related to cleavage, but the anisotropy is smaller. Most of the samples from this transect (SJ2 to SJ9) were discarded because they were found in the hanging-wall of the thrust and correspond to the lower part of the Eocene shale series.

On the other hand, the sites from the La Paúl outcrops (LP1, LP2, LP3) generally correspond to the triaxial or prolate domain, which mark the onset of pencil cleavage in the shales. This also coincides with other sites of the Escalar section (EL7, EL 8, EL 13). In a stage 5 domain we have some of the most anisotropic samples of all those sampled in the footwall of the Leyre thrust (Sites EL10, EL11, EL12, EL17, EL18).

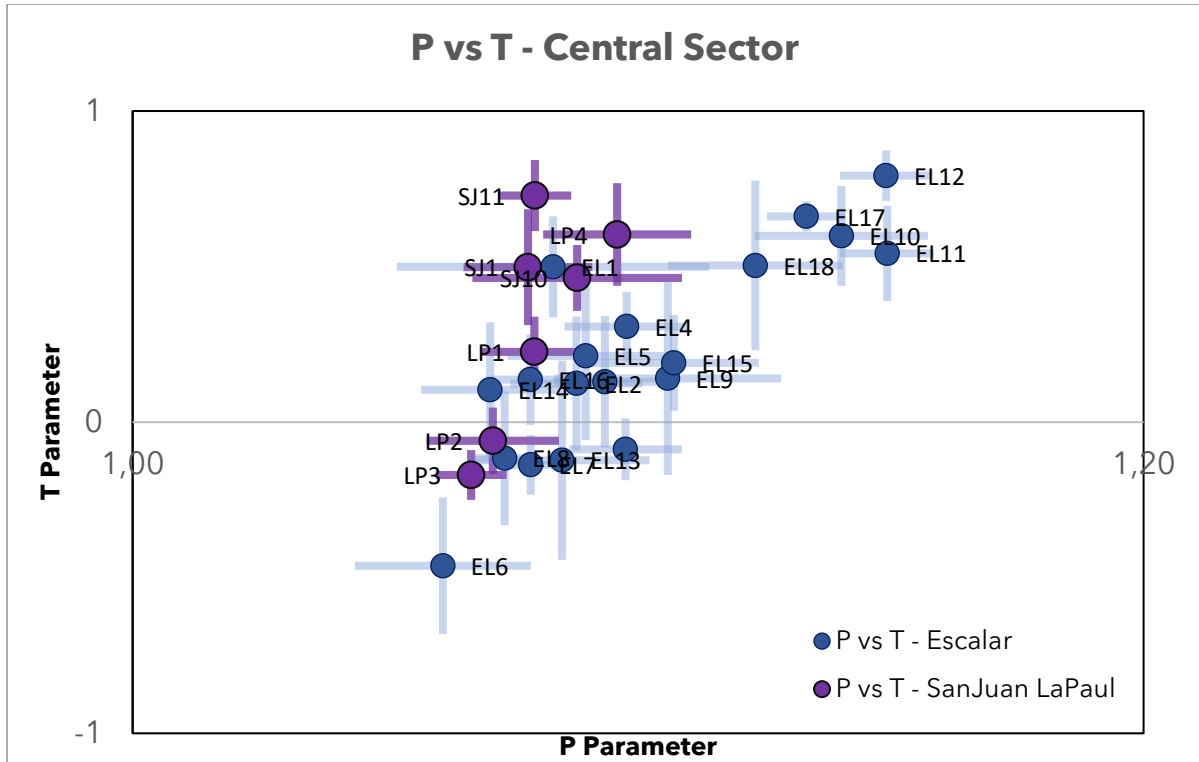


Figure 118: This scheme contains in blue colour the 18 sites of the Escalar transect, the three sites of San Juan and the four sites of La Paul are in purple colour.

Finally, the Sigüés B transect and the Orba transect represent the sampling carried out on the East bank of the river Escá (Figure 119). In both transects, the first sampling sites, farther from the Leyre thrust (Sites 1 and 2 of both sections) are the most oblate ($T > 0.7$) and most anisotropic ($P = 1.09$) according to a typical sedimentary fabric in shales, or stage 1. In the Sigüés B section, a sudden shift to more triaxial shapes is observed (sites 3, 4, 2b, 5b), indicating a pencil cleavage fabric. In any case, this group of sites that in outcrop do appear clearly deformed (Orba 10, and the other above-mentioned Sigüés sites), sometimes with very penetrative pencil cleavage, if not fully developed cleavage. Therefore, this group might not be stage 2, but stage 4, and the lower anisotropy might be conditioned by a very heterogeneous bulk fabric.

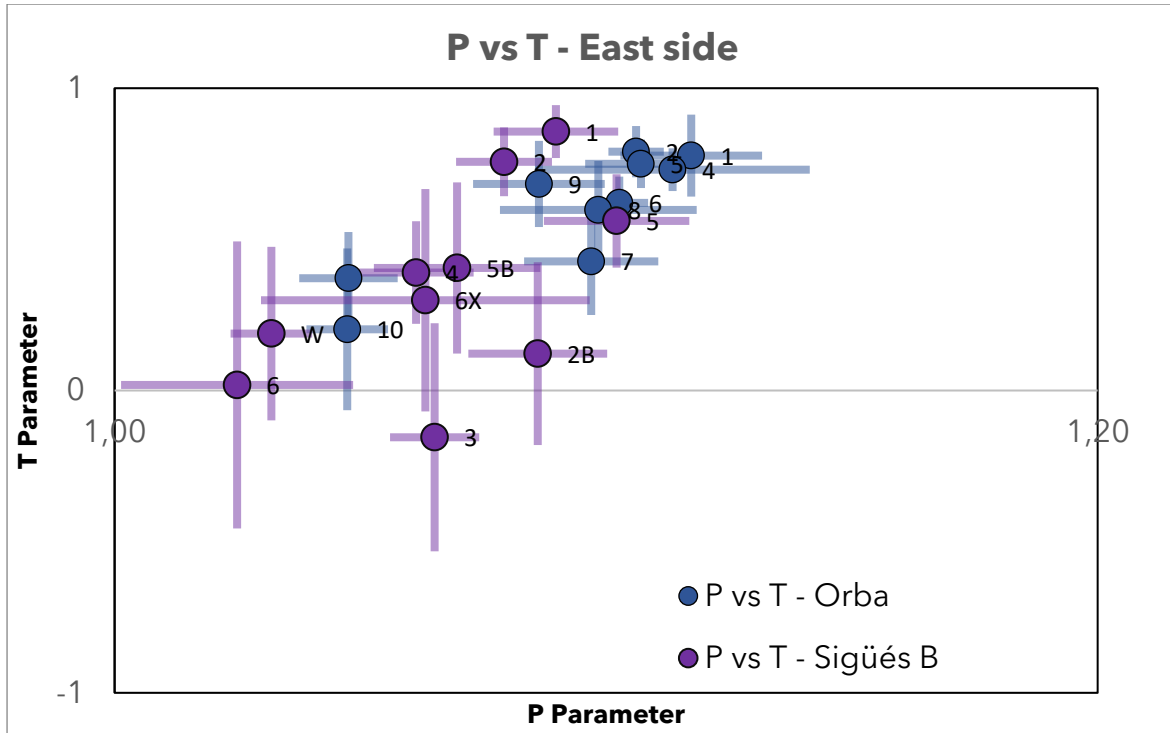


Figure 119: Jelinek diagram including the Orba (blue dots) and Sigüés B (purple dots) sections.

4.3.4 Synthesis of AMS Results near Sigüés footwall

After the presentation of scalar data, we have stated that the analysis of more than 1500 fragments of Eocene shales provides highly reproducible scalar data, thus indicating that the AMS measurement of non-oriented fragments of variable shape is an efficient and reliable technique. This opens the possibility of measuring cuttings from boreholes, or fragments in poorly exposed areas. We demonstrated that the scalar parameters, including the long axis of the confidence ellipse E23, the degree of anisotropy P, and the shape parameter T are independent of the measuring system (Figure 105).

These five steps can be identified on the virtual logs (Figure 120). For the sake of clarity, we focus on the shape parameter T and in two sections among the seven presented. This next figure belongs to the paper published by Gracia-Puzo et al. (2021).

Along the Escó section, only steps 1 to 3 are found. Note that the clearest evidence of step 3 is at ~230 m from the Leyre thrust. This point reaching step 3 is also well marked by the confidence angles E23, and a rather low degree of anisotropy (Figure 115). Step 3 is framed upwards and downwards by sites reaching step 2, suggesting a symmetry of matrix damage. Along the Escalar section, we find instead steps 2 to 5 (Figure 120), without clear evidence of step 1. This indicates more pronounced matrix damage than in the Escó section, in accordance with field observations. Progressive deformation follows a sequence from stage 2 at the bottom of the profile, to stage 3, then 4, to culminate in stage 5 at 230 m from the Leyre thrust, thus defining a continuous deformation gradient. Upwards, deformation decreases (stage 4), recovering again (stage 5) close to the Leyre thrust. The comparison between the two profiles thus shows damage linked to the Leyre thrust (at shallow levels in the virtual boreholes), but also a damage zone culminating in both sections at a depth of about 230 m (reaching stage 3 and 5 in the Escó and Escalar profiles, respectively).

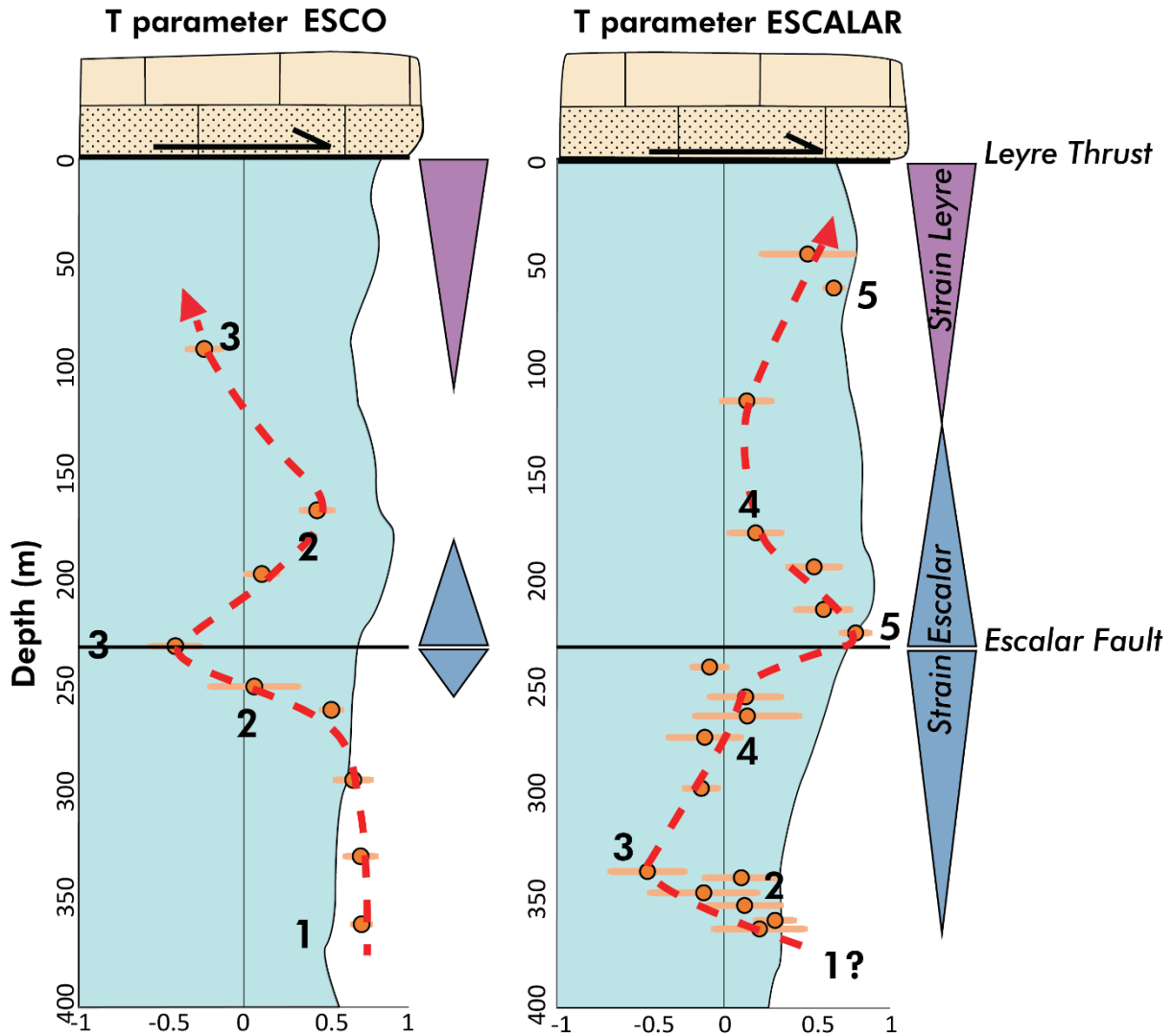


Figure 120: Evolution of the magnetic fabrics along the sampling sections projected onto virtual boreholes. To simplify, we present only the evolution of the shape parameter on which we indicate the different steps 1 to 5, defined in Figure 115. The triangles illustrate the evolution of deformation from stage 1 (no deformation) to stage 5 (maximum deformation).

We interpret this damage zone as related to a South-verging unmapped thrust (Escalar fault) cutting across the footwall of the Leyre thrust (Figure 120). In both profiles, a symmetry of gradients is observed around the maximum damage zone, that reaches a thickness of 140 m in the Escalar profile (Figure 120). In the Escó profile, there is no suggested overlap between the zone of damage related to the Leyre and Escalar thrusts (triangles in Figure 120). Along the Escalar profile, conversely, it is likely that the two damage zones overlap, preventing the clear definition of an upper limit for the deformation associated with the Escalar thrust. Along the Sigüés section, instead, Boiron et al. (2020) did not find anomalies in magnetic scalar parameters suggesting the presence of the Escalar Thrust. This is either due to insufficient sampling (traditional sampling by cylindrical cores), or the fact that the Escalar fault is no longer expressed in the Sigüés section. However, we note that on the Puigdefabregas (1975) map (Figure 92), a fault is mapped, which could be the expression of the Escalar fault. We have not clearly identified this fault along the route in continuity with the sampled outcrops. This latter explanation is plausible because relay zones are very common in thrusts whose strike is oblique to the transport di- rection, as indicated, in this

case by the obliquity between the E-W Leyre thrust and the NNW-SSE transport direction common to most sectors of the Pyrenees.

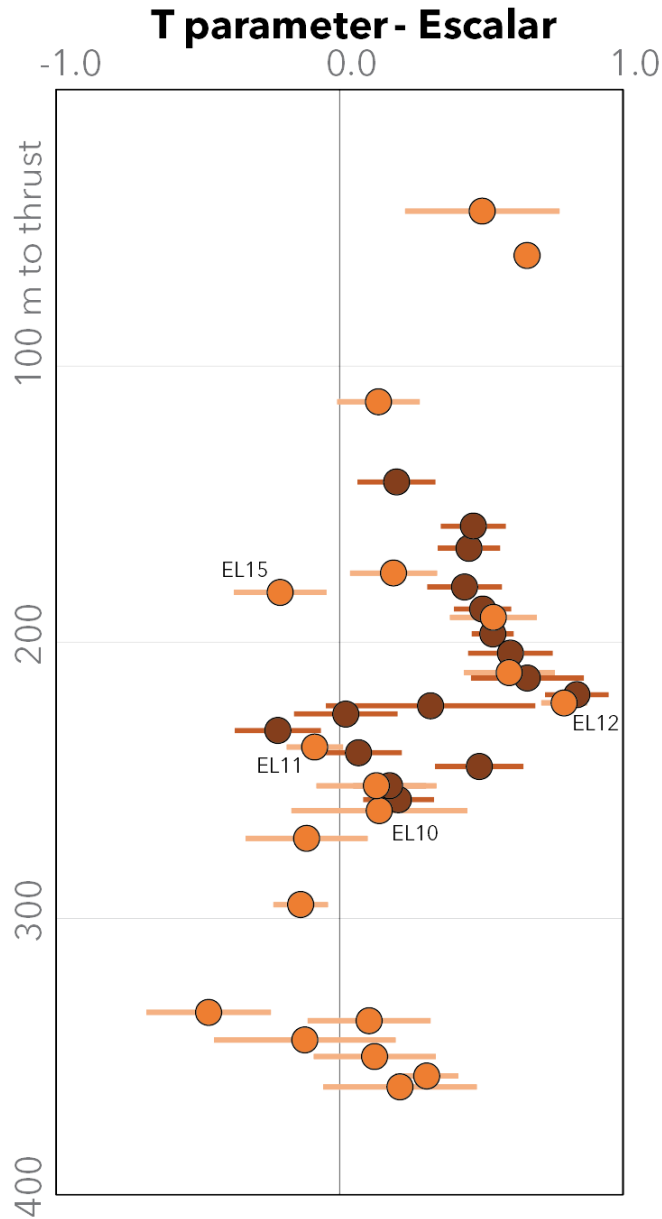


Figure 121: Addition of new data from new sampling points on the same transect. These new points are shown in dark brown, and are compared with the data published in Gracia-Puzo et al., 2021 in orange.

Following the publication of the article by Gracia-Puzo et al. (2021) and the elaboration of these interpretations, a new sampling campaign was undertaken with one main objective, to elucidate with high resolution this intermediate fault in the Escalar section, since a continuous outcrop was available from 270 m vertical distance to the fault to 110 m. This sampling could also demonstrate the continuity of the vertical evolution of the magnetic fabric.

Thus, Figure 121 shows a modification of the vertical scheme already presented in Figure 120, and adds a new batch of 16 sampling sites spread over 115 m vertical distance to the fault, encompassing the point where this secondary Escalar fault was interpreted. These sites

CHAPTER 4 - SHALE FABRIC

are spaced between 4 and 15 m apart, offering much higher vertical resolution of the deformation evolution.

We note that:

- It is remarkable to see that the additional sampling confirms the trends already discussed. In the 230 m to 150 m range, there is a relatively gradual and noiseless decrease in the T parameter. EL15 is a possible outlier, as it displays a prolate shape. However, it can also be interpreted as a stage 3 marker.
- Between EL10 and EL12 (maximum oblate at 230 m) there is a peak of negative T-value, which develops in just 40 m vertical distance. EL11 is not an outlier, and re-sampling confirms this rapid evolution.
 - We have previously interpreted EL9 and EL10 as stage 4, but EL11 would be something close to fabric stage 3 (triaxial-prolate fabric with cleavage). This decrease in deformation means that there are two deformation peaks in the vicinity of this secondary fault, EL12 which we already knew, but also EL10, 260 m from the main fault, approx.

Therefore, there are two possible interpretations: either there is a branch of the Escalar blind fault on the footwall of the Leyre fault, which is expressed in another deformation peak, although less intense, 30 m below the "main" peak. Or there is a mineralogical or sedimentary factor (e.g. some shale layers with a lithological assemblage), which would condition the tectonic fabric, making it less expressive.

In any case, the idea of the symmetrical "deformation shadow" that the Escalar fault would generate on the footwall of the Leyre thrust (shown in Figure 120), would not be so symmetrical around the deformation maximum. This sampling, with a smaller spacing between the points measured in AMS, has shown us that although the previous sampling was largely representative, local variations can occur.

Finally, returning to the Gracia-Puzo et al. (2021) article, we considered deformation under a 3D perspective (Figure 122), a lateral decrease is observed related to the thickness of the damage zones associated with both the Leyre and Escalar thrusts (30 m in the Esco profile). The propagation of the latter fault would rapidly diminish towards the west since only stage 3 is observed on the Esco profile. The two virtual profiles provide a first mapping of the deformation induced by the Leyre thrust and the newly identified Escalar thrust.

CHAPTER 4 - SHALE FABRIC

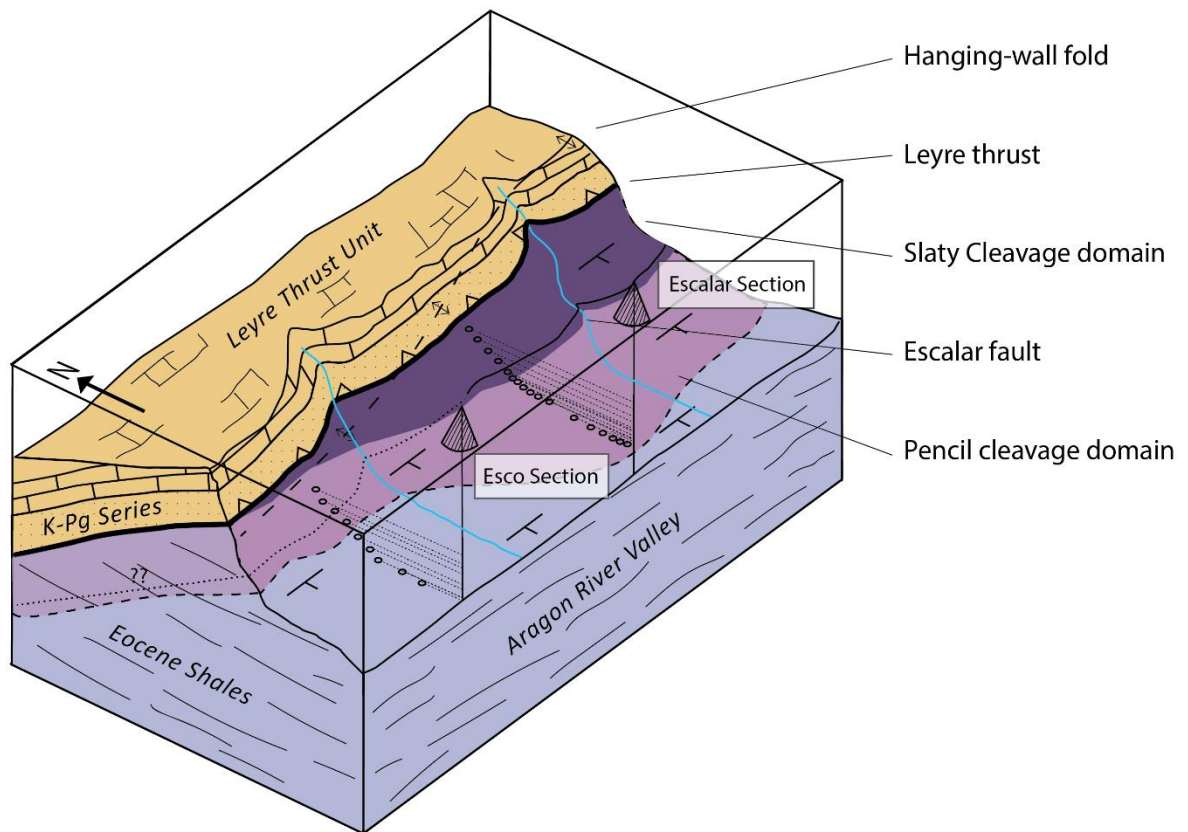


Figure 122: Block-Diagram for the Leyre thrust and the structures in its footwall (not at scale). Dots represent sampling sites. Domains of pencil cleavage (pale violet) and slaty cleavage (strong purple) are indicated. The newly found Escalar thrust is represented.

This map is a figure that was published in Gracia-Puzo et al. (2021) and represents classical geological mapping, constructed from field visits and observation of outcrops. However, throughout this thesis, and thanks to the extended sampling in the Leyre thrust footwall, not only in the two transects presented in the paper, it was possible to propose an improved quantification of the deformation, added in section 4.4. Strain quantification at the Sigüés site.

Firstly, however, we present another data acquisition related to the shale fabrics.

4.4. Strain quantification at the Sigüés site

Previous chapters have presented how the measurement of magnetic fabrics could be used to quantify strain. In general, the use of this methodology poses an important advantage, and could be used to extend strain measurements over large areas, beyond point boreholes.

Several authors (Borradaile, 1991; Kneen, 1976; Parés and van der Pluijm, 2004b; Wood et al., 1976) have proposed the use of scalar parameters to correlate the fabric with strain (T-parameter, Pj-parameter), although it has also been discussed how correlations between these results and strain may be unreliable outside the specifically analysed regions. Precisely, we are using a method previously presented by Humbert et al. (2014) that has already been used in this same geological environment (Boiron et al., 2020).

This method is based on the use of the eigenvalues of the AMS tensor to estimate the ductile horizontal strain. Humbert et al. (2014) stress that sedimentary rocks rich in detrital clays are the main subject of their calculation proposal. Based on the rigid rotation model of March (1932), two issues need to be assessed: 1) the carrier of the magnetic signal measured in AMS are flat particles and 2) the flat particles respond to LPS by crenulation, their magnetic susceptibility axes being rotated.

X-Ray diffraction show that the clay assemblage is largely dominated by illite, with some chlorite. This assemblage is typical of buried shales such as those exposed at Sigüés. Besides, the rock mag studies show a very high dominance of paramagnetism (90-99%) linked to this phyllosilicate (Figure 99). Therefore, it can be stated that AMS is a proxy to the clay fabric. On the other hand, there is the question of rigid rotation, an issue appreciated by Saur (2022) who interprets that particles rotate rigidly in a similar way to quartz.

In attempts to quantify finite deformation using AMS, the Lehigh Gap study (see section 2.4 The Lehigh Gap, a classical shale-to-slates transition), showed how much the question of rigid rotation or crystallization of clays had to be asked. If crystallization phenomena dominate, March's model cannot be applied (Ho et al., 1995). In shale diagenesis, the illite-smectite transformation is well understood and there is little doubt that the illites at Sigüés are authigenic. However, the important point is the timing of illitization relative to deformation.

If illitization occurs during deformation, March's model should not work well. For example, Saur et al. (2020) show that calcites rapidly reorient parallel to pencil cleavage by solution pressure phenomena, whereas quartz on average remains controlled by bedding.

If illitization takes place before deformation, these particles can be expected to act as rigid particles. Boiron et al. (2020) in finding deformation gradient consistent with field observations, seem to favour the dominance of rigid particle rotation. SEM image observations show that illites in the slaty cleavage zone are oriented at 90° to each other, supporting particle rotation. Finally, the illite fabric in the most deformed zones shows a pole between bedding and cleavage, indicating that a fraction of illite is still controlled by cleavage. If illites crystallize during deformation, they should be largely controlled by cleavage.

CHAPTER 4 - SHALE FABRIC

It has been already presented in section 2.3.7 AMS as a strain gouge, conditions of use. the development of the formula for calculating the horizontal incremental strain (dl/l also expressed as % shortening) equivalent to the shortening, using the eigenvalues K_1 and K_3 .

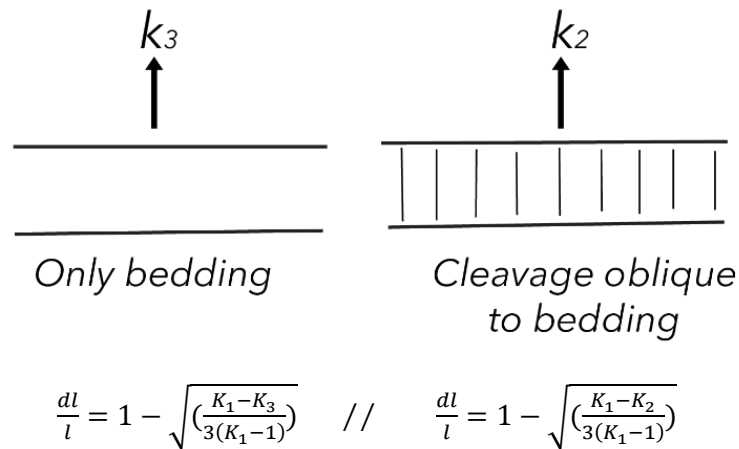


Figure 123: The two end-members of the fabric configuration in shales for the calculation of the shortening through the formulas of Humbert et al. (2014). To the left we find end-member 1 (k_3 is vertical) and to the right we find end-member 2 (k_2 is vertical) after Boiron et al. (2020)

Developing this first formula, Boiron et al. (2020) proposes a second situation, which would be another end-member to calculate the lateral shortening. The original option would be useful when the K_3 axes are vertical, i.e. perpendicular to bedding. This can be used for those sites where we do not see deformation in the outcrops, and are interpreted as setage 1 or stage 2 fabrics (Figure 115). A different situation occurs when the K_2 axes are vertical (in Boiron's article, these fabrics appear close to the cleavage front at 440 m of lateral distance to the fault), which in our case would correspond to outcrops with clear pencil cleavage, and stage 3, 4 or 5 in the gradient of fabrics.

Figure 124 shows the Jelinek P-T diagram of Sigüés data published by Boiron et al. (2020). It shows the same trend as that presented in our article (Gracia-Puzo et al., 2021 and data from Figure 116, Figure 117 and Figure 118). Figure 125A shows the evolution of parameter T as a function of horizontal distance from the fault. It can be seen that the most prolate stage is approximately 440 m from the fault. Beyond this point, as we enter the slaty cleavage domain, the T parameter becomes oblate again, with some instability. Note that this diagram excludes samples located in the footwall syncline, with bedding almost parallel to the cleavage.

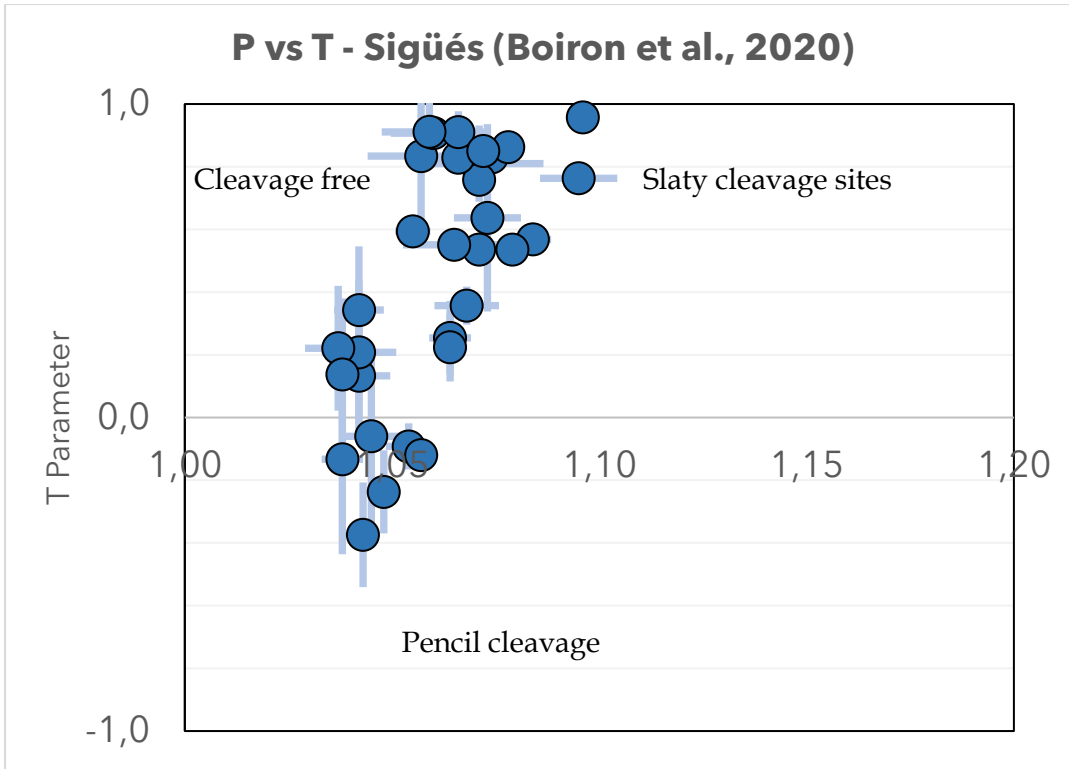


Figure 124: Jelinek diagram of Sigüés transect data from Boiron et al. (2020).

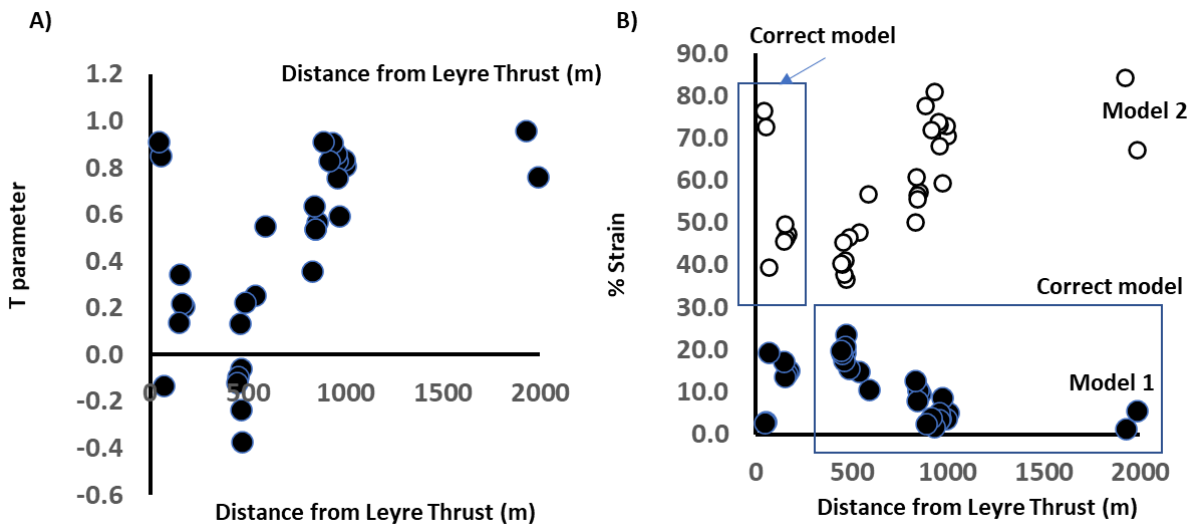


Figure 125: A) Shape parameter T versus distance from the Leyre thrust ($x=0$). B) Strain derived from AMS measurements ($\%strain = 100 (dl/l)$). Black (open) symbols: model 1 (2). All data from Boiron et al. (2020)

Figure 125B shows the application of both models 1 and 2 in this strain gradient context. Here, the strain is

$$\%_{strain} = 100 \left(\frac{dl}{l} \right)$$

If only model 1 is used, the strain does not exceed 30%, which is not realistic with field observations. If only model 2 is used, the deformation is $>40\%$, which is of course unrealistic

CHAPTER 4 - SHALE FABRIC

in areas where no cleavage is observed. So, we have to work with both models. In the path from the oblate (cleavage-free) to the prolate stage, model 1 is applied. In this case, it is possible to observe a gradient ranging from a few % to ~25% in the most prolate stage. In the second path, prolate to oblate, deformation ranges from ~40% to ~80%. In other words, the choice of model 1 over model 2 is due to the fact that the clay fabric tends to be predominantly controlled by cleavage. We can therefore see that the application of model 1 or 2 requires an idea of the deformation gradient. Note that the gradient illustrated and published in Boiron et al. (2020) is consistent with that which would be expected in a Trishear-type mechanism during fault propagation (Hardy and Allmendinger, 2011).

Therefore, with the eigenvalues already arranged, the boundary between both end-members was chosen for each transect, applying in consequence the first or the second formulae. The fundamental criterion of “cleavage front” is the occurrence of stage 3 fabrics, and the observation of pencil cleavage in the field outcrops.

With these criteria we can calculate the % of strain values for the two transects presented in the article (Gracia-puzo et al., 2021) (see Figure 120). Projecting the data into the virtual borehole, the results would be as follows:

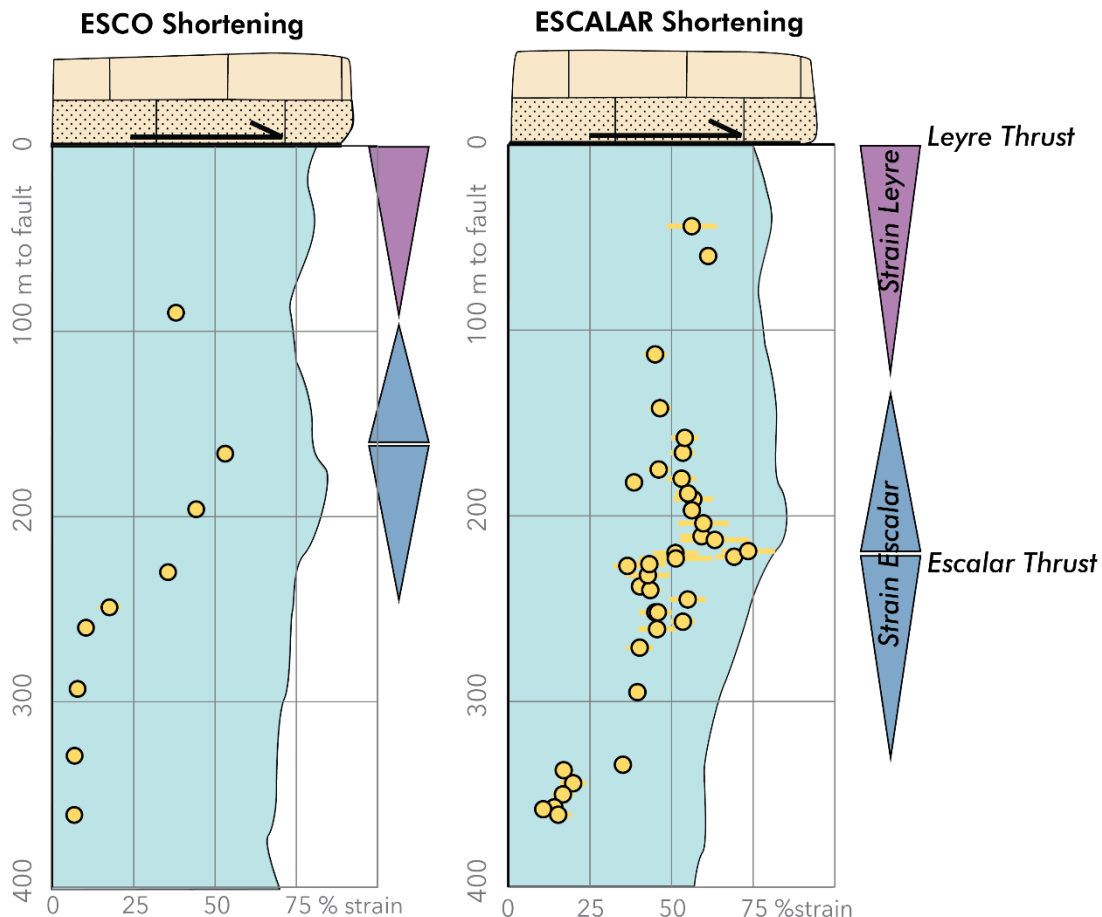


Figure 126: Modification of Figure 120 when the calculated shortening (dl/l) is plotted. The deformed thickness in both sections does not vary if compared to the T parameter vertical section, but the geometry and intensity is slightly different.

The Figure 126 shows a rather similar evolution to the T parameter presented in Figure 120. This indicates that this parameter is also relevant when studying its deformation, although it

CHAPTER 4 - SHALE FABRIC

is also more difficult to read because one oblate value can mean two different things from shale fabrics.

For Esco, the lower part of the profile shows very little deformation (%strain<10%). This increases rapidly at a distance of 230 m from the Leyre thrust, reaching a value of the order of ~50% at ~180 m. For the Escalar section, the deformation footprint is different. At the base of the section, deformation is a bit more pronounced than Escó (10-20%), but increases significantly to a peak of ~75% at 220 m from the Leyre thrust. Then, the rest of the upper section shows 45-60% of strain. Both cross-sections therefore suggest greater deformation ~200 m from the Leyre fault, which we interpreted in our article as the existence of a blind secondary fault; the Escalar fault.

The rest of the sampling transects are plotted in Figure 127, in which the vertical evolution of the deformation can be analysed. In the westernmost sector of our cross-sections, the Leyre section shows little footwall deformation (<15%) up to 80 m from the Leyre thrust (Figure 127). Close to the fault trace, the marls show slaty cleavage and maximum deformation close to 50%.

The Llarto transect (Figure 127) shows a first increasing deformation gradient from a vertical distance of 300 m. At ~300 m, several sites show deformation ~20%. But from 200 m, deformation becomes more significant (~50%) and the calculation results are stable for the rest of the vertical section.

For both the San Juan and La Paul sections (named as San Juan in Figure 127), sampling was carried out 200 m from the Leyre fault. Also a strain gradient is detected, as lower sites show ~20% and from 120 m strain is > 50%

For Sigüés B, a shortening band showing >40% in the last 20 m along the fault is calculated. Nevertheless, as we have explained, this transect presented the dilemma of using one of the two endmembers of the formulas even though the observed deformation did not coincide with the threshold used, which could lead to an over-calculation of the deformation in case of using the End-Member linked to the cleavage front. On the east side of the Escá river, in the Sigüés B and Orba transects, it poses a problem, because of the non-appearance of stage 3 fabrics in these sampling sections and the eigenvalue data available. Considering the cleavage front at 440 m horizontal distance as Boiron et al. (2020) did, with our fabric data implies obtaining shortenings of >80% in areas far from the fault, which does not correspond to the marl appearance what we observed. Therefore, we decided to consider the cleavage front at 100 m horizontal distance from the main fault, in the sites where there are outcrops with obvious cleavage, both in the Sigüés B and the Orba transects.

For the Orba section, which is the most easterly of the cross-sections (Figure 127) in the footwall of the Orba thrust, we find relatively low deformation (<10%) up to 100 m from the fault. The last two sampling sites, strain is ~50%.

CHAPTER 4 - SHALE FABRIC

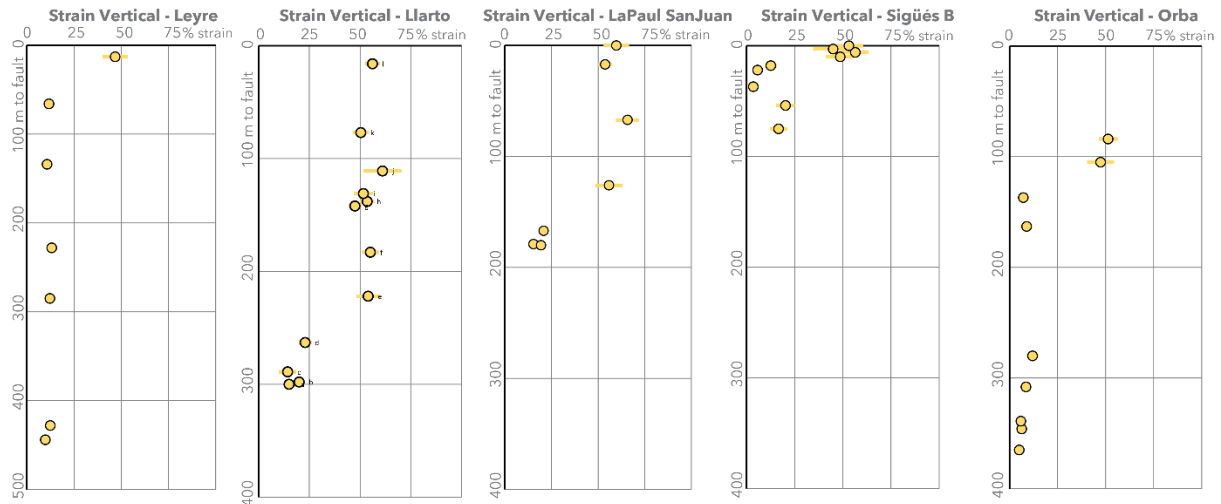


Figure 127: Vertical sections as the ones shown in Figure 113 and Figure 114 in this case showing the calculated d/l shortenings for each sampling site in the remaining five sections of the Sigüés site

To summarize the various cross-sections studied, we note:

- ✓ The cleavage-free zone shows deformations <15%. This low deformation would be linked to the general Layer Parallel Shortening in the Jaca Basin.
- ✓ The zone less than 100 m from the fault shows deformation of 50%-60%. This deformation, as we will discuss later, would be linked to Leyre-Orba thrust propagation. Note that this intense deformation, marked in the field by slaty cleavage, is visible from the westernmost structure (Leyre section) to the easternmost structure (Orba section).
- ✓ For the intermediate zones, we note several results and vertical data evolutions. Which are either related to blind faults (Escalar section, Esco, Llarto...) or to a single gradient distribution of strain (La Paul, Sigüés, Orba)
- ✓ In the Escalar section, the deformation generated by the blind fault is relatively symmetrical to the maximum recorded. This implies that both the footwall and the hanging-wall of the fault are deformed.

With the precedent of calculating deformation on a single transect, which provides a linear graph, the sampling carried out in this thesis made it possible to extend the graph and construct a 2-D map with shortening calculations for a small region of a ~12 km² in area.

The map in Figure 128 is produced with the Surfer v16 software, and the choice is made to produce a contour map, calculating the levels of interpolation between points with the kriging method.

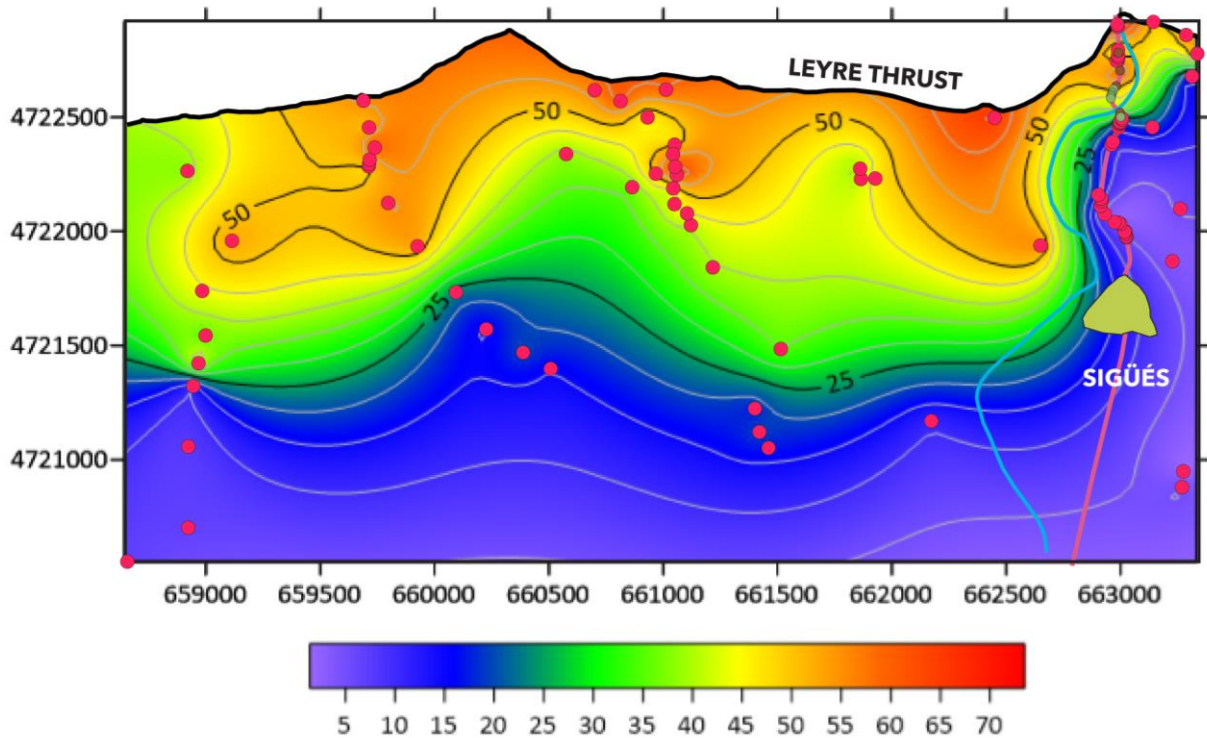


Figure 128: Interpolation map of shortening data calculated from the sampling sites of the footwall of the Leyre thrust.

A main result after using this data processing methodology is to underline the dimensions of the cleavage front on the right bank of the Escá river and the surface that has been covered to the west. The Leyre thrust has produced an important deformation zone in this region, up to 300 m thick in a vertical section, with a frontal extension of up to 1100 m at its widest points. This cleavage-affected surface in the footwall has already been described in section 3.3. Sampling of shales, but now with this methodology it is possible to map accurately areas of several square kilometres from an extensive sampling campaign.

The calculation of shortening for the footwall of this thrust can help to visualise geometric features that transcend conventional geological mapping. On the one hand, it is worth noting the along strike difference in the mapped zone. The ambiguity in the choice of the shortening calculation in the Sigüés B section appears on the map as a “blue” gap, indicating lower shortening values for the east zone. We have decided not to include the Orba section in Figure 128 due to the poor quality of the interpolation calculation, as the sampling sites are far apart and produce artefacts in the intermediate zone between Orba and Sigüés B.

Besides that, we observe that the deformation zone in the footwall of the Leyre fault is heterogeneous. There is not a single, smooth gradient, but within the cleavage front there are sites where there is punctually more %strain within the deformation zone (See Escalar section for example, Figure 121).

Despite this heterogeneity, a certain lateral banding parallel to Leyre thrust can be interpreted, and a shortening peak can be seen at a horizontal distance of about 600 m from the main thrust. It is possible to attribute peaks of the deformation to the shale-on-shale fault which appears in Escó, in a along strike position in relation to the Escalar blind thrust. The secondary fault at Llarto section, contradictorily, has no lateral continuity to the other two contiguous sections. This may be due to no sampling sites in the upper part of the Escó

section, or to the covering of this other secondary fault in the upper part of the Escalar transect.

4.5 Microtomography results

The use of this analysis technique in Sigüés has a background presented in the section 4.1.3 X Ray Microtomography observations.

4.5.1 XCT Technique

X-ray microtomography is an imaging technique, which uses the principle of attenuation of an X-ray emission through a sample. After passing through this material, the attenuated X-ray beam is converted into visible light and collected in a detector or camera. Acquisitions of this technique are usually made on millimetre-sized samples, and a multitude of photos are collected by rotating the sample through 360°. The set of these photos is used to reconstruct a 3D image in digital form using algorithms (see Saur's 2022 PhD thesis, Methodology section, for more details). These 3D digital images are composed of so-called voxels, which have an intensity value in grayscale. Those used in this thesis were calculated in 16 bits offering a spectrum of grey values from 0 to 65,535. This value attributed to each voxel is an expression of the attenuation coefficient of the components corresponding to the volume located in the photograph. Some references on XCT microtomography applied in geosciences are reviews such as Carlson (2006) and Hanna and Ketcham (2017), for various materials Baker et al. (2012) for igneous rocks, or the aforementioned Saur (2022) thesis for fine grained sedimentary rocks.

In the laboratory, marls fragment samples which had been previously measured for AMS were taken as a starting point. 2 mm thick and 4 mm high sample cylinders were drilled at the samples. In order to complete the petrographic study and to complete the microtomography, thin sections were prepared on other fragments sampled from the same sites (Figure 130).

It is worth mentioning that since the fragments have not been oriented, the data relating to the microtomography and microfabric observations should be interpreted in sample coordinate only. The vertical axis on which the fragments measured in AMS and the drilling of the XCT sample have been performed in the same way. However, the horizontal plane of the core is different when the XCT data is acquired.

The two XCT scans were carried out at the DMEX laboratory of the UPPA (Pau, France). A Zeiss Xradia Versa 510 X-ray tomograph was used. This tomograph can obtain high resolution images thanks to the optical magnification and geometry, acquiring radiographs with 2,048² pixels. This apparatus uses an XRM Reconstructor (Zeiss, version 11) which makes it possible to obtain a stack of horizontal sections of the fragment analysed, reconstructed from the frontal X-rays taken of the sample. Thus, a digital volume is formed, in which the voxels have a size of 2 microns, programmed before the acquisition of images for these two samples. Images are subsequently processed with Avizo software (FEI, Version 9.0.0.). The software processing followed to obtain the fabric results include the following steps.

CHAPTER 4 - SHALE FABRIC

The software performs its measurements on a cubic Volume of Interest. In our case we chose the cube of maximum possible volume in the cylinder with no irregularities on its faces or corners, approximately 1.2 mm³.

Subsequently, the X-ray images are treated by various processes. Firstly, an anisotropic diffusion filter is applied to separate the "noise" from the grey bands obtained, and focus on the part of the spectrum that corresponds to the observed matter.

Afterwards, the different mineral phases in the image are segmented. This is done by elucidating the grey bands that could correspond to the different phases, although it is possible to distinguish the type of phase by the geometry of the crystals observed in the photos. This was done with the help of Hugo Saur. Quartz, calcite, pores, and pyrite were separated. A homogeneous mass, which is not crystalline and corresponds to the matrix of the shales, which also contains micrite and phyllosilicates.

By separating these phases in the image stack, grains are therefore obtained for each phase (e.g. quartz grains at Figure 129). At a later stage, those grains that are tangential to the VOI limits are eliminated, since their shape is not complete and could mislead the analysis of their parameters. Very small grains, less than 12 voxels in size, whose shape could also induce large errors, are also eliminated, thus focusing on detrital grains (Saur et al., 2021). The size for this threshold is chosen manually in order to reduce noise but without removing too many grains from the subsequent statistical analysis.

Afterwards, each grain is labelled and geometrically characterised, so the inertia tensor method is used to carry out analyses for the individual grains.

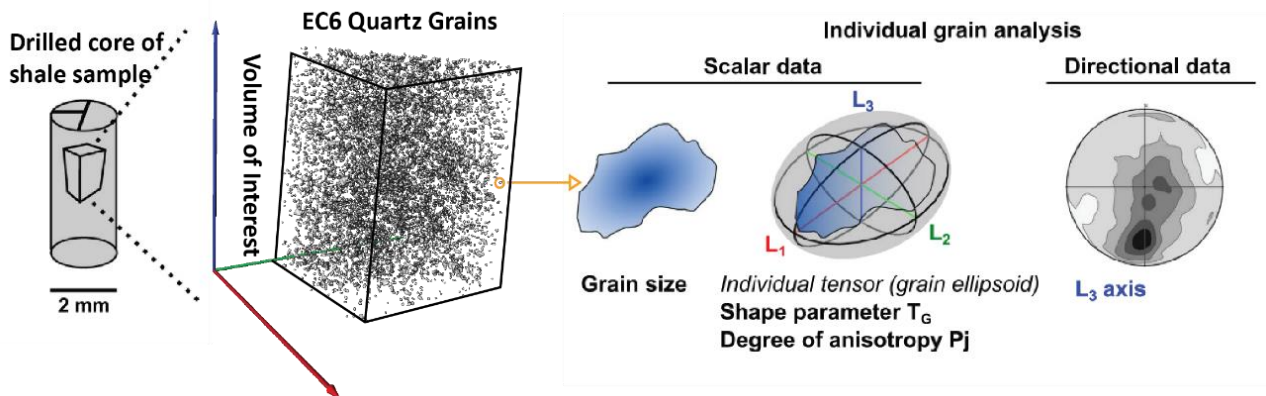


Figure 129: Summary scheme from 3D photos as in Figure 23 to the study of the grain fabric from image processing and statistics. Modified from Saur et al. (2021).

For this reason, the Aviso software allows the construction of a best-fit ellipsoid using second order moments. The inertia tensor of each grain is expressed with the central moments as follows:

$$M_2 = \begin{pmatrix} M_{2,0,0} & M_{1,1,0} & M_{1,0,1} \\ M_{1,1,0} & M_{0,2,0} & M_{0,1,1} \\ M_{1,0,1} & M_{0,1,1} & M_{0,0,2} \end{pmatrix}$$

Equation 26

And the generic expression of the central moments of given $m + n + p$ is:

$$M_{m,n,p} = \frac{1}{V} \sum_i (x_i - x_c)^m (y_i - y_c)^n (z_i - z_c)^p$$

Equation 27

Where V is the volume of the grain, x_i , y_i and z_i are the coordinates of the voxels belonging to the studied grain, and x_c , y_c and z_c correspond to the centre of mass of the same grain. Thus, a best-fit ellipsoid is calculated assuming three orthogonal directions with their respective magnitudes (the eigenvalues $L1 \geq L2 \geq L3$)

This is the information that allows access to statistical calculations on the grain fabric of a shale sample. In this chapter, we will present these results, which are the ones that have been worked on throughout this thesis. Nevertheless, Hugo Saur's thesis (2022) demonstrates the enormous potential of data acquisition from the microtomography of a rock sample. Following this image processing process up to this point, it is possible to develop other analyses, beyond the grain fabric.

In Saur (2022), two methodologies are proposed for the study of the fabric: the analysis of subvolumes within the same sample, and a discussion on the representativeness of the VOI (Volume of Interest) chosen to study a sample; on top on, other statistical studies on frequency and grain size. In this thesis, microtomography is restricted to the study of the grain fabric of those mineral phases of the shales that are masked by AMS due to their magnetic characteristics.

4.5.2 Results

The series of photos presented in Figure 130 present the microscale architecture of the shales that have been studied throughout this thesis.

We see optical microscope images belonging to 5 thin-section samples. Two sites show no evidence of cleavage (EC1 and Orba 1). Samples EC6 and Llarto A show pencil cleavage. Site EL-12 shows slaty cleavage.

The brown colour corresponds to a fine-grained matrix corresponding to the micrite and clays that compose most of the samples studied. Occasionally, micrometric-sized grains of quartz and calcite appear. In the case of cleavage-free samples, bedding is very loosely defined by the elongation of certain minerals. However, no traces of dissolution are visible, particularly on the fossils present. In the pencil cleavage samples, some fracturing is occasionally observed (see Llarto A in Figure 130f). A foliation is observed in slaty cleavage EL 12 sample (Figure 130g). Figure 130h shows how pressure-dissolution processes occur in the calcite grains of the slaty cleavage sample, as is the case of this foraminifera dissolved by half according to the foliation that appears in the sample.

CHAPTER 4 - SHALE FABRIC

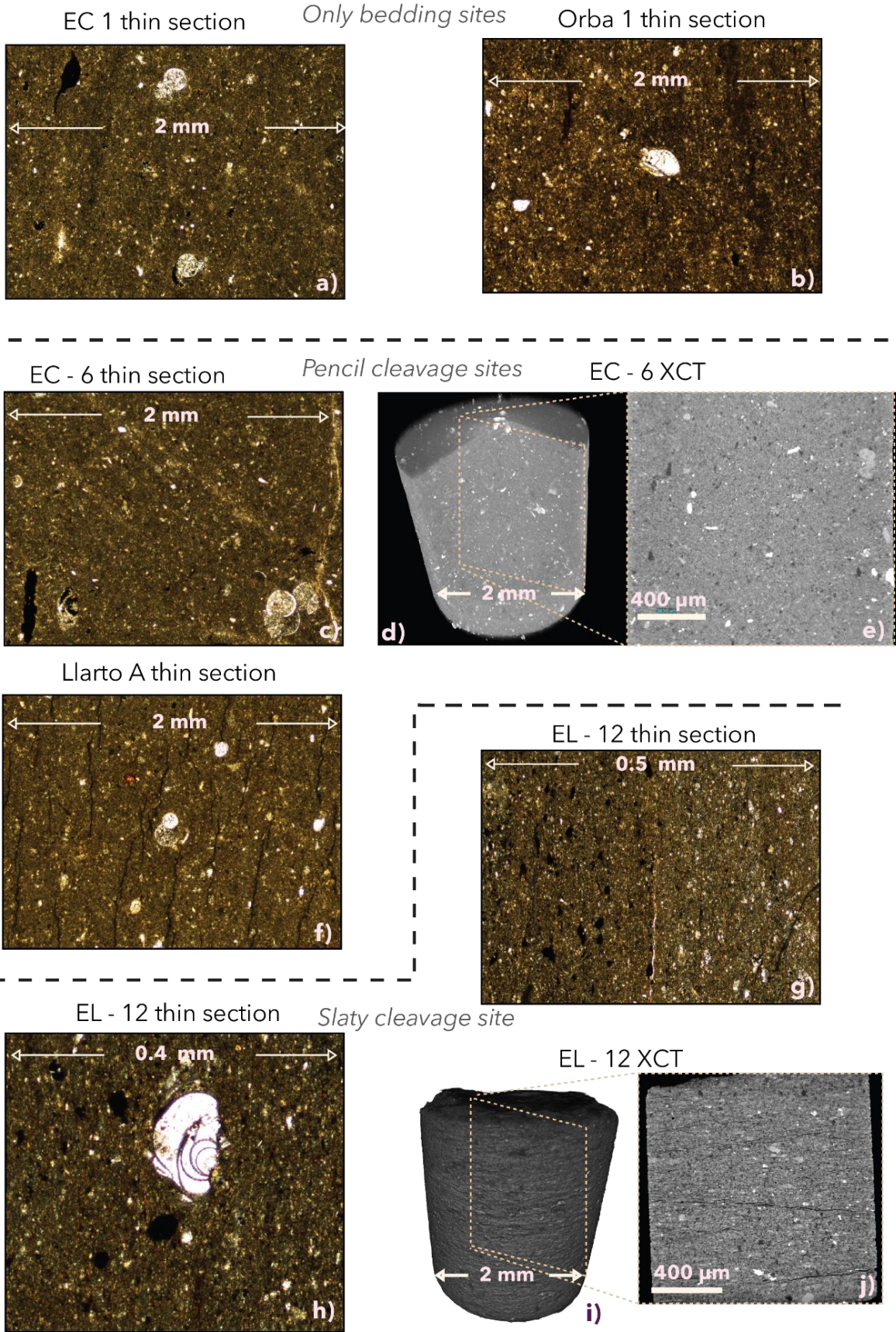


Figure 130: Several examples of thin sections obtained from marls taken at the sampling sites analysed. At the top (a and b) are marls from sites without cleavage, only with bedding. In the middle part (c and f) they belong to sites with pencil

CHAPTER 4 - SHALE FABRIC

cleavage. From EC-6 an XCT scan has been performed (d and e). In the lower part, we have images (g and h) of a sample from a site with slaty cleavage, which has also been imaged by XCT (i and j).

One fragment from site Escalar 12 (EL12, fragment 17) was selected because this site is one of the most deformed marls encountered in this study. Fragments have the most oblate and anisotropic fabric of all the sites. The confidence angle E23 is also very small ($<3^\circ$). In addition, slaty cleavage has been observed. Site EL12 therefore corresponds to a highly deformed state. This outcrop is coincident with a secondary fault in the Leyre Thrust footwall (See section 3.3. Sampling of shales) . The thin section (Figure 130g and h) shows intense foliation in the matrix. One fossil shows a beautiful pressure solution zone. The XCT shows foliation with a spacing of the order of tens of μm . These observations confirm the presence of a slaty cleavage zone where the sample was collected.

One fragment from site Esco 6 (EC6, fragment 12) has the most prolate AMS fabric ($T < 0$) among studied sites (see Figure 113). The confidence angles E23 have a mean value of $\sim 13^\circ$, typical of samples where there is a competitive fabric between a bedding and a cleavage. This outcrop is characterised by a pencil cleavage, spaced 0.5 cm. On examination of the thin section (Figure 130c) the fabric shows no clearly defined planes. The matrix is micritic, with a few millimetric microfossils.

It should be pointed out that XCT measurements are presented in the sample frame, which may be slightly different from the sample frame for which the fragment was studied in AMS.

For each of these two XCT acquisition, grey bands have been segmented from the X-ray image for the calcite, quartz, pores and pyrites. The micrite and clays which form a large part of the matrix cannot be segmented at the scale of observation (voxel = 2 μm)

For sample EL12, fragment 17 (see Figure 131) we observe:

- (i) calcite grains, which show a well-defined sub-horizontal fabric (maximum density ~ 9 for L3)
- (ii) Quartz and pyrite grains show a similar structure to calcite, but with less spatial organization of L3 (maximum density < 5). Particularly noteworthy is the slight garland-like dispersion of pyrites.

For this highly deformed sample, the illite (AMS) and quartz, calcite and pyrite fabrics are very comparable, and largely controlled by slaty cleavage. It should be noted, however, that in the case of pyrites, there may be still be some residual competition between bedding (vertical in the sample frame) and cleavage (horizontal in this frame).

CHAPTER 4 - SHALE FABRIC

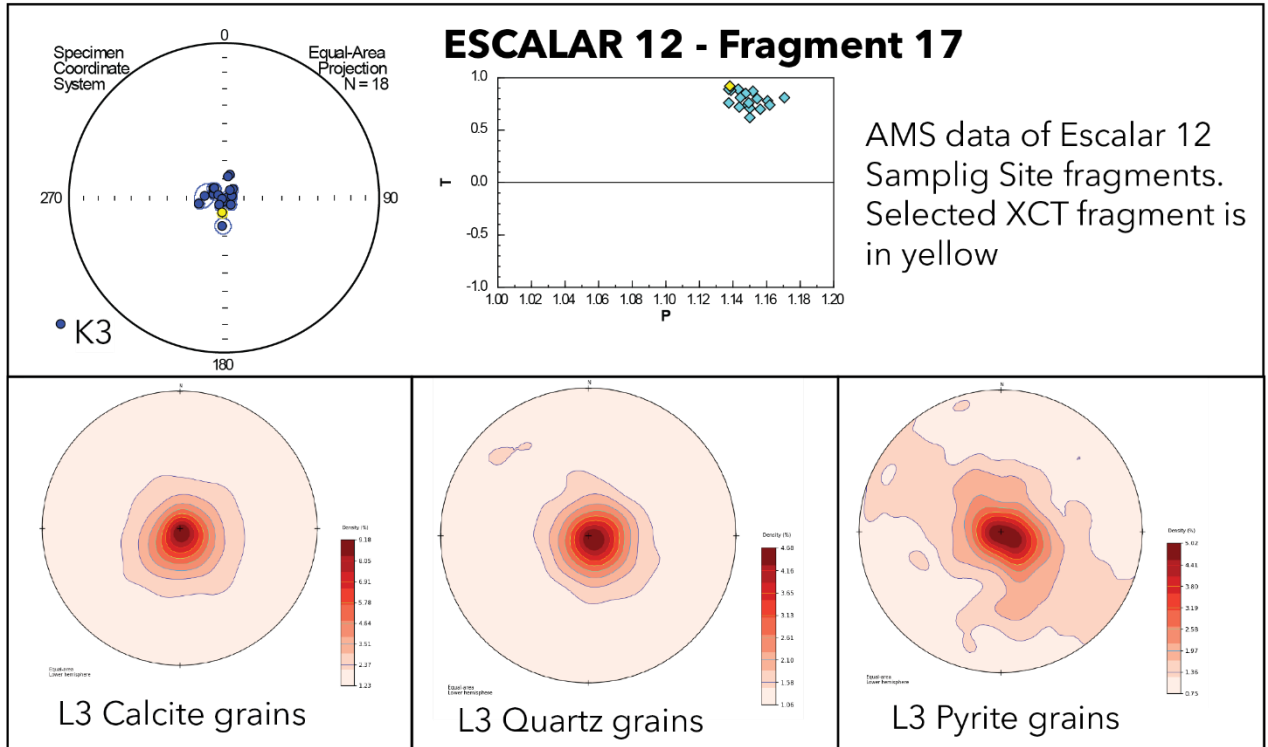


Figure 131: Results for fragment 17 of site EL12. In the upper half we see the scalar parameters P , T and $E23$ of the magnetic fabric of this fragment highlighted in yellow together with the rest of the fragments from the same sampling site. In the lower half, stereoplots display density contours for the L3 of the grains of each mineral component.

For sample EC6#12 (Figure 132), the mineral grain fabrics vary from each other. Overall, the spatial organization of the small L3 inertia tensor axes is more dispersed than for sample EL12#17 (maximum density < 3). The quartz fabric coincides with the pyrite fabric. On the other hand, the L3s of calcite grains show an orientation practically perpendicular to the L3s of quartz and pyrites. Saur et al (2020) observed the same behaviour in the pencil cleavage domain in the marls of the Sigüés section. They observed that quartz is controlled by bedding, while calcite is controlled by cleavage. In this area of pencil cleavage, the highly effective solution pressure in calcites results in an early preferential orientation controlled by cleavage.

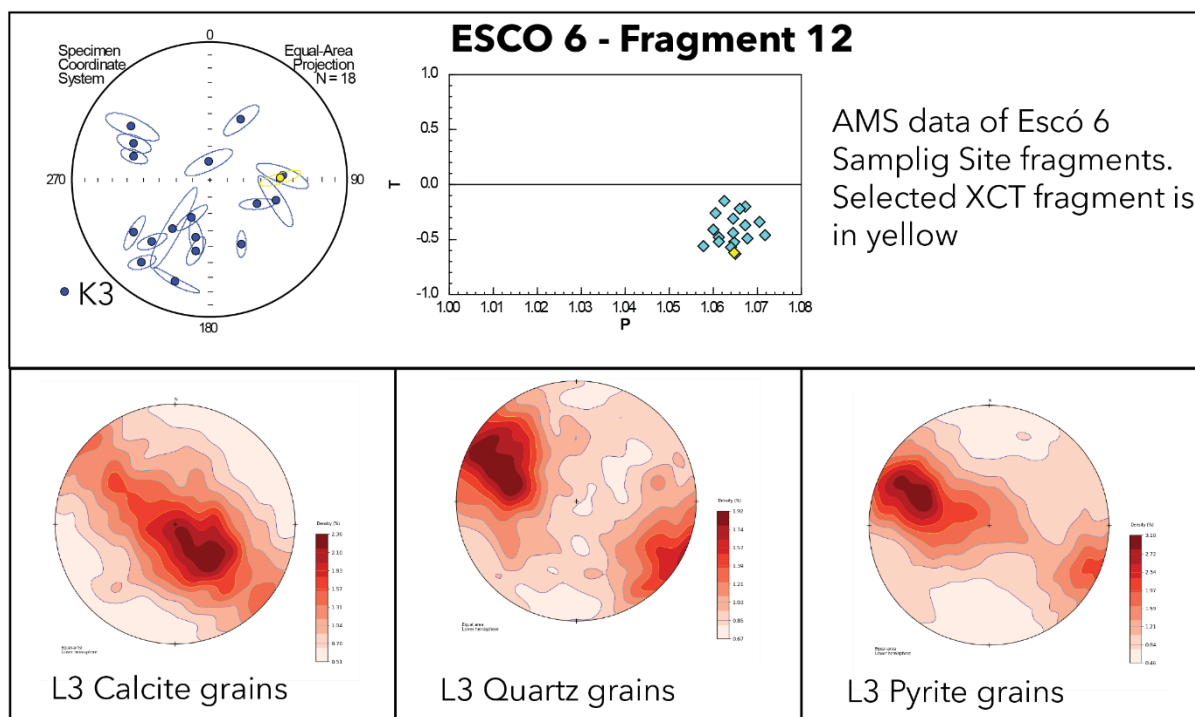


Figure 132: Results for fragment 12 from site EC6. In the upper half we see the scalar parameters P , T and $E23$ of the magnetic fabric of this fragment highlighted in yellow together with the rest of the fragments from the same sampling site. Besides, a stereoplot with the L3 calculated for the pores detected in the sample is shown. At the bottom, we have stereoplots showing density contours for the L3 of the grains of each mineral component. Note that the orientation of the L3 axes is in a sample frame of reference, not a geographical one. The L3 and K3 frames are not comparable.

These multimodal fabrics could be explained by resorting to the study of Saur et al. (2020) where the authors already highlight this difference in behaviour between the mineral components, as explained in 4.1.3 X Ray Microtomography observations. Saur et al. (2020) raise this situation as a similar situation in the fragment A-3 is detected, being a fragment also sampled in the pencil cleavage domain of the Sigüés transect. In this previous case, the authors present their results from oriented samples, thus correlating the calcite grain fabric with the occurrence of cleavage fracturing in these pencil-type outcrops where this component appears "rotated" with respect to the rest. The orientation of the L3 of the other mineral components corresponds to the pole of the stratification.

This situation corresponds to the high chemical mobility of calcite (Gratier et al., 2013) for burial conditions similar to those expected at this site (Izquierdo-Llavall et al., 2013 and further new RSCM data in section 5.2 Additional RSCM and Rock-Eval data.). Our Raman data allow us to estimate a temperature $\sim 180^{\circ}\text{C}$. In this temperature range, it has been shown that the dissolution-pressure of calcites is much higher than that of quartz. This would be an argument to state that calcite recrystallises according to the cleavage geometry in the footwall of the Leyre thrust.

In short, these two samples reinforce the results proposed by Saur et al. (2020), and Saur (2022). The pencil cleavage corresponds to a "conflictive" fabric where each mineral component reacts differently to the strain, given its "intermediate" shortening condition. The

CHAPTER 4 - SHALE FABRIC

determination of bulk fabrics, as in the case of AMS, does not complete the characterisation of the internal architecture of these shales, as microtomography does in sample EC6.

On the other hand, sample EL12#17 shows in a case of penetrative slaty cleavage, how the shale fabric in the most deformed Sigüés sites comes to govern all the parameters, opening the door to interpret a very intense deformation, or cleavage formation conditions favourable to the rotation of all the mineral components.

Finally, this chapter continues by showing other sites in the region to answer interesting questions; could the footwall deformation zone develop in other similar geological settings?, what extent of deformation do we find?, what observations allow us to elucidate similar mechanisms and conditions? For this reason, some other outcrops have been visited and sampled in this thesis, the results of which can be found in next section

4.6. The Jaca thrust

After verifying the successful application of this sampling methodology at the Sigüés site, it was decided to test the technique in other outcrops with similar characteristics. As we have seen, the lithological characteristics and the conditions of finding a similar paramagnetic mineralogy made it necessary to look for rocks with high clay content.

Consequently, several nearby sites belonging to the Jaca Basin, with a relatively similar geological architecture were chosen for this purpose. In fact, these sites share a common structural position: they are sampled on the same thrust, the Jaca-Javierregay thrust, striking N110. This thrust puts in contact the Hecho group turbidites in the hanging-wall, with the (also Eocene) Larrés Fm. in the footwall for more than 40 km, from the Sierra de Illón in the W to the area around Jaca to the E. Only at its eastern end, in the area around Jaca, does the fault show similar lithologies in both walls, in this case the lower part of the Larrés Fm.

Much of the fault trace is recognizable on cartography (Figure 133), however, outcrops are scarce as they are usually covered. Therefore, it is in the vicinity of rivers where we find eroded slopes that expose this contact. In this thesis, we visited the Biniés site, which coincides with the Veral river crossing this contact; and also the Javierregay site, which coincides with the Aragón Subordán river. The Jaca site is also located near the Gas ravine, where a road slope has exposed a portion of shale rock where the fault zone can be recognised.

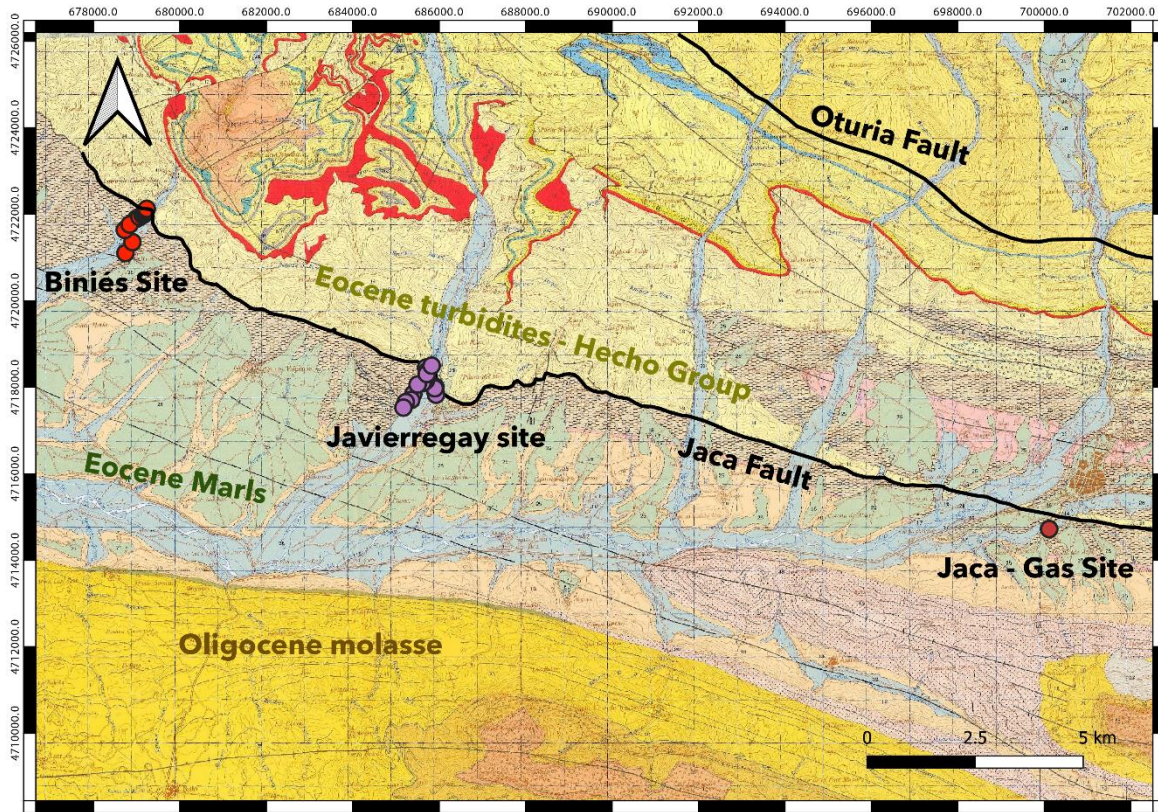


Figure 133: The three sampling zones are marked in this figure: the Biniés section to the west (red dots), the Javierregay section (purple dots) and the Jaca-Gas outcrop (brown dot).

4.6.2 Biniés site

The samples taken in Biniés generally correspond to the outcrops parallel to the A-1602 road, which runs parallel to the Veral river. In this case, the fieldwork was carried out in the reverse way: the thrust contact between the hanging-wall and the marls of the footwall was found, and from there the sample sites were progressively located towards the S. We interpret this thrust as the Jaca thrust, because its trace is aligned with the fault that other authors have described under the same name (de Rojas and Latorre, 1972; Labaume and Teixell, 2018; Teixell, 1994). Here we are about 30 km to the west, but from the cartographic point of view it is the same thrust.

The Hecho Group crops out in the hanging-wall of the thrust. It is composed of turbidites that are often folded, and a few hundred metres to the N there are even carbonate megabeds several tens of metres thick. In the footwall of the thrust lies the Larrés Fm., composed of Eocene Marls (Teixell, 1994), the same lithology found in Sigüés site.

CHAPTER 4 - SHALE FABRIC

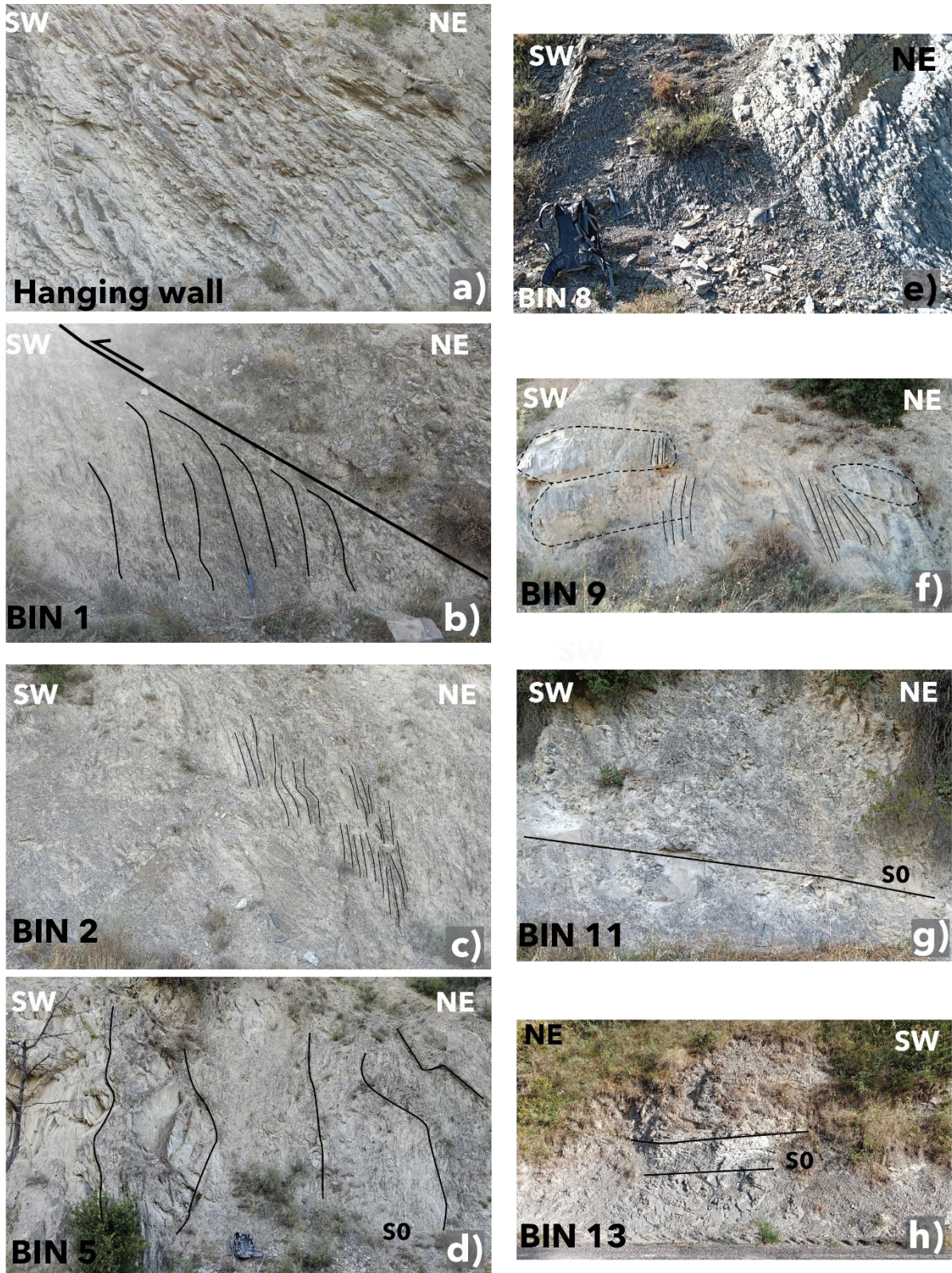


Figure 134: Several field photos of the footwall of the Jaca Thrust next to the A-1602 road.

In the hanging-wall of the Jaca thrust, the flysch belonging to the Hecho Group is observed. Cleavage is detected in the shaly strata (E layer of the Bouma sequence) of the turbidite, but not in the sandy layers (Figure 134a). Folds, of metric wavelength, are also visible towards the N, although they do not follow a consistent pattern.

CHAPTER 4 - SHALE FABRIC

The fault exposure (Figure 134b) shows a plane dipping about 25° to the north, and a shaly footwall with signs of intense shearing at a thickness of about 2 m. Cleavage in the footwall is slaty, penetrative, but is often folded or sheared, showing shifting orientation with dips of about 60°-90° to the N. A few metres to the south there are also subvertical, slightly warped calcite veins (Figure 134c). Bedding is not recognised in these shale outcrops.

At 60 m from the main thrust, subvertical beds are observed (Figure 134.4). Cleavage affects differently certain blocks with a higher clay content, being more penetrative in the latter. In general, it is less penetrative in the more calcareous layers.

Cleavage penetrativity and signs of shear start to diminish ~ 100 m away (horizontally) from the main thrust. Cleavage with intermediate morphology between pencil and slaty (Figure 134.5) appear in the marly outcrops. The marls are fractured, and appear as large boulders or discontinuous and curved beds (Figure 134f), probably indicative of sedimentary processes on the marine slope.

At a distance of ~250 m from the fault, the marls seem homogeneous and a more clayey character is observed (Figure 134g). The bedding is always difficult to distinguish, fractures appears on shales likely to pencil cleavage but it is not homogeneously distributed. The orientation of fracture planes is difficult to define. The sampling performed is less dense and more distance is covered. Signs of sub-horizontal bedding in marls do appear, and can be followed to outcrops more than 500 m far from the fault. The last sampling site, 900 m from the fault, consists of marls with fracturing difficult to distinguish from cleavage (Figure 134h).

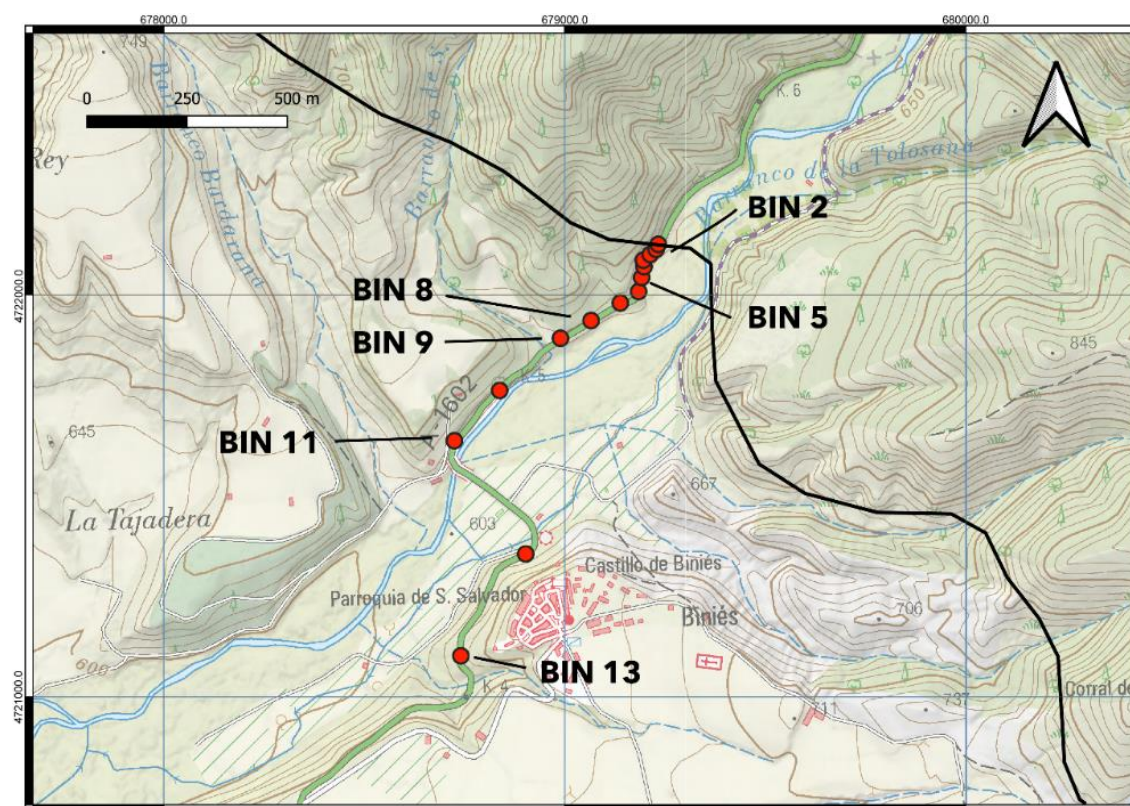


Figure 135: Detailed map of the sampling sites south of the Jaca thrust (solid black trace). The sites are numbered consecutively to the south. All outcrops correspond to the Pamplona Marls (Jaca n°176 sheet of the Geological Map of Spain, MAGNA-IGME).

CHAPTER 4 - SHALE FABRIC

Scalar data results

The methodology of sampling shales, sample preparation and measurement of non-oriented shale fragments is exactly the same as explained in previous section 4.2. The “sampling by fragments” approach. Fifteen shale fragments were prepared for each sampling site to obtain the mean results for the P parameter, T parameter and the E23 angle (plotted in Figure 136). We focus on these parameters in order to make observations on the evolution of the fabric in a simple way. The bulk susceptibility measured in the shale samples is very stable, between 144 and 147 SI, which are values close to those obtained in Sigüés site (Table 6: Summary of data for each sampling section).

The T parameter, as we have seen in the Sigüés area, is more sensitive to strain. In the first sites, at less than 100 m from the fault, T is slightly oblate (0.4-0.6). Then, it approaches triaxial values ($T \sim 0$) in sites Bin 7 to Bin 10. The oblate character is recovered from Bin 11 (450 m from the fault) and is clearer in Bin 12 ($T=0.7$). Finally, site Bin 13 is prolate $T = -0.2$.

The P parameter shows no clear evolution. On the one hand, the site next to the fault does not indicate high anisotropy despite the observed penetrative cleavage. Subsequently, the following sites up to 50 m south of the thrust do show a high anisotropy, ether. P values range from 1.10 to 1.11. In the more distant sites the anisotropy values range between 1.06 and 1.10. The highest values correspond with the more oblate shapes (site Bin 12), although this is not always the case.

The data is shown taking into account the lateral distance of the sampling site to the south with respect to the thrust, and also, were plotted using the Jelinek disposition P vs T . The results show how the sites could be comparable to the deformation states described on section 4.3.3. Data treatment and analysis of scalar parameters. As depicted by each of these parameters, there is no single evolution gradient, with sites intermingling regardless of their distance from the fault.

CHAPTER 4 - SHALE FABRIC

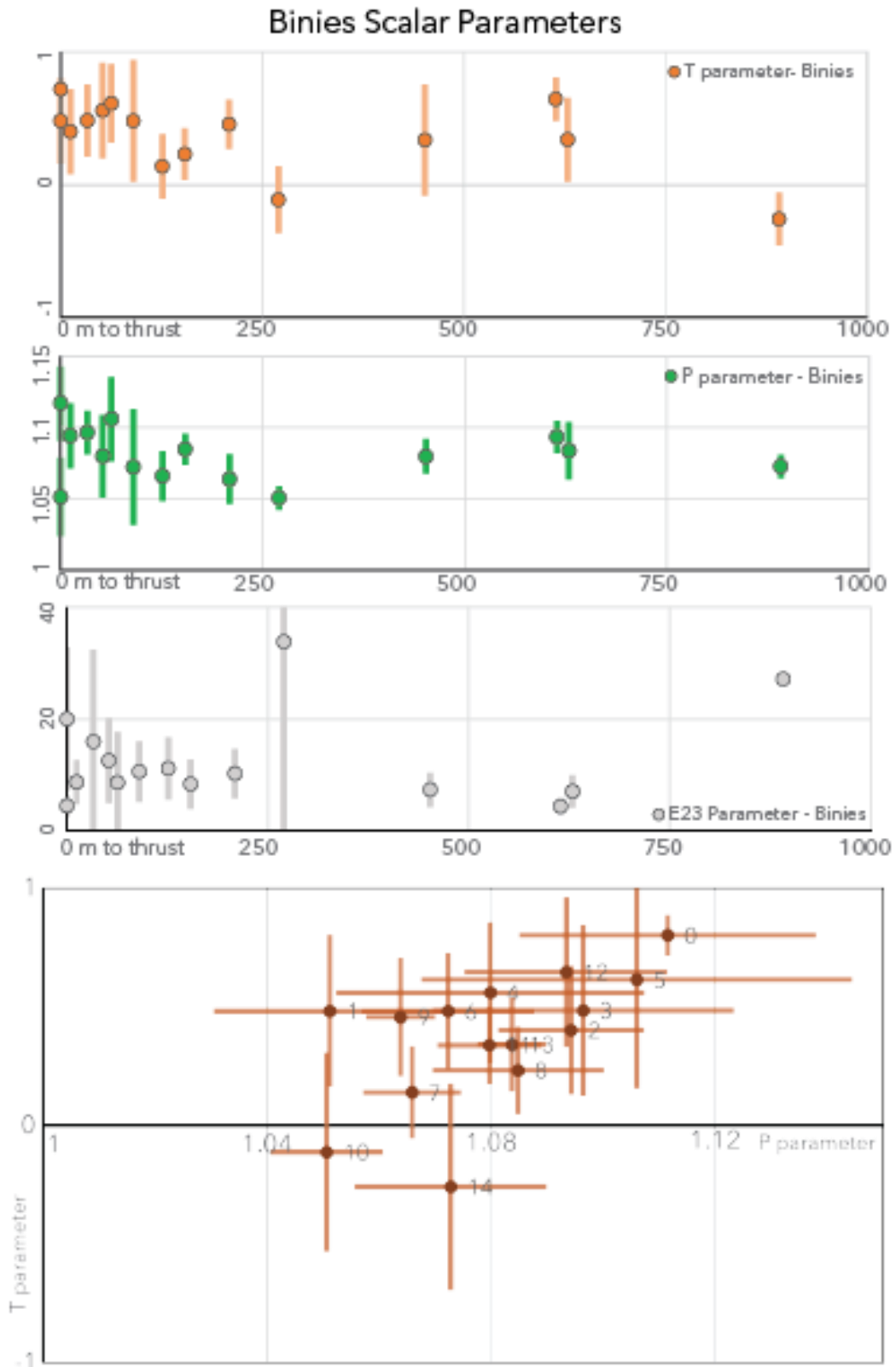


Figure 136: Scalar parameters from Biniés transect. Sampling sites go from 0 (on the fault) to 14 (furthest and southernmost from thrust). Below, the Jelinek diagram plots the P and T parameter data.

CHAPTER 4 - SHALE FABRIC

It could be interpreted that **state 1** is found at *sites 9, 11 and 12*, state 2 at *sites 7 and 8*, state 3 at *sites 10 and 14*, state 4 at *sites 2, 3 and 4* and state 5 at *sites 5 and 0*. However, the value of the P and T parameters are very variable, and the classification is difficult.

The confidence angle E23 with respect to the distance to the fault have also been plotted. The parameter E23, also visible in the confidence angles shown in the stereoplots (Figure 137), indicates that this angle is not very large over most of the transect. Indeed, it does not develop in parallel to other scalar parameters. For example, at site 1 we have high E23 angles ≈ 20 . Since slaty cleavage is the structure present in the site we would not expect so high an angle in relation to site 8, where $E23 \sim 9^\circ$ and a marked pencil cleavage is present. The characteristic relationship between high confidence angle and pencil cleavage fabrics is re-established at the last site where the scalar parameters corresponding to a pencil cleavage type fabric are accompanied by high confidence angles ($E23 \sim 28^\circ$) on average.

As a result, it is interpreted that there is a variability of deformed fabrics, ranging from types 4 / 5 in the first 50 m, towards stage 3 and stage 2 up to 300 m. This is perceived through the "competing fabrics", those in which the coexistence of deformational and sedimentary fabrics produces high confidence angles, triaxial shape parameters, and high anisotropies, as it occurs in sites 5 to 8. In general, with a greater or lesser degree of strain, these are expressed in almost all the transect, except in BIN 12, where there seems to be a clear sedimentary fabric, characterized by its oblate shape and low confidence angle E23 (Figure 137).

Site BIN 14, despite being far from the thrust, shows pencil cleavage-type fabric parameters with its E23 angle values indicating again a competition between two sub-fabrics. It seems likely that the sedimentary structures observed along the transect may have conditioned the way in which the fabric is detected, since the particles responsible for the signal may have different orientations. Pueyo-Anchuela et al. (2011b) suggest that the magnetic signal is defined very early in the basin history. Therefore, we would observe the appearance of cleavage on this heterogeneous sedimentary slope beds observed at Biniés transect, which would not have the oblate-horizontal fabric linked to quiet sedimentary deposits.

Hence, the Biniés transect sites host fabrics that show this competition between sedimentary and tectonic fabrics, where the deformation gradients are also somewhat masked. It can be stated that there is a strip of materials showing stage 4 deformation next to the fault, but then a clear development towards the prolate stage 3 phase is missing between 50 and 250 m. In the rest of the transect the fabric can be interpreted as belonging to stage 2. It is possible that there are other secondary faults in the footwall, as would be the case at the farthest site, BIN14, that shows a pencil cleavage fabric. However, the deformation does not increase linearly towards the fault, since site BIN12 shows a magnetic sedimentary fabric, and is closer to the main thrust.

In summary, this transect cannot be considered for a study of shortening and strain quantification. In particular, we interpret this as a result of the lack of clarity of the initial sedimentary fabric, possibly irregular, and the difficulty of understanding its relationship with the overprinted cleavage, which makes it difficult to use the calculation formulae of Humbert et al. (2014) used in the previous

CHAPTER 4 - SHALE FABRIC

4.4. Strain quantification at the Sigüés site.

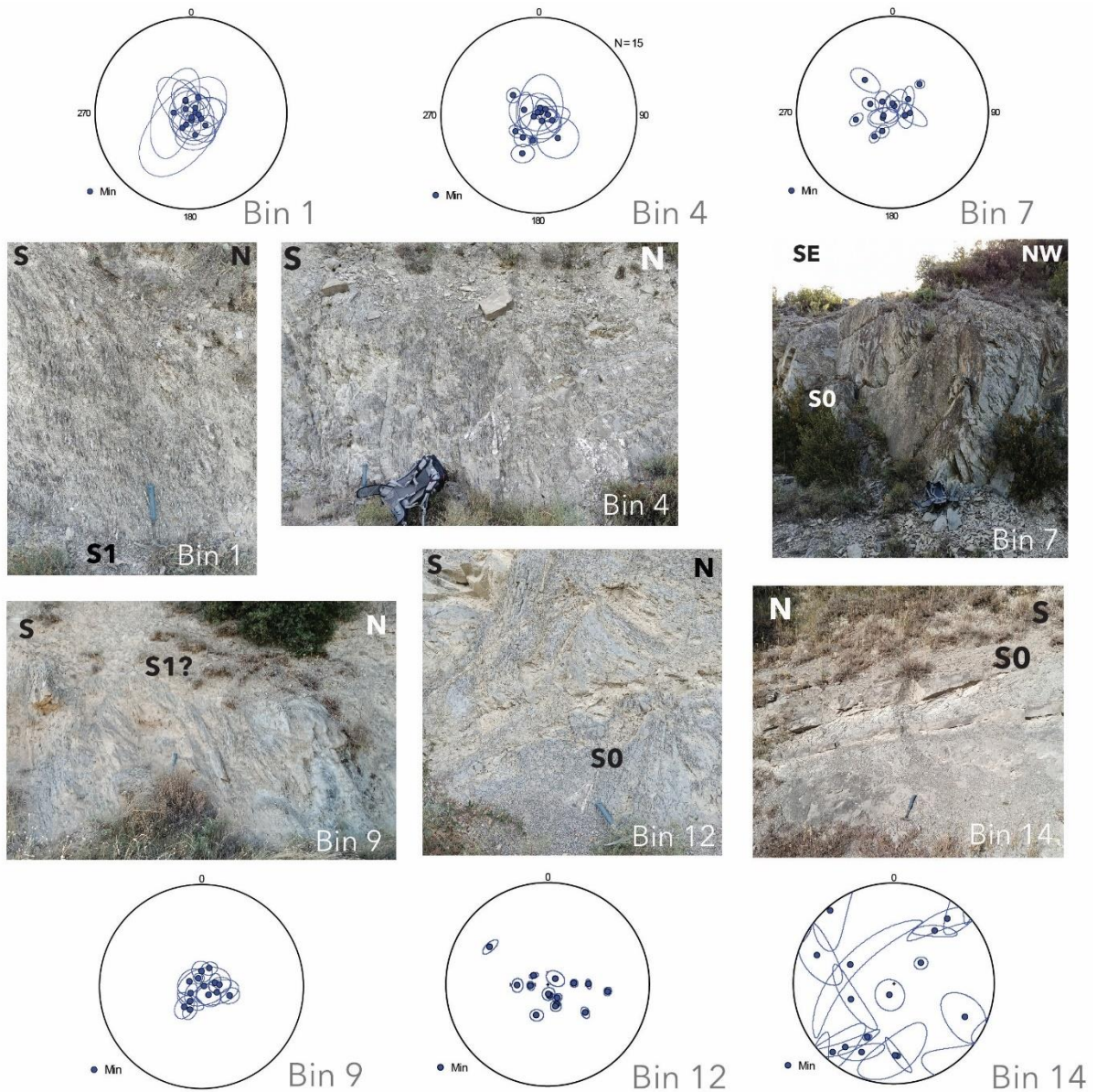


Figure 137: Photos of some key outcrops in the Biniés section. Added to each outcrop, a stereonet of the K3 of the non-oriented fragments. The size of E23 ellipse of confidence is visible.

4.6.2 Javierregay Site

Two sampling sections were done in the Javierregay area. One to the east of the Aragón Subordán river, with a length and lateral distance (slightly more than 1000 m) from the main fault similar to that of Biniés or Sigüés (Figure 138). This has been called JAV-D as it is located on the right bank of the Aragón Subordán river. On the left bank, the sites are named JAV-I.

However, there are differences in the location of the JAV-I sampling sites in relation to other sections.

To the south there are not continuous shale outcrops, and only a couple of samples are taken in the marls at 160 and 120 m (JAV-I1 and JAV-I2 respectively) from the thrust exposure. In contrast, a spectacular fault exposure is observed in the cut of the A-176 road, which shows

CHAPTER 4 - SHALE FABRIC

the deformation approximately 40 m thick associated with the Jaca thrust. Consequently, it was decided to sample this outcrop in detail with seven sampling points in these 40 m. Four of them belong to several layers of the footwall with a clear cleavage 40 m from the fault. And three of them belong to the last few metres of cleaved shales in the footwall.

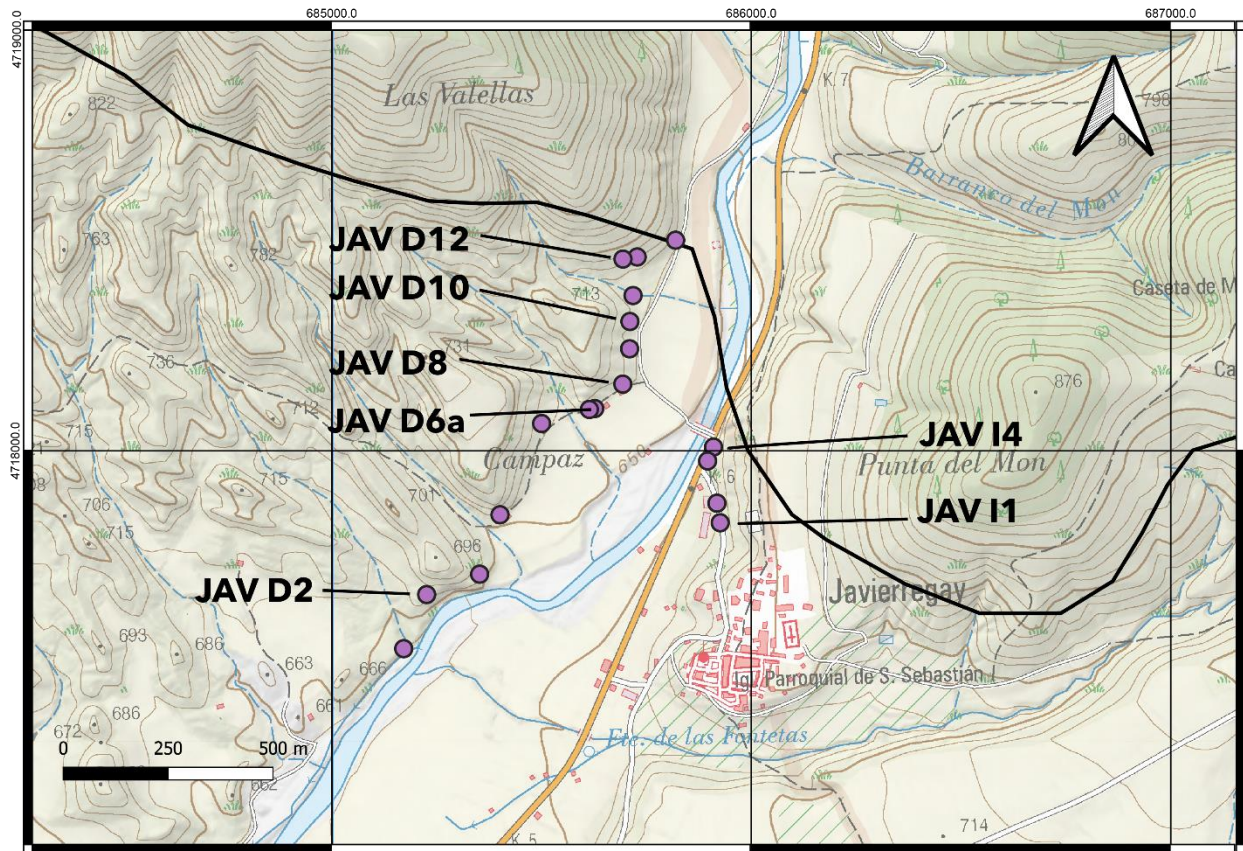


Figure 138: Map of sampling sections in Javierregay Site. Main Jaca thrust is traced in black line.

Outcrop description

The JAV-D transect has a marly appearance although with a more clayey and less carbonate texture than other outcrops visited in the Jaca basin. It is possible to recognise at just over 1000 m from the fault outcrop folds in the marls, with wavelengths of >100m and flanks with open geometry. Between this position and the rest of the sampled transect to the north, the bedding maintains a strike of 100-110 and a dip of between 16 and 35 N.

In general, fracturing, which can be mistaken for pencil cleavage, is visible along the whole transect. However, in the most distant sites, this fracturing is irregular and has a centimetric spacing (D2), revealing the bedding. This fracturing does resemble pencil cleavage from 450 m away from the fault, at site D6A, where it becomes more penetrative (spacing < 1 mm) than in the more distant beds, in all cases dipping to the north (50,298)

This cleavage becomes progressively more penetrative and less spaced. In the last 150m the orientation of the bedding is lost, and marly outcrops with fracturing without recognisable geometries are seen. Small patches and blocks of more clayey shales appear (D10), which we interpret as sedimentary structures of the marly slope. Finally, next to the fault, we find very

CHAPTER 4 - SHALE FABRIC

damaged outcrops, with many calcite veins, and signs of shearing changing the regular dip of the cleavage (D12).

On the left bank of the Aragón Subordán river sampling started 160 m south from the main thrust. There, at sites I1 and I2, outcrops are similar to those on the southernmost sites of the right bank of the river (D2), where the pencil cleavage is either subtle or confused with the natural fracturing of the shales.

Within 50 m of the fault cleavage spacing decreases, giving rise to slaty cleavage, and in the last 30 m of the fault there are numerous fractures, slaty cleavage in the shales of the footwall and signs of shearing producing blocks of metric thickness.

Scalar data results

Susceptibilities (Km) range from 125 μ SI on the right bank of the Aragón Subordán river to 146 μ SI on the left bank staying the bulk measurements of shale samplings between these two values. These values are in the range of the Biniés and Sigüés sites results of bulk susceptibility on Larrés Fm marls. The scalar data obtained from the measurement of the magnetic fabric of non-oriented fragments indicates that:

On the JAV-D section, the samples with more anisotropy and more oblate shapes of the magnetic anisotropy ellipsoid, can be *grosso modo* related to the slaty cleavage zones, i.e. stage 4 or stage 5 fabrics for sites 12, 11, 9, 10. Site 13, next to the fault, is not more oblate than these, and the site with more typical stage 5 fabric is D7. On the other hand, D1, the southernmost site, shows a prolate fabric, which would indicate that the fabric is not sedimentary, and would correspond to the development of pencil cleavage. This evolution towards types 3 and 4 occurs at sites 2 to 6. However, sites 7 and 8 represent two end-members in the middle of the gradient from stage 3 to 5, indicating a possible irregularity in the footwall. In fact, D-7 site shows a penetrative cleavage. However, no signs of thrusting or shearing have been found.

Parameter E23 indicates the competition between the bedding fabric and the cleavage fabrics at sites D3 and D8, with confidence angles $>25^\circ$. On the other hand, in the rest of the sites it remains between 5 and 10° .

CHAPTER 4 - SHALE FABRIC

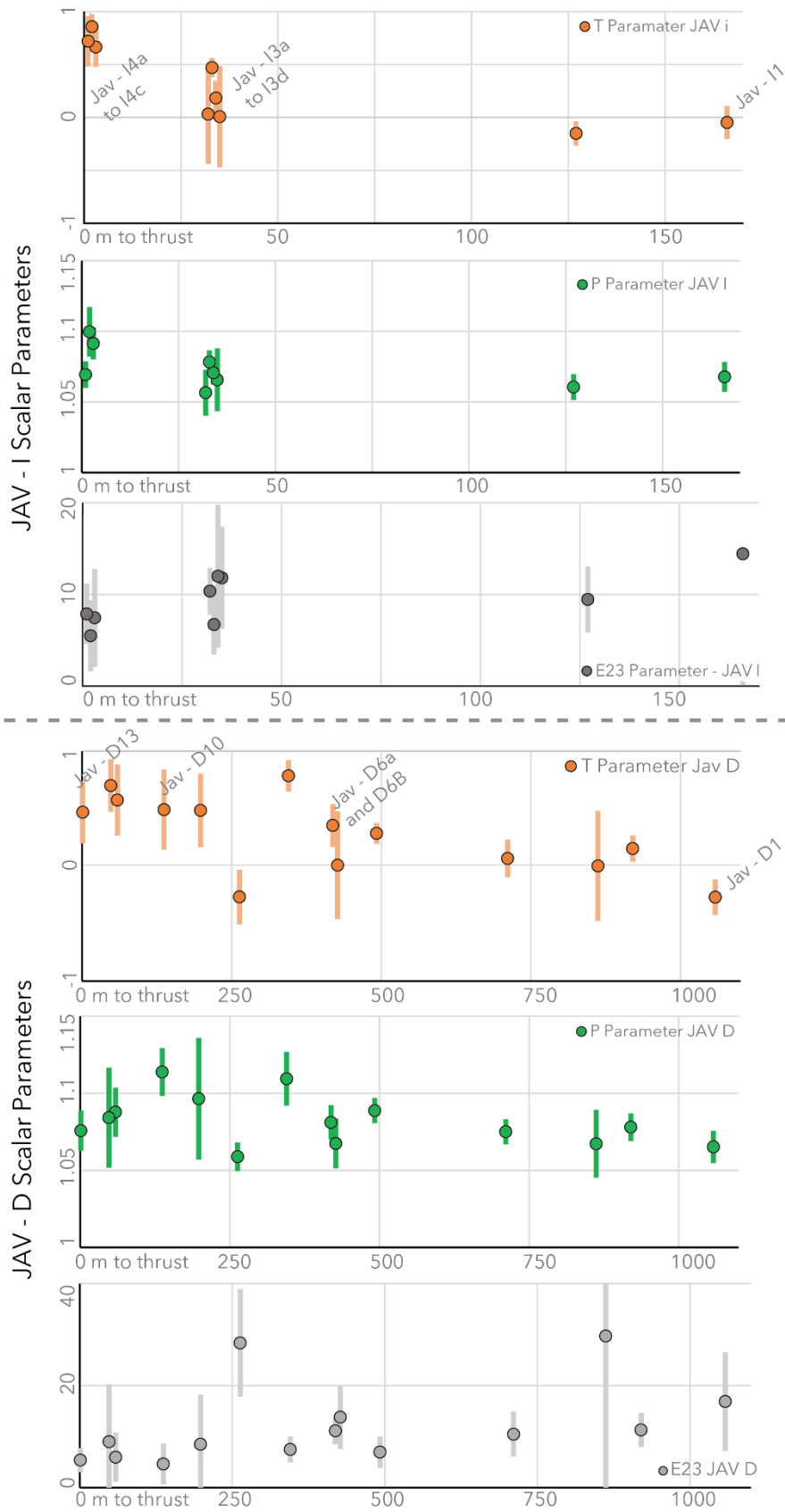


Figure 139: JAV-I (left bank) and JAV-D (right bank) scalar parameters plotted with respect to distance to thrust. Numeration of sites goes from the southernmost site (n°1 on both transects) to the “thrust sampling site” (n°4 on JAV-I, n°13 on JAV-D)

CHAPTER 4 - SHALE FABRIC

On the JAV-I section (left bank of Aragón Subordán River), the results are similar, and define a diagonal trend in Jelinek's plot, although this trend is not a straight line if we order the sites by distance. Sites I1 and I2 are the most prolate (T between -0.2 and -0.1) and on average, the I3 set of sites and the I4 set are more oblate and anisotropic. However, within each set, there is some variability in the parameters: site I3D is less anisotropic and triaxial (it could belong to a stage 2 fabric) and site I3C is more anisotropic (1.08) and oblate (0.5).

Site JAV-I3, which is 40 m from the thrust, probably has variable fabrics depending on the particular sampled layer, varying ~4 m within the marls. In contrast, the I4 sampling site is notably oblate, indicating this strong slaty cleavage observed in the shales along the fault. Anisotropy varies from 1.07 to 1.10 at the three sites of the I4 set. This variability of fabrics in the same sampling area has already been described by Saur (2022) in the Hecho Group.

The L parameter also shows some variability in these sets I3 and I4. However, broadly speaking, they indicate that I4 has low values, about 1.01 indicating how pronounced the planar and not elongated fabric is. In the rest of the transect the value of this parameter is around 1.035, which indicates that although there is cleavage, the composite fabric between bedding and cleavage also gives some elongation to the bulk susceptibility ellipsoid. Finally, the E23 angles decrease in size along this transect, from 15° in I1 to less than 7° in I4.

CHAPTER 4 - SHALE FABRIC

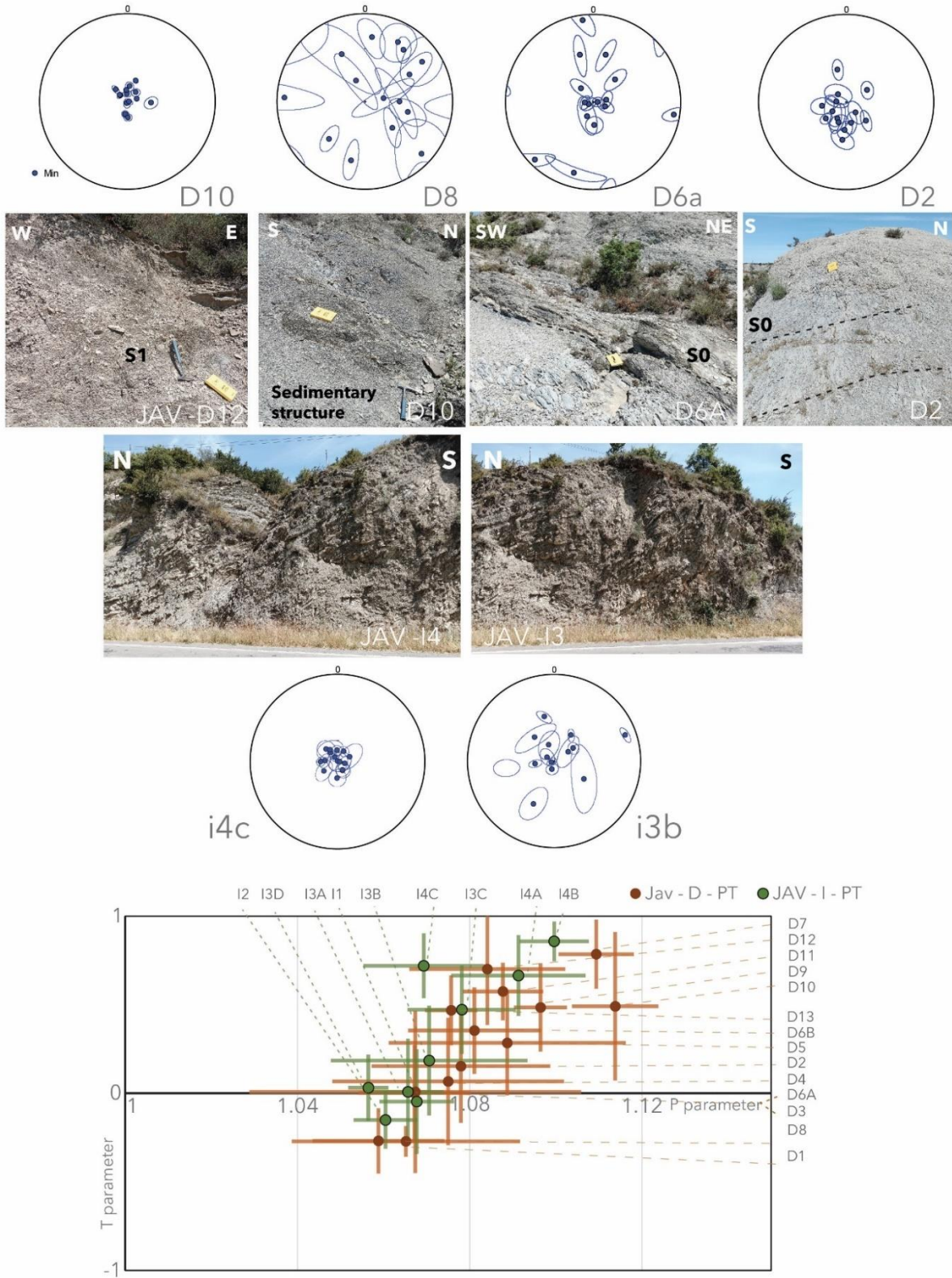


Figure 140: Scalar data on Javierregay sampling sections and outcrop pictures. Jelinek plot is provided to see the evolution of the two main scalar parameters.

4.6.3 Jaca-Gas Site

The Jaca-Gas outcrop is ~25 m in size, on the slope at the edge of the local A-1205 road 900 m south after leaving the town of Jaca. The marls of the Larrés Fm. also crops out at this site, although they are often covered in this part of the basin. The fault trace from Javierregay to this point is difficult to follow. However, the strike of the thrust and the alignment of this outcrop confirm that it is one segment of Jaca thrust (See Figure 133).

A reverse fault zone is observed, with a main fault plane dipping 15° to the N. Shear indicators are visible next to the fault plane and associated slaty cleavage is observed in the 2 m close to the central plane. The cleavage is attenuated in just a few meters towards the hanging-wall and footwall.

Ten sites were sampled at distances within a few metres from each other, located in different sections of the structure of this thrust zone (see Figure 141). The results indicate the following:

Susceptibility is ranging between 140 and 149 SI in the outcrop.

Site 1 corresponds to a stage 2 fabric related to the 5-stage fabric evolution. The T parameter in site 1 reaches a 0.4 value and the parameter P ~ 1.05 , denoting a slight deformation of the initial state expected for stage 1.

Sites 2 to 7 have a triaxial-prolate T-value (from 0 to -0.5), and an even weaker anisotropy $P < 1.03$. This could correspond to stage 2 fabric for site 2, and stage 3 fabric for sites 3, 4, 5 and 6 which have a clearly prolate T-value ($T < -0.2$).

Sites 6 and 7 are located within a few centimetres of the fault plane in areas with high proportion of shale. Site 7 fits with both stage 2 and stage 4 fabrics, while the confidence angle E23 is relatively wide ($37 \pm 24^\circ$) denoting a competing fabric as in sites 3, 4 and 5, but these correspond to the stage 3 fabric.

Finally, sites 8 (on the fault plane) and 9 and 10 (in the footwall, a few metres below) show an oblate fabric ($T > 0.5$). Nevertheless, their position and the degree of anisotropy are different. Site 8 would correspond to a stage 5 fabric, a slaty cleavage conditioned by the fault cleavage, with $P \approx 1.08$. On the contrary, sites 9 and 10, which are located in an outcrop without cleavage, could correspond to stage 1 or 2 fabrics, similar to site 1.

CHAPTER 4 – SHALE FABRIC

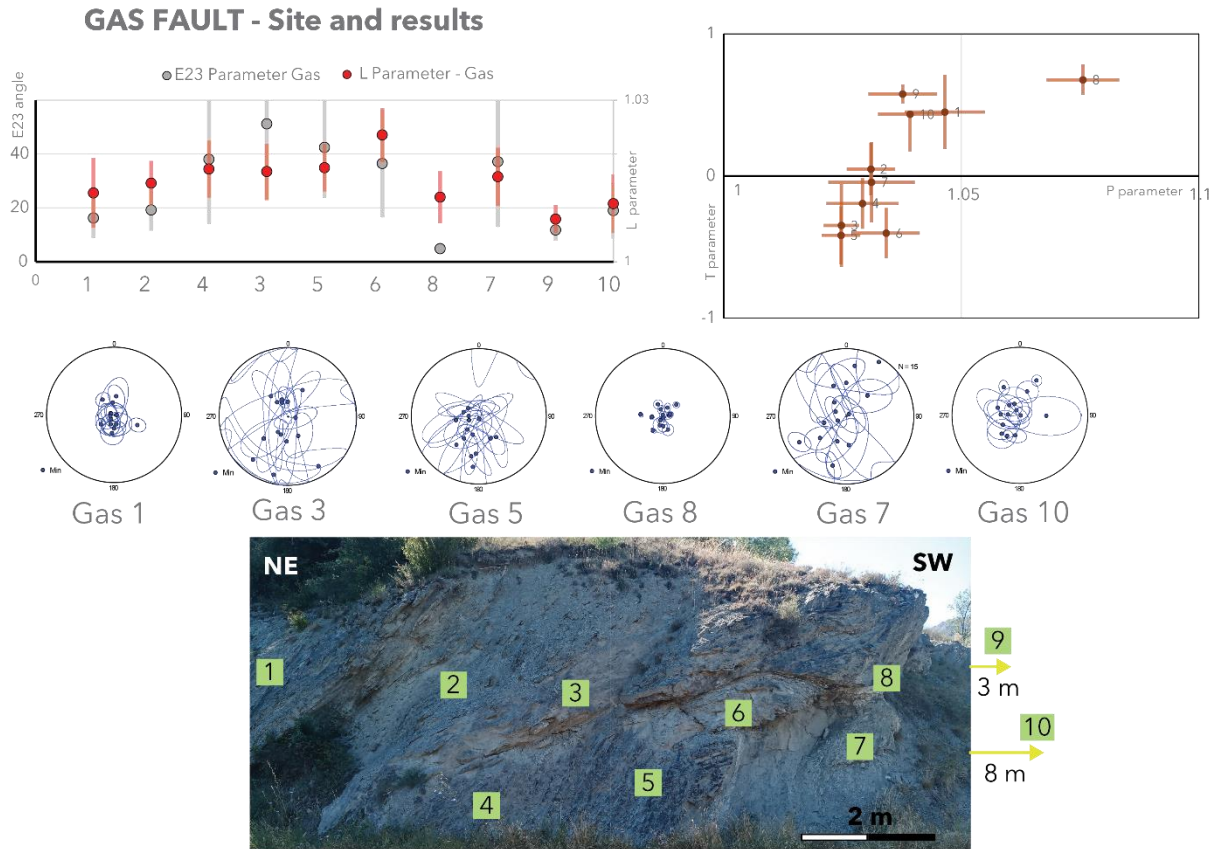


Figure 141: Scalar parameters for sampling at the Jaca Gas site. At the bottom, we see the photo of the outcrop and the precise points where non-oriented fragments were collected.

A vague symmetry in the scalar parameters can be appreciated on both sides of the fault plane in this area. Site 8 would correspond to the most cleavage-controlled site (Stade 5), with a low E23, and a high P parameter value, and towards the two walls we have this fabric in which the primary fabric and the imposition of cleavage coexist. The measurement of the bulk magnetic fabric indicates this competition expressed by high E23 angles ($> 40^\circ$, sites 3, 5 or 7) which diminish as we move away from the fault plane. Site 1 towards the hanging-wall, about 7 m from the fault plane, and site 9 in the footwall, about 3 m away from it, confirm the deformation associated with the fault plane at this point.

4.7 Discussion

In this chapter >1500 fragments of the Eocene marls of the Jaca basin have been analysed, in the Sigüés Area where two thrusts are emerging (Leyre and Orba thrusts), and are close to three well exposed thrusts: Biniés, Javierregay and Jaca-Gas. These thrusts are located 15, 23 and 38 km to the east of Sigüés and belong to the same Jaca thrust system, significant from the regional point of view. They separate the turbiditic domain from the molasse domain of the Jaca Basin. All these faults show a highly deformed footwall, which can be related to the propagation of the. The damage zone of a fault is a classic observation, but to observe and quantify deformation at distances of more than a hundred meters from the fault is, in our view, unprecedented.

CHAPTER 4 - SHALE FABRIC

The main site of investigation (>1500 fragments) is Sigüés, with two main faults: the Leyre thrust and the Orba thrust.

Here are some of the most important points:

- ✓ The magnetic fabric of the Eocene marls is largely controlled by authigenic illite. This is due to a diagenetic state in which the ferromagnetic fraction has virtually disappeared.
- ✓ We have defined five stages of fabric evolution in Jelinek's diagram (T vs P), comparable to the stages of evolution proposed by other studies (Parés et al., 1999; Parés and van der Pluijm, 2004a).
- ✓ The shape parameter T is a sensitive marker of deformation. In particular, the prolate stage may be difficult to detect in the field, especially in shales. In AMS, it is perfectly detectable.
- ✓ The anisotropy parameter P can paradoxically reach very low values where deformation is well expressed. This is due to competition between bedding and almost perpendicular cleavage.
- ✓ The angle of confidence parameter E23, generally underestimated or even absent in the literature turns out to be a very sensitive marker of deformation. We can see that between stage 1 and stage 2, this parameter changes markedly, even though there is no evidence of this in the field.
- ✓ The seven sampling sections made between the western and eastern parts of the Sigüés zone show that stage 5 of deformation can be detected at more than 200 meters from the fault wall.
- ✓ Using a rigid particle rotation model, we document a deformation rate ranging from 5%, mainly related to the LPS, to almost 70% close to the fault.
- ✓ Deformation is detected without seeing the corresponding fault in the field (Escalar cross-section). This zone of deformation develops at the apex of a blind fault. We will see in the section 6.4 Characteristics of the calculated deformation that this will have consequences for the model that accounts for the deformation.
- ✓ A map of the footwall zone of the Leyre and Orba faults is proposed (Figure 128). In our opinion, this is the first mapping of this kind made possible by the fragment method.

For the Biniés and Javierregay faults, the AMS data do not allow us to quantify the deformation, probably for reasons of magnetic mineralogy (with the more turbiditic facies) or a more complex bedding-cleavage geometric relation. The main points to note are as follows:

- ✓ Stages 1 to 5 are present, with stage 5 located close to the thrust.
- ✓ Overall, the Jelinek diagram shows a path comparable to that observed for the Sigüés marls.
- ✓ The organization of the bedding in the footwall, which is rather folded or slumped, makes it difficult to monitor its evolution.
- ✓ Secondary faults probably disrupt the overall scheme.

The Jaca-Gas reverse fault, near the town of Jaca, propagates in the Larrés formation (Figure 141). In a way, this fault can be compared to the blind faults detected in the Escalar section, but in this case the core of the fault is visible. The key points are as follows.

CHAPTER 4 - SHALE FABRIC

- ✓ All stages of fabric are observed
- ✓ Stage 3 prolate is observed in both the footwall and the hanging-wall of the fault, less than 2 m from the fault contact.
- ✓ Stage 5 is unsurprisingly represented in the core of the fault.
- ✓ At distances greater than around 2 m, the fabrics are stage 1 to 2, but with a T parameter (~0.5) that reflects significant matrix damage.

When these data are taken collectively, the following points emerge:

- The footwall of the Leyre and Orba faults is remarkably simple compared to the Biniés and Javierregay faults. Indeed, the bedding is sub-horizontal, and the imprinting cleavage is almost perpendicular. This favours progressive rotation of illite particles during deformation. To the best of our knowledge, there is no equivalent example in the literature. Lehigh Gap, as we have described (2.4 The Lehigh Gap, a classical shale-to-slates transition), has no visible fault, and the cleavage gradient is probably imposed by a transition from simple shear to pure shear, in an LPS-type regime
- Cleavage is fault-related. This is demonstrated in several ways, but the most obvious is the observation of south-dipping slaty cleavage in the footwall of the backthrust of the Pop-Up structure, in the Escá Gorge (see Figure 79). It is therefore reasonable to assume that the cleavage and deformation gradient are associated with the geometry and kinematics of the fault.
- Both the hanging-wall and the footwall of the fault are deformed. This is demonstrated in the Jaca-Gas fault, but also in the blind faults in the Escalar section (as in model from Figure 122). This implies the need for proposing a mechanism that can account for this observation.
- Deformation can commonly reach 80% close to the fault. Yet even at this degree of deformation, not all illite particles are oriented parallel to the cleavage. The resulting fabric has an average magnetic foliation pole intermediate between bedding and cleavage (Boiron et al., 2020). This is also observed for pyrite or quartz grains, as discussed by Saur (2022) in his thesis, and reinforced by our own XCT observation (Figure 103). This shows the heterogeneity of rigid particle rotation. In spite of this, our quantification approach seems to follow the deformation gradient very well, showing that the fragment technique, in this ultimately frequent type of context (gas-window type diagenesis in shales, LPS) can prove a powerful tool for detecting and quantifying strain.

The analysis of the Jaca thrust sites has shown that, in spite of having a very similar structure (a regional thrust over Eocene marls), deformation gradients similar to those obtained in the Leyre thrust are not found. Shale strain and fault-related deformation were observed, generally increasing in the metres adjacent to the fault plane. However, the size of the deformation and cleavage zone in the footwall of the thrust vary in the different transects.

At Sigüés, the cleavage front is located between 440 and 1000 m of lateral distance to the thrust trace. At Biniés, the cleavage front is not clear, but the cleavage is very much attenuated from 230 m lateral distance to the Jaca thrust. At Javierregay, the cleavage front is 450 m from the front fault on the right bank of the Aragón Subordán, and on the left bank it would be less than 50 m.

CHAPTER 4 - SHALE FABRIC

A fundamental factor is the architecture of the footwall, since the internal structure of the Larrés Fm and the Pamplona Fm can vary greatly despite the apparently homogeneous appearance of the marl outcrops.

At Sigüés, the footwall is composed of layers dipping subhorizontal to the south, except in the last 70 m next to the Leyre fault, where a footwall syncline can be seen overturning the layers on its northern flank. In general, the cleavage gradient appears almost in its entirety, and deformation in shales varies homogeneously.

In Biniés, the structure of the Larrés Fm is more difficult to describe, as the bedding is hardly visible, indicating thick shale layers. However, there are some carbonate layers with subvertical attitude, as well as irregular beds of metric thickness with a higher clay content, where the cleavage is more penetrative. The slope on which these shales were deposited may have been steeper, and therefore, thick strata may be found, with internal slumps and other heterogeneities in the sedimentary series.

The Javierregay site appears to be complex. On the left bank of the Aragón Subordán river, folds are visible about 1000 m away from the fault. And, although in the sampled sector the bedding seems to be stable in its geometry, the last 200 m before reaching the fault show heterogeneities in the sediment, with more "clayey" patches making the bedding unrecognisable.

It is for these reasons that the Sigüés site becomes a preferential site for shale fabric analysis, because relationships between AMS results and outcrop observations can be easily established. This can also facilitate the collection of non-oriented fragments, which in sites without geometrical references could be very difficult to interpret, as is the case in some sampling sites of the Jaca thrust transects. The five-stage model of magnetic fabrics evolution also has limitations, and the clear explanation of the "deformation path" in Jelinek's plot presented in Figure 115 is not so clear at the other sites.

Therefore, the elaboration of shortening calculations based on Humbert et al. (2014) formulae and the construction of regional-scale deformation maps could be an imprecise and difficult-to-interpret approach.

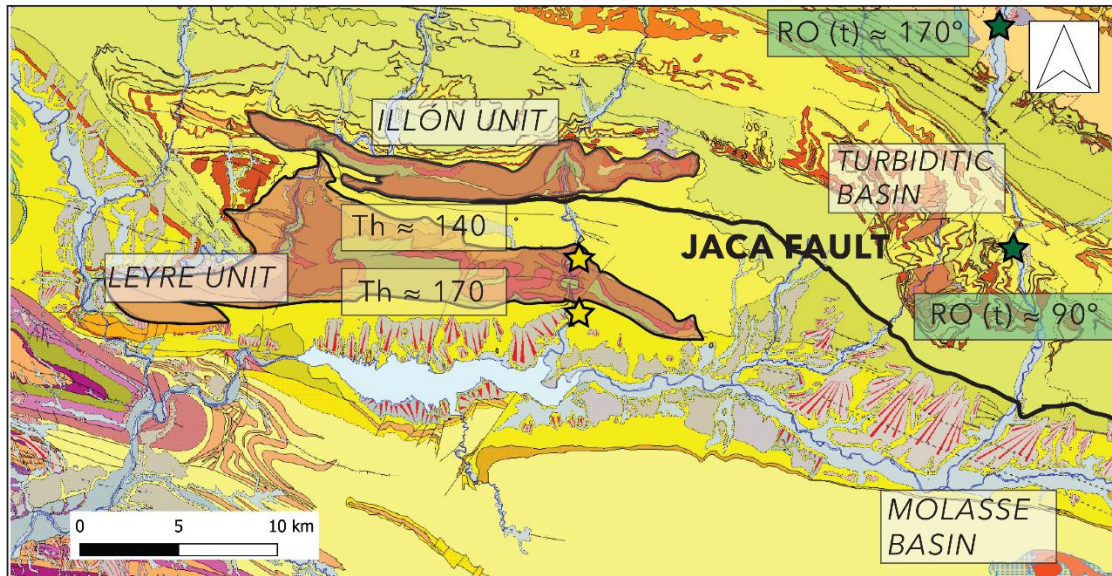
4.8 Conclusion

We have proposed a new approach to study shale strain based on the analysis of non-oriented fragments of a few grams. The scalar data resulting from the analysis can be exploited correctly, as our statistical tests have shown. The advantages of this approach are 1) to be able to take a broader statistical approach to shale deformation, 2) to show that this approach can be adapted to drilling cuttings, for example.

All in all, the presented map (Figure 128) allows us to have a more precise characterization of this phenomenon in a sector Pyrenean region. Therefore, it is possible to advance in the understanding of the complexity of the processes that take place along with the history of the Leyre thrust, which is the fundamental cause of the mechanical stress that produced this cleavage. The conditions under which the cleavage appears have already been introduced in section 2.1. Shales cleavage, and this will be analysed and discussed again in section 5.1 Background. In conclusion, the application of the technique of sampling and measuring unoriented shale fragments presented in this chapter has served to demonstrate advantages,

CHAPTER 4 - SHALE FABRIC

such as rapid sampling campaigns, and obtaining data on the fabric quickly. However, it also has limitations, linked to outcrop conditions, the internal architecture of the marls sampled, and the conditions of burial and acquisition of the internal fabric of the rocks.

5. PALEOTHERMOMETRY AND FLUIDS**5.1 Background**

★ IZQUIERDO LLAPELL ET AL., 2013 ★ CROGNIER ET AL., 2018

Figure 142: Various studies on diagenesis and burial performed on Sigiüés Area. The data of Izquierdo-Llavall et al. (2013) come from studies on the organic matter contained in the turbidites of the Hecho group. The data of Crognier et al. (2018) come from Th obtained in fluid inclusions of calcite veins.

Paleothermometry is a crucial issue in cleavage studies because mechanical properties of rocks are strongly depending on the geothermal gradient and the depth at which deformation takes place (Izquierdo-Llavall et al., 2013a). Regarding the diagenesis and fluid circulation in these geological units during the Pyrenean construction, several contributions have helped to unravel this issue. An overview map presents previous research on (Figure 142).

Crognier (2016) analysed the calcite veins in different areas of the Jaca basin, including Sigiüés. His work included sampling of calcite veins, mineralogical and microthermometric studies, analysis of clumped-isotopes, fluid inclusions, and studies of organic matter in the host-rocks. With these data, the author constructed a palaeohydrological model and paleotemperature map for the southern Pyrenean zone presented in Figure 143.

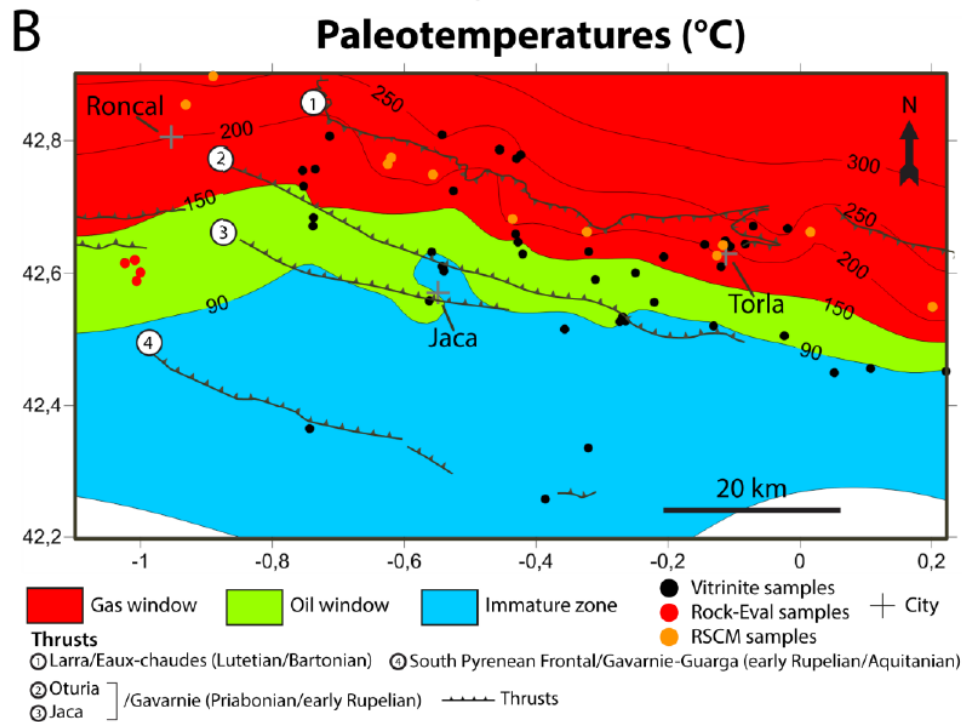


Figure 143: Paleotemperature modelling map for Jaca Basin, Internal and External Sierras. Sigüés zone is located in Oil window (left zone of map). From Crognier (2016)

Some key results from Crognier's (2016) work are the following:

- Extensional calcite veins sampled in Sigüés are interpreted to correspond to a H₂O-NaCl system, as it happens for a large part of the South Pyrenean zone. In the surroundings of the Leyre thrust, two T_h (140 and 170 °C) were obtained from fluid inclusions. In similar veins in more internal areas of the turbiditic basin, higher temperatures are found, between 156°C and 215°C (Crognier et al., 2013).
- Isotopic data (with stable O and C isotopes) show that the veins are mainly buffered by the sediments resulting in a rock-fluid interaction.
- Using other geothermometers techniques, such as Raman spectroscopy and vitrinite reflectance, similar temperatures are proposed for the inner zones of the cleavage domain and inner zones of the orogen. However, an upper limit of 90°C is also proposed for the molasse basin and the External Sierras (see Figure 143). In between, there is a relatively narrow temperature transition zone, corresponding to the study area.

In this same line of work, and using similar techniques to know the conditions and diagenetic history, two master internships at the UPPA obtained additional data for the Sigüés area, Grignard (2018) and Léon (2022). Both works are developed in more detail in section 5.3 Calcite-filled faults. From this new dataset, Grignard (Pers.Com. 2021) proposed a revised version of Figure 143 at the scale of the Jaca Basin (Figure 144)

CHAPTER 5 - PALEOTHERMOMETRY AND FLUIDS

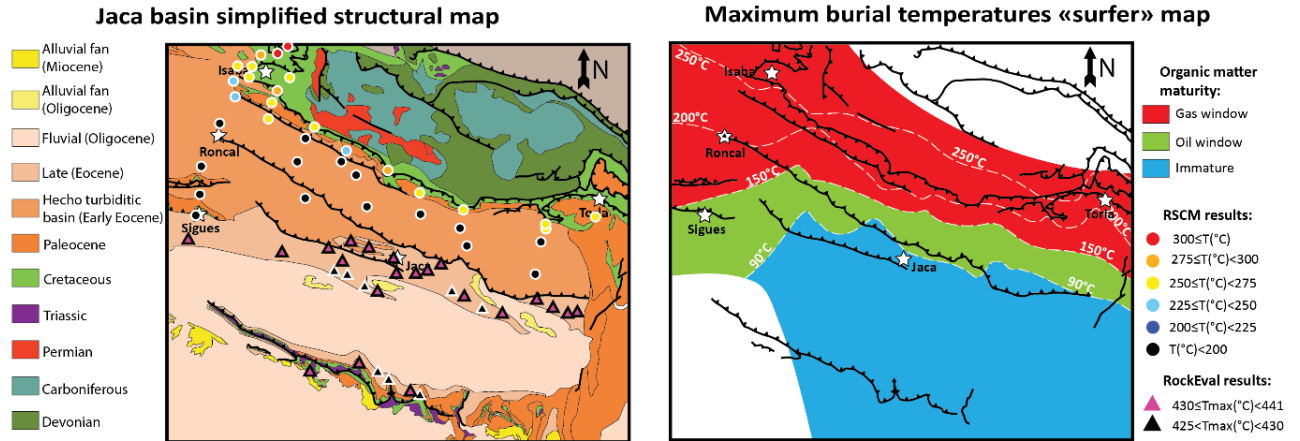


Figure 144: Synthesis of peak burial data (Rock Eval, RSCM). Unpublished figures from Grignard (Personal communication, 2021)

In the area of Sigüés, Grignard's (2018) focuses on the footwall of the Leyre thrust, covering the transition between the southern molasse basin and the shale (Eocene marls) domain (Figure 145). RSCM data are consistent with temperatures of up to 175°C, higher than the previously obtained. By means of Rock-eval analysis, this temperature drops to 130°C south of the Canal de Berdún. Grignard (2018) also studied fluid inclusions from calcite veins. The results are in agreement with those of Crognier (PhD, 2016), with homogenization temperature (T_h) for the inclusions between 70 and 130°C, and fluids with NaCl content in some inclusions. However, a T_h temperature of 215°C is recorded at the boundary between the Larrés Marls and the Pamplona marls. This shows that there is circulation of hydrothermal fluids, which are not in equilibrium with the surrounding rock. Izquierdo-Llavall et al. (2013) have documented a T_h range between 112 and 136°C, i.e. in a lower range than that recorded by Crognier (2016) and Grignard (2018). This temperature range is lower than the burial temperatures of the rocks studied in the Jaca turbiditic basin. A summary of data is shown in Figure 145.

CHAPTER 5 – PALEOTHERMOMETRY AND FLUIDS

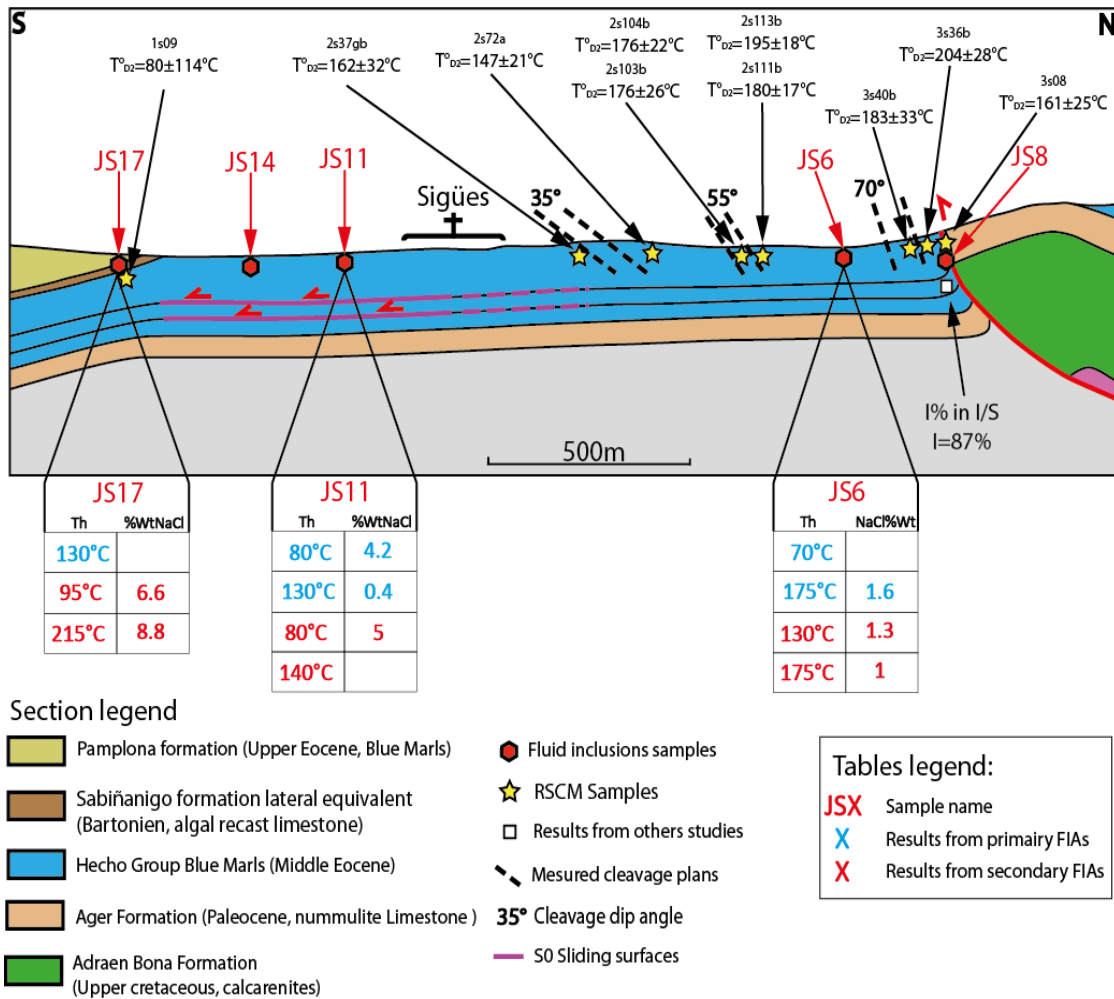


Figure 145: Results from fluid inclusion in calcite veins with their Th are plotted. In addition, some Ts calculated from RSCM are shown. Calibration of the temperatures calculated from the spectra was performed using (Kouketsu et al., 2014). From Grignard (2018)

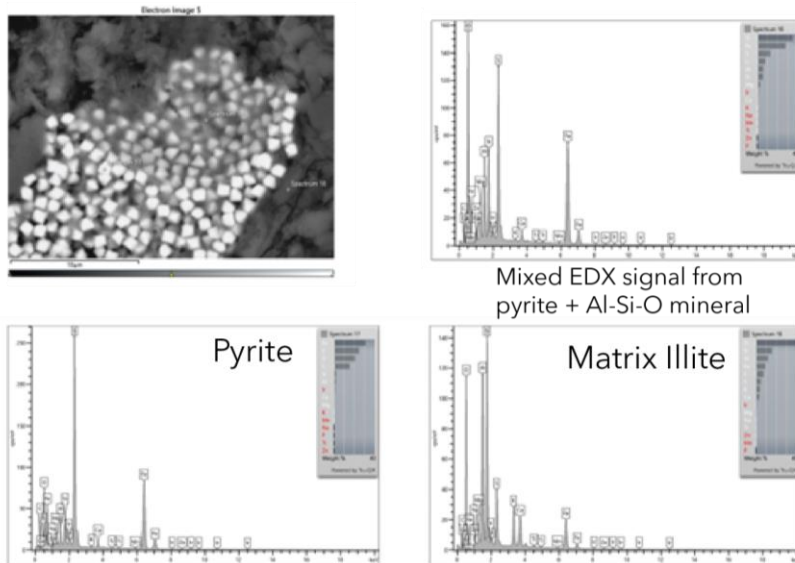
Léon (2022, unpublished internship under supervision of Dr. Beaudoin) carried out a study on calcite veins, which also provide information on the diagenetic evolution of the rocks. He sampled two sets of veins in the southern slope of the Orba Range (see Figure 153), one with E-W direction, and the other oriented N060, which he interprets to be formed along an anticline. Two groups of veins have been distinguished according to their isotopic signal. One of them would have to do with meteoric waters (open system), and the other would be in equilibrium with the overthrust (closed system). Along with the fluid inclusions, this author found a large majority of Th values between 70 and 80 °C. See Figure 156 on section 5.4 Fluid data on calcite faults. The temperatures are interpreted to correspond to 2 km depth and in equilibrium with the rock.

5.2 Additional RSCM and Rock-Eval data.

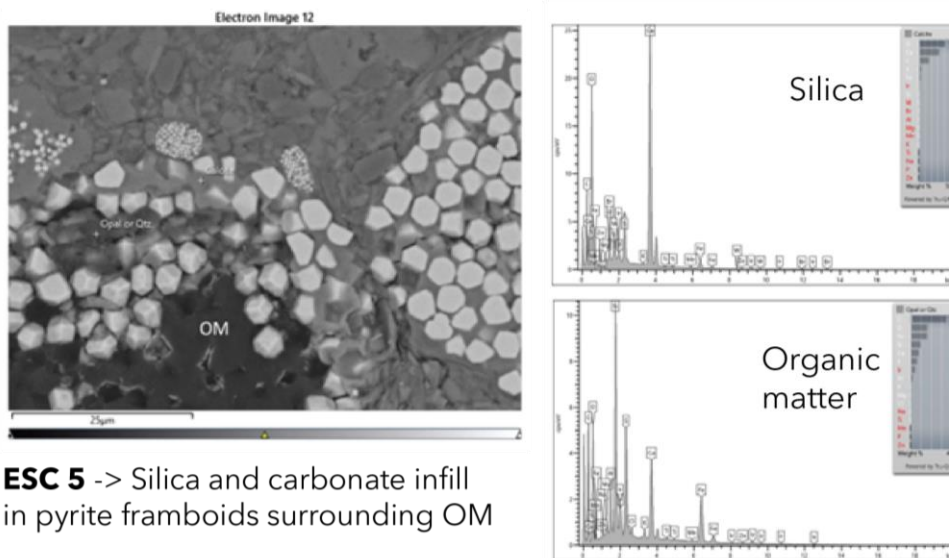
The Sigüés transect has been part of a collaboration in 2021 with Dr Rebecca Stokes from the USGS. Five representative samples of the footwall of the Sierra de Leyre have been analyzed using RSCM thermometry. The aim of the USGS geologists is to examine how organic matter can be influenced or affected by the stress gradient.

5.2.1 Mineralogy

We present some examples of the five samples observed by backscattered electron microscopy (SEM, obtained at the USGS). We note the close relationship between the location of the organic matter and the framboids. Pyrite crystals are oxidized and a crown of magnetite is widely visible on virtually all samples (Figure 146 and Figure 147). Aubourg et al. (2021) have shown that this process is very common in shales. This process is part of the diagenesis of magnetic minerals, and paradoxically contributes to increasing the paramagnetic contribution to susceptibility. In fact, most neoformed magnetites are mostly superparamagnetic (<20nm).



ESC 2 -> Clay matting around pyrite grains



ESC 5 -> Silica and carbonate infill in pyrite framboids surrounding OM

Figure 146: SEM observation of sample ESC2 (Escó cross-section, non-deformed site) and ESC5 (Escó cross-section, pencil cleavage site)

CHAPTER 5 - PALEOTHERMOMETRY AND FLUIDS

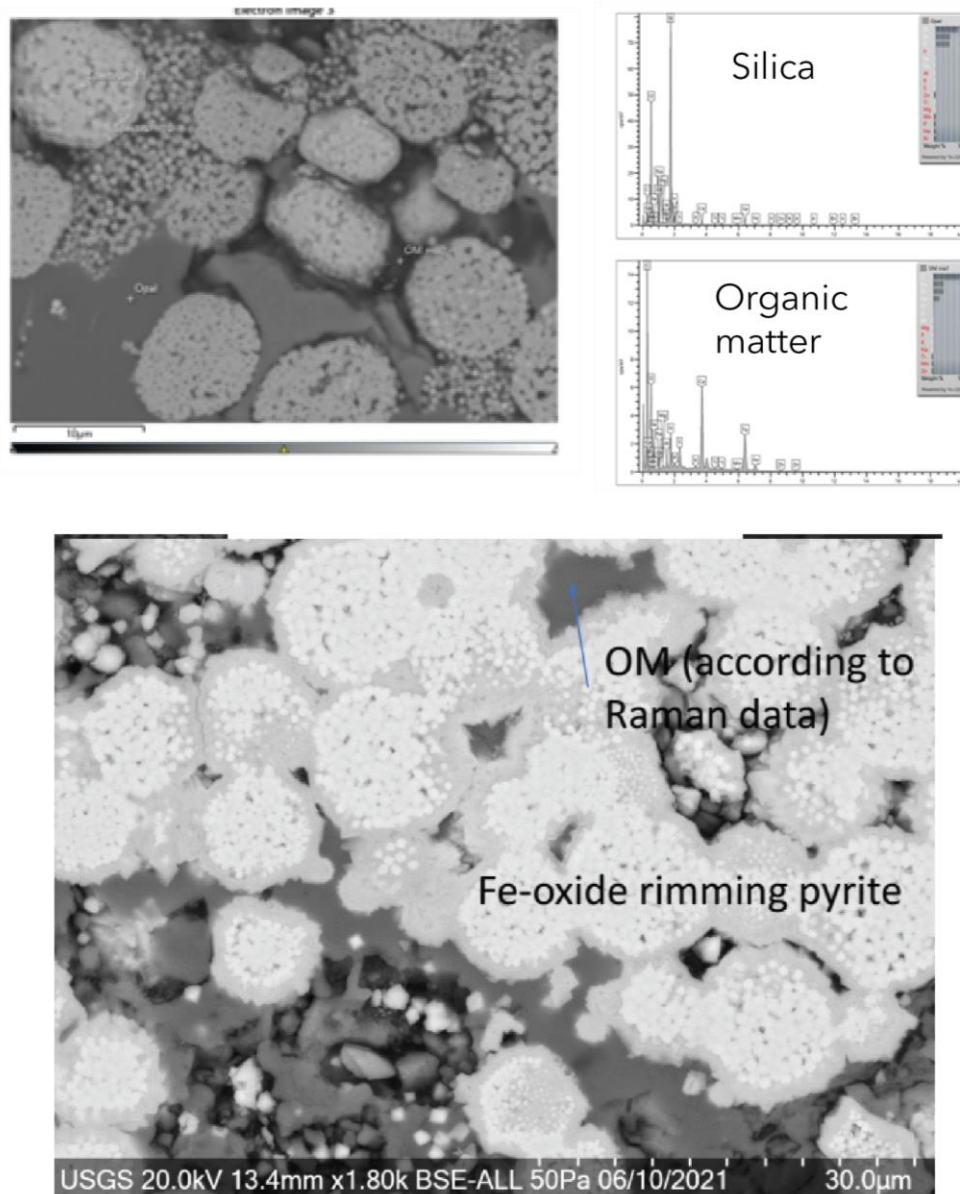


Figure 147: SEM observation of sample CLR5 (Escalar cross-section, slaty cleavage site), and sample CLR 7 (Escalar cross-section, slaty cleavage site). Pyrite are framed by iron oxide, likely magnetite.

Boiron (unpublished data, UPPA) obtained transmission electron microscope (TEM) images showing magnetite crystals growing in the pores of the clay matrix (Sample 3S40B, Sigüés). These data also show authigenetic illites and chlorites oriented parallel to the cleavage.

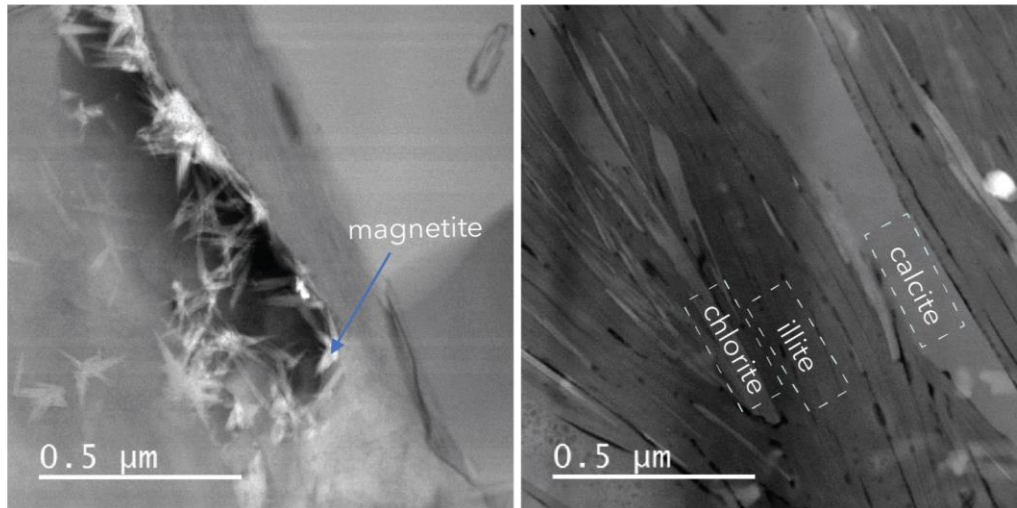


Figure 148. Left: Nanometric magnetites incorporated into the pores. Right: Illite and chlorite crystallites parallel to the cleavage. Note the regular shape, indicating that these are authigenic crystals.

5.2.2. RSCM

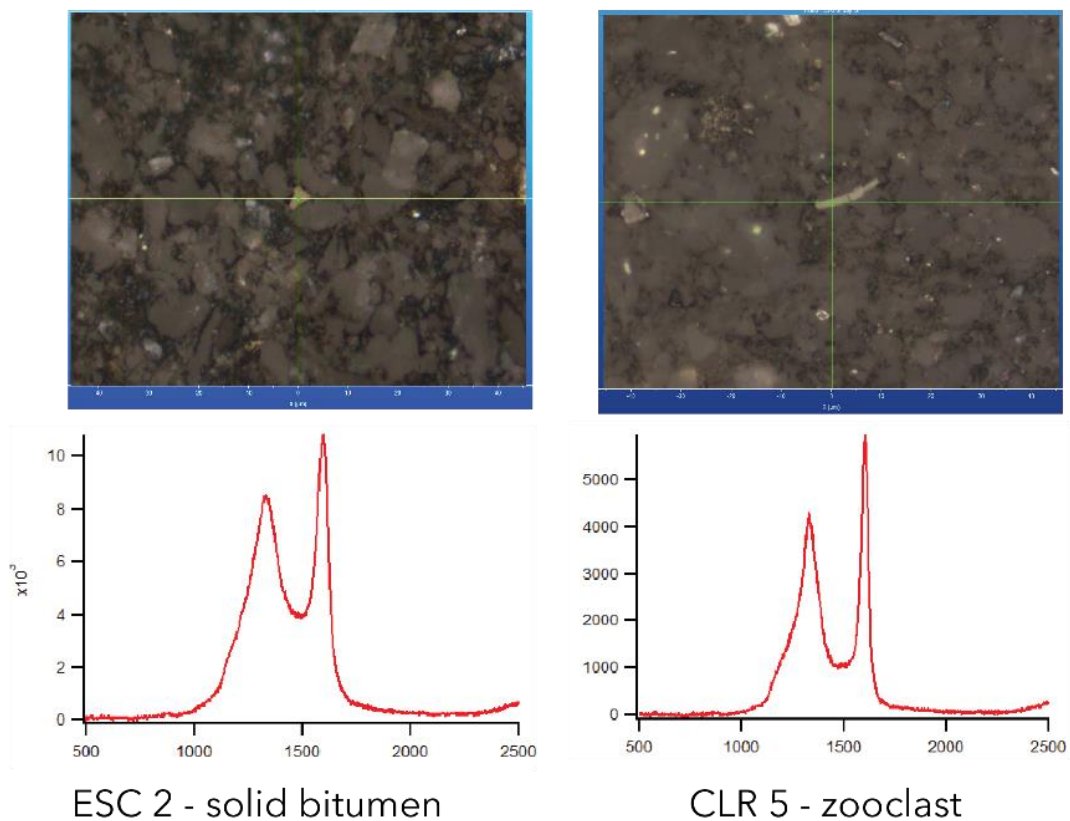


Figure 149: RSCM on carbonaceous materials. Spectra were collected on a Horiba Xplora Plus Raman microscope system using a 532nm laser, 1200 groove/mm spectral grating, 300 μm confocal pinhole diameter, 100 μm spectrometer slit, 75 μW power at the sample surface, and 100 \times objective with a numerical aperture of 0.9. Each analysis was collected across a spectral range of 50-2664 cm^{-1} in 3 accumulations of 30 s.

For burial temperatures close to 200°C, there are few methods for correctly estimating the burial temperature of rocks. The Raman method (RSCM) has undergone considerable

CHAPTER 5 - PALEOTHERMOMETRY AND FLUIDS

development in recent years (Beyssac et al., 2002; Kouketsu et al., 2014; Lahfid et al., 2010; Lünsdorf et al., 2017) but the calibration between burial temperature obtained from other geothermometers and RSCM is not robust for temperature <200°C.

RSCM was performed on three of the five samples. Using the most recent calibration curve (Lünsdorf et al., 2017), a peak burial temperature close to 210°C is calculated (Stokes, personal communication, 2021). Using Kouketsu et al. (2014) calibration (see Table 7) like Grignard, 2018 did, the temperature range obtained shows great variability from 150°C to 277°C, demonstrating the unreliability of the RSCM technique for these temperatures ranges. A trend may emerge if we take only the D2 band as a basis for calibration, with an increase in burial temperatures from ~150°C to ~280°C towards the fault. This trend is not confirmed by the analysis of band D1 (Table 1), and we concur with Grignard's preliminary conclusion that it is not possible to demonstrate a temperature gradient related to the degree of deformation.

Note that Grignard gives a slightly lower temperature range (150-200°C) than that proposed on the Escalar section (190-250°C) using Kouketsu et al. (2014) D2 band calibration curve.

Sample, analysis	Kouketsu (2014) D1-FWHM temperature $\pm 30^{\circ}\text{C}$	Kouketsu (2014) D2-FWHM temperature $\pm 50^{\circ}\text{C}$	Average $^{\circ}\text{C}$
CLR5_1 (Slaty cleavage)	249	277	247
CLR5_3	229	228	
CLR5_5	232	233	
CLR7_14 (Pencil Cleavage)	222	191	190
CLR7_9	234	196	
CLR7_10	207	181	
ECS2_2 (Cleavage free)	230	251	223
ECS2_6	244	267	
ECS2_9	280	150	
ECS5_1	247	164	

Table 7: RSCM Data from USGS.

A Rock-Eval pyrolysis was performed on five samples from the Escalar section, Total Organic Carbon is <0.37% (see Table 8). The Larrés Marls of the Sigüés section (Boiron et al., 2020) are in the same TOC range. The Tmax values, which relate to the burial temperature, are between 456 and 464 °C, placing the maturation of the organic matter in the overmature range. This is in line with RSCM data.

Samples	Tmax Pyrolysis (°C)	TOC Values (%)
Esc 2 - 1	464	0.23
Esc 5 - 2	456	0.27
Clr 1 - 3	465	0.30
Clr 7 - 4	469	0.37
Clr 5 - 5	464	0.32

Table 8: Rock-Eval data from Pyrolysis performed by Stokes (Pers. Comm., 2021)

In short, these new data confirm a burial temperature close to 200°C, with no clear relationship to the degree of deformation of the rock. Grignard (2018) and Crognier (2016) placed the temperature in the 160-180°C range. The RSCM technique shows its limitations in this <200°C temperature range, and more samples are needed to be better constrain this temperature.

Compared with Grignard compilation of burial temperatures in the Jaca Basin (Figure 144) a temperature close to 200°C at Sigüés is particularly high. Further east, the 200°C isotherm is close to Torla, i.e. in the heart of the turbiditic basin.

5.3 Calcite-filled faults

5.3.1. Description of faults

In the Larrés and Pamplona formations there are several set of fractures, some of them joints, and others veins filled with calcite (Crognier et al., 2018). These fractures are a potential source of information about the deformation and burial history which these units have been subjected. Precipitated minerals in the veins provide information about the diagenetic system, which in the study zone is exclusively calcite. To clarify the terminology, there are three types of fractures: joints, which are not filled with calcite precipitation and have no displacement marks; calcite veins, which are filled with this mineral, but generally have no shear marks; and calcite faults, which are calcite-filled fractures with slip lineations and shear indicators.

This information has already been sought in the Jaca Basin and in this part of the Sierra de Leyre as shown in section 3.1.1 (Crognier, 2016; Grignard, 2018; Léon, 2022). In addition to finding a structural characterization of the fractures in this area, this previous work has also obtained data of the calcite precipitated in these rocks. Some of the methodologies used have been the following:

- **Stable oxygen and carbon isotopes**, with mass spectrometric analysis the signal in these isotopes, which gives a reference about the characteristics of the circulating fluids, and which can be compared with the isotopic characteristics of the host rocks is obtained. Therefore, fluid-rock interactions and circulation episodes during burial and diagenesis could be constrained.
- **Geothermometry on calcite clumped-isotopes**, which analyze the thermodynamic dependence for the ¹³C and ¹⁸O isotopes to associate in their precipitation in

CHAPTER 5 - PALEOTHERMOMETRY AND FLUIDS

carbonates. For this purpose, the δ^{47} factor in the CO_2 expelled by the sample when attacked with phosphoric acid is used, which is independent of the isotopic composition. Calibrations such as Kluge et al. (2015), are used to detect this factor for temperatures between 25 and 250°C of thermal activity. Some data are available in Crognier (2016)

- **Microthermometry on Fluid Inclusions**, to constrain the T of the fluid at the moment of its trapping during the formation or fracturing of the mineral, i.e. in studied calcite veins. Mainly, biphased fluid inclusions with gas bubbles coexisting within fluid inclusions are searched for.
- **Raman spectrometry on Fluid Inclusion**, which allows to know the qualitative composition (and depending on the instrument, quantitatively) of the fluid contained in fluid inclusions, by recording the spectra (Crognier, 2016).

In this PhD, we have decided to obtain similar data, in the footwall of the Leyre thrust. The calcite veins appear scattered in the shale units, with various orientations, which could be classified into the following sets (Figure 150)

- A set of **N60 fractures**, both joints and calcite veins, which is present at various points of the Sigüés section footwall. This set seems to be older than the next one, according to the crosscut relationships observed by Léon (2022). Our field observations along the Sigüés section show that the N060 set is passively rotated in the syncline footwall. This set was therefore developed prior to the activity of the Leyre thrust.

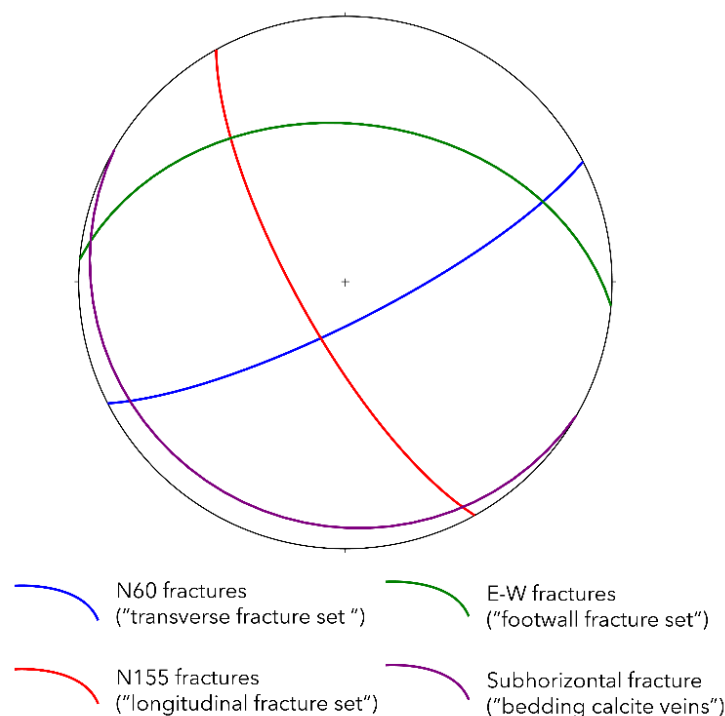


Figure 150: The four sets of fractures described in the Sigüés-Orba footwall

- A set of joints with **N160 direction**, called longitudinal fractures, which appears in the metric rock domains between the N60 fractures (Grignard, 2018).
- **E-W fractures** which are found mainly in the outcrops closest to the Orba thrust (Léon, 2022; Grignard, 2018).

CHAPTER 5 - PALEOTHERMOMETRY AND FLUIDS

- A set of **sub-horizontal calcite faults**, parallel to bedding.

In this PhD, we focused on the calcite faults. These planes, generally parallel to the bedding, are observed in the footwall of the Leyre fault. Thicknesses range from a few mm to cm, with several calcite bands stacked on top of each other. These planes resemble those described by Deville et al. (2020) (Figure 151, left below) in the shales of the Parras Basin (México). The latter are described in the shales of the Parras Basin in Mexico. In the Illón frontal anticline, we observed a calcite-fault in its footwall syncline (Figure 151d), which would indicate its precocity in the system with respect to folding. Some faults are intersected by N60 fracturing initiated before folding (Crognier, 2016). These two observations, folding of the calcite fault and fracturing, therefore indicate that some of these faults are set up early, before folding.

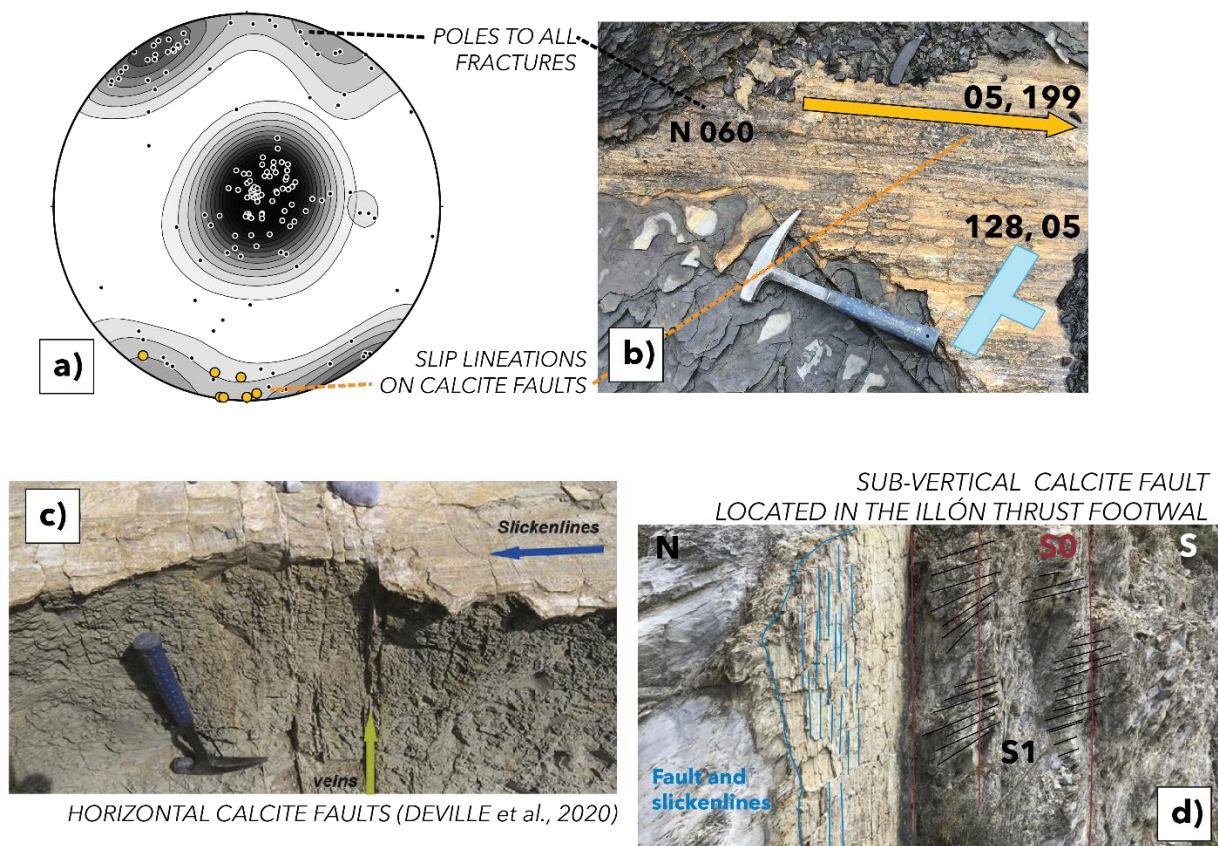


Figure 151: a) Stereoplot of the vein orientation measured in the fieldwork of this thesis ($n=160$). Contours show mostly subhorizontal calcite faults, and also the subvertical N060 set. Some representative lineations are plotted in yellow, but not all of them. For a detail of the lineations, see Figure 168 .b)An example of subhorizontal calcite fault. It exhibits lineation striations, and also an N060 fracture. C) Horizontal calcite fault from Deville et al. (2020), it is also parallel to bedding in a similar context to Sigués site. D) Calcite fault belonging to the same set as fault B, but arranged subvertically. This occurs in the footwall syncline of the Illón range, indicating its earliest occurrence in the system, even before the folding stage.

Plane orientation and striation are shown in Figure 151a. A close picture of one of these fault planes is shown in Figure 151b. The bedding-parallel faults are crosscut by the N60 fracture, thus demonstrating that calcite faults predated this set of fractures.

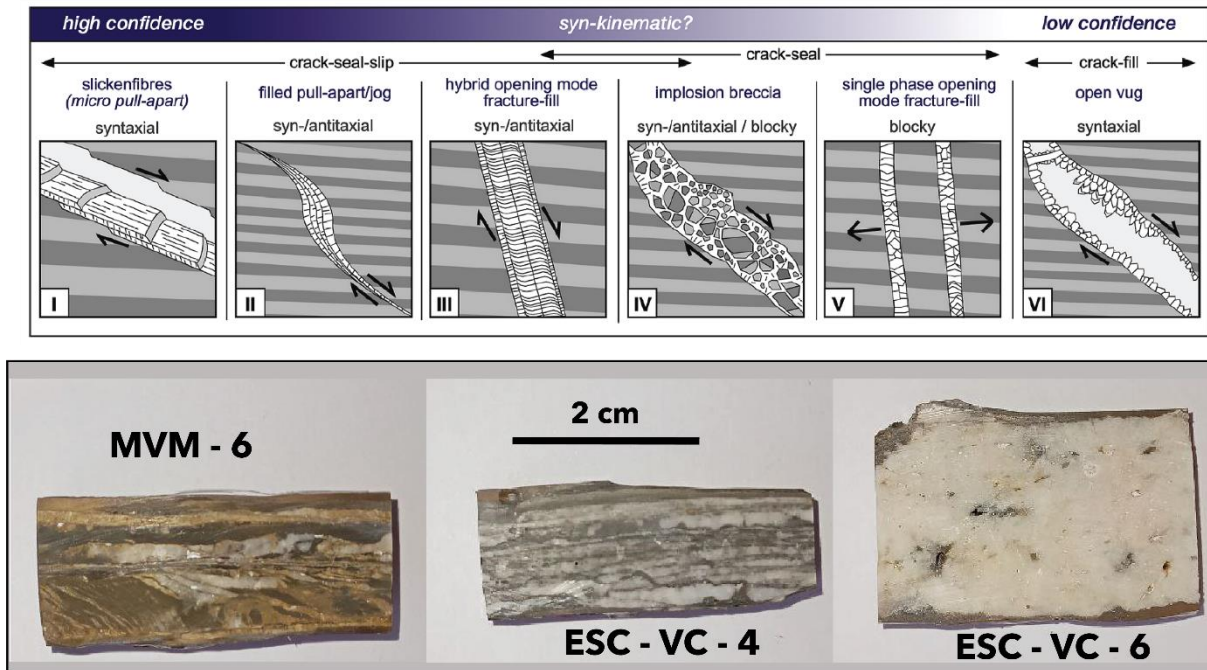


Figure 152: Hand-cut samples of the calcite faults. These can be summarized in these three samples: faults with strong signs of shear such as MVM-6; faults with several sub-parallel segments as ESC-VC-4; and faults with massive crystals as ESC-VC-6.

Fault section display several types of internal architecture (Figure 152). Roberts and Holdsworth (2022) study calcite faults for dating, and in their review propose several types of structure based on their confidence in dating calcite crystals. At the bottom of Figure 152 we have placed three calcite faults representative of all those sampled. The vast majority are Type I faults according to Roberts and Holdsworth's classification, where several layers of crystallization and movement episodes are visible (ESC-VC-4). It can be seen how the same calcite-filled fracture has a complex activity, composed of several episodes of crystallisation that thicken the fracture. Some other faults with massive infills, although with striations in their faces appear occasionally (ESC-VC-6). And also, we have found an example similar to Type III, hybrid, with sinusoidal forms in the crystallization of the fault (MVM-6). This type of sheared crystals would indicate crystallisation contemporaneous with the creep-type fault slip.

The calcite faults sampled correspond to those shown in Figure 152 as blue crosses . Other calcite-filled fractures are also indicated in orange, but have not been studied in this thesis.

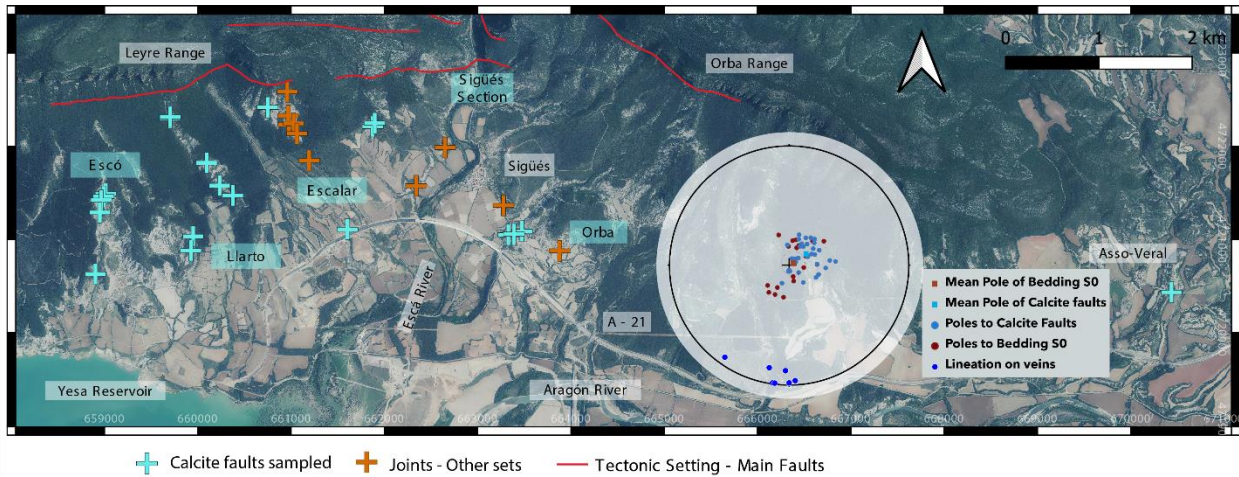


Figure 153: Map of sampled veins in Sigüés - Orba footwall.

These sub-horizontal calcite faults occur at several beds of the Larrés and Pamplona fms, although either due to lack of shale outcrops or difficulty of access, none of them occur in the immediate vicinity of the fault (< 100 m horizontal distance). The calcite faults can appear next to highly deformed shale levels, such as Llarto or Escó, or also in the middle of large marly beds, in areas far from the main fault, such as in Orba.

The map also shows other points (orange crosses) with calcite veins that have not been sampled because they do not coincide with the calcite faults, but which show that fracturing and fluid circulation appear in several areas of the footwall of the Leyre system.

In summary, with these veins it is expected to obtain data on the kinematics of the Leyre frontal thrust and the associated cleavage in the footwall. The objectives and methodology will be based on the following techniques:

- **Microthermometry**, for which it is expected to analyse the fluid inclusions trapped in the calcite veins and obtain temperatures of biphased inclusions.
- **Dating**, for which the samples for studying by means of U-Pb isotopy are prepared, something that has already been applied to calcite veins.
- And **Stable isotope data**, as it is possible to analyse the fluid-rock relationships in these faults, and their relationship with the regional structure.

5.3.2 Methodology

The samples are collected and prepared as shown in Figure 154



Figure 154: Methodology of calcite fault sampling.

From a hand sample of the calcite fault it has been prepared a thin section (polished to 40 nm) and, a thick section (polished on both sides to 100 nm). The thick section is prepared for

CHAPTER 5 - PALEOTHERMOMETRY AND FLUIDS

the study of fluid inclusions. Targeted points were drilled with a Dremell and powder was collected for isotopy.

This preparation work has been carried out mainly at the University of Zaragoza, where the Research Assistance Service - Rock Preparation (SAI) has cut, polished and mounted all the thick sections, and up to 20 thin sections. The laboratory staff also prepared the calcite powders. Besides this, seven thin sections were prepared at the University of Pau LFCR-laboratory. The list of samples and preparation is as follows:

NAME	SECTION OR SITE	STRIKE	LINEATION	Thick section	Thin section	Calcite powder
LPLe - VC2	La Paul	16, 186	02, 179	No	Yes	Yes
LPLe - VC1	La Paul	11, 167	-	Yes	Yes	Yes
EVC - 1	Escalar	12,161	11,023	No	Yes	Yes
VCG 2	Escalar	24, 128	-	No	Yes	No
ESC-VC6	Llarto	30, 311	01, 310	Yes	Yes	Yes
ESC-VC7	Llarto	26, 230	24, 317	No	Yes	No
ESC-VC1	Escó	05, 248	02, 165	No	Yes	No
ESC-VC2	Escó	11, 097	11, 191	Yes	Yes	Yes
ESC-VC3	Escó	17, 333	13, 025	Yes	Yes	Yes
ESC-VC4	Escó	21, 277	-	Yes	Yes	Yes
ESC-VC5	Escó	17, 256	22, 014	Yes	Yes	No
EVCO-1	Orba	09,111	02,183	Yes	Yes	Prepared by Léon (2022)
EVCO-2	Orba	05,099	07,173	Yes	Yes	
EVCO-4	Orba	06,136	02,209	No		
AV - 1	Asso veral	12, 348	10, 036	No	Yes	
Mvm1	Llarto	06, 131	-	Yes	Yes	Yes
Mvm2	Llarto	25, 184	-	Yes 2a	Yes 2a	Yes 2b
		14, 152	14, 191	Yes 2b	Yes 2b	
		13, 292	-	Yes 2c	Yes 2c	
Mvm3	Llarto	21, 197	04, 177	Yes	Yes	Yes
Mvm4	Esco	05, 153	01, 188	Yes	Yes	Yes
Mvm5	Esco	19, 130	03, 222	Yes	Yes 5a	Yes
		14, 085	05, 197		Yes 5b	
Mvm6	San Juan	04, 277	-	Yes	yes	Yes

Table 9: List of prepared samples, and type of preparations each sample had.

The Orba samples (EVCO 1 to 4, and AV-1) were given to Léon (2022) during his master thesis' research.

The **thin section** is primarily used for petrographic characterization. In first instance, by optical microscopy (Nikon-LB150-ND microscope coupled to a Nikon MK1 camera and a PC), but also by means of an OPEA Cathodine cathodoluminescence system that allows to observe the different generations of crystallisation of the calcite in the veins.

Subsequently, these thin sections were subjected to a U-Pb isotopic dating study using an LA-ICP-MS spectrometer, located at CEREGE Laboratory of Université Aix Marseille, assisted by Abel Guihou.

CHAPTER 5 - PALEOTHERMOMETRY AND FLUIDS

The **thick sections** were primarily used for the search and analysis of fluid inclusions. These are observed under the Nikon LV-150-ND optical microscope in the LFCR laboratory, but in this case the mineral is detached from the sample crystal and introduced into a isolated capsule where the Linkam Automatic THMSG600 cooling-heating stage controls temperature.

The **calcite powdered** were sent to the ISTEP - Sorbonne Université Laboratory. There, stable isotope analyses were performed, where the sample is attacked with phosphoric acid in a Kiel IV carbonate device, and the emitted CO₂ is collected and analysed by mass spectroscopy (Delta V).

5.4 Fluid data on calcite faults

In this thesis, 16 thick sections were prepared to study fluid inclusions. Two of them come from Léon (2022) master’s internship supervised by N. Beaudoin. The process of searching for fluid inclusions in the calcite veins was much slower and heavier than expected. Three weeks were spent searching for fluid inclusions, and the results are shown in the table below.

Calcite Fault	FIA	Th	Tm
MVM1	1	188 °C	Not found
	2	174 °C	- 2°C
	3	174 °C	- 4 °C
	4	146 °C	Not found
MVM 2b	1	126 °C	- 9 °C
MVM 4	1	110 °C	Not found
MVMV 6	1	94 °C	- 9 °C
ESC - VC - 6	1	116 °C	- 6 °C
	2	137 °C	- 7 °C
	3	142 °C	- 11°C
LP - VC - 1	1	106 °C	2 °C
MVM 2a	Not found		
MVM 3a	Not found		
MVM 2c	Not found		

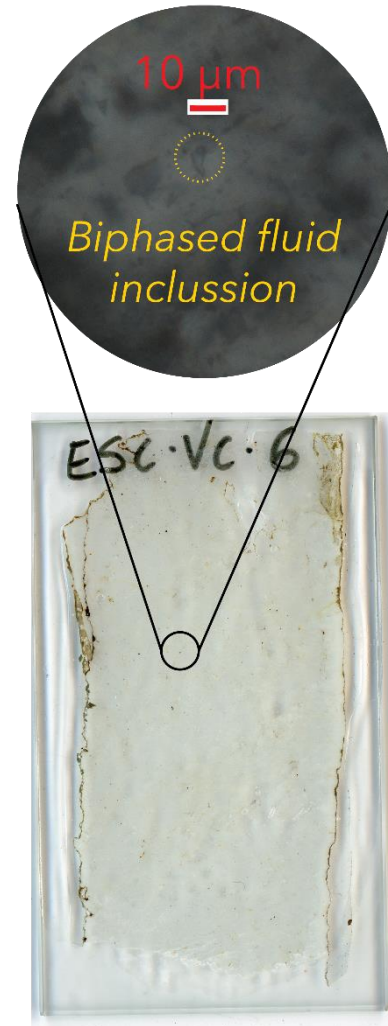


Figure 155: Fluid inclusion in a thick section. (X50 magnification).

Table 10: Summary of microthermometry data on Fluid Inclusions. FIA: Fluid Inclusion Assemblage. Th: Homogenization Temperature. Tm: Melting temperature

Only 6 of 16 thick sections have measurable fluid inclusions with visible phase changes, all between 2 µm (minimum size to observe the two phases and their changes) and 6 µm (Figure 155). The work on searching for fluid inclusions was abandoned after unsuccessful attempts. Practically all are isolated inclusions, in the middle of large crystals without

fractures. This would be related to primary type FIA, corresponding to normal crystalline growth in the calcite phases of the fault.

Léon (2022) adds another 6 veins to the study, in which he could only measure Th as the inclusions were also small (<10 µm). The histogram presenting the different sets measured is attached in Figure 156 . In general, the most frequent temperatures coincide between 60 and 110°C, with a peak around 70°. From this study, it is worth highlighting the sample EVCO-1, corresponding to the “Calcite Faults” marked in grey in the histograms. It belongs to the same set of calcite faults described in this PhD.

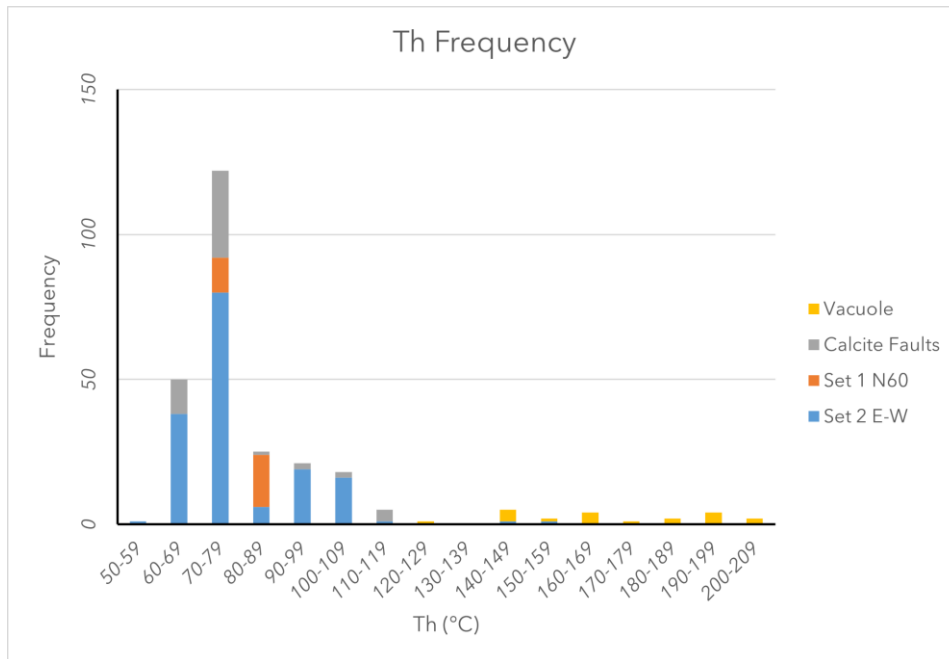


Figure 156: Fluid inclusion data by Léon 2022. For EVCO-1 calcite fault, brought for this sampling campaign (it corresponds to “Calcite faults”, plotted in grey bars), the data is comparable to the rest of the veins presented. Mainly, with Th cooler than any other calcite fault from the same set.

5.5. Dating calcite faults.

In this structural geology work, one of the primary expected results is to obtain a time range for the system of the Leyre thrust, including calcite faults. Field observations show that calcite faults can develop prior to folding and N60 fractures. It remains possible that these faults developed just as late, hence the interest in dating them.

U-Pb isotopy with laser ablation techniques on calcite is now a robust technique in carbonate-composed rocks (Roberts and Holdsworth, 2022; and references therein). Its wide age window (< 1Ma and for the entire Phanerozoic, Roberts et al., 2020) makes it more advantageous than other isotopic decay sequences. Also, with respect to U-Th it requires less U, a trace element (<1000 ppm) in these shale lithologies (Roberts and Holdsworth, 2022).

For this study, the LA-ICP-MS methodology was used, which allows in-situ analysis on the sample, without the need for spraying or drilling. Twenty thin sections were prepared at a

CHAPTER 5 - PALEOTHERMOMETRY AND FLUIDS

thickness of 40 nm (indicated in the list in the Table 9), although later was found out that a thickness of 100 nm would be optimal.

As seen in the description (Figure 152), these prepared faults contained several distinct crystallisation stages. For this reason, and to better understand the phases of the calcitic cement, a cathodoluminescence study was carried out on these faults prior to dating.

The CL image was acquired with a Cathodyne OPEA attached to a Nikon BH2 benchtop optical microscope at the LFCR of the University of Pau and Pays de l'Adour. The imaging conditions are obtained in a vacuum chamber in which the film is placed, and the cathodoluminescence beam is at voltages between 12.5kv and 200-300 mA.

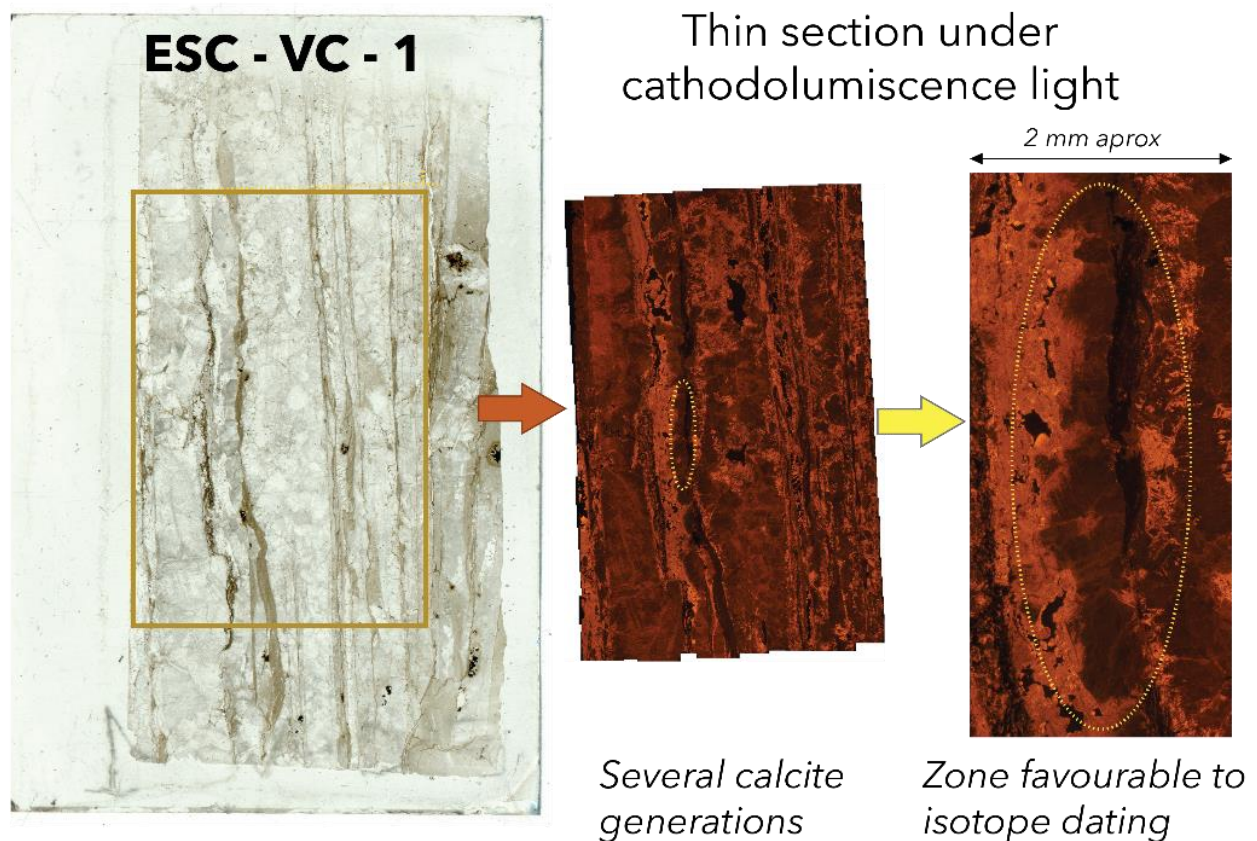


Figure 157: Cathodoluminescence picture on a thin section. The range of reddish to dark colours indicates different generations of calcite crystals. In the pre-dating screenings, it was confirmed that some crystals, such as the one marked, had a favourable isotopy for dating, due to their U content.

Cathodoluminescence photographs confirms that faults contain multiple phases of crystallisation. As seen on Figure 152, three types of fracture architecture were observed: parallel bands (such as the one shown in Figure 157), sheared, or homogeneous phases of millimetre dimensions. The use of Laser Ablation allows quite finely targeting of a particular crystal and obtaining data with precise locations, rather than less precise drilling averages (Roberts and Holdsworth, 2022). In other words, knowledge of this “cement mapping” is important for establishing the fault’s operating agenda.

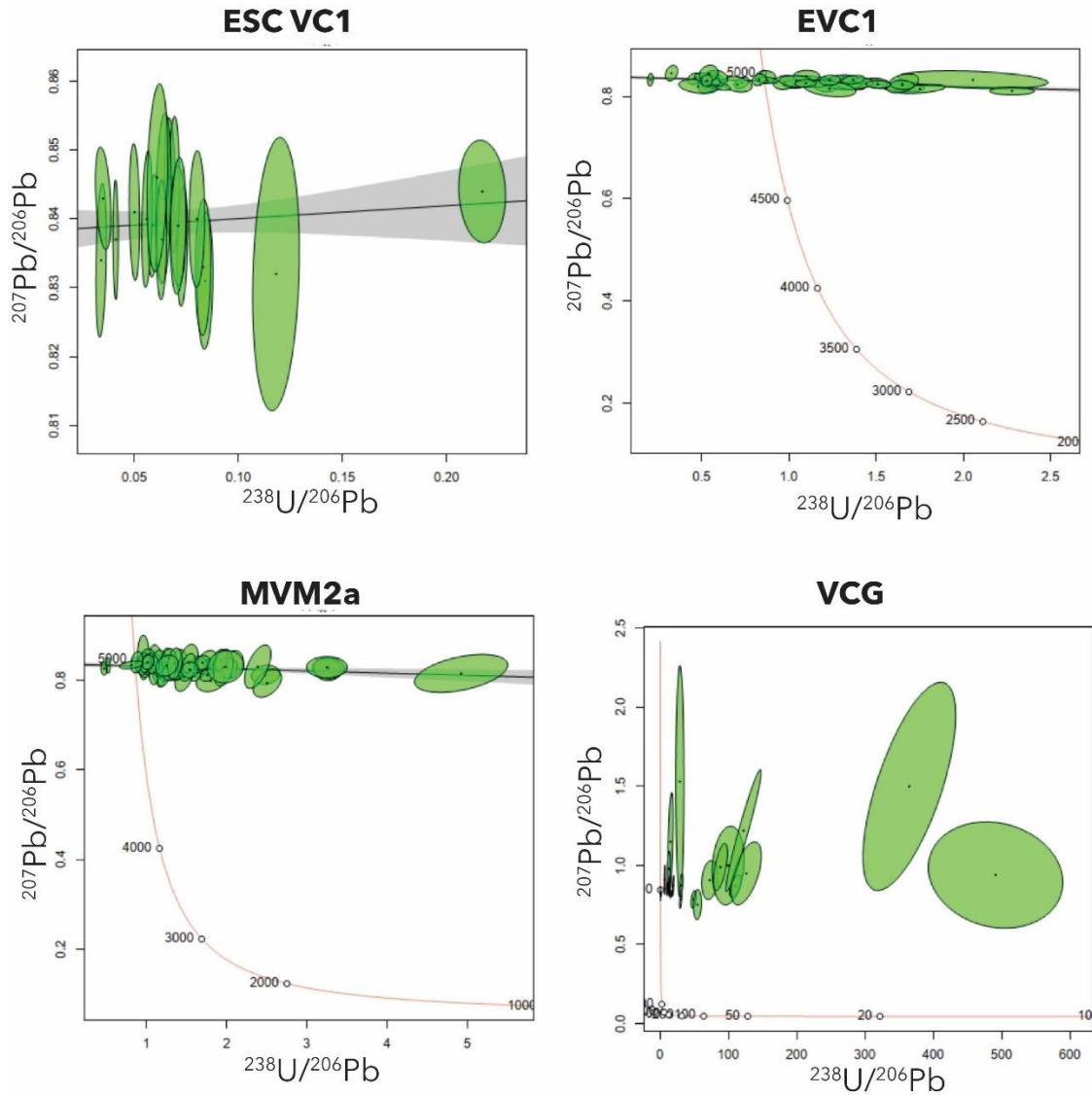
At the CEREGE laboratory of the Aix-Marseille University, hosted by the team of Dr. Pierre Deschamps and Abel Guihou the following methodology was applied:

CHAPTER 5 - PALEOTHERMOMETRY AND FLUIDS

- The thin sections are placed in the ablation instrument, next to the ICP-MS which receives a flow of He that collects the particles denudated by the laser.
- There, before each ablation, the detections of key elements is calibrated with specific standards for each analysis to be performed.
- At first, preliminary ablations are performed in selected areas of the veins, where the cathodoluminescence image is plotted together with a real-time view of the thin section. The aim of this first screening is to select crystals whose isotopic chemistry is favourable for dating, due to their U/Pb ratios. Before any analysis, the surface of the sample is pre-cleaned with 5 s of laser pulses that detach a fraction of the thin section.
- The actual analysis is done in designated areas, within marked crystals, and a few measurement points are programmed on the surface. The mapping of sampling could be different, such as lines, areas... (Roberts et al., 2022). However, in these thin sections, only few areas with a slightly favourable isotopic composition were found. The analysis was done pointing out crystals that seemed to offer a U/Pb ratio close to what it is required for dating, which is 5/1.

In general, before launching the final analysis, the pre-screening phase yielded very negative results. Sixteen of the twenty thin sections were discarded as they did not contain favourable U-Pb ratios: in general, the Pb content was much higher than the U. Only a few crystals from certain veins appeared to be favourable, and these were analysed (between 5/1 and 3/1 ratio).

CHAPTER 5 - PALEOTHERMOMETRY AND FLUIDS



Name	ESC VC1	EVC 1	MVM2a	VCG
U (µg/g)	<0.1	0.001-0.3	0.05-1	0.05-0.8
Pb(µg/g)	1-2	0.05-1.8	0.5-3	<0.05
Age	Unfavourable ratio, non-usable age	Unfavourable ratio, non-usable age	Unfavourable ratio, non-usable age	Good U/Pb ratio, but $^{207}\text{Pb}/^{206}\text{Pb}$ unfavourable Age < 1Ma aprox

Table 11: U-Pb dating results obtained thanks to LA-IMP-MS on CEREGE laboratory (Université-Aix-Marseille). The poor U/Pb isotope ratio means that the concordance lines constructed are not useful, and a coherent age is not obtained.

However, the results were not satisfactory. In all thin sections the U-Pb ratio is unfavourable, due to the large content of Pb isotopes over U isotopes, invalidating the construction of any useable Concordia line on the disintegration curve. This geochemical

composition, persistently unfavourable, drives to not go deeper into the results, which are summarised in Table 11. The Concordia lines shown on Table 5 do not display any useful data, and are solely shown to indicate the absurdity of the calculation without the expected good U-Pb decay ratios, with a mathematical indeterminacy beyond any acceptable statistics.

Only one exception, VCG, has a favourable U-Pb ratio (Table 11). Nevertheless, to prepare for Concordia line, the ratio of the Pb isotopes ^{207}Pb and ^{206}Pb is found insufficient. This type of isotopic set is related with veins that are < 1 Ma, as this isotope of Pb has not disintegrated into its daughter product enough to construct the Concordia line. This recent age needs to be confirmed in future analysis of the regional calcite faults.

This part of the work, with the great interest in obtaining a precise dating, turned out to be a failure. This experiment, in which up to 20 thin sections were used, and 19 of them seem to respond to an unfavourable but recurring isotopic signal, can also encapsulate a coherent reading. Sampling of these calcite faults was carried out at several points along the footwall of the Leyre fault. i.e. the results cannot be fitted into a poorly contextualised sampling, but are recursive of the calcite faults. In the discussion this information along with other about the calcite faults will be revisited.

Some summary points of these isotopic dating analyses are:

- These faults correspond to sub-horizontal slip planes that have hosted displacement several times with N-S kinematics.
- These faults appear to have operated in a period preceding the operation of the large regional thrusts and their associated deformation (Figure 151), and could potentially be active recently, as suggested by the only age dating that we have been able to obtain ($<1\text{Ma}$).
- To support this hypothesis of recent activity, note the seismic activity of the Aragón Valley (Martes Earthquake; Carbonel et al., 2019; García-Mayordomo and Insua-Arévalo, 2011), the hydrothermal source points such as Tiermas (Blasco et al., 2017; Navarro et al., 2004) or near Asso-Veral (Léon, 2022) with hot water and gas emissions ~ 30 °C.

5.6 Isotopic data.

In this section the results of the last two analyses done on calcite faults will be reviewed: oxygen and carbon stable isotopes and chemical cartography, i.e. isotopic maps.

5.6.1 Stable isotopes:

To obtain isotopic data, spots were drilled in 14 of the sampled veins (listed in Table 9: List of prepared samples, and type of preparations each sample had.). According to the complexity of the veins, homogeneous crystals were marked to avoid mixing phases of vein growth. Powders were analysed with KIEV IV carbonate device connected to a DELTA V mass spectrometer (ISTeP laboratory, Paris, France).

The samples are attacked in a vacuum with anhydrous orthophosphoric acid (density 1.945 g/cm³), and the reaction temperature is 70°C . The CO_2 obtained is purified and cryogenically separated. In this thesis, several series of measurements from the sampling described above are included, but also from other sets of veins related to the sampling performed by Léon

CHAPTER 5 - PALEOTHERMOMETRY AND FLUIDS

(2022). The results are normalized and calibrated using an NBS-19 standard, obtaining deviations of 0.01‰ and 0.02‰ for $\delta^{13}\text{C}$, and 0.06 ‰ and 0.10‰ for $\delta^{18}\text{O}$.

Figure 158 includes datasets relating to the calcite fault set, as well as host-rock. The variability in the measurements is quite high, but some observations that will help in the interpretation are that:

- The host rocks in the footwall (Larrés Fm) have a generally similar isotopic signal in a cluster of $\delta^{13}\text{C}$ content close to 0 and $\delta^{18}\text{O}$ content between -8 and -5.
- Most stable isotopes of the faults can be assimilated to this cluster, even if there are some outliers.

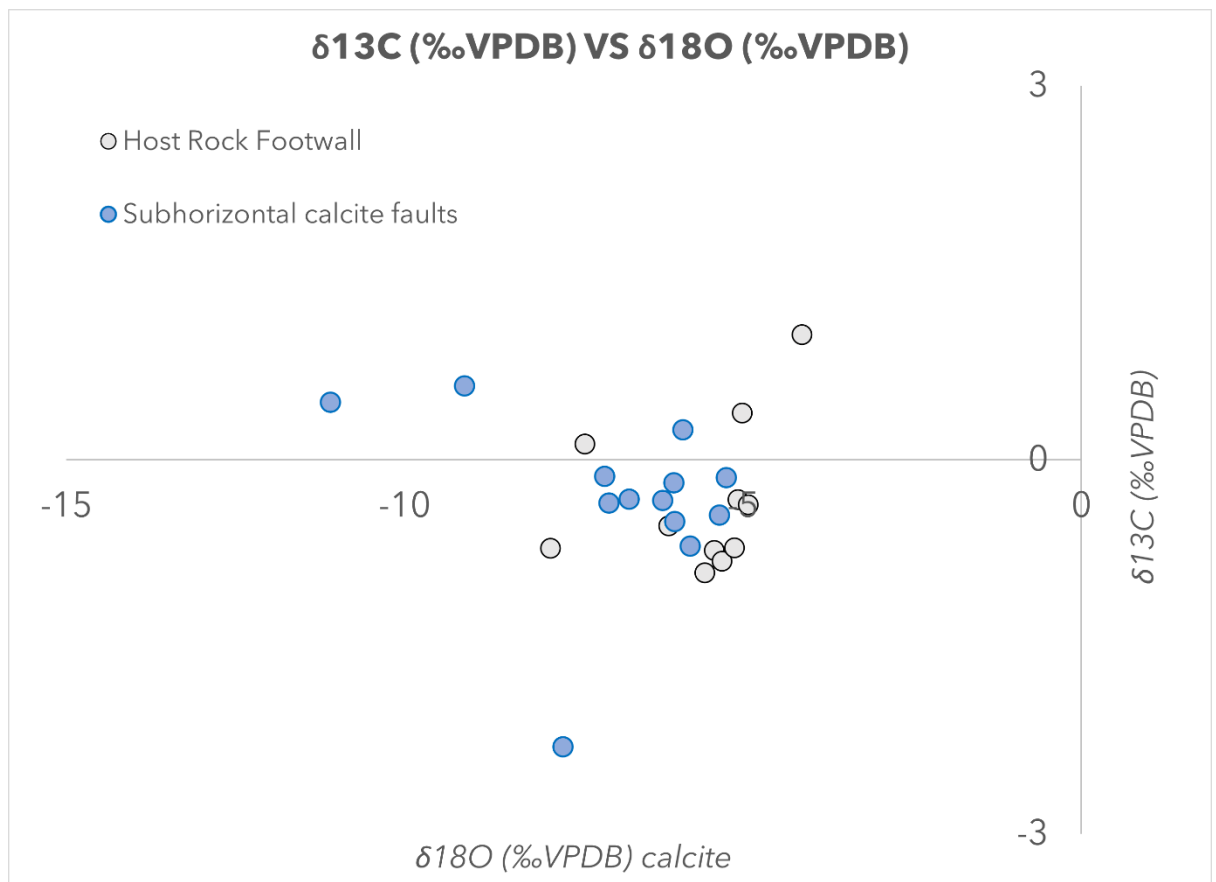


Figure 158: Isotopic data obtained from subhorizontal calcite fault set sampled in this thesis.

5.6.2 Chemical mapping:

In the same CEREGE laboratory that has been used for U-Pb analysis, and with the same laser ablation technology (LA-IMP-MS), it is possible to perform a "chemical mapping" of elements on a mineral surface.

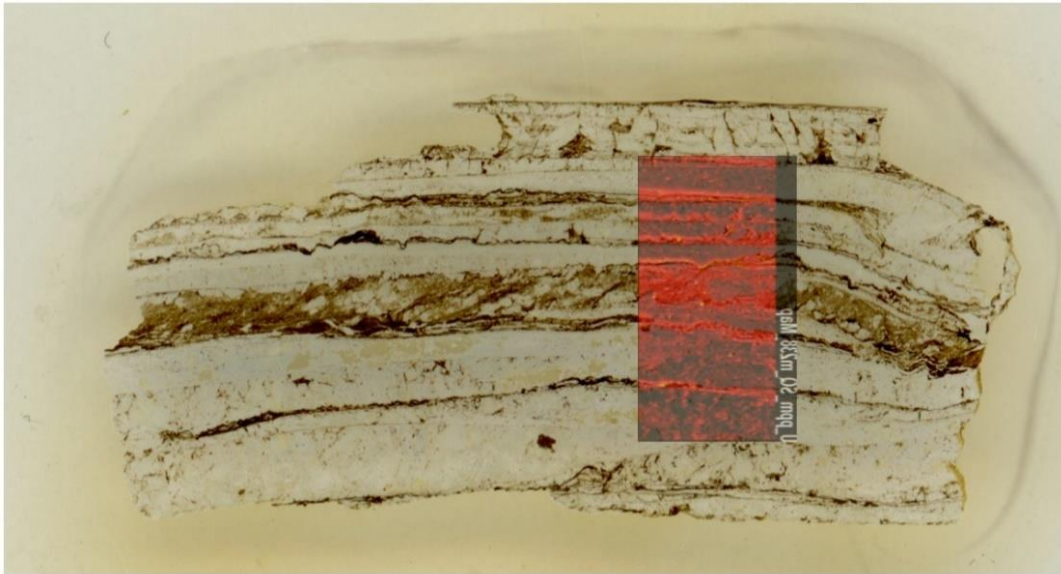


Figure 159: Chemical mapping on the thin section of a calcite fault (specimen EVC - 1). Isotopes are detailed on Figure 160.

The laser ablation beam is programmed in such a way that it makes lines on the surface of the thin section, and obtains an analysis of the detached mass synchronised with the laser displacement. In this case, 50 μm lines were programmed on the surface of two thin sections. This gives a detailed map of $\approx 1\text{mm} \times 0.3\text{mm}$ in size of a mineral surface (Figure 159). This thin section is made up of ten or so layers, each of which can be used to trace the activity of this fault over time. The central layer shows S-C planes that indicate top shearing towards the left of the image, i.e. towards the south

The mass spectrometer is programmed to detect a list of isotopes with unique nuclear mass, thus the detection for each isotope is individualised. In this case, the chemical content for each of the 22 selected isotopes is shown in Figure 160.

We find three types of distribution:

- Isotopes that coincide with the cleanest and most homogeneous calcite crystals in the fault. This is the case of Sr, Ba, or Mn.
- Another type is the opaque zones, more enriched in clay minerals, which coincide with the relative concentration of elements such as B, Mg, Al, Si, Ti, V, V, Zr, Pb (various), Th or U.
- A few elements have a *quasi* homogeneous distribution, such as Ca, La, Ce, Nd or Sm.

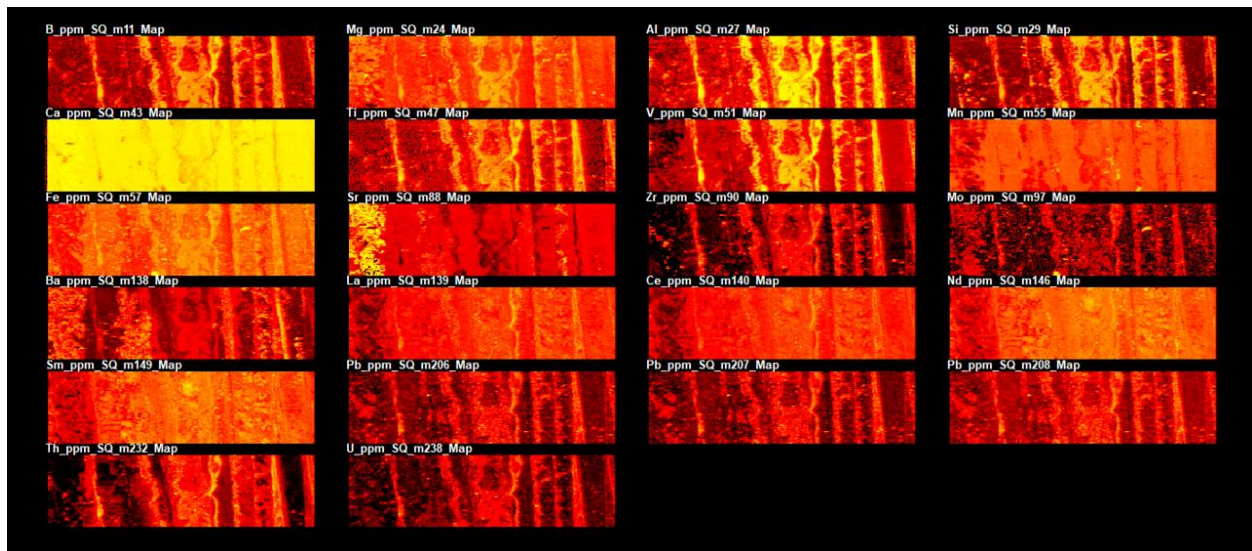


Figure 160: Isotopic chemical map performed on EVC-1 calcite fault. Size for the map is 1mm * 0.3 mm

5.7 Synthesis

In this chapter, we have clarified the burial conditions of the Larrés formation using Raman spectroscopy (RSCM), and we have focused an isotopic study on an object that we found interesting in the Leyre and Orba fault system, subhorizontal fault planes filled with several levels of calcite.

5.7.1 Burial temperature

The new temperature obtained by the RSCM technique (Figure 161) is of the order of 200°C and is not well constrained with this technique. It is, however, significantly higher than the values attributed by Crognier (2016) and Izquierdo-Llavall et al. (2013) (<180°C). The Sigüés area therefore seems to be affected by a higher temperature than initially thought. This is particularly true if we compare this burial temperature with that observed in the Jaca Basin further east. In fact, a temperature of 200°C is more frequently observed at the heart of the turbidite basin (Figure 144). This fairly high temperature also explains the numerous dissolution crystallisation phenomena affecting the calcitic phase (Saur et al., 2020).

CHAPTER 5 - PALEOTHERMOMETRY AND FLUIDS

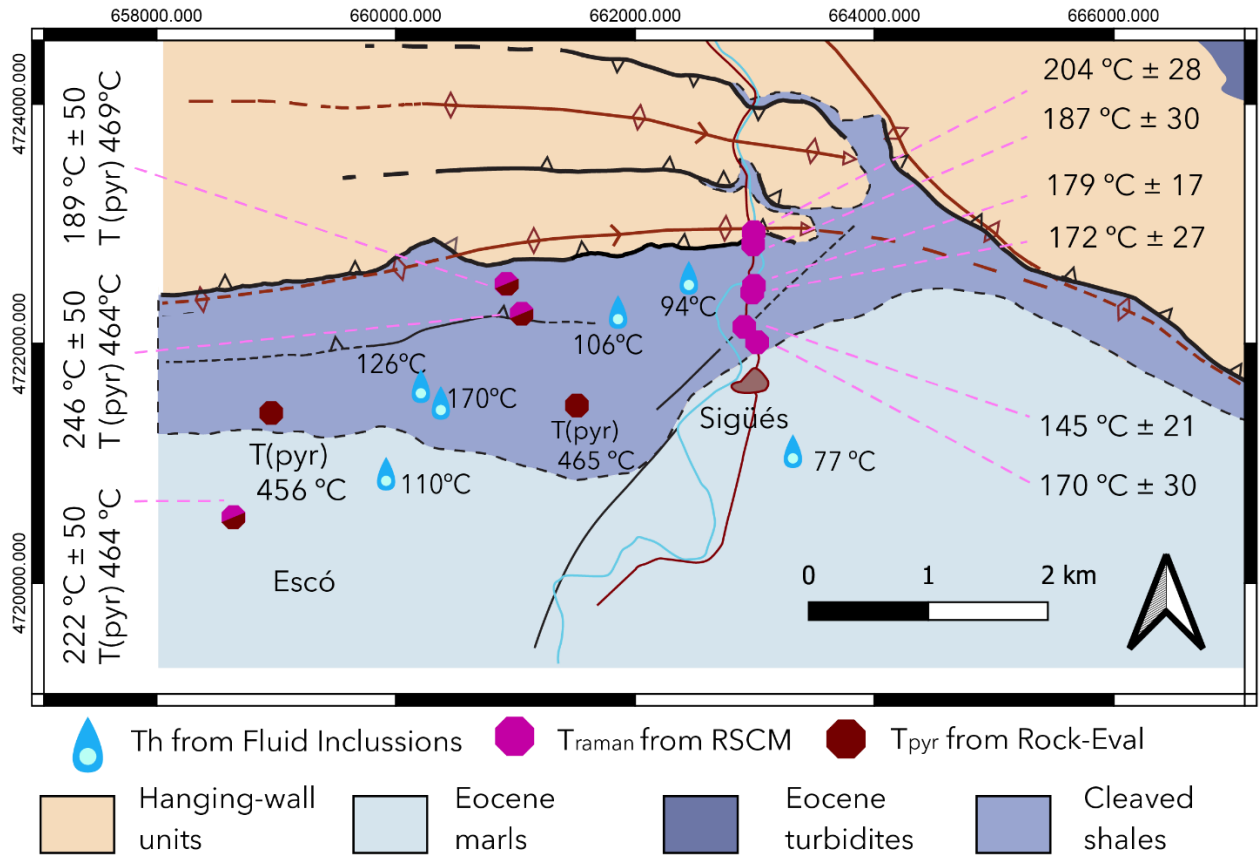


Figure 161: Summary map with data collected by Crognier (2019), Grignard (2018), Léon (2022) and Gracia-Puzo in this thesis.

Several hypotheses can be put forward to explain this abnormal temperature to the west of the Jaca Basin. Tectonic stacking may lead to thermal anomalies beneath the nappes (Deville and Sassi, 2006). We present the classic example of the Appalachians, with thermal anomalies extending over several kilometres (Figure 162) in the footwall of the orogenic zone. However, the compilation of thermal data from the Jaca Basin does not show any particular relationship with the proposed zonation of isotherms and the major fault system (Figure 144). So, without ruling out the hypothesis of a putative role for the Leyre fault, for example, we find it unconvincing to invoke a local thermal anomaly.

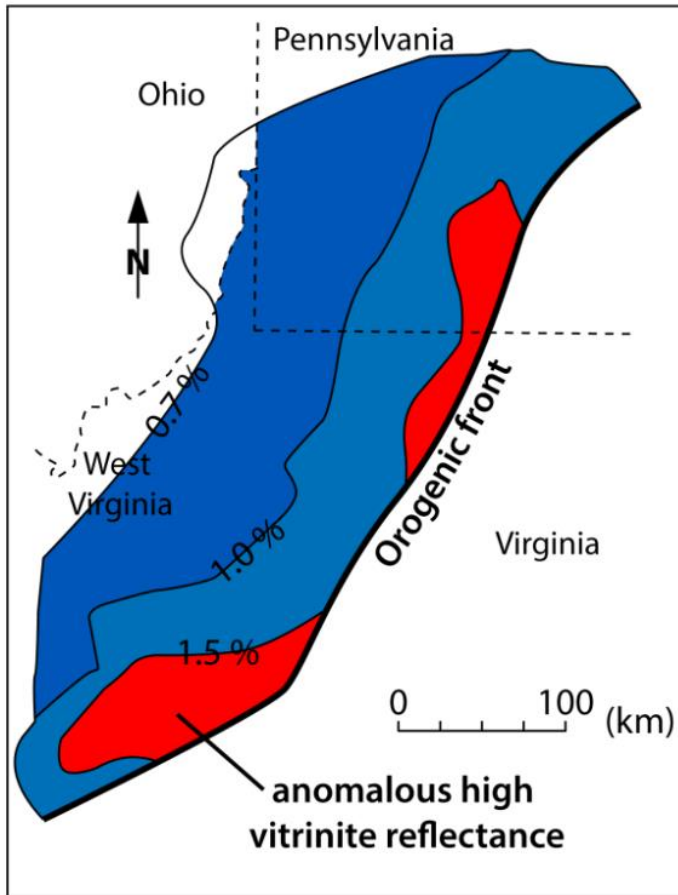


Figure 162: Vitrinite reflectance distribution map of the Appalachians, showing anomalies (red) of high vitrinite reflectance. These zones are located close to the orogenic front (and thrust fronts), and extend up to 50 km westward into the foreland basin. From Evans and Battles (1999) modified by Crognier (2016b)

A thermal anomaly can be linked to fluid circulation (Monte Perdido thrust unit, Lacroix et al., 2011). In the footwall of the Leyre and Orba thrusts there is little evidence of massive fluid injections. The horizontal faults we have studied are not capable of heating a sedimentary series, especially as the rare fluid inclusion data we have do not show temperatures close to 200°C. The same applies to the filling of fracturing systems (Crognier et al., 2018). The footwall of the Leyre thrust is clearly visible next to the Sigüés gorge, along A-176 road. Just a few metres from the fault, the deformation intensifies drastically, without the expression of fluid circulation through the fractures and cleavage. We therefore think it unlikely that fluids acted to heat up this part of the cover.

Crognier et al. (2018) carried out 1D thermal modelling on Sigüés (Figure 163) and found a theoretical temperature of the order of 200°C at the base of the Larrés formation, based on the strong assumption that the Campodarbe clastic formation was filled in for more than 2 km, and that this formation has now disappeared as a result of erosion. This thickness is fairly consistent with that observed further south. The extra thickness of Campodarbe formation (or Oligo-Miocene clastic equivalent) at this point in the chain, if confirmed by other data, may help to explain the thermal anomaly at Sigüés

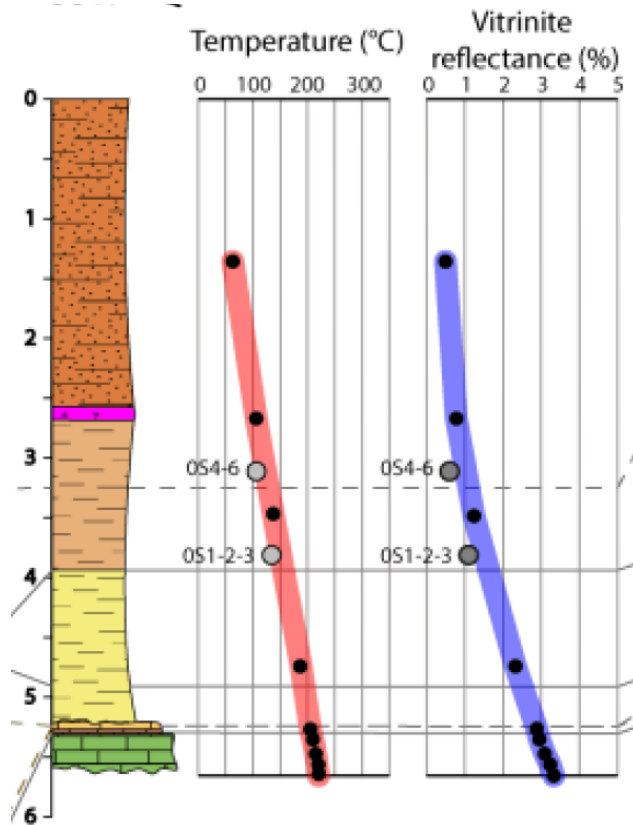


Figure 163: From Crognier (2016). 1D thermal modellisation of Southern Roncal section (corresponds to Leyre system).

Our new RSCM data, with those of Grignard (2018), do not support the existence of a gradient linked to fault activity. This indicates that the deformation-related degradation of organic matter does not prevent a signal that can be exploited in Raman.

5.7.2 Isotopes on calcite faults

These calcite faults regularly outcrop in the footwall of the Leyre thrust. Initially, we thought that they were linked to the thrust, but the observation of such faults, tilted with folding (Figure 151) in the Orba range, suggests that there are multiple planes that accompany the basal thrusting, from which the Leyre and Orba thrusts emerge as ramps. Similar faults are described by Deville et al. (2020) in the Parras Basin (Mexico). These faults have not been specifically studied by either Izquierdo-Llavall et al. (2013a) or Grignard (2018). A preliminary study was carried out by Léon (2022) on a single calcite fault.

Our cathodoluminescence optical microscopy observations show the stacking of several layers (Figure 157) sometimes showing top-to-south horizontal shear and lineations mainly N-S. These calcite faults therefore represent an accumulation of various slip events. Figure 156 shows that fluid temperature range from 90°C to around 120°C (grey triangle). This suggests a burial path if the fluid is at equilibrium during the fault's activity. It is therefore likely that this fault operated at burial depths of 3-4 km to 4-5 km depending on the gradient (25°C/km to 30°C/km).

The fluid inclusion study proved unsuccessful, as it did not allow for a statistical approach. The only prepared section used to describe several inclusions (4) gives a high temperature

CHAPTER 5 - PALEOTHERMOMETRY AND FLUIDS

range (Th between 146 and 188°C), similar to those reported by Crognier (2016) and Grignard (2018). However, if confirmed, these temperatures are higher than those recorded by (Izquierdo-Llavall et al., 2013a) or Léon (2022). There appear to be two different systems, with a meteoric water input, and an in situ water input as proposed by Léon (2022). Our data at this stage do not allow us to decide between the two possibilities.

Ten out of 14 calcite powder samples give a $\delta^{18}\text{O}$ isotopic signature close to -5, and $\delta^{13}\text{C}$ close to 0 (Figure 164). It should be noted that a large number of the data collected by Crognier et al. (2018) and Léon (2022) are in the same range. This background remains enigmatic.

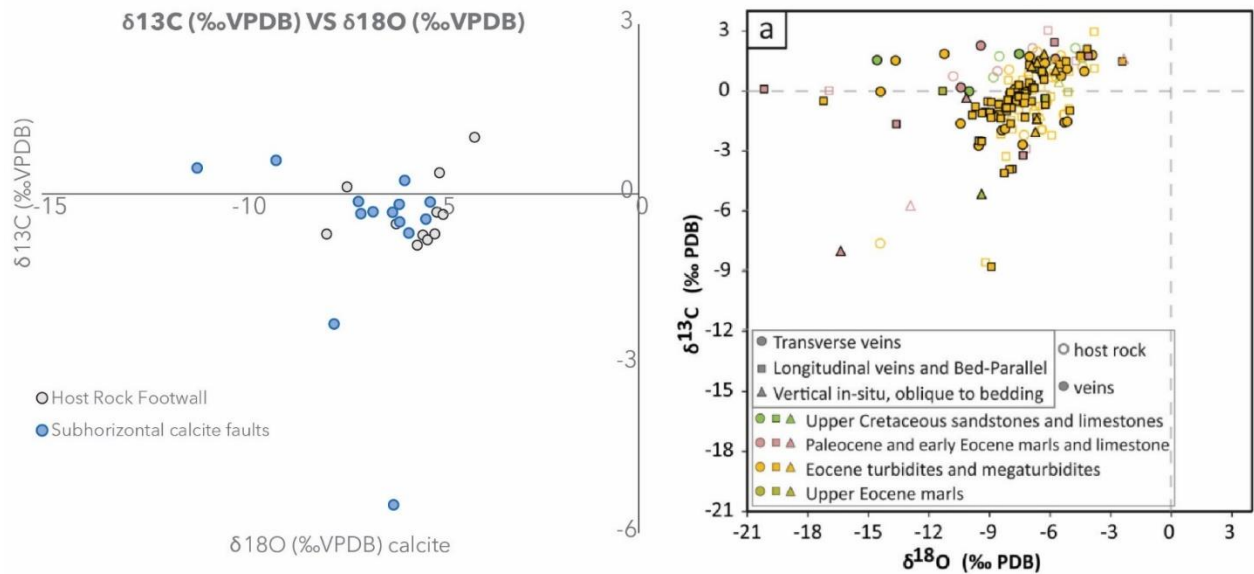


Figure 164: Separate isotope data from subhorizontal calcite faults and host rock (Larrés Fm), compared with data obtained by Crognier (2016) in the Jaca Basin.

Attempts to date U/Pb using laser ablation have proved unsuccessful. We do not give any real credit to the only dating obtained, which gives an age younger than 1 Ma, a data that needs to be confirmed.

However, it seems possible that the basal detachment system is still operating, as evidenced by the significant seismic activity in the region and the circulation of hot fluids within Eocene shales (Tiermas hot springs).

5.8 Conclusions

The main work following fluid studies and thermometry has been the sampling of calcite veins. These had the potential to provide information on several geochemical and genetic dimensions of the Eocene marls. However, the data obtained are few, statistically poor compared to magnetic fabric studies in this same thesis, or other fluid-related published articles (Crognier et al., 2018; Hoareau et al., 2021). Fluid inclusions have had a low occurrence in the sampled calcite faults. Dating has been a failure because of the poor U-Pb ratio. Isotopic studies do not correspond to the core knowledge of this thesis and provide very little information. In general, the fluid circulation story is interpreted as "in equilibrium" with the host-rock.

CHAPTER 5 - PALEOTHERMOMETRY AND FLUIDS

On the other hand, a number of unpublished data have been recompiled in order to compile information on burial temperatures for the Eocene marls. This includes a series of Raman spectroscopies, Rock-Eval data and other isotopies that the author of this thesis has not performed in the laboratory. But they are included in order to add a new set of data with respect to the rock under study in this thesis. This data, in addition to the fluid inclusion data, gives an expected maximum T_{burial} of $\sim 180^{\circ}\text{C}$, similar to data already available in the literature. This confirms burial conditions suitable for those studies on the shortening calculation performed in section 4.4. Strain quantification at the Sigüés site.

6. DISCUSSION

6.1 Introduction

The Jaca basin is the setting in which all the research in this thesis takes place. The Jaca Basin can be defined as an initially orogenic foreland basin, with a sequence of piggyback thrusts towards the foreland, subsequently transported southwards as a piggyback basin (Hogan and Burbank, 1995; Ori and Friend, 1984). Indeed, the Jaca basin is not a unique, atypical geological setting with rare deformation sequences. The South Pyrenean slope corresponds to a very classical deformed foreland basin, and has been extensively studied as demonstrated in section 2.5 The Southern Pyrenees, a natural laboratory of magnetic fabric in shales and slates. It is in this context that we study our "deformation gradient" phenomenon, which, although it corresponds to a local observation, is linked to the Leyre structure. We should not neglect the regional framework of this thrust, which may be familiar and parallel to many other known geological environments and can be used as a deformational model for other orogenic belts in the world.

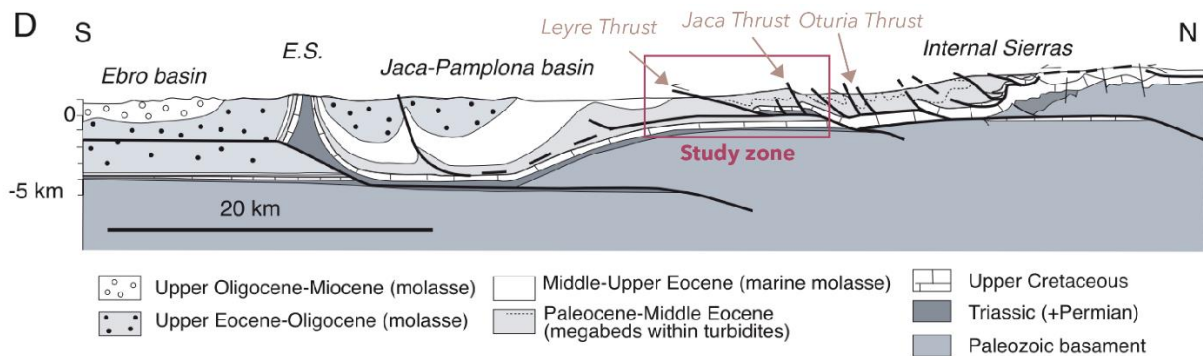


Figure 165: Cross-section of the Central Pyrenees in the western part of the Axial Zone. From Oliva-Urcia et al. (2012), modified from Teixell and García-Sansegundo (1995).

Hence, the South-Pyrenean foreland basin is the pro-foreland in the Iberian plate whose crust subducts under the European plate (Campanyà et al., 2011; Garcés et al., 2020; Muñoz, 1992; Teixell, 1998 and references therein). Progressive compression and stacking of thrust sheets occurred in a piggy-back sequence from the Late Cretaceous to the Early Miocene (Cámara and Klimovitz, 2010). There are exceptions of break-back thrust sequence during the Eocene-Oligocene boundary such as the sequence of thrusts of the Sierras Marginales in the Catalan Pyrenees (Muñoz 2002, Verges and Muñoz 1990) or in the Sierras Exteriores in the Aragonese sector (Millán-Garrido et al., 2000; Millán, 1996).

The sequence of events proposed by Labaume and Teixell (2018) for the eastern sector of the Jaca Basin is as follows:

- 1) Emplacement of the Monte Perdido unit of Séguret (1972) which includes several thrust episodes, from oldest to youngest: Peña-Montañesa thrust, the Larra thrust system (branching also towards the turbidite basin) and the Ordesa thrust. All these mostly involve the K-Pg sequence, and are mostly detached at the base of the Campanian-Santonian units, coinciding with the marls of the Zuriza Fm.

CHAPTER 6 - DISCUSSION

- 2) The Gavarnie basement thrust emerges as the Oturia thrust in the southern part of the outcrop of the Hecho Group turbidites, and overlies the Bartonian-Priabonian deposits.
- 3) The Jaca thrust emerges in the Larrés marls, settles eastwards, and eastwards involves the Illón and Leyre units. They are considered acting coevally, although somewhat earlier than the Oturia system (Labaume et al., 2016).
- 4) The South Pyrenean Frontal Thrust system, which outcrops at the southern boundary of the entire south Pyrenean basin marking the limit of the piggyback basins. It is related to the Guarga basal thrust, and it is a structure that may be more complex, with N-S branching and folding (Anastasio and Holl, 2001; Millán-Garrido et al., 2000; Millán, 1996; Pueyo-Morer et al., 1997).

This entire system has been extensively studied in the literature, thanks to the exceptional nature of its outcrops, and the preservation of the sedimentary series which has allowed growth strata and unconformities to be matched with outcropping structures. In contrast, there is no precise dating study for these basal thrusts in the literature (Labaume and Teixell, 2018).

Despite the local levels of décollement, described for the Larra system, the thrust system has its main detachment level in the Middle-Upper Triassic layers, in the Muschelkak and Keuper facies. It is mainly a thin-skinned system, in which there is a structural decoupling between the layers above this level (corresponding to the piggyback foreland basin), and the Lower Triassic and Paleozoic (here including the post-Variscan Upper carboniferous and Permian units) levels below, generally considered a "basement" and/or "tegment".

It is the band lateral to the orogen axis, parallel to the Jaca thrust the one that we have been studying in the Roncal transect. The cross-sections, showing building of folds associated with emerging thrust ramps are a classic subject of regional tectonics (see section

3.4. Structural frame and serial Cross -Sections.). But on the other hand, so is the phenomenon of cleavage, and more precisely the study of the cleavage gradient discovered in the footwall of the Leyre thrust.

We have already made a synthesis of the burial conditions in this sector, framed within the study of the Jaca basin previously carried out by Crognier et al. (2018), Izquierdo-Llavall et al. (2013) and completed by Grignard (unpublished, pers. Comm.).

CHAPTER 6 - DISCUSSION

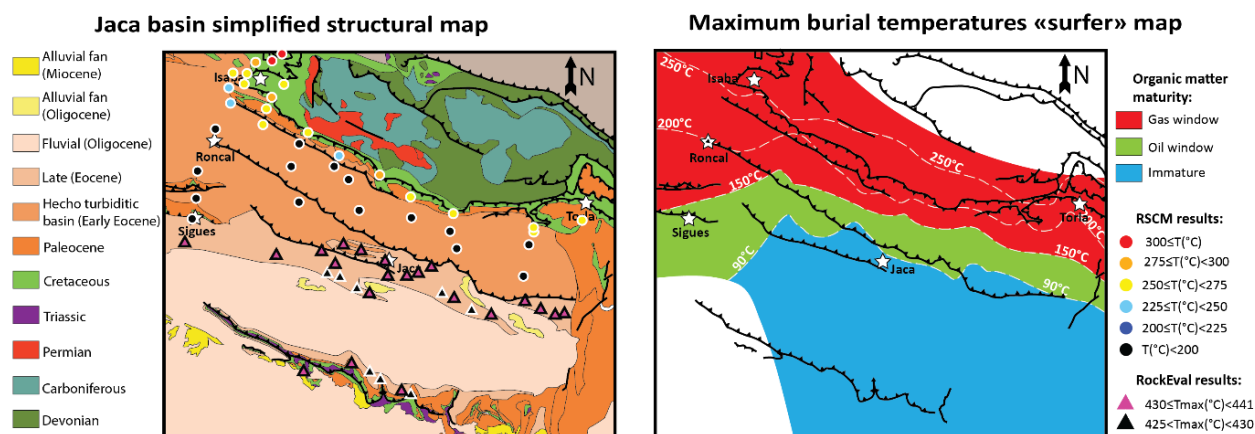


Figure 166: Modelling of burial temperatures after extensive sampling and RSCM acquisition in the Jaca Basin. Unpublished figures from Grignard (Pers. Comm.). Note the lack of correlation between the thermal isotherms and the faults mapped in the Sigüés zone

The calculation of peak burial temperatures in this sector of the orogen also reveals a gradation of temperatures at the foreland basin. We can observe that the domain of higher temperatures corresponds to the Eocene turbiditic basin, which accumulates the higher thicknesses, and the stacking of the thrust sheets of the Larra system. This zone corresponds to the Cleavage domain proposed by Izquierdo-Llavall et al. (2013). Grignard proposes a lower temperature transition to the molasse basin (Larrés to Belsué Atarés Fm, Eocene), in which the Oturia thrust acts as a boundary between the oil and gas windows, presuming <150°C. Finally, southwards there is a progradation of the molasse deposits, and in the Oligocene fluvial sediments (Campodarbe Fm) the maximum burial temperature of the rocks would be progressively lower.

It is therefore at this mid-point of the foreland basin represented by the Leyre structure (peak burial temperature near 180°C), with the development of the ramp and fold structures mentioned above, that this transition of conditions occurs, and where the characteristics of the deformation become of interest.

6.2 Early deformation

The Sigüés area corresponds to the entire block of the South Pyrenean area in which large basal thrusts propagate southwards and form thrust sheets within the cover and the syntectonic units (See 3.4. Structural frame and serial Cross -Sections.).

We will focus now on the local structure that corresponds especially to the Roncal - Sigüés area. The cross-sections following this transect of the orogen (Figure 95 and Figure 96) coincide in drawing a sub-horizontal basal thrust rooted and developed in the Triassic, the overall décollement level for the cover units. Authors who have studied the structure of the Jaca Basin agree that: there is a basement thrust corresponding to the "Fiscal thrust" (after Labaume and Teixell, 2018) which raises the "Gavarnie unit". This Fiscal thrust would die out ~10 km south of this Leyre-Orba structure (Labaume and Teixell, 2018; Oliva-Urcia et al., 2012; Teixell, 1996).

CHAPTER 6 - DISCUSSION

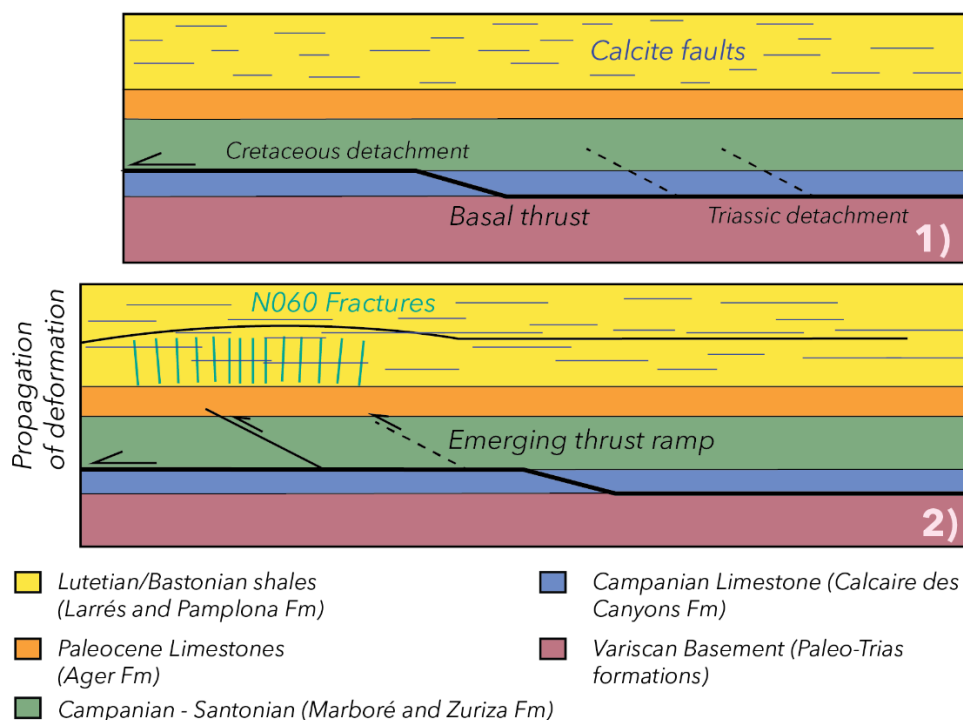
To describe the relative sequence of events related with the structures described in this work at different scales, we propose to place the beginning in the Bartonian (Middle Eocene) at a time when the South Pyrenean basins show transitional-deltaic deposition the Belsué-Atarés Fm. The South-Pyrenean basin is prograding, and underlying the depositing formation there are 2000 m of Priabonian marls, belonging to the Larrés and Pamplona Fms.

The orogenic context provides a constant compressive setting for the deposition of these formations. A few kilometres to the north, the Lakora thrust sheets and the inner branches of Gavarnie are raising the formations of the Internal Sierras and the Lutetian turbiditic basin.

At this time, there are two regional detachment levels that probably also accommodate shortening during the Eocene (and so do they in other inner parts of the orogen). The basal thrust in the Triassic (Keuper Facies) is considered to be the preferred detachment level for the large sheets of the South Pyrenean foreland basin which progrades southwards in the vicinity of our study area. In addition, there is a secondary but significant detachment in the Zuriza marls, of Cretaceous age underlying the Marboré Formation. This is the detachment levels that allows the development of the Internal Sierras: Paleocene limestones and Cretaceous sandstones. As these thrusting units appear in the hanging-wall of the Leyre Mountains, it can be interpreted that this formation is underlain, and therefore, could be responsible for local detachments of thrust ramps in this part of the Jaca Basin.

In the model of Figure 167 we leave aside the tip point of the thrust towards the foreland, as well as the interior structures towards the N, to focus on a more horizontal section and where the new thin-skinned tectonic ramps are expected to emerge.

Oliva-Urcia et al. (2012) and Turner (1990) agree in describing how orogenic compression affects the formations differently, and there are different structural styles depending on the mechanical stratigraphy.



CHAPTER 6 - DISCUSSION

Figure 167: Propagation of deformation from emerging thrust ramps, reconstruction model (not to scale) for the compression in the Jaca Basin.

Our interpretation is that at a very early stage in this Leyre system, gentle basal thrust propagation is accompanied by both calcite faults, LPS, and gentle flexure, a precursor to the Leyre thrust belt. This long-wave flexure and the LPS will encourage the formation of N60 fracturing, which has been shown to post-date certain calcite faults, but predate the folding itself. The sub horizontal calcite faults are early in our system as shown by the cross-cutting relationships with other joint sets (Figure 168).

These calcite faults, which combine several episodes of activity with a top-shouth shear direction, propagate without visible damage to the marls. The onset of these faults is probably very early, before folding, as we have identified a tilted fault, in the Sierra de Illión (Figure 151). This activity may still be going on today, in the footwall of the Leyre fault. One of the ages we obtained is very recent (Table 11) and the activity of the Tiermas thermal waters in the footwall of the Leyre fault suggest the existence of active drainage, perhaps along these faults.

The absence of deformation in the marles, and the stacking of several layers of calcite (in some veins there are more than 5 phases of crystallisation, see Figure 168b) suggest a propagation mode in a zone where the fluids were under overpressure. Numerous striations witness several slip toward the south, with slight rotations of 10-20° in the same vein.

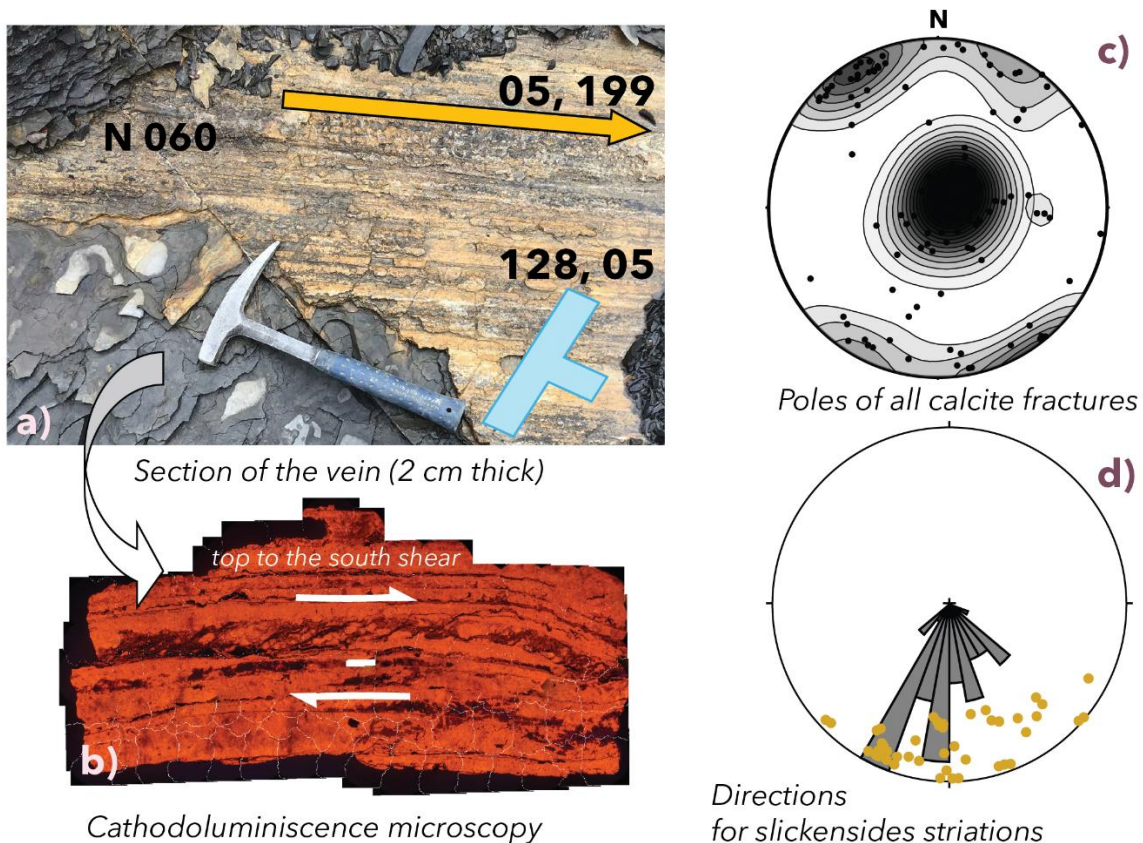


Figure 168: Summary of observations from calcite veins. The shear relationship with the 060 direction Veins can be observed. Also, the internal complexity of the veins (b). A contour plot of the studied veins, mostly subhorizontal, has been added (c). And finally, a direction diagram for the lineaments measured on the surface of these faults, indicating a mostly south direction.

CHAPTER 6 - DISCUSSION

There is a diversity of fault displacement directions to the south. The fan ranges from 130 to 210. The fan is expressed in different faults at different levels, and there does not seem to be a specific pattern, as it often occurs in thrust systems involving large-scale thrusts (Casas-Sainz and Simón-Gómez, 1992; Muniesa and Liesa, 2017; Simón and Liesa, 2011). There are often faults with two directions printed on the same surface. We can distinguish in any case three main sets:

- A 140-170 set, which is expressed in the intermediate fault of Llarto, in La Paul, and in the lower part of the Sigüés section.
- A N-S set, present in almost all sections except Escalar.
- And a 200-210 set, numerically the majority over the rest, very present in the Orba, Escalar and Escó sections.

This the expression of a complex history of fracturing and shortening hosted in the internal Larrés Fm. Calcite faults. In a second stage of this story, but directly linked to the generalised compression in this environment, we have the formation of an incipient thrust. Linked to the flexural response to the fault uplift a second set of calcite joints strike N60 would appear. Its development is also relatively early, and our interpretation is that this set of calcite joints is linked to the flexural response of the Larrés Formation to the propagation of an underlying thrust ramp. In the next section of this chapter, we will discuss the propagation of this fault.

6.3 Fault propagation in marls

In the various chapters of this thesis, we have been able to show the relationship between a zone of deformation marked by cleavage and the fault. The best illustration is undoubtedly the northern fault of the pop-up structure (Figure 169, and Figure 79), where the footwall records a south-dipping slaty cleavage, which is very rare if not unique in the Jaca Basin.

Therefore, we will discuss the mechanism of a fault that not only work as a brittle fracture with slip that accommodates shortening, but also has an associated deformation zone. In summary, the geometries of the deformation features associated with the fault, according to my observations in the sector of the Jaca Basin studied. We will distinguish several types of fault to discuss the deformation observed (Figure 169)

Type 1 thrust:

In type 1, the fault is gently dipping (subhorizontal to 20-30° dip), with a hanging-wall of carbonates or turbidites and a footwall composed of Eocene marls. The **Leyre thrust (west of Sigüés) and Orba thrust (East of Sigüés)**, have type 1 with hanging-wall composed of the Cretaceous-Palaeocene units, and a footwall of hundreds of metres thick of shales (Figure 169). In this context we have found a cleavage gradient with respect to the main thrust. Secondary faulting in the Leyre footwall is notable.

The Javierregay and Biniés and thrust (dip ~20°N) are Type 1. However, the footwall is complex, with slumps, debris flows and turbiditic facies (See Figure 137). In the Leyre-Orba system instead, Eocene marls are homogeneous, subhorizontal, slightly dipping to the south, although secondary gentle folds with long wavelengths are observed. The Biniés footwall has sedimentary irregularities that we interpret as being linked to an unstable submarine

CHAPTER 6 - DISCUSSION

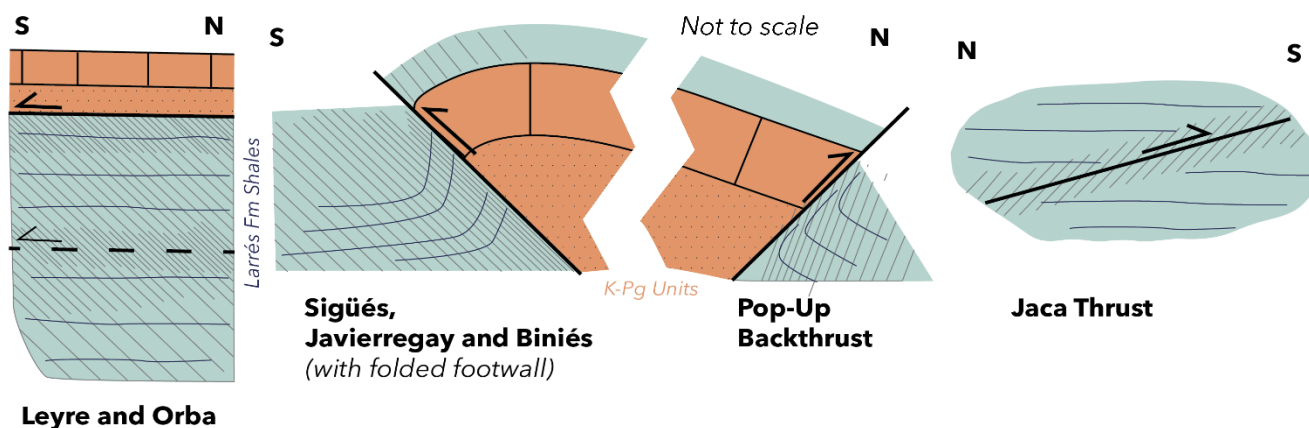
slope at the time of deposition. The footwall of the Javierregay thrust contains some metric folds, and also rapid lithological changes (more sandy layers, or more carbonate than clayey marls) which mask the development of cleavage. It is worth mentioning that Javierregay-Biniés is located on Jaca fault, few km north of the piggyback sequence of the South Pyrenean basin. The Jaca thrust brings the turbiditic basin up over the Eocene marls in the central sector of the Jaca basin. This means that the hanging-wall does not show the K-Pg units, but the Hecho Group.

Type 2 thrust:

Type 2 faults are steeper, with an angle of more than 30°. The footwall consist of Eocene marl, and the hanging-wall is generally dominated by Cretaceous and Palaeocene carbonate facies. To the north of Sigüés, there are three Type 2 faults: the Leyre thrust, and the forethrust and backthrust of the pop-up structure. The Leyre thrust is steeper (>30°, Figure 169). A decametric footwall syncline is observed, and a cleavage gradient towards the Leyre thrust is observed similar to other sections. The hanging-wall shows cleavage in the clay levels, but this is much less pronounced than in the footwall. In type 1 faults, the hanging-wall appears to be less deformed. The steep dip of the Leyre fault can be interpreted in different ways. Either it is local complication imposed by the development of pop-up anticline, or it is a steep ramp. In the latter, the Leyre fault further west would be a flat ramp. Boiron et al. (2020) interpret this segment of the Leyre fault as the expression of the triangular trishear zone (see Figure 183). This interpretation suggest that what is classically considered to be the Leyre Fault (visible from the road) is mainly an expression of intense shearing associated with the trishear; the ramp is blind according to this interpretation. Strong shearing over a distance of few meters has been observed at the extremity of the layers of the Ager formation.

The conjugate thrusts of the pop – up anticline are type 2 (Figure 169). The N-dipping fault to the south shows a strain gradient in the footwall. The cleavage is slaty near the fault. It is possible that the strain observed in the hanging-wall of the Leyre fault is the halo of the strain gradient of the pop-up fault.

The S-dipping fault to the north also shows a strain gradient in the footwall. The cleavage is slaty near the fault. Numerous S-C planes are evidence of top-to-the-north shearing (Figure 79). The southern dip of the cleavage planes, sub-parallel to the trace of the backthrust suggests a genesis related to the propagation of this reverse fault.



CHAPTER 6 - DISCUSSION

Figure 169: The different thrust settings we have observed in the studied sector of the Jaca basin. The cleavage associated with a fault is expressed with different magnitudes, and associated with different geometries. Bedding attitude is shown in blue lines.

Type 3 thrust:

The type 3 thrust is a reverse fault that propagates in the Eocene marls (Figure 169). The ~N100° Jaca thrust near Jaca, propagates within the Larrés Formation. Observations on the deformation zone is here limited to ~50 m exposure. A 4-5 m thick band is visible in which the marls show intense shearing, cleavage, fracturing, and branching planes (see Figure 141). Outside this deformation band, the fractures also appear, but after a few metres they subside and the marls appear in their sedimentary aspect. This has also been corroborated by the study of the magnetic fabric (see section 4.6.3 Jaca-Gas Site).

Having defined these 3 types of faults, we will now discuss the strain observed. We start with type 3.

6.4 Characteristics of the calculated deformation

6.4.1 Extent

a) Type 3 Fault

A study of the magnetic fabric in the Jaca Gas fault shows that both the footwall and the hanging-wall exhibit a symmetrical strain halo limited to a few metres (Figure 170). The fabric can become prolate, and shows an evolution up to stage 5 (Slaty cleavage) in the centimetric gouge. Figure 170 shows a comparison between the calcite fault and the type 3 fault. These two faults propagate in the Eocene marls, but with very different associated strain. The calcite fault does not damage the marls. The type 3 fault symmetrically damages the marls. To explain this difference in behaviour, it is plausible to imagine that the calcite fault is associated with fluid overpressure, whereas the type 3 fault operates as a creep fault.

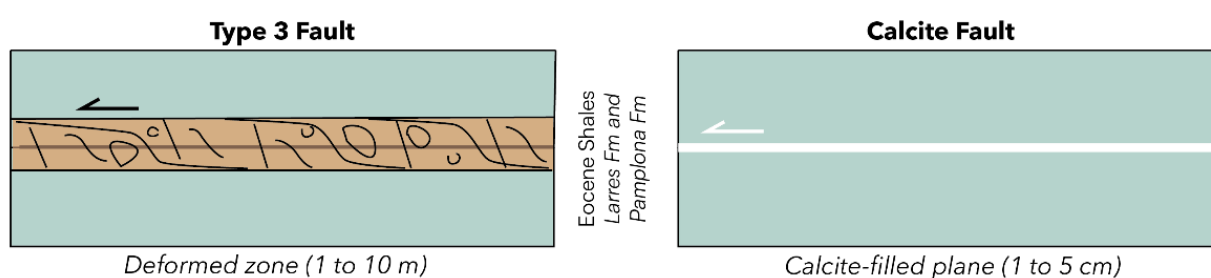


Figure 170: Model sketch for two fault styles propagating within a mudrock formation.

Type 3 faults are also observed in the footwall of the Leyre fault, particularly along the Escó, Llarro and Escalar cross-sections. They may appear clearly in the field at Escó and Llarro, or they may be suggested by the appearance of a zone of slaty cleavage at Escalar. It is in this context that the use of the fragment technique has revealed its full potential (Figure 6). These type 3 faults exhibit strain that interferes with the halo of deformation generated by the Leyre fault. This complication is not observed at the outcrop of the Jaca Gas fault

CHAPTER 6 - DISCUSSION

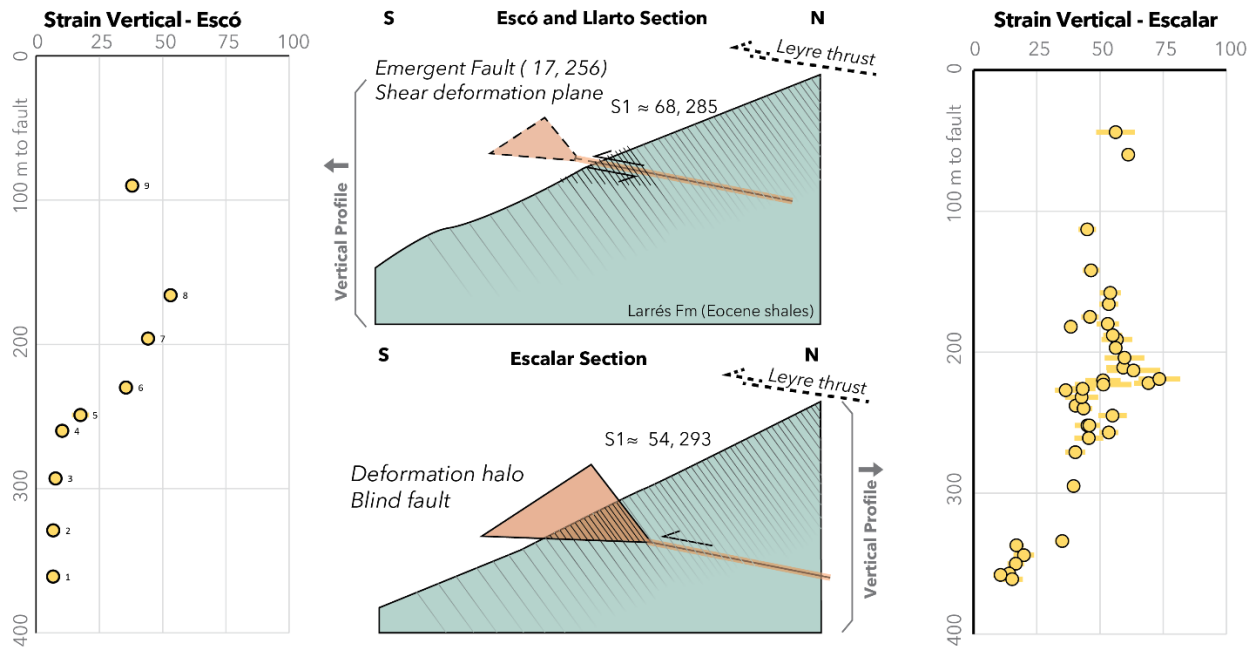


Figure 171: The figure above corresponds to outcrops in the Llarto and Escó sections, in which a fault zone appears. The lower figure corresponds to the Escalar section, in which an intense slaty cleavage appears, but no deformation structures assimilable to a fault plane. All of them are located in the footwall of the Leyre thrust.

We have not been able to find evidence to state whether this phase of deformation linked to the Leyre thrust is prior to the appearance of the secondary thrust. However, the internal structures of these "secondary" faults resemble each other, metric-thick bands of deformation with significant internal deformation, shearing and fracturing. Conversely, damage zones with large blocks (cataclastites) appearing in other scenarios, such as strike-slip faults, are here absent (see synthesis in Marcén-Albero, 2020)

Looking at the evolution of strain derived from the magnetic fabric data, we can see two trends. At Escó there is a rise from ~30 to ~50% strain that begins at ~220 m (and peaks at ~160m), which is consistent with observations of an emerging Type 3 fault at ~220 m. In this case it is difficult to know whether the strain in the hanging-wall is related to the Leyre fault or to this fault. At Escalar, a strain peak of ~75% occurs at ~220m, consistent with the observation of intense shale cleavage. However, our observations in the field did not reveal the clear emergence of a fault. It is therefore plausible that we are seeing the surface strain of a hidden fault. In this example, we can see strain in both the footwall and the hanging-wall of this type 3 fault. The strain background >25% from 320 m to the contact with the Leyre fault will be discussed below.

b) Type 1 and 2 faults

We propose to compare two sections, that of Escalar with 38 sites (~600 fragments) and that of Sigüés with 32 sites (244 samples oriented sites represented at Figure 172) (Boiron et al., 2020). The distance to the fault is projected on a vertical axis in the Escalar section and on a horizontal axis in the Sigüés section.

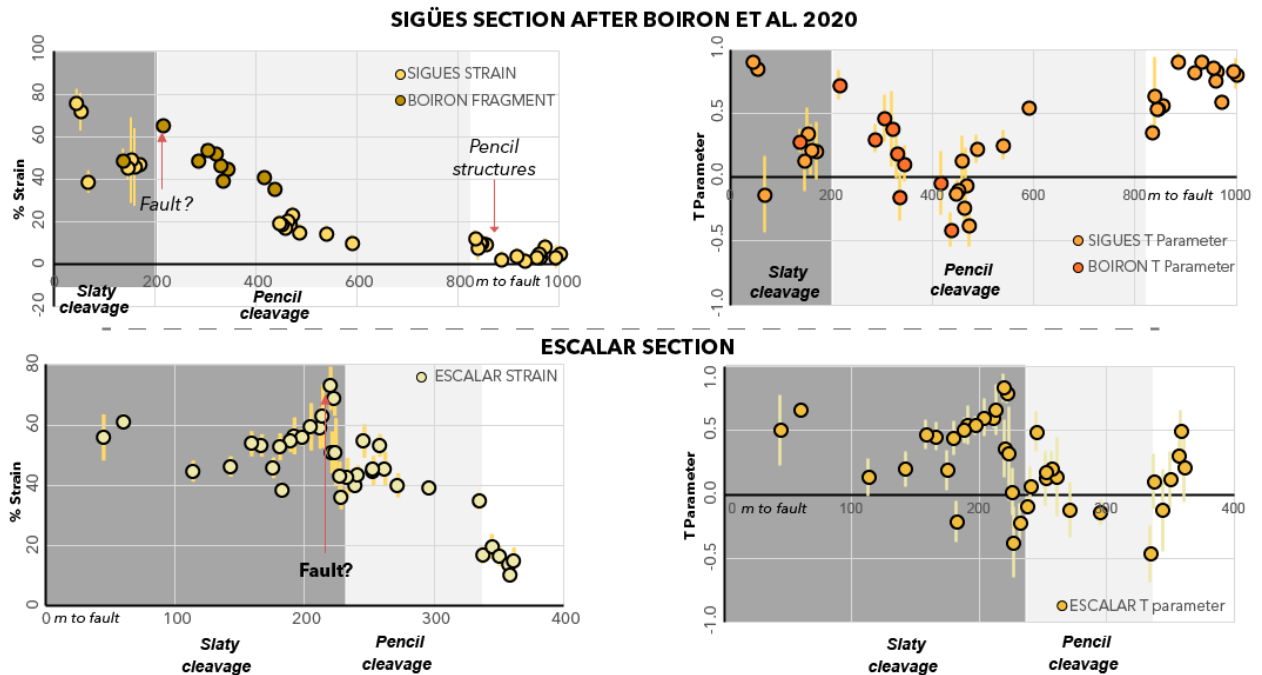
The extent of deformation in the footwall of the Leyre fault has already been presented in section 4.3. Sigüés results. For comparison, we show the strain calculated using the method of Humbert et al. (2014) and the evolution of the T parameter. We also give the observed

CHAPTER 6 - DISCUSSION

thickness of the slaty cleavage and the pencil cleavage. In that sense, showing these two parameters allows us to clearly discern the characteristics of the deformation zone in this footwall of the Leyre thrust. Boiron et al. (2020) locates the onset of the pencil cleavage at ~865 m from the Leyre thrust in the Sigüés sector. The transition between slaty and pencil cleavage is difficult to estimate. Saur et al. (2020) suggest that this boundary should be 200 m from the Leyre fault. In the Escalar section, the slaty cleavage corresponds to a thickness of around 200m, followed by a zone of pencil cleavage of around 100 m (Figure 172).

The slaty cleavage zone is generally well defined visually because the outcrops are much more resistant to erosion. The fragments break into platelets, whereas in the pencil cleavage zone they are fritted. However, there is a little correlation between the calculated strain and the slaty cleavage zone. The strain is greater than 40%, but such values are also found in what we have defined as pencil cleavage zone. This illustrates the difficulty in defining slaty cleavage and pencil cleavage. The calculation of strain is based on the assumption that equation 1 (K3 statistically perpendicular to the bedding) and equation 2 (K2 statistically perpendicular to the bedding) are selected (see Figure 123). The gradients shown are very realistic. In the footwall, the influence of the Leyre fault is felt as early as 800 m in the Sigüés section and as late as 300 m in the Escalar section.

Although the projection system is different, the zone of >40% strain is around 400 m in both sections. This background can be explained by the halo of strain from invisible type 3 faults, as identified at Escalar. In this sense, it is quite possible that the peak strain observed in the Sigüés section at ~ 200 m is the result of an unidentified secondary fault. The geological map proposed by Puigdefabregas (1975) (Figure 70) suggests an additional fault in the footwall of the Leyre thrust in the Sigüés section. Whether the background is due to the influence of a single fault or several type 3 faults remains an open question. Along the Escalar section, with the evolution of the magnetic fabric parameters, it is possible to propose the existence of at least three type 3 faults; at ~250 m, ~220 m and ~160 m



CHAPTER 6 - DISCUSSION

Figure 172: Strain profiles calculated according to the magnetic fabric of the shales. The Sigüés profile is shown horizontal (the dip of the frontal thrust is $>40^\circ$) and the Escalar profile is shown vertical (the frontal thrust dips $<10^\circ$) to understand the extent of the strain acquired in the footwall shales.

Figure 173 shows all the sections of the Leyre and Orba thrusts. The Orba and Leyre sections are the furthest from the area of the pop-up anticlinal structure. The halo of strain greater than 40% is approximately 100 m away, perhaps less for the Leyre section. On the other hand, this halo is more than 350 m away for the other sections. Note that in the Escó and Llarto sections, which are the furthest from the pop-up, the halo $>40\%$ is 250 m away, suggesting an attenuation towards the west. These data therefore suggest a relationship between the strong halo $>40\%$ and the pop-up anticlinal structure.

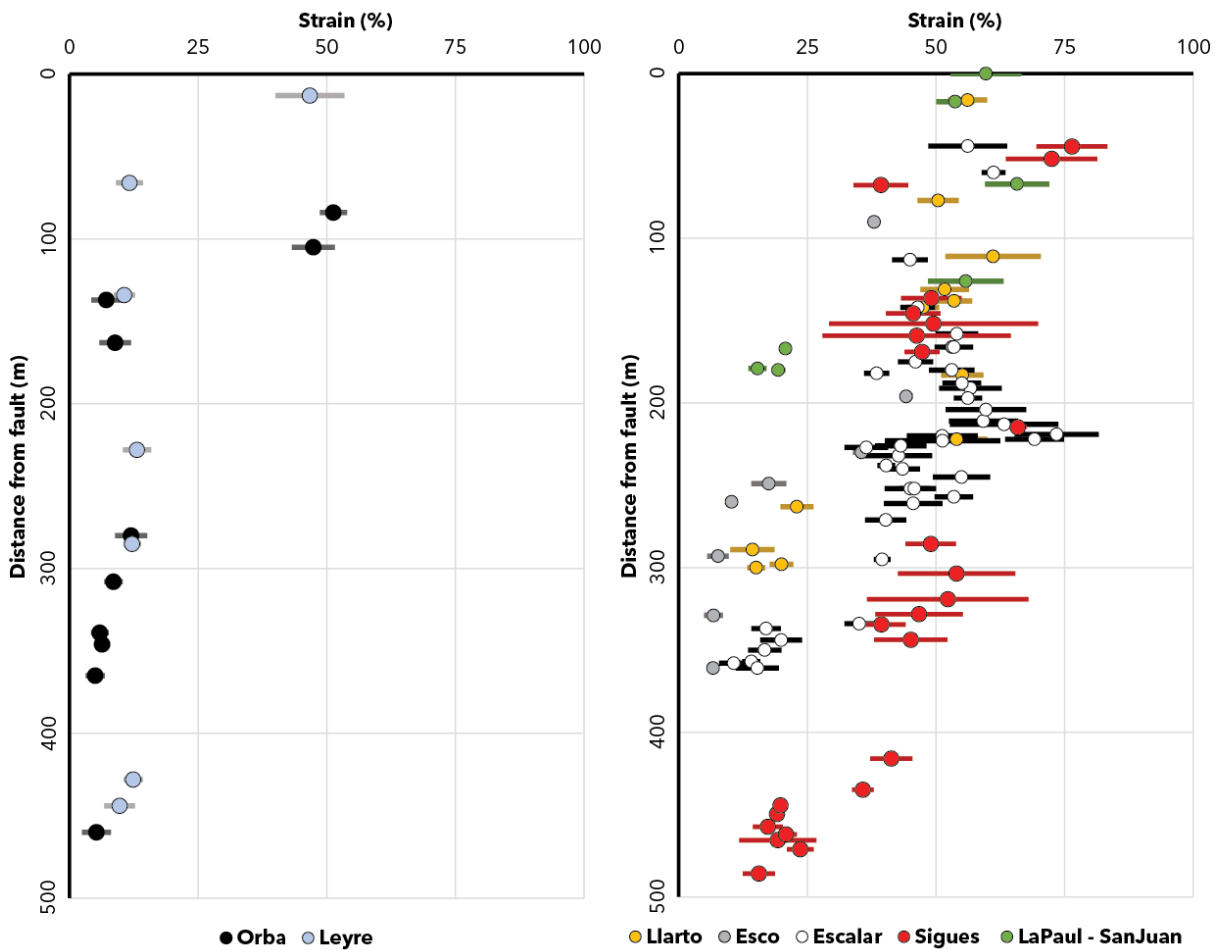


Figure 173: Figure summarising the vertical strain data with respect to the Leyre and Orba fault. Exception: for the Sigüés shear (data from Boiron et al., 2020) are horizontal distances.

At this point in this thesis, we recall the interpolation map we presented in Figure 128 and which it is again presented in this discussion (Figure 174). This map allows us to see in a direct and simple way a quantification of the strain that the marls undergo in their internal fabric. It is one of the main results of this thesis, and it is also one of the future applications of the non-oriented fragment sampling methodology.

As mentioned in

CHAPTER 6 - DISCUSSION

4.4. Strain quantification at the Sigüés site, there is an along-strike E-W difference in the way that the Larrés Fm hosts the strain. Specifically, in the Escó, Escalar and Llarro sections, we can observe the amount of the strain of more than 25% extends more than 1000 m to the south (Figure 174). Meanwhile, in the Sigüés section, parallel to the road, it can be seen that at 500 m the marls no longer have this 25%. The lateral change is especially pronounced if we look at some of the sites of San Juan and La Paul, which are 300 and 1100 m away (along strike) from the Sigüés section, and exceed 40% strain at the same horizontal distance from the fault trace.

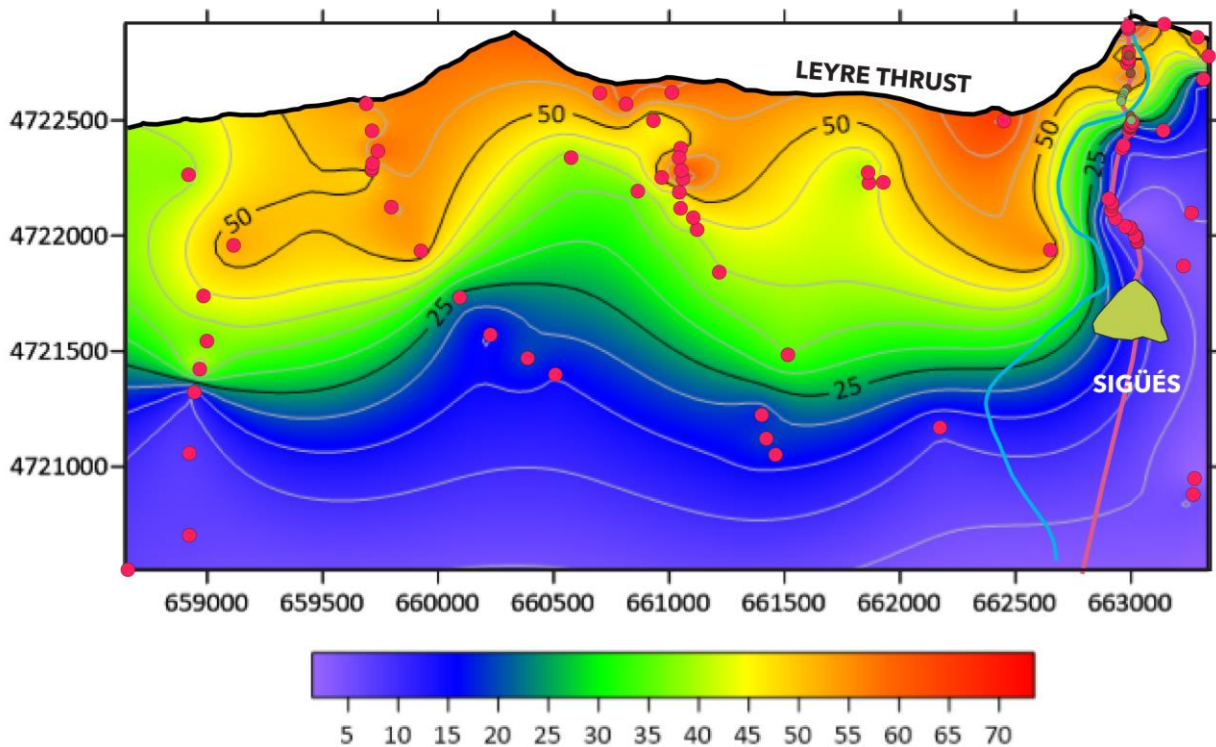


Figure 174: Interpolation map for the strain results calculated at the sampling points (see red dots). The map represents from the Escó section (farther W) to the Sigüés B samples, 100 m to the East of the Sigüés section (Boiron et al., 2020), parallel to the A-137 road.

This West-to-East shift may be due to several factors.

First, there is a possible topographical effect. The topographic profile shows a greater slope to the west than in the Sigüés section parallel to the road. The dip of the fault is different: subhorizontal to the west (type 1 fault), steeper along the Sigüés section (type 2 fault). The combination of these two effects, if we assume a halo of homogeneous deformation linked to the movement of the fault, does not explain the significant cartographic difference observed (Figure 174). The section on the right bank of the Escá river shows an extension of the shale cleavage from the beginning of the Ermita de San Juan road, which contrasts with the extension of the shale cleavage on the left bank of the Escá (Sigüés section). It therefore seems that the topographical effect, combined with the geometry of the faults, cannot explain this transition in the extension of the fault.

CHAPTER 6 - DISCUSSION

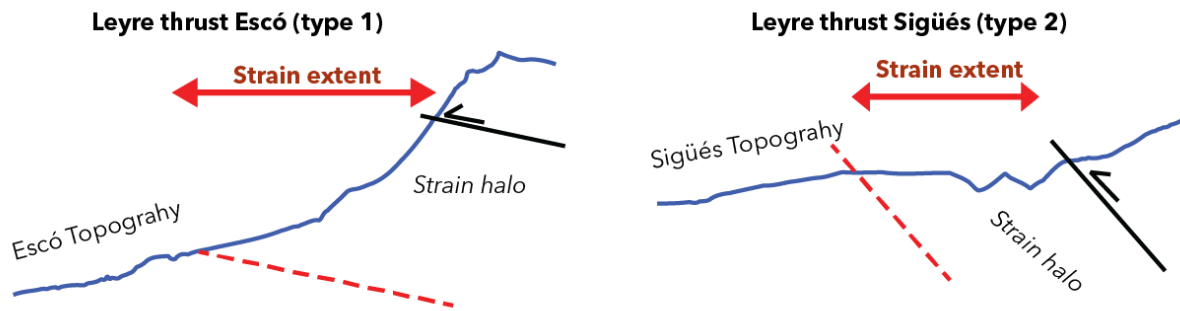


Figure 175: Relationships between the extent of the strain halo in the marls of the footwall, and the geometry of the Leyre thrust.

Second, a change in lithology. Puigdefábregas foresees the change between the Larrés Fm and the Pamplona Marl Fm in the vicinity of the thrust (see Figure 176), something that also fits with the geometry and elevation of the outcrops. A change in lithology, for example with more carbonate content, may alter the expression of the strain. Also, sampling is usually biased towards this type of rocks because they are more competent than the shales, whose fissility precludes in many cases sampling by means of drilling machines. However, examination of the Puigdefábregas map shows that variation in lateral extension of the strain already occurs within the Larrés Fm.

Third, a change in the shortening and propagation of the fault. In the Escá river gorge (north of the Sigüés section) the shortening of the structure is accommodated in two forethrusts, a backthrust and a 400 m thick pop-up fold (see Figure 95 in section

3.4. Structural frame and serial Cross -Sections.). As we move westwards (Escalar or Escó sections) the pop-up structure attenuates, and the geometry of the Leyre thrust rapidly becomes flatter (type 1 fault).

However, in this regard, we must also look at the footwall's shortcomings. These flaws undoubtedly affect the footprint of strain measurement. If each secondary fault, in Escó, Escalar and Llarto, has a strain halo capable of affecting 50-100 m thick shales and generating intense cleavage, the damping of these faults towards the E makes the gradient only related to the Leyre thrust to be isolated in relation of the complexity of the footwall towards the western part of the map. It was along these sections that secondary faults were identified, for which we suggested that although they were not emergent, the deformation halo was identified in the field (slaty cleavage) and confirmed by magnetic fabric measurements.

The fault that appears at 130 m (vertical distance) from the Leyre thrust at Llarto is also much closer to the fault trace than the one at Escalar and Escó, which appears at 230 m of vertical distance and at the same topographic elevation. We have already seen how the Escó fault does not seem to have much lateral continuity in the surrounding marl outcrops, and how at Escalar there is a possible second fault after the results of the detailed sampling are known. Therefore, it is possible that the Llarto fault in the upper part has not been detected in the other parallel sections. Thus, we can state that this footwall is quite complex from the structural point of view. The difficulty of finding good quality outcrops in a part of the piggyback basin where the marls reach thicknesses of up to 1 km combining the Larrés and

CHAPTER 6 - DISCUSSION

Pamplona Fm, makes it complicated detecting this type of faults, without seeing the exposures or detailed sampling.

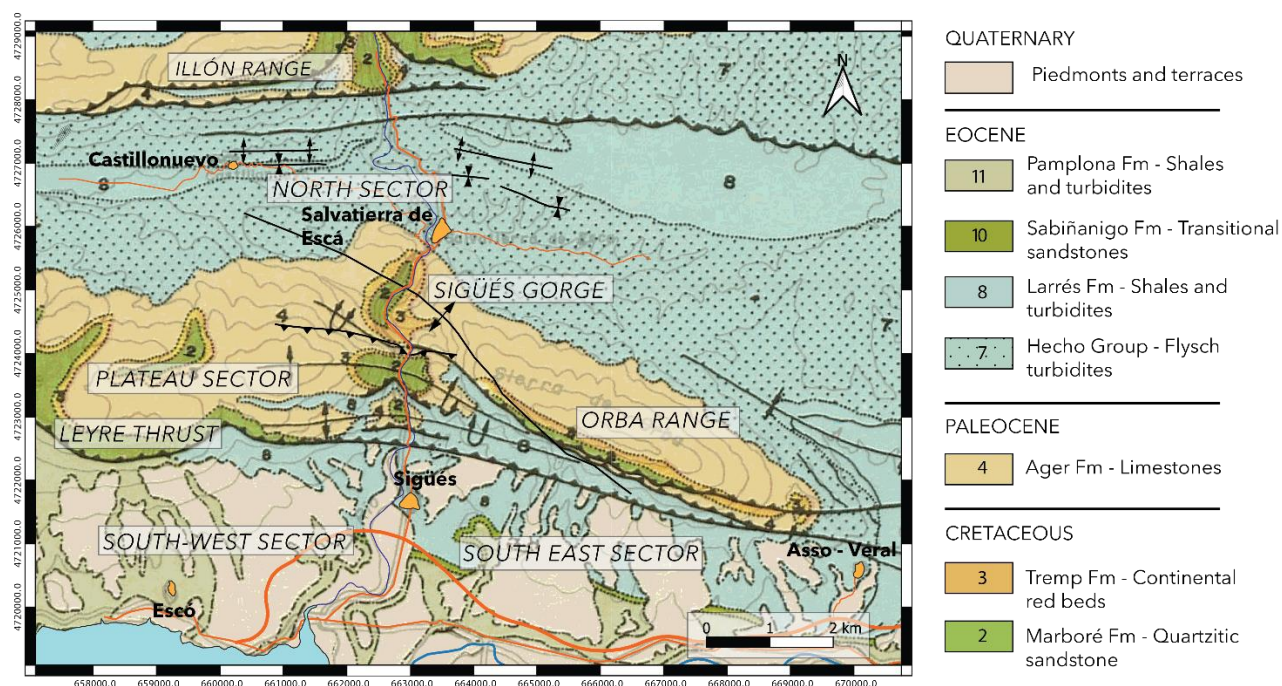


Figure 176: Part of Puigdefábregas (1975) map, with description of the sites of the Leyre-Orba system.

It is interesting to note the cartography of Puigdefábregas (1975), as it does foresee a change in the lithology of the Arro-Fiscal Fm (synonymous with Larrés Fm) vs the Pamplona Fm towards the west. Puigdefábregas (1975) also draws three forethrusts in the Sigüés transect. We can see the one corresponding to the Pop-Up anticline, the one corresponding to the Leyre frontal thrust, and also a third trace to the south, which the author assumes to be subvertical (very rectilinear trace in some segments), and which affects the marls. To the W, he makes it equivalent to the Leyre frontal thrust, with which we do not agree. But this does mean that the author highlighted a fault in the footwall of those main ones (Leyre and Orba).

Therefore, we can establish a relationship between the observations of shale-on-shale faults (type 3) in the Leyre thrust footwall and those we have detected with our sampling and observations towards the W of the Sigüés section.

6.4.2 Fabric development

The relationship between strain and magnetic fabric has already been described in previous chapters. In this discussion we will focus on the correlation presented by Parés and van der Pluijm (2004). They proposed a diagram combining the T parameter and the deformation calculated from the aspect ratio of the pencil structures in the range 10 to 30% (Figure 177). We propose to combine this plot with the strain values from the magnetic fabric data. The very strong coupling between T and the strain value is normal, as these two parameters are calculated from the 3 eigenvalues of the tensor. In this type of diagram, we propose the data from our study along the most complete sections (Escalar, Sigüés), the data from the Cantabric Arc (Parés and van der Pluijm, 2003) and the Lehigh Gap data proposed by

CHAPTER 6 - DISCUSSION

Housen and van der Pluijm (1990). The choice of equations 1 and 2 is subject to our interpretation.

Data from the Cantabrian Arc (Parés and van der Pluijm, 2003) covers a range from 11 to 40% of the shortening. The Lehigh Gap data show a conformal increase in deformation of the order of ~10% (pencil cleavage) to 25% (slaty cleavage). These values are consistent with those estimated by Hirt et al. (1993) and also with our observations of penetrative pencil cleavage and prolate T values. The diagram shows that our strain values cover a wider range in the prolate-oblate path of the T parameter. This V-shaped curve therefore presents two solutions for a measured fabric. For example, for T=0 (triaxial shape), the deformation can be 20% or ~45%. In the Escalar and Sigüés sections at 45%, the cleavage is slaty with the fragments flowing in platelets. At 20%, the cleavage is pencil type, and the fragments are pencil-shaped.

This type of diagram is based on:

- 1) A magnetic mineralogy dominated by clays;
- 2) Very little recrystallisation of clays during deformation
- 3) Cleavage that develops at a distinct angle, ideally perpendicular to the bedding

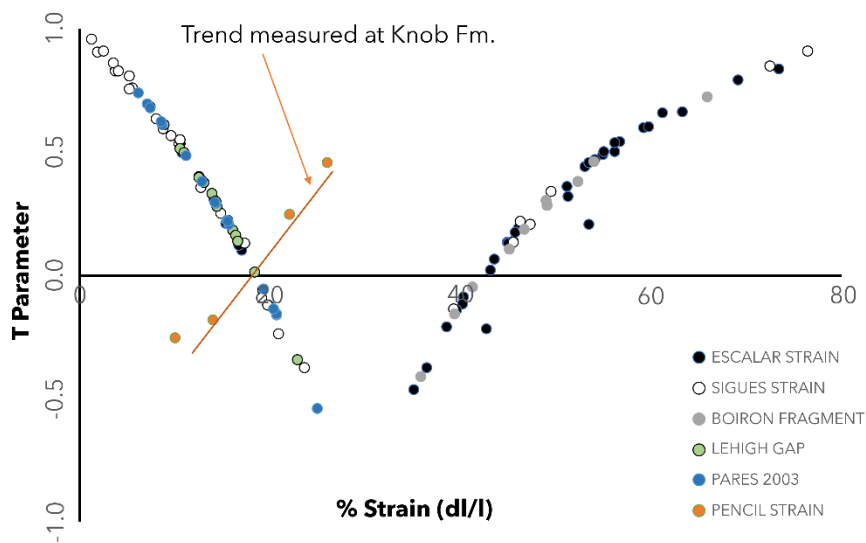


Figure 177: T parameter vs % Strain for shales with cleavage. Various sampling sections are included, such as Escalar, Sigüés (from the Pyrenees), Cantabrian Arc (from Parés and van der Pluijm, 2003), Lehigh Gap (data calculated from Housen and van der Pluijm, 1990). Modified from Parés and van der Pluijm (2004)

This discussion also needs to consider how the fabric of the Larrés Fm shale acquires this deformation. In their paper, Boiron et al. (2020) showed that the distribution of clays is controlled by bedding or cleavage, even in the most deformed facies. In our XCT study we were able to show that in one of the facies showing slaty cleavage, the calcites were almost all oriented along the cleavage line (pressure solution), whereas the quartz was distributed between the bedding and cleavage poles (see Figure 131). We think that the clays react in the same way as the quartz and rotate rigidly in the matrix. This means that there are still zones where the clays remain controlled by the cleavage, even when the deformation is significant.

CHAPTER 6 - DISCUSSION

The AMS of oriented samples from Boiron et al. (2020) along the Sigüés section is shown in Figure 178. In the pencil cleavage section, the K3 axes are distributed between the poles of layering and cleavage. The magnetic lineation (K1 group) is unsurprisingly oriented \sim N100. In the slaty cleavage zone, where the cleavage almost completely overlies the bedding (Figure 178) a fairly homogeneous groupings of K3s are obtained, fairly close to the cleavage pole but with an obliquity of \sim 20°. This suggests a distribution of clays controlled either by cleavage or bedding. Saur (2022) in his thesis, showed that by selecting grain subfabrics (obtained from μ CT) in the marls, he found zones where the quartz was mainly controlled by cleavage or quartz that was still mainly controlled by bedding. In other words, in the absence of chemical processes, the rotation of the particles is not complete and there remain protected islands that preserve the sedimentary fabric. This type of model has already been proposed by Pueyo-Anchuela (personal communication) for shales.

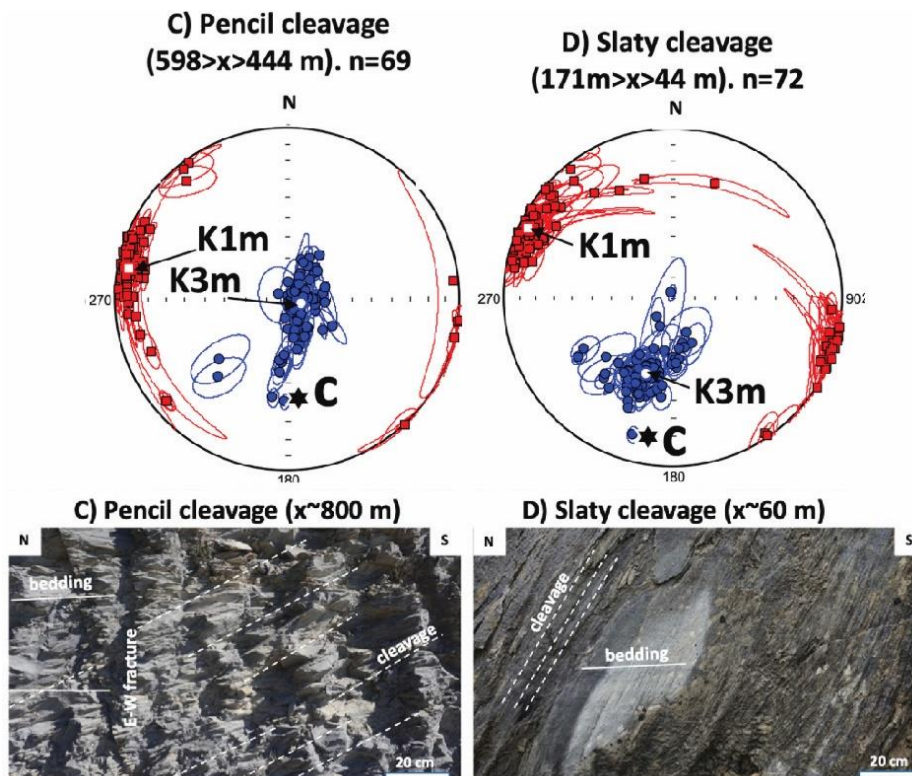


Figure 178: A summary of the data from the AMS oriented on the Sigüés transect. We see the magnetic fabrics measured at the Pencil cleavage site (C is the cleavage pole) and slaty cleavage site (from Boiron et al., 2020).

The AMS measurement can be further conditioned in the scalar parameter spectrum depending on which proportions of the planar particles are rotated or not. That is, the more prolific the sample, the more equality there will be between rotated particles and particles remaining in the bedding, and the more uncertainty the measurement will have (monitored by confidence angle E23, corresponding to stages 2 to 3 of magnetic fabric after Gracia-puzo et al., 2021). But the more particles having undergone rotation, the more we will see the mean K3 rotate towards the pole position of S1, and a bulk oblate shape will appear (stages 4 to 5 of magnetic fabric).

We propose to illustrate an alternative vision of AMS fabrics in Figure 179. In the classical pure shear model, imposed for example by the LPS, we observe a progressive dispersion of

CHAPTER 6 - DISCUSSION

the K3 axes around the bedding pole until they are parallel to the cleavage pole. The magnetic lineation is a zonal axis of the K3 dispersion

In contrast, under a simple shear regime (Layer Parallel Shearing of Parés, 2015), the fabric has a different evolution. The K3 axes are distributed asymmetrically, preferentially between the bedding pole and the cleavage pole. This is observed in the pencil cleavage zone along the Sigüés cross-section (Figure 178). However, where we differ from the conceptual model of Parés (2015) is that, at the final stage, the mean pole K3 is located between the bedding pole and the cleavage pole. This is similar to what we observed in the slaty cleavage zone of the Sigüés cross-section (Figure 178).

Pueyo-Anchuela et al. (2011) proposed that LPS conditioned the fabric of the Larrés Formation in the Jaca Basin. In contrast, data from Boiron et al. (2020), indicate that the Sigüés deformation gradient would fit the top-to-the-south shear model.

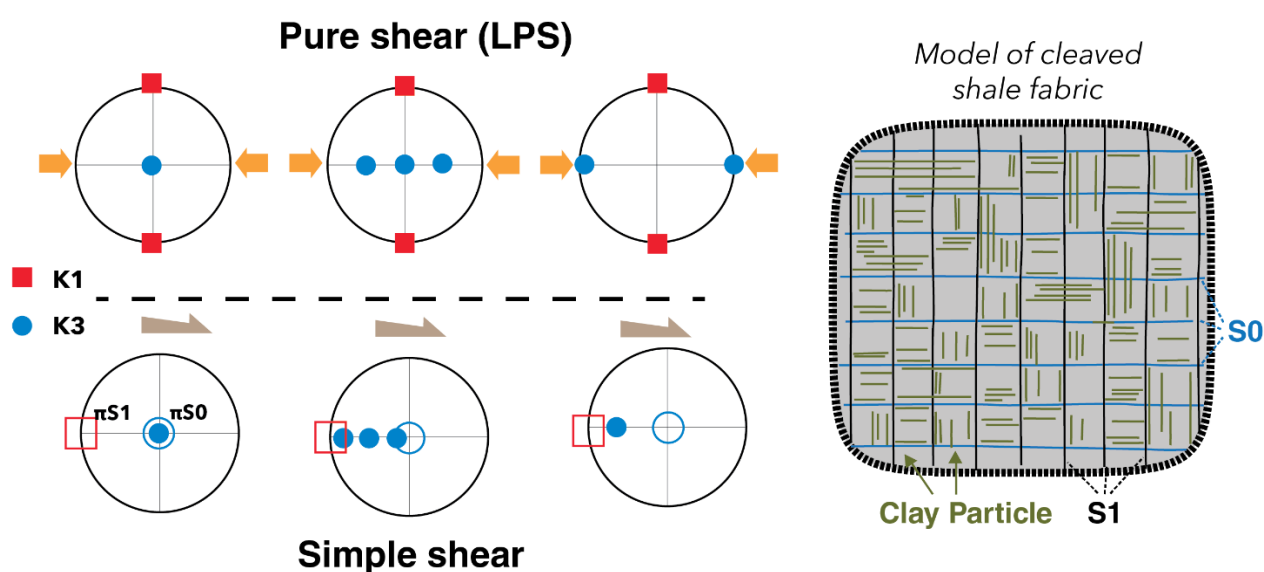


Figure 179: On the left, two models of magnetic ellipsoid evolution measured in ASM for two different compressional kinematics: Layer Parallel Shortening and Simple shear. On the right, a model for an internal fabric of a microscale shale fragment. The clay particles (green colour) would be oriented parallel to S0 or S1.

The AMS fabric of a shale is conditioned by the evolution of its components under burial and mechanical conditions. In section 2.3.7 AMS as a strain gauge, conditions of use. we discussed the importance of constraining the conditions under which shortening occurs. This is crucial to understand whether the fabric being measured is representative of a rotational process, or whether the minerals carrying the magnetic signal are the result of recrystallisation. Saur et al. (2020) and Saur (2022) have demonstrated the rigid rotation of quartz using X-ray microtomography. In contrast, calcite has been shown to be a rapidly recrystallising mineral (see results in section 4.5 Microtomography results) and is rapidly rearranged according to the S1 affecting shales.

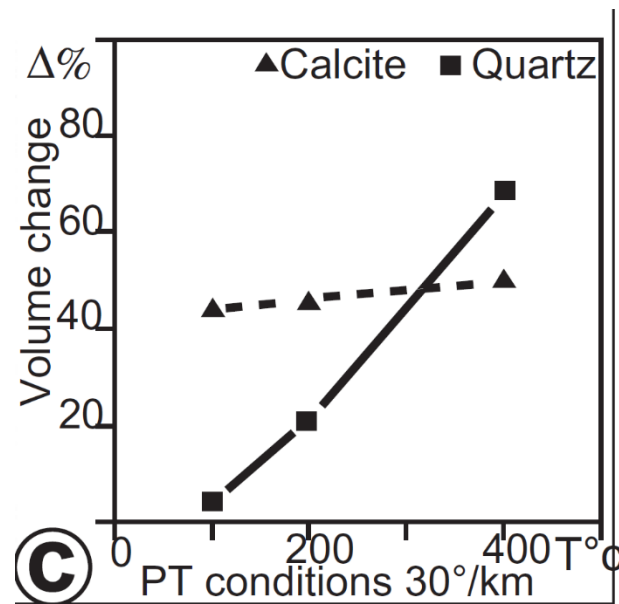


Figure 180: Change in variation in the amount of dissolution of quartz and calcite versus temperature and depth in the sedimentary cover of the Alps. From Gratier et al. (2013)

The RSCM data show that the maximum temperature reached at Sigüés was close to 180°C (see section 5.2 Additional RSCM and Rock-Eval data.). This is in good agreement with the complete illitization of the clay fraction, which occurs within a temperature window of 60° to 200° (Meunier and Velde, 2004). To constrain the timing of illitization, it would be necessary either to be able to date the illites or to model the basin. However, we have a good argument that illitization occurred before strain was generated by fault propagation. AMS strain calculations are consistent with field observations and gradients are well characterised. If illite were formed during the illitization phase, we would expect to see behaviour similar to that of calcite, which reorganises rapidly following cleavage. In Sigüés we can see that the calcites show solution pressure and little quartz. The quartz reacts somewhat as observed using the EBSD technique (Saur, pers. Comm) but certainly in a very marginal way compared to the calcites. In the diagram proposed by Gratier et al. (2013) (Figure 180), we can see that between 100°C and 200°C burial temperature, calcites show a volume change of about 40%, while quartz shows less than 20%. Faults can therefore operate in a temperature range between 100°C and 200°C. Given the apparently low chemical reactivity of quartz grains, it is likely that the faults are operating at $T > 200^{\circ}\text{C}$ i.e. during a tectonic exhumation phase.

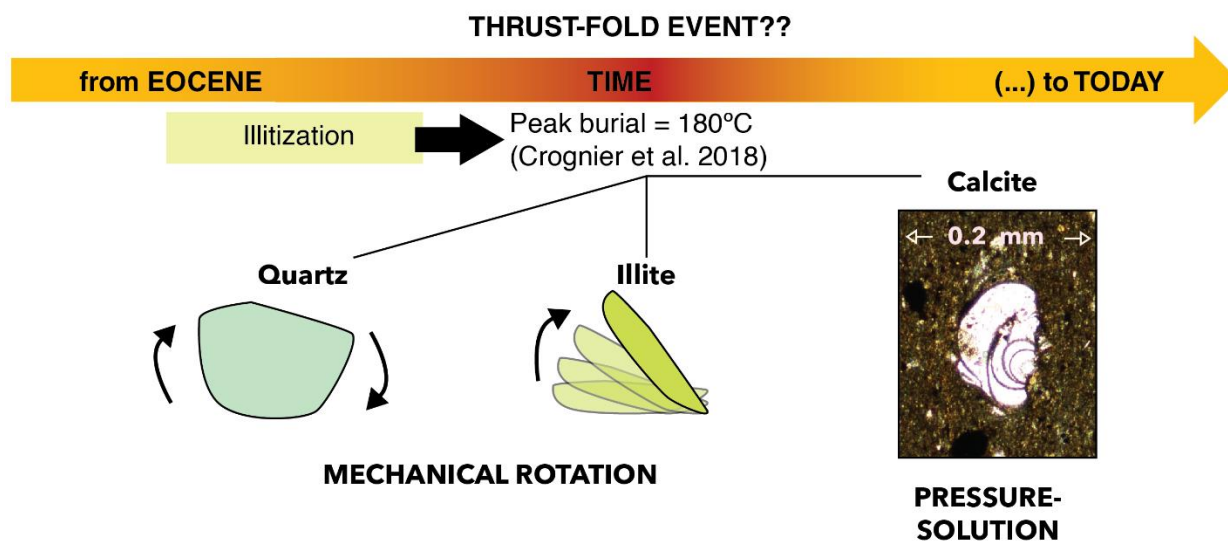


Figure 181: Under the peak burial conditions considered in the Sigüés environment, we expect a complete illitization, and a rigid behaviour of both quartz and illite present in the Larrés Fm shales. In contrast, microscopic observation has shown several signs of pressure-solution in the calcite grains, as it is the case of the foraminifera shown on the right.

The thermal history elaborated by Crognier (2016) suggests that the thermal peak coincides with the deposition of the Oligocene clastic deposits of Lutetian to Rupelian age. Already at the end of chapter 5 (See Figure 163) we propose the burial depth factor as the fundamental control to explain the thermal increase with respect to other areas of the Jaca Basin (a burial temperature of 120°C is estimated a few kilometres to the east after Crognier, 2016).

The stacking of the Gavarnie thrust and the displacement of its hanging-wall seems to be more notable than the stacking generated by the Javierre-Jaca fault. The displacement of the Jaca fault dies out to the east, as suggested by the cartography (in Jaca, the thrust brings into contact materials belonging to the same unit in both fault walls).

In addition, the depocenter of the Guarga synclinorium, which contains an Upper Eocene-Oligocene series up to 4 km thick, could be located above the Sigüés area as it migrated southwards (Teixell et al., 2016).

No arguments have been presented in order to explain a local anomaly linked to other phenomena such as fluid circulation, nor do the data given by the analysis of fluid inclusions allow us to establish this hypothesis. In this sense, we resort to Crognier's model to correlate the faults appearing in Sigüés with the first generation of veins, which occurs contemporaneously with the advance of the Gavarnie thrust. According to Crognier, this fluid is not hydrothermal, its source is local and could correspond to the host-rock/infill that we have described after the isotopic analysis in section 5.6 Isotopic data. (Figure 158).

6.5 The origin of deformation: discussion of mechanisms

In several chapters of this thesis it has been hypothesised that thrusts or reverse faults are the main responsible for the occurrence of cleavage in the footwall of the Leyre thrust (and lateral equivalents, such as Orba, Jaca...).

What makes a fault function only as a fracture, with a very concentrated (seismic-like) slip such as subhorizontal calcite faults? And what makes a fault generate a deformation zone of

CHAPTER 6 - DISCUSSION

one to several meters of intense shearing and fracturing instead? What makes it also generate a halo of deformation and cleavage in shales several tens of meters thick?

Here are some observations on the relationship between faulting and cleavage.

- ✓ Intense cleavage develops when the burial temperature remains below 200°C. This suggests a mainly mechanical origin
- ✓ As the fault dips to the north, the cleavage dips to the north and viceversa
- ✓ Gradients are observed in several sections, passing through stages of pencil cleavage and then slaty cleavage
- ✓ Both the footwall and the hanging-wall are stressed. This is well demonstrated in the Jaca Gas type 3 fault, but also on the right bank of the Rio Escá, where the footwall marls show slaty cleavage
- ✓ According to the Sigüés cross-section, a variation in dip that becomes straighter towards the fault is observed.

We, therefore need to find a model that fits all these observations.

Boiron et al. (2020) first proposed the use of the trishear model to explain the observed cleavage. Erslev (1991) presents the trishear model of deformation and explains that there may be a heterogeneity of the strain suffered by the triangular zone of deformation. This would open the door to possible symmetries, concentrating the deformation in the centre of the triangular area. Hardy and Ford (1997), who return to the triangular zone concept, add two new keys to describe the strain rate in two dimensions. They add horizontal and vertical vectors that explain the shear in the triangular zone, which are what allow us to carry out the modelling that we have presented (Figure 182).

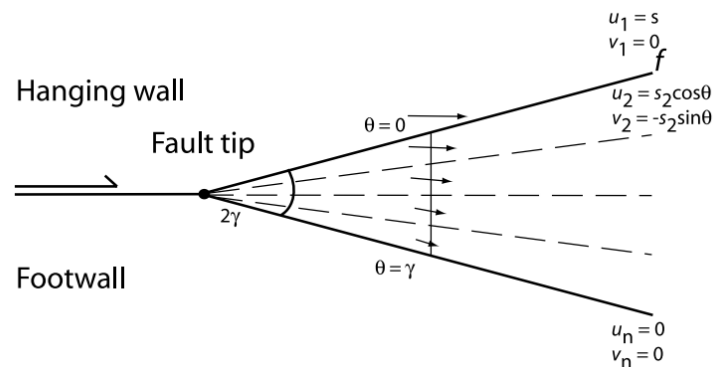


Figure 182: Kinematic model of trishear, velocity vectors within the hanging-wall and shear zone, and sectors of equal velocity are illustrated schematically. The symmetric shear zone has an apical angle of 2γ ; (redrawn from Hardy and Ford, 1997).

The description of the velocity field was taken up and recalculated by Zehnder and Allmendinger (2000), presenting a formulation that assumes linear variations of the velocity vectors in the zone. Unlike the Erslev model, a rigid hanging-wall and a locked footwall are assumed. The shear field could be calculated assuming an asymmetry well present in nature (Allmendinger, 2011).

Boiron et al. (2020), point out that the frontal contact of the Leyre thrust is not the outcrop of the main ramp which would be buried, but the upper part of the trishear triangle. Their best

CHAPTER 6 - DISCUSSION

solution is an apical angle of 100° , and the propagating fault and shortening would be assumed to progress at the same time (P/S ratio =1).

This type of deformation propagation not only has a geometrical and structural description, but it is also possible to offer a modelling of how much this structure can affect the rock. Allmendinger (2011) has built a software called Fault Fold (Allmendinger, 2019) which includes the equations describing this type of structure, published in Zehnder and Allmendinger (2000).

This software allows the construction of geometries and their evolution, in such a way that structures can be obtained to be compared with the geological problems encountered in the field. It is also a relatively simple software, and it is therefore necessary to be cautious with regard to the data obtained, which correspond to calculations and may differ from the real deformation measured in AMS, the result of which depends on numerous parameters that cannot be controlled in this software.

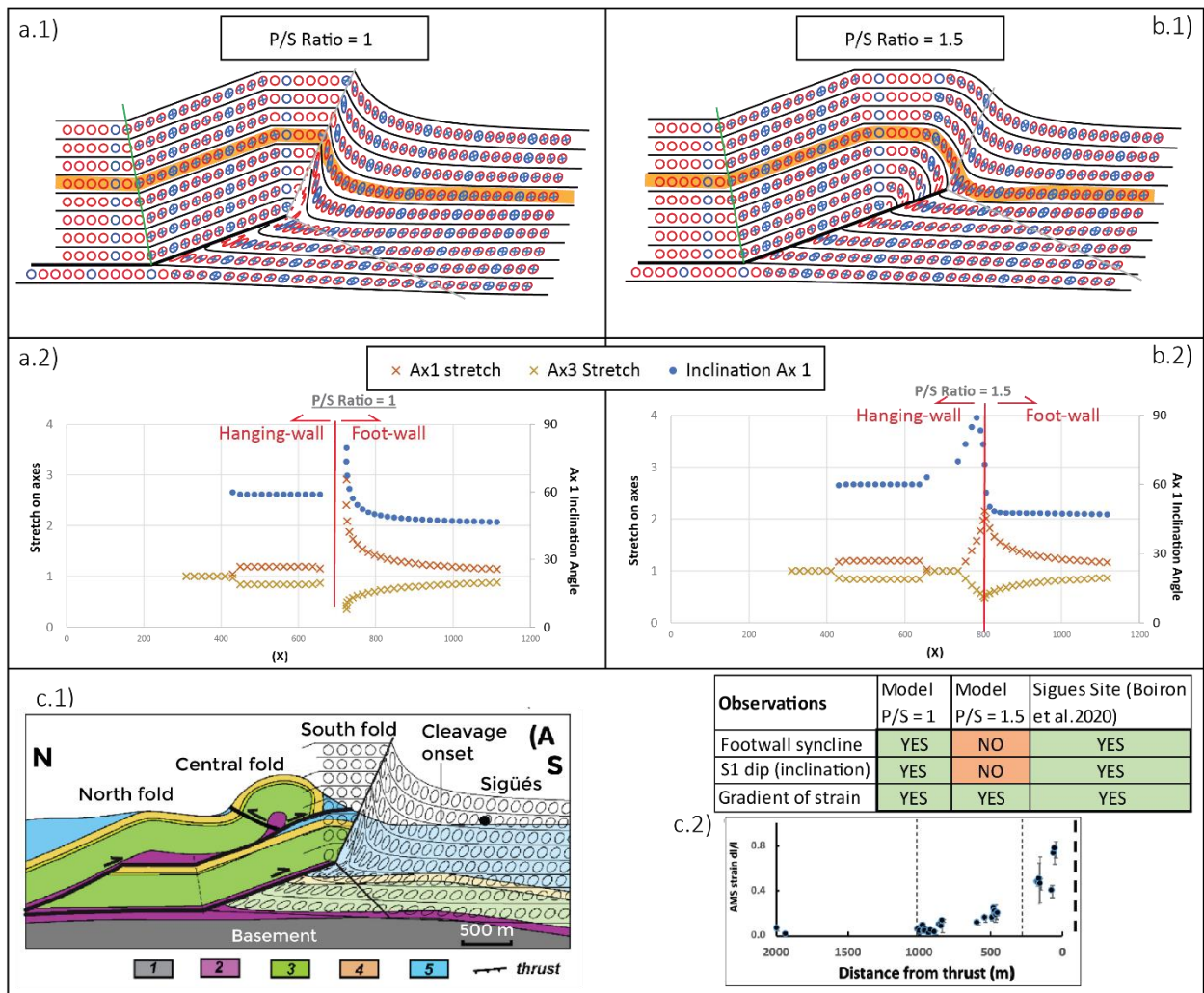


Figure 183: Re-modelling of the Sigüés transect, presented by Boiron et al. (2020). We compare with another possible case of P/S ratio, 1 vs 1.5. It is compared with the strain gradient calculated from the magnetic fabrics in the footwall.

CHAPTER 6 - DISCUSSION

The two sections in the table above have the same initial stratigraphy. The two models (apical angle = 110°) have undergone the same shortening, but by changing the P/S ratio, we can see that the thrust has not progressed in the same way. Here is an example, comparing the P/S ratio=1 case with the P/S ratio=1.5 case, and, at the bottom (Figure 183c.1 and c.2) the data from Boiron et al. (2020).

Different geometries change depending on the P/S ratio. These include:

- Footwall syncline, and its occurrence.
- The length of the fault, as we said, progresses and affects more units at a higher P/S ratio.
- The length of the flat that we see in the hanging-wall of the thrusts, larger the higher the P/S ratio.

Furthermore, the footwall is affected with slightly different geometries, a zone of high deformation is observed next to the fault, and also in the upper part of the triangular shear zone, attenuating towards lower and distant positions of this tip point. But, on the other hand, the development of a drag syncline fold in this footwall seems to disappear in the case of high P/S ratio.

These models confirm with the validity of the trishear model as a deformation process in the Sigüés area. However, we might be compelled to choose one of the options for a P/S ratio according to our observations.

Allmendinger's software allows to extract the data of the circumferences that are plotted in order to know how they suffer a stretching in their axes (small blue lines that can be seen in the figures). Thanks to these calculations, we can evaluate, not only visually, but also extract virtual deformation data point by point. For simplicity, we have decided to present data transects following beds, whose points are affected by the trishear zone, mimicking what would be a layer that has been affected by the structure and its growth (highlighted in yellow in Figure 183 .a.1 and Figure 183.b.1).

The data on strain associated with trishear zones allow us to conclude the following.

- For case b) (P/S=1.5) we observe a stretch peak value coinciding with the trishear zone. This stretch is laterally reduced. Something similar occurs in case a), although quantitatively, the stretch is more significant (almost 3 points).
- With respect to the inclination of the major axis, comparable to the cleavage, it is curious to observe how in case b) this would be acquired in the hanging-wall, and almost all of the footwall, the cleavage would lose inclination. However, in case a) the cleavage decreases its inclination along the footwall. With respect to geometry, we have already commented on the absence of a footwall syncline in case b).

This simple modelling therefore allows us to explain the existence of a deformation gradient in the footwall of the Leyre thrust, as presented by Boiron et al. (2020). We have included a table, in which we can note these observations and compare which model could be the most accurate to explain the Sigüés zone. And although the deformation gradient is well described, thanks to the differential shear characteristics of the trishear proposed by Allmendinger (1998), whatever the P/S ratio, the geometrical characteristics lead us to

CHAPTER 6 - DISCUSSION

conclude that it is highly probable that the P/S ratio = 1 correspond to the Sigüés transect. The $P/S=1$ model gives a good illustration of the Sigüés section. The $P/S=1.5$ model gives a good illustration of the strain observed in the forelimb of the fold on the left bank of the Escar river.

In addition to modelling the Sigüés shear zone, we propose to model the interaction with a second fault affecting the already that affects footwall. This is the case of the Escalar, Llarto or Esco sections. To model these secondary faults, we have decided to add a new fault with a P/S ratio of 1 to the model already presented, with a lower dip (10°) and a smaller trishear angle (20°), as the differences in strain are noticeable within a few meters. Another disadvantage that we find in the previous model is the scale with which we obtain the strain ellipses, which could leave small changes and gradients unexpressed. Therefore, in this case, the thickness of the modelled layers will be reduced to one third of the size in the initial model.

To compare it quantitatively, we make two transects marked in yellow in Figure 5, to see the stretch that these ellipsoids have acquired. The horizontal one shows a graph nearly similar to the one seen in Figure 2 for a single fault. We can see the gradient, especially from the second fault towards the left. However, between the two faults, the gradient of the first fault can be observed, and how the second one raises the acquired stretch again. The imprint of the two faults is detectable in stretch. The vertical transect that we have drawn is different, showing a steep evolution. It is around the triangular zone of the second fault that we see a clear increase in stretch. In upper and lower positions the stretch increases as the ellipse approaches the deformation zone.

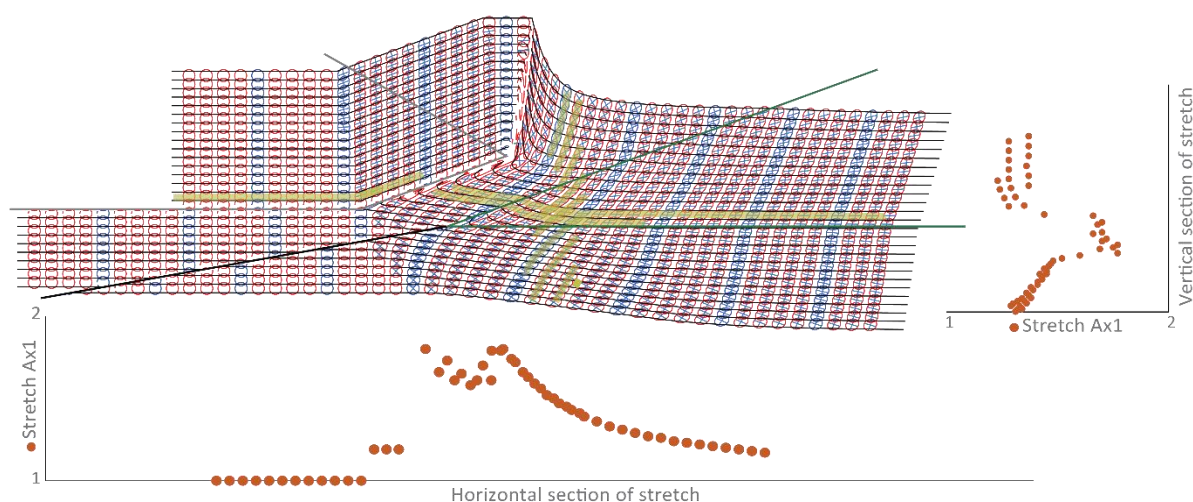


Figure 184: Plotted data for modelling a two-fault system. A first fault with Trishear deformation propagation is prepared. And in the second instance, a second ramp is propagated on the footwall of the first one. This second one has been prepared with a smaller apical angle of 20° . The stretch is calculated for the long axis of the ellipses in which the strain is modelled, and ranges from 1 (original state) to 2 depending on the elongation factor.

This modelling and the extracted transects can explain some of the phenomena observed in the field. Although the scale is a very difficult factor to control in this software (FaultFold), we can try to discuss the geometrical evolution of the stretching in the footwall vs AMS data.

CHAPTER 6 - DISCUSSION

The vertical transect shows an apparent symmetry, if the sampling were so taken. This is reminiscent of what is shown in the virtual boreholes in Figure 171. As we can see, it is also the triangular zone of the secondary footwall fault that is responsible for this deformation peak. Therefore, at this scale of observation, it could serve to explain these peaks.

However, the sampling is not strictly vertical, since in real conditions, the samplings, although inclined, are carried out horizontally with respect to the main fault. And, to discuss this, the horizontal transect of ellipses shows us a different, more skewed data geometry, where the upper flank of the trishear zones has generated a strong stretching. Although, contrary to the vertical section, this transect does reveal a gap between the stretching peaks between the two faults, as shown by the fabrics on virtual borehole in Figure 171.

Some key factors for this may be the separation between the two faults, because if they are close together they can add their deformations, but if they are too far apart they will deform the rock independently, creating each of them a singular triangle of deformation. Also, proximity is important, as we may miss the effect of the secondary fault creating a deformation peak, on a pre-existent shadow of a main fault.

The Trishear model seems to explain well the Leyre fault in the Sigüés transect. The Escalar fault could also be included, being precise with the parameters. However, the symmetry of the deformation observed in both hanging-wall and footwall AMS raises some doubts.

Symmetries on transects can be quite difficult to explain with the trishear model. This model, as proposed in Figure 183b, suggest weaker strain in the hanging-wall and stronger strain in the footwall. This is not consistent with the observation of the Jaca Gas Fault, where a symmetrical strain pattern is observed in the footwall and hanging-wall (Figure 185)

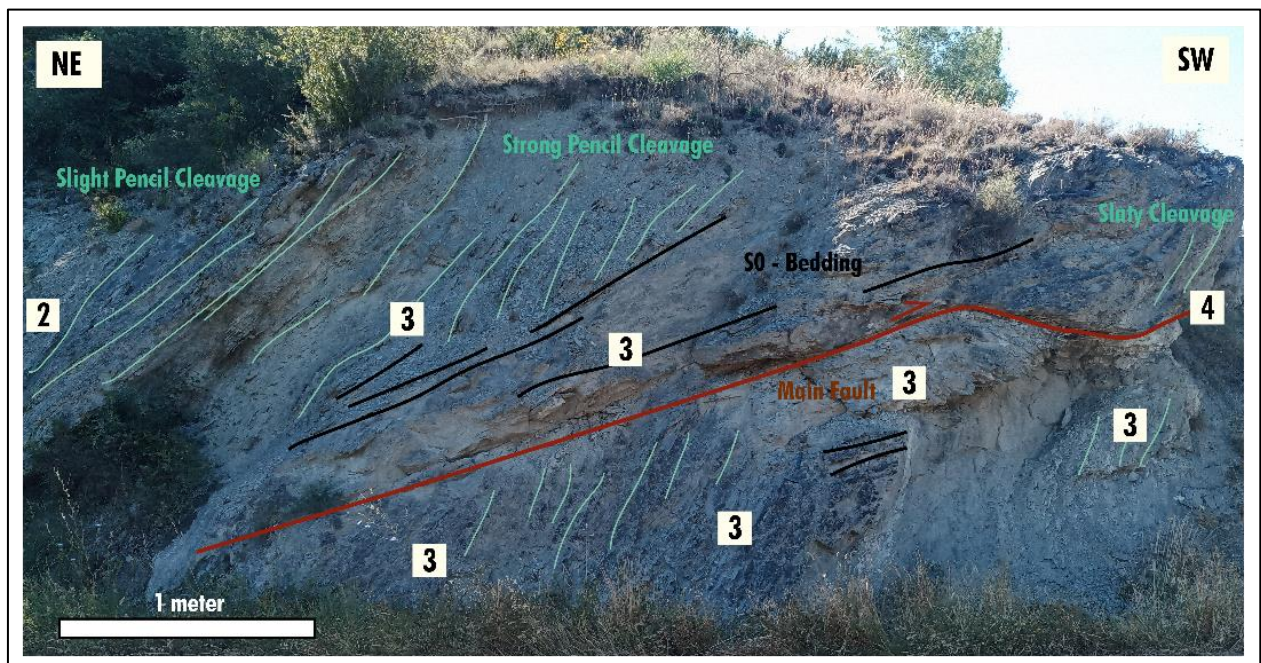


Figure 185: Jaca -Gas fault outcrop. Sampling has been described in Section 4.6.3 Jaca-Gas Site. The numbers for each outcrop point correspond to the stage from 1 to 5 assigned to each magnetic fabric measured. Two more points to go for SW with type 2 fabric. This shows a certain symmetry around the fault zone core.

This type of symmetry is not particularly consistent with what is expected for trishear propagation according to the Hardy and Ford (1997) model, but rather resembles a

CHAPTER 6 - DISCUSSION

décollement fault zone in shales, similar to those described by Morley et al. (2018) (in the Barbados accretionary prism) or Deville et al. (2020) (in the Parras Basin, Mexico). Such structures can have thicknesses of metric size and accumulate various signs of shearing, as well as calcite-filled fractures, cataclastic rocks and tectonic breccias.

Interestingly, this type of structure has also been found outcropping in the Sigüés section (see section 3.2.1.3 Sigüés Gorge, Figure 77). The site for which we interpret coincides with the typical trishear model. It is possible, therefore, that these two types of structures exist: shale-on-shale thrust décollements affecting metric-thick bands in the marly formation (Type 3 faults), but also large triangular zones of trishear-type shear deformation, preceding the thrust ramp itself, and encompassing decametric-thick strain fans in their propagation. In that sense, Figure 171 envisages the different surface manifestations of such a structure: a deformation halo observed in the marls propagating above a narrower fault structure that fractures the previously sheared formations.

6.6 Folding stage

To complete the succession of events, let us revisit the structural observations, and how we can construct a relative tectonic sequence that allows us to understand the finite deformation that the current geometry allows us to reconstruct.

The Orba (strike ≈ 110) and Leyre (strike ≈ 090) thrusts correspond to two different regional stress states, in which a $\delta 1$ of direction 200 and 180 respectively can be expected for each tectonic feature. This would explain the occurrence of these two dominant slickenside sets in Figure 168. The relative timing inferred from the structural study in section 3.4.3 Structural synthesis suggests that the Leyre thrust worked in the first instance, and the Orba thrust later affected the same units to the E. However, the calcite faults in the footwall showing these two lineations on the same surface confirm that the stress states of these two thrusts were relatively close, and that $\delta 1$ rotated rapidly.

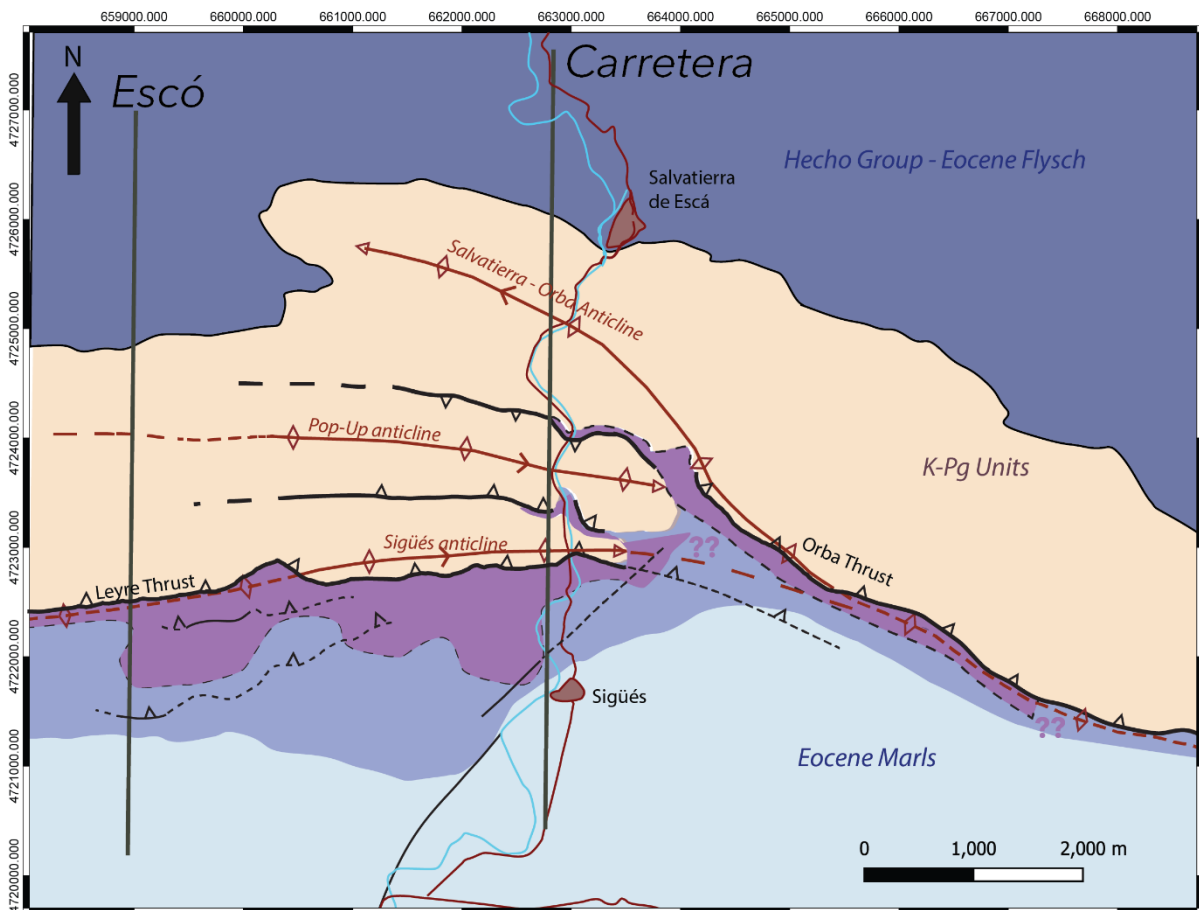


Figure 186: Structural map for the Leyre-Orba system. The pre-ASM data version is available in Figure 93. On this occasion, we have added the updated mapping of the footwall after the observations made thanks to the results of the magnetic fabric and associated calculations. Only the two cross-sections shown in figure 15 are indicated.

Slaty cleavage zones and a remodelling of the footwall faults have been added to the map in figure 13, adding detail to these structures following the study of the magnetic fabrics in chapter 4. As mentioned above, it is difficult to draw the lateral extent of these faults. We do interpret that the fault observed at Escó is the same as the one observed at Escalar. On the

CHAPTER 6 - DISCUSSION

other hand, the extension of the slaty cleavage, painted in a more intense purple colour, is done according to the calculated strain extension $> 40\%$ from the interpolation map in Figure 174.

Although it has not been the object of study in this thesis, the Ruesta fault, a subvertical structure that crosses the area with a N030 strike, is worth mentioning. This fault is associated with post-orogenic or even Quaternary processes (Carbonel et al., 2019). However, we could discuss the possibility that this fracture existed at some point during the thrust-fold event that formed the Leyre and Orba structure.

Interestingly, its strike and position mark the separation between two main configurations in the studied area: the Leyre thrust and the Orba thrust. It also, to a certain extent, marks the limit of the main cleavage zone, to the E of the river Escá. It is therefore possible that this fault may have represented some kind of tectonic discontinuity for the LPS and shortening processes in the Larrés Fm.

On the other hand, as already mentioned in the 3.4.3 Structural synthesis, there are important **along-strike variations** in the hanging-wall of the Leyre fault. The formation of the pop-up, which does not exist in the E margin of the map, but which has an important entity in the central sector, speaks of a change in the way in which shortening is accommodated at a regional level. It is possible that there is a blocking of the structure that we do not see in our map, but which causes the shortening to accumulate in the thrusts and folds of the hanging-wall, and not in the frontal fault. This is suggested by the cross-sections in Figure 18, where the fault dip of the Leyre thrust is higher to the E (Escó section) than in the central part of the map (Carretera section). Besides, the existence of secondary thrusts in the footwall could accommodate further shortening, invisible in the footwall, but related to the same structure at depth. The propagation of these secondary faults could enlarge the cleavage footprint mapped on the surface and calculated from the magnetic fabrics.

An alternative explanation for the formation of the backthrust linked to the pop-up in the hanging-wall of the structure is the possibility of decreasing the friction angle of the décollement (in this case the Zuriza marls) during the process of ascent along the ramp and the displacement along the footwall flat. The development of backthrusts and other structures with non-univocal vergence is typical of orogenic wedges with low-friction décollements vs. wedges with high-friction floors in which a dominant vergence develops (Borderie et al., 2018 and references therein). In the case of Sigüés, the low-friction décollement could be related to high fluid pressure responsible for the formation of calcite faults. The fact that the Cretaceous detachment is not involved in the Orba system (that does not show changes of vergence, either), would also support this hypothesis. In any case, the development of opposite-verging thrust systems sharing in some cases two stepped décollements (Upper Triassic and Zuriza marls) would also favour the balance of shortening in different part of the Leyre-Orba (thin-skin) thrust belt.

An important feature, which we have left out of the previous figure, but which in this discussion we want to integrate, are the trajectories of the cleavage recorded within the cleavage front. We observed that there is no homogeneity or pattern as far as the inclination of the cleavage planes is concerned, although there is an average and a median of around 49° dip. In contrast, the S1 strike does have a certain order.

CHAPTER 6 - DISCUSSION

Firstly, in the Figure 93 of Chapter 3, we could see punctual data of cleavage planes. On the basis of these measurements, it was observed that in the vicinity of the two thrusts there is a cleavage with strike parallel to the thrust trace, both in Leyre and Orba. However, when moving away from the Leyre thrust (> 200 m southwards), even in the previously associated deformation zone we find that the cleavage shows an oblique strike, rather parallel to the Orba strike (200-210°). As the Cleavage is classically interpreted as direct concordance of the LPS and main regional stress field, we can say that there is an LPS in line with the Orba thrust, which hypothetically affects shales in the footwall of Leyre thrusts, 3 to 5 km of lateral distance.

In general, even if we discard this option and it is not directly related to the deformation associated with the advance of the Orba thrust front., we can interpret that the dominant $\delta 1$ stress - LPS direction is rotated in the footwall of Leyre thrust relatively to this main thrust. This explains the appearance of slickensides with strike 200-210 in the Escalar and Escó sections, even though they are not directly near Orba. Briefly, we dare to say that there is an LPS episode in the footwall of the Leyre fault that is not directly related to it, but in which the conditions are the same.

Looking at the present literature, we can raise some questions regarding the relationship with these main thrusts, Orba and Leyre. Oliva-Urcia et al. (2012) states that the basal basement thrust interpreted at depth below the detachment level accommodates 11-13 km of shortening, and is responsible for the uplift of the marine platform towards the surface (the outcrop of Cretaceous-Paleocene at Leyre and Illón mountain ranges). The structural style in this "thin skin" above the Triassic depends on the mechanical stratigraphy: the thin limestone units form a system of imbricate thrusts with low individual displacements and fault-related folds in the hanging-wall of the thrusts. This is in relative agreement with our cross-sections, for which we estimate between 1.3 and 1.9 km for the Leyre and Orba thrusts.

Turner (1990) proposes a sequence of major structures. He states that the first structure is the Sierra de Orba, the Upper Eocene being the last unit affected by it, and its "lack of effect on the Upper Oligocene molasse". This is disputed because there is simply no direct relationship, and our relative chronology for the Leyre area suggests that this is the most recent thrust of this system. Turner (1990) also points out the structure of the vertical backthrust, but relates it to the Sierra de Orba and does not observe how this same mountain range covers the backthrust (figures of section 3.2. Field description of the Jaca Basin sites.). We do, however, welcome his comment that this backthrust is the resolution of "a resistance offered to thrusting".

Turner (1990) also suggests that the Orba and Leyre thrust sequence (formation of the pop-up and imbricated thrust fans to the W of the Leyre mountain range) show signs of having formed in a prolonged sequence, even by thrust propagation from the Upper Eocene to much of the Oligocene.

The studied area is also the area of intersection between the clockwise rotated area of the External Sierras, and the non-rotated area of the Pamplona basin (Larrasoana et al., 2003; Pueyo Anchuela et al., 2012b; Pueyo, 2006). The different strike of the Leyre thrust and the Orba thrust could also suggest a different origin not based on the changing of the maximum compressional stress but rather on the existence of vertical axes rotations in particular segments of the chain (Pueyo et al., 2002). This also agrees with the relative chronology

CHAPTER 6 - DISCUSSION

proposed in this work for the different thrusts and the transfer of displacement between the different thrusts rooted in the Upper Triassic. However, more detailed paleomagnetic studies are needed to strictly determine the position of the hinge zone for the rotated and non rotated areas of the Southern Pyrenees. As we have mentioned before it is interesting to note that the horizontal shortening associated with each structure is not necessarily related to the deformation found in the marly levels of their footwalls. However, the fact that cleavage with a N110 (Orba) strike can be found in the foreland of the Leyre thrust point to an interaction between the two thrust systems, both acting below a significant sedimentary pile (i.e. previous to exhumation). Basement thrusting, both at the local (responsible for the uplift of the Leyre – Orba-Illón system) and the regional (uplifting of an important segment of the Axial zone, see Figure 67, and other regional cross-sections from Chapter 3) would be the ultimate responsible for the final geometry of the Leyre-Orba thrust system.

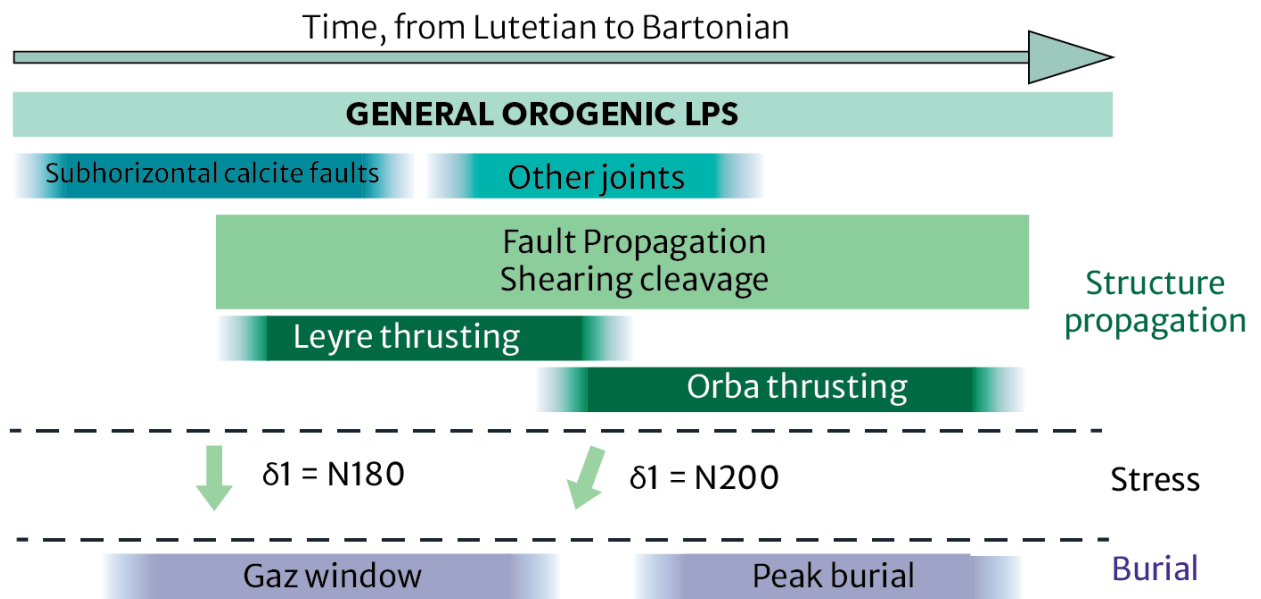


Figure 187: Schema for the timeline of events at Leyre-Orba system. Timeline is from left (Lutetian) to right (Bartonian). Events of different nature (strain, structures, stress field, burial) are arranged in rectangles indicating a relative sequence.

Ultimately, our interpretation of the local history is related to the sequence shown in Figure 167, and now plotted on the scheme of Figure 187.

- An early episode of subhorizontal calcite fault formation occurs.
- Subsequently, fault propagation with associated deformation zones takes root in the Triassic, affecting the Cretaceous and Palaeocene formations in a "brittle" way. Locally, they would use the Zuriza Fm marls as a detachment.
- Subsequently, the propagation of the deformation and its geometry on the fault tip affect the Eocene marls, generating cleavage associated with the strain generated by the thrust.
- At a later stage, probably with the progressive burial of this unit, and the significant deposition of fluvial materials (Campodarbe Fm.) to the south, the Leyre system would come to a halt, and the pop-up backthrust would be born. This resistance would also be accommodated by the Salvatierra fold from behind.
- The Salvatierra fold shows a strike rotated with respect to the Leyre mountain range, demonstrating this change of $\delta 1$. The continuation of compression through this

CHAPTER 6 - DISCUSSION

tectonic feature generates its rupture towards the E, and the Orba backthrust is born, which covers the Leyre system.

- At this time, the burial peak is also approximately produced, and under this $\delta 1$, cleavage is also generated in the Larrés and Pamplona Formation, as well as the reactivation of the secondary calcite faults, superimposed on the compression markers under the previous $\delta 1$.
- To conclude, this final configuration works until the stop of the Gavarnie sheet, with the transfer of compression to the south, and the Guarga system in the External sierras.

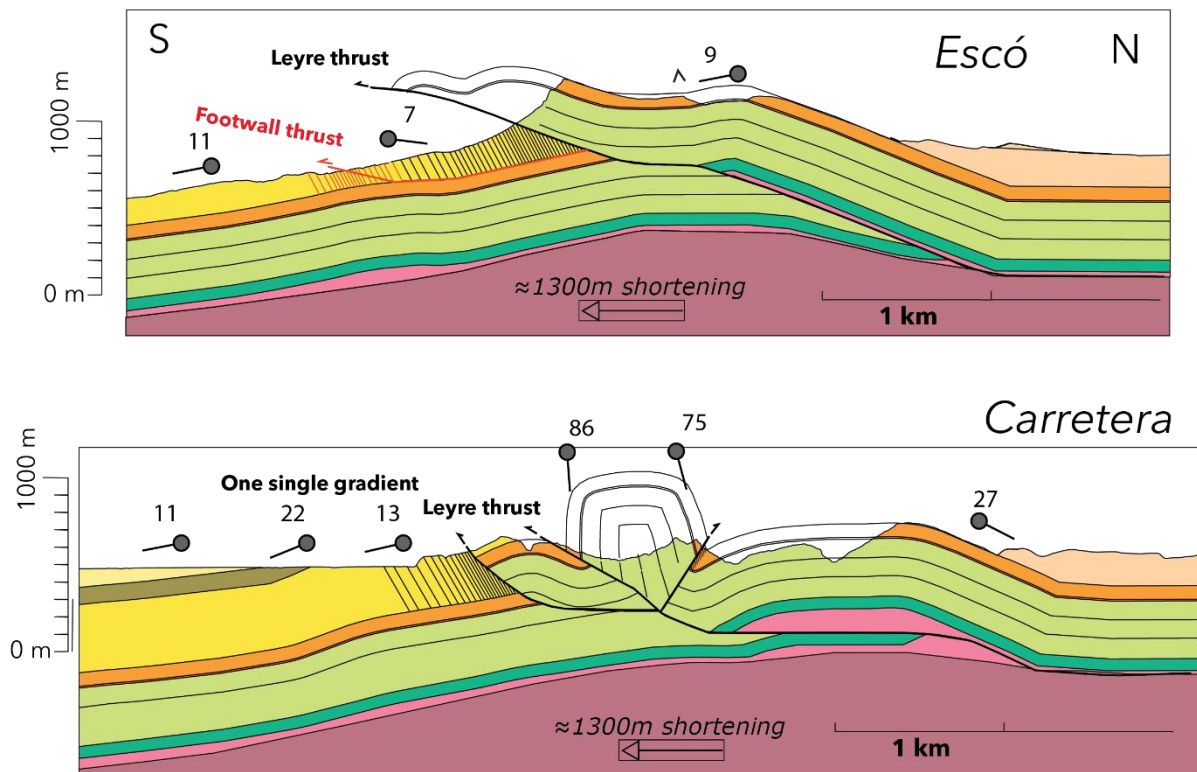


Figure 188: Two cross-sections for the Leyre structure, their traces are shown in Figure 13. In contrast to what was presented in Chapter 3, in these sections we have added the cleavage in the footwall of the Leyre thrust, following our interpretations of the deformation in the Larrés Fm. shales.

After making our interpretations of the extent of cleavage in the Leyre thrust footwall, and studying the secondary faults that appear in it, we propose a small modification to the sections presented in section 3.4.2. Serial cross-sections (traces in map shown in Figure 188). In this case, we have added a fault in the Leyre thrust footwall at the Escó site, as we have seen it in the field, and in the way it affects the Larrés Fm shales. In the Carretera cross-section, a simple cleavage gradient has been added, as explained in this discussion.

In all cases analysed in this thesis we find an accentuation of the Layer Parallel Shortening expected in this geological framework (piggyback basin in a foreland). This accentuation is clearly linked to the proximity to faults affecting the same lithological formation. Only the case of the Leyre footwall seems to reach farther, and also with a greater occurrence of slaty cleavage if we compare it with the Orba sites, or those linked to the Jaca thrust (including Biniés, Javierregay... etc).

6.6.1 Do the conditions under which the strain occurs favour the development of cleavage?

One issue discussed in the literature is the possibility that the thermal conditions of the peak burial may have favoured the appearance of cleavage. Our approach in this discussion establishes that fault-associated strain propagation is the main factor for the occurrence of cleavage. However, the estimated temperature does partially favour the mobility of mineral components. Moreover, the observation of this cleavage band at the Jaca basin sites could indicate common burial conditions in which a precise strain could generate sharp deformation. Izquierdo-Llavall et al. (2013) interprets the Sigüés site within the cleavage front for the regional schistosity affecting the turbidite basin. Therefore, we have to discuss this factor on the basis of two end-members

1. The **observed cleavage is regional**, as the structural factor of kilometre-thick stacking would have a remarkable regional extent. Also, the cleavage trajectories, and the directions of the slickensides are not strictly coincident with the LPS direction expected for the local structures, especially the Leyre thrust. The view of the extensive deformation zone in the Escó or Escalar sections suggests that not all the thickness of cleaved shales is related to the Leyre thrust front.

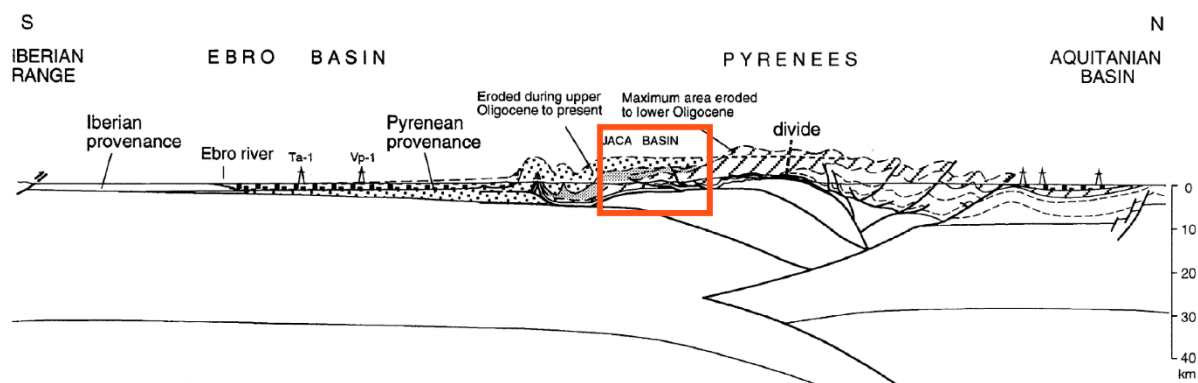


Figure 189: An evaluation of surface material budget, which shows the interpreted sedimentary thick for our section in Jaca Basin. The author interprets up to 4km of sediment thickness in Jaca Basin. From Teixell, (1998).

2. The **observed cleavage is related to the Orba and Leyre structure**. There is a narrow lateral band with respect to the thrust trace that does seem to condition the cleavage geometry. This occurs in the Sierra de Orba, Sierra de Leyre, the pop-up backthrust (Figure 79) and also the deformation gradient next to the Illón thrust (see Figure 71) seems to indicate that local structures are the ones that condition the appearance of cleavage.

However, either of these two "theoretically" separate views is incomplete, and does not resolve the heterogeneity of strain and stress that structural analysis reveals, especially in the Leyre footwall. We can say that the sequence of events in is expressed in the same Larrés formation but printing different geometric expressions of the strain. The peak burial would coincide with the moment when a $\delta 1$ (N010) is dominantly expressed in the deformation

CHAPTER 6 - DISCUSSION

zone. Note the direction of K1 magnetic axis (interpreted perpendicular to the LPS) in the oriented samples of Boiron et al. (2020) indicating this direction (see Figure 178). We have not found a clarifying site where the frontal thrust-related cleavage and the LPS-related cleavage overlap.

In short, we interpret that there is a complex process behind the formation of the large deformation zone with cleaved shales that have been described throughout this thesis. There is a part of the deformation features that correspond to the propagation of thrusts, which also have different directions. Part of the events are related to the regional LPS (Calcite faults), part to thrusts (cleavage gradient) and part to a mixture of the two (secondary faults, and cleavage front extension).

6.7 General conclusions:

The central theme of this thesis has been the study of fault induced strain propagation. The context is that of a foreland basin incorporated in a piggyback sequence to an orogen, in this case, the Jaca Basin and the Pyrenean orogen. The main conclusions linked to the issues, methodologies and hypotheses addressed in this thesis are:

The Leyre thrust is a fault in a sequence of piggyback thrusts within the Jaca Basin. In the hanging-wall, the Marboré Fm, Tremp Fm and Ager Fm appear and ride on Eocene marls (Pamplona Fm and Larrés Fm) which are indistinguishable, but show a joint thickness of > 2300 m.

In these marls of the footwall there is cleavage, which, although it has been reported in the literature (Izquierdo-Llavall et al., 2013a; Labaume et al., 1985a), has not been studied in detail. Boiron et al. (2020) sampled and measured the magnetic fabric of these marls, and showed a strain gradient, 900 m long, from an undeformed fabric to intense slaty cleavage next to the Leyre frontal thrust contact.

This cleavage extends east and west, outcropping adjacent to the Leyre and Orba thrusts. A sampling campaign was planned to extend the analysis of this shale gradient and to extend the interpretation of Boiron et al. (2020). This was done by means of a sampling campaign of non-oriented shale fragments.

The fieldwork is based on the sampling of shales, the mapping of the two fault walls, but also includes the study of calcite faults that appear, and the study of new outcrops of secondary faults at the foot of the Leyre thrust, not previously detected.

The main source of data for understanding the strain has been the study of the scalar parameters of the non-oriented magnetic fabric. This has allowed us to analyse data such as the shape parameter, the anisotropy parameter, or the confidence angles of the magnetic ellipsoid axes.

Previous rock magnetism and microtomography studies on rocks of the same formation reveal that illite is the mineral responsible for the magnetic signal. And that this phyllosilicate rotates in a rigid way reacting to the strain undergone by the Larrés Fm.

We also have RSCM burial new data and isotopic data from the literature and from unpublished studies. These indicate that these rocks have undergone a Tmax of ~180°C, allowing complete illitization of the marls. There are no thermal anomalies or recrystallisations, except for the calcite grains in the marls.

Rigid rotation of illite grains makes it possible to use the March's model to calculate the shortening that occurred in the Larrés formation. By having dozens of sampling points in the Leyre fault footwall affected by cleavage, we have been able to prepare a map in which these strain calculations are interpolated.

The main conclusion about the deformation zone is that west of the Escá river is a complex zone. Other faults appear 100 and 200 m below the Leyre thrust ramp. Also, a blind fault with intense slaty cleavage (strain > 70%) similar to the most deformed samples of the Sigüés section.

CHAPTER 6 - DISCUSSION

Next to, and east of, the river Escá we have fewer samples, but the gradient is unique, and only seems to be controlled by the deformation associated with the Leyre thrust and the Orba thrust.

In the course of this thesis it was decided to visit other outcrops in the Jaca basin, where these same marls exist in the footwall of the Jaca-Javierregay fault. These are the sites of Biniés, Javierregay and Jaca. And the visits also reveal some 300-400 m of outcrops of the Larrés Fm with more or less penetrative cleavage.

However, the results of the magnetic fabrics are more confusing, and complications such as sedimentary structures, folding or shorter outcrops are observed. Strain calculations can be misleading, and are not performed at these sites.

In general, the conditions in the Leyre-Orba system are optimal for deformation analysis with this non-oriented fragment methodology.

This has allowed us to describe a rock unit, the Eocene marls, which is much more complex and deformed than had been described previously or than has been reported in the literature.

This study can be used to avoid simplifying the mechanical and porous role of the marls, which risk being assumed to be homogeneous, watertight and plastic. However, the study of the magnetic fabric, which is quick and easy, has made it possible to construct a deformation map which warns of an important strain in these marl formations.

In conclusion, the methodology of this thesis can be used to propose new surface studies of large mudrocks outcrops, especially in formations of storage interest. But also with scientific interest, in compressional contexts to know the evolution of deformation in basins with similar characteristics to the Jaca Basin.

6.8 General perspectives

In the course of this thesis, a number of questions were raised which, for various reasons, could not be answered. In the face of some of the unknowns that this thesis leaves open, numerous perspectives appear that could complete the conclusions raised or in any case open up other points of interest.

- Firstly, the exceptional outcrop of the Sigüés section (or other sections) can allow numerous studies to be carried out in which different parameters are contrasted against a cleavage gradient. To take just one example, how does organic matter evolve in a stress gradient zone? This is the question that prompted our collaboration with Stokes from the USGS.
- The Sigüés site shows the association of two faults that may represent end-members calcite faults where no damage is observed in the marls, and more dry faults (few veins) with an associated strain halo. This association may be a key to understanding co-seismic displacement with fluids in overpressure (which give rise to calcite faults) and displacements by creep as the fault propagates in the absence of fluid. This can be compared with the history of the basin (expulsion of interfacial water from the clays during diagenesis), the depth of nucleation of the fault displacement and other

CHAPTER 6 - DISCUSSION

parameters. We therefore believe that a dating study could be attempted again to clarify the timing of the propagation of these various faults.

- In this work, we have clearly established the relationship between fault propagation and associated strain in both the footwall and the hanging-wall. We have suggested that the trishear model could explain some of these features, but it is a geometric model that lacks mechanical parameters. We therefore believe that the area around Sigüés site would allow the development of a model that incorporates the mechanical properties of the rocks, as the Leyre thrust (or equivalent) propagates along the carbonate/marl and marl/marl interfaces.
- The structural study for the Sierra de Leyre, the Sierra de Orba, or even the Sierra de Illón could be completed with different cartographic techniques. Likewise, in order to understand the strike difference between Leyre and Orba ranges, sampling for palaeomagnetism could be considered, as well as a possible study of vertical axis rotations, as has been (and is also being) done in other areas in the Pyrenees.
- Small-scale gravimetric studies could also provide accurate information on the subsurface, as other cross-sections suggest a large thickness of Triassic evaporites, in contrast to our cross-sections which suggest basement uplift.
- The fragment method raised questions in the rock magnetism community. I have received numerous invitations to test the fabric data presented with oriented samples (i.e. cylindrical, standard paleomagnetic samples). This has not been done because the data of Boiron et al. (2020) are available, but it could be interesting to have oriented AMS data in the outcrops of Esco, Escalar or Orba. This opens a new door for the use of unoriented fragments to study shale damage, for example in wells but also in areas where outcrops do not allow the collection of oriented samples. The sensitivity of the shape parameter (T) to strain can be used to detect and map damage in geological reservoir systems. My collaboration with Menzer (Menzer et al., 2024 in press) enabled us to map strain in a detachment fold.
- The authors, after discussion with other members of the structural geology community, are aware of the shortening numbers (>80%) presented in chapter 4 for the Larrés Fm and its component marls. Figures of more than 50% shortening for a formation are very rare in the bibliography, and already represent very pronounced physical shortenings. The shortening quantification methodology presented, and the elements on which it is based (the illite platelet magnetic fabric) allow for a specific analysis, which must be framed within the heterogeneity of the rock. This marl formation being somewhat more complex than the study of the deformation by means of the magnetic fabric would reflect. Comments at the end of this thesis suggest adding other perspectives on the fabric, composition and geochemical evolution to complete this analysis.

Finally, during this thesis, the possibility of extending this type of sampling of non-oriented fabrics to other orogens and fault zones on the planet has been raised. The possibility of using this technique in large areas, in fold-and-thrust belts could bring strain maps as presented in Figure 128 for other mudrock-based foreland basins. This would give a new perspective to the study of deformation and strain in similar contexts.

In general terms, the Sigüés area offers potential for exploration in a wide range of areas. These include the study of tectonic interference (Leyre fold, Orba fold) and the circulation of hot water (Tiermas springs in the footwall of the Leyre thrust). I think it would be useful to

CHAPTER 6 - DISCUSSION

find an equivalent outcrop in another orogenic system to gain a better understanding of this complex system

CONCLUSIONES

El tema central de esta tesis ha sido el estudio de la propagación de la deformación asociada a una falla. El contexto estudiado corresponde a una cuenca de antepaís incorporada en una secuencia de tipo *piggyback*, en este caso, la Cuenca de Jaca que ha sido incorporada al orógeno pirenaico. Las principales conclusiones vinculadas a las cuestiones, metodologías e hipótesis abordadas en esta tesis son:

El cabalgamiento de Leyre es una falla que se enmarca en la secuencia de cabalgamientos *piggyback* dentro de la Cuenca de Jaca. En el bloque superior aparecen la Fm Marboré, la Fm Tremp y la Fm Ager, que cabalgan sobre margas eocenas (Fm Pamplona y Fm Larrés) que son indistinguibles, pero muestran un espesor conjunto de > 2300 m.

En estas margas del bloque inferior se observa esquistosidad que, aunque ha sido citada en la bibliografía (Izquierdo-Llavall et al., 2013a; Labaume et al., 1985a), no ha sido estudiado en detalle. Boiron et al. (2020) muestrearon y midieron la fábrica magnética de estas margas, mostrando un gradiente de deformación de 900 m de longitud. Que evolucionad de una fábrica no deformada hasta un intensa esquistosidad de tipo “*slaty*” junto al contacto con el cabalgamiento frontal de Leyre.

Esta esquistosidad se extiende hacia el Este y el Oeste, aflorando junto a los cabalgamientos de Leyre y Orba. Se ha realizado una campaña de muestreo para ampliar el análisis de este gradiente de esquistosidad y extender las observaciones de Boiron et al. (2020). Esto se hizo mediante una campaña de muestreo de fragmentos de roca no orientados.

El trabajo de campo se basa en el muestreo de margas, la cartografía de las dos bloques del cabalgamiento de Leyre. También incluye el estudio de las fallas de calcita que aparecen, y el estudio de nuevos afloramientos de fallas secundarias al pie del cabalgamiento de Leyre, no detectadas anteriormente.

La principal fuente de datos para comprender la deformación ha sido el estudio de los parámetros escalares de la fábrica magnética no orientada. Esto nos ha permitido analizar datos como el parámetro de forma, el parámetro de anisotropía o los ángulos de confianza de los ejes del elipsoide magnético.

Estudios previos de magnetismo de rocas y microtomografía en rocas de la misma formación revelan que la illita es el mineral responsable de la señal magnética. Y que este filossilicato rota de forma rígida reaccionando a la deformación sufrida por las margas eocenas.

También disponemos de nuevos datos del enterramiento provenientes de Espectroscopía Raman (RSCM) y de datos isotópicos procedentes de la literatura así como de estudios no publicados. Éstos indican que estas rocas han sufrido una $T_{\text{máx}}$ de $\sim 180^{\circ}\text{C}$, lo que ha permitido la completa ilitización de las margas. No hay anomalías térmicas ni recristalizaciones, salvo en los granos de calcita de las margas.

La rotación rígida de los granos de illita permite utilizar el modelo de March para calcular el acortamiento que se produjo en la Fm Larrés y Fm Pamplona. Al disponer de decenas de puntos de muestreo en el bloque inferior del cabalgamiento de Leyre afectada por la esquistosidad, hemos podido elaborar un mapa en el que se interpolan estos cálculos de deformación.

CHAPTER 6 - DISCUSSION

La principal conclusión sobre la zona de deformación es que al oeste del río Escá es una zona compleja. Aparecen otras fallas a 100 y 200 m por debajo de la traza del cabalgamiento de Leyre. También aparece una falla ciega con una intensidad esquistosidad de tipo slaty (deformación > 70%) similar al de las muestras más deformadas de la sección de Sigüés.

Junto al río, y más al este del río Esca, hacia la sierra de Orba tenemos menos muestras, pero el gradiente es único, y sólo parece estar controlado por la deformación asociada al cabalgamiento de Leyre y al cabalgamiento de Orba.

En el transcurso de esta tesis se decidió visitar otros afloramientos de la cuenca de Jaca, donde existen estas mismas margas en el bloque inferior de la falla Jaca-Javierregay. Se trata de los yacimientos de Biniés, Javierregay y Jaca. Y las visitas también revelan unos 300-400 m de afloramientos de la Fm Larrés con esquistosidad en gradiente hacia la falla.

Sin embargo, los resultados de las fábricas magnéticas son más confusos, y se observan complicaciones como estructuras sedimentarias, plegamientos o afloramientos más cortos. Los cálculos de deformación pueden ser engañosos y no se realizan en estos yacimientos.

En general, las condiciones del sistema Leyre-Orba son óptimas para el análisis de la deformación con esta metodología de fragmentos no orientados. Esto nos ha permitido describir una unidad rocosa, las margas del Eoceno, mucho más compleja y deformada de lo que se había descrito anteriormente o de lo que se ha informado en la bibliografía.

Este estudio puede servir para no simplificar el papel mecánico y poroso de las margas, que corren el riesgo de ser asumidas como homogéneas, impermeables y plásticas. Sin embargo, el estudio de la fábrica magnética, rápido y sencillo, ha permitido construir un mapa de deformación que advierte de una importante deformación en estas formaciones de margas.

En conclusión, la metodología de esta tesis puede utilizarse para proponer nuevos estudios de superficie de grandes afloramientos de margas, especialmente en formaciones de interés de almacenamiento geológico. Pero también con interés científico, en contextos compresionales para conocer la evolución de la deformación en cuencas con características similares a la Cuenca de Jaca.

CONCLUSIONS

Le thème central de cette thèse a été l'étude de la propagation de la déformation associée à une faille. Le contexte est un bassin d'avant-pays incorporé dans une séquence de *piggyback* à un orogène. Plus précisément, le bassin de Jaca et l'orogène pyrénéen. Les principales conclusions liées aux questions, méthodologies et hypothèses abordées dans cette thèse sont les suivantes :

Le chevauchement de Leyre est une faille qui est incluse dans la séquence de chevauchements en *piggyback* dans le bassin de Jaca. Dans le toit de faille, les Marboré Fm, Tremp Fm et Ager Fm apparaissent et reposent sur des marnes éocènes (Pamplona Fm et Larrés Fm) qui sont impossibles à distinguer, mais qui montrent une épaisseur commune de > 2300 m.

Dans ces marnes du mur de faille inférieure, il existe une schistosité qui, bien que signalée dans la littérature (Izquierdo-Llavall et al., 2013a ; Labaume et al., 1985a), n'a pas été étudiée en détail. Boiron et al. (2020) ont échantillonné et mesuré la fabrique magnétique de ces marnes et ont montré un gradient de déformation de 900 m de long, d'une fabrique non déformée à une schistosité type « *slaty* » intense à côté du contact du chevauchement frontal de la Leyre.

Cette schistosité s'étend à l'est et à l'ouest, affleurant à proximité des chevauchements de Leyre et d'Orba. Une campagne d'échantillonnage a été planifiée afin d'étendre l'analyse de ce gradient de schistosité, et de grandir l'interprétation de Boiron et al. (2020). Pour ce faire, une campagne d'échantillonnage de fragments de marnes non orientés a été réalisée.

Le travail de terrain est basé sur l'échantillonnage des marnes, la cartographie des deux blocs de faille, mais comprend également l'étude des failles de calcite qui apparaissent, et l'étude de nouveaux affleurements de failles secondaires au mur du chevauchement de Leyre, non détectés auparavant.

La principale source de données pour comprendre la déformation a été l'étude des paramètres scalaires de la fabrique magnétique non orientée. Cela nous a permis d'analyser des données telles que le paramètre de forme, le paramètre d'anisotropie ou les angles de confiance des axes de l'ellipsoïde magnétique.

Des études antérieures de magnétisme de roche et de microtomographie sur des roches de la même formation révèlent que l'illite est le minéral responsable du signal magnétique. Et que ce phyllosilicate tourne de manière rigide en réagissant à la déformation subie par le Fm Larrés et Fm Pamplona.

Nous disposons également de nouvelles données de températures issues de la Spectroscopie Raman (RSCM) et de données isotopiques provenant de la littérature et d'études non publiées. Celles-ci indiquent que ces roches ont subi un T_{max} de ~180°C, permettant une illitisation complète des marnes. Il n'y a pas d'anomalies thermiques ou de recristallisations, à l'exception des grains de calcite dans les marnes.

La rotation rigide des grains d'illite permet d'utiliser le modèle de March pour calculer le raccourcissement qui s'est produit dans les marnes éocènes. En disposant des dizaines de points d'échantillonnage dans le mur du chevauchement de Leyre affectée par la schistosité, nous avons pu préparer une carte dans laquelle ces calculs de déformation sont interpolés.

CHAPTER 6 - DISCUSSION

La principale conclusion concernant la zone de déformation est qu'à l'ouest de la rivière Escá se trouve une zone complexe. D'autres failles apparaissent à 100 et 200 m sous la rampe de chevauchement de Leyre. En outre, une faille aveugle avec une schistosité « *slaty* » intense (déformation > 70 %) similaire aux échantillons les plus déformés de la section de Sigüés.

À l'est de la rivière Escá, et à côté, nous avons moins d'échantillons, mais le gradient est unique et semble être contrôlé seulement par la déformation associée au chevauchement d'Orba et de Leyre.

Au cours de cette thèse, il a été décidé de visiter d'autres affleurements dans le bassin de Jaca, où ces mêmes marnes existent dans le mur de la faille de Jaca-Javierregay. Il s'agit des sites de Biniés, Javierregay et Jaca. Les visites révèlent également quelques 300-400 m d'affleurements du Fm Larrés avec une schistosité plus ou moins pénétrant.

Cependant, les résultats des fabriques magnétiques sont plus confus et des complications telles que des structures sédimentaires, des plissements ou des affleurements plus courts sont observés. Les calculs de contrainte peuvent être trompeurs et ne sont pas effectués sur ces sites.

En général, les conditions dans le système Leyre-Orba sont optimales pour l'analyse de la déformation avec cette méthodologie des fragments non orientés. Cela nous a permis de décrire une unité rocheuse, les marnes éocènes, qui est beaucoup plus complexe et déformée que ce qui a été décrit précédemment ou que ce qui a été rapporté dans la littérature.

Cette étude permet de ne pas simplifier le rôle mécanique et poreux des marnes, qui risquent d'être supposées homogènes, étanches et plastiques. Cependant, l'étude de la fabrique magnétique, rapide et facile, a permis de construire une carte des déformations qui alerte sur une déformation importante de ces formations marneuses.

En conclusion, la méthodologie de cette thèse peut être utilisée pour proposer de nouvelles études de surface de grands affleurements de mudrocks, notamment dans des formations d'intérêt pour le stockage. Mais aussi avec un intérêt scientifique, dans des contextes de compression pour connaître l'évolution de la déformation dans des bassins avec des caractéristiques similaires au Bassin de Jaca.

BIBLIOGRAPHY

7. BIBLIOGRAPHY

- Ábalos, B., 2016. Geologic map of the Basque-Cantabrian Basin and a new tectonic interpretation of the Basque Arc. *Int. J. Earth Sci.* 105, 2327–2354. <https://doi.org/10.1007/s00531-016-1291-6>
- Ábalos, B., Carreras, J., Druguet, E., Escuder-Virueite, J., Gómez-Pugnaire, M.T., Lorenzo-Álvarez, S., Quesada, C., Rodríguez-Fernández, R., Gil-Ibarguchi, J.I., 2002. Variscan and pre-Variscan tectonics., in: Gibbons, W., Moreno, T. (Eds.), *The Geology of Spain*. pp. 155–183.
- Abdelmalak, M.M., Polteau, S., 2020. The thermal maturity of sedimentary basins as revealed by magnetic mineralogy. *Basin Res.* 32, 1510–1531. <https://doi.org/10.1111/bre.12439>
- Aguirre, J., Alonso, B., Barnolas, A., Braga, J.C., Casas, D., Civis, J., Cunha, P.P., de Vicente, G., Ercilla, G., Estrada, F., Galindo-Zaldívar, J., García-Castellanos, D., García-Alix, A., 2019. *The Geology of Iberia: A Geodynamic Approach (Volume 3: The Alpine Cycle)*.
- Allmendinger, R.W., 2019. *FaultFold*.
- Almar, Y., Ferrer, O., Roca, E., Puigvert, M., Amilibia, A., 2008. A geological cross-section along the Basque Pyrenees and the Parentis Basib (Western Pyrenees). *Geotemas (Madrid)* 2, 422–424.
- Alonso, J.L., Pulgar, J.A., García-Ramos, J.C., Barba, P., 1996. Tertiary basins and Alpine tectonics in the Cantabrian Mountains (NW Spain). *Trab. Geol.* 21, 214–227.
- Alvarez, W., Engelder, T., Geiser, P.A., 1978. Classification of solution cleavage in pelagic limestones. *Geology* 6, 263–266. [https://doi.org/10.1130/0091-7613\(1978\)6<263:CO&2.0.CO;2](https://doi.org/10.1130/0091-7613(1978)6<263:CO&2.0.CO;2)
- Anastasio, D., Parés, J.M., Kodama, K.P., Troy, J., Pueyo, E.L., 2016. Anisotropy of magnetic susceptibility (AMS) records synsedimentary deformation kinematics at Pico del Aguila anticline, Pyrenees, Spain. *Geol. Soc. Spec. Publ.* 425, 129–144. <https://doi.org/10.1144/SP425.8>
- Anastasio, D.J., Holl, J.E., 2001. Transverse fold evolution in the External Sierra, Southern Pyrenees, Spain. *J. Struct. Geol.* 23, 379–392. [https://doi.org/10.1016/S0191-8141\(00\)00102-4](https://doi.org/10.1016/S0191-8141(00)00102-4)
- Aplin, A.C., Macquaker, J.H.S., 2011. Mudstone diversity: Origin and implications for source, seal, and reservoir properties in petroleum systems. *Am. Assoc. Pet. Geol. Bull.* 95, 2031–2059. <https://doi.org/10.1306/03281110162>
- Aranguren, A., Cuevas, J., Tubía, J.M., 1996. Composite magnetic fabrics from S-C mylonites. *J. Struct. Geol.* 18, 863–869. [https://doi.org/10.1016/0191-8141\(96\)00013-2](https://doi.org/10.1016/0191-8141(96)00013-2)
- Aubourg, C., Jackson, M., Ducoux, M., Mansour, M., 2019. Magnetite-out and pyrrhotite-in temperatures in shales and slates. *Terra Nov.* 31, 534–539. <https://doi.org/10.1111/ter.12424>
- Aubourg, C., Kars, M., Pozzi, J.P., Mazurek, M., Grauby, O., 2021. A magnetic geothermometer in moderately buried shales. *Minerals* 11.

BIBLIOGRAPHY

<https://doi.org/10.3390/min11090957>

- Aubourg, C., Pozzi, J.P., Kars, M., 2012. Burial, claystones remagnetization and some consequences for magnetostratigraphy. *Geol. Soc. Spec. Publ.* 371, 181–188. <https://doi.org/10.1144/SP371.4>
- Aubourg, C., Robion, P., 2002. Composite ferromagnetic fabrics (magnetite, greigite) measured by AMS and partial AARM in weakly strained sandstones from western Makran, Iran. *Geophys. J. Int.* 151, 729–737. <https://doi.org/10.1046/j.1365-246X.2002.01800.x>
- Aubourg, C., Rochette, P., Bergmüller, F., 1995. Composite magnetic fabric in weakly deformed black shales. *Phys. Earth Planet. Inter.* 87, 267–278. [https://doi.org/10.1016/0031-9201\(94\)02962-B](https://doi.org/10.1016/0031-9201(94)02962-B)
- Aubourg, C., Smith, B., Bakhtari, H., Guya, N., Eshragi, A., Lallemand, S., Molinaro, M., Braud, X., Delaunay, S., 2004. Post-Miocene shortening pictured by magnetic fabric across the Zagors-Makran syntaxis (Iran). *Spec. Pap. Geol. Soc. Am.* 383, 131–144. [https://doi.org/10.1130/0-8137-2383-3\(2004\)383\[131:OOTBSS\]2.0.CO;2](https://doi.org/10.1130/0-8137-2383-3(2004)383[131:OOTBSS]2.0.CO;2)
- Averbuch, O., Frizon de Lamotte, D., Kissel, C., 1992. Magnetic fabric as a structural indicator of the deformation path within a fold-thrust structure: a test case from the Corbières (NE Pyrenees, France). *J. Struct. Geol.* 14, 461–474. [https://doi.org/10.1016/0191-8141\(92\)90106-7](https://doi.org/10.1016/0191-8141(92)90106-7)
- Baker, D.R., Mancini, L., Polacci, M., Higgins, M.D., Gualda, G.A.R., Hill, R.J., Rivers, M.L., 2012. An introduction to the application of X-ray microtomography to the three-dimensional study of igneous rocks. *Lithos* 148, 262–276. <https://doi.org/10.1016/j.lithos.2012.06.008>
- Bakhtari, H.R., De Lamotte, D.F., Aubourg, C., Hassanzadeh, J., 1998. Magnetic fabrics of tertiary sandstones from the Arc of Fars (Eastern Zagros, Iran). *Tectonophysics* 284, 299–316. [https://doi.org/10.1016/S0040-1951\(97\)00179-0](https://doi.org/10.1016/S0040-1951(97)00179-0)
- Balsley, J.R., Buddington, A.F., 1960. Magnetic susceptibility anisotropy and fabric of some Adirondack granites and orthogneisses. *Am. J. Sci.* 258, e20.
- Barbed, F., Martínez-Peña, M.B., Millán, H., Navarro, J.J., Pocoví, A., 1988. Observaciones sobre la “klippe” de San Felices (Extremo occidental de las Sierras Exteriores del Prepirineo meridional).
- Barnolas, A., Gil-Peña, I., 2001. Ejemplos de relleno sedimentario multiepisódico en una cuenca de antepaís fragmentada: La Cuenca Surpirenaica. *Bol. Geológico y Min.* 112, 17–38.
- Bauluz, B., Gonzalez-Lopez, J.M., Yuste, A., Mayayo, M.J., 2008. Evolución Diagenética de las Turbiditas del Grupo Hecho (Eoceno) en la Cuenca de Jaca (España). *Rev. la Soc. Española Mineral.* 9, 47–48.
- Beaumont, C., Muñoz, J.A., Hamilton, J., Fullsack, P., 2000. Factors controlling the Alpine evolution of the central Pyrenees inferred from a comparison of observations and geodynamical models. *J. Geophys. Res.* 105, 8121–8145.
- Beutner, E.C., 1978. Slaty Cleavage and Related Strain in Martinsburg Slate, Delaware Water Gap, New Jersey. *Am J Sci.* <https://doi.org/10.2475/ajs.278.1.1>

BIBLIOGRAPHY

- Beysac, O., Goffé, B., Chopin, C., Rouzaud, J.N., 2002. Raman spectra of carbonaceous material in metasediments: A new geothermometer. *J. Metamorph. Geol.* 20, 859–871. <https://doi.org/10.1046/j.1525-1314.2002.00408.x>
- Beysac, O., Simoes, M., Avouac, J.P., Farley, K.A., Chen, Y.G., Chan, Y.C., Goffé, B., 2007. Late Cenozoic metamorphic evolution and exhumation of Taiwan. *Tectonics* 26. <https://doi.org/10.1029/2006TC002064>
- Biteau, J.J., Le Marrec, A., Le Vot, M., Masset, J.M., 2006. The Aquitaine Basin. *Pet. Geosci.* 12, 247–273. <https://doi.org/10.1144/1354-079305-674>
- Bixel, F., Lucas, C., 1983. Magmatisme, tectonique et sédimentation dans les fossés stéphano-permiens des Pyrénées occidentales. *Rev. géologie Dyn. géographie Phys.* 24, 329–342.
- Bjørlykke, K., 1998. Clay Mineral Diagenesis in Sedimentary Basins – A Key to the Prediction of Rock Properties. Examples from the North Sea Basin. *Clay Miner.* 33, 15–34. <https://doi.org/10.1180/claymin.1998.033.1.03>
- Blasco, M., Auqué, L.F., Gimeno, M.J., Acero, P., Asta, M.P., 2017. Geochemistry, geothermometry and influence of the concentration of mobile elements in the chemical characteristics of carbonate-evaporitic thermal systems. The case of the Tiermas geothermal system (Spain). *Chem. Geol.* 466, 696–709. <https://doi.org/10.1016/j.chemgeo.2017.07.013>
- Boiron, T., Aubourg, C., Grignard, P.A., Callot, J.P., 2020. The clay fabric of shales is a strain gauge. *J. Struct. Geol.* 138, 104130. <https://doi.org/10.1016/j.jsg.2020.104130>
- Borderie, S., Graveleau, F., Witt, C., Vendeville, B.C., 2018. Impact of an interbedded viscous décollement on the structural and kinematic coupling in fold-and-thrust belts: Insights from analogue modeling. *Tectonophysics* 722, 118–137. <https://doi.org/10.1016/j.tecto.2017.10.019>
- Borradaile, G.J., 1991. Correlation of strain with anisotropy of magnetic susceptibility (AMS). *Pure Appl. Geophys. PAGEOPH* 135, 15–29. <https://doi.org/10.1007/BF00877006>
- Borradaile, G.J., 1988. Magnetic susceptibility, petrofabrics and strain. *Tectonophysics* 156, 1–20.
- Borradaile, G.J., Henry, B., 1997. Tectonic application of magnetic susceptibility and its anisotropy. *Earth-Science Rev.* 42, 49–93. <https://doi.org/10.1097/MJT.0b013e31824e2b9f>
- Borradaile, G.J., Jackson, M., 2010. Structural geology, petrofabrics and magnetic fabrics (AMS, AARM, AIRM). *J. Struct. Geol.* 32, 1519–1551. <https://doi.org/10.1016/j.jsg.2009.09.006>
- Borradaile, G.J., Tarling, D.H., 1981. The influence of deformation mechanisms on magnetic fabrics in weakly deformed rocks. *Tectonophysics* 77, 151–168. [https://doi.org/10.1016/0040-1951\(81\)90165-7](https://doi.org/10.1016/0040-1951(81)90165-7)
- Bosch, G. V., Teixell, A., Jolivet, M., Labaume, P., Stockli, D., Domènech, M., Monié, P., 2016. Timing of Eocene-Miocene thrust activity in the Western Axial Zone and Chaînons Béarnais (west-central Pyrenees) revealed by multi-method thermochronology. *Comptes Rendus - Geosci.* 348, 246–256. <https://doi.org/10.1016/j.crte.2016.01.001>
- Boyer, S.E., Elliott, D., 1982. Thrust systems. *Am. Assoc. Pet. Geol. Bull.* 66, 1196–1230.

BIBLIOGRAPHY

<https://doi.org/10.1306/03b5a77d-16d1-11d7-8645000102c1865d>

- Branellec, M., Callot, J.P., Nivière, B., Ringenbach, J.C., 2015. The fracture network, a proxy for mesoscale deformation: Constraints on layer parallel shortening history from the Malargüe fold and thrust belt, Argentina. *Tectonics* 34, 623–647. <https://doi.org/10.1002/2014TC003738>
- Bruijn, R.H.C., Almqvist, B.S.G., Hirt, A.M., Benson, P.M., 2013. Decoupling of paramagnetic and ferrimagnetic AMS development during the experimental chemical compaction of illite shale powder. *Geophys. J. Int.* 192, 975–985. <https://doi.org/10.1093/gji/ggs086>
- Butler, R.W.H., 1987. Thrust sequences. *J. Geol. Soc. London.* 144, 619–634.
- Calvín, P., Santolaria, P., Casas, A.M., Pueyo, E.L., 2018. Detachment fold vs. ramp anticline: a gravity survey in the southern Pyrenean front (External Sierras). *Geol. J.* 53, 178–190. <https://doi.org/10.1002/gj.2884>
- Cámara, P., Flinch, J.F., 2017. The Southern Pyrenees, Permo-Triassic Salt Provinces of Europe, North Africa and the Atlantic Margins: Tectonics and Hydrocarbon Potential. Elsevier Inc. <https://doi.org/10.1016/B978-0-12-809417-4.00019-7>
- Campanyà, J., Ledo, J., Queralt, P., Marcuello, A., Liesa, M., Muñoz, J.A., 2012. New geoelectrical characterisation of a continental collision zone in the West-Central Pyrenees: Constraints from long period and broadband magnetotellurics. *Earth Planet. Sci. Lett.* 333–334, 112–121. <https://doi.org/10.1016/j.epsl.2012.04.018>
- Campanyà, J., Ledo, J., Queralt, P., Marcuello, A., Liesa, M., Muñoz, J.A., 2011. Lithospheric characterization of the Central Pyrenees based on new magnetotelluric data. *Terra Nov.* 23, 213–219. <https://doi.org/10.1111/j.1365-3121.2011.01001.x>
- Canérot, J., 1991. Comparative study of the Eastern Iberides (Spain) and the Western Pyrenees (France) Mesozoic basins. *Palaeogeogr. Palaeoclimatol. Palaeoecol.* 87, 1–28. [https://doi.org/10.1016/0031-0182\(91\)90128-E](https://doi.org/10.1016/0031-0182(91)90128-E)
- Canérot, J., Majesté-menjoulas, C., Ternet, Y., 2004. Nouvelle interprétation structurale de la « faille Nord- Pyrénéenne » en vallée d'Aspe (Pyrénées-Atlantiques). Remise en question d'un plutonisme ophitique danien dans le secteur de Bedous 336, 135–142. <https://doi.org/10.1016/j.crte.2003.11.004>
- Cantarelli, V., Aldega, L., Corrado, S., Invernizzi, C., Casas-Sainz, A., 2013. Thermal history of the aragón-béarn basin (late paleozoic, western pyrenees, Spain); insights into basin tectonic evolution. *Ital. J. Geosci.* 132, 443–462. <https://doi.org/10.3301/IJG.2012.41>
- Carbonel, D., Gutiérrez, F., Sevil, J., McCalpin, J.P., 2019. Evaluating Quaternary activity versus inactivity on faults and folds using geomorphological mapping and trenching: Seismic hazard implications. *Geomorphology* 338, 43–60. <https://doi.org/10.1016/j.geomorph.2019.04.015>
- Caricchi, C., Cifelli, F., Kissel, C., Sagnotti, L., Mattei, M., 2016. Distinct magnetic fabric in weakly deformed sediments from extensional basins and fold-and-thrust structures in the Northern Apennine orogenic belt (Italy). *Tectonics* 35, 238–256. <https://doi.org/10.1002/2015TC003940>
- Carlson, W.D., 2006. Three-dimensional imaging of earth and planetary materials. *Earth Planet. Sci. Lett.* 249, 133–147. <https://doi.org/10.1016/j.epsl.2006.06.020>

BIBLIOGRAPHY

- Carreras, J., Capella, I., 1994. Tectonic levels in the Palaeozoic basement of the Pyrenees: a review and a new interpretation. *J. Struct. Geol.* 16, 1509–1524. [https://doi.org/10.1016/0191-8141\(94\)90029-9](https://doi.org/10.1016/0191-8141(94)90029-9)
- Casas-Sainz, A.M., Pardo, G., 2004. Estructura pirenaica y evolución de las cuencas sedimentarias en la transversal Huesca-Oloron.
- Casas-Sainz, A.M., Simón-Gómez, J.L., 1992. Stress field and thrust kinematics: a model for the tectonic inversion of the cameros massif (Spain). *J. Struct. Geol.* 14, 521–530. [https://doi.org/10.1016/0191-8141\(92\)90154-O](https://doi.org/10.1016/0191-8141(92)90154-O)
- Casas Sainz, A.M., Faccenna, C., 2001. Tertiary compressional deformation of the Iberian plate. *Terra Nov.* 13, 281–288. <https://doi.org/10.1046/j.1365-3121.2001.00355.x>
- Chadima, M., 2019. Anisoft, Advanced Treatment of Magnetic Anisotropy Data.
- Chevrot, S., Sylvander, M., Diaz, J., Martin, R., Mouthereau, F., Manatschal, G., Masini, E., Calassou, S., Grimaud, F., Pauchet, H., Ruiz, M., 2018. The non-cylindrical crustal architecture of the Pyrenees. *Sci. Rep.* 8, 1–8. <https://doi.org/10.1038/s41598-018-27889-x>
- Chevrot, S., Sylvander, M., Diaz, J., Ruiz, M., Paul, A., Cougoulat, G., Péquegnat, C., Wolyniec, D., Delmas, P., Grimaud, F., Benahmed, S., Pauchet, H., de Saint Blanquat, M., Lagabrielle, Y., Manatschal, G., 2015. The Pyrenean architecture as revealed by teleseismic P-to-S converted waves recorded along two dense transects. *Geophys. J. Int.* 200, 1096–1107. <https://doi.org/10.1093/gji/ggu400>
- Chevrot, S., Villasenor, A., Sylvander, M., Benahmed, S., Beucler, E., Cougoulat, G., Delmas, P., Blanquat, M.D. Saint, Diaz, J., Gallart, J., Grimaud, F., Lagabrielle, Y., Manatschal, G., Mocquet, A., Pauchet, H., Paul, A., Péquegnat, C., Quillard, O., Roussel, S., Ruiz, M., Wolyniec, D., 2014. High-resolution imaging of the Pyrenees and Massif Central from the data of the PYROPE and IBERARRAY portable array deployments. *J. Geophys. Res. Solid Earth* 119, 6399–6420. <https://doi.org/10.1002/2014JB010953>
- Chou, Y.M., Aubourg, C., Yeh, E.C., Song, S.R., Lin, Y.K., Humbert, F., Jiang, X., Lee, T.Q., 2020. The Magnetic Fabric of Gouge Mimics the Coseismic Focal Mechanism of the Chi-Chi Earthquake (1999, Mw 7.6). *Geophys. Res. Lett.* 47. <https://doi.org/10.1029/2020GL090111>
- Choukroune, P., 1992. Tectonic evolution of the Pyrenees. *Annu. Rev. Earth Planet. Sci.* Vol. 20 143–158. <https://doi.org/10.1146/annurev.ea.20.050192.001043>
- Choukroune, P., 1989. The ECORS Pyrenean deep seismic profile reflection data and the overall structure of an orogenic belt. *Tectonics* 8, 23–39.
- Choukroune, P., Roure, F., Pinet, B., Team, E.P., 1990. Main results of the ECORS Pyrenees profile. *Tectonophysics* 173, 411–423.
- Choukroune, P., Séguret, M., 1973. Carte structurale des Pyrénées, 1/500.000. Univ. Montpellier-ELF Aquitaine.
- Cifelli, F., Mattei, M., Hirt, A.M., Günther, A., 2004. The origin of tectonic fabrics in “undeformed” clays: The early stages of deformation in extensional sedimentary basins. *Geophys. Res. Lett.* 31, 2–5. <https://doi.org/10.1029/2004GL019609>
- Clariana, P., Soto, R., Ayala, C., Casas-Sainz, A.M., Román-Berdiel, T., Oliva-Urcia, B.,

BIBLIOGRAPHY

- Pueyo, E.L., Beamud, E., Rey-Moral, C., Rubio, F., Margalef, A., Schamuells, S., Bach, N., Martí, J., 2022. Basement and cover architecture in the Central Pyrenees constrained by gravity data. *Int. J. Earth Sci.* 111, 641–658. <https://doi.org/10.1007/s00531-021-02137-2>
- Coll, X., Gómez-Gras, D., Roigé, M., Teixell, A., Boya, S., Mestres, N., 2020. Heavy-mineral provenance signatures during the infill and uplift of a foreland basin: An example from the Jaca basin (southern pyrenees, Spain). *J. Sediment. Res.* 90, 1747–1769. <https://doi.org/10.2110/JSR.2020.084>
- Comas, R.M.J., Goy, A., Melendez, G., Millan, H., Navarro, J.J., Pocovi, A., 1988. El Lias de San Felices (prepirineo meridional, extremo occidental de las Sierras Exteriores); biostratigrafia y paleontologia. See Notes ?, ?-?
- Cooper, M.A., Trayner, P.M., 1986. Thrust-surface geometry: implications for thrust-belt evolution and section-balancing techniques. *J. Struct. Geol.* 8, 305–312. [https://doi.org/10.1016/0191-8141\(86\)90051-9](https://doi.org/10.1016/0191-8141(86)90051-9)
- Costa, E., Garcés, M., López-Blanco, M., Beamud, E., Gómez-Paccard, M., Larrasoña, J.C., 2010. Closing and continentalization of the South Pyrenean foreland basin (NE Spain): Magnetochronological constraints. *Basin Res.* 22, 904–917. <https://doi.org/10.1111/j.1365-2117.2009.00452.x>
- Crognier, N., 2016. Évolution Thermique, Circulation De Fluides Et Fracturation Associées À La Structuration Du Bassin D'Avant-Pays Sud-Pyrénéen. *Univ. Pau Des Pays L'Adour* 339.
- Crognier, N., Hoareau, G., Aubourg, C., Dubois, M., Lacroix, B., Branellec, M., Callot, J.P., Vennemann, T., 2018. Syn-orogenic fluid flow in the Jaca basin (south Pyrenean fold and thrust belt) from fracture and vein analyses. *Basin Res.* 30, 187–216. <https://doi.org/10.1111/bre.12249>
- Dahlstrom, C.D.A., 1969. Balanced cross sections. *Can. J. Earth Sci.* 6, 743–757. <https://doi.org/10.1139/e69-069>
- Daignières, M., Séguret, M., Specht, M., 1994. The Arzacq-Western Pyrenees ECORS Deep Seismic Profile. *Hydrocarb. Pet. Geol. Fr.* 199–208. https://doi.org/10.1007/978-3-642-78849-9_15
- Daly, L., 1967. L'anisotropie magnétique des roches et sa mesure par un inductomètre à translation. *Ann. Géophys.* 23.
- de Rojas, B.J., Latorre, F., 1972. Mapa Geológico de España - Sigüés (175).
- Debacker, T.N., Robion, P., Sintubin, M., 2004. The anisotropy of magnetic susceptibility (AMS) in low-grade, cleaved pelitic rocks: influence of cleavage/bedding angle and type and relative orientation of magnetic carriers. *Geol. Soc. London, Special Publ.* 238, 77–107.
- DeFelipe, I., Pulgar, J.A., Pedreira, D., 2018. Crustal structure of the eastern Basque-cantabrian zone – Western Pyrenees: From the Cretaceous hyperextension to the Cenozoic inversion. *Rev. la Soc. Geol. Espana* 31, 69–82.
- Denèle, Y., Laumonier, B., Paquette, J.L., Olivier, P., Gleizes, G., Barbey, P., 2014. Timing of granite emplacement, crustal flow and gneiss dome formation in the Variscan segment of the Pyrenees. *Geol. Soc. Spec. Publ.* 405, 265–287. <https://doi.org/10.1144/SP405.5>

BIBLIOGRAPHY

- Denèle, Y., Paquette, J.L., Olivier, P., Barbey, P., 2012. Permian granites in the Pyrenees: The Aya pluton (Basque Country). *Terra Nov.* 24, 105–113. <https://doi.org/10.1111/j.1365-3121.2011.01043.x>
- Deramond, J., Souquet, P., Fondécave-Wallez, M.J., Specht, M., 1993. Relationships between thrust tectonics and sequence stratigraphy surfaces in foredeeps: Model and examples from the Pyrenees (Cretaceous-Eocene, France, Spain). *Geol. Soc. Spec. Publ.* 71, 193–219. <https://doi.org/10.1144/GSL.SP.1993.071.01.09>
- Deville, E., Dutrannoy, C., Schmitz, J., Vincent, B., Kohler, E., Lahfid, A., 2020. Shale tectonic processes: Field evidence from the Parras Basin (north-eastern Mexico). *Mar. Pet. Geol.* 122, 104688. <https://doi.org/10.1016/j.marpetgeo.2020.104688>
- Deville, É., Sassi, W., 2006. Contrasting thermal evolution of thrust systems: An analytical and modeling approach in the front of the western Alps. *Am. Assoc. Pet. Geol. Bull.* 90, 887–907. <https://doi.org/10.1306/01090605046>
- Diaz, J., Gallart, J., Carbonell, R., 2016. Moho topography beneath the Iberian-Western Mediterranean region mapped from controlled-source and natural seismicity surveys. *Tectonophysics* 692, 74–85. <https://doi.org/10.1016/j.tecto.2016.08.023>
- Ducoux, M., Jolivet, L., Cagnard, F., Baudin, T., 2021. Basement-Cover Decoupling During the Inversion of a Hyperextended Basin Insights From the Eastern Pyrenees. *Tectonics* 40, 1–23.
- Ducoux, M., Jolivet, L., Callot, J.P., Aubourg, C., Masini, E., Lahfid, A., Homonnay, E., Cagnard, F., Gumiaux, C., Baudin, T., 2019. The Nappe des Marbres Unit of the Basque-Cantabrian Basin: The Tectono-thermal Evolution of a Fossil Hyperextended Rift Basin. *Tectonics* 38, 3881–3915. <https://doi.org/10.1029/2018TC005348>
- Egan, S.S., Buddin, T.S., Kane, S., Williams, G.D., 1997. Three-dimensional modelling and visualisation in structural geology: New techniques for the restoration and balancing of volumes. 1996 *Geosci. Inf. Gr. Conf. Geol. Vis. Electron Geol.* 67–82.
- Elliott, D., 1976. The Energy Balance and Deformation Mechanisms of Thrust Sheets *Philosophical Transactions of the Royal Society of London . Series A , Mathematical and Physical Sciences , Vol . 283 , No . 1312 , A Discussion on Natural Strain and Geological Structure . (. Strain 283, 289–312.*
- Epstein, A.G., Epstein, J.B., Harris, L.D., 1977. Conodont color alteration - an index to organic metamorphism. *USGS Prof. Pap.* 995, 27pp.
- Epstein, J.B., Epstein, A.G., 1967. *Geology in the region of the Delaware to Lehigh Water Gaps*, Field Conf. ed. Pennsylvania Geological Survey.
- Erslev, E.A., 1991. Trishear fault-propagation folding B . Simple Shear. *Geology* 617–620.
- Espurt, N., Angrand, P., Teixell, A., Labaume, P., Ford, M., de Saint Blanquat, M., Chevrot, S., 2019. Crustal-scale balanced cross-section and restorations of the Central Pyrenean belt (Nestes-Cinca transect): Highlighting the structural control of Variscan belt and Permian-Mesozoic rift systems on mountain building. *Tectonophysics* 764, 25–45. <https://doi.org/10.1016/j.tecto.2019.04.026>
- Evans, M.A., Battles, D.A., 1999. Fluid inclusion and stable isotope analyses of veins from the central Appalachian Valley and Ridge province: Implications for regional synorogenic hydrologic structure and fluid migration. *Bull. Geol. Soc. Am.* 111, 1841–

BIBLIOGRAPHY

1860. [https://doi.org/10.1130/0016-7606\(1999\)111<1841:FIASIA>2.3.CO;2](https://doi.org/10.1130/0016-7606(1999)111<1841:FIASIA>2.3.CO;2)
- Faccenna, C., Speranza, F., Caracciolo, F.D.A., Mattei, M., Oggiano, G., 2002. Extensional tectonics on Sardinia (Italy): Insights into the arc-back-arc transitional regime. *Tectonophysics* 356, 213–232. [https://doi.org/10.1016/S0040-1951\(02\)00287-1](https://doi.org/10.1016/S0040-1951(02)00287-1)
- Faulkner, D.R., Jackson, C.A.L., Lunn, R.J., Schlische, R.W., Shipton, Z.K., Wibberley, C.A.J., Withjack, M.O., 2010. A review of recent developments concerning the structure, mechanics and fluid flow properties of fault zones. *J. Struct. Geol.* 32, 1557–1575. <https://doi.org/10.1016/j.jsg.2010.06.009>
- Ferré, E.C., Chou, Y.M., Kuo, R.L., Yeh, E.C., Leibovitz, N.R., Meado, A.L., Campbell, L., Geissman, J.W., 2016. Deciphering viscous flow of frictional melts with the mini-AMS method. *J. Struct. Geol.* 90, 15–26. <https://doi.org/10.1016/j.jsg.2016.07.002>
- Ferrer, O., Jackson, M.P.A., Roca, E., Rubinat, M., 2012. Evolution of salt structures during extension and inversion of the Offshore Parentis Basin (Eastern Bay of Biscay). *Geol. Soc. Spec. Publ.* 363, 361–380. <https://doi.org/10.1144/SP363.16>
- Flegmann, A.W., 1969. Rheological studies on kaolinite suspensions. *Proc. Brit. Ceram. Soc.* 13, 31–45.
- Flemming, B.W., 2000. A revised textural classification of gravel-free muddy sediments on the basis of ternary diagrams. *Cont. Shelf Res.* 20, 1125–1137. [https://doi.org/10.1016/S0278-4343\(00\)00015-7](https://doi.org/10.1016/S0278-4343(00)00015-7)
- Fossen, H., 2010. *Structural Geology*. Cambridge University Press, New York.
- Freed, R.L., 1989. Variability in Temperature of the Smectite/Illite Reaction in Gulf Coast Sediments†. *Clay Miner.* 24, 171–180. <https://doi.org/10.1180/claymin.1989.024.2.05>
- Frizon de Lamotte, D., Souque, C., Grelaud, S., Robion, P., 2002. Early record of tectonic magnetic fabric during inversion of a sedimentary basin. Short review and examples from the Corbières transfer zone (France). *2Bull.Soc.Geol.France* 173, 461–469.
- Fuller, M.D., 1963. Magnetic Anisotropy and Paleomagnetism. *J. Geophys. Res.* 68, 293–309.
- Gabaldón, V., Hernández-Samaniego, A., Simó-Marja, A., 1985. Mapa Geológico de España 1:50.000, hoja nº174 (Sangüesa).
- Gale, J.F.W., Laubach, S.E., Olson, J.E., Eichhubl, P., Fall, A., 2017. Natural fractures in shale: A review and new observations. *Am. Assoc. Pet. Geol. Bull.* 101, 2165–2216. <https://doi.org/10.1306/08121413151>
- Garcés, M., López-Blanco, M., Valero, L., Beamud, E., Muñoz, J.A., Oliva-Urcia, B., Vinyoles, A., Arbués, P., Cabello, P., Cabrera, L., 2020. Paleogeographic and sedimentary evolution of the south-pyrenean foreland basin. *Mar. Pet. Geol.* 113, 104105. <https://doi.org/10.1016/j.marpetgeo.2019.104105>
- García-Lasanta, C., 2016. Magnetic fabric analyses and paleomagnetism applied to study the Mesozoic evolution of the Iberian Range. Universidad de Zaragoza.
- García-Mayordomo, J., Insua-Arévalo, J.M., 2011. Seismic hazard assessment for the Itoiz dam site (Western Pyrenees, Spain). *Soil Dyn. Earthq. Eng.* 31, 1051–1063. <https://doi.org/10.1016/j.soildyn.2011.03.011>
- Gil-Imaz, A., Lago-San José, M., Galé, C., Pueyo-Anchuela, Ó., Ubide, T., Tierz, P., Oliva-

BIBLIOGRAPHY

- Urcia, B., 2012. The Permian mafic dyke swarm of the Panticosa pluton (Pyrenean Axial Zone, Spain): Simultaneous emplacement with the late-Variscan extension. *J. Struct. Geol.* 42, 171–183. <https://doi.org/10.1016/j.jsg.2012.05.008>
- Girdler, R.W., 1961. The Measurement and Computation of Anisotropy of Magnetic Susceptibility of Rocks. *Geophys. J. R. Astron. Soc.* 5, 34–44. <https://doi.org/10.1111/j.1365-246X.1961.tb02927.x>
- Gisbert Aguilar, J., 1983. El Pérmico de los Pirineos españoles, in: *Carbonífero y Pérmico de España*. pp. 403–420.
- Gleizes, G., Leblanc, D., Bouchez, J.L., 1998. The main phase of the Hercynian orogeny in the Pyrenees is a dextral transpression. *Geol. Soc. Spec. Publ.* 135, 267–273. <https://doi.org/10.1144/GSL.SP.1998.135.01.17>
- Gleizes, G., Leblanc, D., Bouchez, J.L., 1997. Variscan granites of the Pyrenees revisited: Their role as syntectonic markers of the orogen. *Terra Nov.* 9, 38–41. <https://doi.org/10.1046/j.1365-3121.1997.d01-9.x>
- Goguel, J., 1965. *Tectonics: Traité de tectonique*, 2nd ed. Paris.
- Gómez-Romeu, J., Masini, E., Tugend, J., Ducoux, M., Kuszniir, N., 2019. Role of rift structural inheritance in orogeny highlighted by the Western Pyrenees case-study. *Tectonophysics* 766, 131–150. <https://doi.org/10.1016/j.tecto.2019.05.022>
- Gómez, M., Vergés, J., Riaza, C., 2002. Inversion tectonics of the northern margin of the Basque Cantabrian Basin. *Bull. la Société Géologique Fr.* 173, 449–459. <https://doi.org/10.2113/173.5.449>
- Gracia-puzo, F., Aubourg, C., Casas-sainz, A., 2021. A fast way to estimate the clay fabric from shale fragments . Key example from a strained thrust footwall (Pyrenees). *J. Struct. Geol.* 152, 104443. <https://doi.org/10.1016/j.jsg.2021.104443>
- Graham, J.W., 1954. Magnetic anisotropy, an unexploited petrofabric element. *Geol. Soc. Am. Bull.* 65, 1257–1258.
- Graham, R., Hossack, J., Deramond, J., Soula, J.C., 1987. Géométrie des surfaces de chevauchement. *Bull. la Soc. géologique Fr.* 3, 169–181.
- Gratier, J.P., 1983. Estimation of volume changes by comparative chemical analyses in heterogeneously deformed rocks (folds with mass transfer). *J. Struct. Geol.* 5, 329–339.
- Gratier, J.P., Dysthe, D.K., Renard, F., 2013. The Role of Pressure Solution Creep in the Ductility of the Earth's Upper Crust, *Advances in Geophysics*. Elsevier Inc. <https://doi.org/10.1016/B978-0-12-380940-7.00002-0>
- Gray, D.R., 1997. Volume loss and slaty cleavage development. *Evol. Geol. Struct. Micro- to Macro-scales I*, 273–291. https://doi.org/10.1007/978-94-011-5870-1_17
- Grool, A.R., Ford, M., Vergés, J., Huismans, R.S., Christophoul, F., Dielforder, A., 2018. Insights Into the Crustal-Scale Dynamics of a Doubly Vergent Orogen From a Quantitative Analysis of Its Forelands: A Case Study of the Eastern Pyrenees. *Tectonics* 37, 450–476. <https://doi.org/10.1002/2017TC004731>
- Hanna, R.D., Ketcham, R.A., 2017. X-ray computed tomography of planetary materials: A primer and review of recent studies. *Chemie der Erde* 77, 547–572. <https://doi.org/10.1016/j.chemer.2017.01.006>

BIBLIOGRAPHY

- Hardy, S., Allmendinger, R.W., 2011. Trishear: A review of kinematics, mechanics, and applications. AAPG Mem. 95-119. <https://doi.org/10.1306/13251334M943429>
- Hardy, S., Ford, M., 1997. Numerical modeling of trishear fault propagation folding. *Tectonics* 16, 841-854. <https://doi.org/10.1029/97TC01171>
- Henry, B., Daly, L., 1983. From qualitative to quantitative magnetic anisotropy analysis: the prospect of finite strain calibration. *Tectonophysics* 98, 327-336.
- Hirt, A.M., Lowrie, W., Clendenen, W.S., Kligfield, R., 1993. Correlation of strain and the anisotropy of magnetic susceptibility in the Onaping Formation: evidence for a near-circular origin of the Sudbury Basin. *Tectonophysics* 225, 231-254. [https://doi.org/10.1016/0040-1951\(93\)90300-9](https://doi.org/10.1016/0040-1951(93)90300-9)
- Hirt, A.M., Lowrie, W., Lüneburg, C., Lebit, H., Engelder, T., 2004. Magnetic and mineral fabric development in the ordovician Martinsburg Formation in the Central Appalachian Fold and Thrust Belt, Pennsylvania. *Geol. Soc. Spec. Publ.* 238, 109-126. <https://doi.org/10.1144/GSL.SP.2004.238.01.09>
- Ho, N., Peacor, D.R., van der Pluijm, B.A., 1995. Reorientation mechanisms of phyllosilicates in the mudstone-to-slate transition at Lehigh Gap, Pennsylvania. *J. Struct. Geol.* 17, 345-356.
- Ho, N.C., Peacor, D.R., Van Der Pluijm, B.A., 1996. Contrasting roles of detrital and authigenic phyllosilicates during slaty cleavage development. *J. Struct. Geol.* 18, 615-623. [https://doi.org/10.1016/S0191-8141\(96\)80028-9](https://doi.org/10.1016/S0191-8141(96)80028-9)
- Hoareau, G., Crognier, N., Lacroix, B., Aubourg, C., Roberts, N.M.W., Niemi, N., Branellec, M., Beaudoin, N., Suárez Ruiz, I., 2021. Combination of $\Delta 47$ and U-Pb dating in tectonic calcite veins unravel the last pulses related to the Pyrenean Shortening (Spain). *Earth Planet. Sci. Lett.* 553, 116636. <https://doi.org/10.1016/j.epsl.2020.116636>
- HOFFMAN, J., HOWER, J., 1979. Clay Mineral Assemblages As Low Grade Metamorphic Geothermometers: Application To the Thrust Faulted Disturbed Belt of Montana, U.S.a. *Asp. Diagenes.* 55-79. <https://doi.org/10.2110/pec.79.26.0055>
- Hogan, P.J., Burbank, D.W., 1995. Evolution of the Jaca piggyback basin and emergence of the External Sierra, southern Pyrenees. *World Reg. Geol.* 1, 153-160.
- Holeywell, R.C., Tullis, T.E., 1975. Mineral reorientation and slaty cleavage in the martinsburg formation, Lehigh Gap, Pennsylvania. *Bull. Geol. Soc. Am.* 86, 1296-1304. [https://doi.org/10.1130/0016-7606\(1975\)86<1296:MRASCI>2.0.CO;2](https://doi.org/10.1130/0016-7606(1975)86<1296:MRASCI>2.0.CO;2)
- Holl, J.E., Anastasio, D.J., 1995. Cleavage development within a foreland fold and thrust belt, southern Pyrenees, Spain. *J. Struct. Geol.* 17, 357-369. [https://doi.org/10.1016/0191-8141\(94\)00062-5](https://doi.org/10.1016/0191-8141(94)00062-5)
- Hoth, S., Kukowski, N., Oncken, O., 2008. Distant effects in bivergent orogenic belts - How retro-wedge erosion triggers resource formation in pro-foreland basins. *Earth Planet. Sci. Lett.* 273, 28-37. <https://doi.org/10.1016/j.epsl.2008.05.033>
- Housen, B.A., van der Pluijm, B.A., 1990. Chlorite control of correlations between strain and anisotropy of magnetic susceptibility. *Phys. Earth Planet. Inter.* 61, 315-323. [https://doi.org/10.1016/0031-9201\(90\)90114-D](https://doi.org/10.1016/0031-9201(90)90114-D)

BIBLIOGRAPHY

- Housen, B.A., Van Der Pluijm, B.A., 1991. Slaty cleavage development and magnetic anisotropy fabrics. *J. Geophys. Res.* 96, 9937–9946. <https://doi.org/10.1029/91JB00605>
- Housen, B.A., van der Pluijm, B.A., Voo, R. Van Der, 1993. Magnetite Dissolution and Neocrystallization During Cleavage Formation: Palcomagnetic Study of the Martinsburg Formation, Lehigh Gap, Pennsylvan. *J. Geophys. Res.* 98, 799–813.
- Hower, J., Eslinger, E. V., Hower, M.E., Perry, E.A., 1976. Mechanism of burial metamorphism of argillaceous sediment: 1. Mineralogical and chemical evidence. *Bull. Geol. Soc. Am.* 87, 725–737. [https://doi.org/10.1130/0016-7606\(1976\)87<725:MOBMOA>2.0.CO;2](https://doi.org/10.1130/0016-7606(1976)87<725:MOBMOA>2.0.CO;2)
- Hrouda, F., 1993. Theoretical models of magnetic anisotropy to strain relationship revisited. *Phys. Earth Planet. Inter.* 77, 237–249. [https://doi.org/10.1016/0031-9201\(93\)90101-E](https://doi.org/10.1016/0031-9201(93)90101-E)
- Hrouda, F., Tarling, D.H., 1993. The Magnetic anisotropy of Rocks.
- Hrouda, F.Š., 1987. Mathematical model relationship between the paramagnetic anisotropy and strain in slates. *Tectonophysics* 142, 323–327. [https://doi.org/10.1016/0040-1951\(87\)90131-4](https://doi.org/10.1016/0040-1951(87)90131-4)
- Humbert, F., Louis, L., Robion, P., 2014. Method for estimating ductile horizontal strain from magnetic fabrics in poorly consolidated clay-rich sediments. *Tectonophysics* 629, 335–352. <https://doi.org/10.1016/j.tecto.2014.07.003>
- Ising, G., 1942. On the magnetic properties of varved clay. *Almqvist & Wiksell.*
- Izquierdo-Llavall, E., Aldega, L., Cantarelli, V., Corrado, S., Gil-Peña, I., Invernizzi, C., Casas, A.M., 2013a. On the origin of cleavage in the Central Pyrenees: Structural and paleo-thermal study. *Tectonophysics* 608, 303–318. <https://doi.org/10.1016/j.tecto.2013.09.027>
- Izquierdo-Llavall, E., Casas-Sainz, A.M., Oliva-Urcia, B., 2013b. Heterogeneous deformation recorded by magnetic fabrics in the Pyrenean Axial Zone. *J. Struct. Geol.* 57, 97–113. <https://doi.org/10.1016/j.jsg.2013.10.005>
- Izquierdo-Llavall, E., Menant, A., Aubourg, C., Callot, J.P., Hoareau, G., Camps, P., Péré, E., Lahfid, A., 2020. Preorogenic Folds and Syn-Orogenic Basement Tilts in an Inverted Hyperextended Margin: The Northern Pyrenees Case Study. *Tectonics* 39, 1–32. <https://doi.org/10.1029/2019TC005719>
- Izquierdo-Llavall, E., Sainz, A.C., Oliva-Urcia, B., Burmester, R., Pueyo, E.L., Housen, B., 2015. Multi-episodic remagnetization related to deformation in the Pyrenean Internal Sierras. *Geophys. J. Int.* 201, 891–914. <https://doi.org/10.1093/gji/ggv042>
- Jammes, S., Manatschal, G., Lavier, L., 2010. Interaction between prerift salt and detachment faulting in hyperextended rift systems: The example of the Parentis and Mauléon basins (Bay of Biscay and western Pyrenees). *Am. Assoc. Pet. Geol. Bull.* 94, 957–975. <https://doi.org/10.1306/12090909116>
- Jammes, S., Manatschal, G., Lavier, L., Masini, E., 2009. Tectonosedimentary evolution related to extreme crustal thinning ahead of a propagating ocean: Example of the western Pyrenees. *Tectonics* 28. <https://doi.org/10.1029/2008TC002406>
- Jelinek, V., 1981. Characterization of the magnetic fabric of rocks. *Tectonophysics* 79, 63–67. [https://doi.org/10.1016/0040-1951\(81\)90110-4](https://doi.org/10.1016/0040-1951(81)90110-4)

BIBLIOGRAPHY

- Jelinek, V., 1977. The statistical theory of measuring anisotropy of magnetic susceptibility of rocks and its application.
- Jelínek, V., Kropáček, V., 1978. Statistical processing of anisotropy of magnetic susceptibility measured on groups of specimens. *Stud. Geophys. Geod.* 22, 50–62. <https://doi.org/10.1007/BF01613632>
- Jolivet, M., Labaume, P., Monie, P., Brunel, M., Arnaud, N., Campani, M., 2007. Thermochemistry constraints for the propagation sequence of the south Pyrenean basement thrust system (France-Spain) 26. <https://doi.org/10.1029/2006TC002080>
- Judge, P.A., Allmendinger, R.W., 2011. Assessing uncertainties in balanced cross sections. *J. Struct. Geol.* 33, 458–467. <https://doi.org/10.1016/j.jsg.2011.01.006>
- Kanamatsu, T., Parés, J.M., Kitamura, Y., 2012. Pliocene shortening direction in Nankai Trough off Kumano, southwest Japan, Sites IODP C0001 and C0002, Expedition 315: Anisotropy of magnetic susceptibility analysis for paleostress. *Geochemistry, Geophys. Geosystems* 13, 1–13. <https://doi.org/10.1029/2011GC003782>
- Kars, M., Aubourg, C., Pozzi, J.P., 2011. Low temperature magnetic behaviour near 35 K in unmetamorphosed claystones. *Geophys. J. Int.* 186, 1029–1035. <https://doi.org/10.1111/j.1365-246X.2011.05121.x>
- Kars, M., Aubourg, C., Suárez-Ruiz, I., 2015. Neoformed magnetic minerals as an indicator of moderate burial: The key example of middle Paleozoic sedimentary rocks, West Virginia. *Am. Assoc. Pet. Geol. Bull.* 99, 389–401. <https://doi.org/10.1306/06301413006>
- KISCH, H.J., 1991. Development of slaty cleavage and degree of very-low-grade metamorphism: a review. *J. Metamorph. Geol.* 9, 735–750. <https://doi.org/10.1111/j.1525-1314.1991.tb00562.x>
- Kissel, C., Barrier, E., Laj, C., 1986. Magnetic fabric in “undeformed” marine clays from compressional zones. *Tectonics* 5, 769–781.
- Kligfield, R., Owens, W.H., Lowrie, W., 1981. Magnetic susceptibility anisotropy, strain, and progressive deformation in Permian sediments from the Maritime Alps (France). *Earth Planet. Sci. Lett.* 55, 181–189. [https://doi.org/10.1016/0012-821X\(81\)90097-2](https://doi.org/10.1016/0012-821X(81)90097-2)
- Kluge, T., John, C.M., Jourdan, A.L., Davis, S., Crawshaw, J., 2015. Laboratory calibration of the calcium carbonate clumped isotope thermometer in the 25–250°C temperature range. *Geochim. Cosmochim. Acta* 157, 213–227. <https://doi.org/10.1016/j.gca.2015.02.028>
- Kneen, S.J., 1976. The relationship between the magnetic and strain fabrics of some haematite-bearing Welsh slates. *Earth Planet. Sci. Lett.* 31, 413–416. [https://doi.org/10.1016/0012-821X\(76\)90123-0](https://doi.org/10.1016/0012-821X(76)90123-0)
- Kouketsu, Y., Mizukami, T., Mori, H., Shunsuke, E., Aoya, M., Hidetoshi, H., Nakamura, D., Wallis, S., 2014. A new approach to develop the Raman carbonaceous material geothermometer for low-grade metamorphism using peak width. *Isl. Arc* 23, 33–50.
- Labaume, P., Meresse, F., Jolivet, M., Teixell, A., Lahfid, 2016. Tectonothermal history of an exhumed thrust-sheet-top basin - An example from the south Pyrenean thrust belt. *Tectonics* 35, 1280–1313.
- Labaume, P., Séguret, M., Seyve, C., 1985a. Evolution of a turbiditic foreland basin and

BIBLIOGRAPHY

- analogy with an accretionary prism: Example of the Eocene South-Pyrenean Basin. *Tectonics* 4, 661–685. <https://doi.org/10.1029/TC004i007p00661>
- Labaume, P., Séguret, M., Seyve, C., 1985b. Evolution of a turbiditic foreland basin and analogy with an accretionary prism: Example of the Eocene South-Pyrenean basin. *Tectonics* 4, 661–685.
- Labaume, P., Séguret, M., Seyve, C., 1985c. Evolution of a turbiditic foreland basin and analogy with an accretionary prism: Example of the Eocene South-Pyrenean Basin. *Tectonics* 4, 661–685.
- Labaume, P., Teixell, A., 2020. Evolution of salt structures of the Pyrenean rift (Chaînons Béarnais, France): From hyper-extension to tectonic inversion. *Tectonophysics* 785, 228451. <https://doi.org/10.1016/j.tecto.2020.228451>
- Labaume, P., Teixell, A., 2018. 3d structure of subsurface thrusts in the eastern Jaca Basin, southern pyrenees. *Geol. Acta* 16, 477–498. <https://doi.org/10.1344/GeologicaActa2018.16.4.9>
- Lacroix, B., Buatier, M., Labaume, P., Travé, A., Dubois, M., Charpentier, D., Ventalon, S., Convert-Gaubier, D., 2011. Microtectonic and geochemical characterization of thrusting in a foreland basin: Example of the South-Pyrenean orogenic wedge (Spain). *J. Struct. Geol.* 33, 1359–1377. <https://doi.org/10.1016/j.jsg.2011.06.006>
- Lagabrielle, Y., Labaume, P., De Saint Blanquat, M., 2010. Mantle exhumation, crustal denudation, and gravity tectonics during Cretaceous rifting in the Pyrenean realm (SW Europe): Insights from the geological setting of the Iherzolite bodies. *Tectonics* 29. <https://doi.org/10.1029/2009TC002588>
- Lago, M., Arranz, E., Pocoví, A., Galé, C., Gil-Imaz, A., 2004. Permian magmatism and basin dynamics in the southern Pyrenees: A record of the transition from late Variscan transtension to early Alpine extension. *Geol. Soc. Spec. Publ.* 223, 439–464. <https://doi.org/10.1144/GSL.SP.2004.223.01.19>
- Lago, M., Gil, A., Arranz, E., Galé, C., Pocoví, A., 2005. Magmatism in the intracratonic Central Iberian basins during the Permian: Palaeoenvironmental consequences. *Palaeogeogr. Palaeoclimatol. Palaeoecol.* 229, 83–103. <https://doi.org/10.1016/j.palaeo.2005.06.032>
- Lahfid, A., Beyssac, O., Deville, E., Negro, F., Chopin, C., Goffé, B., 2010. Evolution of the Raman spectrum of carbonaceous material in low-grade metasediments of the Glarus Alps (Switzerland). *Terra Nov.* 22, 354–360. <https://doi.org/10.1111/j.1365-3121.2010.00956.x>
- Lamarche, G., Rochette, P., 1987. Microstructural analysis and origin of lineations in the magnetic fabric of some Alpine slates. *Tectonophysics* 139, 285–293. [https://doi.org/10.1016/0040-1951\(87\)90102-8](https://doi.org/10.1016/0040-1951(87)90102-8)
- Lanaja, J.M., 1987. Contribución de la exploración petrolífera al conocimiento de la geología de España.
- Larrasoana, J.C., Parés, J.M., Millán, H., del Valle, J., Pueyo, E.L., 2003. Paleomagnetic, structural, and stratigraphic constraints on transverse fault kinematics during basin inversion: The Pamplona Fault (Pyrenees, north Spain). *Tectonics* 22. <https://doi.org/10.1029/2002tc001446>

BIBLIOGRAPHY

- Larrasoana, J.C., Pueyo-Morer, E.L., Millán-Garrido, H., Parés, J.M., Del Valle, J., 1997. Deformation mechanisms deduced from AMS data in the Jaca-Pamplona basin (Southern Pyrenees). *Phys. Chem. Earth* 22, 147–152. [https://doi.org/10.1016/s0079-1946\(97\)00093-1](https://doi.org/10.1016/s0079-1946(97)00093-1)
- Larrasoana, J.C., Pueyo, E.L., Parés, J.M., 2004. An integrated AMS, structural, palaeo- and rock-magnetic study of Eocene marine marls from the Jaca-Pamplona basin (Pyrenees, N Spain); new insights into the timing of magnetic fabric acquisition in weakly deformed mudrocks. *Geol. Soc. Spec. Publ.* 238, 127–143. <https://doi.org/10.1144/GSL.SP.2004.238.01.10>
- Lash, G., 1978. The structure and stratigraphy of the Pen Argyl Member of the MARTINSBURG FORMATION IN LEHIGH AND BERKS COUNTIES, PENNSYLVANIA. USGS Open File Rep. 78-391 212.
- Lee, J.H., Ahn, J.H., Peacor, D.R., 1985. Textures in layered silicates: Progressive changes through diagenesis and Low-Temperature metamorphism. *J. Sediment. Petrol.* 55, 532–540.
- Lee, J.H., Peacor, D.R., Lewis, D.D., Wintsch, R.P., 1986. Evidence for syntectonic crystallization for the mudstone to slate transition at Lehigh gap, Pennsylvania, U.S.A. *J. Struct. Geol.* 8, 767–780. [https://doi.org/10.1016/0191-8141\(86\)90024-6](https://doi.org/10.1016/0191-8141(86)90024-6)
- Lescoutre, R., Manatschal, G., 2020. Role of rift-inheritance and segmentation for orogenic evolution: Example from the Pyrenean-Cantabrian system. *BSGF - Earth Sci. Bull.* 191. <https://doi.org/10.1051/bsgf/2020021>
- López-Gómez, J., Alonso-Azcárate, J., Arche, A., Arribas, J., Fernández Barrenechea, J., Borruel-Abadía, V., Bourquin, S., Cadenas, P., Cuevas, J., De la Horra, R., Díez, J.B., Escudero-Mozo, M.J., Fernández-Viejo, G., Galán-Abellán, B., Galé, C., Gaspar-Escribano, J., Gisbert Aguilar, J., Gómez-Gras, D., Goy, A., Gretter, N., Heredia Carballo, N., Lago, M., Lloret, J., Luque, J., Márquez, L., Márquez-Aliaga, A., Martín-Algarra, A., Martín-Chivelet, J., Martín-González, F., Marzo, M., Mercedes-Martín, R., Ortí, F., Pérez-López, A., Pérez-Valera, F., Pérez-Valera, J.A., Plasencia, P., Ramos, E., Rodríguez-Méndez, L., Ronchi, A., Salas, R., Sánchez-Fernández, D., Sánchez-Moya, Y., Sopena, A., Suárez-Rodríguez, Á., Tubía, J.M., Ubide, T., Valero Garcés, B., Vargas, H., Viseras, C., 2019. Permian-Triassic Rifting Stage. https://doi.org/10.1007/978-3-030-11295-0_3
- Lopez-Mir, B., 2019. Cross-Section Construction and Balancing: Examples From the Spanish Pyrenees, 1st ed, Problems and Solutions in Structural Geology and Tectonics. Elsevier Inc. <https://doi.org/10.1016/b978-0-12-814048-2.00001-6>
- Louis, L., David, C., Robion, P., 2003. Comparison of the anisotropic behaviour of undeformed sandstones under dry and saturated conditions. *Tectonophysics* 370, 193–212. [https://doi.org/10.1016/S0040-1951\(03\)00186-0](https://doi.org/10.1016/S0040-1951(03)00186-0)
- Lüneburg, C.M., Lampert, S.A., Lebit, H.D., Hirt, A.M., Casey, M., Lowrie, W., 1999. Magnetic anisotropy, rock fabrics and finite strain in deformed sediments of SW Sardinia (Italy). *Tectonophysics* 307, 51–74. [https://doi.org/10.1016/S0040-1951\(99\)00118-3](https://doi.org/10.1016/S0040-1951(99)00118-3)
- Lünsdorf, N.K., Dunkl, I., Schmidt, B.C., Rantitsch, G., von Eynatten, H., 2017. Towards a Higher Comparability of Geothermometric Data Obtained by Raman Spectroscopy of Carbonaceous Material. Part 2: A Revised Geothermometer. *Geostand. Geoanalytical*

BIBLIOGRAPHY

- Res. 41, 593–612. <https://doi.org/10.1111/ggr.12178>
- Macchiavelli, C., Vergés, J., Schettino, A., Fernandez, M., Turco, E., Casciello, E., Torne, M., Pierantoni, P.P., Tunini, L., 2017. A New Southern North Atlantic Isochron Map: Insights into the Drift of the Iberian Plate since the Late Cretaceous. *J. Geophys. Res.* 122, 9603–9626. <https://doi.org/10.1002/2017JB014769>
- Marcén-Albero, M., 2020. *Fábricas Magnéticas aplicadas al estudio de Zonas de Falla: Ejemplos de la Península Ibérica*. Universidad de Zaragoza.
- Marcén, M., Casas-Sainz, A.M., Román-Berdiel, T., Oliva-Urcia, B., Soto, R., Aldega, L., 2018. Kinematics and strain distribution in an orogen-scale shear zone: Insights from structural analyses and magnetic fabrics in the Gavarnie thrust, Pyrenees. *J. Struct. Geol.* 117, 105–123. <https://doi.org/10.1016/j.jsg.2018.09.008>
- March, A., 1932. Mathematische Theorie der Regelung nach der Korngestalt bei affiner Deformation. *Z. Krist.* 81, 285–297.
- Marshak, S., Engelder, T., 1985. Development of cleavage in limestones of a fold-thrust belt in eastern New York. *J. Struct. Geol.* 7, 345–359. [https://doi.org/10.1016/0191-8141\(85\)90040-9](https://doi.org/10.1016/0191-8141(85)90040-9)
- Martín-Hernández, F., Ferré, E.C., 2007. Separation of paramagnetic and ferrimagnetic anisotropies: A review. *J. Geophys. Res. Solid Earth* 112. <https://doi.org/10.1029/2006JB004340>
- Martín-Hernández, F., Hirt, A.M., 2003. The anisotropy of magnetic susceptibility in biotite, muscovite and chlorite single crystals. *Tectonophysics* 367, 13–28. [https://doi.org/10.1016/S0040-1951\(03\)00127-6](https://doi.org/10.1016/S0040-1951(03)00127-6)
- Masini, E., Manatschal, G., Tugend, J., Mohn, G., Flament, J.M., 2014. The tectono-sedimentary evolution of a hyper-extended rift basin: The example of the Arzacq-Mauléon rift system (Western Pyrenees, SW France). *Int. J. Earth Sci.* 103, 1569–1596. <https://doi.org/10.1007/s00531-014-1023-8>
- Mattauer, M., 1990. Une autre interprétation du profil ECORS Pyrénées. *Bull. la Soc. géologique Fr.* 6, 307–311.
- Mattauer, M., 1985. Présentation d'un modèle lithosphérique de la chaîne des Pyrénées. *Comptes-rendus des séances l'Académie des Sci. Série 2, Mécanique-physique, Chim. Sci. l'univers, Sci. la terre* 300, 71–74.
- Matte, P., 2002. Les plis hercyniens kilométriques couchés vers l'ouest-sud-ouest dans la région du pic du Midi d'Ossau-col du Somport (zone axiale des Pyrénées occidentales). *Comptes Rendus - Geosci.* 334, 773–779. [https://doi.org/10.1016/S1631-0713\(02\)01808-4](https://doi.org/10.1016/S1631-0713(02)01808-4)
- Mattei, M., Speranza, F., Argentieri, A., Rossetti, F., Sagnotti, L., Funicello, R., 1999. Extensional tectonics in the Amantea basin (Calabria, Italy): A comparison between structural and magnetic anisotropy data. *Tectonophysics* 307, 33–49. [https://doi.org/10.1016/S0040-1951\(99\)00117-1](https://doi.org/10.1016/S0040-1951(99)00117-1)
- Maxwell, J.C., 1962. Origin of slaty and fracture cleavage in the Delaware Water Gap area, New Jersey and Pennsylvania. *Geol. Soc. Am. Bull.* 281–311.
- Meunier, A., n.d. *Clays*.

BIBLIOGRAPHY

- Meunier, A., Velde, B., 2004. Illite: Origins, Evolution and Metamorphism.
- Millán-Garrido, H., Oliva-Urcia, B., Pocoví Juan, A., 2006. La transversal de Gavarnie-Guara. Estructura y edad de los mantos de Gavarnie , Guara-Gèdre y Guarga (Pirineo centro-occidental). *Geogaceta* 40, 35–38.
- Millán-Garrido, H., Pueyo-Morer, E.L., Aurell, M., Luzón, A., Oliva-Urcia, B., Martínez-Peña, M.B., Pocovi-Juan, A., 2000. Actividad tectónica registrada en los depósitos terciarios del frente meridional del Pirineo Central. *Rev. la Soc. Geológica España* 13, 279–300.
- Millán, H., 1996. Estructura y cinemática del frente de cabalgamiento surpirenaico. Universidad de Zaragoza.
- Mitra, G., Yonkee, W.A., Gentry, D.L., 1984. Solution cleavage and its relationship to major structures in the Idaho-Utah-Wyoming thrust belt. *Geology* 12, 354–358. [https://doi.org/10.1130/0091-7613\(1984\)12<354:SCAIRT>2.0.CO;2](https://doi.org/10.1130/0091-7613(1984)12<354:SCAIRT>2.0.CO;2)
- Mitra, S., 1987. Regional variations in deformation mechanisms and structural styles in the central Appalachian orogenic belt. *Bull. Geol. Soc. Am.* 98, 569–590. [https://doi.org/10.1130/0016-7606\(1987\)98<569:RVIDMA>2.0.CO;2](https://doi.org/10.1130/0016-7606(1987)98<569:RVIDMA>2.0.CO;2)
- Mochales, T., Pueyo, E.L., Casas, A.M., Barnolas, A., Oliva-Urcia, B., 2010. Anisotropic magnetic susceptibility record of the kinematics of the Boltaña Anticline (Southern Pyrenees). *Geol. J.* 45, 562–581. <https://doi.org/10.1002/gj.1207>
- Montes, M.J., 2002. Estratigrafía del Eoceno-Oligoceno de la Cuenca de Jaca (Sinclinorio del Guarga). Universitat de Barcelona.
- Moon, C.F., Hurst, C.W., 1984. Fabric of muds and shales: An overview. *Geol. Soc. Spec. Publ.* 15, 579–593. <https://doi.org/10.1144/GSL.SP.1984.015.01.36>
- Moore, D.M., Reynolds, R.C., 1997. X-Ray Diffraction and the Identification and Analysis of Clay Minerals. Oxford University Press, Oxford.
- Moreno, E., Homberg, C., Schnyder, J., Person, A., David, C., du Peloux, A., Moubeche, E., Bonnelye, A., Dick, P., 2018. Fault imprint in clay units: Magnetic fabric, p-wave velocity, structural and mineralogical signatures. *Tectonophysics* 745, 264–277. <https://doi.org/10.1016/j.tecto.2018.07.017>
- Morley, C.K., von Hagke, C., Hansberry, R., Collins, A., Kanitpanyacharoen, W., King, R., 2018. Review of major shale-dominated detachment and thrust characteristics in the diagenetic zone: Part II, rock mechanics and microscopic scale. *Earth-Science Rev.* 176, 19–50. <https://doi.org/10.1016/j.earscirev.2017.09.015>
- Morley, C.K., von Hagke, C., Hansberry, R.L., Collins, A.S., Kanitpanyacharoen, W., King, R., 2017. Review of major shale-dominated detachment and thrust characteristics in the diagenetic zone: Part I, meso- and macro-scopic scale. *Earth-Science Rev.* 173, 168–228. <https://doi.org/10.1016/j.earscirev.2017.07.019>
- Mouthereau, F., Filleaudeau, P.Y., Vacherat, A., Pik, R., Lacombe, O., Fellin, M.G., Castelltort, S., Christophoul, F., Masini, E., 2014. Placing limits to shortening evolution in the Pyrenees: Role of margin architecture and implications for the Iberia/Europe convergence. *Tectonics* 33, 2283–2314. <https://doi.org/10.1002/2014TC003663>. Received

BIBLIOGRAPHY

- Muniesa, P., Liesa, C.L., 2017. Dirección de transporte de los cabalgamientos del sistema de Larra en la sección de Aragüés (Sierras Interiores, Pirineos centrales). *Geogaceta* 61, 91–94.
- Muñoz, A., Arenas, C., González, A., Luzón, A., Pardo, G., Pérez, A., Villena, J., 2002. Ebro basin (northeastern Spain), in: London, G.S. (Ed.), *The Geology of Spain*. pp. 301–309.
- Muñoz, J.A., 2019. *Alpine Orogeny: Deformation and Structure in the Northern Iberian Margin (Pyrenees s.l.)*. Springer International Publishing. https://doi.org/10.1007/978-3-030-11295-0_9
- Muñoz, J.A., 1992. Evolution of a continental collision belt: ECORS-Pyrenees crustal balanced.
- Muñoz, J.A., Beamud, E., Fernández, O., Arbués, P., Dinarès-Turell, J., Poblet, J., 2013. The Ainsa Fold and thrust oblique zone of the central Pyrenees: Kinematics of a curved contractional system from paleomagnetic and structural data. *Tectonics* 32, 1142–1175. <https://doi.org/10.1002/tect.20070>
- Navarro, J.Á.S., López, P.C., Perez-Garcia, A., 2004. Evaluation of geothermal flow at the springs in Aragón (Spain), and its relation to geologic structure. *Hydrogeol. J.* 12, 601–609. <https://doi.org/10.1007/s10040-004-0330-8>
- Nieto, F., Ortega-Huertas, M., Peacor, D.R., Arostegui, J., 1996. Evolution of illite/smectite from early diagenesis through incipient metamorphism in sediments of the Basque-Cantabrian Basin. *Clays Clay Miner.* 44, 304–323. <https://doi.org/10.1346/CCMN.1996.0440302>
- Oliva-Urcia, B., Beamud, E., Arenas, C., Pueyo, E.L., Garcés, M., Soto, R., Valero, L., Pérez-Rivarés, F.J., 2019. Dating the northern deposits of the Ebro foreland basin; implications for the kinematics of the SW Pyrenean front. *Tectonophysics* 765, 11–34. <https://doi.org/10.1016/j.tecto.2019.05.007>
- Oliva-Urcia, B., Casas, A.M., Pueyo, E.L., Pocovi-Juan, A., 2012. Structural and paleomagnetic evidence for non-rotational kinematics of the South Pyrenean Frontal Thrust at the western termination of the External Sierras (southwestern central Pyrenees). *Geol. Acta* 10, 125–144. <https://doi.org/10.1344/105.000001704>
- Oliva-Urcia, B., Casas, A.M., Pueyo, E.L., Román-Berdiel, T., Geissman, J.W., 2010. Paleomagnetic evidence for dextral strike-slip motion in the Pyrenees during alpine convergence (Mauléon basin, France). *Tectonophysics* 494, 165–179. <https://doi.org/10.1016/j.tecto.2010.09.018>
- Oliva-Urcia, B., Casas, A.M., Soto, R., Villalaín, J.J., Kodama, K., 2011. A transtensional basin model for the Organyà basin (central southern Pyrenees) based on magnetic fabric and brittle structures. *Geophys. J. Int.* 184, 111–130. <https://doi.org/10.1111/j.1365-246X.2010.04865.x>
- Oliva-Urcia, B., Larrasoaña, J.C., Pueyo, E.L., Gil, A., Mata, P., Parés, J.M., Schleicher, A.M., Pueyo, O., 2009. Disentangling magnetic subfabrics and their link to deformation processes in cleaved sedimentary rocks from the Internal Sierras (west central Pyrenees, Spain). *J. Struct. Geol.* 31, 163–176. <https://doi.org/10.1016/j.jsg.2008.11.002>
- Oliva-Urcia, B., Román-Berdiel, T., Casas, A.M., Bógalo, M.F., Osácar, M.C., García-Lasanta, C., 2013. Transition from extensional to compressional magnetic fabrics in the Cretaceous Cabuérniga basin (North Spain). *J. Struct. Geol.* 46, 220–234.

BIBLIOGRAPHY

<https://doi.org/10.1016/j.jsg.2012.09.001>

- Oliva-Urcia, Belén, Román-Berdiel, T., Casas, A.M., Pueyo, E.L., Osácar, C., 2010. Tertiary compressional overprint on Aptian-Albian extensional magnetic fabrics, North-Pyrenean Zone. *J. Struct. Geol.* 32, 362–376. <https://doi.org/10.1016/j.jsg.2010.01.009>
- Oliva Urcia, B., Pueyo Morer, E., 2007. Gradient of shortening and vertical-axis rotations in the Southern Pyrenees (Spain), insights from a synthesis of paleomagnetic data. *Rev. la Soc. Geológica España* 20, 105–118.
- Oliván, C., Pueyo, E., Pocoví, A., Luzón, A., Martínez-Peña, M.B., 2008. Fábricas magnéticas (ASM) en el anticlinal de Barbastro-Balaguer (Pirineo Central): implicaciones cinemáticas. *Geotemas* 10.
- Ori, G.G., Friend, P.F., 1984. Sedimentary basins formed and carried piggyback on active thrust sheets. *Geology* 12, 475–478. [https://doi.org/10.1130/0091-7613\(1984\)12<475:SBFACP>2.0.CO;2](https://doi.org/10.1130/0091-7613(1984)12<475:SBFACP>2.0.CO;2)
- Ougier-Simonin, A., Renard, F., Boehm, C., Vidal-Gilbert, S., 2016. Microfracturing and microporosity in shales. *Earth-Science Rev.* 162, 198–226. <https://doi.org/10.1016/j.earscirev.2016.09.006>
- Parés, J.M., 2015. Sixty years of anisotropy of magnetic susceptibility in deformed sedimentary rocks. *Front. Earth Sci.* 3, 1–13. <https://doi.org/10.3389/feart.2015.00004>
- Parés, J.M., Dinarés-Turell, J., 1993. Magnetic Fabric in two Sedimentary Rock-Types from the Southern Pyrenees. *J. Geomagn. Geoelectr.* 45, 193–205.
- Parés, J.M., van der Pluijm, B.A., 2004a. Correlating magnetic fabrics with finite strain: Comparing results from mudrocks in the Variscan and Appalachian Orogens. *Geol. Acta* 2, 213–220.
- Parés, J.M., van der Pluijm, B.A., 2004b. Correlating magnetic fabrics with finite strain: Comparing results from mudrocks in the Variscan and Appalachian Orogens. *Geol. Acta* 2, 213–220. <https://doi.org/10.1344/105.000001428>
- Parés, J.M., van der Pluijm, B.A., 2003. Magnetic fabrics and strain in pencil structures of the Knobs Formation, Valley and Ridge Province, US Appalachians. *J. Struct. Geol.* 25, 1349–1358. [https://doi.org/10.1016/S0191-8141\(02\)00197-9](https://doi.org/10.1016/S0191-8141(02)00197-9)
- Parés, J.M., Van Der Pluijm, B.A., 2002. Evaluating magnetic lineations (AMS) in deformed rocks. *Tectonophysics* 350, 283–298. [https://doi.org/10.1016/S0040-1951\(02\)00119-1](https://doi.org/10.1016/S0040-1951(02)00119-1)
- Parés, J.M., Van der Pluijm, B.A., Dinarès-Turell, J., 1999. Evolution of magnetic fabrics during incipient deformation of mudrocks (Pyrenees, northern Spain). *Tectonophysics* 307, 1–14. [https://doi.org/10.1016/S0040-1951\(99\)00115-8](https://doi.org/10.1016/S0040-1951(99)00115-8)
- Pascual, J.O., Parés, J.M., 1990. Estudio preliminar de los materiales comprendidos en el tránsito Eoceno–Oligoceno en el borde SE de la Cuenca del Ebro. *Rev. la Soc. Geológica España* 3, 323–333.
- Payros, A., Orue-Etxebarria, X., Pujalte, V., 2006. Covarying sedimentary and biotic fluctuations in Lower-Middle Eocene Pyrenean deep-sea deposits: Palaeoenvironmental implications. *Palaeogeogr. Palaeoclimatol. Palaeoecol.* 234, 258–276. <https://doi.org/10.1016/j.palaeo.2005.10.013>
- Payros, A., Pujalte, V., Orue-Etxebarria, X., 1999. The South Pyrenean Eocene carbonate

BIBLIOGRAPHY

- megabreccias revisited: New interpretation based on evidence from the Pamplona Basin. *Sediment. Geol.* 125, 165–194. [https://doi.org/10.1016/S0037-0738\(99\)00004-4](https://doi.org/10.1016/S0037-0738(99)00004-4)
- Payros, A., Tosquella, J., Bernaola, G., Dinarès-Turell, J., Orue-Etxebarria, X., Pujalte, V., 2009. Filling the North European Early/Middle Eocene (Ypresian/Lutetian) boundary gap: Insights from the Pyrenean continental to deep-marine record. *Palaeogeogr. Palaeoclimatol. Palaeoecol.* 280, 313–332. <https://doi.org/10.1016/j.palaeo.2009.06.018>
- Pereira, M.F., Castro, A., Chichorro, M., Fernández, C., Díaz-Alvarado, J., Martí, J., Rodríguez, C., 2014. Chronological link between deep-seated processes in magma chambers and eruptions: Permo-Carboniferous magmatism in the core of Pangaea (Southern Pyrenees). *Gondwana Res.* 25, 290–308. <https://doi.org/10.1016/j.gr.2013.03.009>
- Piña-Varas, P., Soto, R., Clariana, P., Ayala, C., Rubio, F., Ledo, J., Pueyo, E., n.d. High-Resolution Scan of the Pyrenean Crustal Structure Combining Magnetotelluric and Gravity Data.
- Pocoví Juan, A., Pueyo Anchuela, Pueyo, E.L., Casas-Sainz, A.M., Román Berdiel, M.T., Gil Imaz, A., Ramajo Cordero, J., Mochales, T., García Lasanta, C., Izquierdo-Llavall, E., Parés, J.M., Sánchez, E., Soto Marín, R., Oliván, C., Rodríguez Pintó, A., Oliva-Urcia, B., Villalaín, J.J., 2014. Magnetic fabrics in the Western Central-Pyrenees: An overview. *Tectonophysics* 629, 303–318. <https://doi.org/10.1016/j.tecto.2014.03.027>
- Potter, D.K., Corbett, P.W.M., Barclay, S.A., Haszeldine, R.S., 2004. Quantification of illite content in sedimentary rocks using magnetic susceptibility - A rapid complement or alternative to X-ray diffraction. *J. Sediment. Res.* 74, 730–735. <https://doi.org/10.1306/021304740730>
- Potter, P.E., Maynard, J.B., Depetris, P.J., 2005. Mud and Mudstones. *Mud Mudstones*. <https://doi.org/10.1007/b138571>
- Potter, P.E., Maynard, J.B., Pryor, W.A., 2012. *Sedimentology of shale: study guide and reference source*.
- Potter, P.E., Maynard, J.B., Pryor, W.A., 1980. *Sedimentology of shale*. Springer-Verlag, New York.
- Powell, C.M., 1979. A morphological classification of rock cleavage. *Tectonophysics* 58, 21–34. [https://doi.org/10.1016/0040-1951\(79\)90320-2](https://doi.org/10.1016/0040-1951(79)90320-2)
- Pueyo-Anchuela, O., 2012a. Estudio de fábricas magnéticas y su relación con la deformación en el sector centro-occidental del Pirineo central (Aragón y Navarra).
- Pueyo-Anchuela, O., 2012b. Estudio de fábricas magnéticas y su relación con la deformación en el sector centro-occidental del Pirineo Central (Aragón y Navarra).
- Pueyo-Anchuela, O., Casas-sainz, A.M., Pueyo, E.L., Pocoví Juan, A., Gil-Imaz, A., 2013a. Analysis of the ferromagnetic contribution to the susceptibility by low field and high field methods in sedimentary rocks of the Southern Pyrenees and Northern Ebro foreland basin (Spain). *Terra Nov.* 25, 307–314. <https://doi.org/10.1111/ter.12037>
- Pueyo-Anchuela, O., Gil-Imaz, A., Pocovi-Juan, A., 2011a. Lithology-dependent reliability of AMS analysis: A case study of the Eocene turbidities in the southern Pyrenees (Aragón, Spain). *Comptes Rendus - Geosci.* 343, 11–19. <https://doi.org/10.1016/j.crte.2010.11.003>

BIBLIOGRAPHY

- Pueyo-Anchuela, O., Gil-Imaz, A., Pocovi-Juan, A., 2010. What does AMS mean in multilayer systems? Regional and detailed study from the Southern Pyrenees (Aragón, Spain). *Trab. Geol.* 162, 155–162.
- Pueyo-Anchuela, O., Gil-Imaz, A., Pocovi-Juan, A., Ipas-Lloréns, J.F., 2011b. Acquisition and blocking of magnetic fabrics in synsedimentary structures, Eocene Pyrenees, Spain O. *J. Geophys. J. Int.* 186, 1015–1028. <https://doi.org/10.1111/j.1365-246X.2011.05136.x>
- Pueyo-Anchuela, O., Pocovi-Juan, A., Gil-Imaz, A., Casas-Sainz, A.M., 2013b. Factors influencing magnetic susceptibility in the southern Pyrenees. *Stud. Geophys. Geod.* 57, 692–709. <https://doi.org/10.1007/s11200-013-0919-2>
- Pueyo-Morer, E.L., Millán-Garrido, H., Pocovi-Juan, A., Parés, J.M., 1997. Determination of the folding mechanism by AMS data. Study of the relation between shortening and magnetic anisotropy in the Pico del Aguila anticline (southern Pyrenees). *Phys. Chem. Earth* 22, 195–201.
- Pueyo Anchuela, Ó., Gil Imaz, A., Pocoví Juan, A., 2012a. Factors affecting the record of strain fabrics at the anisotropy of magnetic susceptibility: West-Central South-Pyrenean cleavage domain (Southern Pyrenees; NE Spain). *Tectonophysics* 554–557, 1–17. <https://doi.org/10.1016/j.tecto.2012.05.028>
- Pueyo Anchuela, Ó., Gil Imaz, A., Pocoví Juan, A., 2010a. Significance of AMS in multilayer systems in fold-and-thrust belts. A case study from the Eocene turbidites in the Southern Pyrenees (Spain). *Geol. J.* 45, 544–561. <https://doi.org/10.1002/gj.1194>
- Pueyo Anchuela, Ó., Pocoví Juan, A., Gil Imaz, A., 2010b. Tectonic imprint in magnetic fabrics in foreland basins: A case study from the Ebro Basin, N Spain. *Tectonophysics* 492, 150–163. <https://doi.org/10.1016/j.tecto.2010.06.016>
- Pueyo Anchuela, Ó., Pueyo, E.L., Pocoví Juan, A., Gil Imaz, A., 2012b. Vertical axis rotations in fold and thrust belts: Comparison of AMS and paleomagnetic data in the Western External Sierras (Southern Pyrenees). *Tectonophysics* 532–535, 119–133. <https://doi.org/10.1016/j.tecto.2012.01.023>
- Pueyo, E.L., 2006. The Pyrenean AMS database, state of the art and future task The Pyrenean AMS database, state of the art and future task 1–9.
- Pueyo, E.L., Millán, H., Pocoví, A., 2002. Rotation velocity of a thrust: A paleomagnetic study in the External Sierras (Southern Pyrenees). *Sediment. Geol.* 146, 191–208. [https://doi.org/10.1016/S0037-0738\(01\)00172-5](https://doi.org/10.1016/S0037-0738(01)00172-5)
- Puigdefàbregas, C., Souquet, P., 1986. Tecto-sedimentary cycles and depositional sequences of the Mesozoic and Tertiary from the Pyrenees. *Tectonophysics* 129, 173–203. [https://doi.org/10.1016/0040-1951\(86\)90251-9](https://doi.org/10.1016/0040-1951(86)90251-9)
- Puigdefàbregas, T., 1975. La sedimentación de la cuenca de Jaca. *Pirineos* 104, 1–118.
- Pujalte, V., Schmitz, B., Baceta, J.I., 2014. Sea-level changes across the Paleocene-Eocene interval in the Spanish Pyrenees, and their possible relationship with North Atlantic magmatism. *Palaeogeogr. Palaeoclimatol. Palaeoecol.* 393, 45–60. <https://doi.org/10.1016/j.palaeo.2013.10.016>
- Pulgar, J.A., Alonso, J.L., Espina, J.A., Marín, R.G., 1999. La deformación alpina en el basamento varisco de la Zona Cantábrica. *Trab. Geol. Univ. Oviedo* 21, 283–294.

BIBLIOGRAPHY

- Quintana, L., Pulgar, J.A., Alonso, J.L., 2015. Displacement transfer from borders to interior of a plate: A crustal transect of Iberia. *Tectonophysics* 663, 378–398. <https://doi.org/10.1016/j.tecto.2015.08.046>
- Rathore, J.S., 1979. Magnetic susceptibility anisotropy in the Cambrian slate belt of North Wales and correlation with strain. *Tectonophysics* 53, 83–97. [https://doi.org/10.1016/0040-1951\(79\)90355-X](https://doi.org/10.1016/0040-1951(79)90355-X)
- Reks, I.J., Gray, D.R., 1982. Pencil structure and strain in weakly deformed mudstone and siltstone. *J. Struct. Geol.* 4, 161–176.
- Remacha, E., Fernández, L.P., 2003. High-resolution correlation patterns in the turbidite systems of the Hecho Group (South-Central Pyrenees, Spain). *Mar. Pet. Geol.* 20, 711–726. <https://doi.org/10.1016/j.marpetgeo.2003.09.003>
- Reynolds, R.C., Hower, J., 1970. The nature of interlayering in mixed-layer illite-montmorillonites. *Clays Clay Miner.* 18, 25–36.
- Roberts, A.P., 2015. Magnetic mineral diagenesis. *Earth-Science Rev.* 151, 1–47. <https://doi.org/10.1016/j.earscirev.2015.09.010>
- Roberts, N.M.W., Drost, K., Horstwood, M.S.A., Condon, D.J., Chew, D., Drake, H., Milodowski, A.E., McLean, N.M., Smye, A.J., Walker, R.J., Haslam, R., Hodson, K., Imber, J., Beaudoin, N., Lee, J.K., 2020. Laser ablation inductively coupled plasma mass spectrometry (LA-ICP-MS) U-Pb carbonate geochronology: strategies, progress, and limitations. *Geochronology* 2, 33–61. <https://doi.org/10.5194/gchron-2-33-2020>
- Roberts, N.M.W., Holdsworth, R.E., 2022. Timescales of faulting through calcite geochronology: A review. *J. Struct. Geol.* 158, 104578. <https://doi.org/10.1016/j.jsg.2022.104578>
- Robion, P., David, C., Dautriat, J., Colombier, J.C., Zinsmeister, L., Collin, P.Y., 2014. Pore fabric geometry inferred from magnetic and acoustic anisotropies in rocks with various mineralogy, permeability and porosity. *Tectonophysics* 629, 109–122. <https://doi.org/10.1016/j.tecto.2014.03.029>
- Robion, P., Grelaud, S., Frizon de Lamotte, D., 2007. Pre-folding magnetic fabrics in fold-and-thrust belts: Why the apparent internal deformation of the sedimentary rocks from the Minervois basin (NE - Pyrenees, France) is so high compared to the Potwar basin (SW - Himalaya, Pakistan)? *Sediment. Geol.* 196, 181–200. <https://doi.org/10.1016/j.sedgeo.2006.08.007>
- Rochette, P., Jackson, M., Aubourg, C., 1992. Rock Magnetism and the Interpretation of Magnetic Susceptibility. *Rev. Geophys.* 209–226.
- Rodríguez Méndez, L., 2011. Análisis De La Estructura Varisca Y Alpina En La Transversal Sallent-Biescas (Pirineos Centrales, Huesca).
- Roigé, M., Gómez-Gras, D., Remacha, E., Boya, S., Viaplana-Muzas, M., Teixell, A., 2017. Recycling an uplifted early foreland basin fill: An example from the Jaca basin (Southern Pyrenees, Spain). *Sediment. Geol.* 360, 1–21. <https://doi.org/10.1016/j.sedgeo.2017.08.007>
- Rosenbaum, G., Lister, G.S., Duboz, C., 2002. Relative motion of Africa, Iberia and Europe during Alpine orogeny. *Tectonophysics* 359, 117–129.

BIBLIOGRAPHY

- Roure, F., Choukroune, P., Berastegui, X., Matheron, P., Bareyt, M., Seguret, M., Camara, P., Montpellier, D., 1989. ECORS Deep seismic data and balanced cross sections: Geometric Constraints on the evolution of the Pyrenees. *Tectonics* 8, 41-50.
- Rutter, E.H., 1983. Pressure solution in nature, theory and experiment. *J. Geol. Soc. London*. 140, 725-740. <https://doi.org/10.1144/gsjgs.140.5.0725>
- Sánchez, E., Oliva-Urcia, B., Pueyo, E.L., Bausa, K., Beamud, E., Ramón, M.J., Pocovi-Juan, A., 2012. Geometría no-coaxial del anticlinal de Sto . Domingo (Pirineo Occidental) deducida de la fábrica magnética (ASM). *Geotemas* 13, 1188-1191.
- Sanjuan, F., Aubourg, C., Saur, H., Fasentieux, B., Bernier, M., 2022. Terahertz Dielectric Permittivity Anisotropy and Fabric of Oil Shales: Comparison to Acoustic, Magnetic Susceptibility, and X-ray Microtomography Results. *Energy and Fuels* 36, 12555-12562. <https://doi.org/10.1021/acs.energyfuels.2c02557>
- Saspiturry, N., Allanic, C., Razin, P., Issautier, B., Baudin, T., Lasseur, E., Serrano, O., Leleu, S., 2020. Closure of a hyperextended system in an orogenic lithospheric pop-up, Western Pyrenees: The role of mantle buttressing and rift structural inheritance. *Terra Nov.* 32, 253-260. <https://doi.org/10.1111/ter.12457>
- Saspiturry, N., Allanic, C., Serrano, O., Courrioux, G., Baudin, T., Le Bayon, B., Lahfid, A., Razin, P., Villasenor, A., Chevrot, S., Issautier, B., 2022. Upper lithospheric transfer zones driving the non-cylindricity of the West-Pyrenean orogenic prism (Mauléon hyperextended basin). *J. Struct. Geol.* 156. <https://doi.org/10.1016/j.jsg.2022.104535>
- Saspiturry, N., Razin, P., Baudin, T., Serrano, O., Issautier, B., Lasseur, E., Allanic, C., Thinon, I., Leleu, S., 2019. Symmetry vs. asymmetry of a hyper-thinned rift: Example of the Mauléon Basin (Western Pyrenees, France). *Mar. Pet. Geol.* 104, 86-105. <https://doi.org/10.1016/j.marpetgeo.2019.03.031>
- Saur, H., 2022. Microstructure investigation by means of X-ray computed tomography: application to fine-grained clastic rocks. *Université de Pau et des Pays de l'Adour*.
- Saur, H., Moonen, P., Aubourg, C., 2021. Grain Fabric Heterogeneity in Strained Shales: Insights From XCT Measurements. *J. Geophys. Res. Solid Earth* 126, 1-19. <https://doi.org/10.1029/2021JB022025>
- Saur, H., Sénéchal, P., Boiron, T., Aubourg, C., Derluyn, H., Moonen, P., 2020. First investigation of quartz and calcite shape fabrics in strained shales by means of X-ray tomography. *J. Struct. Geol.* 130. <https://doi.org/10.1016/j.jsg.2019.103905>
- Schweitzer, J., Jennings, B.R., 1971. The association of montmorillonite studied by light scattering in electric fields. *J. Colloid Interface Sci.* 37, 443-457.
- Séguret, M., 1972. Etude Tectonique Des Nappes Et Séries Décollées De La Partie Centrale Du Versant Sud Des Pyrénées: Caractère Syn-sédimentaire, Rôle De La Compression Et De La Gravité. Publications de l'Université des sciences et techniques du Languedoc (USTELA).
- Séguret, M., Daignières, M., 1986. CROSS-SECTIONS OF THE PYRENEES ; The Balanced Cross-Section Technique (BCST) (Dahlstrom , Hossack , 1979 : Elliot , 1983) has been thrust belts and is particularly used successfully in the geometric interpretation of well adapted to the study of them. *Tectonophysics* 129, 303-318.
- Séranne, M., Benedicto, A., Labaum, P., Truffert, C., Pascal, G., 1995. Structural style and

BIBLIOGRAPHY

- evolution of the Gulf of Lion Oligo-Miocene rifting: role of the Pyrenean orogeny. *Mar. Pet. Geol.* 12, 809–820. [https://doi.org/10.1016/0264-8172\(95\)98849-Z](https://doi.org/10.1016/0264-8172(95)98849-Z)
- Silva-Casal, R., Aurell, M., Payros, A., Pueyo, E.L., Serra-Kiel, J., 2019. Carbonate ramp drowning caused by flexural subsidence: The South Pyrenean middle Eocene foreland basin. *Sediment. Geol.* 393–394, 105538. <https://doi.org/10.1016/j.sedgeo.2019.105538>
- Silva-Casal, R., Serra-Kiel, J., Rodríguez-Pintó, A., Pueyo, E.L., Aurell, M., Payros, A., 2021. Systematics of lutetian larger foraminifera and magneto-biostratigraphy from the South Pyrenean Basin (Sierras exteriores, Spain). *Geol. Acta* 19. <https://doi.org/10.1344/GeologicaActa2021.19.7>
- Simón, J.L., Casas-Sainz, A.M., Gil-Imaz, A., 2021. Controversial epiglyptic thrust sheets: The case of the Daroca Thrust (Iberian Chain, Spain). *J. Struct. Geol.* 145. <https://doi.org/10.1016/j.jsg.2021.104298>
- Simón, J.L., Liesa, C.L., 2011. Incremental slip history of a thrust: Diverse transport directions and internal folding of the Utrillas thrust sheet (NE Iberian Chain, Spain). *Geol. Soc. Spec. Publ.* 349, 77–97. <https://doi.org/10.1144/SP349.5>
- Sinclair, H.D., Gibson, M., Naylor, M., Morris, R.G., 2005. Asymmetric growth of the Pyrenees revealed through measurement and modeling of orogenic fluxes. *Am. J. Sci.* 305, 369–406. <https://doi.org/10.2475/ajs.305.5.369>
- Soto, R., 2003. Relationship between AMS and folding in an area of superimposed folding (Cotiella-Bóixols nappe, Southern Pyrenees). *Geodin. Acta* 16, 171–185. <https://doi.org/10.1016/j.geoact.2003.08.001>
- Soto, R., Casas-Sainz, A.M., Oliva-Urcia, B., Román-Berdiel, T., 2022. Guía rápida para el estudio de rocas deformadas a partir del análisis de la Anisotropía de la Susceptibilidad Magnética (ASM). *Rev. la Soc. Geológica España* 35, 56–70. <https://doi.org/10.55407/rsge.94884>
- Soto, R., Casas-Sainz, A.M., Villalaín, J.J., Oliva-Urcia, B., 2007. Mesozoic extension in the Basque-Cantabrian basin (N Spain): Contributions from AMS and brittle mesostructures. *Tectonophysics* 445, 373–394. <https://doi.org/10.1016/j.tecto.2007.09.007>
- Soto, R., Larrasoaña, J.C., Arlegui, L.E., Beamud, E., Oliva-Urcia, B., Simón, J.L., 2009. Reliability of magnetic fabric of weakly deformed mudrocks as a palaeostress indicator in compressive settings. *J. Struct. Geol.* 31, 512–522. <https://doi.org/10.1016/j.jsg.2009.03.006>
- Soto, R., Larrasoaña, J.C., Beamud, E., Garcés, M., 2016. Early-Middle Miocene subtle compressional deformation in the Ebro foreland basin (northern Spain); insights from magnetic fabrics. *Comptes Rendus - Geosci.* 348, 213–223. <https://doi.org/10.1016/j.crte.2015.10.009>
- Soto, R., Storti, F., Casas-sainz, A.M., 2006. Impact of backstop thickness lateral variations on the tectonic architecture of orogens: Insights from sandbox analogue modeling and application to the Pyrenees 25, 1–19. <https://doi.org/10.1029/2004TC001693>
- Souque, C., Robion, P., Frizon De Lamotte, D., 2002. Cryptic magnetic fabric of tectonic origin revealed by heating of sedimentary samples from the Corbie`res, France. *Phys. Chem. Earth* 27, 1253–1262. [https://doi.org/10.1016/S1474-7065\(02\)00111-0](https://doi.org/10.1016/S1474-7065(02)00111-0)

BIBLIOGRAPHY

- Souquet, P., 1967. Le crétacé supérieur sud-pyrénéen: en Catalogne, Aragon et Navarre.
- Spears, D.A., 1980. Towards a classification of shales. *J. Geol. Soc.* 137, 125–129.
- Spears, D.A., 1976. The fissility of some Carboniferous shales. *Sedimentology* 23, 721–725.
- Stacey, F.D., 1960. Magnetic Anisotropy of Rocks. *J. Geophys. Res.* 54, 2429–2442.
- Stamatakis, J., Hirt, A.M., Lowrie, W., 1996. The age and timing of folding in the central Appalachians from paleomagnetic results. *Bull. Geol. Soc. Am.* 108, 815–829. [https://doi.org/10.1130/0016-7606\(1996\)108<0815:TAATOF>2.3.CO;2](https://doi.org/10.1130/0016-7606(1996)108<0815:TAATOF>2.3.CO;2)
- Tarling, D.H., Hrouda, F., 1997. *The Magnetic Anisotropy of Rocks*. Chapman and Hall.
- Tavani, S., Muñoz, J.A., 2012. Mesozoic rifting in the Basque-Cantabrian Basin (Spain): Inherited faults, transversal structures and stress perturbation. *Terra Nov.* 24, 70–76. <https://doi.org/10.1111/j.1365-3121.2011.01040.x>
- Teixell, A., 1998. Crustal structure and orogenic material budget in the west central Pyrenees. *Tectonics* 17, 395–406. <https://doi.org/10.1029/98TC00561>
- Teixell, A., 1996. The Ansó transect of the southern Pyrenees: Basement and cover thrust geometries. *J. Geol. Soc. London.* 153, 301–310. <https://doi.org/10.1144/gsjgs.153.2.0301>
- Teixell, A., 1994. Mapa Geológico de España - Escala 1:50.000 - Jaca (176).
- Teixell, A., 1992. Estructura alpina en la transversal de la terminación occidental de la zona axial pirenaica. Universitat de Barcelona.
- Teixell, A., Garcia-Sansegundo, J., 1995. Estructura del sector central de la Cuenca de Jaca (Pirineos Meridionales). *Rev. la Soc. Geológica España* 8, 215–228.
- Teixell, A., Labaume, P., Ayarza, P., Espurt, N., Blanquat, M.D. Saint, Lagabrielle, Y., 2018. Tectonophysics Crustal structure and evolution of the Pyrenean-Cantabrian belt: A review and new interpretations from recent concepts and data. *Tectonophysics* 724–725, 146–170. <https://doi.org/10.1016/j.tecto.2018.01.009>
- Teixell, A., Labaume, P., Lagabrielle, Y., 2016. The crustal evolution of the west-central Pyrenees revisited: Inferences from a new kinematic scenario. *Comptes Rendus - Geosci.* 348, 257–267. <https://doi.org/10.1016/j.crte.2015.10.010>
- Ten Haaf, E., Van der Voo, R., Wensink, H., 1971. The S-external Pyrenees of Huesca. *Geol. Rundschau* 60, 996–1009.
- Tullis, T.E., 1976. Experiments on the origin of slaty cleavage and schistosity. *Bull. Geol. Soc. Am.* 87, 745–753. [https://doi.org/10.1130/0016-7606\(1976\)87<745:EOTOOS>2.0.CO;2](https://doi.org/10.1130/0016-7606(1976)87<745:EOTOOS>2.0.CO;2)
- Turner, J.P., 1990. Structural and stratigraphic evolution of the West Jaca thrust-top basin, Spanish Pyrenees. *J. Geol. Soc. London.* 147, 177–184. <https://doi.org/10.1144/gsjgs.147.1.0177>
- Vacherat, A., Mouthereau, F., Pik, R., Bernet, M., Gautheron, C., Masini, E., Le Pourhiet, L., Tibari, B., Lahfid, A., 2014. Thermal imprint of rift-related processes in orogens as recorded in the Pyrenees. *Earth Planet. Sci. Lett.* 408, 296–306. <https://doi.org/10.1016/j.epsl.2014.10.014>
- Valero-Garcés, B.L., Gisbert Aguilar, J., 2004. El estephaniense y pérmico de los Pirineos., in:

BIBLIOGRAPHY

- Geología de España. SGE-IGME. Madrid, pp. 266–268.
- van der Pluijm, B.A., Ho, N.C., Peacor, D.R., 1994. High-resolution X-ray texture goniometry. *J. Struct. Geol.* 16, 1029–1032. [https://doi.org/10.1016/0191-8141\(94\)90084-1](https://doi.org/10.1016/0191-8141(94)90084-1)
- Van Der Pluijm, B.A., Ho, N.C., Peacor, D.R., Merriman, R.J., 1998. Contradictions of slate formation resolved? [5]. *Nature* 392, 348. <https://doi.org/10.1038/32810>
- Van Der Pluijm, B.A., Marshak, S., 2004. *Earth Structure. An introduction to Structural Geology and Tectonics*, W.W. Norton & Company. <https://doi.org/10.1038/471573a>
- Van der Voo, R., 1966. Geology of the Sierra de Tendenera region, Spanish Pyrenees, province of Huesca. *Estud. Geol.* 22, 61–64.
- Van Olphen, H., 1963. *An Introduction to Clay Colloid Chemistry*. New York.
- Velde, B., Vasseur, G., 1992. Estimation of the diagenetic smectite to illite transformation in time-temperature space. *Am. Mineral.* 77, 967–976.
- Vergés, J., Fernández, M., Martínez, A., 2002. The Pyrenean orogen : pre- , syn- , and post-collisional evolution 55–74.
- Vergés, J., Millan, H., Roca, E., Muñoz, J.A., Marzo, M., Cites, J., Bezemer, T. Den, Zoetemeijer, R., Cloetingh, S., 1995. Eastern Pyrenees and related foreland basins : Ma 12, 893–915.
- Vinyoles, A., López-blanco, M., Garcés, M., Arbués, P., Valero, L., Beamud, E., Oliva-Urcia, B., Cabello, P., 2020. 10 Myr evolution of sedimentation rates in a deep marine to non-marine foreland basin: Tectonic and sedimentary controls (Eocene, Tremp-Jaca Basin, Southern Pyrenees, NE Spain. *Basin Res.* 33, 447–477.
- Voigt, W., Kinoshita, S., 1907. Bestimmung absoluter Werte von Magnetisierungszahlen, insbesondere für Kristalle. *Ann. Phys.* 329, 492–514.
- Wang, Y., Chevrot, S., Monteiller, V., Komatitsch, D., Mouthereau, F., Manatschal, G., Sylvander, M., Diaz, J., Ruiz, M., Grimaud, F., Benahmed, S., Pauchet, H., Martin, R., Toulouse, G.E., Pyrénées, O.M., Sabatier, U.P., 2016. The deep roots of the western Pyrenees revealed by full waveform inversion of teleseismic P waves. *Geol. Soc. Am. Bull.* 475–478. <https://doi.org/10.1130/G37812.1>
- Weaver, C.E., 1989. *Clays, Muds and Shales*. Elsevier B.V.
- Weil, A.B., Yonkee, W.A., 2012. Layer-parallel shortening across the Sevier fold-thrust belt and Laramide foreland of Wyoming: Spatial and temporal evolution of a complex geodynamic system. *Earth Planet. Sci. Lett.* 357–358, 405–420. <https://doi.org/10.1016/j.epsl.2012.09.021>
- Wenk, H.-R., Yu, R., Cárdenes, V., Lopez-Sanchez, M.A., Sintubin, M., 2020. Fabric and anisotropy of slates: From classical studies to new results. *J. Struct. Geol.* 104066. <https://doi.org/10.1016/j.jsg.2020.104066>
- Wenk, H.R., Kanitpanyacharoen, W., Voltolini, M., 2010. Preferred orientation of phyllosilicates: Comparison of fault gouge, shale and schist. *J. Struct. Geol.* 32, 478–489. <https://doi.org/10.1016/j.jsg.2010.02.003>
- Wenk, H.R., Lonardelli, I., Franz, H., Nihei, K., Nakagawa, S., 2007. Preferred orientation

BIBLIOGRAPHY

- and elastic anisotropy of illite-rich shales. *Geophysics* 72, 69–75.
<https://doi.org/10.1190/1.2435966>
- Wenk, H.R., Yu, R., Cárdenes, V., Lopez-Sanchez, M.A., Sintubin, M., 2020. Fabric and anisotropy of slates: From classical studies to new results. *J. Struct. Geol.* 138.
<https://doi.org/10.1016/j.jsg.2020.104066>
- Wintsch, R.P., 1978. A chemical approach to the preferred orientation of mica. *Bull. Geol. Soc. Am.* 89, 1715–1718. [https://doi.org/10.1130/0016-7606\(1978\)89<1715:ACATTP>2.0.CO;2](https://doi.org/10.1130/0016-7606(1978)89<1715:ACATTP>2.0.CO;2)
- Wintsch, R.P., Kunk, M.J., Epstein, J.B., 1996. 40Ar/39Ar whole-rock data constraints on Acadian diagenesis and Alleghanian cleavage in the Martinsburg Formation, eastern Pennsylvania. *Am. J. Sci.* 296, 766–788. <https://doi.org/10.2475/ajs.296.7.766>
- Wintsch, R.P., Kvale, C.M., Kisch, H.J., 1991. Open-system, constant-volume development of slaty cleavage, and strain-induced replacement reactions in the Martinsburg Formation, Lehigh Gap, Pennsylvania. *Geol. Soc. Am. Bull.* 103, 916–927.
- Wood, D.S., 1982. Current views of the problem of slaty cleavage. *Light Res Technol* 14, 31–46.
- Wood, D.S., Oertel, G., Singh, J., Bennett, H.F., Tarling, D.H., 1976. Strain and Anisotropy in Rocks [and Discussion]. *Philos. Trans. R. Soc. A Math. Phys. Eng. Sci.* 283, 27–42.
- Woodland, G., 1982. GRADATIONAL DEVELOPMENT OF DOMAINAL SLATY CLEAVAGE, ITS ORIGIN AND RELATION TO CHLORITE PORPHYROBLASTS IN THE MARTINSBURG FORMATION, EASTERN PENNSYLVANIA 82, 89–124.
- Woodward, N.B., Boyer, S.E., Suppe, J., 1989. Balanced Geological Cross-Sections, International Geological Congress, Short Course in Geology,.
- Zehnder, A.T., Allmendinger, R.W., 2000. Velocity field for the trishear model. *J. Struct. Geol.* 22, 1009–1014. [https://doi.org/10.1016/S0191-8141\(00\)00037-7](https://doi.org/10.1016/S0191-8141(00)00037-7)

AGRADECIMIENTOS

Una tesis te obliga a cruzarte con mucha gente, y tener muchas conversaciones para resolver dudas, aprender técnicas, leer datos... Todas estas personas de alguna forma han resuelto algo, así que muchísimas gracias:

A Antonio Casas y Charles Aubourg,

A Esther Izquierdo,

A Nicolas Beaudoin y a Guilhem Hoareau, Jean-Paul Callot y a Cedric Bonnel,

A Teresa Román, Emilio Pueyo, José Luis Simón, Belén Oliva, Oscar Pueyo,

A Marcos Marcén y a Pablo Calvin

A Pablo Sierra, se venía al campo, y luego resulta que también acabó haciendo la tesis allí!

A Hugo, por su inestimable ayuda en Pau,

A la gente del Cerege en Aix-En-Provence, Abel, Pierre.

A la gente del DMEX en Pau, especialmente Pascale, pero también Peter

Al SAI - Servicio de Preparación de Rocas de la Facultad de Zaragoza,

A Rebecca Stokes (USGS) por su interés y sus datos.

A Aurelie, por acogerme tanto, y a Thomas, Gabriel, Nicolas, Lionel, Landry, Naïm, Marine L. y Marine D, Alexis, Salsa.

A Ana, Rosi y Alba,

A Álvaro, Manu, Edu., compañeros de promo y de Tesis.

A tantos otros compañeros doctorandos y post-docs, Diego T., Elisa, Stephen, Olivia, Maria Heleni, ... gente que ha dedicado algún rato para ayudarme con cualquier cosa. Mil gracias.

Y gente que no ha estado en la uni, pero también lo puso fácil: A mis colocs de Pau, que les dí un poco la brasa, Clemence que me ayudó con el examen del DALF, Flavien, Marine, Donald, Lois, Pauline, Manu, Anouchk...

A mi padre, Miguel, que me preguntó si estaba seguro de estudiar geología, porque se "pasaba mucho tiempo en la facultad".

A mi madre, Ana, por desperdigar libros de geología por casa.

A Carmen, por hacer menos difíciles distancias y ausencias, ¡Gracias!

Por el encuentro del Béarn y de Aragón. Por la cultura montañesa compartida, los paisajes que se sienten vecinos.

Por volver cantar "Cap ta l'inmortela" en una granja perdida con un grupo de paysans.

¡Au, peirot!...¡ a rebrotar, flor immortal!, Aragón y Occitania

¡Au, pedrón, a caminar, a caminar... que hay un país que hallar!